INVESTIGATION OF TIME-DEPENDENT DEFLECTION IN LONG SPAN, HIGH STRENGTH, PRESTRESSED CONCRETE BRIDGE BEAMS

Stephen D. Hinkle

Thesis submitted to the faculty of the
Virginia Polytechnic Institute and State University
in partial fulfillment of the requirements for the degree of

Master of Science

in

Civil Engineering

Dr. Carin L. Roberts-Wollmann, P.E.

Dr. Thomas E. Cousins, P.E.

Dr. Richard E. Weyers, P.E.

August 10, 2006

Blacksburg, VA

Keywords: camber, time-dependent deflection, prestress losses, creep, shrinkage

INVESTIGATION OF TIME-DEPENDENT DEFLECTION IN LONG SPAN, HIGH STRENGTH, PRESTRESSED CONCRETE BRIDGE BEAMS

Stephen D. Hinkle

ABSTRACT

Accurate camber prediction in prestressed concrete bridge beams is important to all parties involved in bridge design and construction. Many current prestress loss prediction methods, necessary for proper camber calculation, were developed many years ago and are predicated on assumptions that may no longer be valid as higher strength concrete, wider beam spacing, and longer span lengths become more commonplace. This throws into question which models are appropriate for use in camber calculation by the bridge engineers and contractors of today.

Twenty-seven high-strength concrete modified 79 in. Bulb Tee beams with a design compressive strength of 9,000 psi were periodically measured to determine camber growth. Most available models for concrete creep and shrinkage were used to calculate creep and shrinkage strain. The modulus of elasticity equation of each model was used to predict modulus of elasticity of the studied mix. The Shams and Kahn compressive strength and modulus of elasticity equations were modified in order to approximate measured modulus of elasticity. The creep, shrinkage, and modulus of elasticity equations were used as inputs to an incremental time step method. The time-dependent change in beam curvature calculated by the time step method was used to calculate theoretical camber using the Moment-Area method. Predicted camber, using inputs from each considered model, was then compared with measured camber to determine the most accurate camber prediction models. Season of casting was also examined to determine what, if any, affect ambient temperature has on camber growth.

For the studied beams, the Shams and Kahn Model for creep, shrinkage, and modulus of elasticity, used as inputs for an incremental time step analysis, were found to most accurately predict camber values. Lower concrete compressive strength was observed for test cylinders from beams cast in summer versus beams cast in winter. Differences in beam deflection based on season of casting showed mixed results.

ACKNOWLEDGEMENTS

First and foremost, I would like to thank Dr. Carin Roberts-Wollmann for her support and guidance throughout this process. She reached out to me more than anyone did after it was not possible to make further progress on a previous thesis topic. This enabled me to find the courage and spirit to start over again and bring my work to fruition. I would also like to thank Dr. Cousins for the valuable insight he provided during this process. I especially thank the Via Foundation for the scholarship that made my graduate studies possible.

Most importantly, I would like to thank my wife, Natalie, for her patience and moral support with this endeavor. It is no understatement to say that I would never have been able to complete this without her. I thank my family for instilling in me the values that continue to guide me throughout my life.

Richard Potts at Standard Concrete Products provided crucial support, allowing me access to his entire plant. He stood behind me and made sure I got the assistance I needed from his crew. I also owe a tremendous deal of gratitude for the mentoring and guidance I received from the late John Durand. His wisdom, patience, and strength, even in the face of an un-winnable battle with cancer, will always serve as an inspiration to me. I could not have asked for a better boss and friend - he is sorely missed.

I would also like to thank everyone at the Caribou Coffee Shop. This is where the majority of this work was written over the last few years, with the aid of many gallons of coffee. During my time there, I have met many people who I now consider to be close friends.

Finally, I would like to thank God, who makes all things possible.

TABLE OF CONTENTS

LIST OF TABLES

LIST OF FIGURES

CHAPTER 1. INTRODUCTION

1.1 PROBLEM STATEMENT

Camber growth is of interest to the many parties involved in a typical bridge construction project for several reasons. The design engineer is concerned because the calculated theoretical camber value is used to set elevations of the beam seats and, by extension, the elevations for the entire bridge. The contractor is concerned because he/she has to fit everything "between the lines". The beam seats are formed to the elevations indicated on the bridge plans and the deck forms must be set so that the finished surface of the bridge deck is constructed to the elevations specified by the plans. If the beams camber more than predicted, and more than can be accomodated by the coping typically present between the beam and deck, the top of the beam at mid-span will rise into the space to be occupied by the bridge deck. If the interference with the reinforcement in the bridge deck cannot be tolerated, then the issue must be resolved in some other way – if at all. The typical state Department of Transportation is concerned primarily due to quality of rideability on the bridge deck, as well as disruption to the construction schedule in a worst-case scenario. All of these parties have a vested interest in both verifying the validity of current camber prediction methods and adjusting those methods if necessary to increase predictive accuracy for those beams designed and constructed by today's common practices.

Camber prediction methods involve the use of prediction models for prestress losses (creep, shrinkage, relaxation, elastic shortening, and anchorage losses) and modulus of elasticity. Many of the commonly used models are based on research from many years ago, or are formulated using assumptions that do not entirely match what is seen in current practice. As higher concrete strengths become more practical for design, and span lengths and beam spacing increase, there is some question as to whether the current models still apply, or if the results are being extrapolated beyond an acceptable limit.

1.2 OBJECTIVES AND SCOPE

This research will examine some of the current methods of predicting camber of prestressed concrete bridge beams and verify their accuracy in predicting the camber of actual beams. Two general types of camber prediction methods will be examined: multiplier methods and an incremental time step method. Many of the available prediction models for creep and shrinkage strains will be used as inputs to the time step method, along with the generally accepted equations for elastic shortening and relaxation, to see what effect model selection has on calculated camber. Prediction equations for concrete modulus of elasticity will also be compared with experimental results from test cylinders made from the concrete mix used to fabricate the studied beams. The variability of calculated camber using the measured and predicted modulus of elasticity will be examined.

The 27 investigated beams in this study are modified 79 in. deep AASHTO Bulb Tees (Figure 3.13) which have lengths between 127 ft - 4 in. and 137 ft - 3 in. These are relatively long spans for prestressed beams. The beams are also widely spaced, with spacing ranging from approximately 11 ft to 13 ft. The concrete was a high strength mix with a specified design strength of 9000 psi. Compressive strength and modulus of elasticity testing was performed to determine concrete material properties. Camber measurements were taken at weekly intervals until the beams were one month old, after which time the measurements were decreased to monthly intervals. The oldest beams were measured over a six month period.

The predicted camber values at various ages are compared with what was observed in the actual beams. The model that produces the “best fit” for individual beams or groups of beams is identified. Differences in measured camber for beams cast in different seasons, spring and summer, are examined.

1.3 THESIS ORGANIZATION

Chapter 2 details previous studies of camber in prestressed concrete bridge beams. Methods of camber calculation are described, including multiplier and approximate time step methods. Additionally, previous summaries of research concerning variables thought to influence camber are presented. These variables include modulus of elasticity, creep, shrinkage, prestress losses, aggregate type, ambient curing conditions, and age at release. Chapter 3 begins by summarizing the beam production methods, materials, and configuration. Following that is a description of the camber measurement method, measurement of thermal-induced camber, fresh concrete properties, and the compressive strength and modulus of elasticity testing methods. Chapter 4 describes the incremental time step analysis procedure used in the study. Chapter 5 presents the compressive strength and modulus of elasticity test results and compares those results with values predicted by the commonly used theoretical models. Shrinkage strain and creep coefficients are calculated using many of the available theoretical models. The predicted creep and shrinkage values are used in conjunction with the predicted and measured modulus of elasticity results to calculate camber with the incremental time step method. Calculated camber is then compared with measured camber. The predicted camber according to commonly-used multiplier methods and the computer program used to design the beams are also compared to measured camber. Chapter 6 presents the study's conclusions and recommendations. The prediction models used for calculating modulus of elasticity, prestress losses, creep, and shrinkage are summarized in Appendix A, along with the experimental results for the remaining beam samples. Appendix B contains measured and predicted camber, residuals, and prediction model rankings for individual beams not grouped in a beam sample.

CHAPTER 2. BACKGROUND

2.1 INTRODUCTION

The following sections examine some previous research studies relevant to the present study. The first section discusses camber in general, while subsequent sections address important variables in camber calculations including modulus of elasticity, creep, shrinkage, prestress losses, influence of aggregate type, influence of ambient and curing conditions, and age at release.

2.2 PREVIOUS INVESTIGATIONS OF CAMBER

Several trends were noted by studies examining camber growth of high strength concrete bridge beams. Kelly, Bradberry, and Breen (1987) found that beams made of lower strength concrete exhibited the greatest camber during erection, the greatest time dependent responses, and the least final camber at the end of service life while higher strength concrete exhibited the opposite trends. In addition to variation in concrete strength, the construction schedule and magnitude of creep were variables that showed the greatest influence on camber. Relative humidity and age at release were observed to have smaller effects. A study by Brown, Nielsen, and Schmeckpeper (1995) also found no correlation between camber growth and relative humidity. The measured camber values compared favorably with the time step prediction model of the study when gross section properties were used in place of transformed section properties.

Ahlborn, French and Shield (2000) measured beam camber from time of release until an age of 840 days for a Minnesota DOT 45M I-girder. The experimental measurements showed the camber to increase until an age of 30 days, at which point the camber growth was observed to stabilize for the duration of measurement.

2.2.1 PCI Method

The PCI Method (1999) applies multipliers to the instantaneous elastic deflections or calculated deflection components. The basic method is based on the work of Martin (1977) and the modified method is based on Tadros, Ghali, and Meyer (1985). Multiplier methods have built-in assumptions regarding curing time, prestress losses, and age at erection, and the multipliers were developed from the results of a time-step analysis

incorporating these assumptions. Specifics of both forms of the PCI Method are discussed in greater detail in Chapter 5.

Byle, Burns, and Carrasquillo (1997) tracked camber and deflection from time of release until the beams were in service. Experimental results were compared to the predictions of the PCI method. The PCI Method worked reasonably well given the simplicity of application, although it over estimated the measured deflections. Ahlborn, French, and Shield (1996) observed that the PCI Method over estimated camber by 7 percent for one beam and 20 percent for the second beam. Woolf, Douglas, and French (1998) also found the PCI Method to over estimate the measured camber values, but by an acceptable amount for the model's simplicity. Stallings and Eskildsen (2001) observed that the PCI Multiplier Method consistently over estimated the camber by an average of 29 percent for twenty-six beams measured at 200 days. Shams and Kahn (2000) studied four 33 ft Type II AASHTO Beams to monitor prestress losses and deflection for one year. The beams were composed of high strength concrete with a 56-day design strength of 10,000 psi.

Study results found that initial deflection calculated using the PCI Method overestimated measured camber by 11 percent. The PCI Method was observed to underestimate long-term camber by nearly 40 percent, or nearly ½" at an age of 6 months and beyond.

2.2.2 Time Step Method

Time step methods divide the life of the prestressed concrete beam into a number of equal or unequal time intervals. This allows for the computation of modulus of elasticity, creep, shrinkage, and relaxation at each considered time interval. Typically, initial curvature due to the initial prestressing force and beam self-weight is calculated, including the effects of elastic shortening. Increase or decrease in curvature due to prestress losses (including creep, shrinkage, and relaxation) is calculated at each time interval, which allows deflection to be determined. A complete discussion of the time step method used in the study is presented in Chapter 4.

Woolf, Douglas, and French (1998) found that the time step method developed by Branson and Kripanarayanan (1971) was the best match with the measured camber in most cases, but did not accurately predict camber in all beams. Byle, Burns, and

Carrasquillo (1997) also found a time step method to be the best predictor of camber when using the measured time-dependent material properties. Stallings and Eskildsen (2001) compared the experimentally measured camber values with theoretically calculated values using an incremental time step method. It was observed that the incremental time step method, combined with the standard parameters for creep and shrinkage, over estimated the camber by 24 percent. Utilizing parameters for High Performance Concrete yielded values an average of 6 percent below the measured camber values. The larger error when using the standard parameters was attributed to over estimating the effects of creep. Deflection calculated by Shams and Kahn (2000) using a time step method produced predicted results that were nearly identical to the measured camber results.

2.2.3 Other Methods

Several studies examined other prediction methods. Woolf, Douglas, and French (1998) used the ACI-209 (1992) and ACI-435 (1995) methods, which produced the best overall results and closest match with the experimentally measured data. The CEB-MC90 (1990) method was found to overestimate camber. Yazdani and Mtenga (1997) predicted theoretical camber using the conjugate beam method utilized by a Florida Department of Transportation (FDOT) computer program. The camber of AASHTO Type III beams considered in the study was consistently under predicted by the FDOT program. The initial difference was 6 percent, with a 10 percent difference at 1 month and a 15 percent difference at 2 months. The AASHTO Type IV beams showed the same trend, as did a modified AASHTO Type VI beam. The only exception to the under prediction of camber by the FDOT program were the Florida 72 in. Bulb Tee beams. The experimental camber measurements for the Florida 72 in. Bulb Tees were 35 percent lower than the values predicted by the FDOT program. After one month, however, the cambers were under predicted by 6 percent.

Sanek (2005) studied beams camber of six 162 ft long 78 in. deep Florida Bulb-Tees with a 28-day design strength of 8,500 psi, three 91 ft long Type IV AASHTO girders with a 28-day design strength of 5,500 psi, and four 81 ft long Type V AASHTO girders with a 28-day design strength of 5,500 psi. Periodic camber measurements were

taken from the time of prestress transfer to as long as 6 months following transfer and compared with the predicted values of the Florida DOT PSBeam LRFD Design Software

Camber measurements of the 78 in. Florida Bulb-Tees following release were 55 percent of the predicted results during the first few weeks and 35 percent of the predicted results at 6 months. Camber measurements of the AASHTO Type IV and Type V beams following release were nearly identical to the predicted results during the first few weeks. Measured deflection at 6 months for the AASHTO Type IV beams were 50 percent of the predicted results, but measured results for the AASHTO Type V beams were very close to the predicted values.

Ahlborn, French and Shield (2000) compared measured camber values to the Moment Area Method using equivalent loading, and the PBeam computer program developed by Suttikan (1978) which uses a finite element method accounting for nonlinearity and time-dependent material properties. The Moment Area Method provided a close approximation to the initial camber in the beam. The PBeam computer program predicted cambers 11 percent and 28 percent higher for two different beams.

Paulson, Nilson, and Hover (1991) used the ACI-318 method (1989), which was observed to be fairly accurate for beams with concrete strengths below 5000 psi, but predicted values were as much as three times greater than the actual deflections of high-strength concrete beams. A modified ACI-318 method by Luebkeman, Nilson, and Slate (1985) was a better predictor of the actual deflections for the high-strength concrete beams. The method is identical to the ACI-318 (1999) method for concrete strengths below 6000 psi, but the long-term deflection multiplier is replaced by the following equation:

$$\lambda = \frac{\mu\xi}{1 + 50\mu\rho'}$$

where , ξ = Time-dependent factor ($\xi = 2.0$ for >5 years ; $\xi = 1.4$ for 12 months ; $\xi = 1.2$ for 6 months ; $\xi = 1.0$ for 3 months)

$$\mu = 1.4 - \frac{f_c'}{10{,}000} \quad \text{for } 0.4 \le \mu \le 1.0$$

ρ' = Compression steel ratio as defined in ACI-318 (1999)

2.3 FACTORS AFFECTING CAMBER

Eccentricity of the prestressing strands in a prestressed concrete beam and some small initial prestress losses result in the initial camber of the beam. Elastic shortening and anchorage losses compose the initial prestress losses. Long term camber growth is affected by several inter-related time-dependent factors. Creep, shrinkage, and relaxation of the prestressing strands all contribute to a gradual reduction of the effective prestressing force in the strands, which creates prestress losses. Shrinkage, which is a volumetric change, results in a shortening of the beam length. Creep occurs as the concrete deforms under the application of a sustained effective upward load (due to prestressing force eccentricity). Meanwhile, the prestressing strand is itself being subjected to relaxation, which is a loss in prestressing force due to elongation of the stressed strand held at constant length. As the force in the strand decreases from relaxation, shrinkage is also occurring, which further decreases the force in the strand as the beam length shortens. As the force in the strand decreases, the creep-inducing upward force component also decreases and the process continues at a decreasing rate as the beam ages.

Other factors also affect camber growth, including modulus of elasticity, aggregate type, ambient and curing conditions, and age at release. These factors, along with creep, shrinkage, and relaxation, will now be discussed individually along with the findings of previous researchers.

2.3.1 MODULUS OF ELASTICITY

Modulus of elasticity and beam deflection exhibit an inverse relationship as evident in the following equation:

$$\frac{d^2y}{dx^2} = \frac{M(x)}{EI}$$

It has been generally accepted that concrete modulus of elasticity is proportional to the square root of compressive strength, therefore higher compressive strength should be associated with higher modulus of elasticity and smaller deflection. This is intuitively logical due to the increased stiffness of materials with higher modulus of elasticity.

Several studies examined the relationship between concrete compressive strength and modulus of elasticity and their effect on camber.

Neville (1997) asserted that there can be no simple relation between modulus of elasticity and compressive strength because the concrete modulus of elasticity is affected by the modulus of elasticity of the aggregate as well as the volumetric content of the aggregate in the mix. None of the current predictive equations for modulus of elasticity account for the bond between the aggregate and the concrete paste. Microcracking occurs at this interface, which is a major factor in the structural behavior of the concrete mix. The curvilinear form of the stress-strain relationship for concrete is a result of this interface bonding and microcracking. This explains why the stress-strain relationship of the constituent materials of the mix (aggregate and cement paste) is linear while the combined relationship is curvilinear. A trade-off is also observed because the increased aggregate size reduces the water requirement but allows more microcracking to occur, since there is a smaller total bonding surface area with increased bonding stresses.

Decreasing the bond stresses by decreasing aggregate particle size (which increases total surface area) allows the fracture surface to pass through the aggregate particles instead of fracturing only through the hardened concrete paste. In high strength concrete, the lower w/c ratios typically result in the modulus of elasticity being similar between the hardened concrete paste and aggregate. This allows the concrete to behave as a more homogeneous material, with a stress-strain relationship that approaches linearity.

Shams and Kahn (2000) observed that a higher concrete compressive strength was associated with a decrease in initial and long-term prestress losses and camber. Results of work by Baalbaki, Aitcin, and Ballivy (1992) indicated that the ACI-363 (1992), CEB-MC90, and Norwegian Council for Building Standardization, NS 3473 (1992) relationships between compressive strength and modulus of elasticity only seem to hold well for normal strength concrete. Their results also indicated that determining the high strength concrete modulus of elasticity based on the aggregate modulus of elasticity worked very well for granite and limestone aggregate, but was a poor indicator of concrete modulus of elasticity for quartzite and sandstone aggregate.

Many studies examined the accuracy of several models to predict modulus of elasticity for high strength concrete. The models used in the current study include the AASHTO Standard Specifications (2002) and AASHTO-LRFD Specifications (1998), ACI-318 (1999), ACI-209 (1992), ACI-363 (1992), and the CEB-MC90 (1990) code. These models are presented in Appendix A. Summaries of their findings are included below.

2.3.1.1 AASHTO Standard Specification

Byle, Burns, and Carrasquillo (1997) found that the AASHTO-Standard Specifications equation for modulus of elasticity in terms of concrete strength overestimated the measured modulus of elasticity values for high strength concrete. Both Huo, Al-Omaishi, and Tadros (2001) and Huo (1997) observed similar trends, with the measured modulus of elasticity values being higher than the predicted values according to the AASHTO equation. Results by Mokarem (2002) showed that modulus of elasticity values calculated using the AASHTO prediction equations were within 10 percent of the experimental test results. Sanek (2005) found that the AASHTO method for calculating concrete modulus of elasticity was accurate compared with experimental measurements.

2.3.1.2 AASHTO LRFD Specification

Will and Sanders (2000) found that the AASHTO LRFD equation for modulus of elasticity slightly over estimated the experimentally measured values obtained.

2.3.1.3 ACI-318

Testing conducted by Ahlborn, French and Shield (1996) indicated that ACI-318 over estimated the experimentally measured values for modulus of elasticity of high strength concrete. Work by Lai, Kahn, et. al. (1999), Slapkus and Kahn (2002), Stallings and Glover (2000), Lai, Kahn, Travis, et al. (1999), and Gardner and Lockman (2001) also indicated that the ACI-318 equation over estimated the measured modulus of elasticity. Will and Sanders (2000) found that the ACI-318 equation for modulus of elasticity slightly over estimated the values obtained experimentally. Testing conducted

by Mokarem (2002) indicated that the modulus of elasticity values calculated using the ACI-318 prediction equations were within 10 percent of the experimental test results. A study by Huo (1997) was the only one which showed the ACI-318 equation to under estimate the experimentally measured values. Canfield (2005) tested the modulus of elasticity of cylinders made from a concrete mix with design strength of 10,000 psi. The results were compared against several theoretical equations. The ACI -318 equation was observed to overestimate measured modulus of elasticity by an average of 35.8 percent.

2.3.1.4 ACI-363

Ahlborn, French and Shield (1996) observed that ACI-363 (1992) over estimated the experimentally measured values for modulus of elasticity. Additional studies by Lai, Kahn, Travis et al. (1999) and Gardner and Lockman (2001) also found that the modulus of elasticity was over-predicted by the ACI-363 equation. Gardner and Lockman (2001), however, showed the ACI-363 equation to match better at later age than at early age. Work by Slapkus and Kahn (2002), although finding the modulus of elasticity to be over predicted by the ACI-363 equation, found that the ACI-363 predicted values were much closer to the measured values than ACI-318. A study by Will and Sanders (2000) found that the ACI-363 equation for modulus of elasticity slightly over estimated the values obtained experimentally. Canfield (2005) found that the ACI-363 equation overestimated measured modulus of elasticity by 15 percent, on average.

Several studies observed that the ACI-363 predicted modulus of elasticity was lower than the experimentally measured values. Byle, Burns, and Carrasquillo (1997), Stallings and Glover (2000), Huo, Al-Omaishi, and Tadros (2001), and Huo (1997) all showed that the measured values were consistently higher than the values predicted by the ACI-363 equation. Sanek (2005) observed that the ACI method for calculating concrete modulus of elasticity was fairly accurate compared with experimental measurements.

2.3.1.5 ACI-209

Testing by Huo, Al-Omaishi, and Tadros (2001) showed that the measured modulus of elasticity values were higher than the predicted values according to the ACI-

209 equation. Work by Huo (1997) also showed the same trend with respect to the ACI-209 equation.

2.3.1.6 CEB-MC 90

Baalbaki, Aitcin, and Ballivy (1992) examined the CEB-MC 90 model and observed that it consistently over estimated the measured values of modulus of elasticity for groups of three 4 in. x 8 in. cylinders tested at each age by an average of 32 percent at 28 days and 29 percent at 91 days. The overestimation varied from 7 to 100 percent at 28 days and from 7 to 81 percent at 91 days.

2.3.1.7 Additional Modulus of Elasticity Prediction Equations

Three studies developed or modified predictive equations for modulus of elasticity. These methods are presented in this section. Alexander (1996) developed a predictive equation for modulus of elasticity based on the British BS 8110 Model Code (1985), which is the British Standard for the structural design of concrete. It is of the form:

$$E_c = K_0 + \alpha f_{cu}$$

where E_c is the concrete modulus of elasticity

f_{cu} is the compressive strength of a test cube at a corresponding age

K_0 is an aggregate stiffness factor

α is a strength factor.

The last two variables were found by regression and for the three samples of granite are shown in Table 2.1.

Table 2.1 Coefficients for Modulus of Elasticity Equation (Alexander, 1996)

Aggregate Type	3 to 28-day values		6-month values	
	K_0	α	K_0	α
Series 1				
Granite (J)	20	0.20	31	0.10
Granite (Rh)	21	0.25	34	0.10
Series 2				
Granite (Ro)	15	0.30	25	0.10

Huo, Al-Omaishi, and Tadros (2001) also developed an equation to better fit the experimental data:

$$E_c = a\sqrt{f_c^{'}} + b \quad \text{(MPa)}$$

where a and b are constants specific to the concrete mix. Modulus of elasticity was observed to increase with increasing coarse aggregate content. Lai, Kahn, Travis, et al. (1999) proposed a best-fit equation as follows:

$$E = \left(38{,}000\sqrt{f_c^{'}} + 730{,}000\right)\left(\frac{w}{145}\right)^{1.5}$$

where w is unit weight of concrete (lb/ft^3)

Shams and Kahn (2000) proposed a prediction equation for compressive strength and modulus of elasticity of moist-cured concrete made with Type III cement and Georgia granite aggregate. The equations are:

$$f_c^{'}(t) = \frac{t^{0.28}}{1.11 + 0.56t^{0.28}}\, f_{c28}^{'}$$

$$E_c = 41000\sqrt{f_c^{'}(t)} + 410000$$

where,

t = Age in days

$f_c^{'}(t)$ = Compressive strength at age t (psi)

$f_{c28}^{'}$ = Compressive strength at 28 days (psi)

E_c = Modulus of elasticity (psi)

Canfield (2005) found that the Shams and Kahn equation was the most accurate predictor of the measured modulus of elasticity, with an average over-estimation of 4.7 percent.

2.3.2 Creep

Creep is a material property resulting in increasing cross-sectional strain under the action of a sustained load over time. In the case of a prestressed concrete beam, the eccentricity of the prestressing strand pattern centroid (normally below the neutral axis) results in an equivalent upward force. This upward force is always present due to the

initial stressing of the strands and the bond between the strands and concrete. The effect of this upward force leads to an increase in beam deflection due to creep of the material. Creep strain prediction methods by AASHTO-LRFD (1998), ACI-209 (1992), ACI-209, modified by Huo (1997), Bazant B3 (1995), CEB-MC90 (1990), Gardner-Lockman (2001), Shams and Kahn (2000), and NCHRP 496 (2003) are presented in Appendix A.

Researchers who experimentally measured creep in their studies did so using two different methods. Some tested concrete cylinders in creep frames while others calculated creep based on measurements from constructed beams.

Mokhtarzadeh and French (2000) observed that the creep of mixes made with soft aggregates was higher than for mixes made with hard coarse aggregates. The grading, particle size, and shape were also observed to have an effect on creep. Higher creep was observed for the smooth coarse aggregates, since there is a weaker bond at the interface between the aggregate and cement paste. Testing by Alexander (1996) indicated that the more aggregate that is included in the mix, the less creep that occurs. A clear trend was also observed that the concrete modulus of elasticity could be considered as an indicator of the overall concrete stiffness and, consequently, the long-term effects of creep and shrinkage. Coarse aggregates with low absorption values (water demand) were found by Alexander (1996) to produce concrete with less creep. Testing by Collins (1989) indicated that use of high-range water-reducing admixtures did not appear to have an effect on creep deformations.

Several studies noted that test specimens with higher compressive strength exhibited less creep than lower compressive strength concrete. Alexander (1996), Huo, Al-Omaishi, and Tadros (2001), Lai, Kahn, Travis, et al. (1999), Shams and Kahn (2000), and Mokhtarzadeh and French (2000) all reported this trend. Testing by Gopalaratnam and Eatherton (2001) indicated that creep strains were 5 percent to 15 percent less than normal strength concrete and Myers and Carrasquillo (1999) noted that, generally, the use of the high performance concrete mixtures resulted in lower creep strains as compared with normal strength concrete. Farrington, Burns and Carrasquillo (1996) observed a linear relationship between the level of stress and creep strain up to a limiting stress of approximately 40 percent of f'_c.

Fekete, Barr, Stanton, Eberhard, and Janssen (2000) conducted creep tests indicating that the total creep coefficient ranged from 1.64 to 2.72 for 6 in. diameter cylinders. The upper end of the range was significantly more than the typical value of 1.60 suggested by others.

Farrington, Burns and Carrasquillo (1996) reported a relationship between creep and loading age. Specific creep values and the ultimate creep coefficient were each higher for specimens loaded at an early age than for specimens loaded at 28 days. Shams and Kahn (2000) also observed greater creep for beams loaded at earlier ages. At approximately one month following loading, however, the creep coefficient curves appear to be parallel, which suggested that long term creep is independent of loading age. It was thought that as concrete ages, hydration creates stronger bonds in the cement paste, which leads to a greater resistance to movement under sustained loading.

2.3.2.1 AASHTO Standard Specification

Testing by Barr, Fekete, Eberhard, Stanton, Khaleghi, and Hsieh (2000) showed that creep losses were over predicted for some beams and under predicted for others. Fifteen bridge beams, 10 with a design span of 80 ft and 5 with a span of 137 ft, were studied. The results of the AASHTO method ranged from 21 percent lower to 19 percent higher compared with measured losses from the actual beams.

2.3.2.2 AASHTO LRFD

Townsend (2003) studied creep specimens cured using steam and moist curing methods. The mix used in the study was the same mix design the precaster used to produce the instrumented beams, and four batches were made to produce the test specimens. The design strength was 8000 psi. Results for ASTM moist-cured cylinders indicated that the AASHTO-LRFD method was the best predictor of creep strain while the ACI-209 method (modified by Huo) was the best predictor of total strain. Shams and Kahn (2000) also found that the AASHTO-LRFD model gave the results closest to the experimentally measured creep values.

2.3.2.3 ACI-209

Several studies examined the ACI-209 method for predicting creep. Most of the studies found that ACI-209 over predicted the measured values of creep, with Huo, Al-Omaishi, and Tadros (2001), Farrington, Burns and Carrasquillo (1996), Slapkus and Kahn (2002), Huo (1997), and Lai, Kahn, Travis, et al. (1999) all reporting this trend. Canfield (2005) also found that the ACI-209 (1992) model significantly overestimated the experimentally measured creep coefficient, as did models by Lai (1999), Slapkus and Kahn (2002), and Shams and Kahn (2000). Townsend (2003) found that the ACI-209, modified by Huo, was the best predictor of creep strain for the match cure batches tested.

Two studies found that the ACI-209 predicted values matched well with the experimentally measured values. Stallings and Glover (2000) measured a specific creep of 0.20 microstrain/psi at 90 days, which compared well with the value of 0.29 microstrain/psi predicted by the ACI-209 equation. Mokhtarzadeh and French (2000) also found that the ACI-209 equations were good predictors of creep for the concrete mixes tested. Ahlborn, French, and Shield (1996) reported mixed results, finding that the ACI-209 equations for creep were a better fit at earlier ages than later in the service life of the member.

2.3.2.4 CEB-MC 90

Lakshmikantam (1999) showed that the CEB-MC 90 model, along with the B3 model, was most accurate for prediction of creep strains, followed in order by the Gardner-Zhao, ACI-209, and Sakata (1993) models.

2.3.2.5 Sakata

Results by Meyerson (2001) indicated that all models over predicted the basic creep. The best predictor of basic creep strain at 28 and 97 days, was the Sakata Model (1993) followed in order by the ACI-209, Bazant B3, CEB-90, and Gardner-Lockman models.

2.3.2.6 PCI Method

Waldron (2004) found that the PCI Method predicted creep with reasonable accuracy. Barr, Fekete, Eberhard, Stanton, Khaleghi, and Hsieh (2000) had mixed conclusions about the accuracy of the PCI method for creep prediction, with results that ranged from matching well to 32 percent lower than the experimentally measured values.

2.3.2.7 NCHRP 496

Waldron (2004) found that the NCHRP model predicted creep strain with reasonable accuracy.

2.3.2.8 Additional Creep Prediction Equations

Huo, (1997) modified the ACI-209 equation for the creep coefficient as a result of experimental test results. The revised equation was tested against the data of other researchers and found to provide a good fit. The equation is:

$$C_t = 2.35\gamma_c \frac{t^{0.6}}{K_c + t^{0.6}}$$

where γ_c is the product of adjustment factors given in ACI-209 and a new strength correction adjustment factor, $\gamma_{st,c}$, which is given by:

$$\gamma_{st,c} = 1.18 - 0.045 f_c^{'} \leq 1.0$$

The adjustment factor K_c is defined by:

$$K_c = 12 - 0.50 f_c^{'}$$

with f_c' being the concrete strength in ksi at 28 days.

2.3.3 Shrinkage

Shrinkage is a property of concrete that occurs during the drying process as concrete cures. There are three main types: autogenous shrinkage, carbonation shrinkage, and drying shrinkage. During the initial time interval after the concrete has been poured, autogenous shrinkage takes place as moisture from the concrete surface evaporates at a higher rate than it can be replaced from water inside the poured concrete. Carbonation shrinkage also occurs a this time due to the reaction between carbon dioxide in the

atmosphere and Calcium Hydroxide in the cement paste. The reaction produces water which then evaporates and results in carbonation shrinkage. Drying shrinkage occurs in the hardened concrete and is the result of the beam losing volume as moisture evaporates. Many of the same factors affecting creep also affect shrinkage. These include volume to surface ratio, relative humidity, aggregate volume, and water to cement ratio. Shrinkage causes the beam to decrease in length and contributes to prestress losses, which in turn results in increased beam camber with time. Most creep models also have corresponding shrinkage models and these models are presented in Appendix A. They include the AASHTO-LRFD (1998), ACI-209 (1992), ACI-209, modified by Huo (1997), Bazant B3 (1995), CEB-MC90 (1990), Gardner-Lockman (2001), Shams and Kahn (2000), and NCHRP 496 (2003) models.

Paulson, Nilson, and Hover (1991) performed tests and the results indicated that drying shrinkage for high-strength concrete was 2/3 of the normal strength concrete shrinkage. Gopalaratnam and Eatherton and Eatherton (2001) observed similar results, noting that shrinkage strains were 40 percent less than those of typical normal strength concrete. Myers and Carrasquillo (1999) noted that, in general, the use of high performance concrete mixtures exhibited lower shrinkage strains as compared with normal strength concrete.

Moisture content is also a significant factor in the amount of shrinkage. Testing by Lai, Kahn, Travis, et al. (1999) indicated that the magnitude of shrinkage strains is directly proportional to the water volume in the mix and not influenced by the compressive strength. Torrenti, Granger, Diruy, and Genin (1999) also found that drying shrinkage is proportional to the variation of moisture content in the material.

Shrinkage testing by Fekete, Barr, Stanton, Eberhard, and Janssen (2000) showed that a natural log function for strain versus age appeared to match the experimental data very well for 100 days, then began to over predict the strains. Shrinkage was also observed to increase as the Volume to Surface Ratio (V/S) decreased. The V/S Ratio is the ratio of the area of the beam cross-section to its perimeter. Granger, Diruy, and Genin (1999) observed that drying is modeled by a nonlinear diffusion equation. Furthermore, shrinkage of the beam is proportional to beam loss of weight. It was also

noted that the diffusion coefficient during the drying cycle is not the same as the diffusion coefficient during the wetting cycle.

Shams and Kahn (2000) conducted shrinkage tests on 9 in. x 18 in. x 24 in. concrete blocks. One block was kept in a controlled environment at 70 $\pm$ 3^{o} F and 50 $\pm$ 4% humidity while the other block was subjected to ambient conditions ranging from 40^{o} F to 85^{o} F with 72% average humidity. Shrinkage was observed to decrease with increased relative humidity. Shrinkage appeared to be less in beams with higher compressive strength, 31 percent to 51 percent less than normal strength drying under similar conditions. Nearly one half of the total shrinkage was observed to occur during the first two weeks of drying.

2.3.3.1 ACI-209

All studies considered found that the ACI-209 equation for shrinkage over predicted the experimentally measured values. Slapkus and Kahn (2002), Huo, Al-Omaishi, and Tadros (2001), Huo, (1997), and Lai, Kahn, Travis, et al. (1999) all noted this trend for high performance concrete. Canfield (2005) observed that the ACI-209 (1992) model significantly overestimated the experimentally measured shrinkage strain, as did models by Lai (1999), Slapkus and Kahn (2002), and Shams and Kahn (2000).

The results by Farrington, Burns and Carrasquillo (1996) showed that the experimental ultimate shrinkage strain was an average of 55 percent lower than that predicted by ACI-209. Testing by Ahlborn, French and Shield (2000) found that the ACI-209 equation was a better fit of the measured shrinkage values at earlier ages than later in the service life of the member. Based on testing of match-cured specimens, Townsend (2003) found that the ACI-209 model, modified by Huo, was the best predictor of shrinkage strain.

2.3.3.2 CEB-90

Mokarem (2002) observed that the CEB-90 Code was the best model for portland cement mixtures, followed by the Bazant B3 Model. McDonald and Roper (1993) performed testing on concrete made in Australia, finding that the model that best predicted the experimental test results was the Australian AS1481 model. This was

followed by the other two Australian models, AS3600 and NAASRA. The CEB-90 Model provided the best fit of the non-Australian models.

2.3.3.3 Sakata

Meyerson (2001) found the best predictor of drying shrinkage strain at 28 days was the Sakata Model (1993), followed in order by the Gardner-Lockman, Bazant B3, CEB-90, and ACI-209 models.

2.3.3.4 Bazant B3

Testing of cylinder shrinkage strain performed by Townsend (2003) found that the Bazant B3 method was the best predictor of shrinkage for ASTM moist-cured cylindrical test specimens. Evaluation of several models by Lakshmikantan (1999) for accuracy in predicting shrinkage strains noted that the Bazant B3 and Gardner-Zhao (GZ) models were the best overall predictors of shrinkage strain, followed in order by ACI-209, CEB-90, and the Sakata Model (1993). Waldron (2004) also found that the Bazant B3 model was the best predictor of shrinkage strains.

2.3.3.5 Gardner-Lockman

Townsend (2003) found that the Gardner-Lockman (GL-2000) Method was the best predictor of prism shrinkage strains for ASTM moist-cured specimens. Mokarem (2002) noted that the GL-2000 model showed the most accurate results for supplemental cementitious mixtures, followed by the Bazant B3 and CEB-90 Models. Testing by Meyerson (2001) found that the best predictor of drying shrinkage strain at 97 days was the GL-2000 Model, followed in order by the Bazant B3, CEB-90, Sakata (1993), and ACI-209 models. Lakshmikantan (1999) found the previous version of Gardner's model, Gardner-Zhao, to be the best overall predictor of shrinkage strain. In fact, the Bazant B3 model was found to be nearly as accurate as the Gardner–Zhao method, despite the fact that the the Bazant B3 model was calibrated to the data bank from which the data sets for comparing studies were obtained.

2.3.3.6 AASHTO

Barr, Fekete, Eberhard, Stanton, Khaleghi, and Hsieh (2000) found the AASHTO method results to range from 21 percent lower to 19 percent higher than actual.

2.3.3.7 PCI Method

Testing by Barr, Fekete, Eberhard, Stanton, Khaleghi, and Hsieh (2000) found the PCI method for shrinkage yielded results that were 0 to 32 percent lower than actual. Waldron (2004) observed that the PCI Bridge Design Manual method predicted creep and shrinkage strains with reasonable accuracy.

2.3.3.8 NCHRP 496

Waldron (2004) found that shrinkage strain was predicted accurately by the NCHRP model.

2.3.3.9 Additional Prediction Equations

A few studies proposed new shrinkage prediction equations for future use. Huo, Al-Omaishi, and Tadros (2001) developed new equations based on experimental data. Huo (1997) also used these equations. The proposed equation for shrinkage strain is:

$$\varepsilon_{sh} = (\varepsilon_{sh})_u \frac{t}{K_s + t}$$

$$K_s = 45 - 2.5 f_c^{'} \quad \text{(ksi)}$$

where, t = time in days

K_s = adjustment factor of early-age shrinkage,

$(\varepsilon_{sh})_u$ = Ultimate Shrinkage (in./in.)

A correction factor was developed to reduce the ultimate shrinkage strain for concrete with high compressive strength. The factor is:

$$\gamma_{st,c} = 1.20 - 0.05 f_c^{'} \leq 1 \quad \text{(ksi)}.$$

Lai, Kahn, Travis, et al. (1999) recommended the following equation for estimating shrinkage strains as a function of time:

$$(\varepsilon_{sh})_t = \frac{t}{20+t}(500\times10^{-6})$$

where,

$(\varepsilon_{sh})_t$ = shrinkage strain at time t, in. / in.

t = time after the onset of drying, days

2.3.4 Prestress Losses

Prestress loss occurs as the initial prestressing force applied during the jacking phase gradually reduces with time. Loss of prestress can be categorized into two main types: immediate elastic losses and time-dependent prestress losses. The immediate elastic losses are caused by friction, anchorage and seating, and elastic shortening following transfer. The long-term time-dependent prestress losses are caused by the inter-related effects of creep and shrinkage of the concrete, and relaxation of the prestressing steel. Prestress losses decrease the rate at which camber growth progresses and uncertainty in estimates of the long term time-dependent components creates difficulty in accurately estimating camber.

Ahlborn, French and Shield (2000) measured actual prestress losses by a combination of vibrating wire and foil strain gages and compared them with theoretical predictions. The results of time step methods were closer to the experimentally measured losses than any of the predictive equations of the established models. The differences were primarily attributed to the fact that the models were developed based on normal strength concrete instead of high strength concrete.

Mortensen, Saiidi, and Ladkany (2003) observed larger losses in box beams than in other beam shapes similar to AASHTO beams. It was suggested that this could be due to the larger volume to surface ratio for the box beam as compared with the solid beams.

Waldron (2004) instrumented nine high-strength concrete bridge beams with strain gages. The design strengths ranged from 8,000 psi to 10,000 psi. Strain data was compared with the values predicted by several creep and shrinkage prediction models. The models underpredicted strains at early ages and over predicted strains at later ages, with the Bazant B3 model resulting in the best match of the experimentally measured

strains. The models specifically developed for high-strength concrete (Shams and Kahn, PCI Bridge Design Manual, and NCHRP 496) fit the measured data better than the models developed using normal weight concrete, generally speaking.

2.3.4.1 PCI Method

Barr, Fekete, Eberhard, Stanton, Khaleghi, and Hsieh (2000) found that the PCI method under predicted the relaxation loss as reported from strand manufacturer testing. The predicted losses due to elastic shortening were also lower than the experimentally measured values by 8 to 16 percent. Total prestress losses ranged from 12 percent lower to 9 percent higher with the PCI method. Kelly, Bradberry, and Breen (1987) also found the PCI model to underestimate losses in general. Testing by Ahlborn, French and Shield (2000) found that the PCI Committee Method (1975) and the PCI Design Handbook (1992) yielded results that were less than the measured losses by 5 to 9 percent. Testing by Shams and Kahn (2000) found that the PCI Method underestimated measured initial losses by an average of 16 percent and overestimated measured long-term losses by greater than 30 percent in most cases. Waldron (2004) found that the PCI Bridge Design method was the best predictor of prestress losses, yielding results within $\pm$ 10 percent of measured losses.

2.3.4.2 AASHTO-Standard Specification

A study by Kelly, Bradberry, and Breen (1987) found that the AASHTO model overestimated losses. Despite its overestimation, however, the AASHTO model was still considered to be the most accurate model. Testing by Huo (1997) also found that the prestress losses calculated using the AASHTO Standard equations overestimated the measured losses for the high performance concrete beams. Similarly, Byle, Burns, and Carrasquillo (1997) found the AASHTO Method over estimated losses for a Texas type U-Beam by nearly 8 percent and was not recommended for use. Barr, Fekete, Eberhard, Stanton, Khaleghi, and Hsieh (2000) found that the AASHTO method under predicted relaxation loss as reported from strand manufacturer testing. The predicted losses due to elastic shortening were also lower than the experimentally measured values by 8 to 16 percent. Total prestress losses were over predicted by the AASHTO method by 1 percent

to 18 percent. Ahlborn, French and Shield (2000) reported that the AASHTO– Standard Specification method under predicted the measured losses by 5 to 9 percent. Work by Canfield (2005) compared measured prestress losses against losses predicted by the AASHTO Standard Specification (2002). The ratio of predicted losses to measured losses was 2.23 for the AASHTO Type IV beams and 1.9 for a modified PCI 56 in. Bulb Tee beam.

2.3.4.3 AASHTO-LRFD

Stallings and Eskildsen (2001) calculated losses using measured strains and compared the values with the AASHTO-LRFD model. The values based on measured losses were an average of 10 percent higher for beams with midspan strain gages and 14 percent higher for the beams with quarter span strain gages. Shams and Kahn (2000) found that the AASHTO-LRFD model predicted initial prestress losses within 7 percent of the measured losses, however it tended to overestimate long-term prestress losses by 31 percent. Waldron (2004) reported that the AASHTO-LRFD model overestimated prestress losses for the studied beams by a wide range of 18 percent to 98 percent.

2.3.4.3.1 NCHRP 496

Waldron (2004) observed that the NCHRP 496 method predicted prestress losses within $\pm$ 18 percent of the measured losses.

2.3.5 Influence of Aggregate Type

Researchers have observed that many properties of the aggregate used in the concrete mix, such as shape, porosity, and modulus of elasticity, affect the behavior of the concrete mix as it sets, cures, and ages. Particularly for high strength concrete, a high aggregate modulus of elasticity greatly contributes to higher modulus of elasticity of the concrete itself. A higher modulus of elasticity increases beam stiffness and decreases the deflection. Aggregate shape and porosity have been observed to be related to creep and shrinkage properties of the concrete material, which affect prestress losses, that in turn affect camber. The findings of researchers regarding the affect of aggregate type on creep, shrinkage, compressive strength, and modulus of elasticity will now be discussed.

2.3.5.1 Creep and Shrinkage

Alexander (1996) asserted that the influence of aggregate type on creep and shrinkage of concrete is due to two effects: water demand of the coarse aggregate, and the stiffness of the aggregate restraining movement of the concrete paste. The water demand of the aggregate has an effect because aggregates with low water demand (absorption) produce concrete with less creep and shrinkage. Additionally, the more aggregate included in the mix the less creep and shrinkage that occurs, since the concrete paste is the primary source of creep and shrinkage. The experimental testing showed that the concrete mixes with granite coarse aggregate exhibited the second lowest shrinkage values from among the 23 aggregate samples considered. Mokhtarzadeh and French (2000) found that the creep of mixes made with soft aggregates was also higher than those made with hard coarse aggregates, and the grading, particle size, and shape were also observed to have an effect on creep. Higher creep was observed for the smooth coarse aggregates, since there is a weaker bond at the interface between the aggregate and cement paste.

Shrinkage testing by Mokhtarzadeh and French (2000) showed that greater shrinkage strains were present for the mixes made with smooth river gravel as opposed to those made with crushed aggregates. The shrinkage was affected by the degree to which the aggregate restrained movement of the cement paste. The mineralogy of the aggregate appeared to have a minimal effect on shrinkage as compared with the surface characteristics. Testing by Will and Sanders (2000) found that the Vega aggregate (rounded, irregular shaped river gravel) mixes showed the least drying shrinkage, followed by the All-Lite and Paiute aggregate mixes, respectively. The aggregate with the lowest absorption showed the least drying shrinkage.

2.3.5.2 Compressive Strength and Modulus of Elasticity

Shams and Kahn (2000) observed that the type of coarse aggregate used greatly affected the measured concrete modulus of elasticity. It was suggested that theoretical equations for concrete modulus of elasticity incorporate a parameter based on aggregate properties. Ahlborn, French and Shield (2000) performed testing using concrete with two

different aggregate types. Mixes containing limestone aggregate had a strength of 9300 psi at release, increasing to 12,100 psi at 28 days. Mixes containing glacial gravel aggregate had a strength of 10,400 psi at release, increasing to 11,100 psi at 28 days. The mix with the harder aggregate appeared to have higher strength initially, but lower strength at twenty-eight days. Will and Sanders (2000) also tested concrete mixes using different coarse aggregate types. The Vega aggregate mixes had the greatest compressive strengths and modulus of elasticity values, followed by the Paiute (quartzite, chert, and siltstone) and All-Lite aggregates (rhyolite). Though all the aggregates were very similar in gradation, mixes containing aggregates with higher specific gravity and lower absorption showed higher compressive strengths. Aitcin and Mehta (1990) evaluated high strength concrete mixes with four different coarse aggregate types for compressive strength and modulus of elasticity in order to determine the effects of aggregate type on these properties. The aggregate types considered were: round and smooth particles of siliceous gravel, diabase, crushed limestone, and crushed granite. The maximum aggregate particle size was ½ in., except the granite particles of ¾ in. The compressive strength testing was performed at 1, 28, and 56 days. The modulus of elasticity was measured at 28 and 56 days.

Testing showed that the granite exhibited failure across the grain and was the weakest of all the aggregates in terms of both compressive strength and modulus of elasticity. However, microscopic evaluation showed that the granite in the sample contained impurities known to cause instability. The gravel aggregate had an 8 to 10 percent lower compressive strength and modulus of elasticity than the diabase and limestone concretes. Failure was observed along the interface zone due to the smooth, rounded aggregate surface. The limestone aggregate produced concrete with the highest modulus of elasticity (5.9×10^6 psi at 56 days), while the diabase aggregate produced concrete with the highest compressive strength (15,200 psi at 56 days).

Another interesting observation was that a common failure plane through the cement paste and aggregate was observed for the limestone and diabase aggregates, while the granite particles showed a separate fracture plane through the aggregate particles than through the cement paste. It was theorized that failure occurred first through the weaker areas of granite particles, then through the cement paste.

Baalbaki, Benmokrane, Chaallal, and Aitcin (1991) observed that concrete made with quartzite exhibited the lowest compressive strength, but the highest modulus of elasticity. The lower compressive strength was attributed to the rigidity of the particles concentrating the stresses at the interface. A sandstone concrete mix exhibited the highest compressive strength, but the lowest modulus of elasticity. The high compressive strength was explained by the aggregate and cement paste having similar modulus of elasticity values that distribute the stresses, as well as the porosity of the sandstone improving the cement paste to aggregate bond at the interface. In general, the compressive strength of the high performance concrete mixes studied appeared to be controlled by the weakest concrete component, as evidenced by testing of the mechanical properties of the rock, cement paste, and combined concrete mix.

Test results by Baalbaki, Aitcin, and Ballivy (1992) indicated that determining the concrete modulus of elasticity based on the aggregate modulus of elasticity worked very well for the granite aggregate concrete. It also worked well for the limestone aggregate concrete, but was a poor indicator of modulus of elasticity for the quartzite and sandstone aggregate concretes.

Myers and Carrasquillo (1999) found that increasing the aggregate content resulted in lower flexural strengths for a given aggregate size. Similarity in aggregate and cement paste modulus of elasticity values resulted in the most efficient mixes in terms of strength. Alexander (1996) performed testing in which the influence of aggregate type on hardened concrete properties was examined. Twenty-three different commonly found aggregate types were selected for study. The testing was conducted in two series, with Series 1 being composed of 13 different aggregate types and Series 2 being composed of 10 additional aggregate types. Series 1 mixes were designed with 28-day strengths of 2900, 4350, 5800, and 8700 psi. Series 2 had fixed water/cement rations of 0.74, 0.61, 0.51, and 0.425. The aggregates were all crushed materials. Three samples of granite were among the considered aggregate types for the studied concrete mixes, characteristics of which are presented in Table 2.2.

Table 2.2 Characteristics of Studied Concrete Mixes (Alexander, 1996)

Stone			Sand		Range of:				
Source	**S.G.**	**E_a GPa**	**Source**	**F.M.**	**water content, l/m^3**	**w/c**	**A/c**	**Slump, mm**	**Bleed Vol, %**
Series 1									
Granite (J)	2.65	79	Same source as stone	2.78	184 – 202	0.80-0.38	9.18-3.18	55-85	6.2-10.9
Granite (Rh)	2.63	70	Pit Sand	1.83	158 – 160	0.80-0.38	10.24-4.55	25-75	9.0-10.3
Series 2									
Granite (Ro)	2.67	77	Same source as stone	3.16	187-192	0.74-0.43	7.40-3.90	55-85	8.1-10.0

The study showed that for a range of concrete strengths between 3000 to 11,500 psi that it is acceptable to model the relationship between concrete modulus of elasticity and compressive strength as linear regressions at different ages.

2.3.6 Influence of Ambient and Curing Conditions

Several researchers have examined the effect of ambient conditions on concrete properties. Most theoretical models for creep and shrinkage incorporate relative humidity into the prediction equations, and temperature is included in the CEB-MC90 model to determine the effective maturity of the concrete. From a construction standpoint, it has been noted that hot weather conditions can negatively affect concrete quality by increasing the rates of moisture loss and cement hydration. Examples of such adverse conditions include elevated ambient temperature, elevated concrete temperature, low relative humidity, high wind speed, and intense solar radiation (ACI-305, 1999). These conditions create an increased water demand in the concrete. Frequently water is added to combat these affects, which results in decreased strength due to higher water/ cement ratio, and increased drying shrinkage (Kosmatka, 2002). Temperature, humidity, and wind affect the amount and rate of prestress losses and the development of concrete strength, which in turn affect camber growth in the beam. Solar radiation can directly cause short-term thermal camber in the beam by creating differential stresses due to the beam being heated unevenly.

A few researchers have studied the effect of temperature on concrete strength development in normal-strength concrete. Klieger (1958) studied concrete made with Type I, II, and III cements and moist-cured at temperatures ranging from 40 to 120 ^{o}F and relative humidity of either 50 percent or 100 percent. Four cylinders were tested at each test date, ranging from one day to one year. Concrete slump decreased as temperature increased when the water content was held constant. Extra water added to the mix to increase slump and workability was observed to decrease concrete strength. Concrete strength at ages less than 3 days was found to increase with casting and curing temperature. Increasing casting and curing temperature, however, was found to decrease concrete strength at 3 months and 1 year. An optimal curing temperature of 55 ^{o}F was suggested for concrete made with Type I and II cement, and 40 ^{o}F was suggested for concrete made with Type III cement.

Verbeck and Helmuth (1968) also observed that higher curing temperatures provide an early compressive strength gain, but result in a decrease in compressive strength at 28 days. Burg (1996) cast fifteen 4 in. x 8 in. test cylinders with water to cement ratio of 0.45 and moist-cured them under controlled laboratory conditions at 50, 73, or 90 ^{o}F. Casting and curing temperatures were varied to determine the effect on concrete strength development. Concrete cast at 73 ^{o}F and cured at 50 ^{o}F showed virtually no effect on strength. Concrete cast and cured at 50 ^{o}F nearly equaled or exceeded specimens cast and cured at 73 ^{o}F. Concrete cast and cured at 90 ^{o}F was observed to have higher early strength than concrete cast and cured at 73 ^{o}F (developing in 3 days what took 7 days at 73 ^{o}F), but exhibited approximately 10 percent less strength at 56 days than concrete cast and cured at 73 ^{o}F.

A testing problem frequently occurs on-site when cylinders are not promptly moved out of the hot sun in the summer. ASTM requirements specify cylinders be stored in conditions ranging from 60 to 80 ^{o}F during the first 24 hours following casting. If a cylinder has been subjected to excessive heating at an early age, testing may result in higher early age compressive strength but lower 28 day compressive strength than the in-place concrete the cylinders are supposed to represent (Hover, 2005).

2.3.6.1 Temperature and Humidity

Some studies examined the influence of ambient temperature and humidity. Others noted general trends regarding internal beam temperatures. Brown, Nielsen, and Schmeckpeper (1995) measured camber and found no correlation between camber growth and relative humidity. Average monthly humidity varied from 40% to 70% during the study period with no observable camber difference for beams cast in different seasons, and subjected to conditions at both ends of the humidity range.

Kelly, Bradberry, and Breen (1987) found that variation in relative humidity did have an initial effect on camber growth. An analysis was performed to simulate the humidity conditions of El Paso, TX (40 percent), Austin, TX (65 percent), and Houston, TX (75 percent). The beam analyzed with 40 percent humidity showed the greatest predicted deflection, while the beam analyzed with 75 percent humidity showed the least deflection. The difference was predicted to be ½" at an age of 60 days, which was the assumed age of beam setting. The difference was predicted to be negligible at the end of the beam's service life.

A study conducted by Mangoba, Mayberry, and Saiidi (1999) in Northern Nevada, where humidity is highly variable, suggested that a period of moist weather following prestressing of a post-tensioned structure can reduce creep and shrinkage losses while dry weather has the opposite effect. Humidity in Northern Nevada has been observed to range from 14 percent to 100 percent during the course of a single day. Instrumentation of a prestressed box girder bridge near Reno, NV by Saiidi, Shields, O'Connor, and Hutchens (1996) indicated creep and shrinkage losses 60 percent higher than the AASHTO Standard Specifications predicted. Measured deflection was one half the predicted value, thought to be caused by the creep and shrinkage losses theorized to result from the dry climate. Shams and Kahn (2000) performed shrinkage tests on 9 in. x 18 in. x 24 in. concrete blocks. One block was kept in a controlled environment at 70 $\pm$ 3^{o} F and 50 $\pm$ 4% humidity while the other block was subjected to ambient conditions ranging from 40^{o} F to 85^{o} F with 72% average humidity. Shrinkage was observed to decrease with increased relative humidity.

Based on readings of internal temperature, Kelly, Bradberry, and Breen (1987) observed that the beam temperature on a hot sunny day, on average, was 4 degrees

Fahrenheit warmer than the ambient air temperature in the morning and 13 degrees Fahrenheit cooler than the ambient air temperature in the afternoon. Temperature readings also indicated that the temperature of the top flange was cooler than the bottom flange in the morning, but was warmer than the bottom flange in the afternoon. Barr, Fekete, Eberhard, Stanton, Khaleghi, and Hsieh (2000) recorded an internal temperature variation of 77 degrees Fahrenheit over the beam height for instrumented Washington State DOT 74G Beams during casting. The coldest temperature was recorded at the bottom of the beam but it was suspected that, due to winter weather, the frozen ground was acting as a heat sink.

Upon measuring the camber of twenty-six beams in a single day, Stallings and Eskildsen (2001) observed a significant amount of variability in the theoretically identical beams. Woolf, Douglas, and French (1998) measured camber of the same 72 in. Bulb Tee beams over the course of a sunny day, when ambient air temperatures increased by 34^{o} Fahrenheit, to observe the effects of solar radiation. The results showed a deflection variation of ½ in. for the same 128 ft-6 in. long beam during the day. Byle, Burns, and Carrasquillo (1997) observed same-beam deflection variation of ½ in. subjected to a 15 degree Fahrenheit temperature variation for Texas Department of Transportation U54 Beams with spans ranging from 110 ft to 125 ft. Kelly, Bradberry, and Breen (1987) measured deflection of AASHTO Type IV beams on a sunny day with temperature variation of 38 degrees Fahrenheit and observed a change of nearly ¼ in. The same beams measured on a cloudy day with a temperature variation of 13 degrees Fahrenheit resulted in an insignificant deflection change. Sanek (2005) monitored thermal camber on a 78 in. Florida Bulb-Tee during the course of a sunny day with high temperature of 85 ^{o}F. Camber was observed to vary by 11/16” during the day, from 7:30 am until 12:30 pm.

2.3.6.2 Curing Method

The method of curing, or even curing conditions, was observed to have a significant effect on several concrete material properties or measured variables. They will be examined individually.

2.3.6.2.1 Compressive Strength and Modulus of Elasticity

Lai, Kahn, et. al. (1999) observed higher compressive strengths in test cylinders that were cured using an insulated method, as opposed to the ASTM standard method. Slapkus and Kahn (2002) cured test cylinders using three different methods: ASTM ambient, insulated, and match-curing. The strengths of the cylinders cured using the insulated method were an average of 35 percent higher than those cured with an ambient method. The match cured cylinder strengths were within approximately 3 percent of the insulated cured cylinder strengths.

Roller, Russell, Bruce, and Hassett (2003) also cast test cylinders, with some being match cured and some being field cured. The beams were instrumented with thermocouples and load cells to collect experimental data. At 20 hours after casting, the average force in the strands decreased almost 11 percent, and decreased nearly 19 percent at 30 hours after casting. It was theorized that this was due to steel relaxation and thermal expansion effects. The thermocouples showed that internal temperatures during curing increased during the first 24 hours and then decreased. Compressive strength testing was performed, and the match cured cylinders exhibited 1000 psi higher strengths than the field cured cylinders at 28 days. The match cured cylinders remained 10 percent higher at 90 days. The measured modulus of elasticity at release for the match cured cylinders was 6 percent higher than that of the field cured cylinders. At 7 days through 90 days and beyond, the measured modulus of elasticity values were virtually identical between the match and field cured cylinders.

Mortensen, Saiidi, and Ladkany (2003) found that the modulus of elasticity for moist-cured cylinders was 20 percent higher than that of cylinders kept in a dry room. Ten high or very high-strength concretes were made for testing by Haque (1996), and test specimens were cured using varying methods. Some were placed in a fog room with nearly 100 percent humidity until testing, some were placed in a fog room for two days and moved to a control room with 40 percent humidity, while the remaining specimens were cured in the fog room for six days before being moved to the control room. The modulus of elasticity testing indicated that the fog room cured concrete had higher values of modulus of elasticity than concrete cured using other methods. Testing at 91 days showed that, regardless of composition, concrete cured exclusively in the fog room

showed higher strengths than concrete cured partly in the fog room and partly in ambient conditions.

A study of temperature effects conducted by Myers and Carrasquillo (1999) showed that test specimens cured with an accelerated heat curing method attained higher early strengths (56 percent), but resulted in lower strengths at later ages (25 percent). The same trend was observed for the modulus of elasticity values: higher accelerated heat curing produced higher early modulus of elasticity, but lower long-term modulus of elasticity compared with non-accelerated heat cured specimens. Testing of paired cylinders by Shams and Kahn (2000) showed that the modulus of elasticity of ASTM moist cured cylinders tended to be lower at earlier ages before converging to similar values after 28 days. Mokhtarzadeh and French (2000) found no difference in compressive strength and modulus of elasticity when curing temperature varied.

2.3.6.2.2 Prestress Losses

Mortensen, Saiidi, and Ladkany (2003) constructed and instrumented two types of normal-weight concrete beams. A single-cell box beam and a solid rectangular beam, were constructed and instrumented to determine prestress losses. The beams were either moist cured or air cured, and were either kept inside under constant temperature and relative humidity or outdoors where there was snow and rain. The indoor beams showed fairly uniform decreasing stresses while the outdoor beams showed oscillation in the stresses. The upward slope of the outdoor beam stresses was thought to be due to the absorption of moisture, causing expansion in the concrete and stresses in the tendons. The dry air of the summer months was thought to contribute to the downward slope of the stresses due to the loss of moisture to the environment, which results in increased shrinkage and decreased strand stresses.

The outdoor moist-cured box beam had measured losses 3 percent less than predicted by AASHTO, while the outdoor air-cured box beam was 15.7 percent higher than the AASHTO prediction. The indoor moist-cured box beam measured losses were 21.5 percent higher than AASHTO predictions, while the indoor air-cured box beam had measured losses 8.9 percent higher than AASHTO predicted. For the solid beams, the outdoor moist-cured beams had measured losses 29 percent lower than predicted by

AASHTO while the outdoor air-cured beam measured losses were 68 percent lower than the predicted values. Moist curing was observed to have a greater effect in reducing losses if there is continued moisture after the initial curing period. The effects of initial moist-curing became less observable when the presence of moisture was removed following the initial curing period.

Shams and Kahn (2000) measured prestress losses in instrumented beams. The results indicated that losses stabilized during winter months and increased in the spring, corresponding with a temperature increase. When the temperature dropped below 60^{o} F, losses were negligible, before increasing again with warmer temperatures. The rate of losses in the beams under controlled conditions decreased continuously over the entire monitoring period. The experimental data suggested that prestress losses in cold climates may be less than in warmer climates.

2.3.6.2.3 Shrinkage

Shrinkage testing was performed by Stallings and Glover (2000) using several different curing methods. One shrinkage specimen sample was air dried for a period of 90 days while another sample was moist cured for 28 days, and then air dried for up to 90 days. The air dried specimens showed higher shrinkage values than did the specimens that were initially moist cured. Collins (1989) observed that specimens moist cured for 7 days exhibited more shrinkage than those moist cured for 28 days. Lai, Kahn, Travis, et al. (1999) found that the shrinkage strain of moist cured cylinders was less than that of insulated cured cylinders. Mokhtarzadeh and French (2000) found that drying shrinkage decreased as concrete curing temperatures increased, since there is less free water to lose.

Torrenti, Granger, Diruy, and Genin (1999) examined a beam composed of non-reinforced concrete, with a cross section of 1m x 30 cm and a length of 3 m, to determine the effects of variable ambient conditions on shrinkage. The beam was cast in 1979 and has been kept outside, sheltered from the rain, ever since. It is instrumented with 21 vibrating wire gages in the middle of the section, 10 strain gages on the surface, and 31 temperature probes. The experiment found that temperature had a minimal effect on variations in the thermal expansion coefficient, however variations in humidity were

observed to have a strong influence. The variations in the thermal expansion coefficient were also observed to follow the variation pattern on shrinkage in the beam.

2.3.6.2.4 Creep

Mokhtarzadeh and French (2000) utilized two different curing methods: moist curing and accelerated heat curing. Moist curing reduced the effect of varying the type of coarse aggregate or type of cement with respect to creep. Lai, Kahn, Travis, et al. (1999) observed that moist cured cylinders underwent a higher rate of specific creep at early ages than did insulated cured cylinders.

2.3.7 Age at Release

If two identical prestressed concrete beams are cast and one is released significantly earlier compared with the other, it could be expected for the first beam to deflect more than the beam released at a later age. This is because the concrete in the first beam would have a lower modulus of elasticity (due to being in the bed for a shorter period of time) than the second beam at the time of prestress transfer. This should also result in the camber of the younger beam being greater than the camber of the older beam at all ages, since it will exhibit a lower modulus of elasticity than the older beam at each time period following release.

Kelly, Bradberry, and Breen (1987) found that camber of an otherwise identical beam released 4 days after the first beam had a camber difference of approximately ½ in. throughout the construction period and service life of the beam.

2.4 SUMMARY OF PREVIOUS RESEARCH

The results observed by various researchers are more easily compared in tabular format. A summary of research results for modulus of elasticity is presented in Table 2.3. A summary of research results for creep coefficient and shrinkage strain is presented in Tables 2.4 and 2.5, respectively. Finally, a summary of research results related to prestress losses is presented in Table 2.6.

Table 2.3 Modulus of Elasticity Research Results

		Ahlborn, French and Shield (2000)	Byle, Burns, and Carrasquillo (1997)	Huo (1997)	Kelly, Bradberry, and Breen (1987)	Stallings and Glover (2000)	Baalbaki, Aitcin, and Ballivy (1992)	Woolf and French (1998)	Waldron (2004)
Info	Concrete Strength (psi)	10500	11600	12000	6500	10000	13,000	8000 to 18600	8700
	C/A Ratio	0.23 / 0.22	0.22	0.35	Unavail.	0.31	0.27	N/A	0.33
	W/C Ratio	0.32 / 0.36	0.28	0.24	0.38	0.29	0.27	0.28 to 0.32	0.30
Model	AASHTO-LRFD	-	-	under [2]	good match	-	-	-	over
	AASHTO-Standard	-	over [1]	under	-	-	-	-	-
	ACI-209	-	-	-	-	-	-	-	-
	ACI-318	over	-	-	-	over	-	over	-
	ACI-363	over	under	under	under	under	good match [3]	good match	over
	CEB-MC90	-	-	-	-	-	over	good match	-

1 "over" indicates the model over predicted the measured values
2 "under" indicates the model under predicted the measured values
3 "good match" indicates the model predicted the measured values well
4 "mixed" indicates the model matched some measured values but not others
- "indicates the model was not examined by the research study

Table 2.3 Modulus of Elasticity Research Results (continued)

		Lai, Kahn, et. al (1999)	Huo, Al-Omaishi, and Tadros (2001)	Mokarem (2002)	Will and Sanders (2000)	Townsend (2003)	Slapkus and Kahn (2002)
Info	Concrete Strength (psi)	10000	8000 to 12000	5,000	5000	8000	14,000
	C/A Ratio	0.39	Varied	0.19	Unavail.	0.29	0.38
	W/C Ratio	0.35	Varied	0.33 to 0.39	0.40	0.30	0.24
Model	AASHTO-LRFD	-	under [2]	-	over [1]	over	-
	AASHTO-Standard	-	under	-	-	-	-
	ACI-209	-	-	-	-	-	-
	ACI-318	over	-	good match [3]	over	-	over
	ACI-363	over	under	-	over	under	over
	NCHRP 496	-	good match	-	-	over	-

1 "over" indicates the model over predicted the measured values
2 "under" indicates the model under predicted the measured values
3 "good match" indicates the model predicted the measured values well
4 "mixed" indicates the model matched some measured values but not others
- "indicates the model was not examined by the research study

Table 2.4 Creep Research Results

		Ahlborn, French and Shield (2000)	Byle, Burns, and Carrasquillo (1997)	Huo (1997)	Meyerson (2001)	Stallings and Eskildsen (2000)	Woolf and French (1998)
Info	Concrete Strength (psi)	10500	11600	12000	6,000 to 7,400	10000	8000 to 18600
	C/A Ratio	0.23 / 0.22	0.22	0.35	0.23 to 0.25	0.31	N/A
	W/C Ratio	0.32 / 0.36	0.28	0.24	0.31 to 0.39	0.29	0.28 to 0.32
Model	ACI-209	-	over [1]	over	over	over	good match [3]
	ACI-318	over	-	-	-	-	-
	ACI-363	over	-	-	-	-	-
	Bazant B3	-	-	-	over	-	-
	CEB-MC90	-	-	-	over	-	-
	Gardner-Lockman	-	-	-	over	-	-
	JSCE (2002)	-	-	-	over	-	-
	PCI (1975)	-	-	-	-	-	-

1 "over" indicates the model over predicted the measured values
2 "under" indicates the model under predicted the measured values
3 "good match" indicates the model predicted the measured values well
4 "mixed" indicates the model matched some measured values but not others
- "indicates the model was not examined by the research study

Table 2.4 Creep Research Results (continued)

		Lai, Kahn, et. al (1999)	Farrington, Burns, and Carrasquillo (1996)	Stallings and Glover (2000)	Townsend (2003)	Huo, Al-Omaishi, and Tadros (2001)	Slapkus and Kahn (2002)	Waldron (2004)
Info	Concrete Strength (psi)	10,000	13,000	10000	8000	8000 to 12000	14,000	8700
	C/A Ratio	0.39	0.35	0.31	0.29	Varied	0.38	0.33
	W/C Ratio	0.35	0.28	0.29	0.30	Varied	0.24	0.30
Model	AASHTO-LRFD	-	-	-	over	over	-	good match [3]
	ACI-209	over [1]	over	over	over	over	over	-
	ACI-209 mod. by Huo	-	-	-	over	-	-	-
	Bazant B3	-	-	-	over	-	-	over
	CEB-MC90	-	-	-	over	-	-	-
	Gardner-Lockman	-	-	-	over	-	-	over
	Shams and Kahn	-	-	-	-	-	under [2]	under
	NCHRP 496	-	-	-	over	good match	-	good match

1 "over" indicates the model over predicted the measured values
2 "under" indicates the model under predicted the measured values
3 "good match" indicates the model predicted the measured values well
4 "mixed" indicates the model matched some measured values but not others
- "indicates the model was not examined by the research study

Table 2.5 Shrinkage Research Results

		Ahlborn, French and Shield (2000)	Byle, Burns, and Carrasquillo (1997)	Huo (1997)	Stallings and Eskildsen (2000)	Stallings and Glover (2000)	Woolf and French (1998)
Info	Concrete Strength (psi)	10500	11600	12000	10000	10000	8000 to 18600
	C/A Ratio	0.23 / 0.22	0.22	0.35	0.31	0.31	N/A
	W/C Ratio	0.32 / 0.36	0.28	0.24	0.29	0.29	0.28 to 0.32
Model	ACI-209	-	over	over	over	over	over
	ACI-318	over [1]	-	-	-	-	-
	ACI-363	over	-	-	-	-	-
	PCI (1975)	-	-	-	-	-	-

1 "over" indicates the model over predicted the measured values
2 "under" indicates the model under predicted the measured values
3 "good match" indicates the model predicted the measured values well
4 "mixed" indicates the model matched some measured values but not others
- "indicates the model was not examined by the research study

Table 2.5 Shrinkage Research Results (continued)

		Lai, Kahn, et. al (1999)	Farrington, Burns, and Carrasquillo (1996)	Slapkus and Kahn (2002)	Huo, Al-Omaishi, and Tadros (2001)	Mokarem (2002)	McDonald and Roper (1993)	Townsend (2003)	Waldron (2004)	Meyerson (2001)
Info	Concrete Strength (psi)	10,000	13,000	14,000	8000 to 12000	5,000	7,250	8000	8700	6,000 to 7,400
	C/A Ratio	0.39	0.35	0.38	Varied	0.19	Unavail.	0.29	0.33	0.23 to 0.25
	W/C Ratio	0.35	0.28	0.24	Varied	0.33 to 0.39	0.47	0.30	0.30	0.31 to 0.39
Model	AASHTO-LRFD	-	-	-	over	-	-	over	over	-
	ACI-209	over [1]	over	over	over	-	over	over	over	under
	ACI-209 mod. by Huo	-	-	-	-	-	-	over	-	-
	Bazant B3	-	-	-	-	under	over	under	-	under
	CEB-MC90	-	-	-	-	under	over	under	under	under
	Gardner-Lockman	-	-	-	-	under	-	over	over	under
	JSCE (2002)	-	-	-	-	over	-	-	-	under
	Shams and Kahn	-	-	under [2]	-	-	-	-	over	-
	NCHRP 496	-	-	-	good match	-	-	over	over	-

1 "over" indicates the model over predicted the measured values
2 "under" indicates the model under predicted the measured values
3 "good match" indicates the model predicted the measured values well
4 "mixed" indicates the model matched some measured values but not others
- "indicates the model was not examined by the research study

Table 2.6 Prestress Losses Research Results

		Ahlborn, French and Shield (2000)	Barr, Fekete, Eberhard, Stanton, Khaleghi, and Hsieh (2000)	Byle, Burns, and Carrasquillo (1997)	Huo, Al-Omaishi, and Tadros (2001)	Huo (1997)	Kelly, Bradberry, and Breen (1987)	Waldron (2004)	Stallings and Eskildsen (2001)
Info	Concrete Strength (psi)	10500	10000	11600	8000 to 12000	12000	6500	8700	10000
	C/A Ratio	0.23 / 0.22	0.25	0.22	Varied	0.35	Unavail.	0.33	0.31
	W/C Ratio	0.32 / 0.36	0.36	0.28	Varied	0.24	0.38	0.30	0.29
Model	AASHTO-LRFD	-	under [2]	-	over	over	-	over	under
	AASHTO-Standard	under	-	over [1]	-	over	over	-	under
	ACI-209	-	-	-	-		-	over	-
	Bazant B3	-	-	-	-	-	-	over	-
	CEB-MC90	-	-	-	-	-	-	over	-
	Gardner-Lockman	-	-	-	-	-	-	over	-
	NCHRP 496	-	-	-	good match	-	-	over	-
	PCI (1975)	under	under	-	-	-	under	-	-
	PCI Design Handbook	under	-	over	mixed	-	-	good match [3]	-
	Shams and Kahn	-	-	-	-	-	-	under	-

1 "over" indicates the model over predicted the measured values
2 "under" indicates the model under predicted the measured values
3 "good match" indicates the model predicted the measured values well
4 "mixed" indicates the model matched some measured values but not others
- "indicates the model was not examined by the research study

2.5 CONCLUSION

Although many prediction models are available, researchers have not reached consensus on which models are the best. Indeed, many researchers have shown conflicting results. Since designers are faced with situations that increasingly "push the envelope", such as high concrete strength, long spans, widely spaced beams, and high levels of prestressing, the choice of a representative model becomes important. Prestress losses and camber may be significantly over or underestimated based on the model chosen.

This study attempts to provide additional clarification concerning the different conditions in which particular models should perhaps be used. There are many variables based on material properties or curing conditions that are already considered by many of the models. Additional variables such as time of day, season, and climate at different geographic locations have not been widely studied as variables. It is important to examine the effects of some of these variables in order to gain a better understanding of camber growth in prestressed concrete beams.

CHAPTER 3. METHODS AND MATERIALS

3.1 INTRODUCTION

To investigate the suitability of currently available methods to predict initial camber and camber growth of long-span, high-strength prestressed concrete beams, 27 beams from the new Cooper River Bridge approach spans were studied. The Cooper River Bridge is an eight-lane, cable-stayed bridge located near downtown Charleston, SC connecting a vital commuter suburb to the Charleston Peninsula, which is surrounded on both sides by the Cooper and Ashley Rivers. Due to constraints imposed by existing buildings, roads, and creeks, the approach spans vary from approximately 120 ft. to 140 ft. The bents are also skewed to avoid these obstacles, creating a variety of beam lengths.

With 25 spans on the mainline of the approach and several ramps providing access to the bridge, the total number of beams exceeds 300. The large number of beams to be fabricated allowed for measurements to be taken on beams cast in different seasons, and with different beam lengths. Additionally, the bridge contractor kept all beams at the precast yard until they were ready to be set (see Figure 3.1). This meant that many of the beams produced early in the project would be accessible for many months until the contractor was ready for them. On smaller projects, the precaster prefers to ship the beams fairly soon after production in order to free up storage space in the yard. In order to meet the contractor's set schedule, the precaster was forced to get a head start on production and allow the beams to accumulate in the yard instead of casting on a just-in-time basis (See Figure 3.1).

Figure 3.1: Beams Stored in the Casting Yard

In addition to the long beam lengths, the beam spacing exceeded 13 ft. on many of the spans. The framing plans for the spans of the bridge including the studied beams are shown below in Figures 3.2 through 3.12. The beams included in the study are indicated with heavier outlines in the following figures.

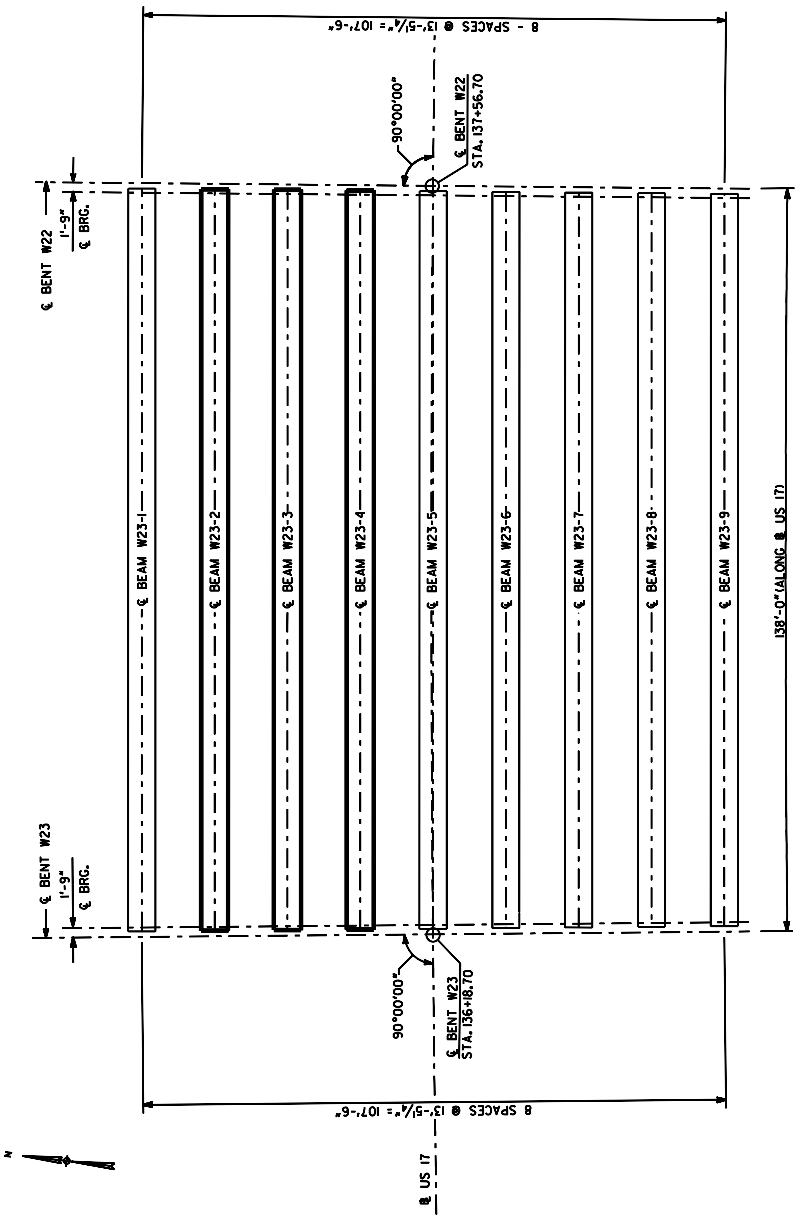

Figure 3.2: Span W23 Framing Plan

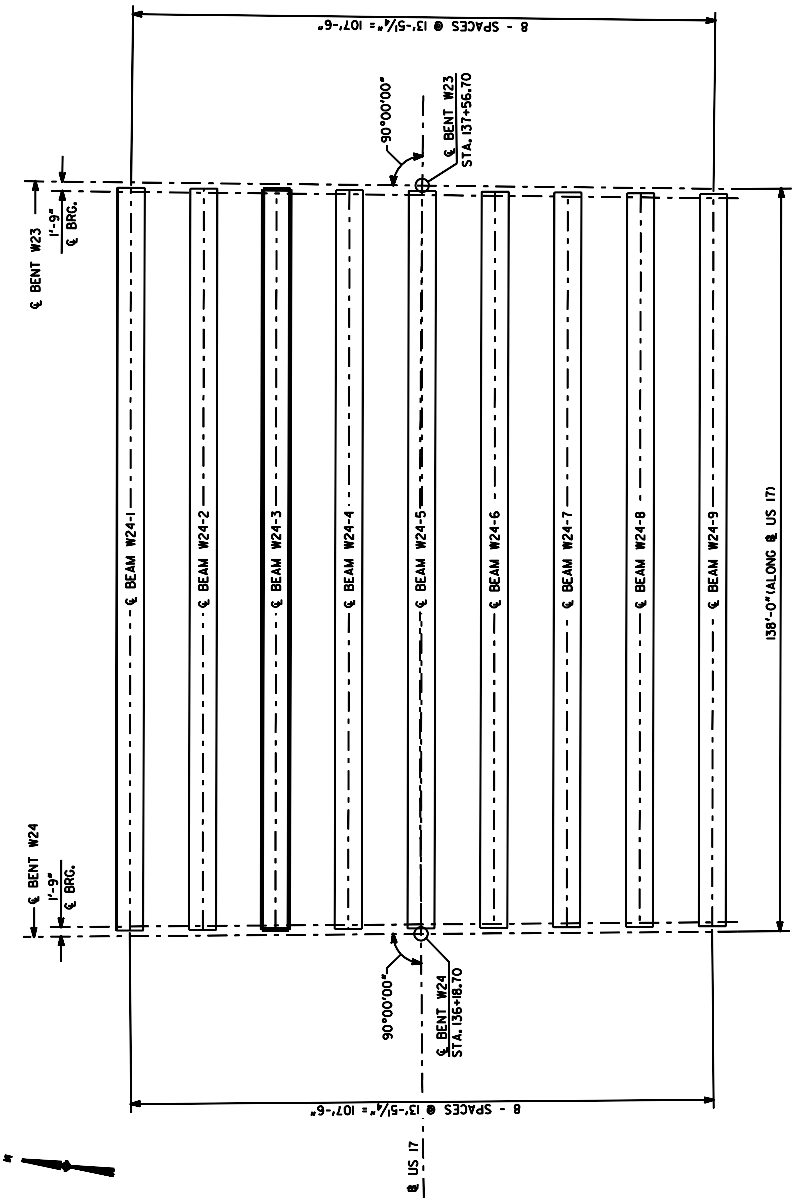

Figure 3.3: Span W24 Framing Plan

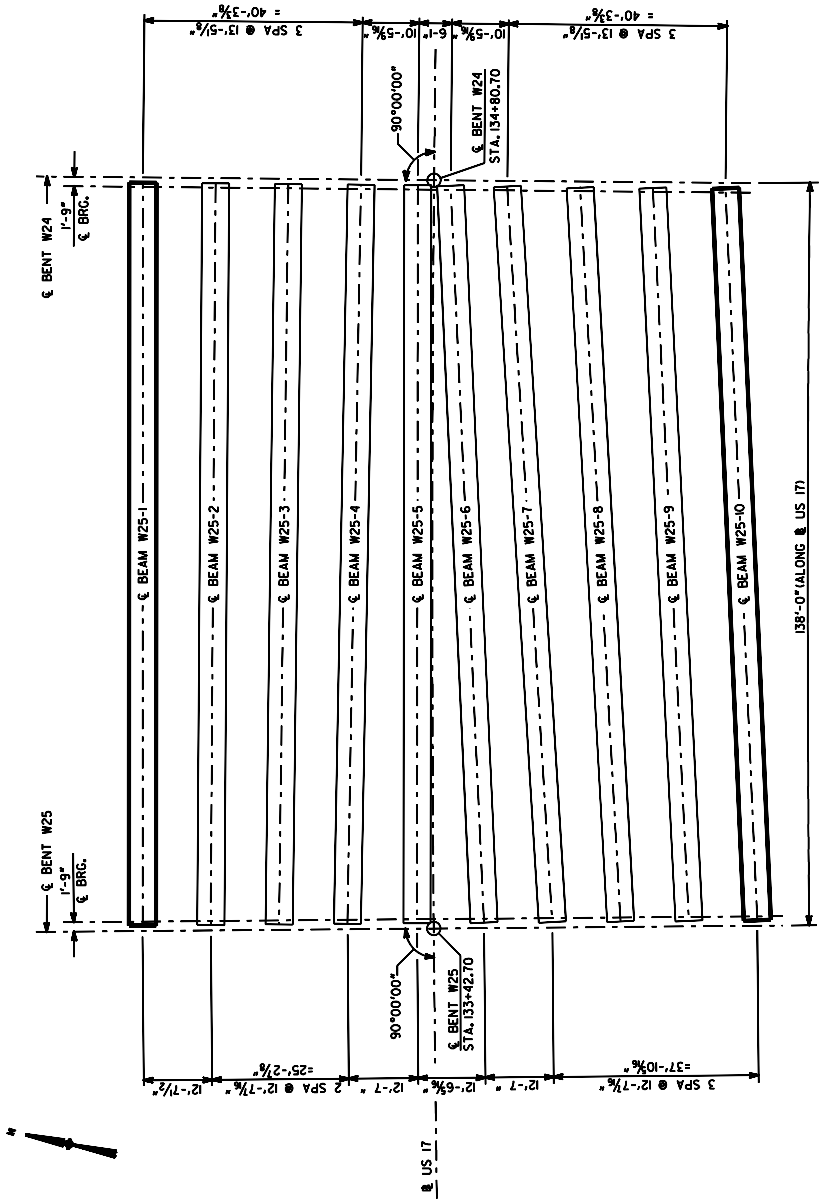

Figure 3.4: Span W25 Framing Plan

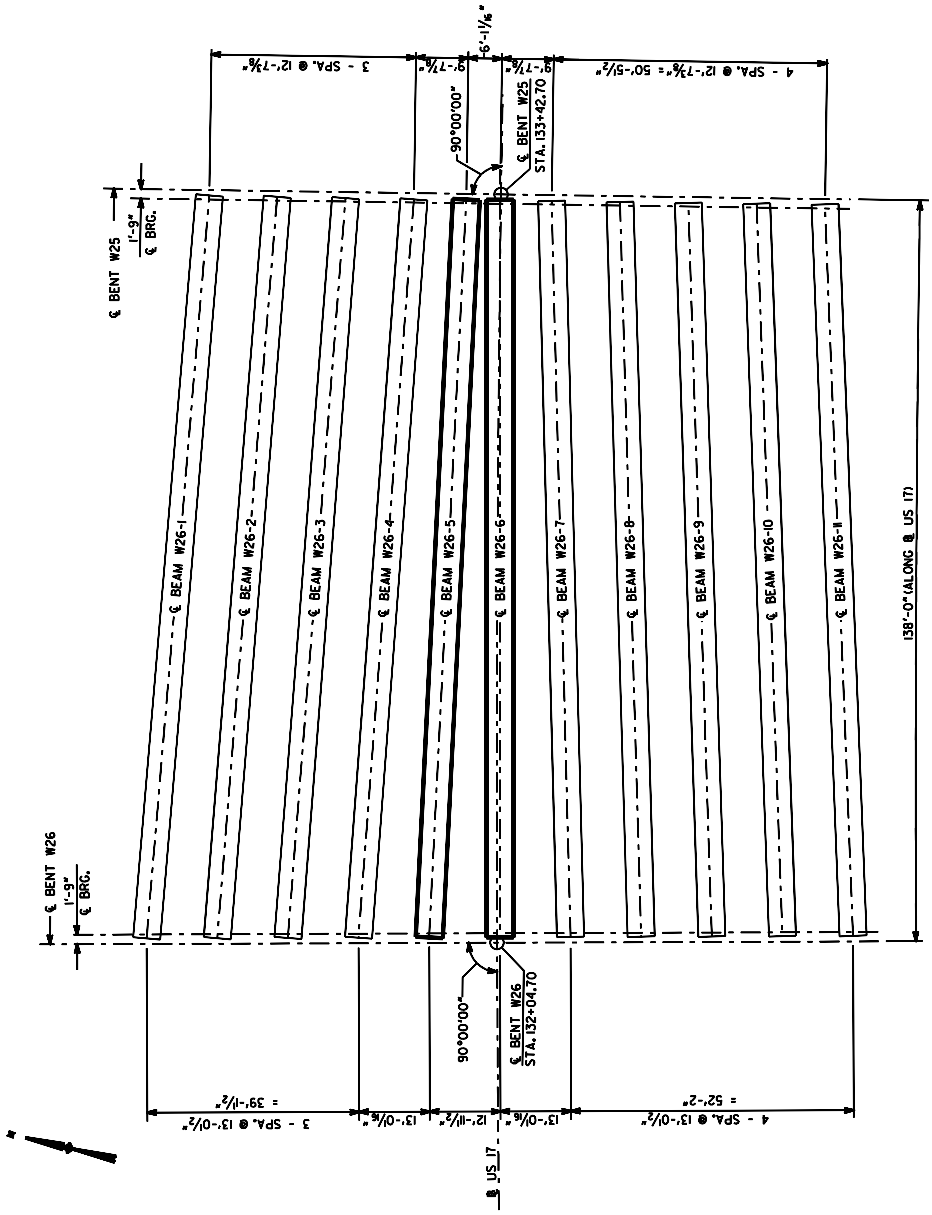

Figure 3.5: Span W26 Framing Plan

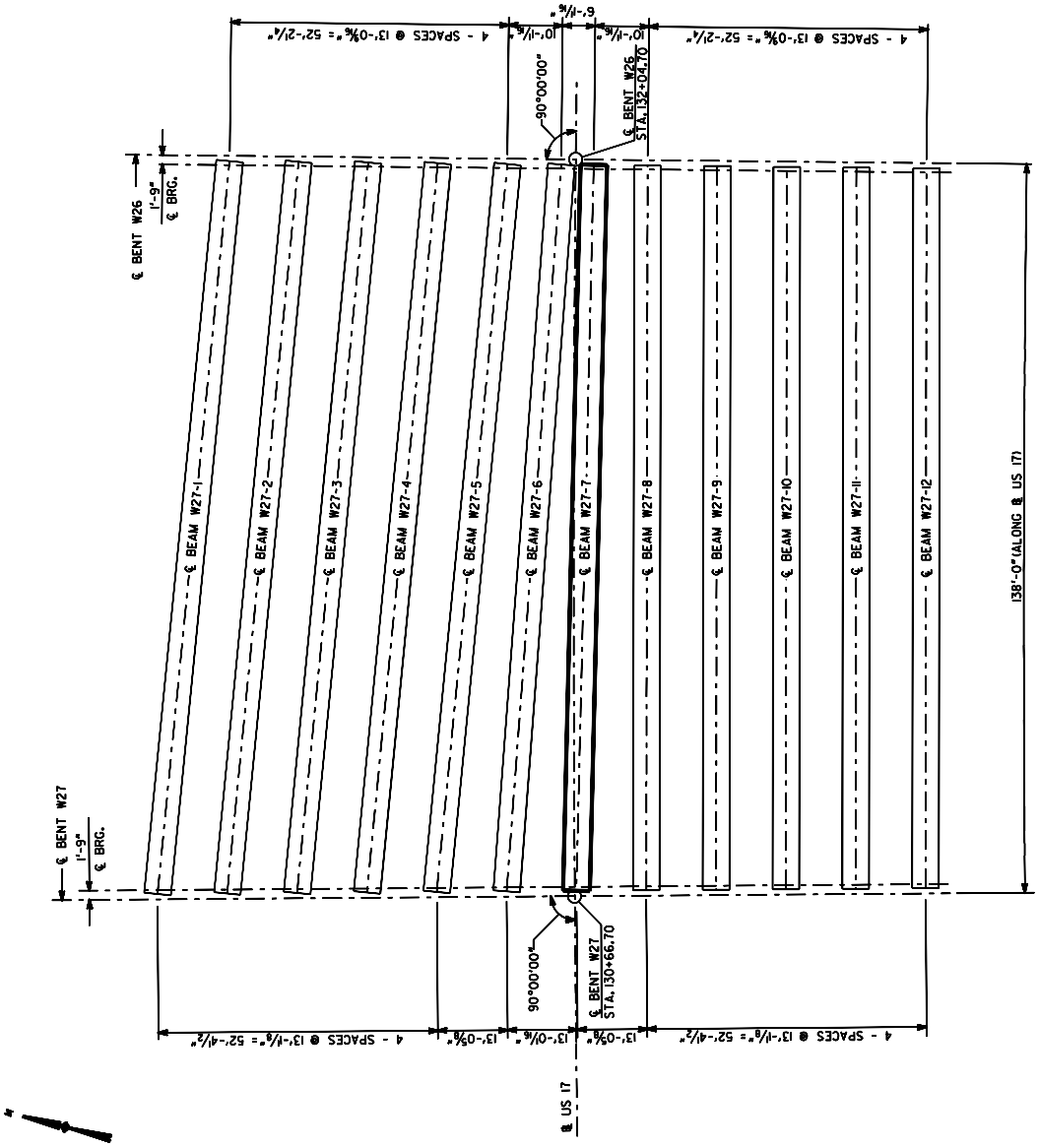

Figure 3.6: Span W27 Framing Plan

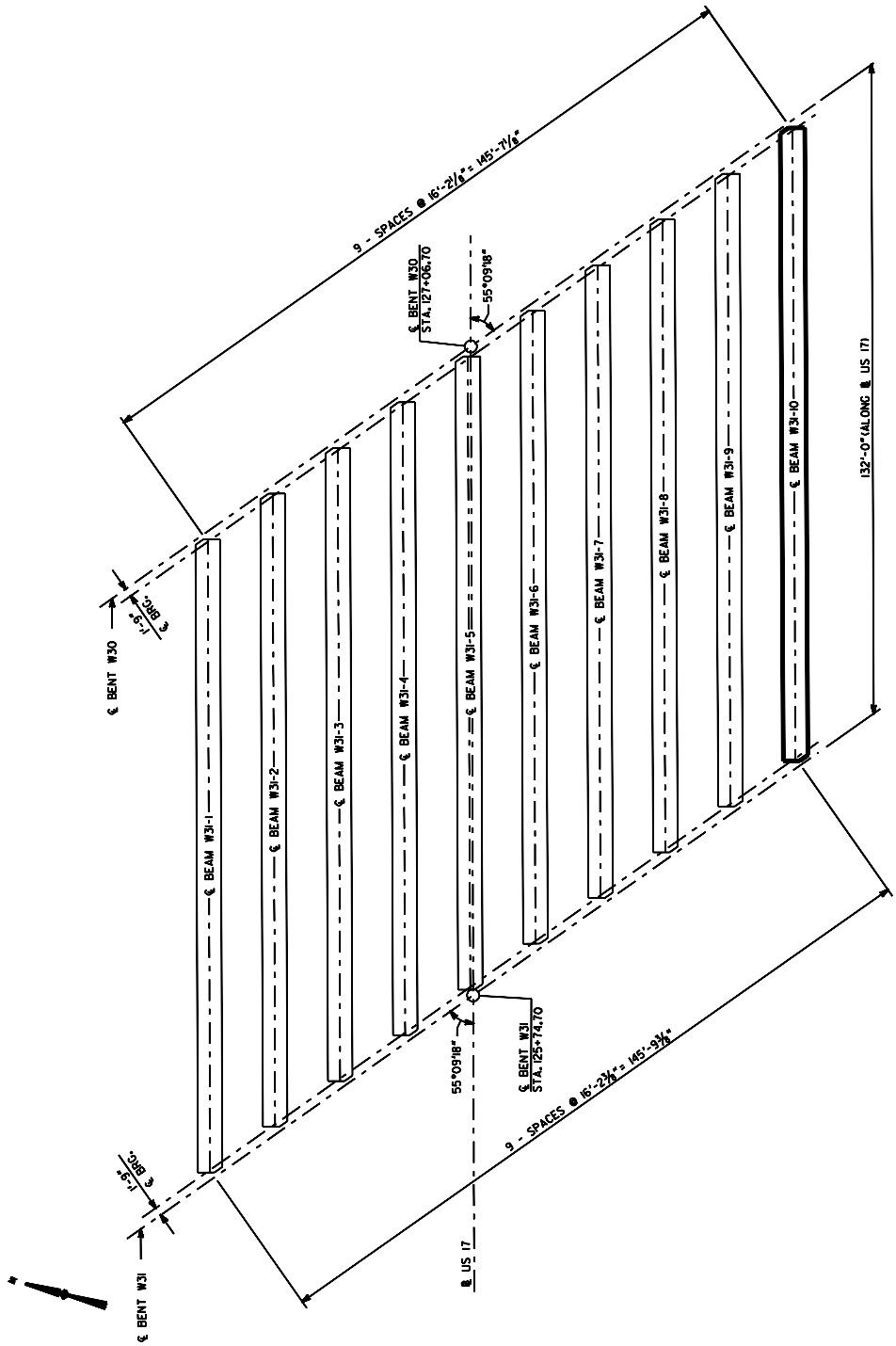

Figure 3.7: Span W31 Framing Plan

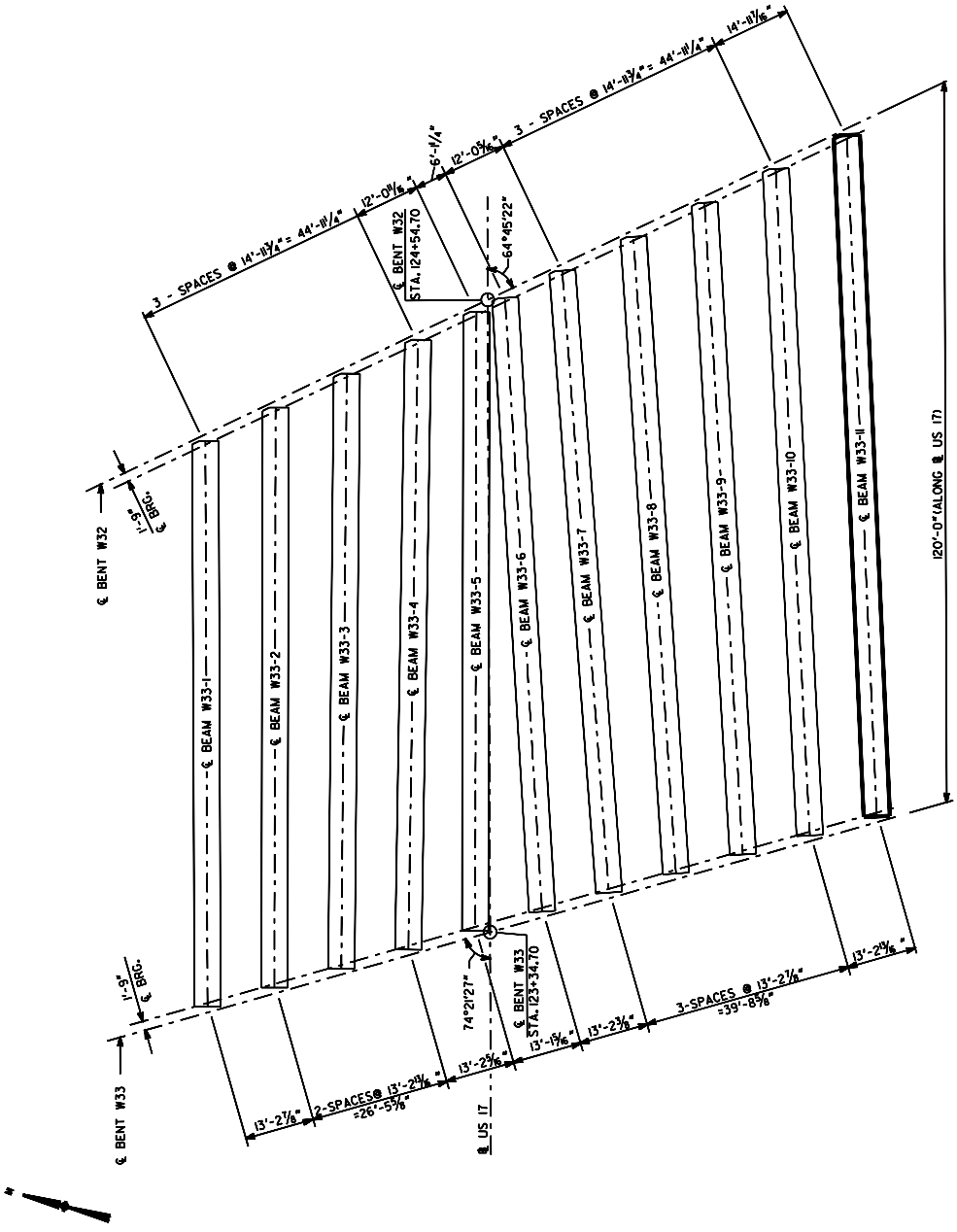

Figure 3.8: Span W33 Framing Plan

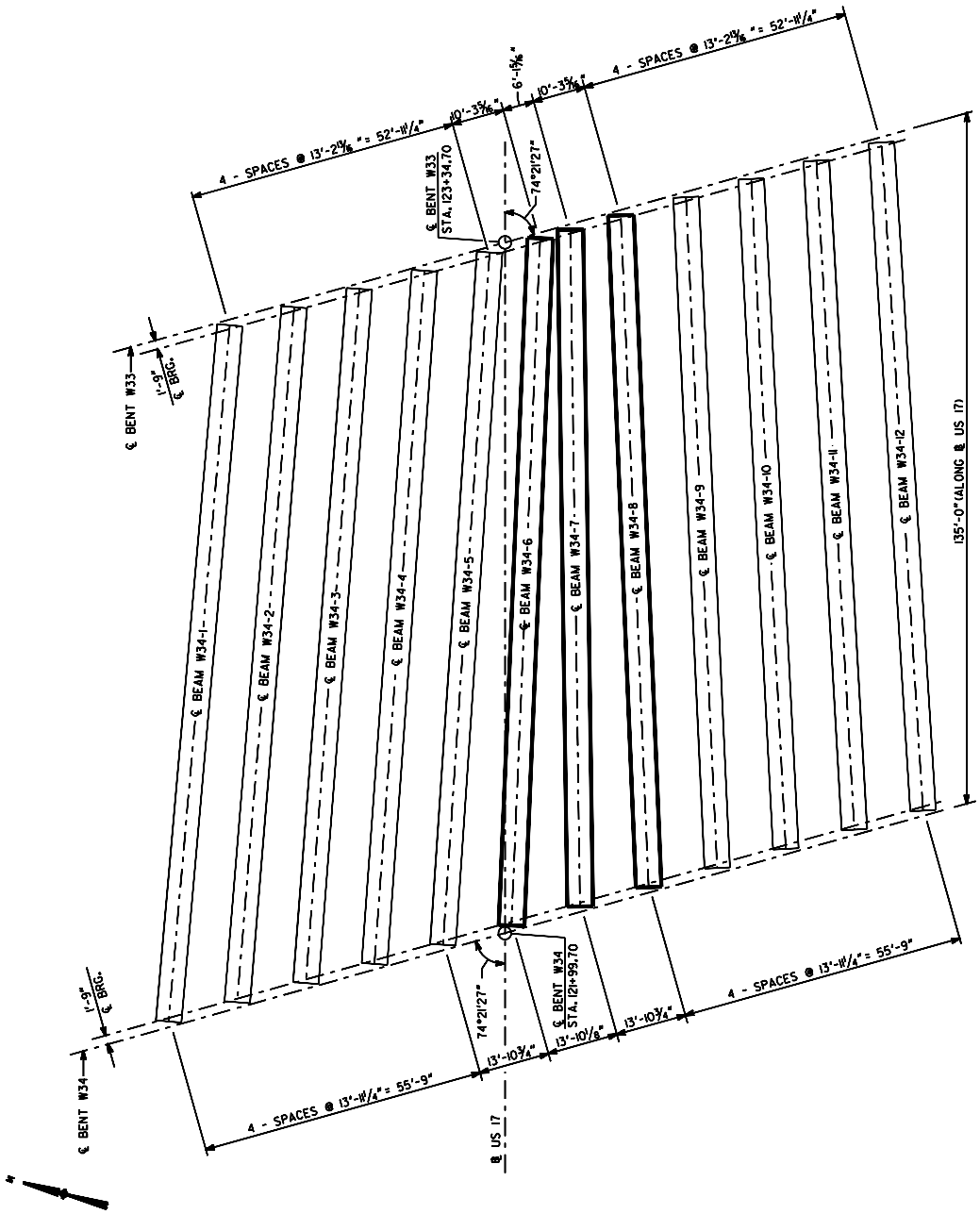

Figure 3.9: Span W34 Framing Plan

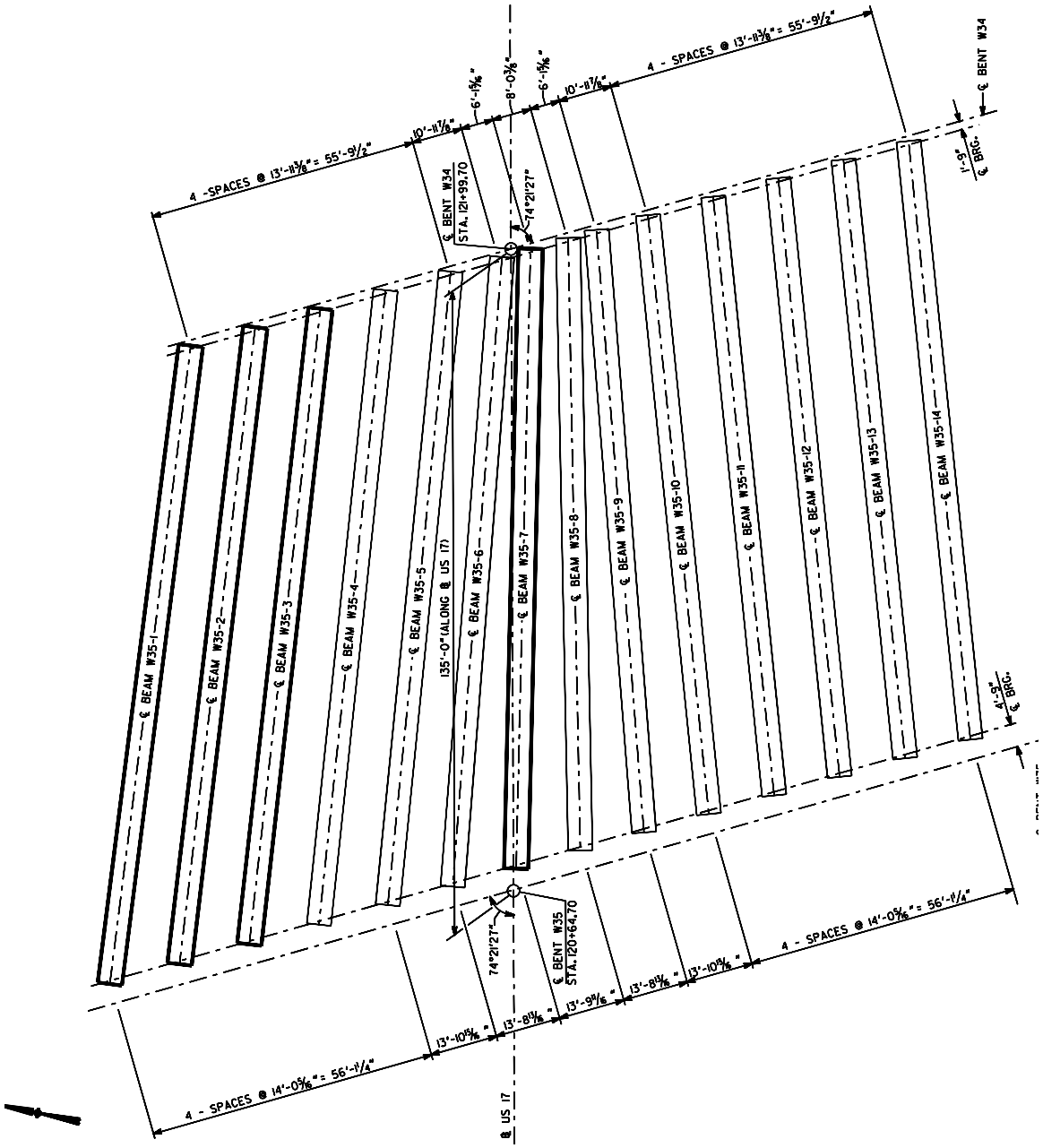

Figure 3.10: Span W35 Framing Plan

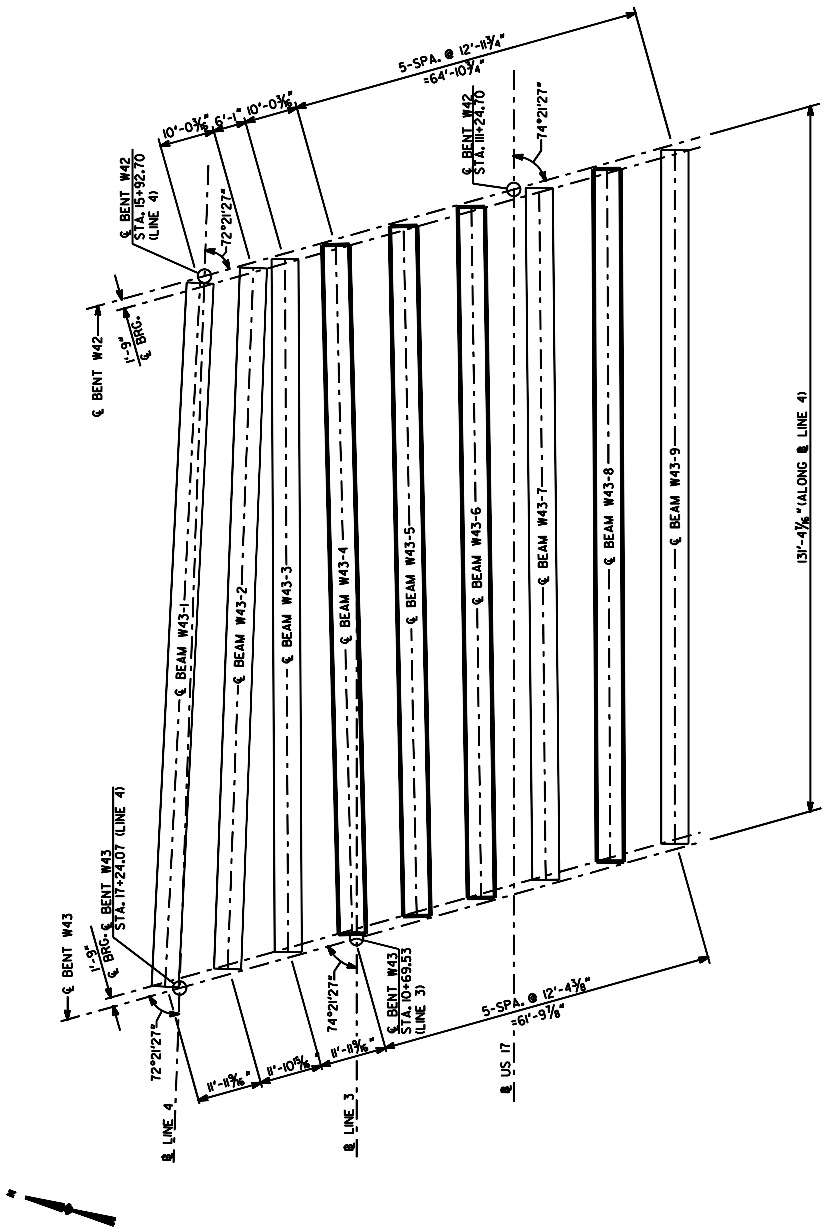

Figure 3.11: Span W43 Framing Plan

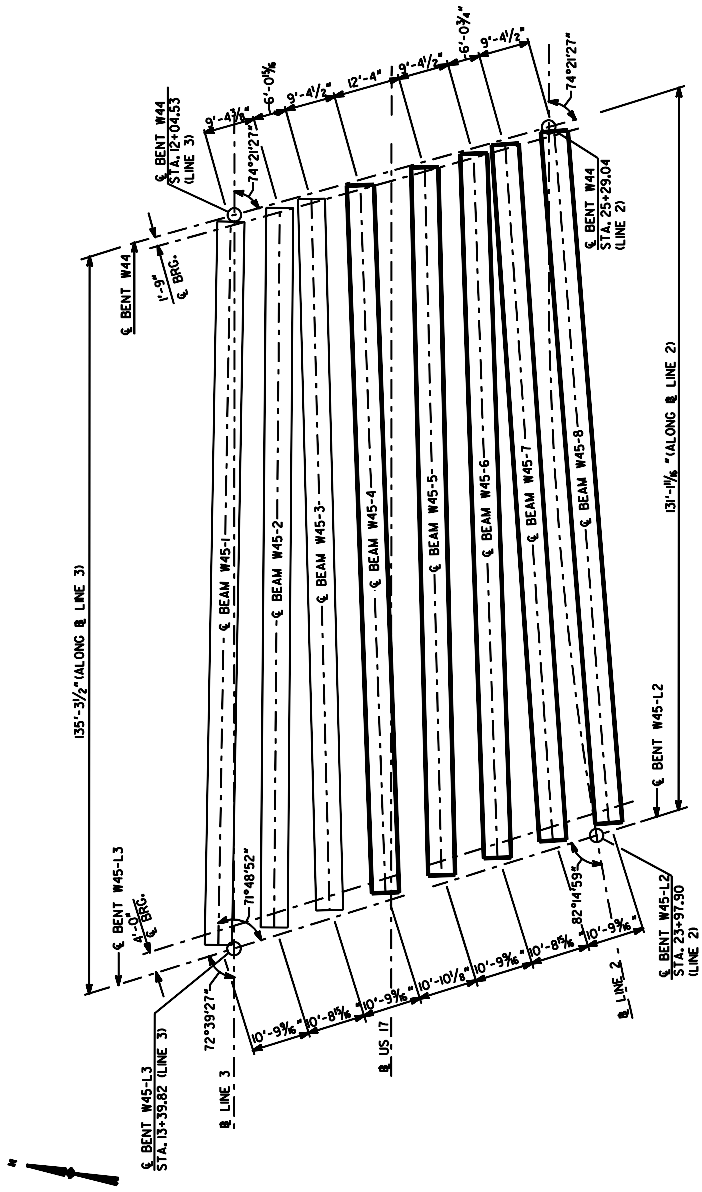

Figure 3.12: Span W45 Framing Plan

3.2 BEAM CONFIGURATION AND MATERIAL PROPERTIES

3.2.1 Beam Cross-Section

All of the prestressed concrete beams measured for deflection in this study were modified Bulb-Tees with a total depth of 79 in. The beam shape and dimensions are shown in Figure 3.13.

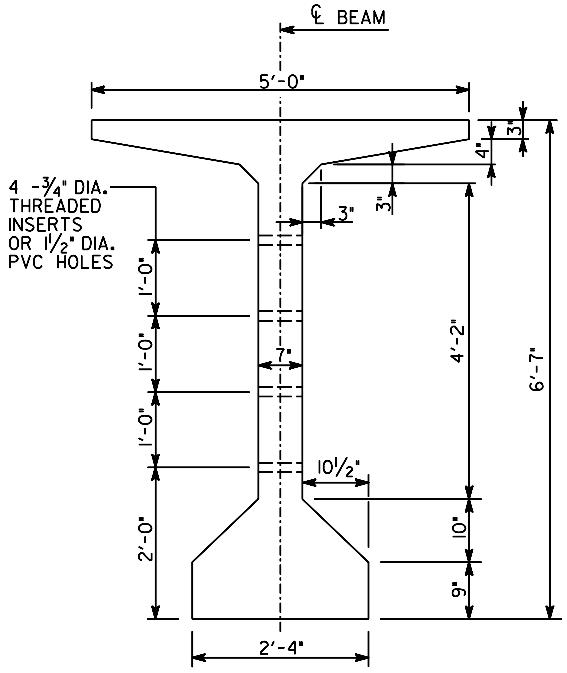

Figure 3.13: 79 in. Modified Bulb Tee

3.2.2 Concrete Mixture

The beams were made with normal weight High Performance Concrete with a 28 day design strength of 9000 psi and a release strength of 6100 psi. The actual concrete strength as determined by cylinder breaks was much higher and is presented later. Summaries of the materials and the mix design are included in Tables 3.1 and 3.2. The produced concrete mix was intended to meet the criteria shown in Table 3.3. The actual fresh concrete properties for each concrete batch are shown in Table 3.10.

Table 3.1: Source of Materials

Component	Source	Type	Specific Gravity	Test Standard
Cement	Lafarge, Harleyville, SC	Type III (II)	3.14 S.G.	ASTM C150
Flyash	Southeastern	Type F	2.20 S.G.	ASTM C618
Coarse Aggregate	Martin-Marietta Granite	#67	2.66 S.G.	ASTM C33
Fine Aggregate	Deerfield	-	2.63 S.G.	ASTM C33
Water Reducing Admixture	W.R. Grace WRDA 64	Type A/D	-	ASTM C494
High-Range Water Reducing Admixture	W.R. Grace ADVA Flow	Type F/G	-	ASTM C494

Table 3.2: Mix Design

Component	Material per Cubic Yard	Absolute Volume	Percent
Cement	770 lb/yd^3	3.93 ft^3	15.5%
Flyash	164 lb/yd^3	1.19 ft^3	4.7%
Coarse Aggregate	1900 lb/yd^3	11.45 ft^3	45.3%
Fine Aggregate	862 lb/yd^3	5.25 ft^3	20.8%
Water Reducing Admixture	38.0 oz/yd^3	-	-
High-Range Water Reducing Admixture	65.2 oz/yd^3	-	-
Mix Water	33.5 gal/yd^3	-	-
Mix Water	279.0 lb/yd^3	3.47 ft^3	13.7%
Design Water	33.5 gal/yd^3	-	-
Design Water	279.0 lb/yd^3	-	-
Total	**3975.0 lb/yd^3**	**27.37 ft^3**	**100%**

Table 3.3: Mix Design Target Criteria

Slump Range	4.0 in. to 9.0 in.
Air Content	0.0% to 4.5%
Unit Weight	145.23 lb/ft^3
Water/Cement Ratio	0.30 lb/lb
Temperature Range	50 ^{o}F to 100 ^{o}F

3.2.3 Beam Length and Strand Patterns

The measured beams were grouped into major samples based on the strand pattern. The beams were further sub-grouped according to beam length, and then cast date. The sample sizes were maximized as much as possible so that the behavior of groups of similar beams could be observed. Figures 3.14 through 3.17 show the different strand patterns and structural plans for all the beams studied. Tables 3.4 through 3.6 detail the major sample grouping, separated by strand pattern and sorted by increasing beam length.

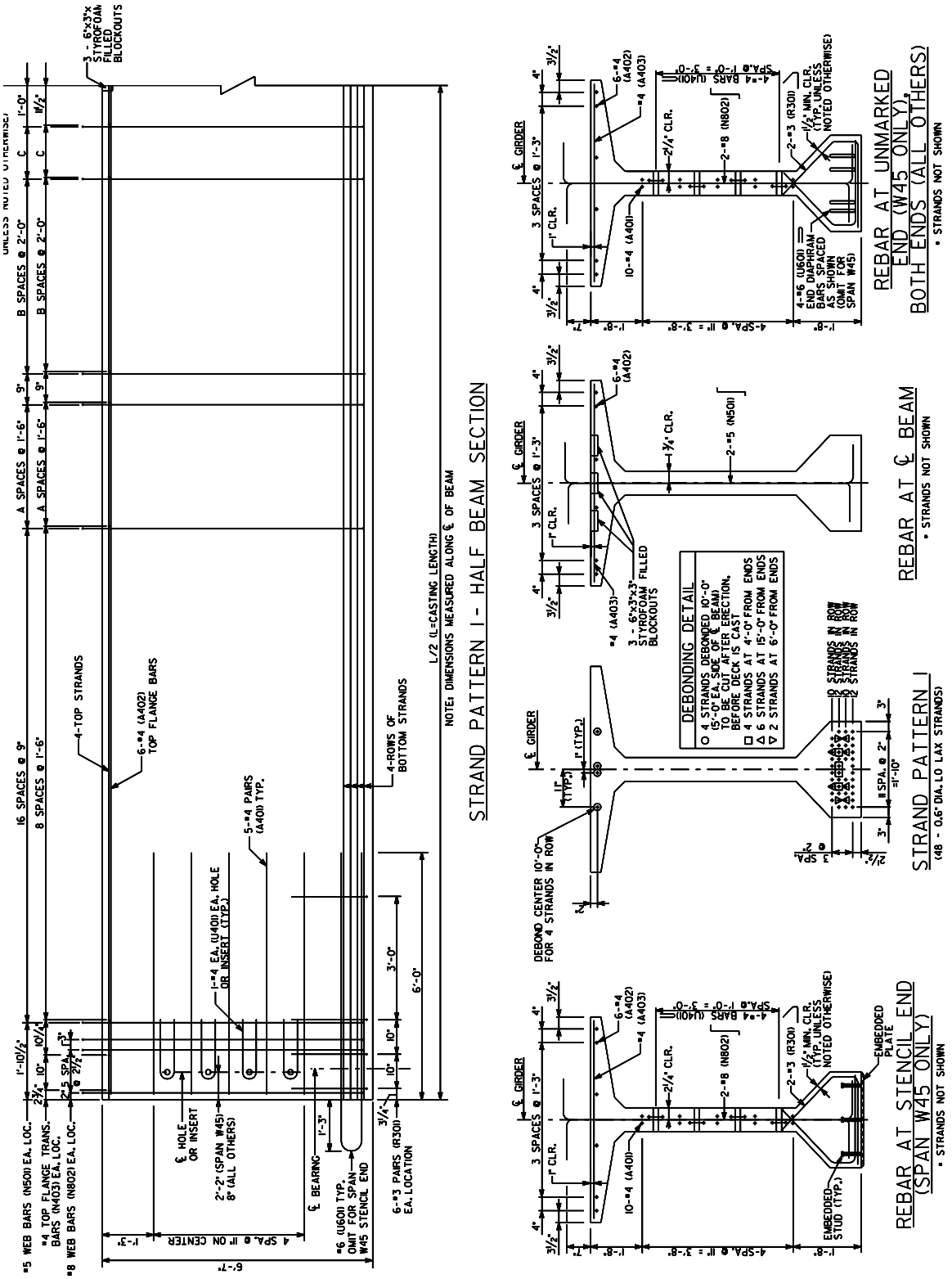

Figure 3.14: Strand Pattern 1 Beam (48 Straight Strands)

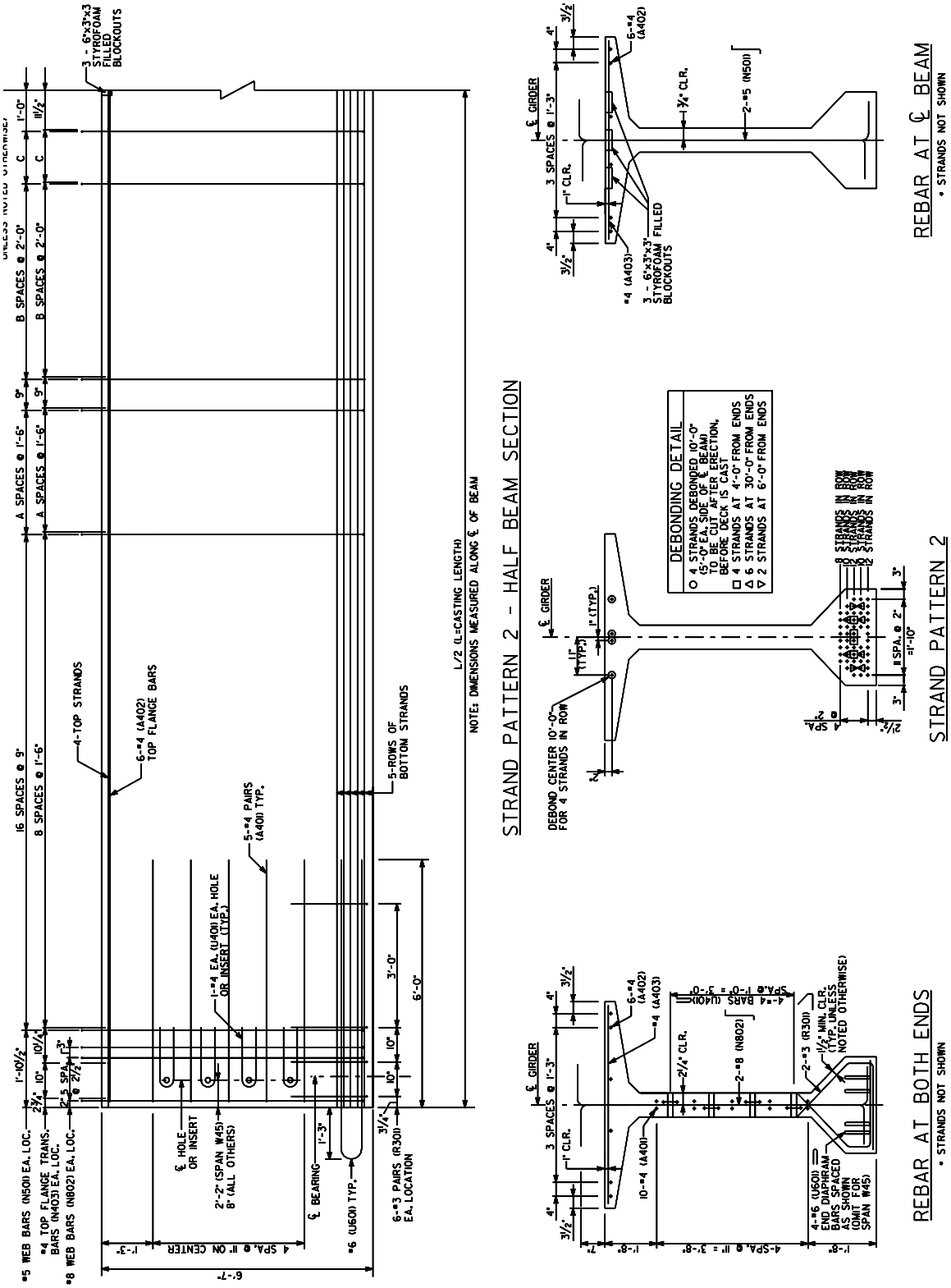

Figure 3.15: Strand Pattern 2 Beam (56 Straight Strands)

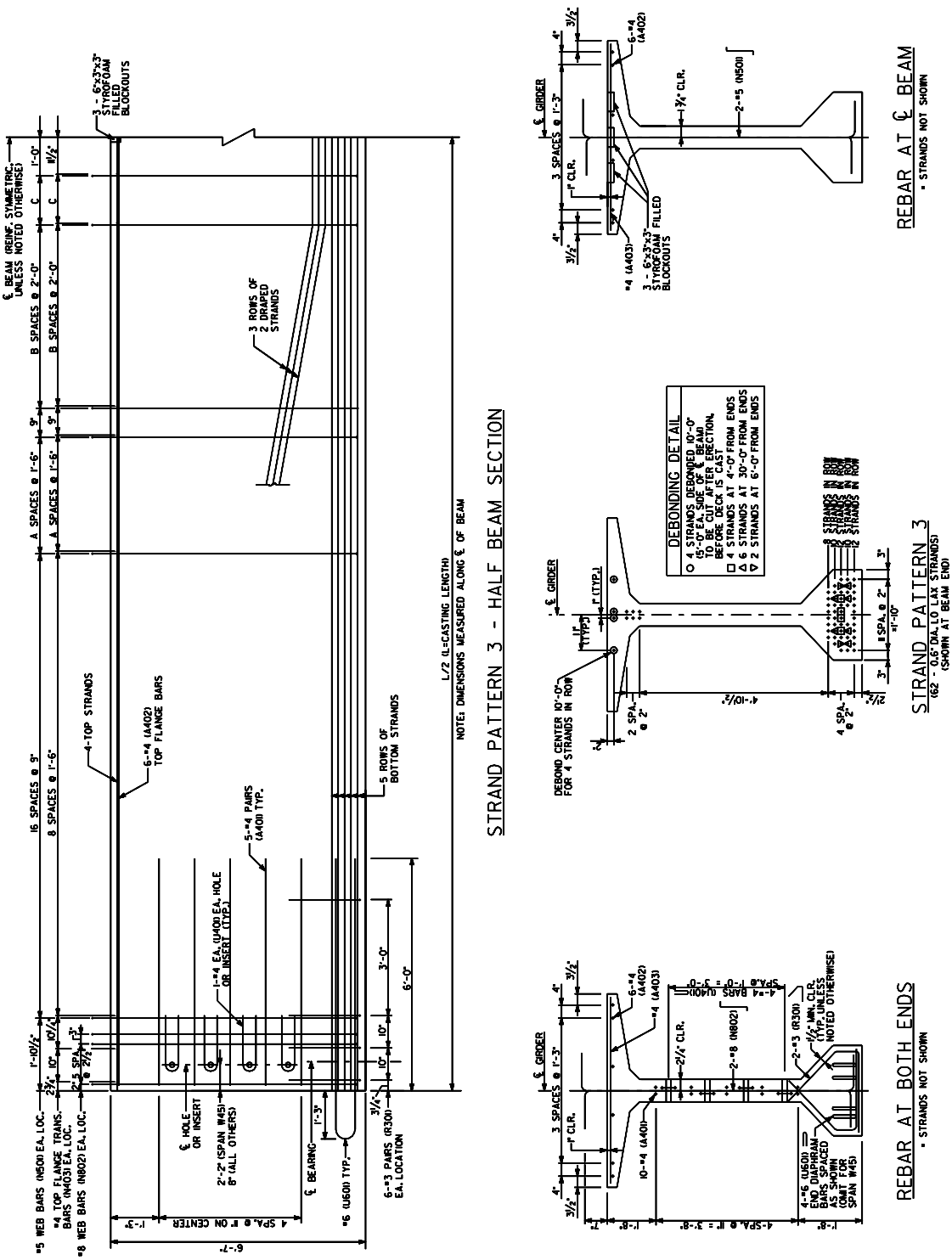

Figure 3.16: Strand Pattern 3 Beam (56 Straight Strands, 6 Draped Strands)

Table 3.4: Strand Pattern 1 Beams

Beam Number	Length	Season	Cast Date	"A" *	"B" *	"C" *
W43-4	127'- 4"	Winter	2/27/03	18	10	1'-0 ½"
W45-8	127'- 5½"	Summer	6/27/03	18	10	1 ¼'
W43-5	127'- 5¾"	Winter	2/27/03	18	10	1'-1 3/8"
W43-6	127'- 7½"	Winter	2/27/03	18	10	1'-2 ¼"
W43-8	127'- 11½"	Winter	3/3/03	0	24	1'-4 ¼"
W45-7	128'- 0¾"	Summer	6/27/03	0	24	1 7/8"
W45-6	129'- 5"	Summer	6/27/03	0	24	1'-1"
W33-11	129'- 9"	Winter	3/13/03	28	3	1'-3"
W45-4	130'- 0"	Summer	6/17/03	0	24	1'-4 ½"
W45-5	130'- 0½"	Summer	6/17/03	0	24	1'-4 ¾"
W35-7	131'- 0¼"	Winter	3/6/03	5	21	4 5/8"
W34-8	131'- 8¾"	Winter	3/11/03	28	4	2 7/8"
W34-7	131'- 0¼"	Winter	3/11/03	0	25	8 ¼"
W34-6	134'- 9½"	Winter	3/11/03	0	25	1'-9 ¼"
W26-6	136'- 6"	Summer	7/11/03	0	26	6"
W26-5	136'- 6½"	Summer	7/11/03	0	26	7 ¾"

*** As shown in Figure 3.14**

Table 3.5: Strand Pattern 2 Beams

Beam Number	Length	Season	Cast Date	"A" *	"B" *	"C" *
W31-10	129'- 4¾"	Winter	3/8/03	28	3	1'-0 7/8"
W25-10	135'- 1¾"	Winter	3/12/03	18	12	1'-0 7/8"
W27-7	136'- 3½"	Summer	7/3/03	28	5	6 ¼"
W23-4	136'- 6½"	Winter	3/12/03	28	5	7 ¾"
W24-3	136'- 9¼"	Winter	2/26/03	28	5	9 1/8"
W23-3	136'- 9¼"	Winter	3/12/03	28	5	9 1/8"
W23-2	137'- 0¼"	Winter	3/8/03	28	5	10 5/8"
W25-1	137'- 3"	Winter	2/28/03	28	5	1'-0"

*** As shown in Figure 3.15**

Table 3.6: Strand Pattern 3 Beams

Beam Number	Length	Season	Cast Date	"A" *	"B" *	"C" *
W35-3	134'- 7¾"	Summer	7/2/03	28	4	1'-8 3/8"
W35-2	134'- 8¼"	Summer	7/2/03	28	4	1'-8 5/8"
W35-1	134'- 8½"	Summer	7/2/03	28	4	1'-8 ¾"

*** As shown in Figure 3.16**

From each strand pattern group, beams were selected that differed in casting length by no more than ½ percent. This equates to less than an 8 in. difference for the shortest beam length in any sample and less than 8 ¼ in. difference for the longest beam in any sample. These beams were considered to be identical for the purposes of this study, and will comprise the sample groups. The results of this grouping are shown in Tables 3.7 through 3.9.

Table 3.7: Beam Sample 1

Beam Number	Length	Strand Pattern	Season	Cast Date
W43-4	127'-4"	1	Winter	2/27/03
W43-5	127'- 5¾"	1	Winter	2/27/03
W43-6	127'- 7½"	1	Winter	2/27/03
W43-8	127'- 11½"	1	Winter	3/3/03
W45-8	127'- 5½"	1	Summer	6/27/03
W45-7	128'- 0¾"	1	Summer	6/27/03

Table 3.8: Beam Sample 2

Beam Number	Length	Strand Pattern	Season	Cast Date
W33-11	129'- 9"	1	Winter	3/13/03
W45-6	129'- 5"	1	Summer	6/27/03
W45-4	130'- 0"	1	Summer	6/17/03
W45-5	130'- 0½"	1	Summer	6/17/03

Table 3.9: Beam Sample 3

Beam Number	Length	Strand Pattern	Season	Cast Date
W23-4	136'- 6½"	2	Winter	3/12/03
W24-3	136'- 9¼"	2	Winter	2/26/03
W23-3	136'- 9¼"	2	Winter	3/12/03
W27-7	136'- 3½"	2	Summer	7/3/03

Table 3.10: Individual Beams

Beam Number	Length	Strand Pattern	Season	Cast Date
W23-2	137’- 0¼”	2	Winter	3/8/03
W25-1	137’- 3”	2	Winter	2/28/03
W25-10	135’- 1¾”	2	Winter	3/10/03
W26-5	136’- 6½”	1	Summer	7/11/03
W26-6	136’- 6”	1	Summer	7/11/03
W31-10	129’- 4¾”	2	Winter	3/8/03
W34-6	134’- 9½”	1	Winter	3/11/03
W34-7	131’- 0¼”	1	Winter	3/11/03
W34-8	131’- 8¾”	1	Winter	3/11/03
W35-1	134’- 8½”	3	Summer	7/2/03
W35-2	134’- 8¼”	3	Summer	7/2/03
W35-3	134’- 7¾”	3	Summer	7/2/03
W35-7	131’- 0¼”	1	Winter	3/6/03

3.3 BEAM PRODUCTION

Bed lengths of 310 ft.-3 in. to 510 ft.-10 in. were used during production of the beams in the sample. Beams were typically produced in lines of three. There were two prestressing abutments that provided for the anchorage of the strands until they were cut. Metal side forms were used for casting the beams. The prestressing steel used was 0.6 in. diameter, Grade 270, Low Relaxation, seven-wire strand. The prestressing strands were individually stressed by hydraulic jacks to a prestressing force of 75 percent of the gross ultimate tensile strength, or approximately 44 kips per strand. Beams were generally allowed to cure, using a moist cure method, for eighteen hours to one day following placement. Steam curing is not used at this plant, since the climate of Savannah, GA makes this method unnecessary. After test cylinder compressive testing indicated satisfactory release strengths, the forms were stripped, allowing for detensioning of the strands. Detensioning was achieved by using torches to cut strands individually and simultaneously at both ends of the bed. Figures 3.17 through 3.19 depict the production methods.

Figure 3.17: Side Form

Figure 3.18: Beam with Strands in Casting Bed

Figure 3.19: Beam Curing in Casting Bed

Once cut from the bed, the beams were lifted by crane and moved to their storage location. Lifting loops embedded in the top of the beam provided the lift points for removal. As the beams were lowered to their storage position, two oak 8 in. x 8 in. wooden beams were symmetrically placed at a specified support point 3 ft. from the end of the beam.

3.4 MEASUREMENT PROCEDURE

Deflections in the beams were measured using a rotating laser level surveying system. This laser level unit had a manufacturer-stated accuracy of 1/16 in. at 100 ft., and is based on the ability of the laser beam source to rotate exclusively in a horizontal plane. The slight magnitude of wobbling of the beam source is directly related to the instrument accuracy, which decreases with increasing distance from the instrument. The

laser level unit was mounted on a surveying tripod and set up at the end of each beam. The longest beam was approximately 137 ft long, so this was the farthest distance at which a reading was taken, corresponding to a 3/32 in. error. The level and rod are shown in Figure 3.20.

Figure 3.20: Taking Readings with Laser Level Surveying System

A laser beam detector with the ability to translate on a graduated aluminum measuring rod was used. The aluminum measuring rod was attached to a base formed to the shape of the edge of the bottom flange. The measuring rod was also capable of rotating in two orthogonal planes to allow plumbing of the rod. The rod is shown in Figures 3.20 and 3.21. Prior to taking deflection measurements for the studied beams, an experiment was conducted to verify the instrument accuracy. Sample readings were taken from one end of the beam. The instrument was then moved to the opposite end of the same beam, and the readings were taken again. A comparison of the elevation differences from both sets of readings confirmed the stated instrument accuracy.

Figure 3.21: Laser Beam Detector and Measurement Apparatus

When measuring the studied beams, marks were placed on the bottom flange/web intersection at points located at ¼, ½, and ¾ of the beam cast length. Duplicate marks were also placed on the side of the top flange. This allowed location and replacement of any marks obscured or worn away due to harsh weather conditions or finishing and rubbing of the concrete surface. The beams were marked when either still on the bed or temporarily adjacent to the bed after release. Once beams were placed into long-term storage, the support midpoints were marked as well. This was to allow a change in support span length, due to moving the beam, to be considered. Fortunately, after being placed in long-term storage, most of the beams were not moved until shipment to the construction site and those that were moved were reset with similar support conditions.

As soon after release as possible, elevation measurements were taken at all marked points, comprised of the marks at the supports, quarter-span, and midspan. The measured elevations were used to calculate the deflections at quarter points and midspan. Measurements were then taken at approximately weekly intervals for three to four weeks before decreasing the measurement frequency to monthly measurements. These measurements were taken early in the morning to avoid the influence of solar radiation on

short-term camber growth, as noted by previous researchers and described in Chapter 2. Results of the deflection measurements are included in Chapter 5. An experimental trial to determine the variability of same-day camber caused by solar radiation was conducted to gain a better understanding of the phenomenon. The results of that trial are now described.

3.5 EFFECT OF SOLAR RADIATION ON SHORT TERM CAMBER VALUES

In order to determine the effect of solar radiation on the change in beam deflection during the course of a warm sunny day, measurements were taken at periodic time intervals. Beams W45-6 and W45-8 were exposed to direct sunlight on one full side in addition to the top flange. Beam W45-7 was surrounded by beams on either side, and was only exposed to direct sunlight on top. The deflected shapes of each beam, for each of the three readings taken during the day, are shown in Figures 3.22 through 3.24. The accuracy of the figures is within $\pm$ 3/32 in., which is based on the 1/16 in. at 100 ft accuracy of the measurement instrument for these beams.

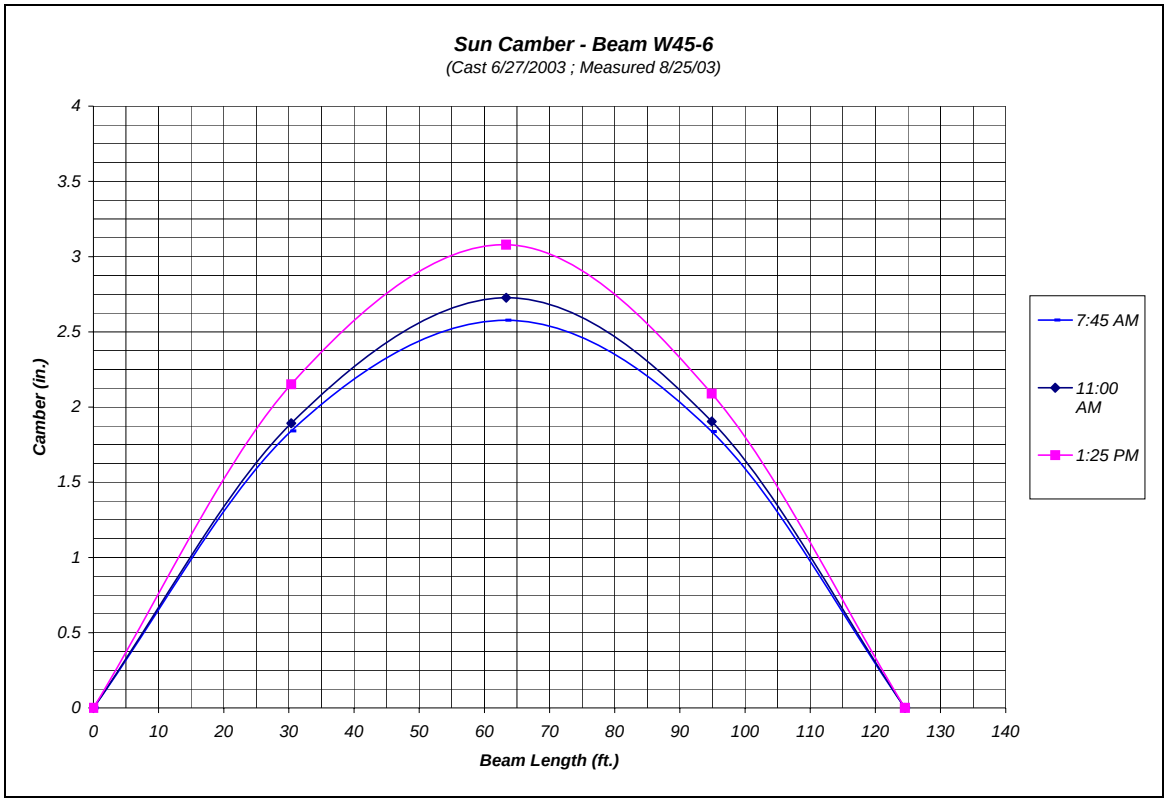

Figure 3.22 Thermal Camber, Beam W45-6

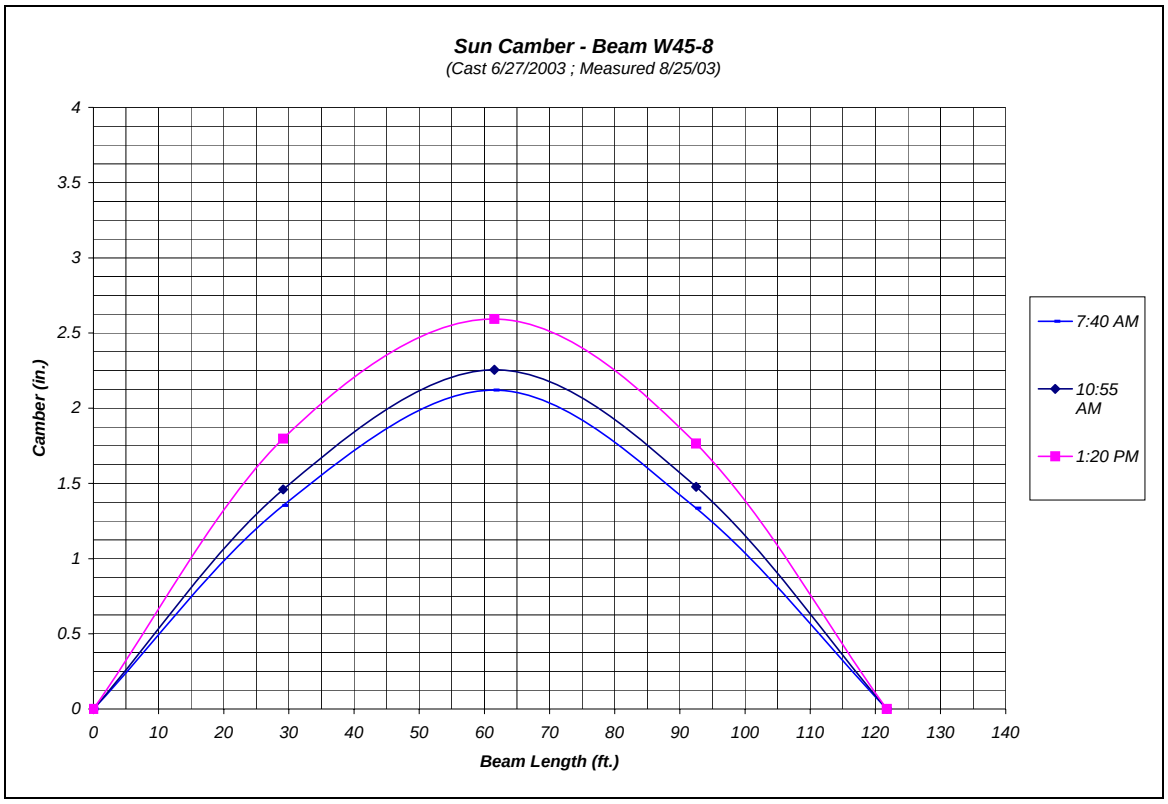

Figure 3.23 Thermal Camber, Beam W45-8

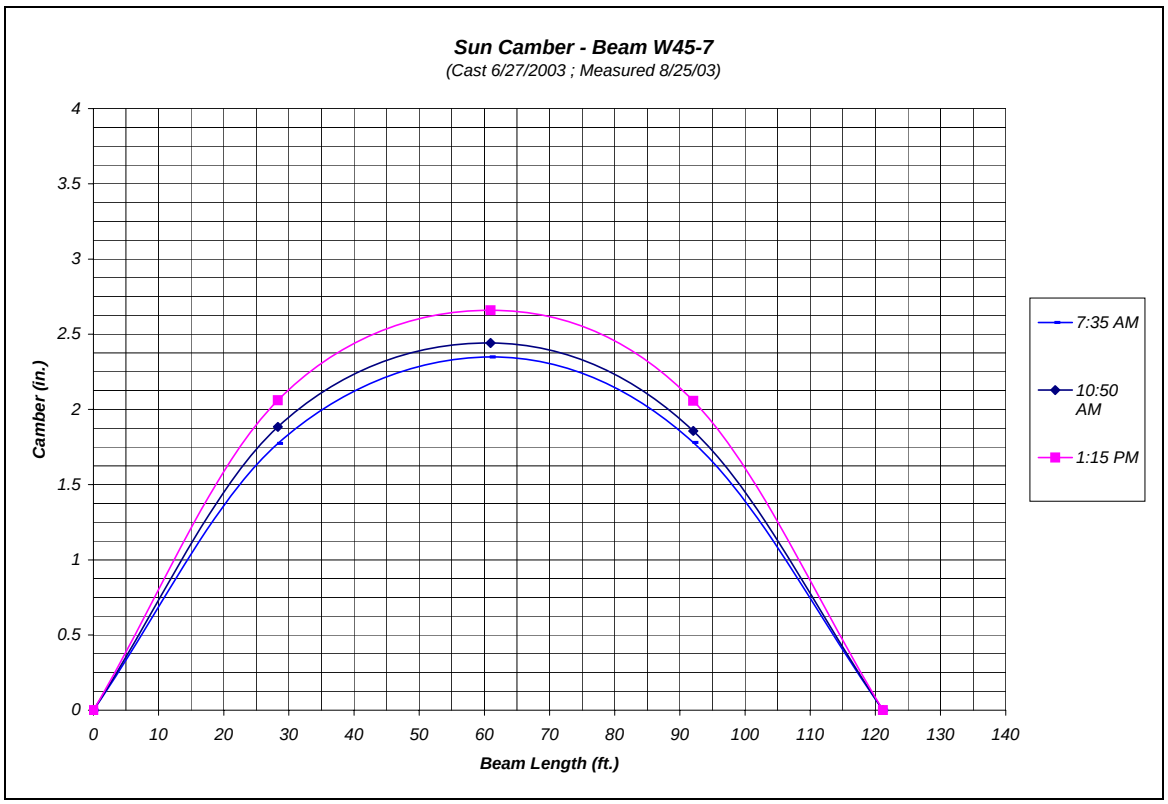

Figure 3.24 Thermal Camber, Beam W45-7

Beams W45-6 and W45-8 exhibited greater change in deflection (approximately ½ in.) than did Beam W45-7 (approximately ¼ in.), which was shaded on two sides. Additionally, it was interesting to observe the change between the first and second, and the second and third measurements. For all beams, the change between the second and third measurement was consistently greater than the change between the first and second measurement. This could be due to a latent effect as the beam is slow to heat up after it has been allowed to cool overnight and during the early morning hours. This observed behavior and magnitude of deflection agrees well with the research discussed in Chapter 2. A plot of the hourly temperature change on this day is shown in Figure 3.25.

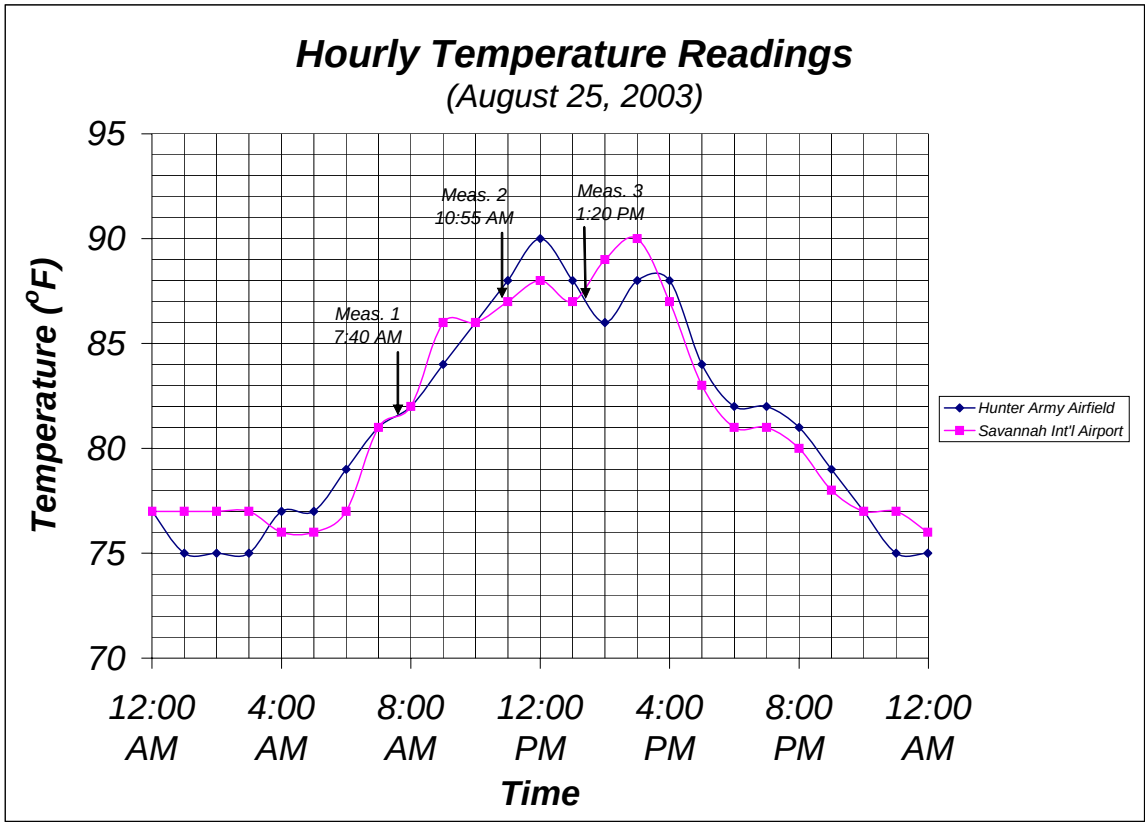

Figure 3.25 Hourly Temperature Readings (August 25, 2003)

The average daily temperature, recorded at two National Weather Service Station Locations in the vicinity of the precasting plant, is shown in Figure 3.26. The two stations are located at the Savannah International Airport and Hunter Army Airfield, each less than ten miles from the plant. By looking at the casting date for each beam, it can be seen that the average temperatures during the measurement intervals of the Winter/Spring and Summer Samples are significantly different. According to the work of previous researchers, discussed in the previous chapter, this magnitude of temperature change between seasons should be enough to affect the rate of compressive strength development and long-term concrete strength. This assertion is evaluated in Chapter 5, where the results of compressive strength testing are presented and examined.

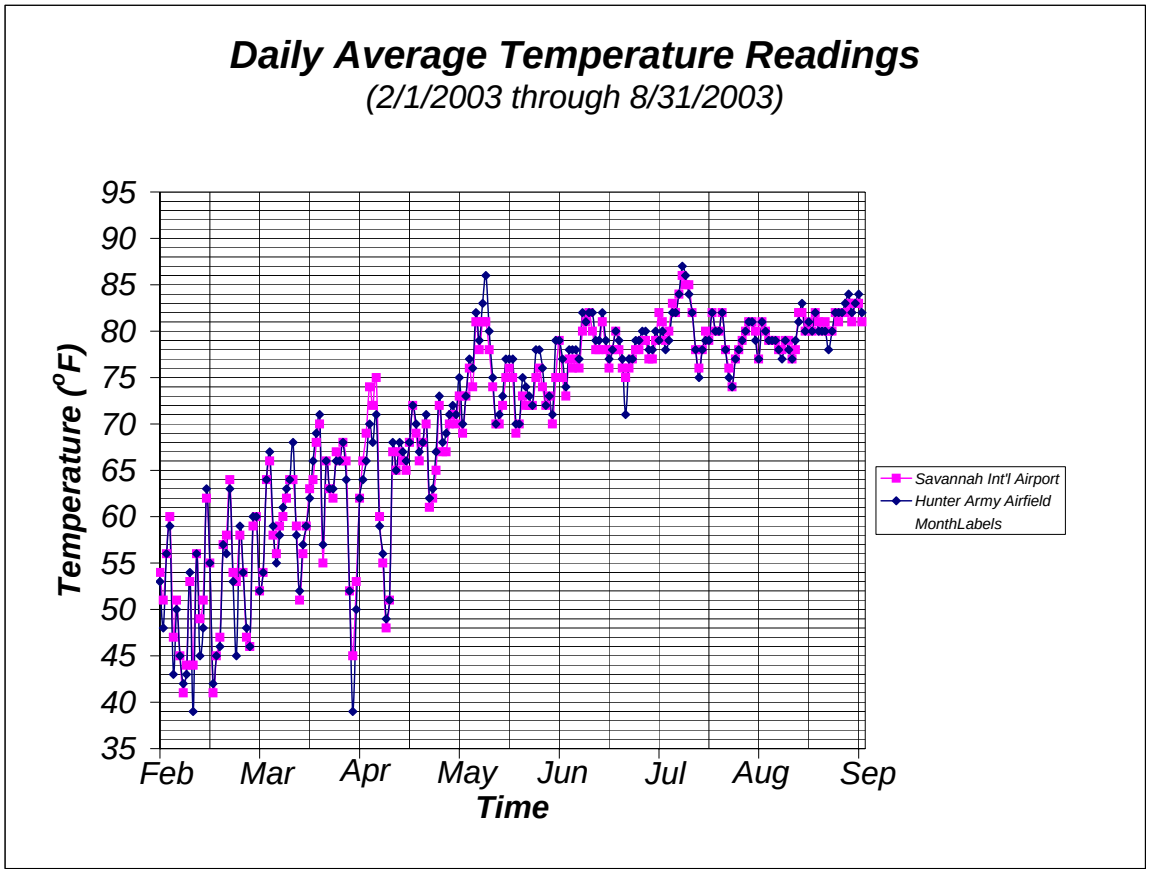

Figure 3.26 Daily Average Temperature Readings (2/1/2003 through 8/31/2003)

3.6 COMPRESSIVE STRENGTH AND MODULUS OF ELASTICITY TESTING

Standard Concrete Products cast several 4 in. diameter by 8 in. long test cylinders for each concrete pour. The beams were typically cast in lines of three, so all three would be cast from the same pour. Two cylinders were taken from the Live End (LE) and two were taken from the Dead End (DE) for a total of four cylinders for each testing age. The Live End is the area of the casting bed adjacent to the prestressing abutments, and closest to where the jacking load is applied. The Dead End is in the middle of the casting bed. All pours had 4 test cylinders for each age, with the exception of the pours for Beams W26-5, W26-6, and W27-7 for which 2 test cylinders were made for each testing age (one from the Live End and one from the Dead End). Both fresh and hardened concrete properties were tested according to their respective ASTM standards.

The fresh concrete properties such as slump and air content were tested, and concrete constituent materials were weighed or measured for each concrete batch. From this data, unit weight, water/cement ratio, and cement/aggregate ratio were calculated for the concrete used to construct each beam. The results of these tests and calculations are included in Table 3.11.

Table 3.11: Fresh Concrete Properties

	Beam Number	Unit Weight (lb/ft^3)	W/C Ratio	C/A Ratio	Ave Slump (in.)	Ave Air (%)
Winter Sample	**W24-2**	148.17	0.30	0.34	7.9	1.9
	W24-3	148.17	0.30	0.34	7.9	1.9
	W43-4	147.80	0.31	0.34	7.9	1.8
	W43-5	147.80	0.31	0.34	7.9	1.8
	W43-6	147.80	0.31	0.34	7.9	1.8
	W25-1	148.20	0.31	0.33	8.5	1.8
	W43-7	148.50	0.30	0.34	8.8	1.7
	W43-8	148.50	0.30	0.34	8.8	1.7
	W43-9	148.50	0.30	0.34	8.8	1.7
	W35-7	148.50	0.30	0.34	8.5	1.8
	W23-2	148.25	0.31	0.34	9.0	1.7
	W31-10	148.25	0.31	0.34	9.0	1.7
	W34-6	148.99	0.30	0.34	8.8	1.5
	W34-7	148.99	0.30	0.34	8.8	1.5
	W34-8	148.99	0.30	0.34	8.8	1.5
	W23-3	148.16	0.31	0.34	7.4	1.8
	W23-4	148.16	0.31	0.34	7.4	1.8
	W25-10	148.16	0.31	0.34	7.4	1.8
	W33-11	148.44	0.30	0.35	8.0	1.6
Summer Sample	**W45-5**	147.36	0.32	0.34	8.8	1.8
	W45-6	146.66	0.33	0.34	8.0	1.9
	W45-7	146.66	0.33	0.34	8.0	1.9
	W45-8	146.66	0.33	0.34	8.0	1.9
	W35-1	146.16	0.35	0.33	7.0	1.9
	W35-2	146.16	0.35	0.33	7.0	1.9
	W35-3	146.16	0.35	0.33	7.0	1.9
	W27-7	146.38	0.34	0.34	6.0	2.0
	W26-5	146.70	0.33	0.34	7.0	1.8
	W26-6	146.70	0.33	0.34	7.0	1.8

Hardened concrete properties tested were compressive strength and modulus of elasticity. The cylinders were cured at the concrete plant, allowing them to be subjected to similar environmental conditions as the beams. The cylinders were tested for compressive strength at an early age of 1 to 4 days, and then at 7, 28, and 56 days in age.

The compressive strength testing was done on four cylinders per test date. Fourteen additional 4 in. x 8 in. cylinders from a typical pour were obtained and taken to be tested at the Virginia Polytechnic Institute and State University's Structures and Materials Laboratory in Blacksburg, VA. They were stored inside the lab until testing. Two cylinders were tested for compressive strength for each test date, at ages of 7, 14, 28, and 56 days. They were also tested to determine the modulus of elasticity corresponding to the time of compressive testing. Each modulus of elasticity test was the average of 3 runs from 0 to 40 percent of f'_c for 2 cylinders. Results of these tests are presented in Chapter 5.

3.7 SUMMARY

This chapter has summarized the materials, details, and production methods for the beams. The camber measurement method has also been discussed, along with the effect of solar radiation. Finally, the testing of compressive strength and modulus of elasticity are discussed, along with some of the various fresh concrete properties and how they varied from the theoretical mix design and target ranges. The next chapter will discuss the theoretical basis for the camber calculations and the theoretical models used to predict modulus of elasticity, creep, shrinkage, and prestress loss. The results of the tests for compressive strength and modulus of elasticity are presented in Chapter 5.

CHAPTER 4. THEORETICAL FORMULATION

4.1 OVERVIEW

Camber is dependent upon many factors: prestressing strand configuration and force, initial losses due to elastic shortening, anchorage seating, and relaxation of the prestressing strands while the beam is still in the casting bed, time-dependent effects of creep, shrinkage, and strand relaxation, and the constant sustained applied loading of the beam self weight. Due to the interrelated and complex nature of these contributing factors, it is desirable to use an approach that calculates the time-dependent change in the effective prestressing force over many discrete time steps.

Deflections for the beams at each time step were calculated according to the Moment Area Method. The Moment-Area Method relates the geometry of the beam's elastic deflection curve to its M/EI, or curvature, Diagram. The beams examined in this study contain harped strands, as well as straight strands above and below the neutral axis of the member, so the Moment-Area Method facilitates the most straight-forward determination of midspan deflection.

4.2 INCREMENTAL TIME STEP METHOD

The curvatures used as input values for the Moment-Area Method are calculated according to the Incremental Time Step Method presented in Nilson (1987). An important deviation from the Nilson Incremental Time Step Method concerned the application of self weight moment. Nilson applies self weight moment separately from the prestressing force and moment. To increase the technical accuracy of the calculations in this study, it was very important to consider self weight and the prestressing force and moment as acting simultaneously during each time step interval. Self weight is a very important factor, especially considering the large cross-sectional area of the beams studied.

The time step method proposed by Nilson (1987) is expressed by the following equation:

$$\phi_{pt} = \frac{-P_i e_x}{E_c I_c} + \sum_0^t (P_{n-1} - P_n)\frac{e_x}{E_c I_c} - \sum_0^t (C_n - C_{n-1})P_{n-1}\frac{e_x}{E_c I_c} \qquad (4.1)$$

where,

ϕ_{pt} = curvature at any section, at any time t

C_{n-1} = Creep coefficient at the beginning of a time interval

C_n = Creep coefficient at the end of a time interval

e_x = Eccentricity of prestressing steel at a distance x from end of beam

E_c = Model Predicted Concrete Modulus of Elasticity during the time interval.

I_c = Cross-sectional Moment of Inertia

P_i = Initial prestress force (at transfer)

P_{n-1} = Prestress force at the beginning of a time interval

P_n = Prestress force at the end of a time interval

This equation reflects that the prestressing force is continuously decreasing due to the effects of creep, shrinkage, and relaxation, which directly affects the contribution due to creep. As the beam concrete undergoes shrinkage and the prestressing strands experience relaxation, the sustained creep-inducing load applied to the concrete is reduced, which gradually reduces concrete creep.

The first term of the equation represents the curvature occurring when the prestress force is transferred to the beam at release. At this time, the time-dependent effects due to creep, shrinkage, and relaxation have just begun, simplifying the calculation. The second term is the decrease in curvature resulting from creep, shrinkage, and relaxation prestress losses. The final term reflects the fact that creep also increases the curvature, as the creep-inducing load acts as an effective upward load. At the end of each time step, the prestress force present at the beginning of the interval is reduced by the creep, shrinkage, and relaxation prestress losses occurring during the time step multiplied by the total area of prestressing steel in the section. The process is then repeated for each time step.

This incremental time step calculation procedure for deflections differs from Lump Sum Methods such as Martin (1977) and the PCI Method in that a distinction is

made between different time intervals in the life of the beam as it ages. The time is divided into two distinct phases. The initial phase, at transfer, is when the force in the member is due to the initial prestress force $P_{eInit,}$ reduced to reflect elastic shortening, anchorage and seating, and initial relaxation losses. The second phase, beginning just after transfer, consists of a continuously decreasing effective prestress force, attributed to the loss of prestress due to creep, shrinkage, and relaxation effects. The method is described in detail with the following sequence of steps:

1. Calculate the initial effective prestress force, reducing the jacking force due to the effect of elastic shortening. The typical AASHTO-LRFD (2004) method of calculating elastic shortening requires iteration to calculate an accurate value by assuming a value for the concrete stress following transfer. This assumed concrete stress is used to calculate the stress at the center of gravity of the prestressing steel, which is then used to calculate the elastic shortening loss and a new after-transfer concrete stress. This value is used to repeat the process as the solution converges to an acceptable level. Alternatively, the PCI Bridge Design Manual (2003) offers a method of calculation allowing a solution without iteration. The PCI elastic shortening method is summarized as:

$$P_{eInit} = \left(f_{pj} - \Delta f_{ES}\right)A_{ps} \tag{4.2}$$

$$\Delta f_{ES} = f_{pj} - f_{po} \tag{4.3}$$

where,

P_{eInit} = Effective Prestress Force at Release

f_{pj} = Stress in strand due to jacking force

f_{po} = Stress in prestressing steel immediately after release

Δf_{ES} = Prestress Loss due to Elastic Shortening at Release

A_{ps} = Area of prestressing steel

$$f_{po} = \frac{f_{pi} + \frac{E_p}{E_{ci}}\frac{M_{sw}e}{I}}{1+\alpha} \tag{4.4}$$

$$\alpha = \frac{E_p}{E_{ci}} \frac{A_p}{A} \left(1 + \frac{e^2}{r^2} \right) \tag{4.5}$$

where,

E_{ci} = Modulus of elasticity of the beam concrete at transfer

E_p = Modulus of elasticity of prestressing steel

I = Moment of inertia of beam

M_{sw} = Moment at section of interest due to beam self-weight

e = Eccentricity of prestressing steel with respect to centroid of section

r = Radius of gyration of gross cross-section = $\sqrt{\frac{I}{A}}$

2. Calculate the prestressing and self weight moments. The prestressing moment is calculated by resolving the individual strand forces into an equivalent prestressing force acting at the centroid of the entire prestressing strand pattern. This includes strands above and below the neutral axis, as well as any harped strands.

$$M_{ps} = P_e(e) \tag{4.6}$$

$$M_{sw} = \frac{\omega \cdot x}{2}(L - x) \tag{4.7}$$

where,

M_{ps} = Moment due to prestressing force

P_e = Effective prestress force

ω = Uniform load due to self-weight

L = Length of beam

x = Distance from end of beam

3. Calculate the stresses at the extreme fibers, beginning with $P_{e\ init}$ and followed by P_e, incorporating the effects of self weight in addition to the prestressing force and moment.

$$f_{Top} = -\frac{P_e}{A_{trans}} + \frac{(M_{ps} - M_{sw})c_{top}}{I_{trans}} \quad (4.8)$$

$$f_{Bott} = -\frac{P_e}{A_{trans}} - \frac{(M_{ps} - M_{sw})c_{bott}}{I_{trans}} \quad (4.9)$$

where,

f_{Top} = Stress at top of beam cross-section

f_{Bott} = Stress at bottom of beam cross-section

c_{top} = Distance from beam centroid to top of beam

c_{bott} = Distance from beam centroid to bottom of beam

4. Calculate the stress at the level of the centroid of the prestressing strand pattern.

$$f_{cgp} = -\frac{P_e}{A_{trans}} + \left(\frac{-P_e \times e^2}{I_{trans}}\right) + \frac{M_{sw}e}{I_{trans}} \quad (4.10)$$

where,

f_{cgp} = Stress at centroid of prestressing steel pattern

5. Using Hooke's Law to express the relationship between stress and strain, calculate values of strain at the extreme fibers and at the level of the prestressing centroid.

$$\varepsilon_{top} = \frac{f_{top}}{E_c} \quad (4.11)$$

$$\varepsilon_{bott} = \frac{f_{bott}}{E_c} \quad (4.12)$$

$$\varepsilon_{ps} = \frac{f_{ps}}{E_c} \quad (4.13)$$

where,

ε_{top} = Strain at top of beam cross-section

ε_{bott} = Strain at bottom of beam cross-section

6. Calculate initial curvature.

$$\phi = \frac{\varepsilon_{bott} - \varepsilon_{top}}{h} \tag{4.14}$$

where,

ϕ = Curvature of deflected beam (rad/in)

h = Height of beam cross-section

7. Choose a model with which to calculate the time-dependent creep coefficients and the shrinkage strains. Calculate relaxation loss according to the generally accepted method, developed by Magura, Sozen, and Siess (1964), shown below:

$$\Delta f_{relax} = f_{pi}\left(\frac{\log(t_n) - \log(t_r)}{45}\right)\left(\frac{f_{pi}}{f_{pe}} - 0.55\right) \tag{4.15}$$

$$f_{pe} = \frac{P_e}{A_{ps}} \tag{4.16}$$

$$f_{pi} = \frac{P_{eInit}}{A_{ps}} \tag{4.17}$$

where,

Δf_{relax} =Prestress loss due to relaxation of prestressing steel

f_{pi} = Initial Stress

t_n = Time (hours)

t_r = Time of release (hours)

f_{pe} = Stress in prestressing steel due to effective prestress force

8. Compute the total change in strain at the prestressing centroid level, and the change in effective prestressing force.

$$\varepsilon_{psTotal} = \varepsilon_{ps}\delta_u + \varepsilon_{sh} \tag{4.18}$$

$$\Delta P_{ps} = \left[\left(\varepsilon_{psTotal} \cdot E_{ps}\right) + \Delta f_{relax}\right] A_{ps} \tag{4.19}$$

where,

$\varepsilon_{psTotal}$ = Total strain at prestressing centroid level

ε_{ps} = Strain due to prestressing force

δ_u = Creep coefficient

ε_{sh} = Shrinkage strain

ΔP_{ps} = Change in effective prestress force

Δf_{relax} = Prestress loss due to relaxation

9. Calculate changes in stress and strain at the extreme fibers due to the decreasing effective prestressing force.

$$\Delta f_{top} = \frac{\Delta P_{ps}}{A_{trans}} - \frac{\Delta P_{ps} \cdot e \cdot c_{top}}{I_{trans}} \tag{4.20}$$

$$\Delta f_{bott} = \frac{\Delta P_{ps}}{A_{trans}} + \frac{\Delta P_{ps} \cdot e \cdot c_{bott}}{I_{trans}} \tag{4.21}$$

$$\Delta \varepsilon_{top} = \frac{\Delta f_{top}}{E_c} \tag{4.22}$$

$$\Delta \varepsilon_{bott} = \frac{\Delta f_{bott}}{E_c} \tag{4.23}$$

where,

Δf_{top} = Change in stress at top of beam cross-section

Δf_{bott} = Change in stress at bottom of beam cross-section

$\Delta \varepsilon_{top}$ = Change in strain at top of beam cross-section

$\Delta \varepsilon_{bott}$ = Change in strain at bottom of beam cross-section

10. Calculate total change in strain at the extreme fibers due to creep, shrinkage, and reduction of the effective prestressing force.

$$\Delta \varepsilon_{topTotal} = \varepsilon_{top} \cdot \delta_u + \varepsilon_{sh} + \Delta \varepsilon_{top} \tag{4.24}$$

$$\Delta\varepsilon_{bottTotal} = \varepsilon_{bott} \cdot \delta_u + \varepsilon_{sh} + \Delta\varepsilon_{bott} \tag{4.25}$$

11. Calculate change in curvature caused by changes in strain at the top and bottom of the section.

$$\Delta\phi = \frac{\Delta\varepsilon_{bottTotal} - \Delta\varepsilon_{topTotal}}{h} \tag{4.26}$$

12. Calculate Steps 1 through 11 for midspan, quarter point, and one transfer length from the end of the beam.
13. Use the Moment-Area Method applied at midspan, quarter point, and transfer location to determine the midspan deflection.
14. Use Moment-Area Method to calculate change in midspan deflection due to change in curvature.
15. Begin new time step, reducing the effective prestress force by the change in effective prestress force that occurred during the previous time step. Repeat this process for as many time steps as desired.

4.3 MODELS FOR MODULUS OF ELASTICITY, CREEP, AND SHRINKAGE

The designer is presented with many models from which to choose in order to calculate modulus of elasticity, creep coefficients, and shrinkage strains. Several of these models were examined by the present study. They include AASHTO-Standard (2002), AASHTO-LRFD (2002), ACI-209 (1992), ACI-209 (modified by Huo) (1997), Bazant B3 (1995), CEB-MC90 (1990), Gardner-Lockman (GL-2000) (2000), Shams and Kahn (2000), and NCHRP-496 (2003). A summary of the input variables and equations for each model is presented in Appendix A.

The time-dependent creep coefficients and shrinkage strains predicted by each model are used as inputs to the incremental time step method described above. Table 4.1 presents a comparison of the input variables used in each of the considered creep and shrinkage models.

Table 4.1 Input Variables for Time-Dependent Creep and Shrinkage Models

	Theoretical Model							
Input Variable	**AASHTO (LRFD)**	**ACI 209**	**ACI 209 (Huo)**	**Bazant B3**	**CEB-MC90**	**GL-2000**	**Shams and Kahn**	**NCHRP 496**
Humidity	X	X	X	X	X	X	X	X
Temperature					X		X	
V/S Ratio	X	X	X	X	X	X	X	X
Shape				X				
28-day strength	X		X	X	X	X	X	X
Strength at loading		X	X					X
Modulus of elasticity					X	X		
W/C Ratio				X				
Cement content		X	X	X				
Cement type				X	X	X		
Fine/Coarse aggregate		X	X					
Cement/Aggregate				X				
Air content		X	X					
Slump		X	X					
Density		X	X					
Drying age				X			X	
Loading age	X	X	X	X	X	X	X	X
Curing Method	X	X	X	X			X	
Loading stress					X		X	

The modulus of elasticity used in the time step method is either the value predicted by each model considered in the study, or an equation by Shams and Kahn (2000) modified to better represent the measured modulus of elasticity values. The modified Shams and Kahn modulus of elasticity equation is described in Chapter 5, and the modulus of elasticity prediction equations for each considered model are presented in Appendix A. Predicted and measured modulus of elasticity values are used as input values to examine how modulus of elasticity affects the predictive accuracy of the time step method. For models without a time-dependent modulus of elasticity prediction equation (AASHTO-LRFD, Bazant B3, and NCHRP 496), the initial modulus of elasticity is calculated based on the design release strength, and the modulus of elasticity following transfer is calculated using the 28-day design compressive strength. Two cases were considered for each model used to predict creep and shrinkage strains: one using the model-predicted modulus of elasticity, and one using the approximated measured

modulus of elasticity. The input variables for each of the compressive strength and modulus of elasticity models are shown in Table 4.2.

Table 4.2 Input Variables for Comp. Strength and Modulus of Elasticity Models

	Theoretical Model							
Input Variable	**AASHTO (LRFD)**	**ACI 209**	**ACI 209 (Huo)**	**Bazant B3**	**CEB-MC90**	**GL-2000**	**Shams and Kahn**	**NCHRP 496**
Time		X	X		X	X	X	
Compressive Strength	X	X	X	X	X	X	X	X
Weight	X	X	X					
Cement Type						X		
Aggregate Type								X

CHAPTER 5. EXPERIMENTAL RESULTS AND DISCUSSION

5.1 COMPRESSIVE STRENGTH AND MODULUS OF ELASTICITY TEST RESULTS

As described in Chapter 3, test cylinders were made for each concrete pour. These test cylinders were tested for compressive strength by Standard Concrete Products. The results of these tests are included in Tables 5.1 and 5.2, and in Figures 5.1 through 5.14. In each table, the release and 28-day compressive strengths are presented for the winter and summer beam samples. The age at release is also shown for each beam.

In each figure the experimentally measured compressive strengths and specified design compressive strengths at release and 28 days are compared to predictions by the ACI-209, CEB-MC90, Gardner-Lockman (GL-2000), and Shams and Kahn models. All theoretical strength gains shown in each figure are based on equations suggested in each model. The prediction equations for each model are included in Appendix A. The predicted time-dependent compressive strength curves of the ACI-209 and Shams and Kahn Models achieve the input concrete design strength at 28 days. It is interesting to note that the CEB-MC90 and Gardner-Lockman (GL-2000) curves predicted compressive strengths that exceed the input 28 day design strength. These equations seem to recognize the fact that the precaster deliberately tries to overshoot the 28-day design strength in order to ensure a high statistical probability that the cylinder breaks exceed the required strength.

A 28-day compressive strength higher than design f'_c better represents experimental observations from the compressive strength testing of the concrete mix examined in this study (Tables 5.1 and 5.2). The average compressive strength for all the cylinders tested at 28 days exceeded 11,000 psi, with a standard deviation of 1050 psi, compared with the 9,000 psi 28-day design concrete strength. The design release strength of 6,100 psi was also significantly less than the average strength observed in the test cylinders at the time of release, which was approximately 7,470 psi, with a standard deviation of 1190 psi. A simple practical explanation of this phenomenon is that the precaster does not want to risk falling short of the concrete release strength or the 28 day design strength, so a concrete mix is used that has a high probability of exceeding these values. The release strength exceeds the design value and concrete strength develops

from this point and exceeds the 28 day design strength as well. The time a beam spends in the casting bed is worth far more than the incremental cost of using a higher quality concrete mix.

Table 5.1 Winter Beam Compressive Strength Test Results

Cylinder Information					Compressive Strength (psi)							
Test Cylinder	Cast Date	Release Age (days)	Break No.	Location	Release	Release Ave.	7 Days	7 Day Ave.	28 Days	28 Day Ave.	56 Days	56 Day Ave.
W24-3	2/26/2003	1	1	LE	7623	7290	10315	10330	12375	12250	12268	12890
				DE	6991		10422		12303		13192	
			2	LE	7560		10191		11309		12815	
				DE	6991		10391		13017		13288	
W43-4, 5 & 6	2/27/2003	1	1	LE	6474	6380	9532	9380	10918	11250	12077	12200
				DE	6129		9295		11782		13118	
			2	LE	6690		9487		10725		11001	
				DE	6210		9205		11579		12621	
W25-1	2/28/2003	3	1	LE	10247	9890	10584	10650	11378	11430	11734	12000
				DE	9876		10627		11503		12357	
			2	LE	9751		11004		11425		11419	
				DE	9695		10368		11419		12502	
W43-7,8,9	3/3/2003	1	1	LE	6165	6390	10361	10630	12444	12850	12217	12570
				DE	6696		10667		12750		13664	
			2	LE	6109		10937		13626		12698	
				DE	6575		10565		12559		11680	
W35-7	3/6/2003	1	1	LE	8207	7860	10709	10660	11950	12290	12317	12130
				DE	7537		10788		12481		11881	
			2	LE	8111		10398		12547		12115	
				DE	7598		10753		12164		12191	
W23-3, 23-4, 25-10	3/12/2003	2	1	LE	9627	9320	10101	10060	13445	13200	12886	12870
				DE	9162		10079		13399		12469	
			2	LE	9963		10097		13295		12883	
				DE	8536		9976		12640		13252	
W33-11	3/13/2003	1	1	LE	7951	7280	10865	10810	12466	12150	12046	12090
				DE	6718		10932		11983		12353	
			2	LE	7769		10234		12044		12366	
				DE	6695		11218		12100		11586	
				Ave:	**7770**		**10360**		**12200**		**12390**	
				Std. Dev:	**1350**		**510**		**760**		**620**	

Table 5.2 Summer Beam Compressive Strength Test Results

Cylinder Information					Compressive Strength (psi)							
Test Cylinder	**Cast Date**	**Release Age (days)**	**Break No.**	**Location**	**Release**	**Release Ave.**	**7 Days**	**7 Day Ave.**	**28 Days**	**28 Day Ave.**	**56 Days**	**56 Day Ave.**
W45-4, 5	6/17/2003	1	1	LE	6200	6350	7917	9010	10469	11420	10740	11670
				DE	6195		9846		12482		12518	
			2	LE	6715		8590		10234		10819	
				DE	6275		9670		12512		12612	
W45-6,7,8	6/27/2003	1	1	LE	7219	6720	9652	8940	11224	10430	10907	10680
				DE	6371		7975		10279		10535	
			2	LE	7145		9477		10064		10699	
				DE	6149		8646		10155		10588	
W35-1, 2, 3	7/2/2003	5	1	LE	7807	7700	8616	8890	10036	10090	10143	10260
				DE	7745		9302		10444		10302	
			2	LE	7691		8597		10093		10223	
				DE	7567		9030		9796		10382	
W27-7	7/3/2003	4	1	LE	7118	7070	8353	8560	11690	11590	11308	11330
				DE	7026		8756		11480		11355	
W26-5, W26-6	7/11/2003	3	1	LE	6878	6790	7842	7710	10674	10780	10888	10850
				DE	6695		7578		10882		10806	
				Ave:	**6930**		**8740**		**10780**		**10930**	
				Std. Dev:	**580**		**710**		**860**		**730**	

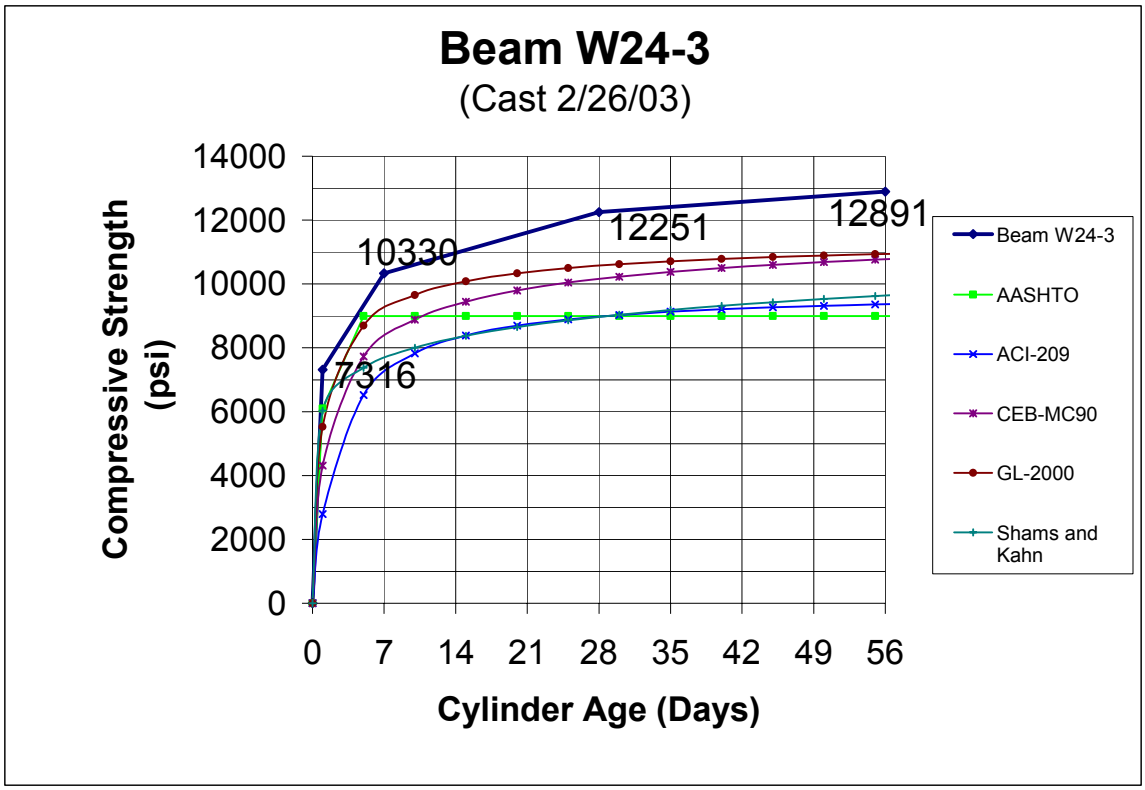

Figure 5.1 Beam W24-3 Compressive Strength vs. Time

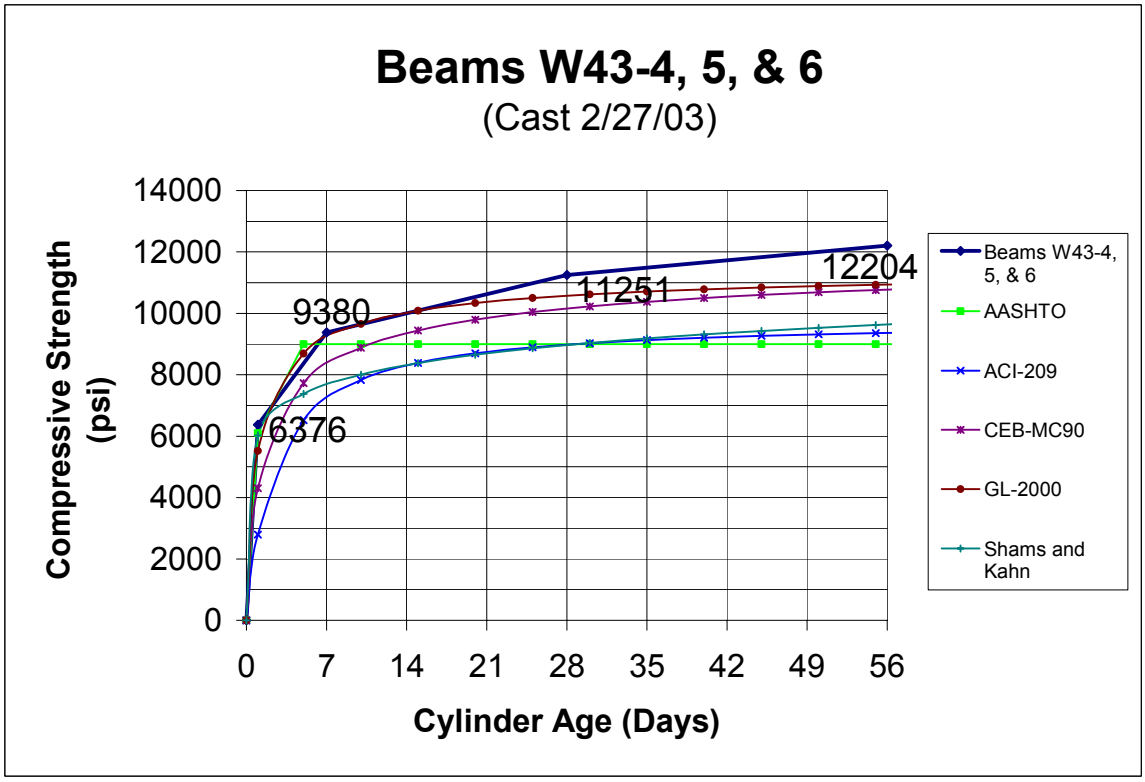

Figure 5.2 Beams W43-4, 5 &6 Compressive Strength vs. Time

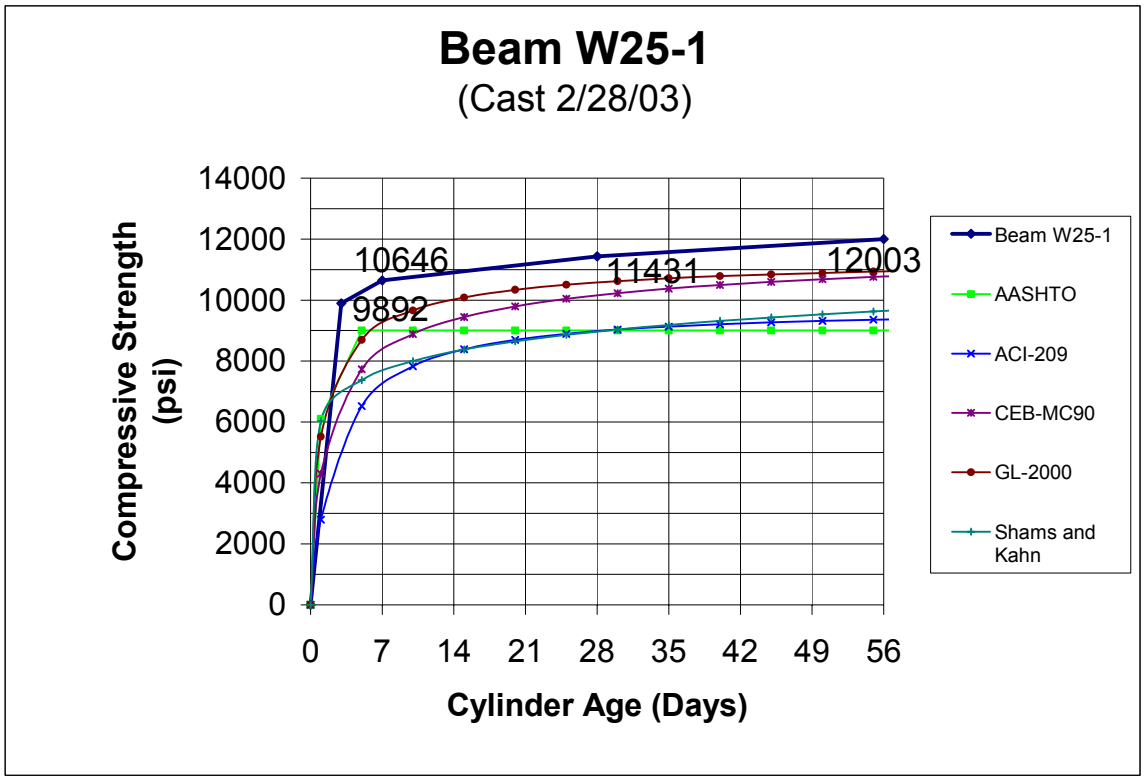

Figure 5.3 Beam W25-1 Compressive Strength vs. Time

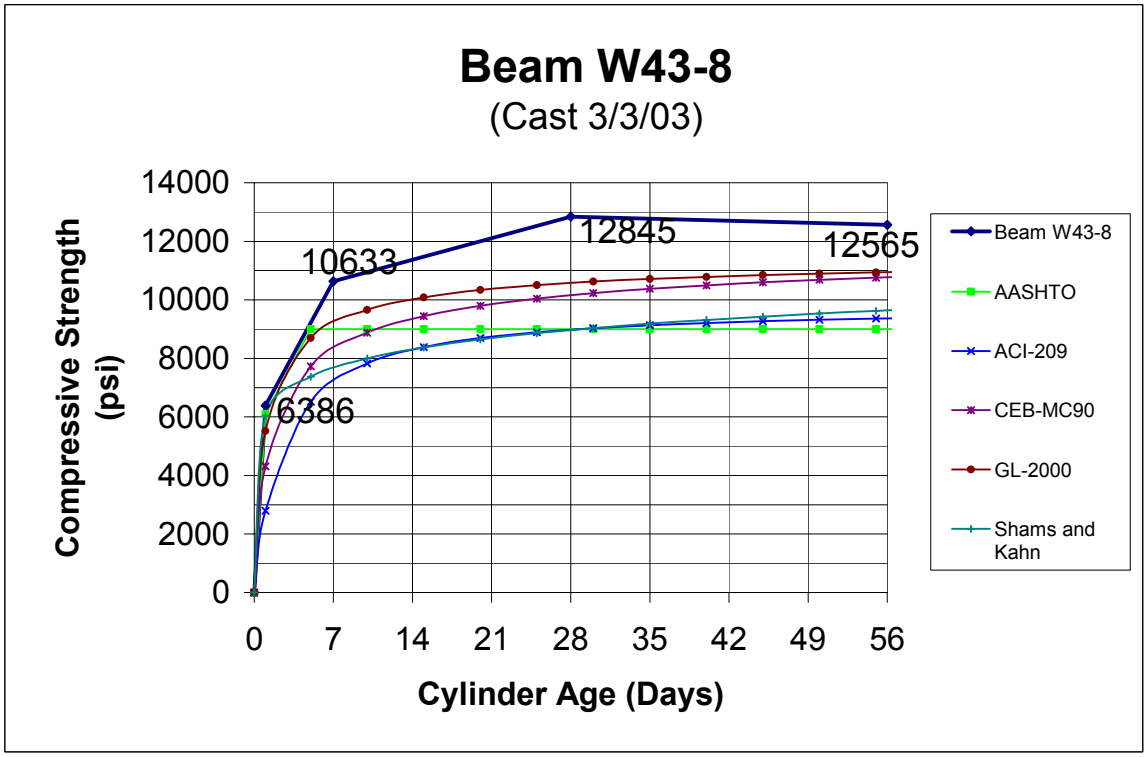

Figure 5.4 Beam W43-8 Compressive Strength vs. Time

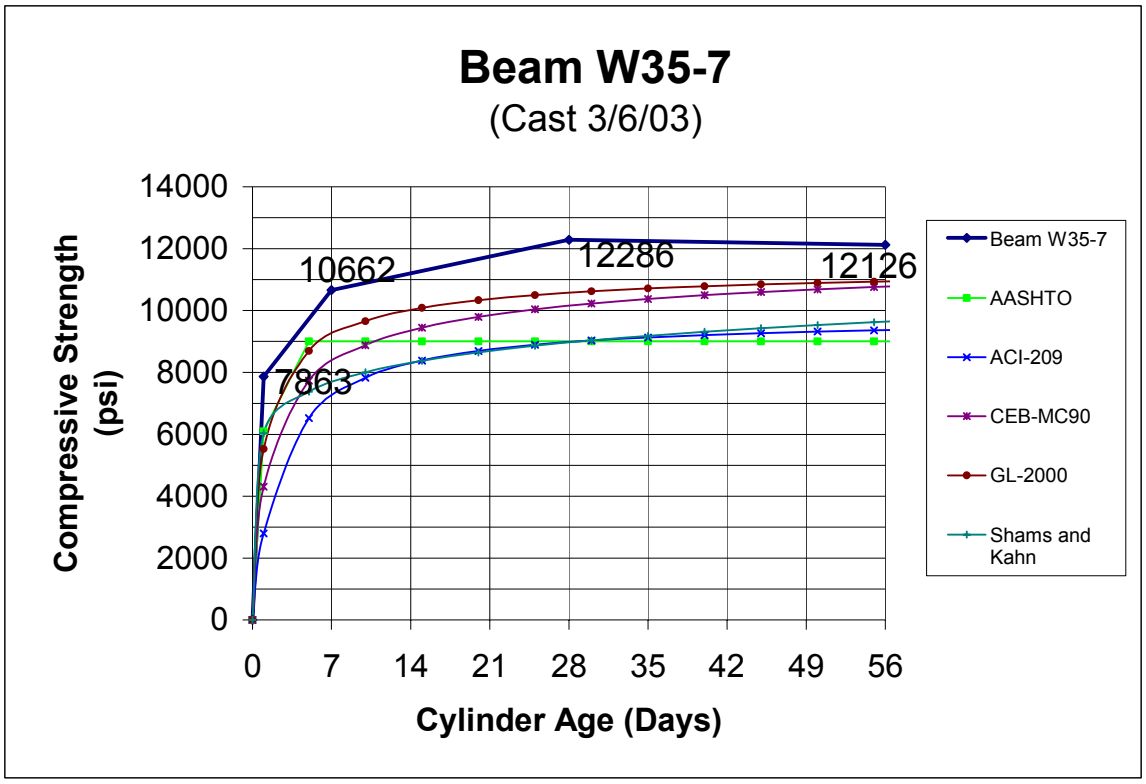

Figure 5.5 Beam W35-7 Compressive Strength vs. Time

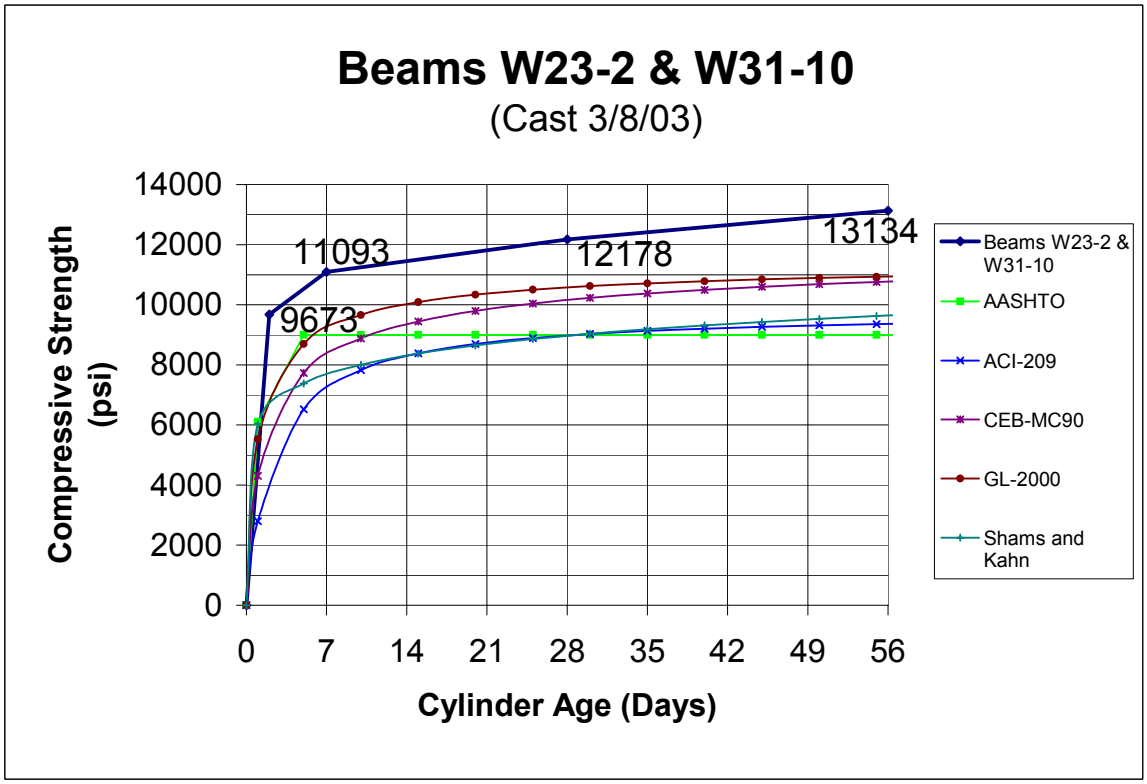

Figure 5.6 Beams W23-2 & W31-10 Compressive Strength vs. Time

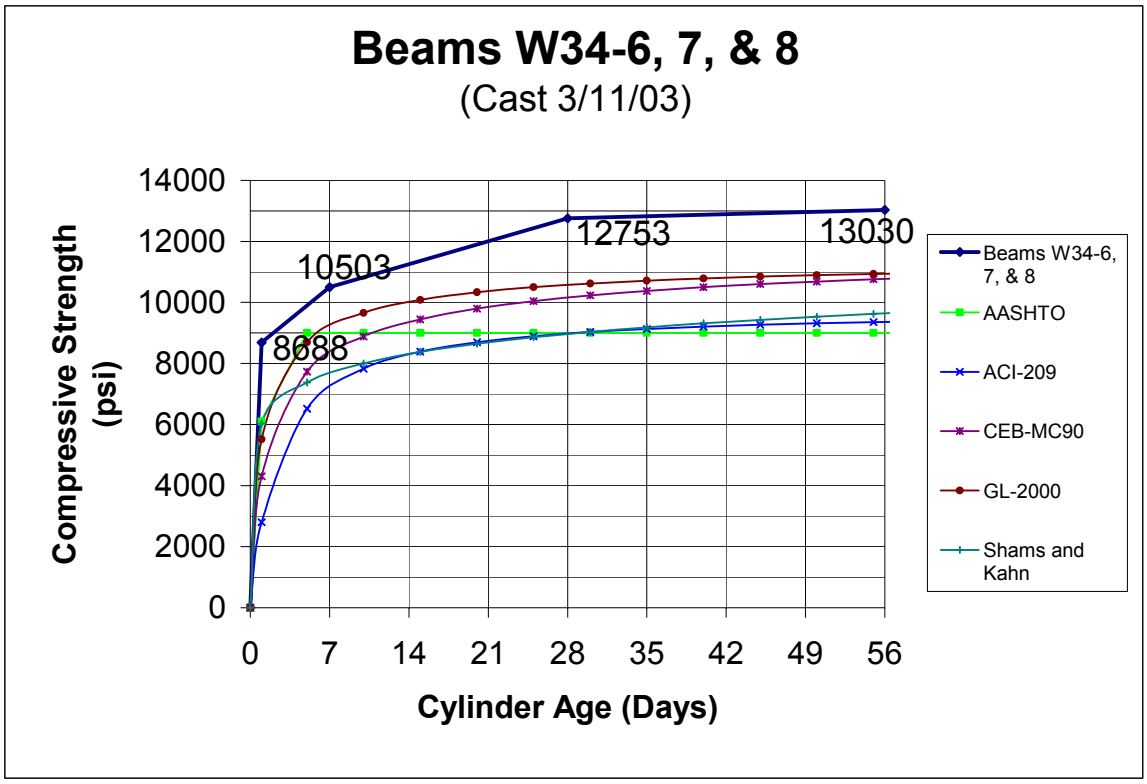

Figure 5.7 Beams W34-6, 7 &8 Compressive Strength vs. Time

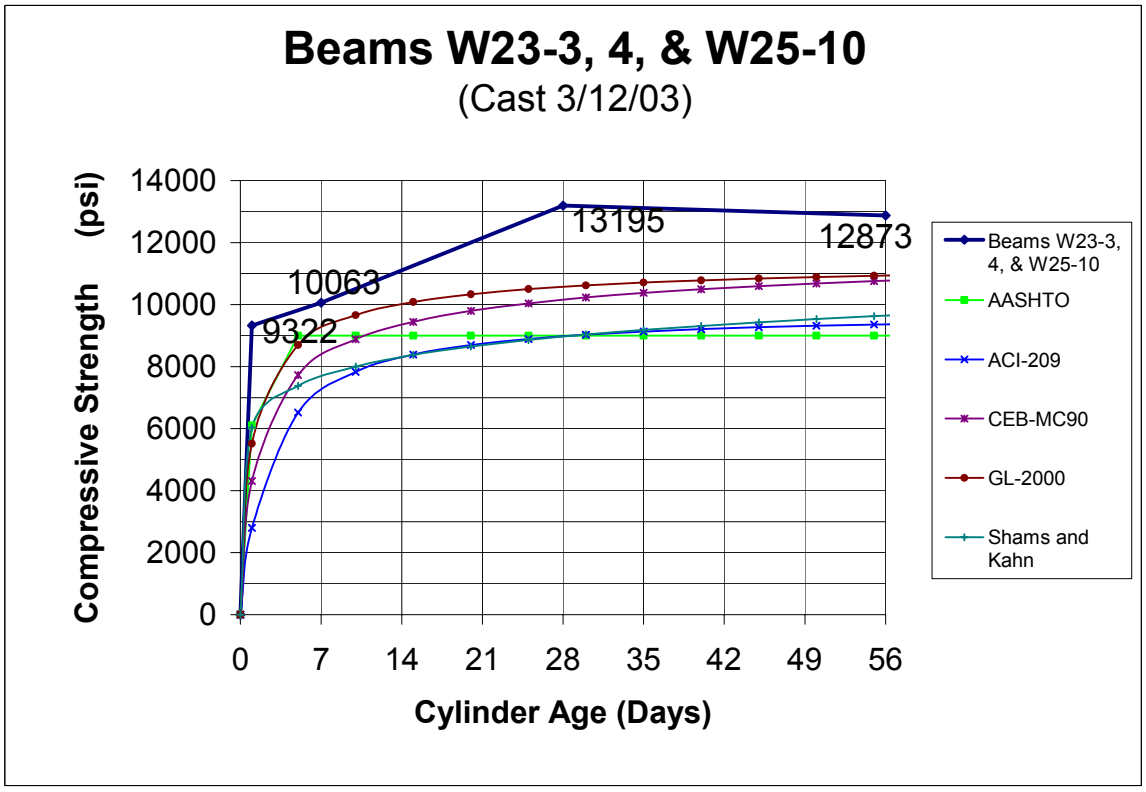

Figure 5.8 Beams W23-3, 4 & W25-10 Compressive Strength vs. Time

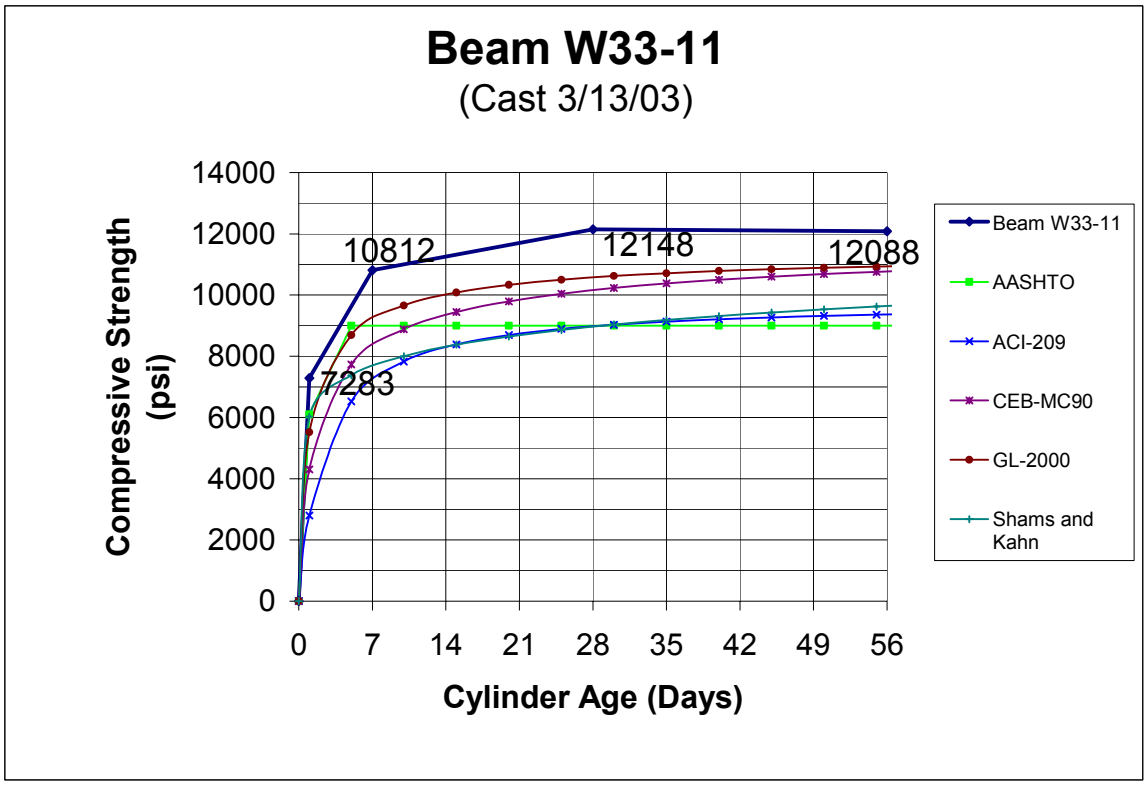

Figure 5.9 Beam W33-11 Compressive Strength vs. Time

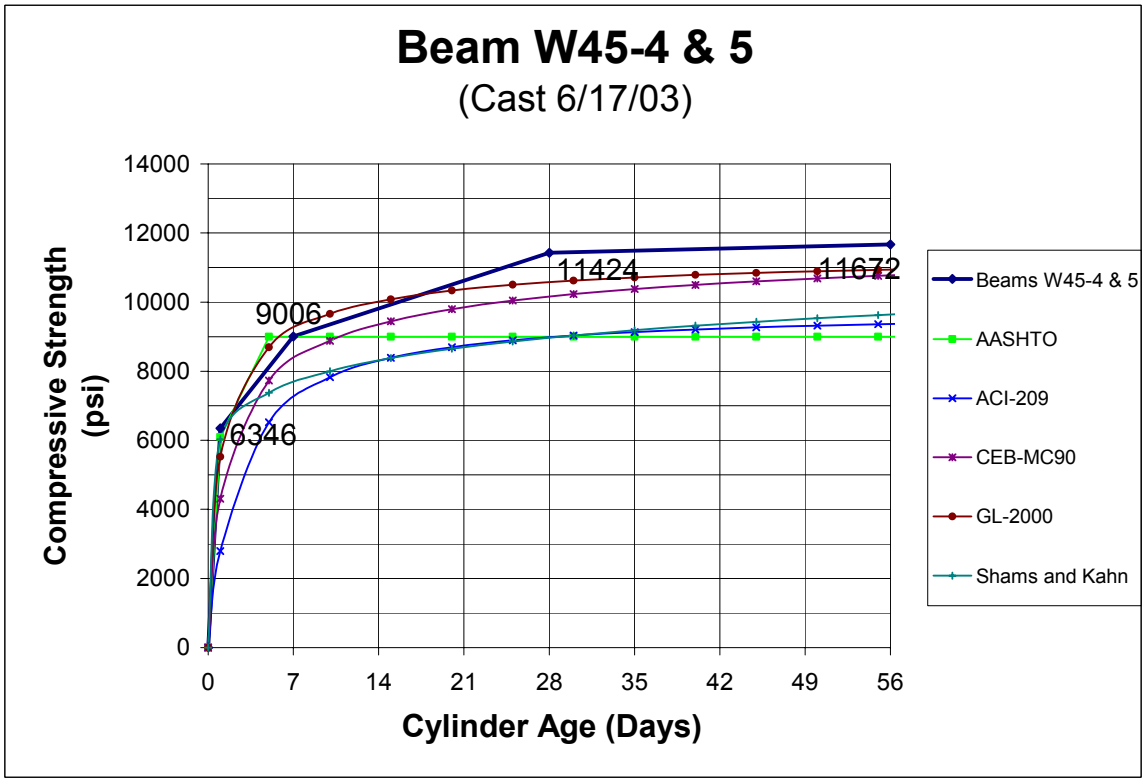

Figure 5.10 Beams W45-4 & 5 Compressive Strength vs. Time

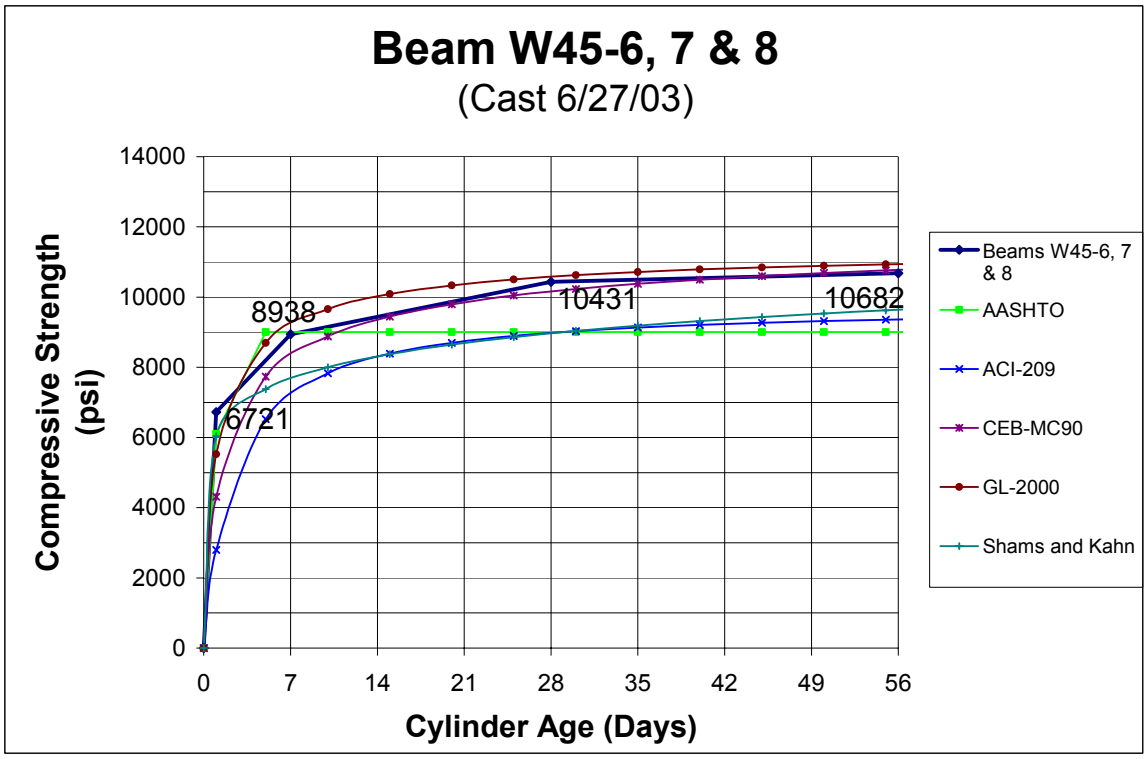

Figure 5.11 Beams W45-6,7 & 8 Compressive Strength vs. Time

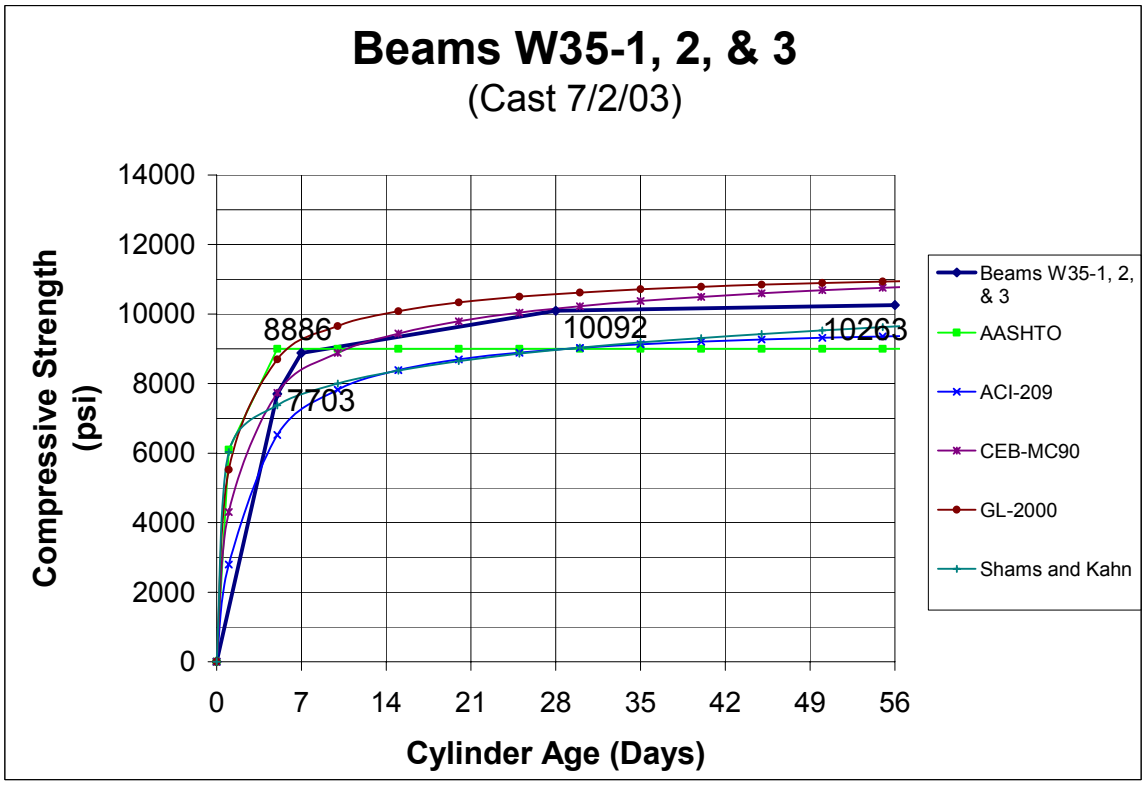

Figure 5.12 Beams W35-1, 2 & 3 Compressive Strength vs. Time

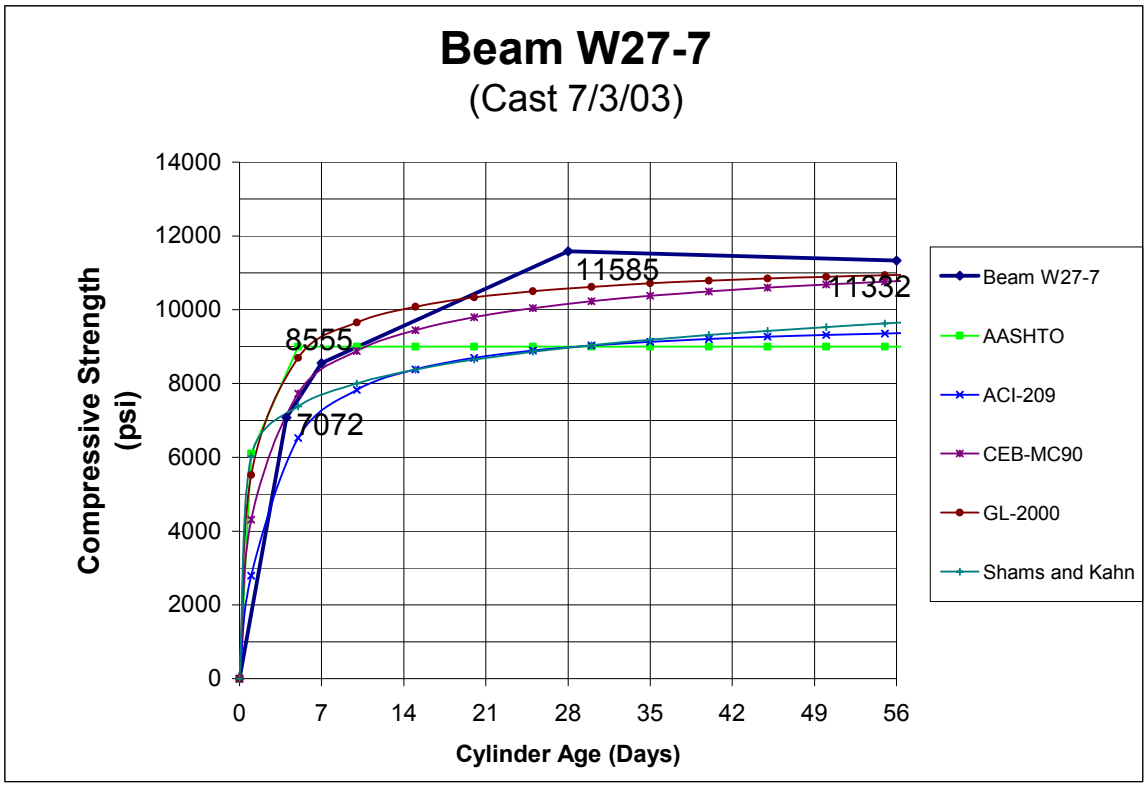

Figure 5.13 Beam W27-7 Compressive Strength vs. Time

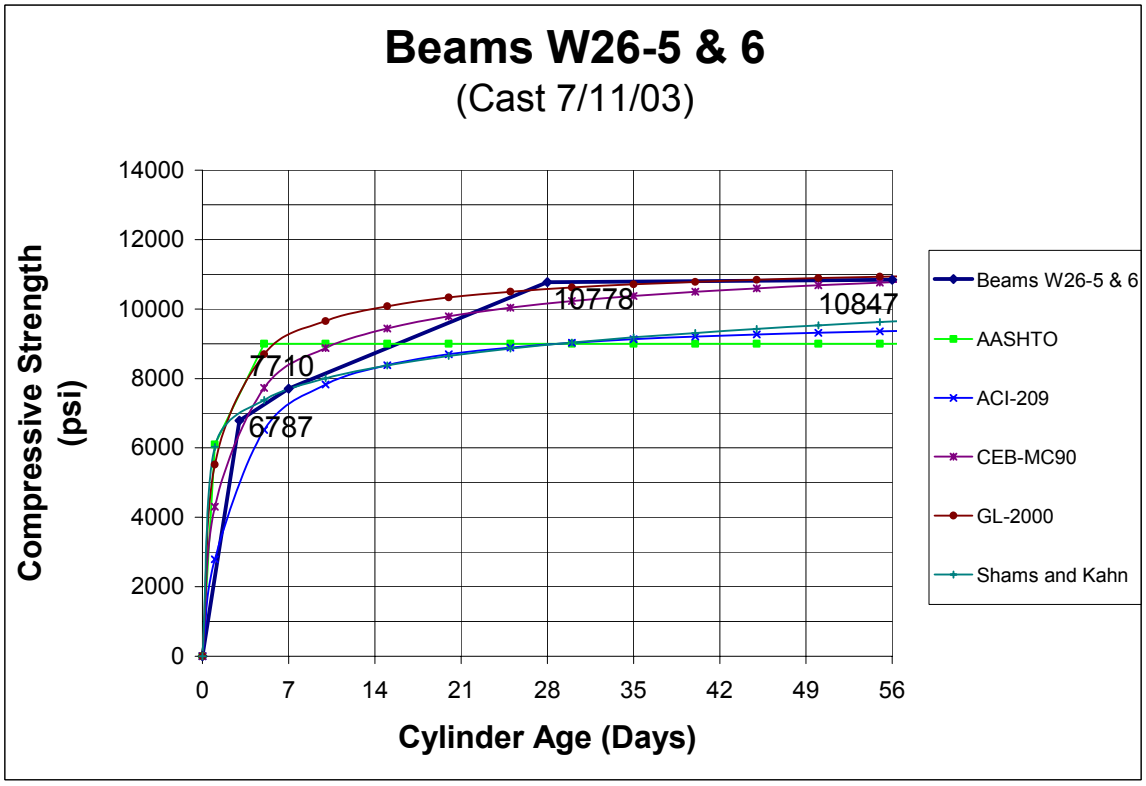

Figure 5.14 Beams W26-5 & 6 Compressive Strength vs. Time

The lowest release strength was 6350 psi for Beams W45-4 and W45-5, which were cast on 6/17/03. The highest release strength was 9890 psi for Beam W25-1, cast on 2/28/03. At an age of seven days the lowest strength was 7710 psi for Beams W26-5 and W26-6, cast on 7/11/03. The highest strength at seven days was 11,090 psi for Beams W23-2 and W31-10, cast on 3/8/03. At twenty-eight days, the lowest strength was 10,090 psi for Beams W35-1, 2, and 3 cast on 7/2/03. The highest twenty-eight day strength was 13,200 psi for Beams W23-3 and 4, and Beam W25-10 cast on 3/12/03. The final compression test was performed at fifty-six days. The lowest strength at this time was 10,260 psi for Beams W35-1, 2, and 3 cast on 7/2/03, while the highest strength was 13,130 psi for Beams W23-2 and W31-10 cast on 3/8/03.

The most noticeable result of these tests was that the predicted compressive strengths according to the various models were often much lower than the experimentally measured compressive strengths. This is not entirely unexpected, since the theoretical prediction equations are based on the 28 day design strength of 9000 psi. The measured 28-day compressive strength was much higher than the design strength for all measured cylinders. It is desirable for the precaster to use a high early strength concrete mix, since much of the cost to produce a prestressed concrete beam is attributable to the length of time that beam is occupying the casting bed. The longer a beam stays in the bed, the longer it is until the next beam can be cast. Also, the precaster does not want to risk rejection of a beam if it exhibits low compressive strength when the cylinders are tested. It is for these reasons that the precaster would prefer to overshoot the specified compressive strength than to supply a concrete mix that barely achieves the required design strength.

Another interesting trend was observed in the compression testing results. The Winter cylinder breaks consistently achieved higher strengths than the Spring/Summer cylinder breaks. This agrees with the findings of Klieger (1958) and Verbeck and Helmuth (1968) as well as the hot weather behavior of concrete described in ACI-305 (1999), which are all discussed in Chapter 2. There are two potential contributing factors for this phenomenon. The first is that extra water was added to the mixes poured in summer to compensate for increased water consumption, and decreased workability and slump experienced in summer ambient conditions approaching 90 ^{o}F. This would

increase the water/cement ratio and, consequently decrease concrete strength. The second factor is that the high temperature itself causes lower long-term compressive strength compared with concrete cast and cured at lower temperatures. This trend is shown in Figure 5.15.

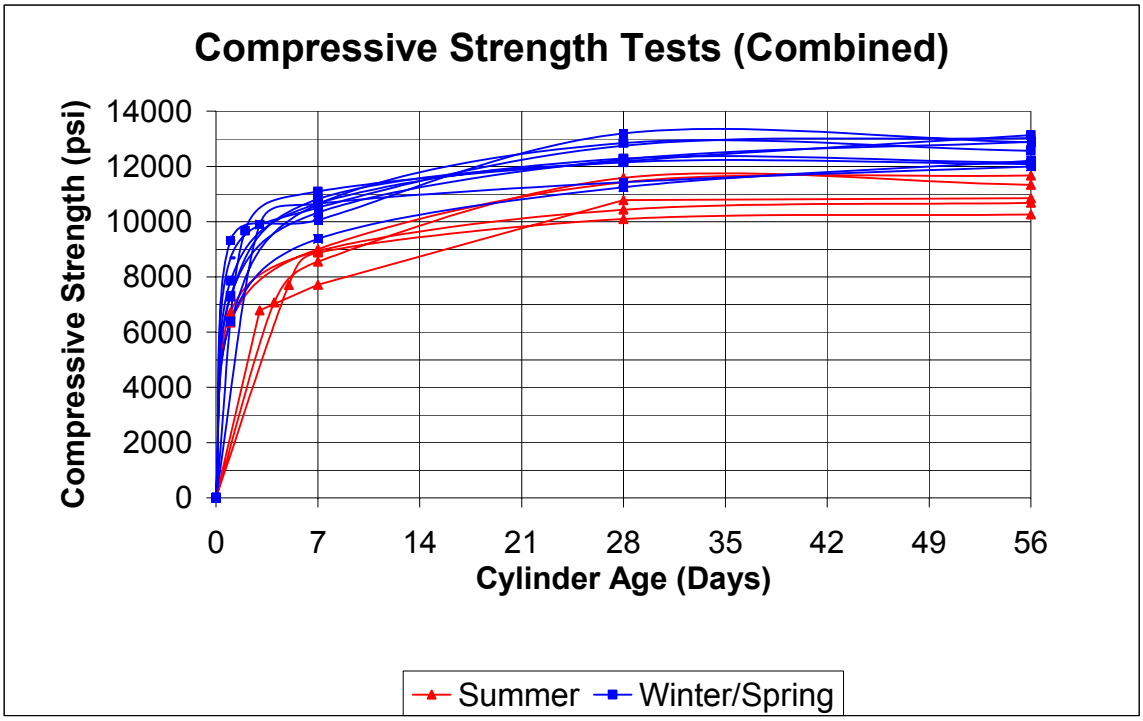

Figure 5.15 Compressive Strength Testing Results (Precaster)

Additional cylinders from a representative pour on 7/3/2003 were cast, as described in Chapter 3, in order to test modulus of elasticity at Virginia Polytechnic Institute and State University (Virginia Tech). The precaster did not perform modulus of elasticity testing. Additional compressive strength testing was also performed at Virginia Tech. The results of these compressive strength tests are shown in Figure 5.16. Each point is an average of 2 cylinders. This testing resulted in compressive strengths that were much lower than the average strengths recorded by the precaster, although the values were closer to the summer cylinder compression strengths recorded by the precaster. The theoretically predicted compressive strengths are also shown in Figure 5.16 for comparison. At early ages, the experimentally measured compressive strengths

are matched best by the CEB-MC90 prediction equation, however the measured strengths appear to flatten out at later ages compared with CEB-MC-90. At ages past 28-days, the experimentally measured compressive strengths do not appear to be matched consistently well by any of the considered models, although at 56 days the experimental strengths seem to approach the Shams and Kahn predicted strengths. The highest time-dependent compressive strength at ages beyond 28-days was predicted by the Gardner-Lockman Model, while the lowest time-dependent compressive strength during that time range was according to the design strength used by the ACI-209 Model.

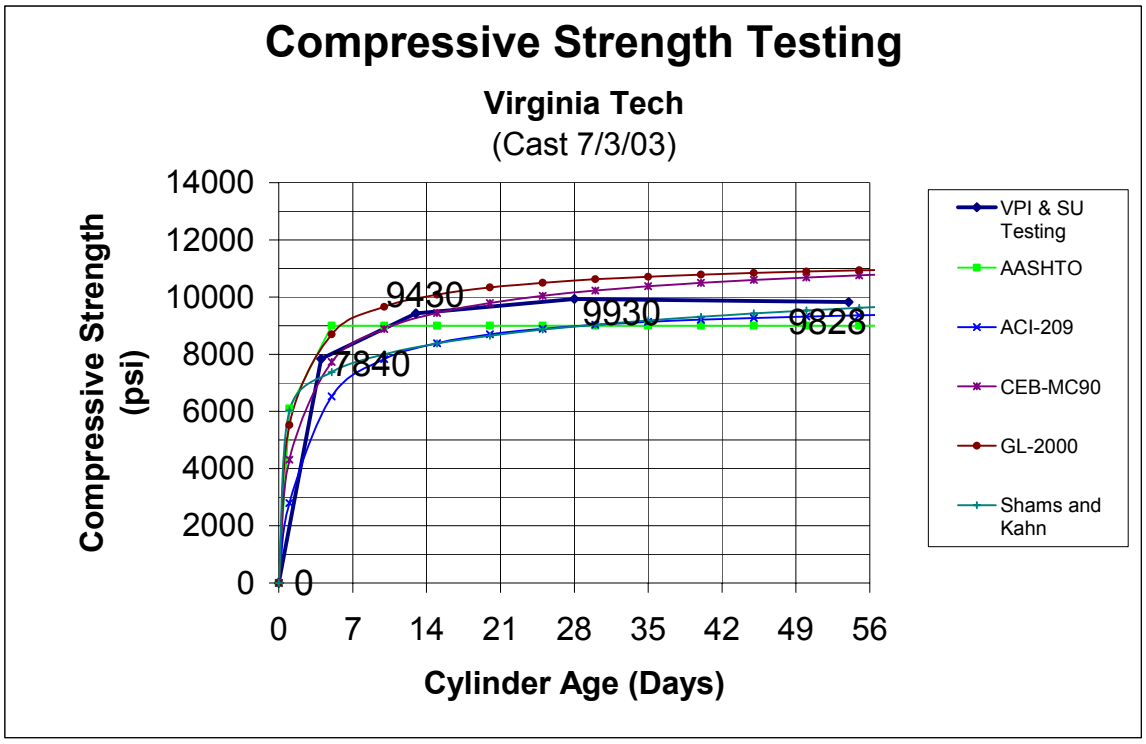

Figure 5.16 Compressive Strength Test Results (Virginia Tech)

The modulus of elasticity experimental test results are shown in Figure 5.17. The predicted values of modulus of elasticity according to the theoretical models are also shown in this figure for comparison. The considered models include the equations of AASHTO (1998), ACI-363, and NCHRP 496 which calculate modulus of elasticity based on the compressive strengths at release and 28 days, and the time-dependent models of ACI-209, CEB-MC90, Gardner-Lockman (GL-2000), and Shams and Kahn.

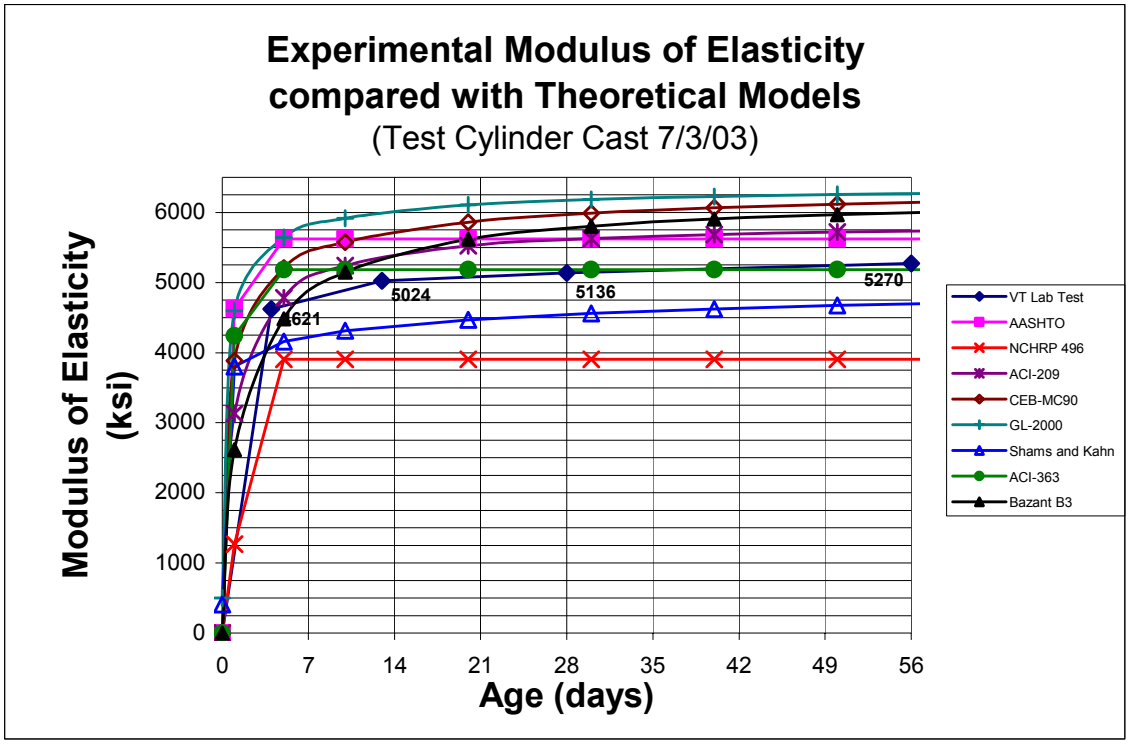

Figure 5.17 Test Cylinder Modulus of Elasticity vs. Age

Of all the models as presented, the ACI-363 equation appeared to produce values most closely representing the experimentally measured modulus of elasticity at 28 days. Due to the gradual increase in the measured modulus of elasticity, the ACI-363 equation with design concrete strength was also the best match of any model beyond 7 days. This is true despite the fact that the ACI-363 equation does not have a time-dependent component. Examining the predicted values of the other equations that are not time-dependent, the NCHRP 496 prediction equation yielded the lowest values for modulus of elasticity and significantly underpredicted the experimentally measured values. The AASHTO (1998) equation significantly overpredicted the experimental test values.

Evaluating the accuracy of the time-dependent modulus of elasticity models, the ACI-209 model produced the closest values to the test results, despite overpredicting at all ages. The Gardner-Lockman (GL-2000) Model predicted the highest values, which significantly overpredicted the experimental results, while the Shams and Kahn model predicted the lowest values. It was interesting to note that the theoretically predicted values of the Shams and Kahn equation appeared to have the same curve shape, or rate of

increase in modulus of elasticity, as the experimental data. The concrete cylinders tested by Shams and Kahn, which were used to generate their prediction equation, were produced by the same precaster that produced the beams and test cylinders for this study. It is for this reason that the Shams and Kahn prediction equation was modified to approximate the measured modulus of elasticity for each beam. The modified Shams and Kahn equation was then used in conjunction with the Incremental Time Step Method to obtain the predicted time-dependent deflections, based on measured modulus of elasticity, summarized later in the chapter.

5.2 APPROXIMATION OF MEASURED COMPRESSIVE STRENGTH AND MODULUS OF ELASTICITY

The modulus of elasticity values used in the time step method were determined using two methods. The first method used predicted values calculated from the equations suggested by each model, all of which use the design concrete strength as an input variable. The second method used values approximating the measured modulus of elasticity, since many of the theoretical creep and shrinkage models allow for the use of measured modulus of elasticity in the calculations.

As seen in Figure 5.17, the predicted modulus of elasticity varied significantly between theoretical models. The Shams and Kahn time-dependent modulus of elasticity equation yielded predicted values that matched the measured values reasonably well, and was observed to best match the shape of the curve fit to the measured modulus of elasticity values. The ACI-209 equation also produced values that were close to the experimentally measured modulus of elasticity values, but the shape of the predicted curve appeared to be different than the curve fitting the experimental measurements. For this reason, the Shams and Kahn modulus of elasticity equation was selected over the ACI-209 modulus of elasticity equation for use as the measured modulus of elasticity curve. Although the Shams and Kahn modulus of elasticity prediction equation appeared to best match the experimental data based on the slope and shape of the curve, the predicted values appeared to be shifted lower compared with the measured values. Looking at the compressive strength test results, the values predicted by the Shams and Kahn compressive strength equation also appeared to match the slope and shape of the

experimental curve and were shifted lower compared with the measured values for most of the beams. The Shams and Kahn compressive strength equation was modified to better fit the experimental compressive strength data for these beams.

The beams for which the Shams and Kahn compressive strength model did not appear to match the shape of the curve fit to the experimental data included beams W26-5, W26-6, W27-7, W35-1, W35-2, and W35-3. For these beams the unmodified ACI-209 compressive strength prediction equation was a closer fit to the experimental test results. These beams were all cast in late summer, and the compressive strength gain at early ages appears to be slower than predicted by the Shams and Kahn equation. The ACI-209 compressive strength equation will be used in conjunction with the Shams and Kahn modulus of elasticity equation for these beams.

The modified Shams and Kahn compressive strength equation and the ACI-209 compressive strength equation are shown with the experimental compressive strengths in Figures 5.18 and 5.19. Figure 5.18 shows a pour for which the modified Shams and Kahn equation was the better match, while Figure 5.19 shows a pour for which the unmodified ACI-209 equation was the better match. The compressive strength prediction curves chosen as the best fit for each test cylinder are shown in Appendix A.

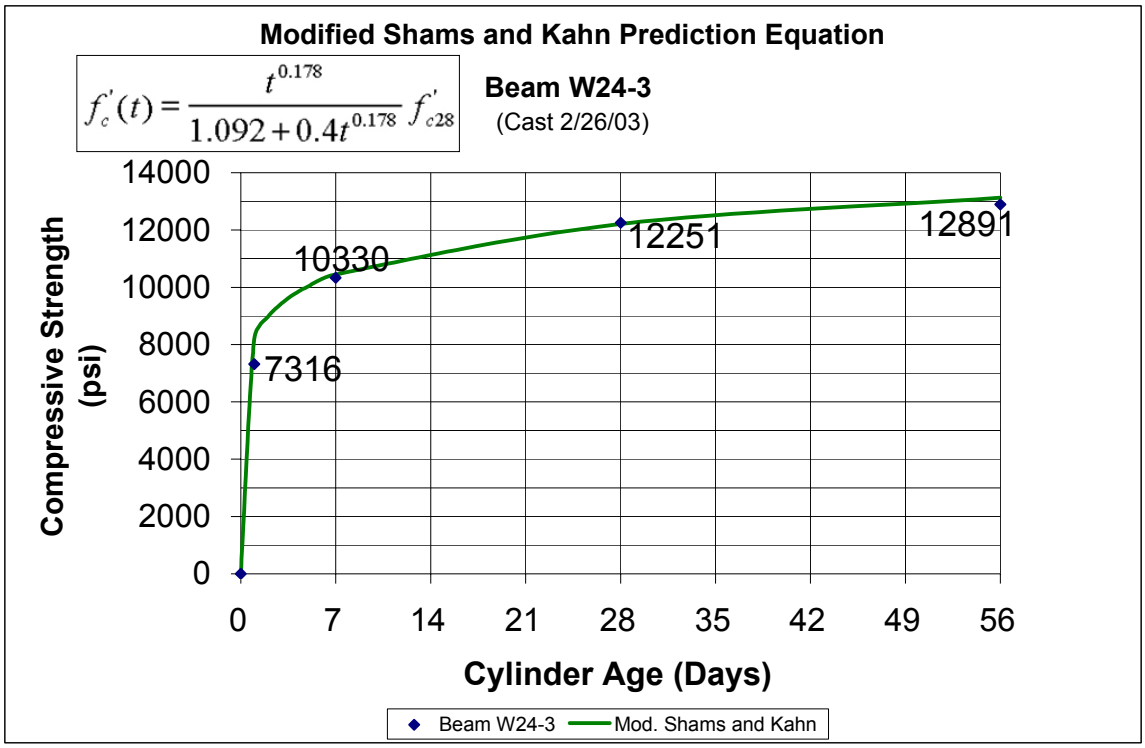

Figure 5.18 **Modified Shams and Kahn Compressive Strength Equation (Beam W24-3)**

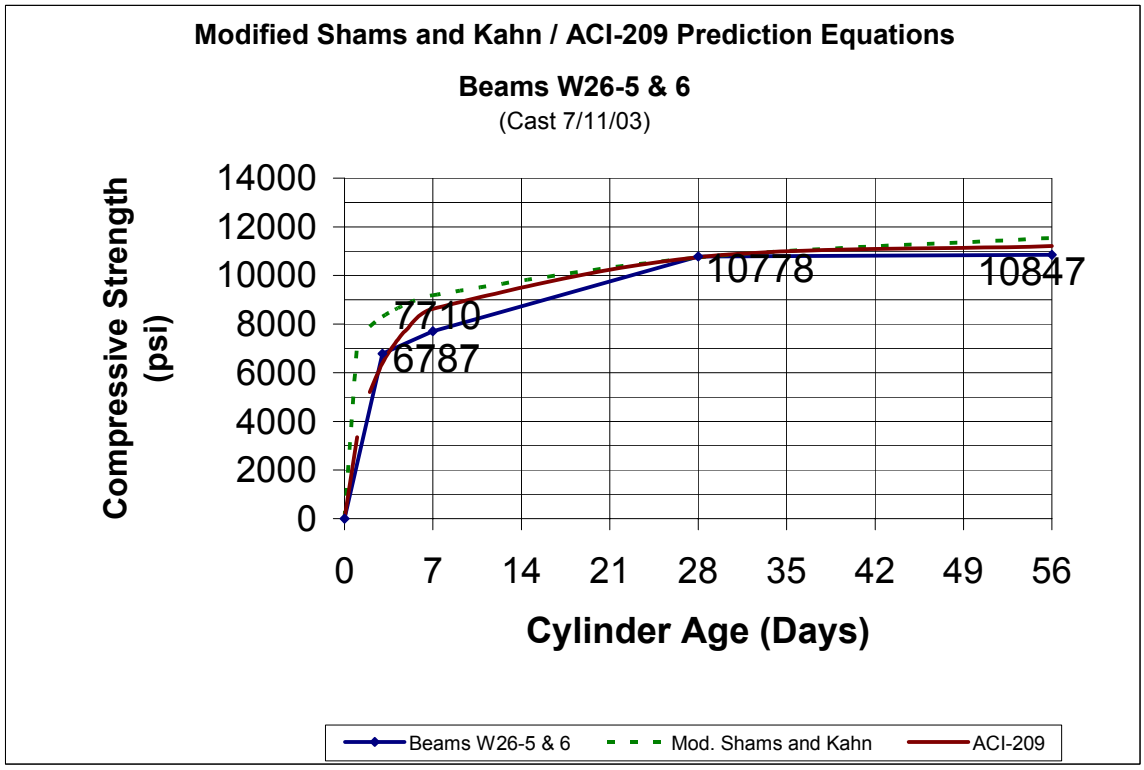

Figure 5.19 **Modified Shams and Kahn / ACI-209 Compressive Strength Equation (Beams W26-5 and W26-6)**

Since the predicted compressive strength is used as an input for the Shams and Kahn predicted modulus of elasticity, the underpredicted compressive strength contributes to the underprediction of the measured modulus of elasticity by the Shams and Kahn prediction equation. Using the modified Shams and Kahn compressive strength equation as an input, the Shams and Kahn modulus of elasticity prediction equation was also modified to better fit the measured values for the Virginia Tech modulus of elasticity test data. The multiplier and Y-Intercept of the original equation were increased until they provided a better fit to the Virginia Tech experimental test data. The results of these modifications are shown in Figure 5.20.

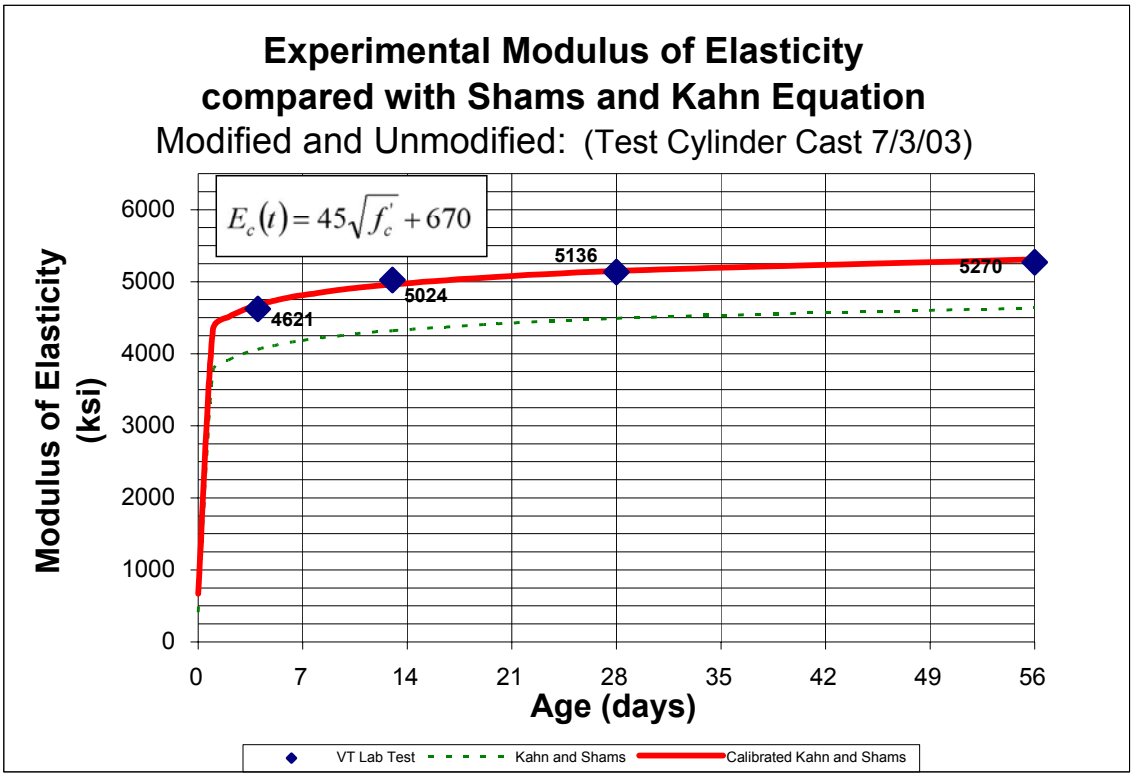

Figure 5.20 Calibrated Shams and Kahn Modulus of Elasticity Equation

5.3 RESULTS OF THEORETICAL SHRINKAGE STRAIN PREDICTION

Since shrinkage specimens were not made, experimental values for shrinkage strains were not obtained. The theoretically predicted values of shrinkage strain for each model are shown in Figure 5.21. The NCHRP 496 Model predicted shrinkage strains that were the highest of all models considered, while the Bazant B3 model predicted shrinkage strains that were the lowest.

These findings agree well with Waldron (2004), who found that the AASHTO-LRFD and ACI-209 models predicted the highest shrinkage strains, and that the CEB-MC90 model predicted the lowest shrinkage strains. These results, as well as the highest and lowest shrinkage strains predicted by several previous researchers, are shown in Table 5.3.

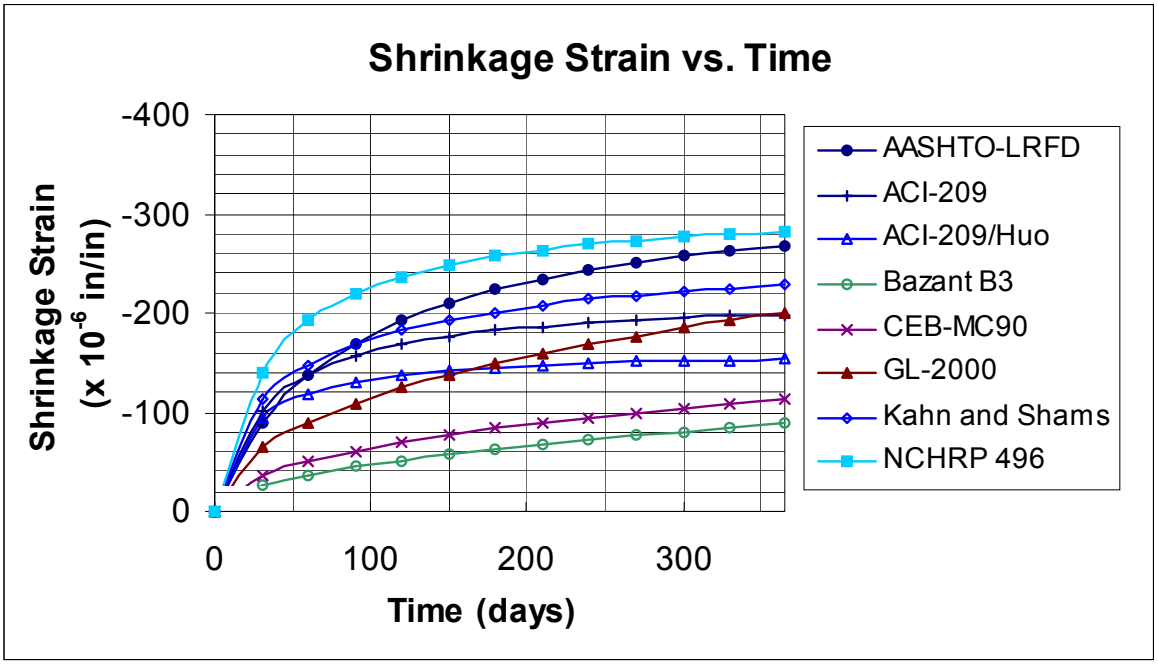

Figure 5.21 Predicted Shrinkage Strain vs. Time

Table 5.3 Maximum and Minimum Shrinkage Strains (Previous Researchers)

	Researcher				
Model	**Waldron (2004)**	**Townsend (2003)**	**Shams and Kahn (2000)**	**Canfield (2005)**	**Slapkus and Kahn (2002)**
AASHTO-LRFD	Highest	Highest	Highest	✘	✘
ACI-209	✔	✔	✔	Highest	Highest
Bazant B3	✔	Lowest	✘	✘	✘
CEB-MC90	Lowest	✔	Lowest	✘	✘
GL-2000	✔	✔		✘	✘
Shams and Kahn	✔	✘	✔	Lowest	Lowest
NCHRP 496	✔	✔	✘	✘	✘

✔ Model was examined by researcher

✘ Model was not examined by researcher

5.4 RESULTS OF THEORETICAL CREEP COEFFICIENT PREDICTION

As was the case with the shrinkage strains, it was not possible to experimentally determine creep coefficients, since specimens were not made. The theoretically predicted creep coefficients according to the considered models are presented below in Figure 5.22. Many of the theoretical models, since they were originally developed for moist-cured, normal-weight, low strength concrete, have minimum loading ages of 7 days. These include AASHTO-LRFD (1998), ACI-209, and NCHRP 496. For these models, the minimum allowed loading age of seven days was used as the input variable, rather than the typical loading age of 1 day for the actual beams. The remaining models did not specify a minimum loading age, so the actual loading age was used. The ACI-209 model also prescribes a minimum moist curing age of 7 days, which was used in the calculations for that model.

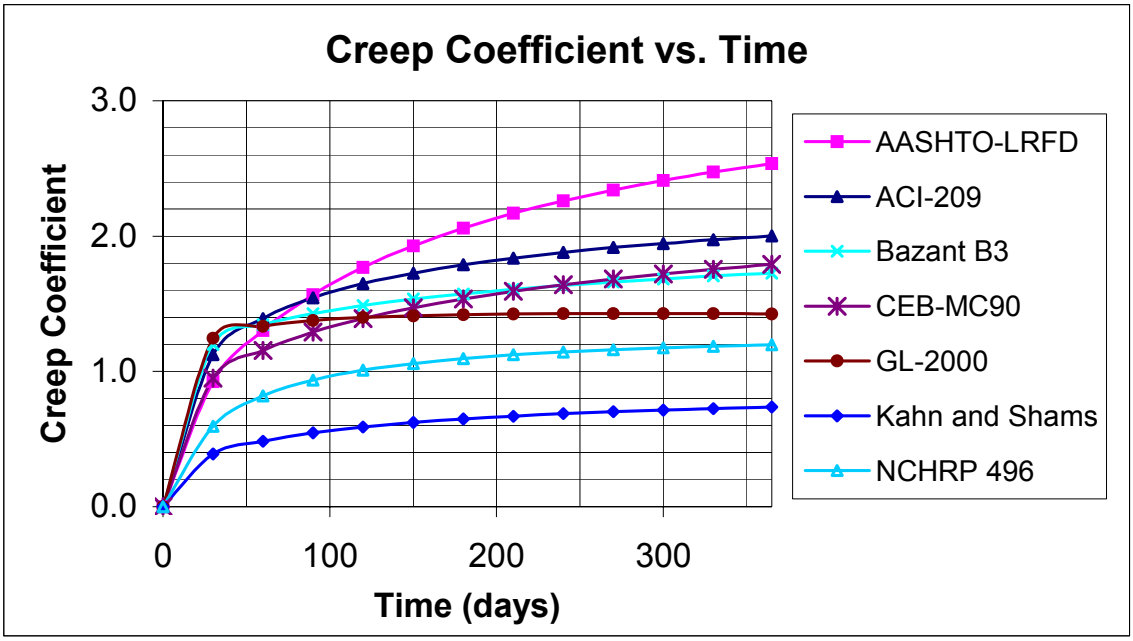

Figure 5.22 Predicted Creep Coefficient vs. Time

The AASHTO-LRFD (1998) Model yielded predicted values that were significantly higher than the predicted values of the other models, especially at later ages. The Shams and Kahn Model predicted the lowest creep coefficient values, followed by the NCHRP 496 Model. The CEB MC90 and Bazant B3 models produced similar values and curves at later ages, but differed significantly in their early age prediction. The Gardner-Lockman Model (GL-2000) exhibited an extremely rapid increase in creep coefficient at early age, with a relatively flat increase at later ages.

The results of previous researchers, indicating the highest and lowest creep coefficients predicted by each study, are shown in Table 5.4.

Table 5.4 Maximum and Minimum Creep Coefficient (Previous Researchers)

	Researcher					
Model	**Waldron (2004)**	**Townsend (2003)**	**Meyerson (2001)**	**Shams and Kahn (2000)**	**Canfield (2005)**	**Slapkus and Kahn (2002)**
AASHTO-LRFD	✔	✔	✔	Lowest	✘	✘
ACI-209	✘	✔	✔	✔	Highest	Highest
ACI-209 (by Huo)	✘	Lowest	✘	✘	✘	✘
Bazant B3	✔	✔	✔	✘	✘	✘
CEB-MC90	Highest	✔	✔	Highest	✘	✘
GL-2000	✔	Highest	Lowest		✘	✘
Sakata	✘	✘	Highest	✘	✘	✘
Shams and Kahn	Lowest	✘	✘	✔	Lowest	Lowest
NCHRP 496	✔	✔	✘	✘	✘	✘

✔ Model was examined by researcher

✘ Model was not examined by researcher

Although none of the cited studies observed AASHTO-LRFD to predict the highest creep coefficients, Shams and Kahn was observed to predict the lowest creep coefficients by three researchers.

5.5 COMPARISON OF MEASURED AND PREDICTED CAMBER VALUES

As was previously stated, beams varying in length by no more than ½ percent were considered identical for the purposes of the study and grouped into samples. The measured deflection versus time of each beam in the sample is shown, as is the predicted deflection curve versus time for each model. The predicted deflection curves are based on the shrinkage strain and creep coefficient predicted by the considered models. The modulus of elasticity values used in the analysis were based either on the model-predicted values, or the approximated measured values obtained from the modified Shams and Kahn equation as previously discussed.

For each beam sample, the 28-day design compressive strength was used to calculate the predicted modulus of elasticity for each model. The average 28-day compressive strength for the entire sample was used with the modified Shams and Kahn modulus of elasticity prediction equation to approximate the measured modulus of elasticity. Additional beams not assigned to a beam sample also used the 28-day design compressive strength for predicted modulus of elasticity and the experimental 28-day compressive strength for that beam as an input for calculating the approximated measured modulus of elasticity. The modulus of elasticity values obtained using the measured compressive strengths and the modified Shams and Kahn modulus of elasticity model will hereafter be referred to as the "measured" modulus of elasticity in subsequent graphs showing predicted beam deflections. It is necessary to refer to these modulus values as "measured" to distinguish them from the entirely theoretically predicted values. The justification for this is that these modulus of elasticity values are based on the experimentally measured compressive strengths, even though modulus of elasticity was not measured for each beam. These quasi-experimental modulus of elasticity values were then used in the incremental time step method in lieu of the modulus of elasticity equation suggested by each considered model.

The residuals, which are the algebraic differences between the measured and predicted deflection values, were plotted for each model as a function of time. The residuals were calculated for each model using the predicted and measured modulus of elasticity values. Residuals are negative when the measured values are underpredicted and positive when the measured values are overpredicted. Figures 5.23 through 5.52 and Tables 5.5 through 5.10 show the results for Beam Sample 1. The summary results for Beam Sample 2 are shown in Figures 5.53 through 5.61 and Tables 5.11 through 5.16. The summary results for Beam Sample 3 are shown in Figures 5.62 through 5.70 and Tables 5.17 through 5.22. For Beam Samples 2 and 3, the detailed charts of each model compared with measured deflections are included in Appendix A. The results for individual beams not included in a sample are presented in Appendix B.

5.5.1 Beam Sample 1

The measured deflections of Beam Sample 1 showed a distinct difference between the beams cast in Summer and those cast in the cooler Winter/Spring seasons. The beams in the Winter/Spring sample exhibited greater measured deflections for all beams than the beams in the Summer Sample. The measured deflections for each beam in Sample 1 are shown in Figure 5.23. The predicted deflections according to all considered models are shown in Figure 5.24. The predicted deflections according to the considered models, using the measured modulus of elasticity, are shown in Figure 5.25.

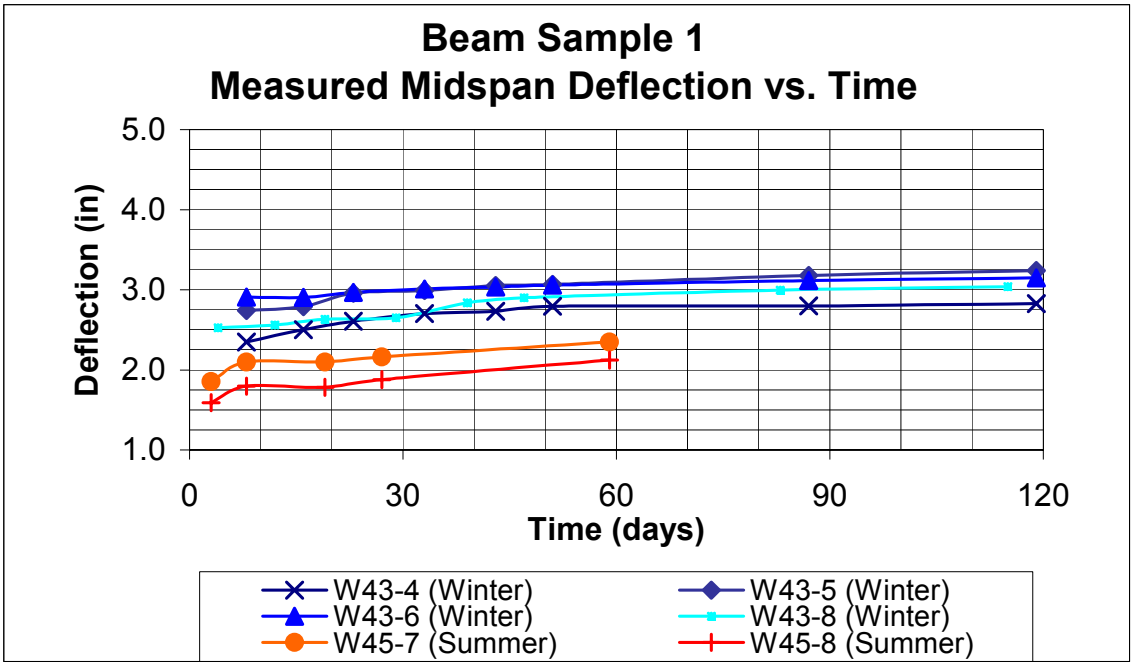

Figure 5.23 Beam Sample 1, Measured Deflection vs. Time

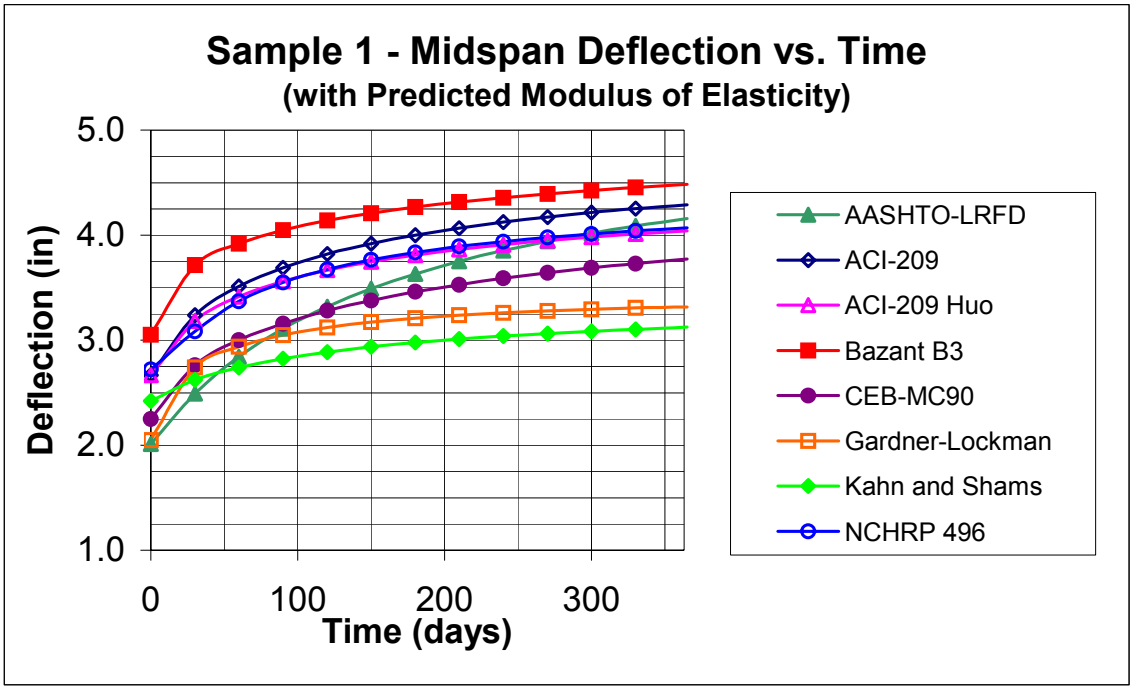

Figure 5.24 Beam Sample 1, Predicted Deflection vs. Time (Predicted E)

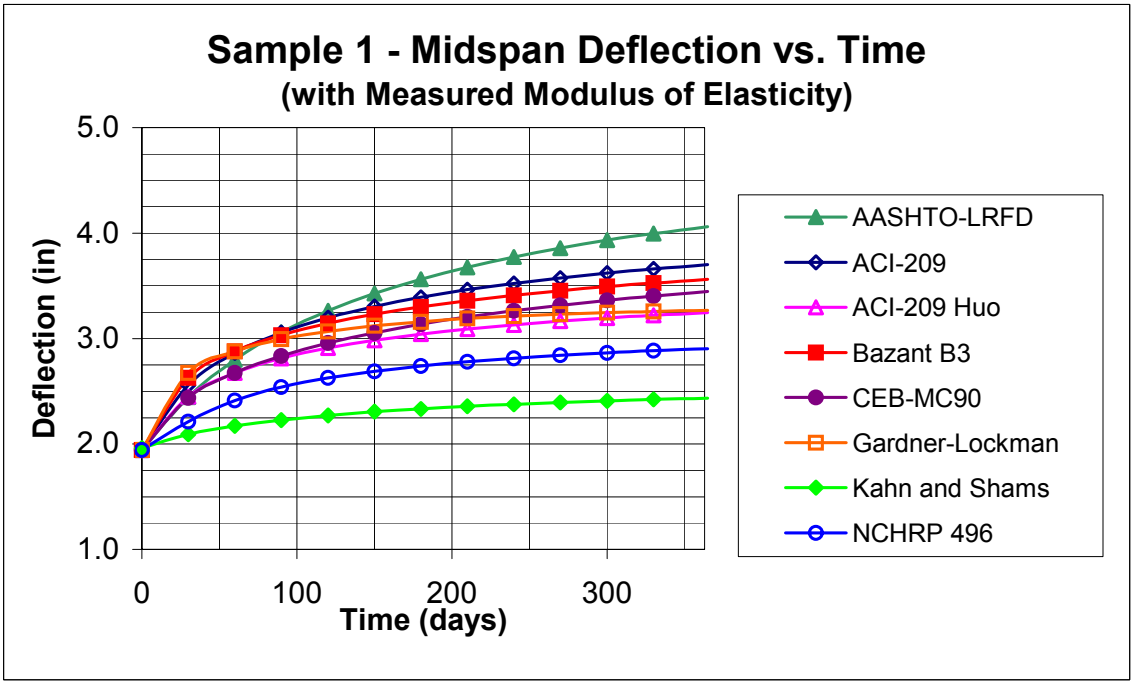

Figure 5.25 Beam Sample 1, Predicted Deflection vs. Time (Measured E)

The measured deflections of each beam in Sample 1 are shown with the predicted deflections of each considered model in Figures 5.26 to 5.49.

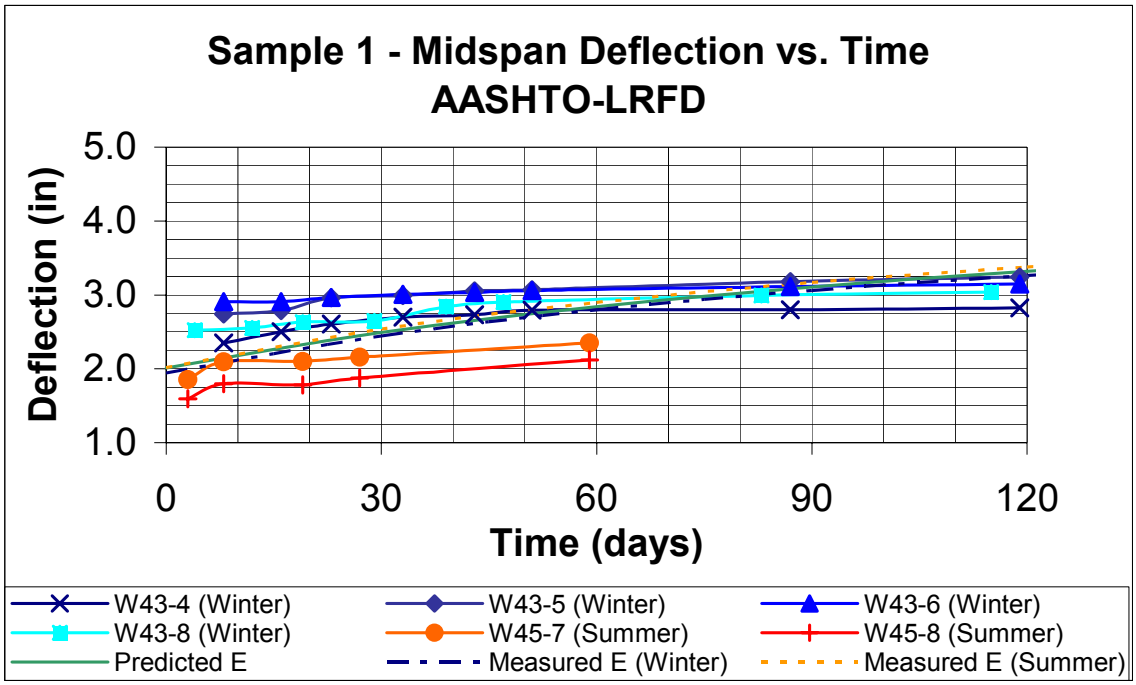

Figure 5.26 Beam Sample 1 - AASHTO-LRFD Predicted Deflection vs. Time

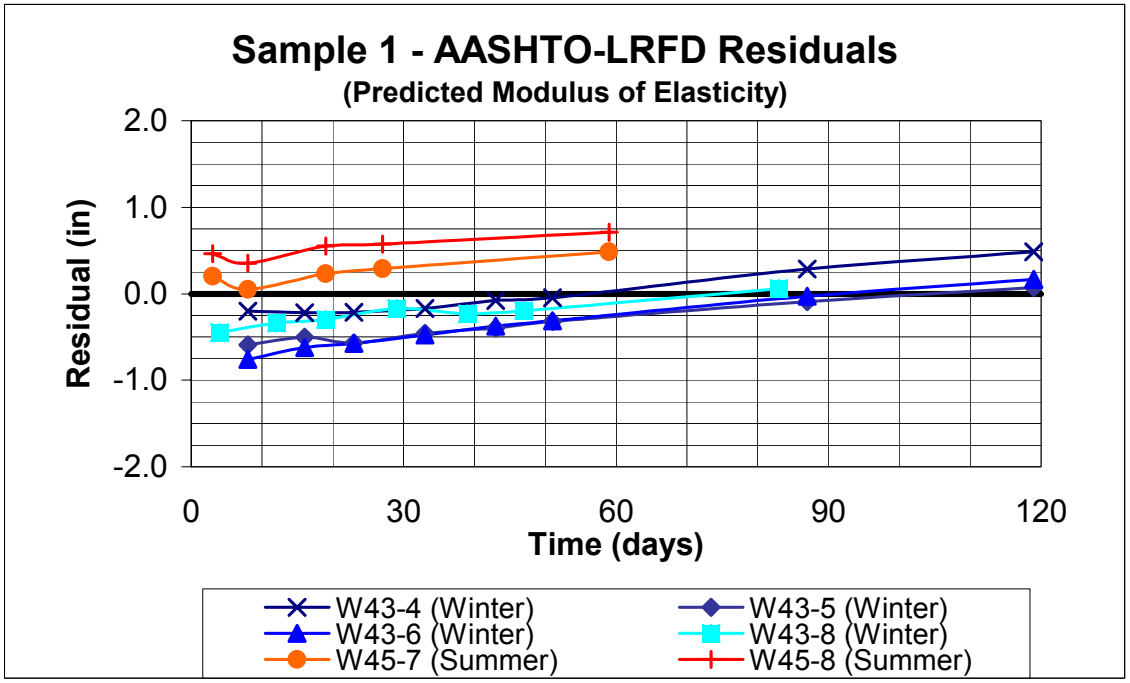

Figure 5.27 Beam Sample 1 - AASHTO-LRFD Residuals vs. Time (Predicted Modulus of Elasticity)

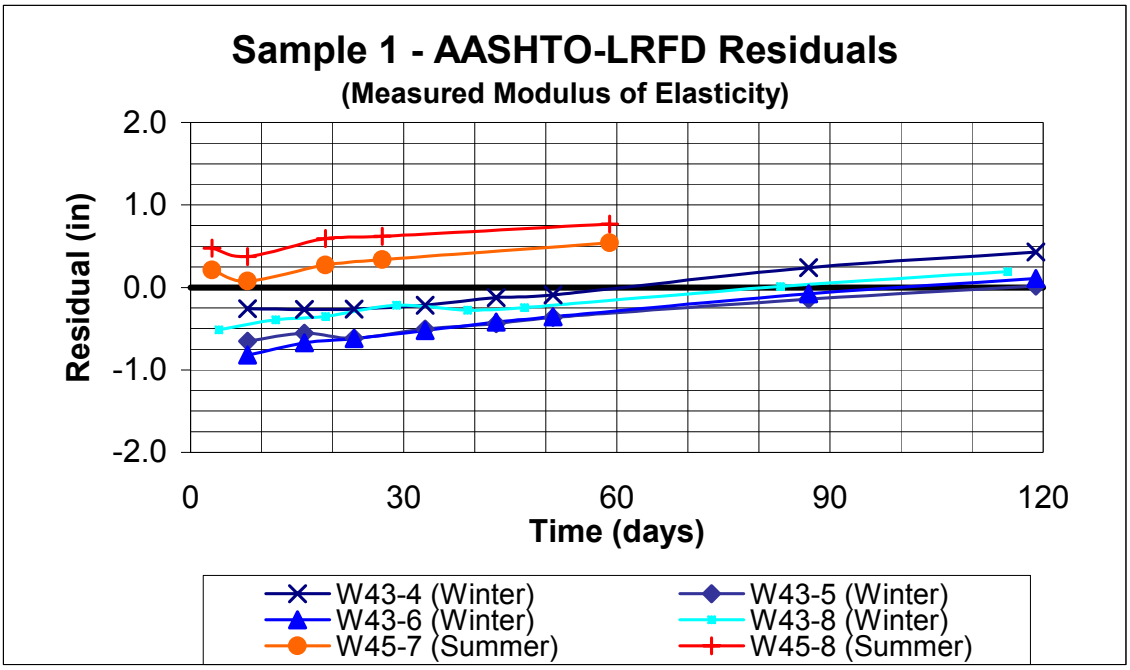

Figure 5.28 Beam Sample 1 - AASHTO-LRFD Residuals vs. Time (Measured Modulus of Elasticity)

The AASHTO-LRFD Model with predicted modulus of elasticity underestimated the measured midspan deflection for Beams W43-5, W43-6, and W43-8 until an approximate age of 90 days. These beams were cast in the winter/spring season. The beams cast in Summer, W45-7 and W45-8, appeared to match fairly well for the first 30 days before being overpredicted at later ages. At early ages, the AASHTO-LRFD Method using the measured modulus of elasticity best represented the Winter/Spring Beams. Overall, the fit for each season's beam sample was not very good for this model. This was true regardless of the modulus of elasticity value used.

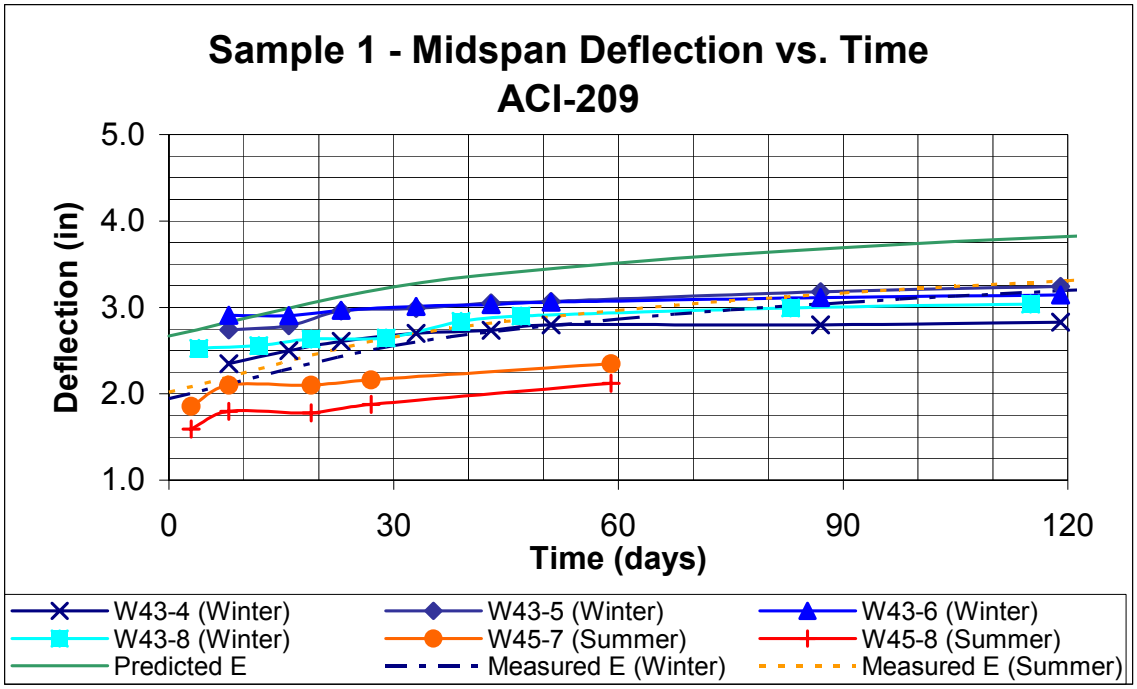

Figure 5.29 Beam Sample 1 - ACI-209 Predicted Deflection vs. Time

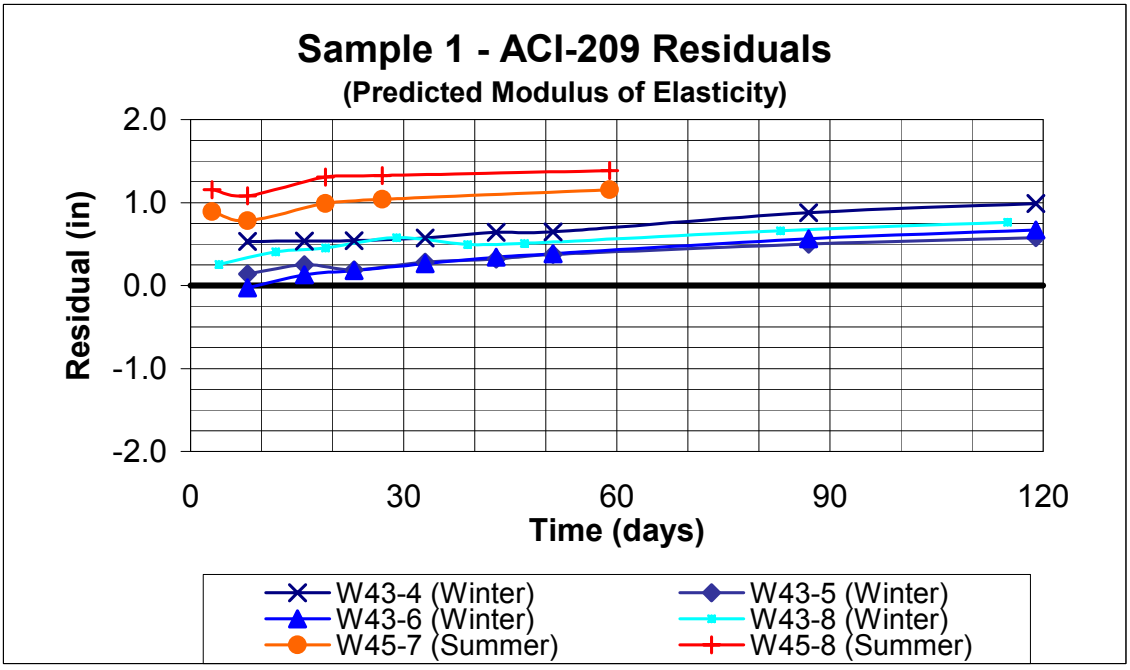

Figure 5.30 Beam Sample 1 - ACI-209 Residuals vs. Time (Predicted Modulus of Elasticity)

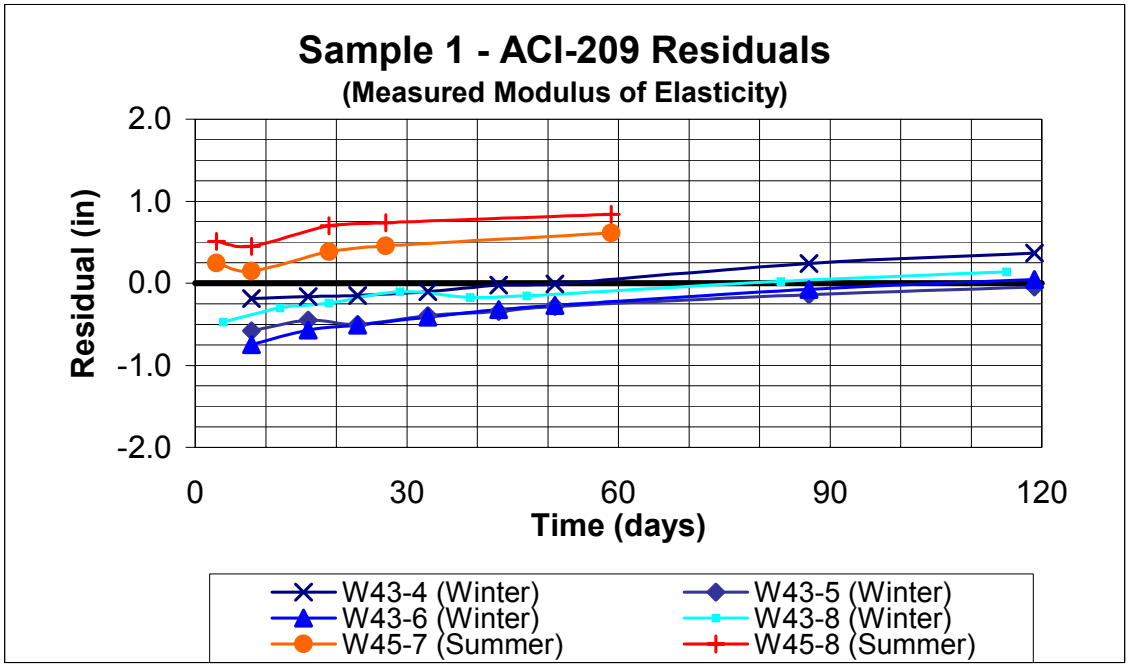

Figure 5.31 Beam Sample 1 - ACI-209 Residuals vs. Time (Measured Modulus of Elasticity)

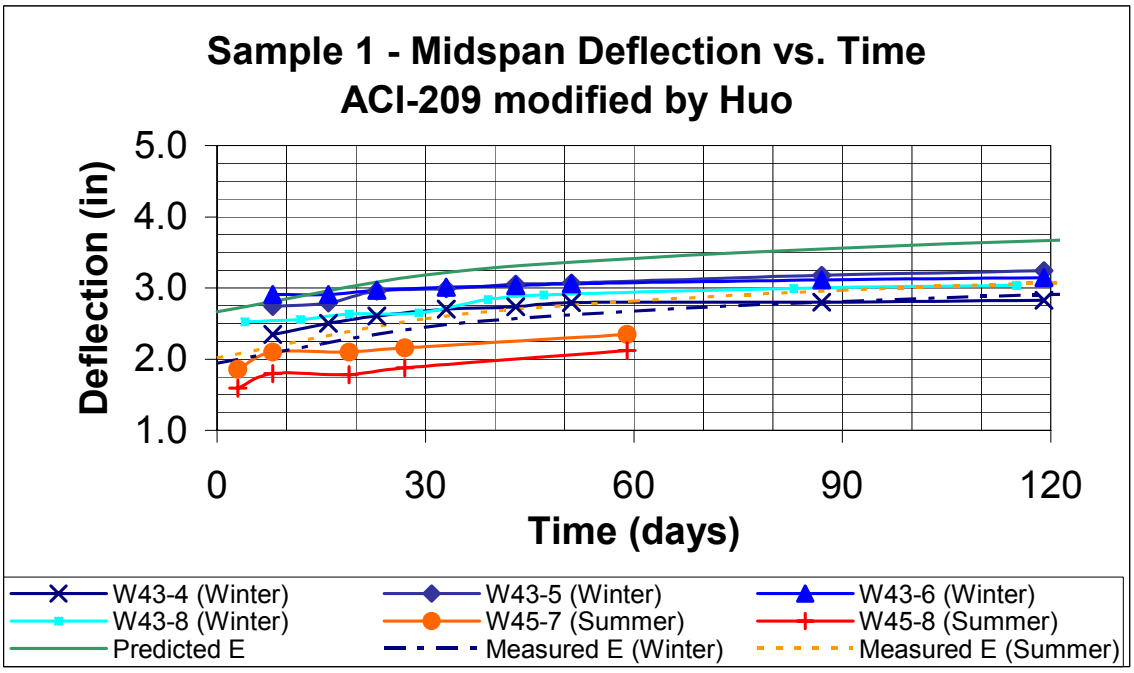

Figure 5.32 Beam Sample 1 - ACI-209 (Modified by Huo) Predicted Deflection vs. Time

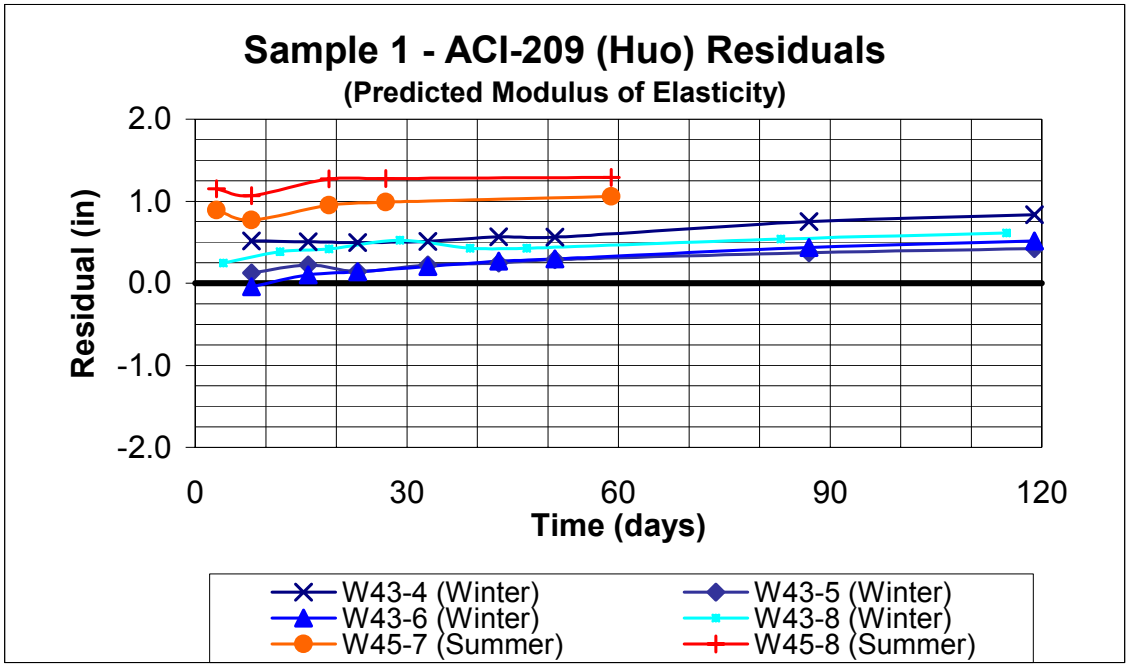

Figure 5.33 Beam Sample 1 - ACI-209 (Modified by Huo) Residuals vs. Time (Predicted Modulus of Elasticity)

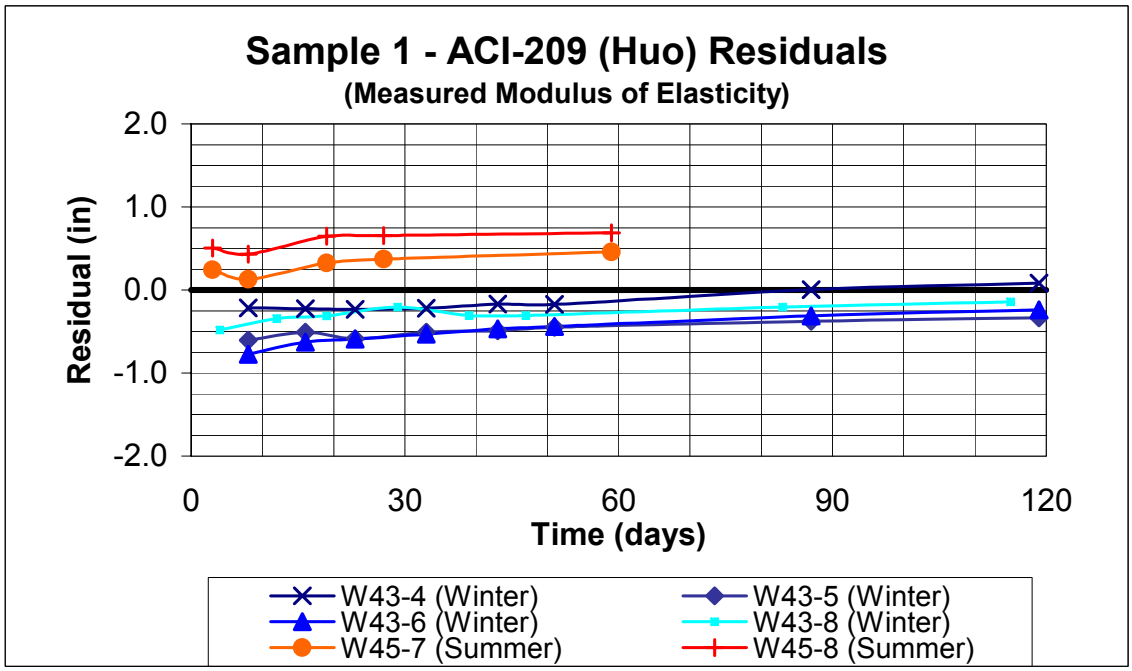

Figure 5.34 Beam Sample 1 - ACI-209 (Modified by Huo) Residuals vs. Time (Measured Modulus of Elasticity)

The ACI-209 Model, and the same model with modifications by Huo (1997) did not appear to yield significantly different predicted deflection values for the concrete mix used in this study. The model, with the predicted modulus of elasticity values, appeared to overpredict the measured deflections, by nearly 1 in. at later ages for the Winter/Spring Sample. The Summer Sample appeared to be overpredicted by a much greater margin, although measurements were not taken beyond 60 days. The ACI-209 model using the measured modulus of elasticity appeared to provide an excellent match for the Winter/Spring Beams for nearly the entire period of deflection measurement. The Summer Sample was overestimated whether measured or predicted modulus of elasticity values were used.

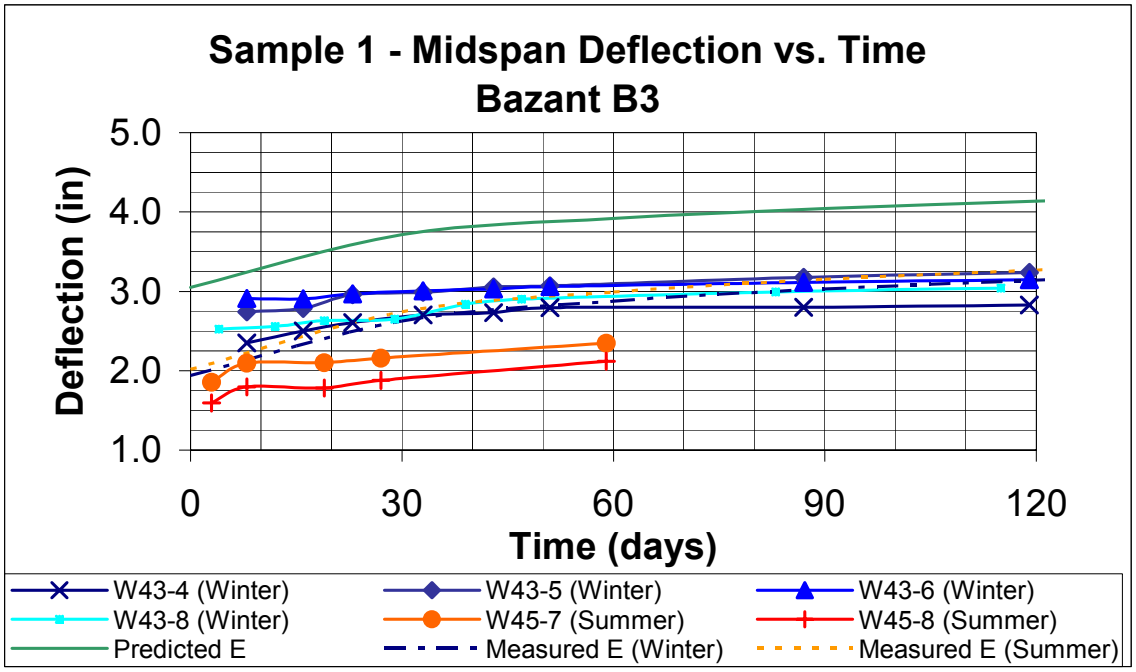

Figure 5.35 Beam Sample 1 - Bazant B3 Predicted Deflection vs. Time

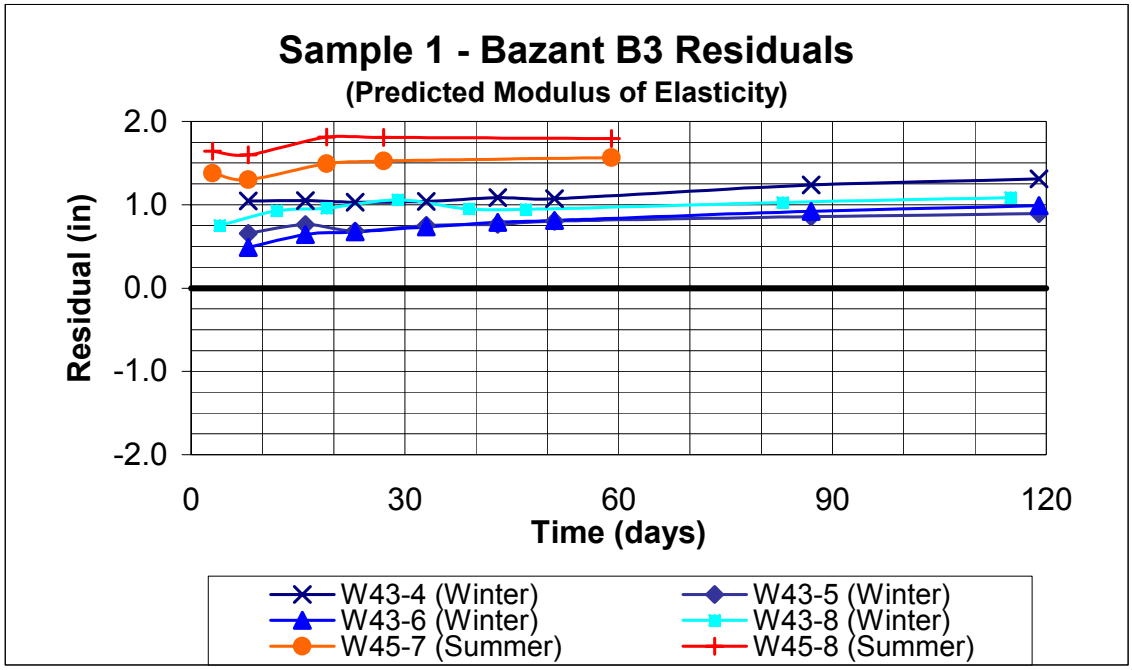

Figure 5.36 Beam Sample 1 - Bazant B3 Residuals vs. Time (Predicted Modulus of Elasticity)

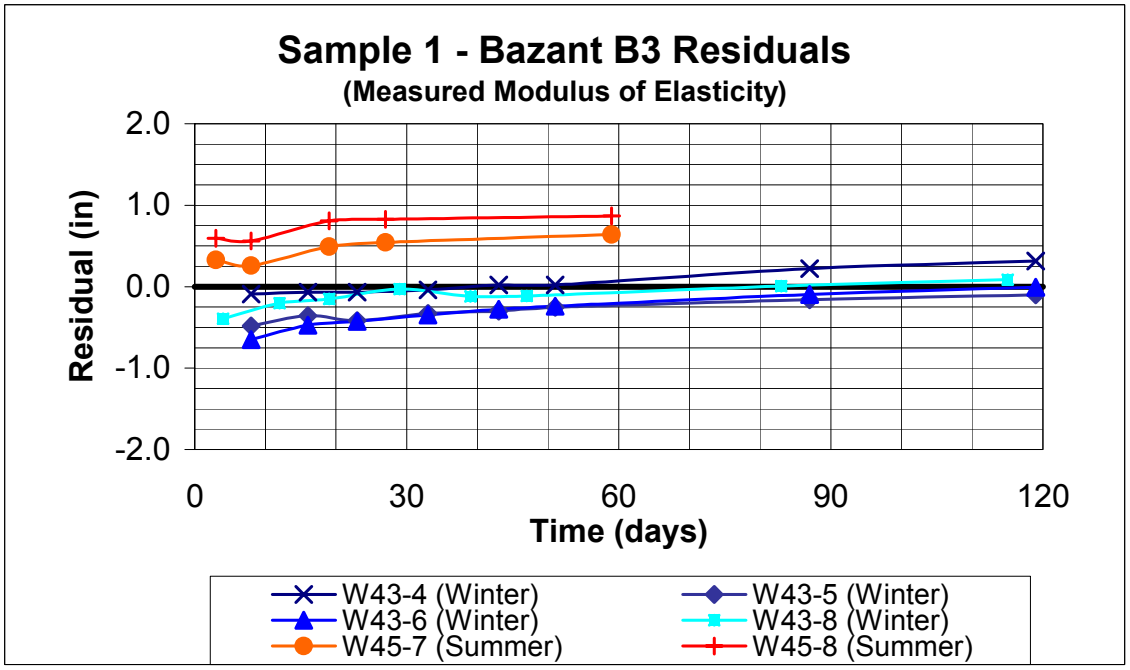

Figure 5.37 Beam Sample 1 - Bazant B3 Residuals vs. Time (Measured Modulus of Elasticity)

When the measured modulus of elasticity values were used, the Bazant B3 Model was a good fit for the Winter/Spring beam sample, but overpredicted the Summer beam sample camber by ½ in. Using the predicted modulus of elasticity values with the Bazant B3 Model resulted in predicted camber nearly 1 in. greater than the measured camber for the Winter/Spring beams and 1 ½ in. greater for the Summer beams

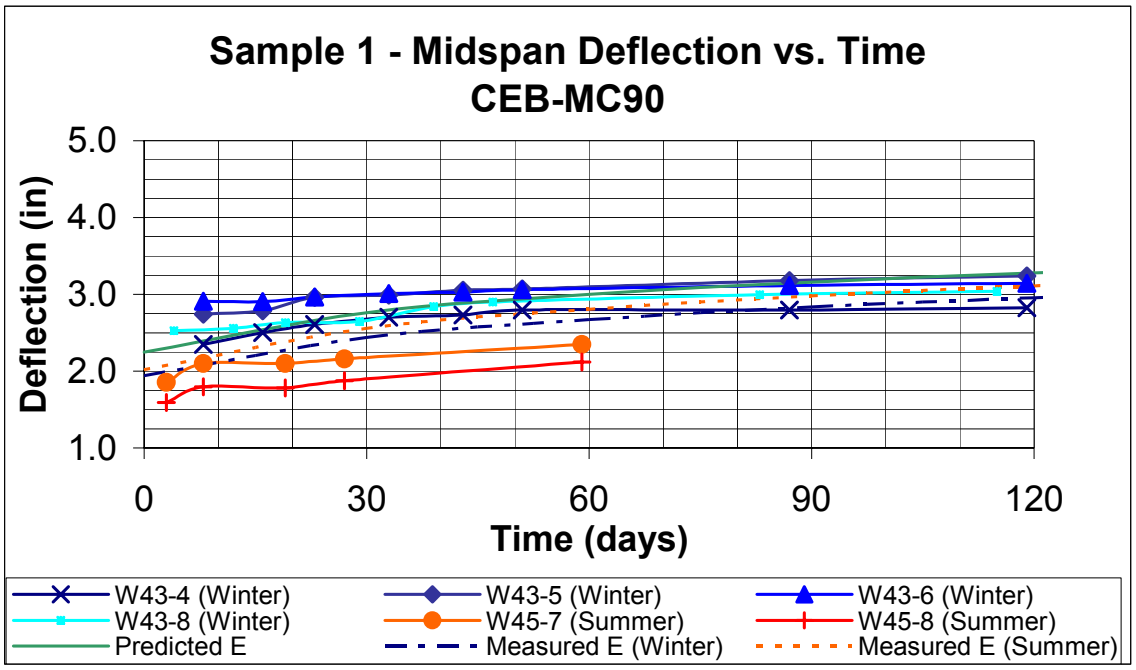

Figure 5.38 Beam Sample 1 - CEB-MC90 Predicted Deflection vs. Time

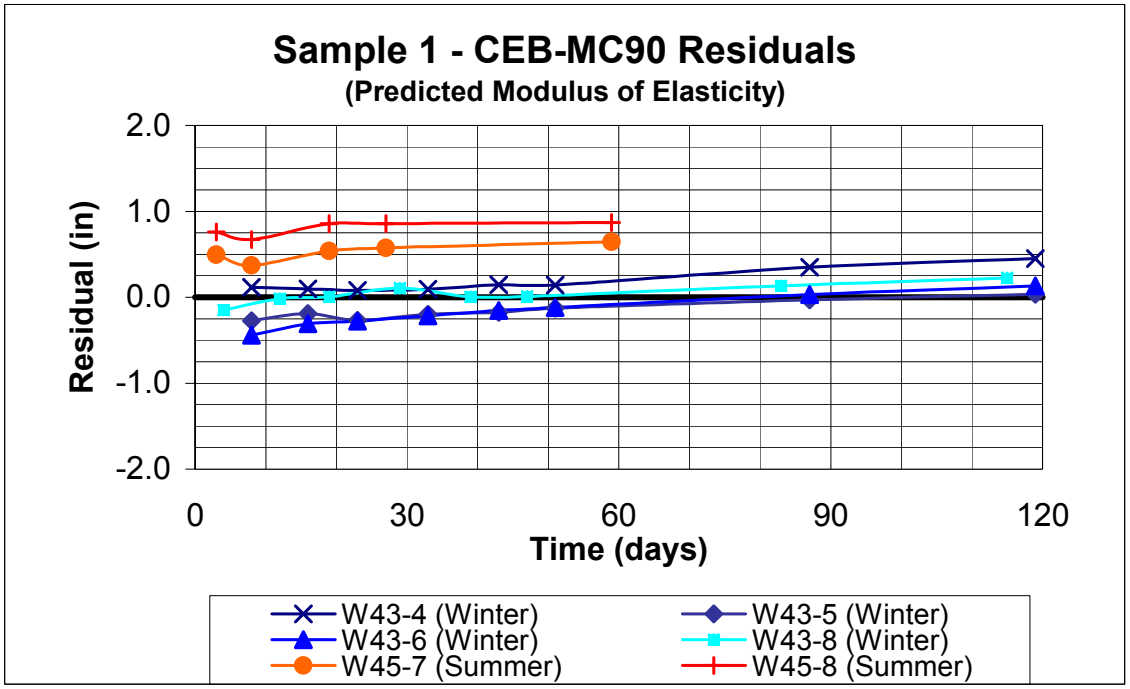

Figure 5.39 Beam Sample 1 - CEB-MC90 Residuals vs. Time (Predicted Modulus of Elasticity)

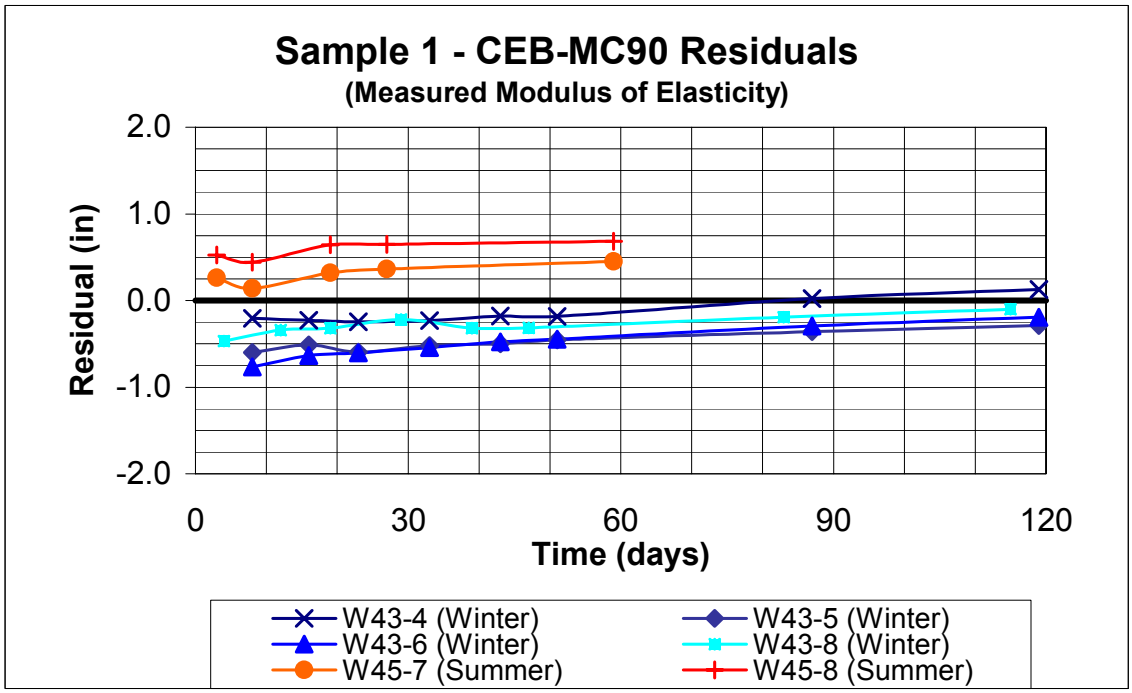

Figure 5.40 Beam Sample 1 - CEB-MC90 Residuals vs. Time (Measured Modulus of Elasticity)

The CEB-MC90 Model provided an excellent fit for the Winter/Spring beam sample using either the measured or predicted modulus of elasticity values. The differences between the deflections predicted using the measured modulus of elasticity and those predicted using the predicted modulus of elasticity values were less than ¼ in.for the entire prediction interval. The deflections of the Summer Sample were overpredicted by the CEB-MC90 Model.

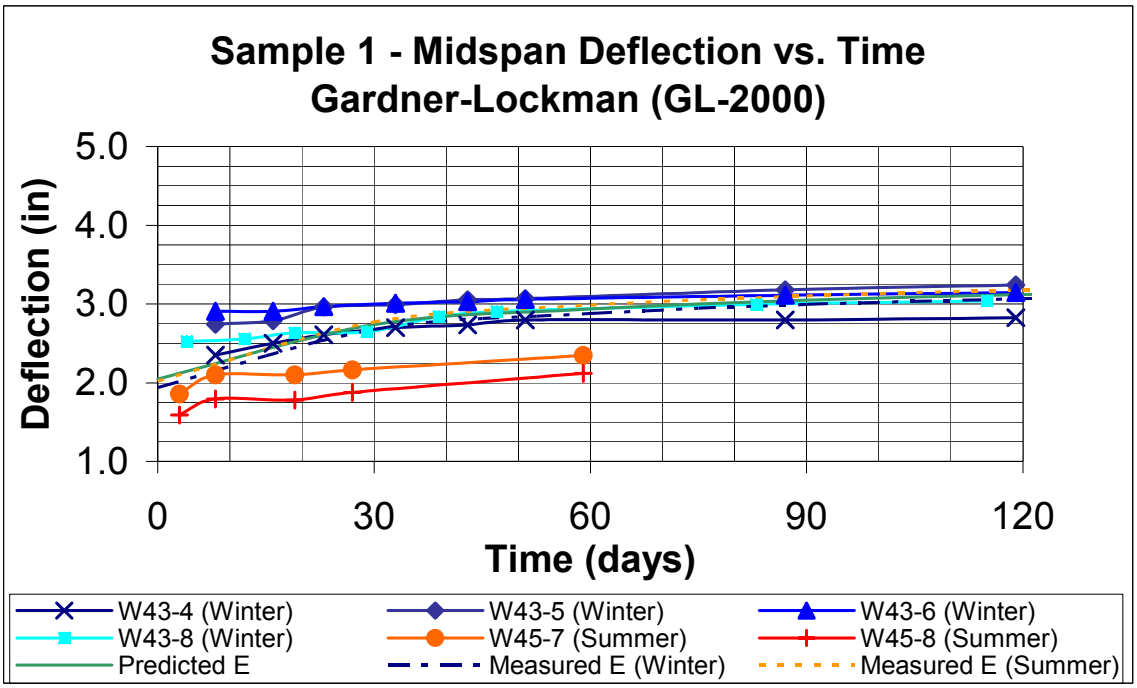

Figure 5.41 Beam Sample 1 - Gardner-Lockman Predicted Deflection vs. Time

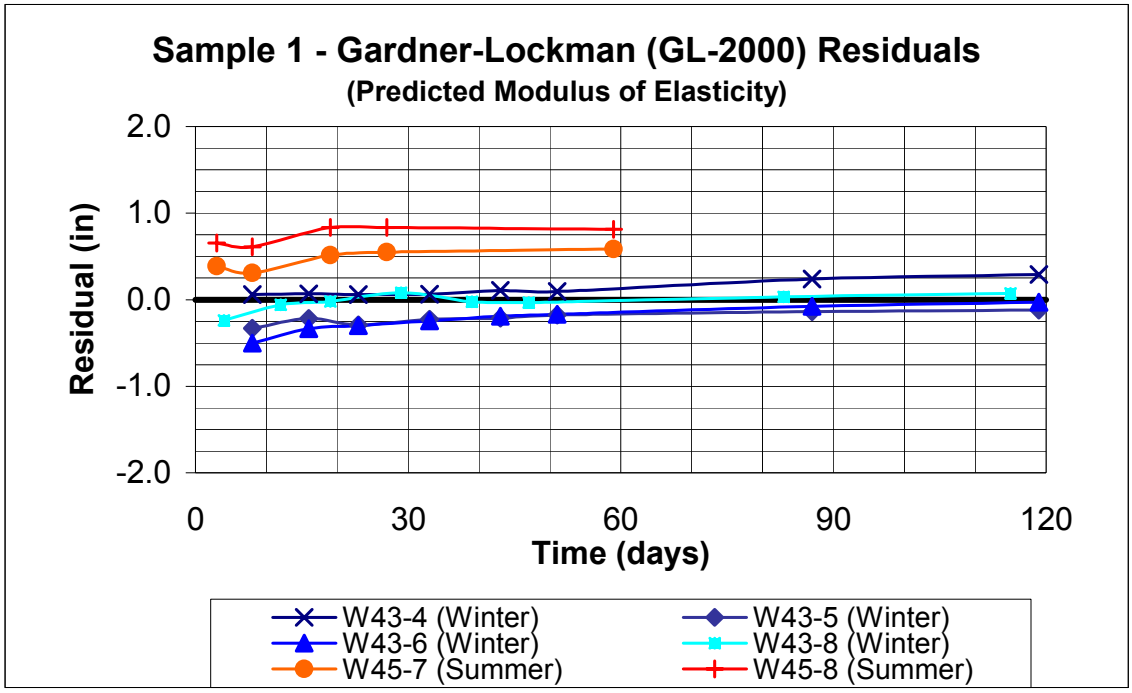

Figure 5.42 Beam Sample 1 - Gardner-Lockman Residuals vs. Time (Predicted Modulus of Elasticity)

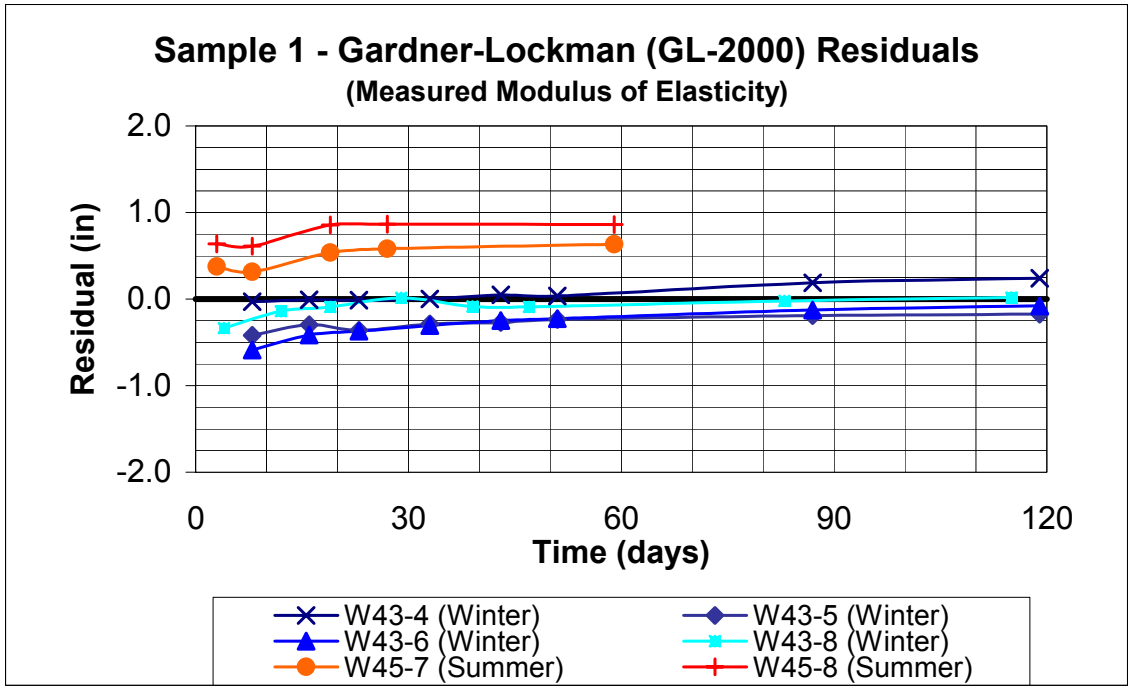

Figure 5.43 Beam Sample 1 - Gardner-Lockman Residuals vs. Time (Measured Modulus of Elasticity)

The Gardner-Lockman (GL-2000) Model was a good fit for the Winter/Spring Beam Sample when either the measured or predicted modulus of elasticity values were used. The use of the predicted and measured modulus of elasticity values did not appear to produce significantly different predicted camber values for this model. The Summer Sample was overpredicted by the Gardner-Lockman Model whether the measured or predicted modulus of elasticity values were used, especially at later ages.

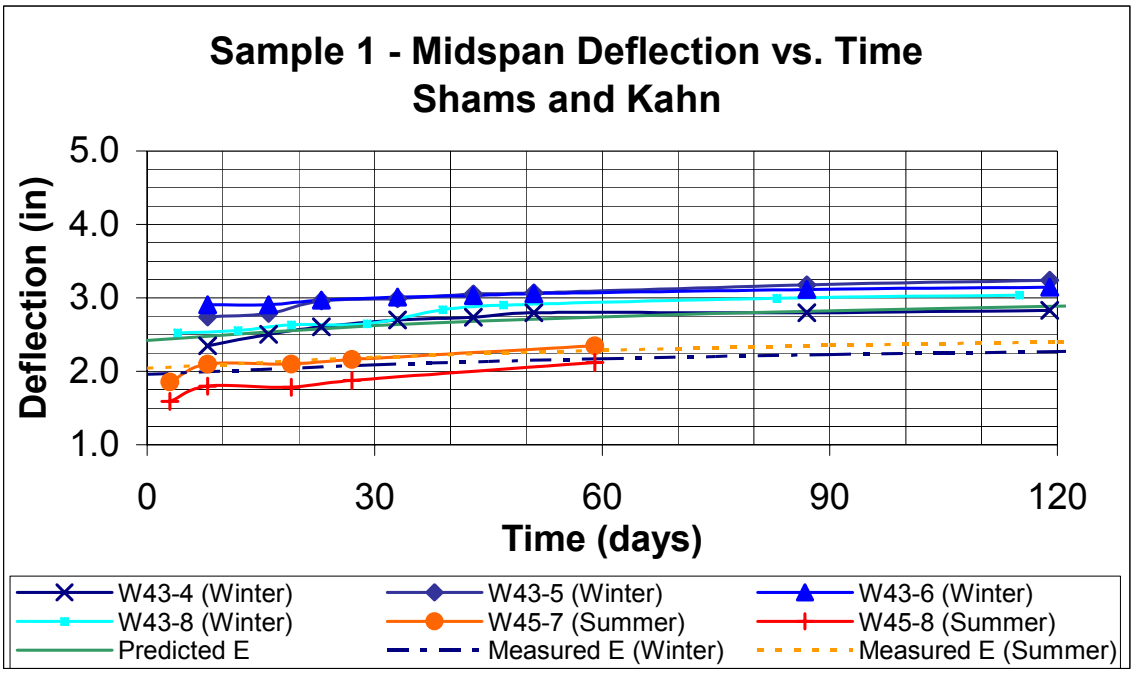

Figure 5.44 Beam Sample 1 - Shams and Kahn Predicted Deflection vs. Time

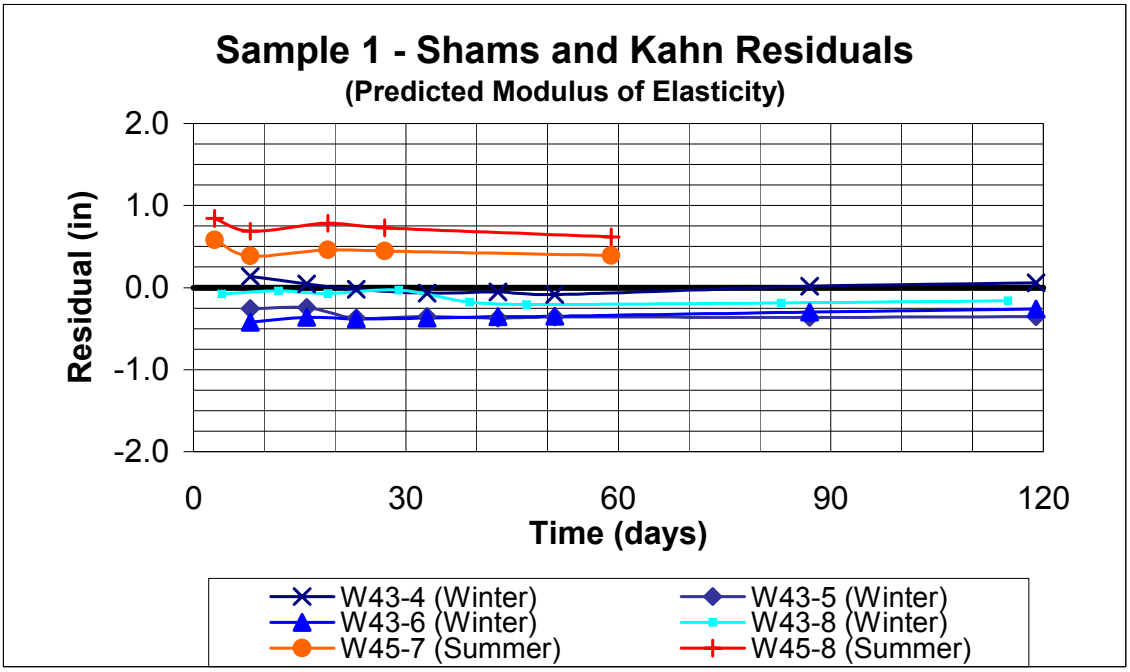

Figure 5.45 Beam Sample 1 - Shams and Kahn Residuals vs. Time (Predicted Modulus of Elasticity)

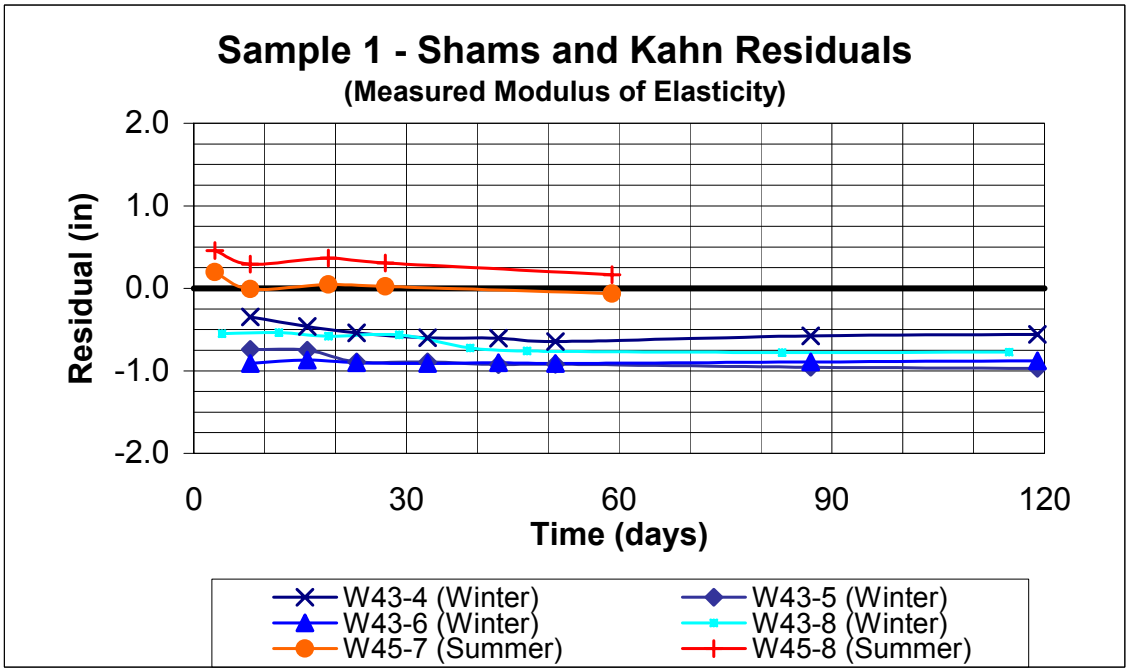

Figure 5.46 Beam Sample 1 - Shams and Kahn Residuals vs. Time (Measured Modulus of Elasticity)

The Shams and Kahn Model yielded a close match to the measured deflections of the Winter/Spring sample when the predicted values for modulus of elasticity were used. Even though the match was close, however, it was a slight underprediction of the measured deflections. Use of the measured modulus of elasticity values underpredicted the measured camber by nearly ¾ in. at all ages. The Summer Sample was reasonably predicted when using the measured modulus of elasticity values, however, producing a good match over the entire time of camber measurement. Using the predicted modulus of elasticity values with the Shams and Kahn model resulted in overprediction of the Summer beam sample by over ½ in.

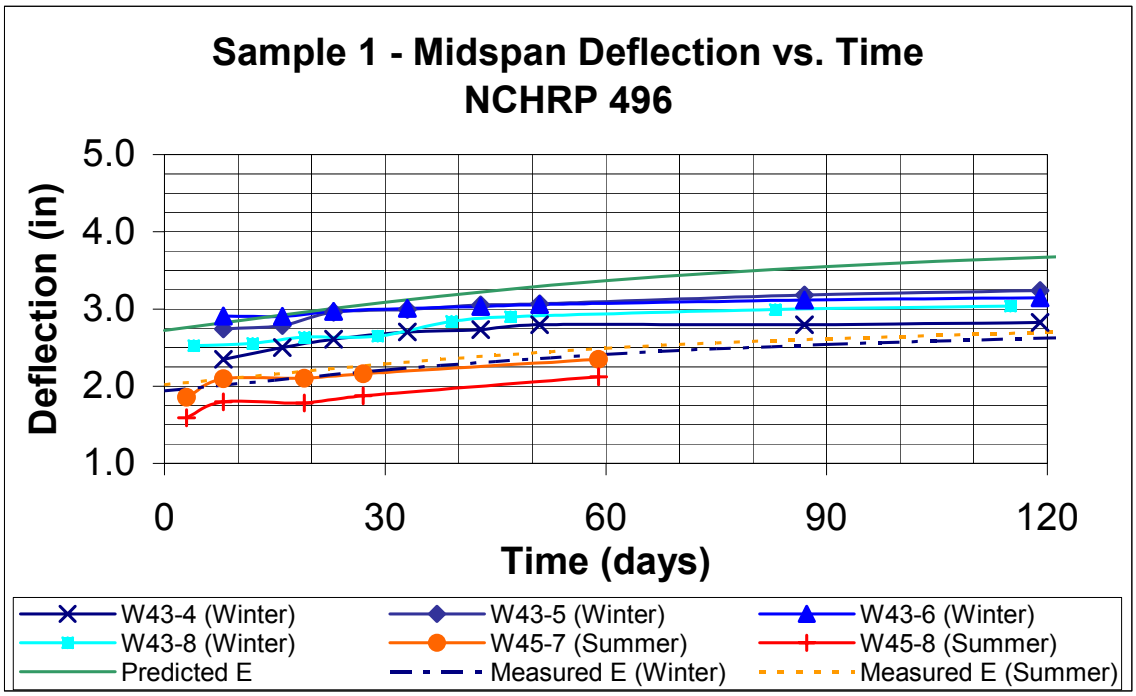

Figure 5.47 Beam Sample 1 - NCHRP 496 Predicted Deflection vs. Time

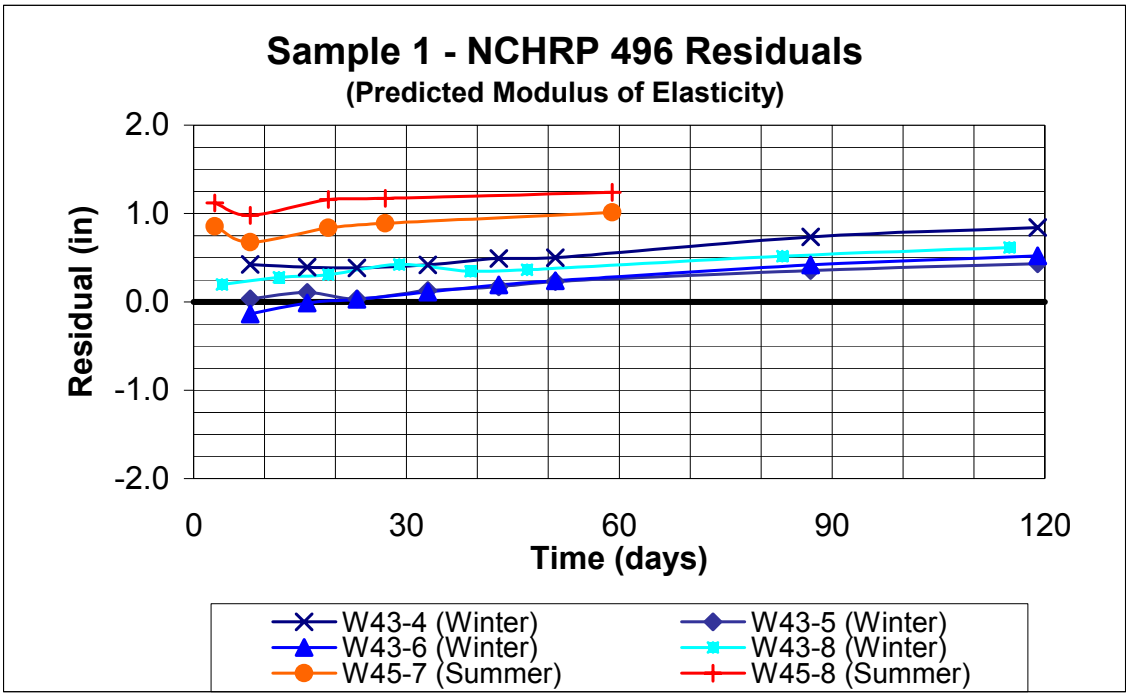

Figure 5.48 **Beam Sample 1 - NCHRP 496 Residuals vs. Time (Predicted Modulus of Elasticity)**

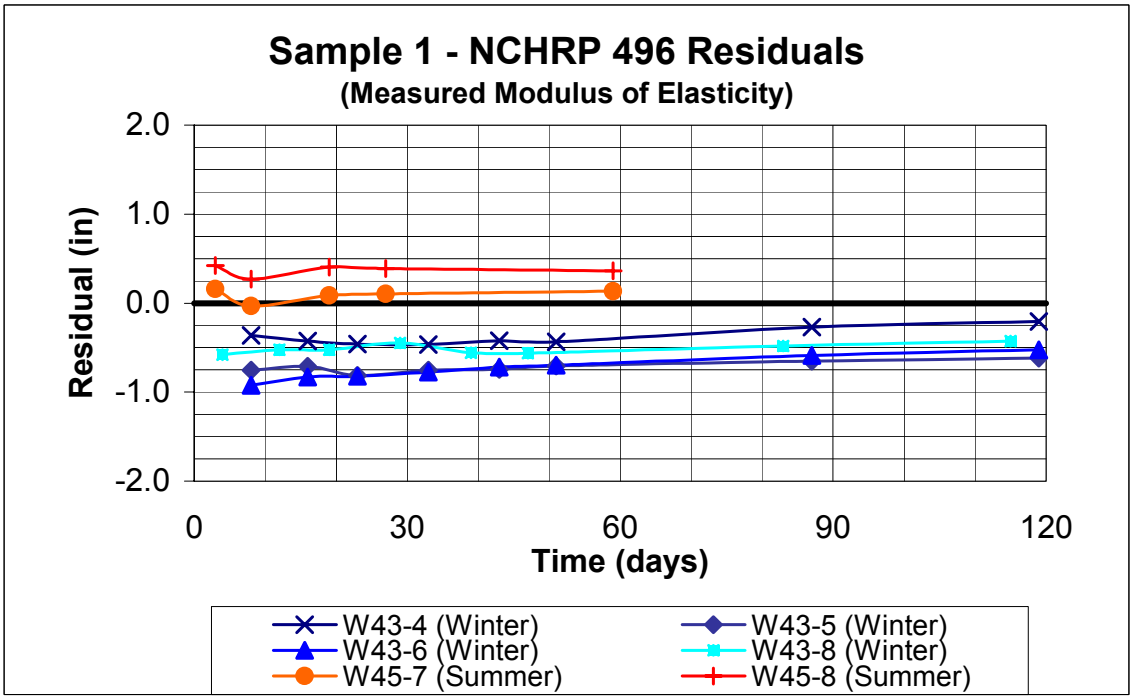

Figure 5.49 **Beam Sample 1 - NCHRP 496 Residuals vs. Time (Measured Modulus of Elasticity)**

The NCHRP 496 Model overpredicted the measured deflections of the Winter/Spring and Summer beam samples when the predicted modulus of elasticity values were used, especially overpredicting camber of the Summer beam sample. The predicted values resulted in the closer match for most of the Winter/Spring beams at early ages before significantly overpredicting camber at later ages. The deflections of the Summer Sample were reasonably matched by the model when the measured modulus of elasticity values were used, however there was overprediction by almost ½ in. when compared with Beam W45-8.

After calculating the predicted camber according to the various models just described, the residual values were then squared and summed in order to rank the various models by their predictive accuracy over the period of camber measurement. These Sum of Residuals Squared values were calculated for all beams in the sample, for both the models using the predicted modulus of elasticity (Figure 5.50) and those using measured modulus of elasticity (Figure 5.51). These categories were then subdivided into the Winter (Figures 5.52 and 5.53) and Summer (Figures 5.54 and 5.55) Beam Samples.

The Gardner-Lockman (GL-2000) Model was observed to be the best match when the beams were considered as one group and the predicted modulus of elasticity was used, while the Shams and Kahn Model was the second best match. The Bazant B3 Model was the worst match, and the ranking of the other models is shown in Table 5.5. When the measured modulus of elasticity value was used, the Gardner-Lockman (GL-2000) Model was the best match. The Gardner-Lockman (GL-2000) Model showed virtually identical results with the second best match, Bazant B3, and the Shams and Kahn Model yielded the worst match when the measured modulus of elasticity was used (Table 5.6).

For the beams cast in Winter, and models using the predicted modulus of elasticity, the Gardner-Lockman (GL-2000) Model was the best match, followed by the CEB-MC90 Model. The Bazant B3 Model was the worst match (Table 5.7). The Winter beams with measured modulus of elasticity showed the Gardner-Lockman (GL-2000) Model to be the best match, followed closely by the Bazant B3 Model. The worst predictor was the Shams and Kahn Model (Table 5.8).

The Summer beams with predicted modulus of elasticity showed the AASHTO-LRFD Model to be the best match, with the Shams and Kahn Model as the second best match. The worst match was the Bazant B3 Model (Table 5.9). For the models using the measured modulus of elasticity, the Shams and Kahn Model was the best match. The NCHRP 496 Model was the second best match, while the ACI-209 Model was the worst match (Table 5.10).

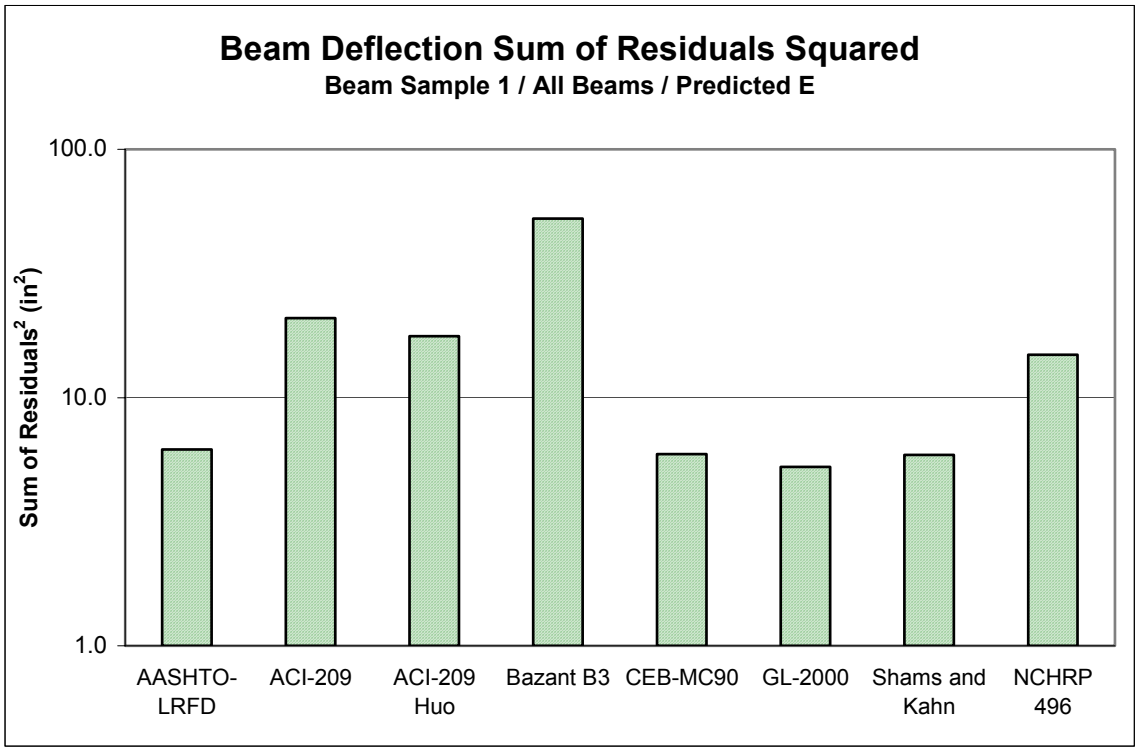

Figure 5.50 Deflection Sum of Residuals Squared, Beam Sample 1, Predicted E

Table 5.5 Model Ranking - Beam Sample 1, Predicted E

Rank	Model
1	**GL-2000**
2	Shams and Kahn
3	CEB-MC90
4	AASHTO-LRFD
5	NCHRP 496
6	ACI-209, modified by Huo
7	ACI-209
8	Bazant B3

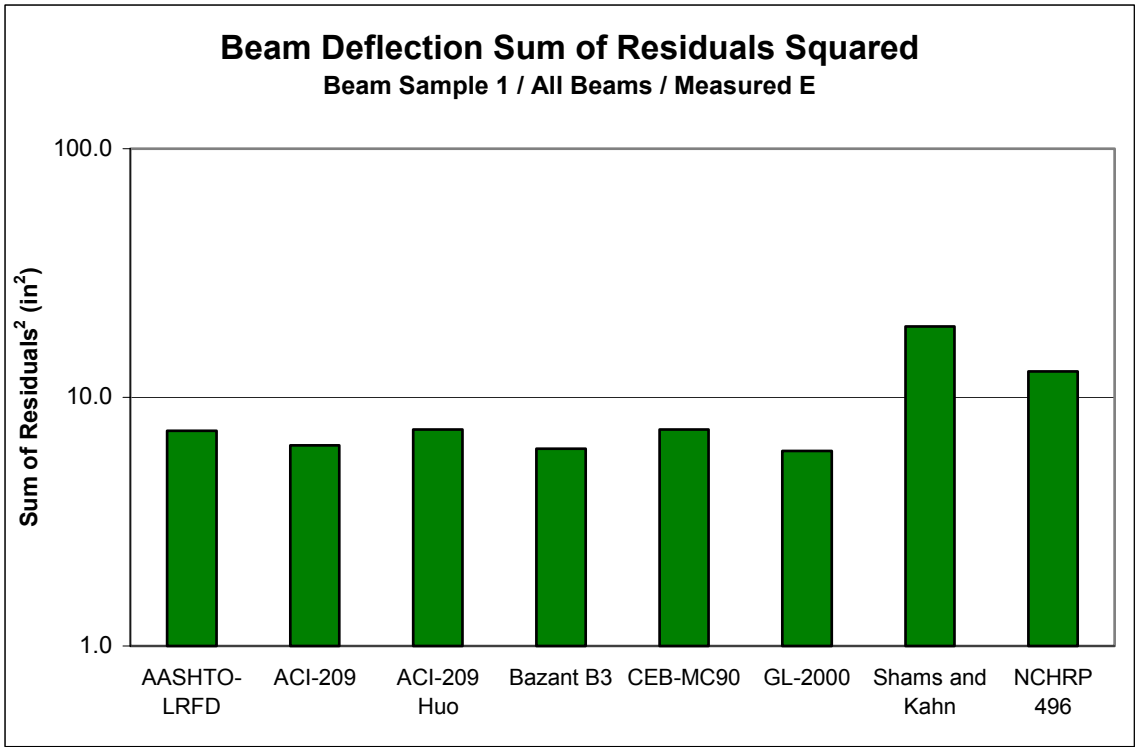

Figure 5.51 Beam Deflection Sum of Residuals Squared, Beam Sample 1, Measured E

Table 5.6 Model Ranking - Beam Sample 1, Measured E

Rank	Model
1	**GL-2000**
2	Bazant B3
3	ACI-209
4	AASHTO-LRFD
5	CEB-MC90
6	ACI-209, modified by Huo
7	NCHRP 496
8	Shams and Kahn

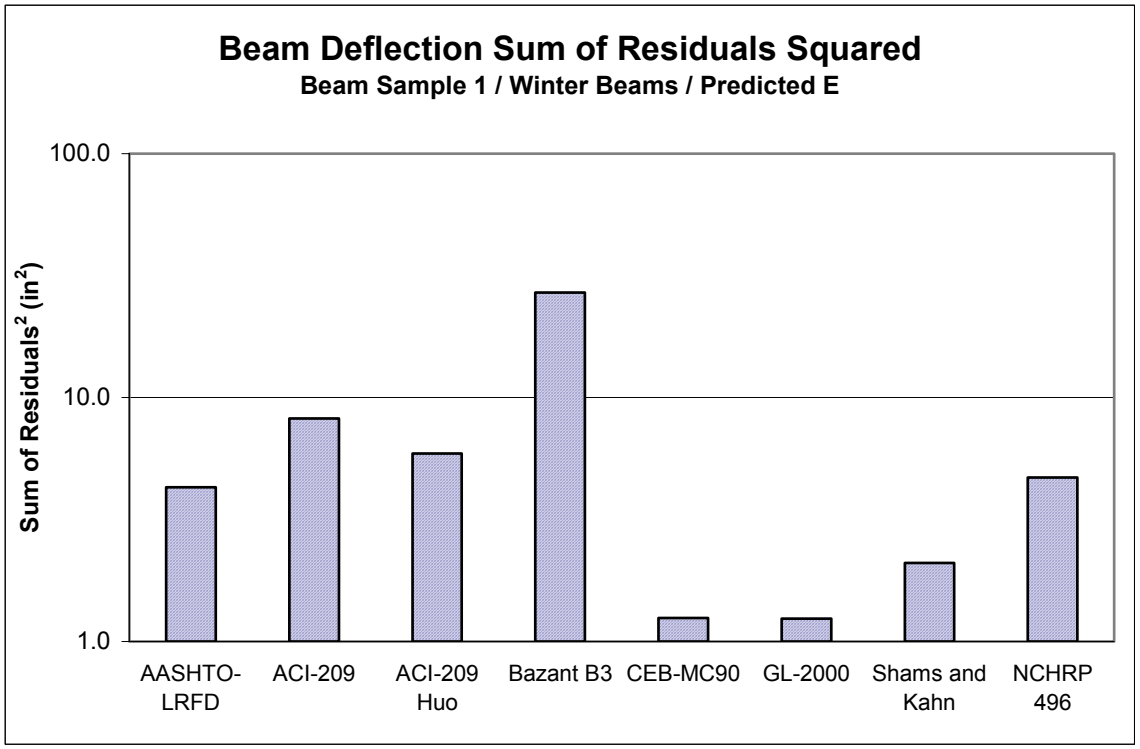

Figure 5.52 Beam Deflection Sum of Residuals Squared, Beam Sample 1 Winter Beams, Predicted E

Table 5.7 Model Ranking - Beam Sample 1, Winter Beams, Predicted E

Rank	Model
1	**GL-2000**
2	CEB-MC90
3	Shams and Kahn
4	AASHTO-LRFD
5	NCHRP 496
6	ACI-209, modified by Huo
7	ACI-209
8	Bazant B3

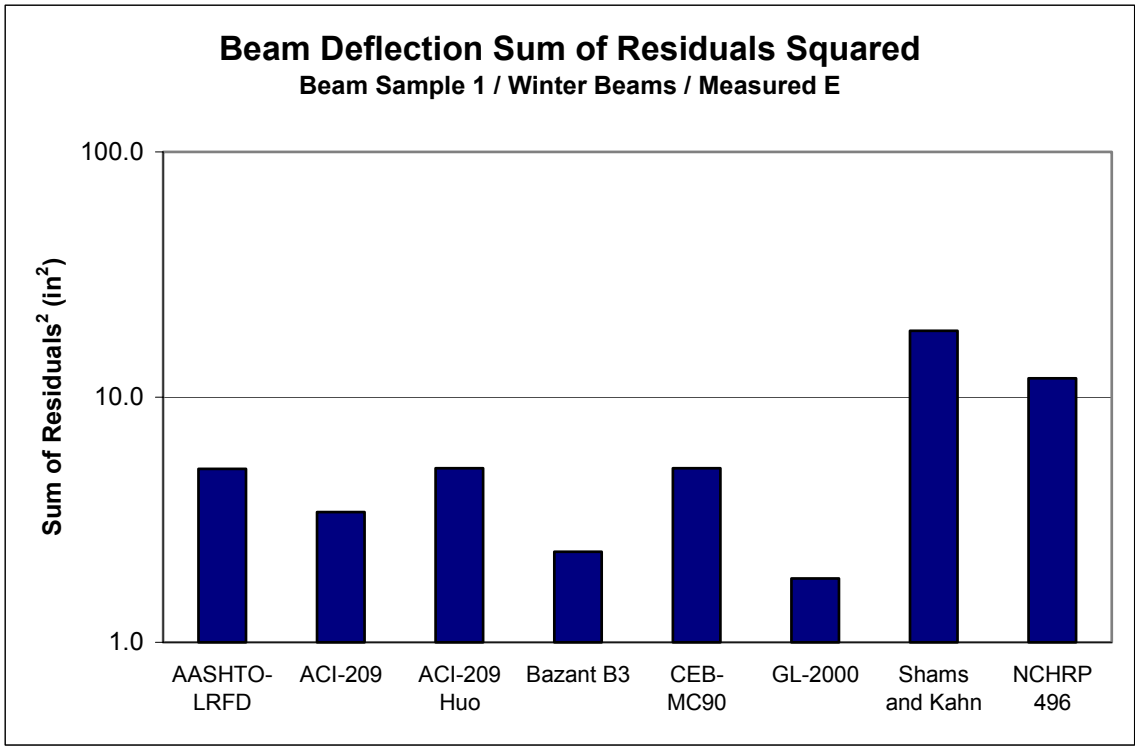

Figure 5.53 Beam Deflection Sum of Residuals Squared, Beam Sample 1 Winter Beams, Measured E

Table 5.8 Model Ranking - Beam Sample 1, Winter Beams, Measured E

Rank	Model
1	**GL-2000**
2	Bazant B3
3	ACI-209
4	AASHTO-LRFD
5	ACI-209, modified by Huo
6	CEB-MC90
7	NCHRP 496
8	Shams and Kahn

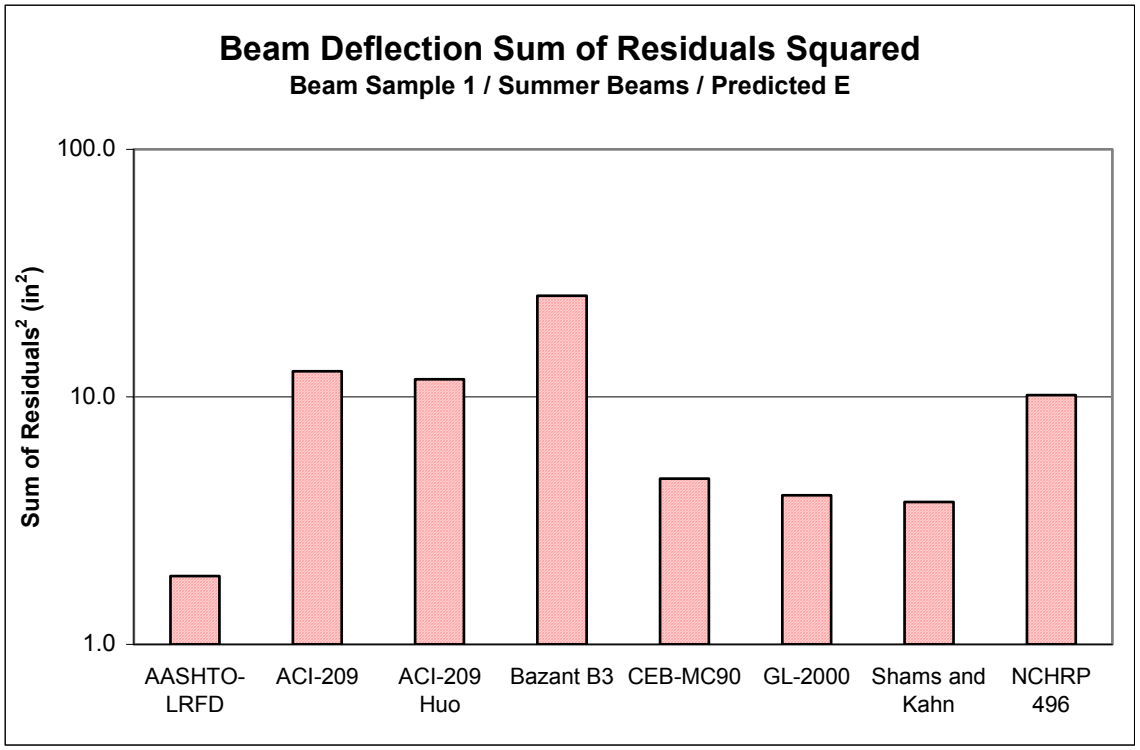

Figure 5.54 Beam Deflection Sum of Residuals Squared, Beam Sample 1 Summer Beams, Predicted E

Table 5.9 Model Ranking - Beam Sample 1, Summer Beams, Predicted E

Rank	Model
1	**AASHTO-LRFD**
2	Shams and Kahn
3	GL-2000
4	CEB-MC90
5	NCHRP 496
6	ACI-209, modified by Huo
7	ACI-209
8	Bazant B3

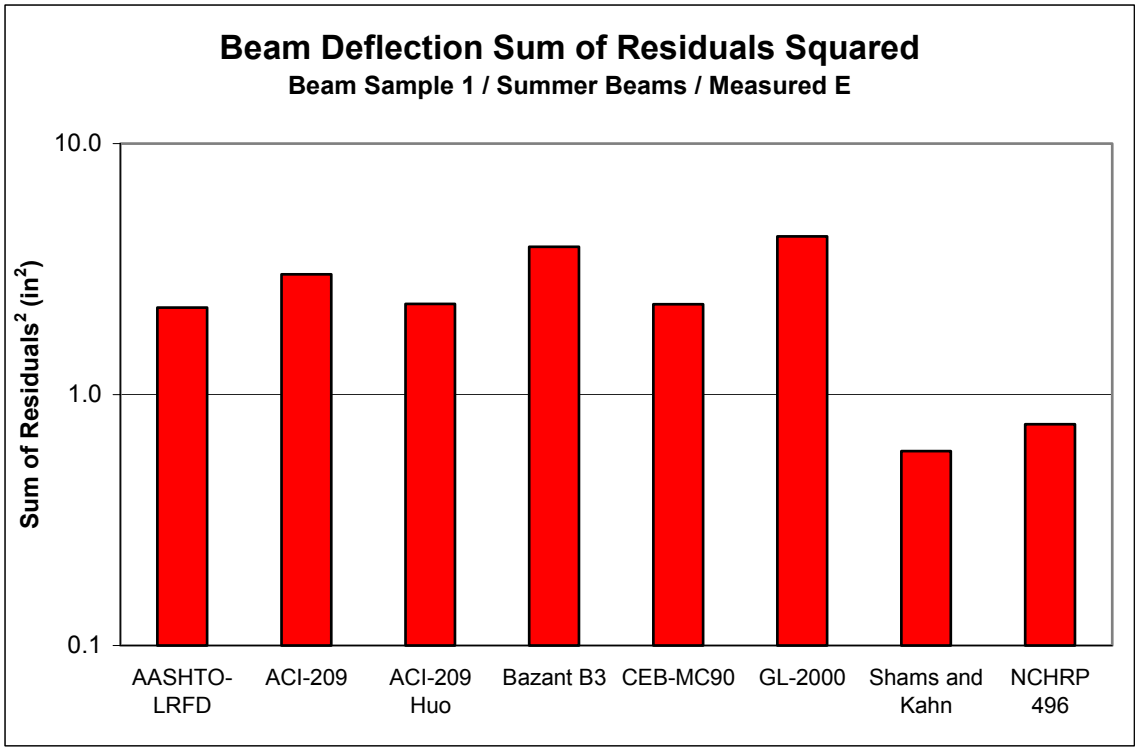

Figure 5.55 Beam Deflection Sum of Residuals Squared, Beam Sample 1 Summer Beams, Measured E

Table 5.10 Model Ranking - Beam Sample 1, Summer Beams, Measured E

Rank	Model
1	**Shams and Kahn**
2	NCHRP 496
3	ACI-209, modified by Huo
4	AASHTO-LRFD
5	NCHRP 496
6	Bazant B3
7	GL-2000
8	ACI-209

5.5.2 Beam Sample 2

The measured deflections of Beam Sample 2 also showed a distinct difference between the beams cast in Summer and those cast in the cooler Winter/Spring seasons. However, unlike in Beam Sample 1, the beams in the Summer Sample exhibited greater deflections for all beams than Beam W33-11 cast in Winter. The deflections for each beam in Sample 2 are shown below in Figure 5.56. The predicted deflections according to all considered models are shown in Figure 5.57. The predicted deflections according to the considered models, using the measured modulus of elasticity, are shown in Figure 5.58.

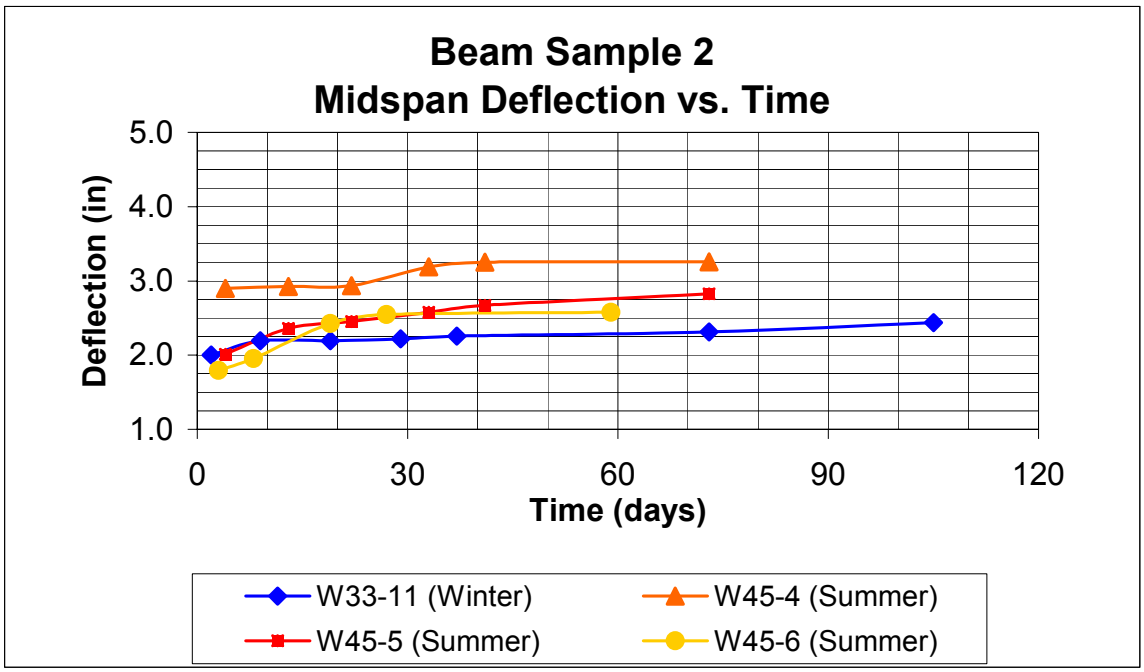

Figure 5.56 Beam Sample 2, Measured Deflection vs. Time

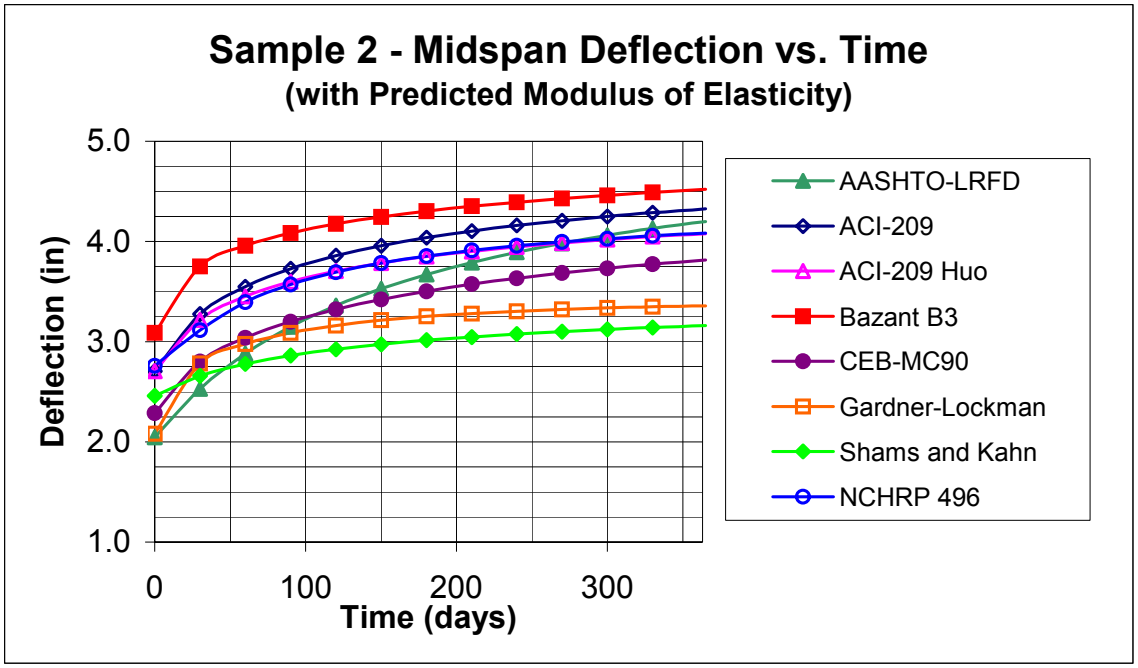

Figure 5.57 Beam Sample 2, Predicted Deflection vs. Time (Predicted E)

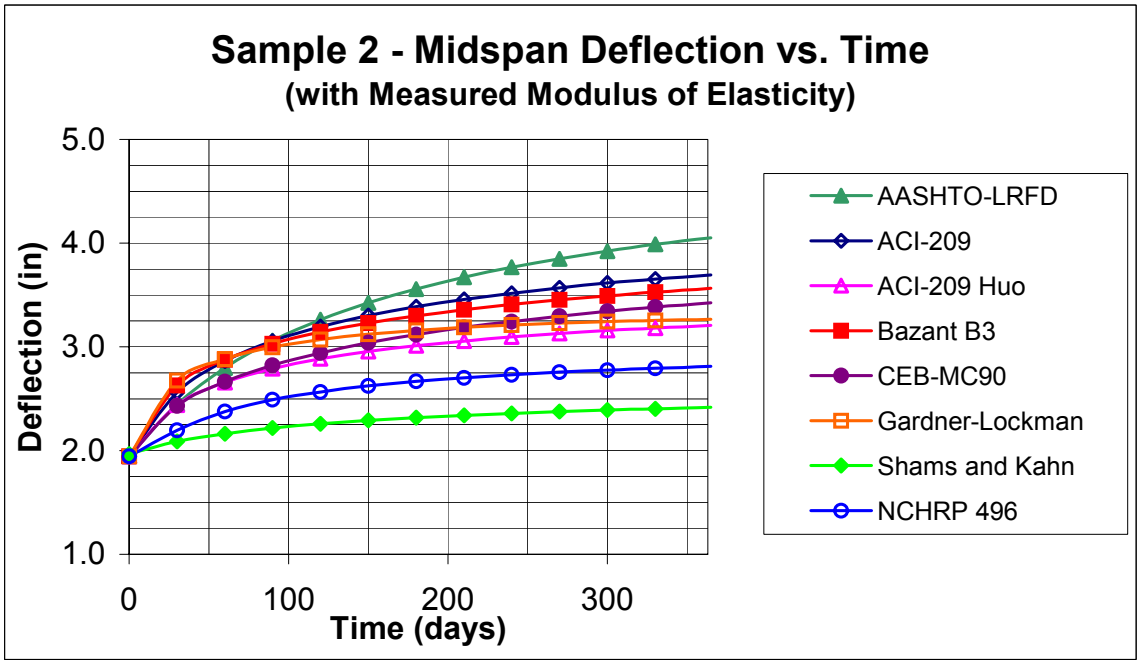

Figure 5.58 Beam Sample 2, Predicted Deflection vs. Time (Measured E)

The deflections of each beam in Sample 2 are shown with the predicted deflections of each considered model in Appendix A. The summary results are now shown and discussed.

The AASHTO-LRFD Model was a better match for most of the Summer Sample, with the exception of Beam W45-4. Beam W45-4, cast in the summer, deflected significantly more than the other beams. The predicted deflections were within ¼ in. of each other whether or not the predicted or measured modulus of elasticity was used. Beam W33-11, the winter beam, was especially overpredicted at later ages (Figure A.15).

The ACI-209 Model using the measured modulus of elasticity showed good agreement with most of the Summer Sample (except Beam W45-4), and poor agreement with Beam W33-11, cast in winter. The use of the predicted modulus of elasticity with the ACI-209 Model resulted in a significantly higher deflection than was measured. Beam W45-4 agreed well with the predicted deflection using the predicted modulus of elasticity at an early age before flattening considerably compared with the predicted deflection (Figure A.18).

The ACI-209 Model with modifications by Huo, and using measured modulus of elasticity, showed an even better match to most of the Summer Sample (except Beam W45-4) than the regular ACI-209 Model. As with the regular ACI-209 Model, use of the predicted modulus of elasticity resulted in significant overprediction for all beams except W45-5, for which it matched reasonably well. The Winter/Spring beam (W33-11) also agreed with the model using predicted modulus of elasticity at early ages before flattening compared with the other beams (Figure A.21).

The Bazant B3 Model using measured modulus of elasticity was a good match for the majority of the Summer Sample, but overpredicted camber for Beam W33-11 by nearly ½ in. at later ages. The model using the predicted modulus of elasticity appeared to significantly overpredict the measured camber of all beams in the sample for the entire life of the beam. The deflection of the Summer beam, W45-4, was not predicted well using either modulus of elasticity value (Figure A.24).

The CEB-MC90 Model with measured modulus of elasticity matched most of the Summer Sample very well, however the deflection of Beam W33-11 was much less than

the predicted values, regardless of whether predicted or measured modulus of elasticity was used. Beam W45-4 deflected more than both of the predicted deflection curves, although it appeared to converge somewhat at an age beyond 60 days (Figure A.27).

The Gardner-Lockman (GL-2000) Model with measured or predicted modulus of elasticity matched the Summer Sample very well, with the exception of Beam W45-4. The predicted deflection curves using predicted or measured modulus of elasticity values did not differ significantly from each other. Beam W33-11, the winter beam, was overpredicted by the Gardner-Lockman (GL-2000) Model by nearly ½ in. at later ages (Figure A.30).

The Shams and Kahn Model using predicted modulus of elasticity overpredicted the summer beam sample (except Beam W45-4) at early ages before converging to a better prediction beyond 30 days. The model using measured modulus of elasticity matched Winter Beam W33-11 almost exactly. The Shams and Kahn model with measured modulus of elasticity was observed to be a poor match for the Summer Sample, underpredicting measured camber by nearly ¾ in. (Figure A.33).

The NCHRP 496 Model with measured modulus of elasticity showed good agreement with the majority of the Summer Sample, and matched Beam W33-11 nearly exactly over the entire life of the beam. The model using the predicted modulus of elasticity overpredicted most of the beams by over ¾ in., but agreed well with the measured deflection of Beam W45-4 until an age of 40 days, beyond which it appeared to flatten when compared with the predicted values (Figure A.36).

As with Beam Sample 1, the residual values for Beam Sample 2 were also squared and summed in order to rank the various models. The Sum of Residuals Squared values for all beams in the sample are shown using the predicted modulus of elasticity (Figure 5.59) and the measured modulus of elasticity (Figure 5.60). The Winter Beam Sample (Figures 5.61 and 5.62) and Summer Beam Sample (Figures 5.63 and 5.64) are also shown below.

The Shams and Kahn Model was observed to be the best match when the beams were considered as one group and the predicted modulus of elasticity was used, while the AASHTO-LRFD Model was the second best match. The Bazant B3 Model was the worst match, and the ranking of the other models is shown in Table 5.11. When the

measured modulus of elasticity value was used, the ACI-209, modified by Huo Model was the best match, followed by the CEB-MC90 Model. The Shams and Kahn Model yielded the worst match when the measured modulus of elasticity was used (Table 5.12).

For the beams cast in Winter, and models using the predicted modulus of elasticity, the Shams and Kahn Model was the best match, followed by the AASHTO-LRFD Model. The Bazant B3 Model was the worst match (Table 5.13). The Winter beams with measured modulus of elasticity showed the NCHRP 496 Model to be the best match, followed by the Shams and Kahn Model. The worst predictor was the Gardner-Lockman (GL-2000) Model (Table 5.14).

The Summer beams with predicted modulus of elasticity showed the Gardner-Lockman (GL-2000) Model to be the best match, with CEB-MC90 as the second best match. The worst match was the Bazant B3 Model (Table 5.15). For the models using the measured modulus of elasticity, the Gardner-Lockman (GL-2000) Model was the best match. The Bazant B3 Model followed closely as the second best match, while the Shams and Kahn Model was the worst match (Table 5.16).

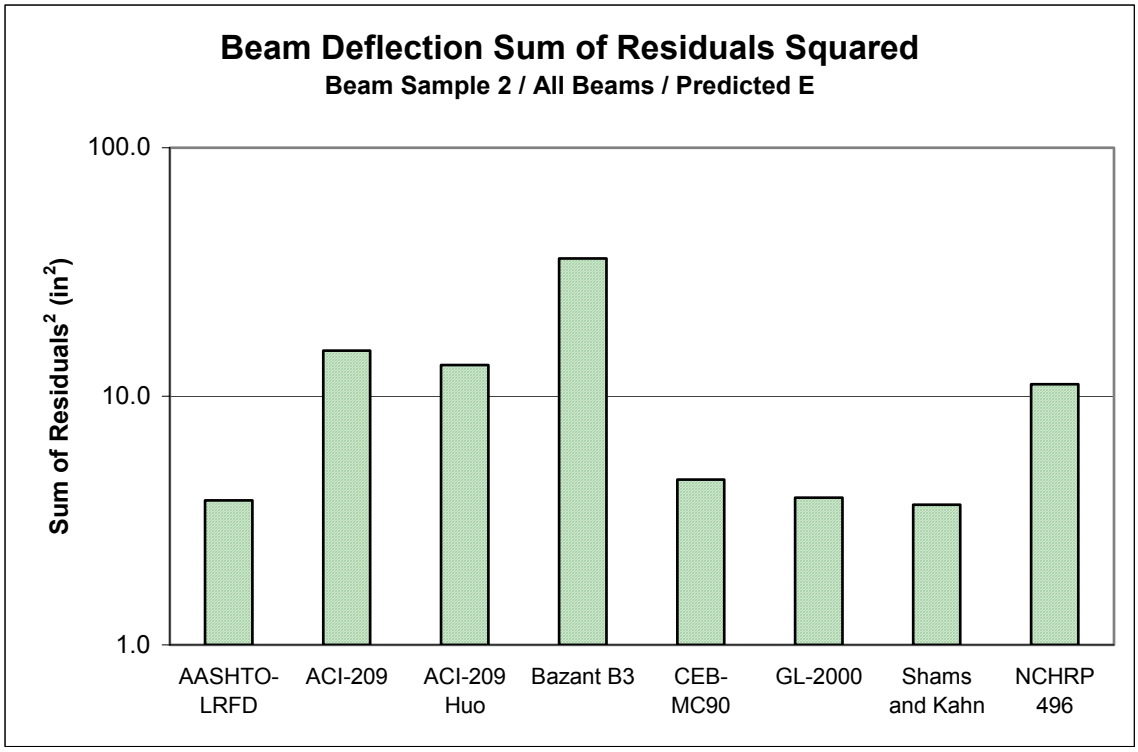

Figure 5.59 Beam Deflection Sum of Residuals Squared, Beam Sample 2, Predicted E

Table 5.11 Model Ranking - Beam Sample 2, Predicted E

Rank	Model
1	**Shams and Kahn**
2	AASHTO-LRFD
3	GL-2000
4	CEB-MC90
5	NCHRP 496
6	ACI-209, modified by Huo
7	ACI-209
8	Bazant B3

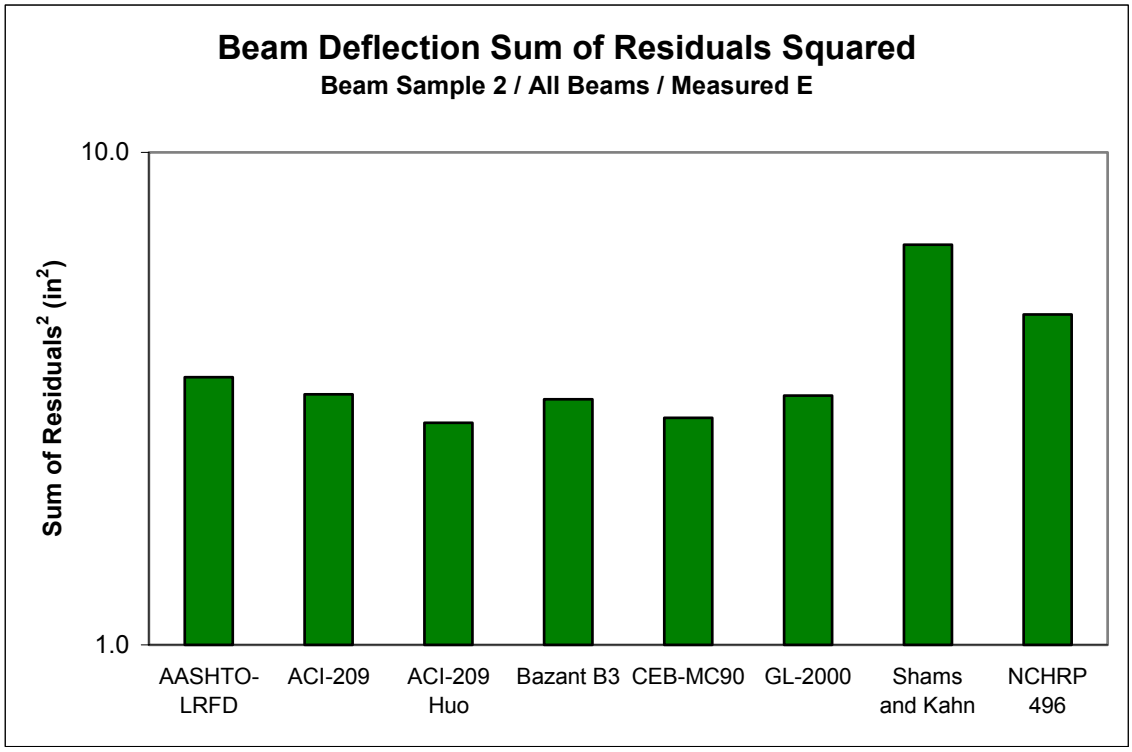

Figure 5.60 Beam Deflection Sum of Residuals Squared, Beam Sample 2, Measured E

Table 5.12 Model Ranking - Beam Sample 2, Measured E

Rank	Model
1	**ACI-209, modified by Huo**
2	CEB-MC90
3	Bazant B3
4	GL-2000
5	ACI-209
6	AASHTO-LRFD
7	NCHRP 496
8	Shams and Kahn

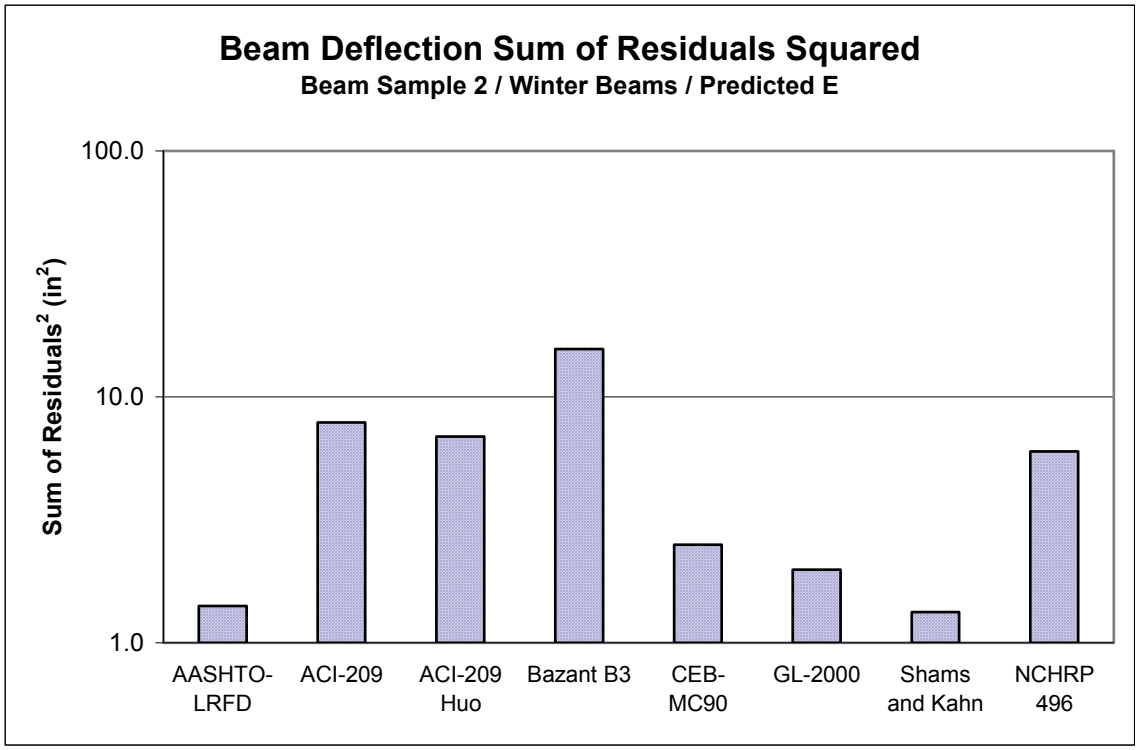

Figure 5.61 Beam Deflection Sum of Residuals Squared, Beam Sample 2 Winter Beams, Predicted E

Table 5.13 Model Ranking - Beam Sample 2, Winter Beams, Predicted E

Rank	Model
1	**Shams and Kahn**
2	AASHTO-LRFD
3	GL-2000
4	CEB-MC90
5	NCHRP 496
6	ACI-209, modified by Huo
7	ACI-209
8	Bazant B3

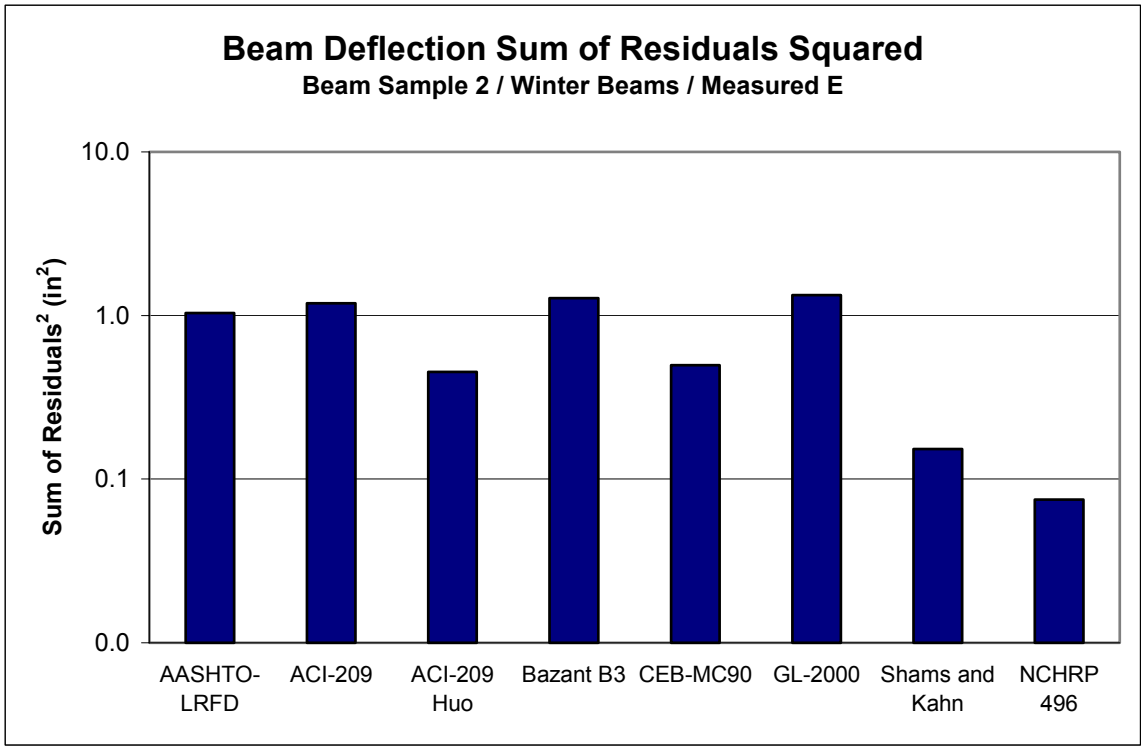

Figure 5.62 Beam Deflection Sum of Residuals Squared, Beam Sample 2 Winter Beams, Measured E

Table 5.14 Model Ranking - Beam Sample 2, Winter Beams, Measured E

Rank	Model
1	**NCHRP 496**
2	Shams and Kahn
3	ACI-209, modified by Huo
4	CEB-MC90
5	AASHTO-LRFD
6	ACI-209
7	Bazant B3
8	GL-2000

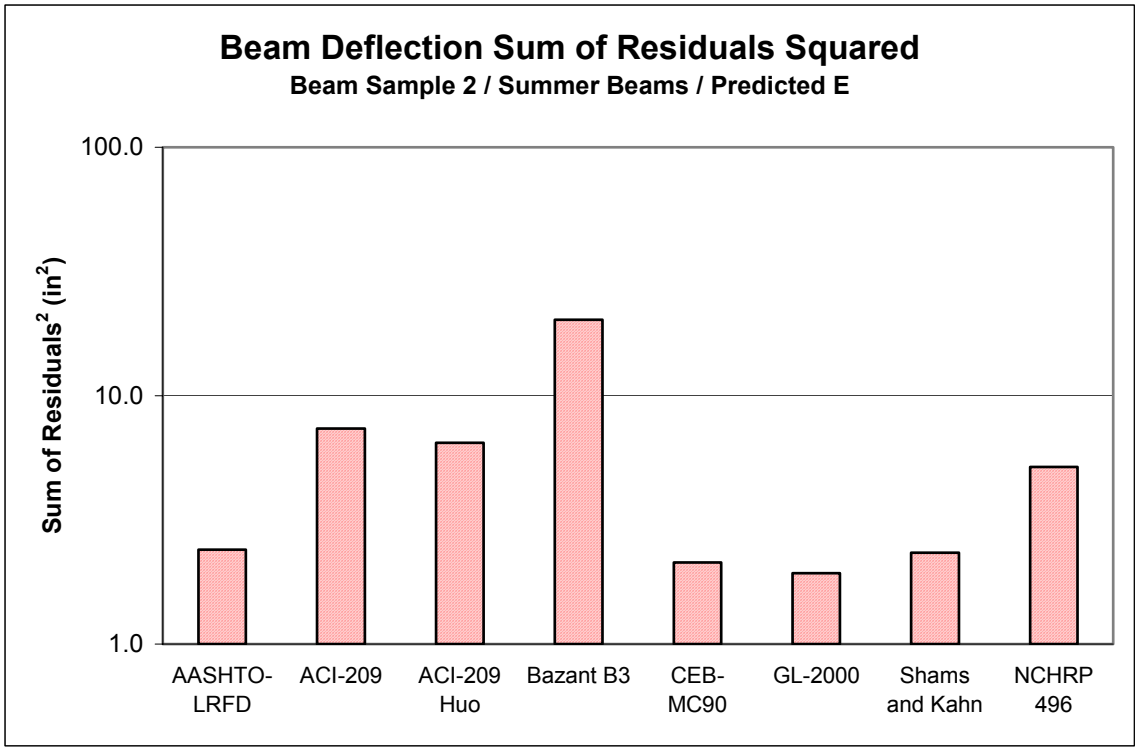

Figure 5.63 Beam Deflection Sum of Residuals Squared, Beam Sample 2 Summer Beams, Predicted E

Table 5.15 Model Ranking - Beam Sample 2, Summer Beams, Predicted E

Rank	Model
1	**GL-2000**
2	CEB-MC90
3	Shams and Kahn
4	AASHTO-LRFD
5	NCHRP 496
6	ACI-209, modified by Huo
7	ACI-209
8	Bazant B3

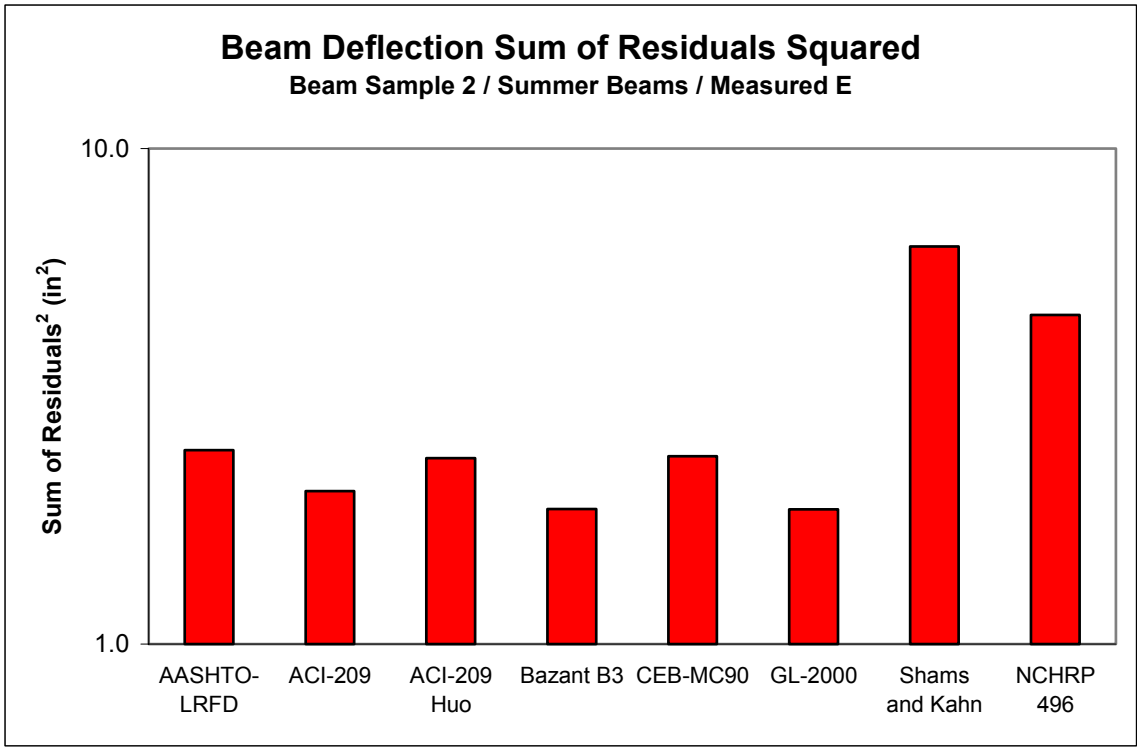

Figure 5.64 Beam Deflection Sum of Residuals Squared, Beam Sample 2 Summer Beams, Measured E

Table 5.16 Model Ranking - Beam Sample 2, Summer Beams, Measured E

Rank	Model
1	**GL-2000**
2	Bazant B3
3	ACI-209
4	ACI-209, modified by Huo
5	CEB-MC90
6	AASHTO-LRFD
7	NCHRP 496
8	Shams and Kahn

5.5.3 Beam Sample 3

The measured deflections of Beam Sample 3 were not distinctively different from each other based upon casting season as were the beams in Beam Sample 1 and Beam Sample 2. For the most part, the deflections were similar with age, and the rate of camber growth appeared to be slower at later ages than most of the beams in the other samples. The measured deflections are shown in Figure 5.65 below. The predicted deflections according to all considered models are shown in Figure 5.66. The predicted deflections according to the considered models, using the measured modulus of elasticity, are shown in Figure 5.67.

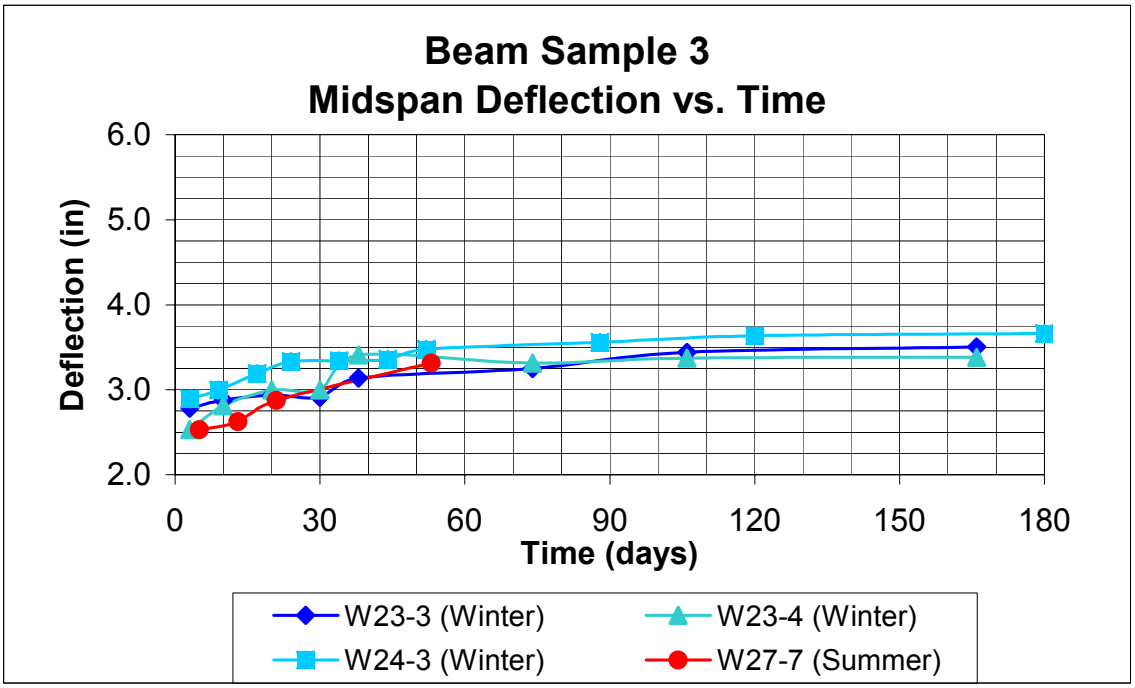

Figure 5.65 Beam Sample 3, Measured Deflection vs. Time

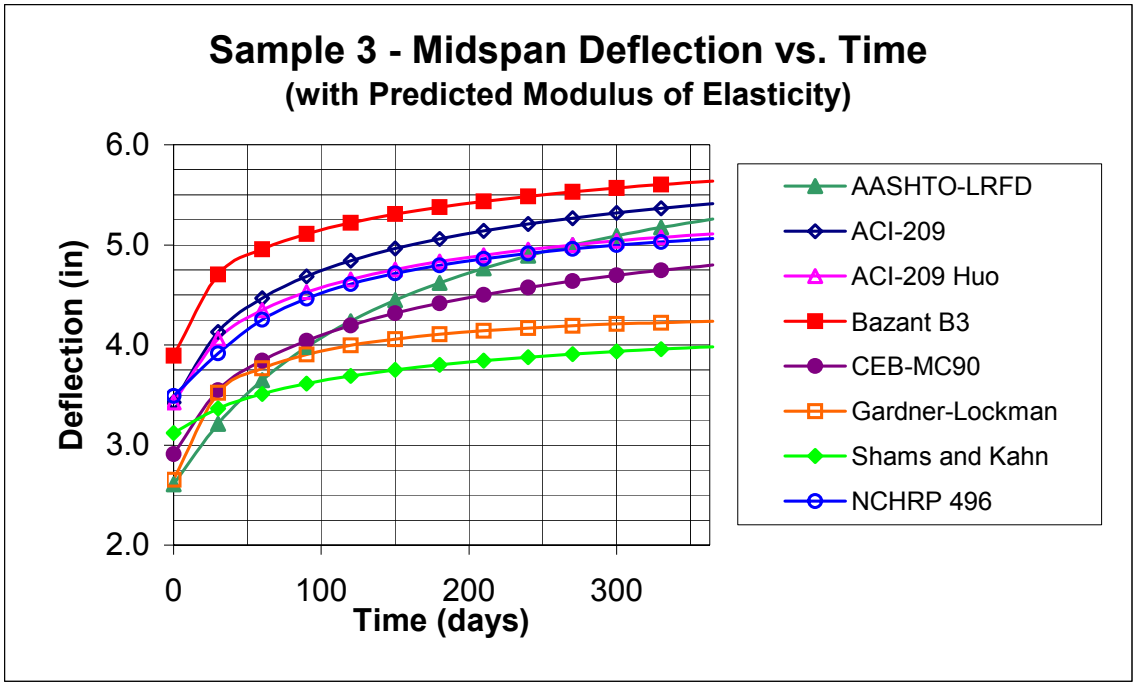

Figure 5.66 Beam Sample 3, Predicted Deflection vs. Time (Predicted E)

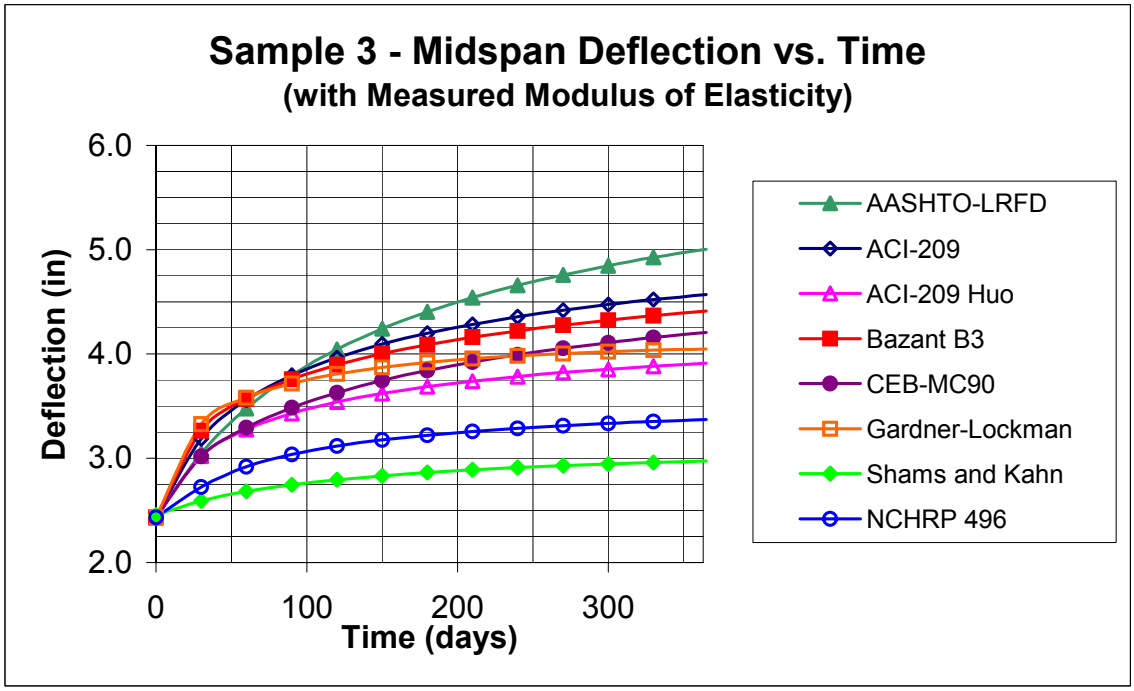

Figure 5.67 Beam Sample 3, Predicted Deflection vs. Time (Measured E)

The deflections of each beam in Sample 3 are shown with the predicted deflections of each considered model in Appendix A. The results will now be discussed.

The AASHTO-LRFD Model using the predicted modulus of elasticity matches the measured deflections for Beam W27-7, cast in Summer, almost exactly for the entire period the deflection was measured. The predicted deflection curve using the measured and predicted modulus of elasticity values appear to be extremely similar. Both curves seem to provide a good match to the measured camber of all beams in the sample until an approximate age of 45 days, beyond which the measured deflection curve appears to flatten and are overpredicted by the model. The difference approaches 1 in. toward the end of the time of camber measurement for these beams (Figure A.38).

The ACI-209 Model for the most part appears to overpredict the measured deflections, regardless of whether the measured or predicted modulus of elasticity is used. The model with the measured modulus of elasticity values matches the measured deflections very well at early ages, however. The predicted deflection using the predicted modulus of elasticity drastically overpredicted the measured deflections of all beams in the sample by nearly 1 ¼ in. at an age of 180 days (Figure A.42).

The ACI-209 Model with modifications by Huo produced results that significantly overpredicted measured camber when the predicted modulus of elasticity values were used with the model. The predicted camber using the measured modulus of elasticity values, however, appeared to match the measured camber almost exactly over the entire time of camber measurement (Figure A.45).

The measured deflections of Beam Sample 3 were overpredicted by nearly 1 ¾" using the Bazant B3 Model with the predicted modulus of elasticity. The predicted camber using measured modulus of elasticity was a very good match at early ages before overpredicting slightly at later ages (Figure A.48).

The CEB-MC90 Model using the predicted modulus of elasticity values overpredicted measured camber at all ages for all beams. The measured deflection of Beam 24-3 seemed to very closely match the model using predicted modulus of elasticity until an approximate age of 25 days beyond which it flattened compared with the predicted curve. The amount of overprediction seemed to increase as the beam aged.

The CEB-MC90 Model with measured modulus of elasticity was a good match to the measured camber at all ages (Figure A.51).

The theoretical deflection curves using the Gardner-Lockman (GL-2000) Model with predicted or measured modulus of elasticity were extremely close to each other, not varying by more than ¼ in. The predicted deflections matched the measured deflections better at early ages before being overpredicted at later ages. In general, the model overpredicted measured deflections regardless of whether the measured or predicted modulus of elasticity was used. The model using the predicted modulus of elasticity significantly overpredicted the measured deflections, where the model using measured modulus of elasticity overpredicted the measured deflections by no more than ½ in. (Figure A.54).

The Shams and Kahn Model with predicted modulus of elasticity overpredicted measured camber at early ages by approximately ½ in., but provided a good match overall at later ages. The model using measured modulus of elasticity underpredicted camber, with the exception of Beams W27-7 and W23-4 at early ages. At ages beyond 30 days, camber was underpredicted by approximately ½ in. (Figure A.57).

The NCHRP Model with predicted modulus of elasticity significantly overpredicted the measured deflections for all beams in the sample, frequently by more than 1 in. The model using the measured modulus of elasticity yielded predicted deflections that matched the measured deflections fairly closely. Deflections were all slightly underpredicted at later ages, while some deflections were overpredicted at early ages (Figure A.60).

As with the other beam samples, the residual values for Beam Sample 3 were also squared and summed in order to rank the various models. The Sum of Residuals Squared values for all beams in the sample are shown using the predicted modulus of elasticity (Figure 5.65) and the measured modulus of elasticity (Figure 5.66). The Winter Beam Sample (Figures 5.67 and 5.68) and Summer Beam Sample (Figures 5.69 and 5.70) are also shown below.

The Shams and Kahn Model was observed to be the best match when the beams were considered as one group and the predicted modulus of elasticity was used, while the AASHTO-LRFD Model was the second best match. The Bazant B3 Model was the

worst match, and the ranking of the other models is shown in Table 5.17. When the measured modulus of elasticity value was used, the ACI-209 Model, with modifications by Huo, was the best match. The CEB-MC90 Model was the second best match, and the Shams and Kahn Model yielded the worst match when the measured modulus of elasticity was used (Table 5.18).

For the beams cast in Winter, and models using the predicted modulus of elasticity, the Shams and Kahn Model was the best match, followed by the Gardner-Lockman (GL-2000) Model. The Bazant B3 Model was the worst match (Table 5.19). The Winter beams with measured modulus of elasticity showed the ACI-209 Model, with modifications by Huo, to be the best match, followed by the CEB-MC90 Model. The worst predictor was the Shams and Kahn Model (Table 5.20).

The Summer beams with predicted modulus of elasticity showed the AASHTO-LRFD Model to be the best match, with the Shams and Kahn Model as the second best match. The worst match was the Bazant B3 Model (Table 5.21). For the models using the measured modulus of elasticity, the NCHRP 496 Model was the best match for the summer beams. The AASHTO-LRFD Model was the second best match, while the Gardner-Lockman (GL-2000) Model was the worst match (Table 5.22).

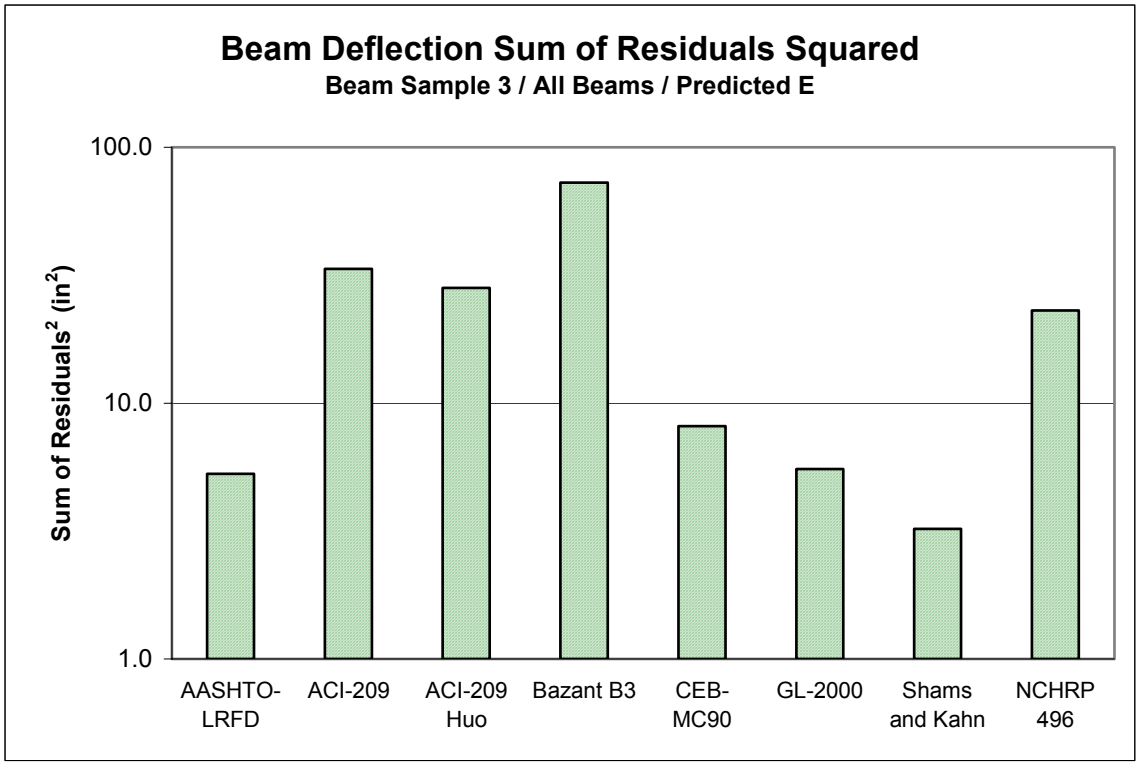

Figure 5.68 Beam Deflection Sum of Residuals Squared, Beam Sample 3, Predicted E

Table 5.17 Model Ranking - Beam Sample 3, Predicted E

Rank	Model
1	**Shams and Kahn**
2	AASHTO-LRFD
3	GL-2000
4	CEB-MC90
5	NCHRP 496
6	ACI-209, modified by Huo
7	ACI-209
8	Bazant B3

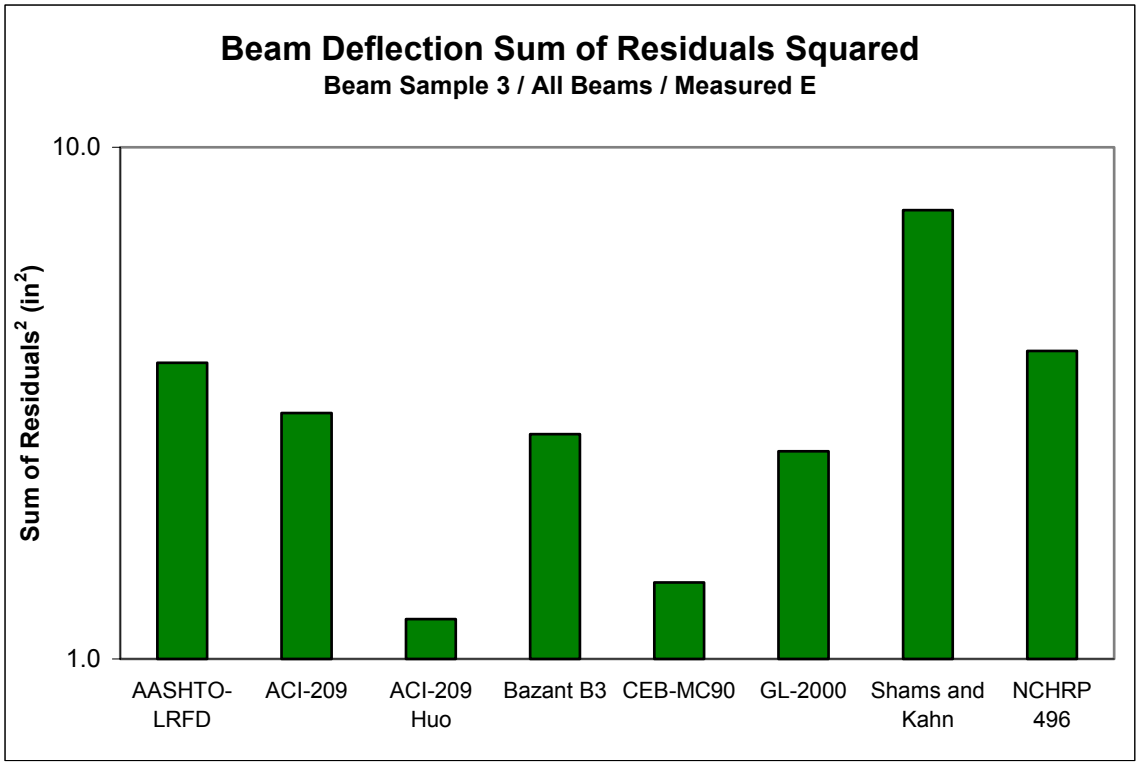

Figure 5.69 Beam Deflection Sum of Residuals Squared, Beam Sample 3, Measured E

Table 5.18 Model Ranking - Beam Sample 3, Measured E

Rank	Model
1	**ACI-209, modified by Huo**
2	CEB-MC90
3	GL-2000
4	Bazant B3
5	ACI-209
6	AASHTO-LRFD
7	NCHRP 496
8	Shams and Kahn

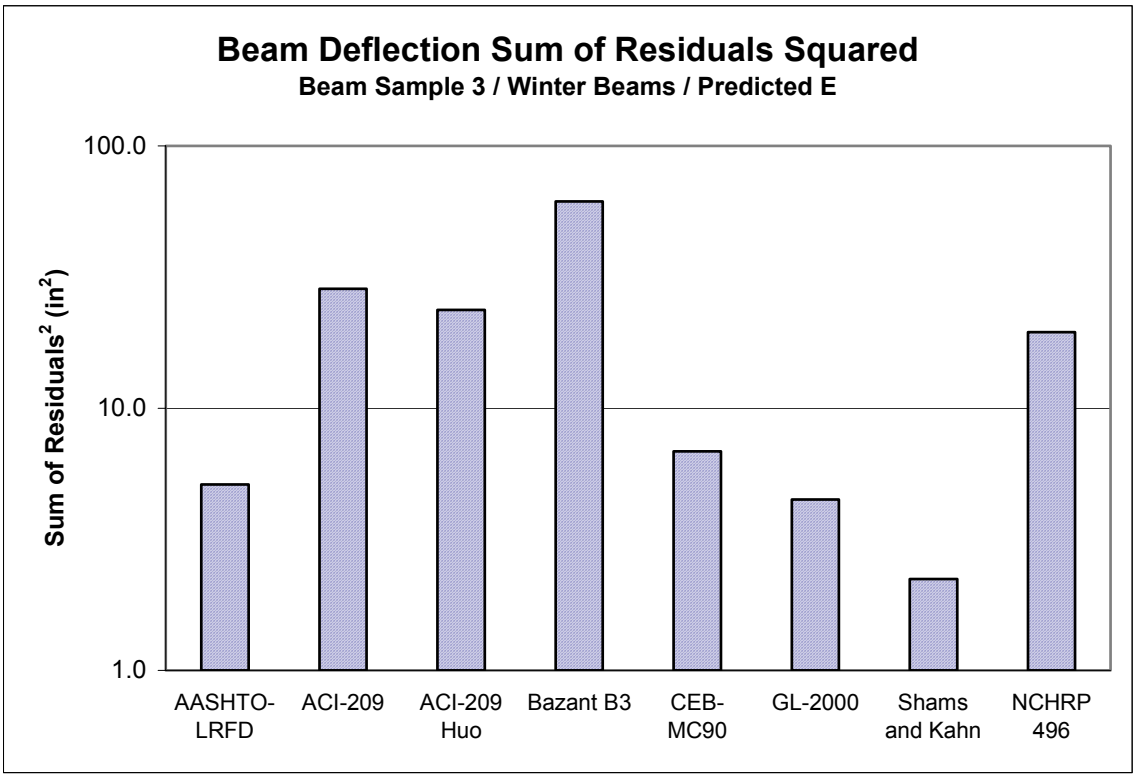

Figure 5.70 Beam Deflection Sum of Residuals Squared, Beam Sample 3 Winter Beams, Predicted E

Table 5.19 Model Ranking - Beam Sample 3, Winter Beams, Predicted E

Rank	Model
1	**Shams and Kahn**
2	GL-2000
3	AASHTO-LRFD
4	CEB-MC90
5	NCHRP 496
6	ACI-209, modified by Huo
7	ACI-209
8	Bazant B3

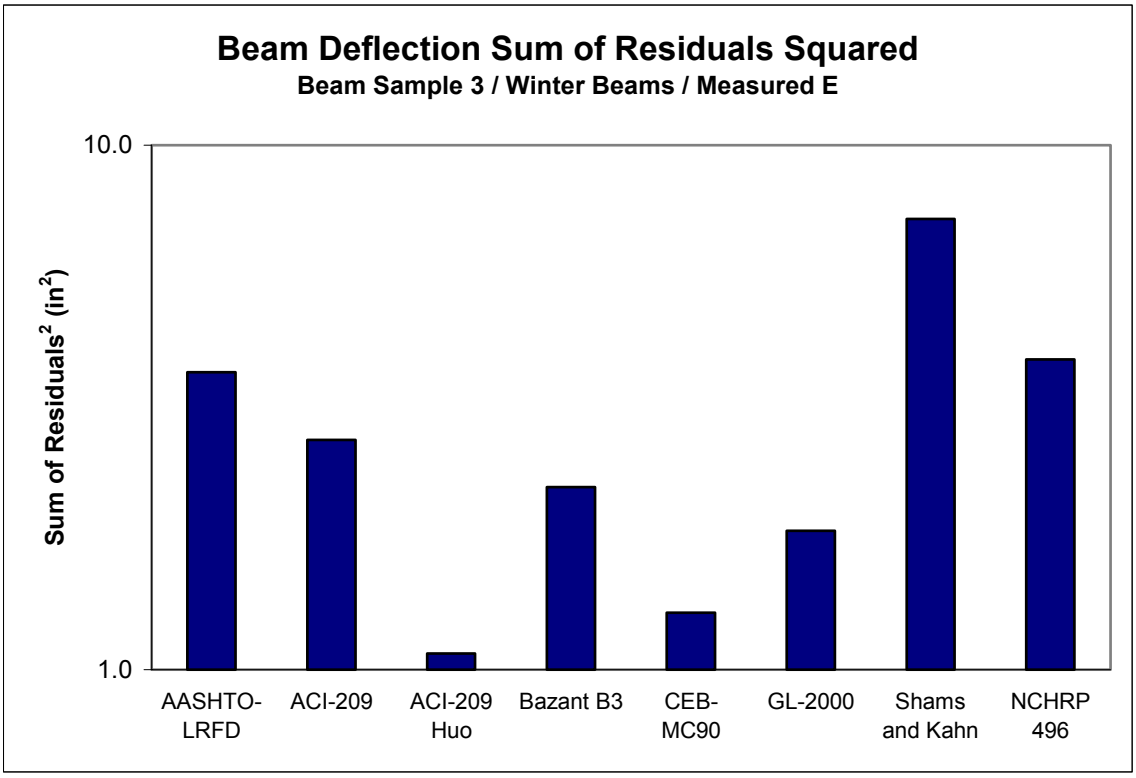

Figure 5.71 Beam Deflection Sum of Residuals Squared, Beam Sample 3 Winter Beams, Measured E

Table 5.20 Model Ranking - Beam Sample 3, Winter Beams, Measured E

Rank	Model
1	**ACI-209, modified by Huo**
2	CEB-MC90
3	GL-2000
4	Bazant B3
5	ACI-209
6	AASHTO-LRFD
7	NCHRP 496
8	Shams and Kahn

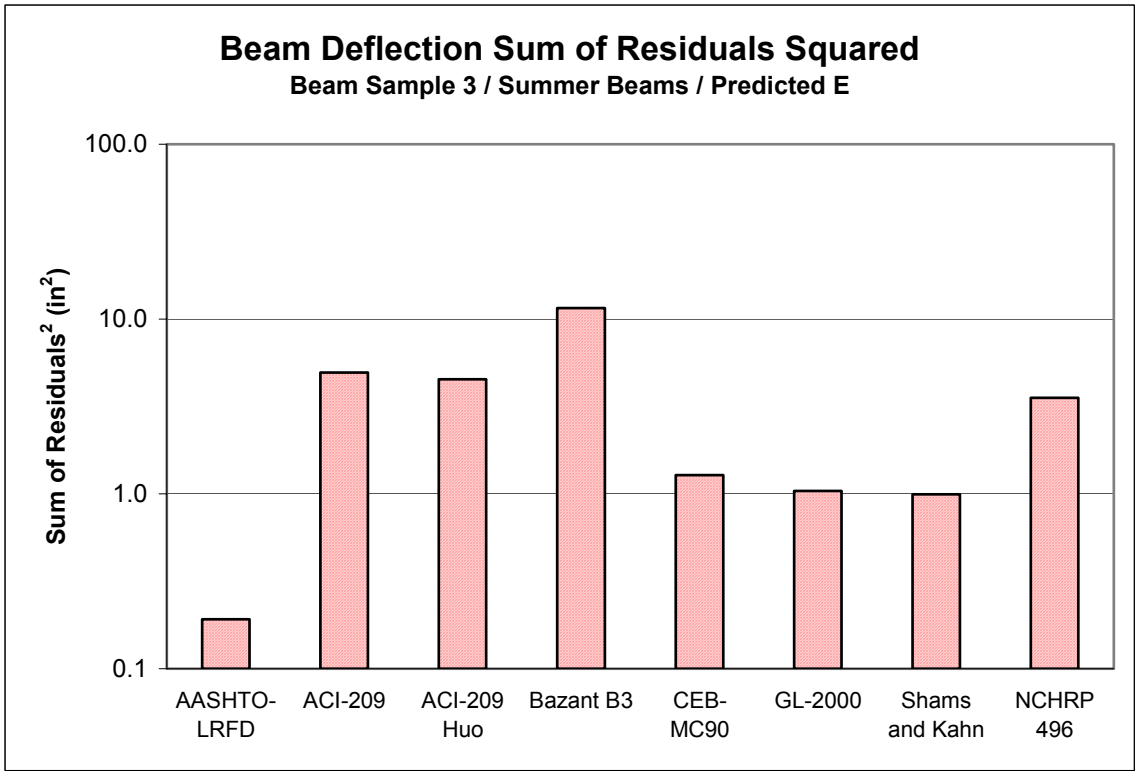

Figure 5.72 Beam Deflection Sum of Residuals Squared, Beam Sample 3 Summer Beams, Predicted E

Table 5.21 Model Ranking - Beam Sample, Summer Beams, Predicted E

Rank	Model
1	**AASHTO-LRFD**
2	Shams and Kahn
3	GL-2000
4	CEB-MC90
5	NCHRP 496
6	ACI-209, modified by Huo
7	ACI-209
8	Bazant B3

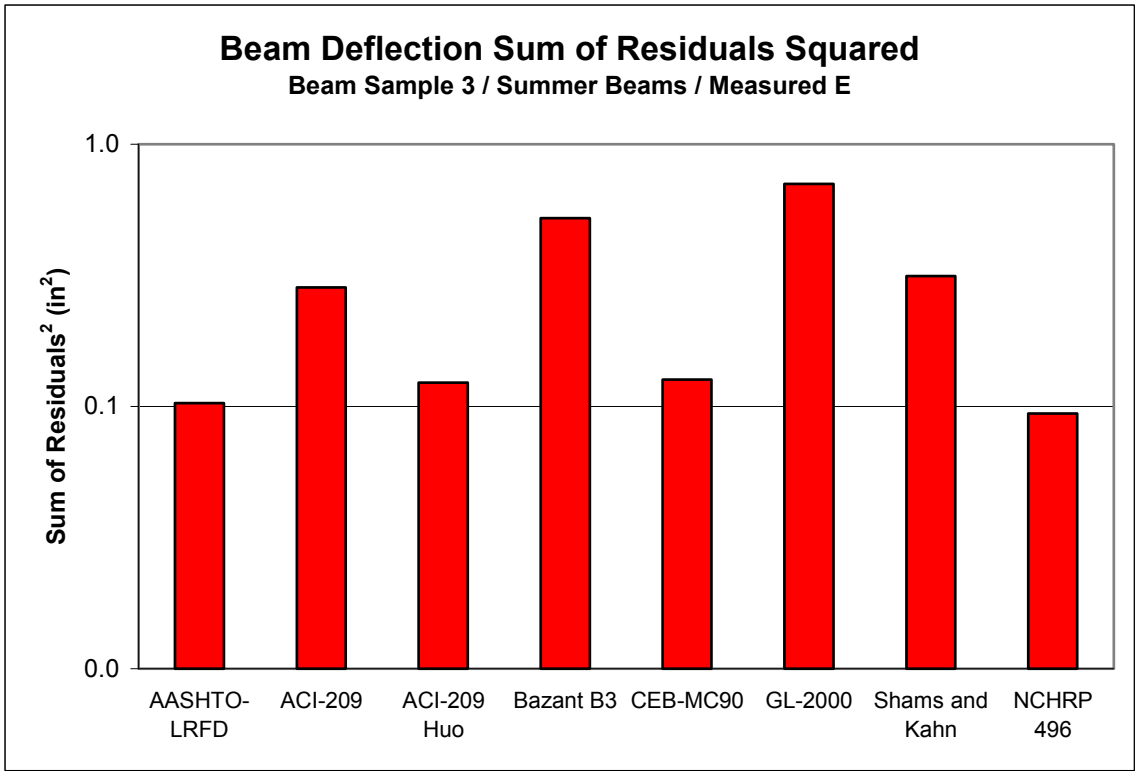

Figure 5.73 Beam Deflection Sum of Residuals Squared, Beam Sample 3 Summer Beams, Measured E

Table 5.22 Model Ranking - Beam Sample 3, Summer Beams, Measured E

Rank	Model
1	**NCHRP 496**
2	AASHTO-LRFD
3	ACI-209, modified by Huo
4	CEB-MC90
5	ACI-209
6	Shams and Kahn
7	Bazant B3
8	GL-2000

5.5.4 All Beams

Results for the 13 beams not able to be grouped in a sample according to the previously stated criteria are shown in Appendix B for the interested reader. These results include the same information as that provided for Beam Samples 1, 2, and 3. This includes measured deflections, residuals, sum of residuals squared, and model rankings for all models, using predicted and measured modulus of elasticity values as before.

Now that the models have been examined and ranked based on all individual beams and beam samples (for different modulus of elasticity values and seasons of casting), the models will be ranked according to their total predictive accuracy for all 27 beams taken as a whole. The residual values for all 27 beams were squared and summed in order to achieve an overall ranking of the various models. The Sum of Residuals Squared values for models using the predicted modulus of elasticity are shown in Figure 5.74 and Sum of Residuals Squared values for the models using measured modulus of elasticity are shown in Figure 5.75. The overall rankings for models using the predicted modulus of elasticity are shown in Table 5.23 and the rankings for models using measured modulus of elasticity are shown in Table 5.24.

Of all models using the predicted modulus of elasticity values, the Shams and Kahn Model had the greatest predictive accuracy for the beams taken as a whole, with the Gardner-Lockman (GL-2000) Model being the next highest. The model with the least predictive accuracy for all beams was the Bazant B3 Model. Of all models using the measured modulus of elasticity, the ACI-209 Model, with modifications by Huo, was the best. The worst model, when measured modulus of elasticity was used, is the AASHTO-LRFD Model. While there was a relatively wide range of predictive accuracy for models using the predicted modulus of elasticity, all models using measured modulus of elasticity had extremely similar predictive accuracies overall. This suggests that the proper selection of modulus elasticity values is extremely important to the predictive accuracy of the model.

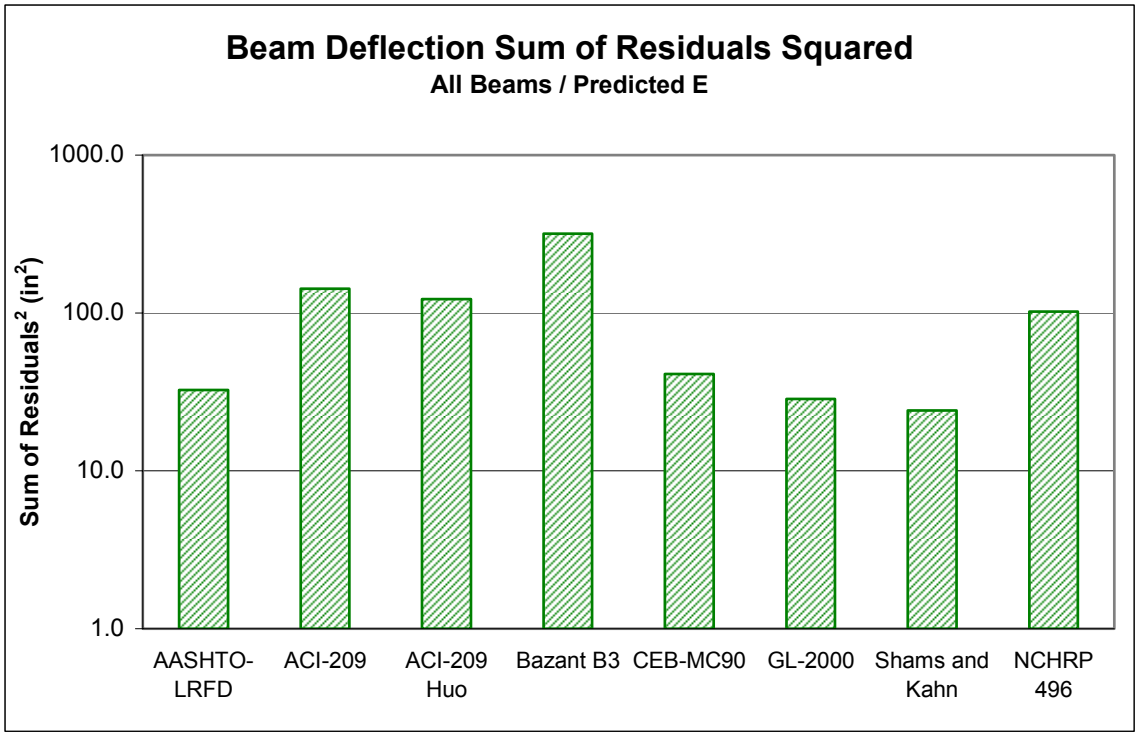

Figure 5.74 Beam Deflection Sum of Residuals Squared, All Beams, Predicted E

Table 5.23 Model Ranking – All Beams, Predicted E

Rank	Model
1	**Shams and Kahn**
2	GL-2000
3	AASHTO-LRFD
4	CEB-MC90
5	NCHRP 496
6	ACI-209, modified by Huo
7	ACI-209
8	Bazant B3

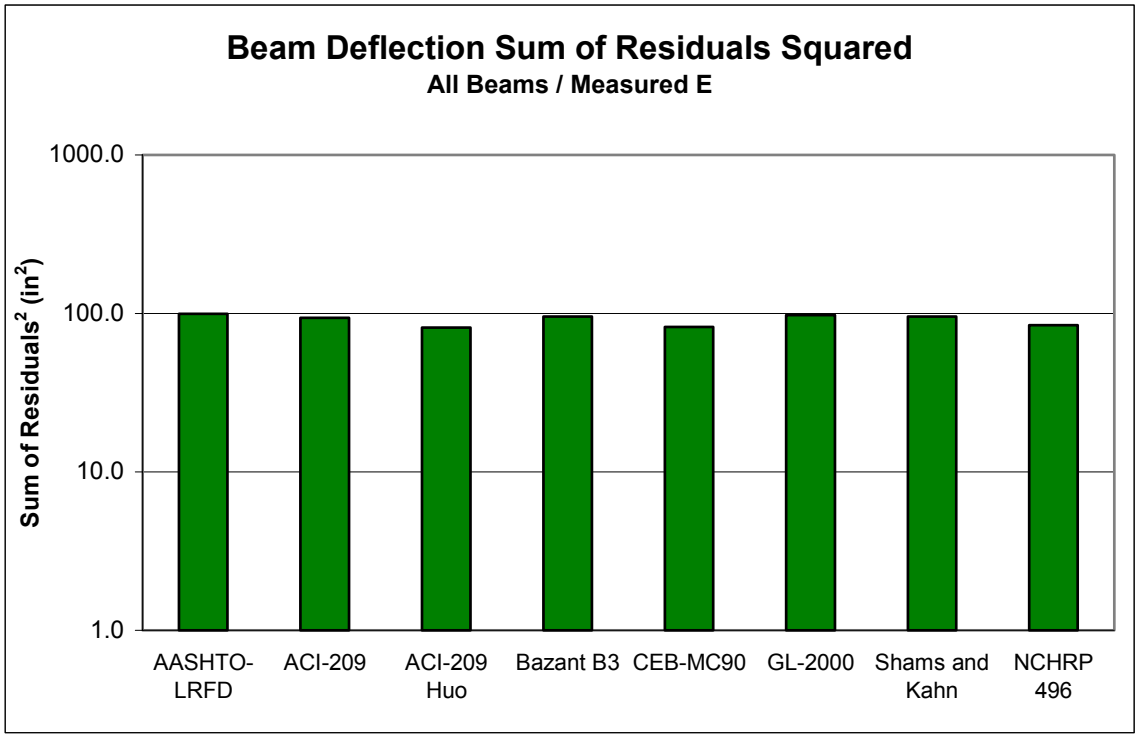

Figure 5.75 Beam Deflection Sum of Residuals Squared, All Beams, Measured E

Table 5.24 Model Ranking – All Beams, Measured E

Rank	Model
1	**ACI-209, modified by Huo**
2	CEB-MC90
3	NCHRP 496
4	ACI-209
5	Bazant B3
6	Shams and Kahn
7	GL-2000
8	AASHTO-LRFD

5.6 COMPARISON OF MEASURED CAMBER TO MULTIPLIER METHODS

In addition to the time-dependent creep and shrinkage models and Incremental Time Step Method used to predict camber growth in prestressed concrete beams, several "multiplier methods" are currently available for use. These methods are very simplistic in that the instantaneous elastic deflection or various components of deflection are increased by suggested multipliers. The AASHTO-LRFD Design Specification includes a suggested method, as well as the PCI Bridge Design Manual, which includes two suggested methods. The first method described by the PCI Bridge Design Manual is based upon previous work by Martin (1977). The second is a more detailed method developed by Tadros, Ghali, and Meyer (1985). It allows for a creep coefficient specific to the concrete mix to be used, as well as using a prestress loss component of deflection based on calculated values. A summary of the three multiplier methods is presented in Tables 5.25, 5.26, and 5.27. The camber predicted by each of the multiplier methods, compared with the average measured camber at 60 days, is presented in Table 5.28 for each beam sample.

Table 5.25 AASHTO-LRFD Multiplier Method - based on Martin (1977)

Deflection Calculation Basis	Multiplier
Instantaneous Deflection Based on I_g	4.0
Instantaneous Deflection Based on I_e	$3.0-1.2(A'_s/A_s) > 1.6$

where,

A'_s = area of compression reinforcement (in^2)

A_s = area of nonprestressed tension reinforcement (in^2)

Table 5.26 PCI Manual Multiplier Method - based on Martin (1977)

Phase	Without Composite Topping	With Composite Topping
At Erection:		
(1) Deflection (↓) component – apply to the elastic deflection due to the member weight at release of prestress	1.85	1.85
(2) Camber (↑) component – apply to the elastic camber due to prestress at the time of release of prestress	1.80	1.80
Final:		
(3) Deflection (↓) component – apply to the elastic deflection due to the member weight at release of prestress	2.70	2.40
(4) Camber (↑) component – apply to the elastic camber due to prestress at the time of release of prestress	2.45	2.20
(5) Deflection (↓) component – apply to elastic deflection due to superimposed dead load only	3.00	3.00
(6) Deflection (↓) component – apply to elastic deflection caused by the composite topping	---	2.30

Table 5.27 PCI Manual Modified Multiplier Method - based on Tadros (1985)

	Erection Time		Final Time	
Load condition	**Formula**	**Average**	**Formula**	**Average**
Initial Prestress	$1+C_a$	1.96	$1+C_u$	2.88
Prestress loss	$\alpha(1+\chi C_a)$	1.00	$(1+\chi C_u)$	2.32
Self-weight	$1+C_a$	1.96	$1+C_u$	2.88
Dead load on plain beam	1.00	1.00	$1+C'_u$	2.50
Dead load on composite beam	1.00	1.00	$1+C'_u$	2.50

where,

C_u = ultimate creep coefficient for loads applied immediately after transfer. Average value is 1.88.

C'_u = ultimate creep coefficient for loads applied at time of erection. Average value is 1.50.

C_a = creep coefficient for loading applied immediately after transfer and strains measured at time of erection. Average value is 0.96.

α_a = time-dependent prestress loss at erection divided by total time-dependent prestress loss. Average value is 0.60.

χ = Bazant's aging coefficient. Average value is 0.70.

Table 5.28 Multiplier Method Predicted Camber vs. Measured Camber

Beam Sample	PCI Multiplier Method (Martin, 1977) (in.)	Modified PCI Multiplier Method (Tadros, 1985) (in.)	Average Measured Camber at 60 days (in.)
1	4	3 1/4	2 5/8
2	3 7/8	3 3/16	2 3/4
3	5	4 1/8	3 5/16

5.7 COMPARISON OF DESIGN, MEASURED, AND THEORETICAL CAMBER

The studied beams were designed using CONSPAN design software. The computer program predicted camber values, which are shown on the bridge plans as the predicted camber at 60 days, are compared against the predicted camber values using the models considered in the study (with predicted and measured modulus of elasticity values) and the measured camber values (Tables 5.29 and 5.30). The CONSPAN predicted design camber significantly overpredicted the measured camber for all beams in the study. For the other models used in conjunction with the Incremental Time Step Method, predicted values within 10 percent of the measured values are shown in bold. It is important to note that, for the every model, the use of measured modulus of elasticity significantly increased the number of predicted camber values falling within 10 percent of the measured camber values.

Table 5.29 Design Camber vs. Measured and Predicted Camber (Predicted E)

Beam	Design (in.)	Meas. (in.)	AASHTO-LRFD (in.)	ACI-209 (in.)	ACI-209 (Huo) (in.)	Bazant B3 (in.)	CEB-MC90 (in.)	GL-2000 (in.)	Shams and Kahn (in.)	NCHRP 496 (in.)
W23-2	5 5/16	3 5/16	1.09	1.34	1.30	1.49	1.15	1.13	1.04	1.28
W23-3	5 5/16	3 3/16	1.14	1.53	1.31	1.55	1.22	1.18	1.10	1.33
W23-4	5 5/16	3 3/8	1.07	1.44	1.24	1.46	1.15	1.11	1.04	1.26
W24-3	5 5/16	3 1/2	1.04	1.39	1.20	1.41	1.11	1.07	1.00	1.21
W25-1	5 5/16	3 1/2	1.04	1.27	1.23	1.41	1.09	1.07	0.98	1.21
W25-10	5 1/4	2 13/16	1.29	1.58	1.53	1.76	1.36	1.31	1.22	1.49
W26-5	4 3/8	2 13/16	1.02	1.27	1.22	1.42	1.09	1.07	1.00	1.20
W26-6	4 3/8	2 9/16	1.12	1.39	1.34	1.56	1.20	1.17	1.10	1.32
W27-7	5 5/16	3 5/16	1.09	1.47	1.26	1.49	1.17	1.13	1.06	1.28
W31-10	5 1/16	3 1/8	1.14	1.40	1.36	1.56	1.20	1.18	1.08	1.34
W33-11	4 1/16	2 5/16	1.24	1.54	1.49	1.70	1.32	1.30	1.19	1.46
W34-6	4 5/16	2 3/16	1.31	1.63	1.57	1.80	1.40	1.37	1.26	1.54
W34-7	4 5/16	2 9/16	1.12	1.39	1.34	1.54	1.17	1.10	1.07	1.32
W34-8	4 1/4	2 3/16	1.31	1.63	1.57	1.80	1.37	1.29	1.26	1.54
W35-1	5 1/2	4 1/16	0.94	1.14	1.11	1.26	0.98	1.02	0.89	1.08
W35-2	5 1/2	4 1/8	0.92	1.12	1.09	1.24	0.97	1.00	0.88	1.06
W35-3	5 1/2	3 15/16	0.97	1.17	1.14	1.30	1.02	1.05	0.92	1.11
W35-7	4 3/16	2 1/2	1.15	1.43	1.38	1.58	1.20	1.13	1.10	1.35
W43-4	4 3/16	2 13/16	1.00	1.24	1.22	1.40	1.07	1.04	0.98	1.20
W43-5	4 3/16	3 1/8	0.90	1.12	1.10	1.26	0.96	0.94	0.88	1.08
W43-6	4 3/16	3 1/16	0.92	1.14	1.12	1.29	0.98	0.96	0.90	1.10
W43-8	4 3/16	2 15/16	0.96	1.19	1.17	1.34	1.02	1.00	0.94	1.15
W45-4	4 3/16	3 1/4	0.88	1.10	1.06	1.21	0.94	0.92	0.85	1.04
W45-5	4 3/16	2 3/4	1.05	1.30	1.25	1.43	1.11	1.09	1.00	1.23
W45-6	4 3/16	2 9/16	1.12	1.39	1.34	1.54	1.20	1.17	1.07	1.32
W45-7	4 3/16	2 3/8	1.18	1.47	1.45	1.66	1.26	1.24	1.16	1.42
W45-8	4 3/16	2 1/8	1.32	1.65	1.62	1.85	1.41	1.38	1.29	1.59

Values corresponding to each model are ratios of the predicted deflection to the measured deflection.

Table 5.30 Design Camber vs. Measured and Predicted Camber (Measured E)

Beam	Design (in.)	Meas. (in.)	AASHTO-LRFD (in.)	ACI-209 (in.)	ACI-209 (Huo) (in.)	Bazant B3 (in.)	CEB-MC90 (in.)	GL-2000 (in.)	Shams and Kahn (in.)	NCHRP 496 (in.)
W23-2	5 5/16	3 5/16	1.08	1.09	1.02	1.09	1.02	1.09	0.83	0.91
W23-3	5 5/16	3 3/16	1.10	1.12	1.02	1.12	1.04	1.12	0.84	0.92
W23-4	5 5/16	3 3/8	1.04	1.06	0.96	1.06	0.98	1.06	0.80	0.87
W24-3	5 5/16	3 1/2	1.00	1.02	0.93	1.02	0.95	1.02	0.77	0.84
W25-1	5 5/16	3 1/2	1.02	1.04	0.96	1.04	0.96	1.04	0.79	0.86
W25-10	5 1/4	2 13/16	1.22	1.24	1.13	1.24	1.16	1.24	0.91	1.00
W26-5	4 3/8	2 13/16	1.04	1.07	1.00	1.07	1.00	1.07	0.82	0.89
W26-6	4 3/8	2 9/16	1.15	1.17	1.10	1.17	1.10	1.17	0.90	0.98
W27-7	5 5/16	3 5/16	1.09	1.11	1.04	1.11	1.04	1.11	0.85	0.92
W31-10	5 1/16	3 1/8	1.10	1.14	1.06	1.14	1.06	1.14	0.86	0.92
W33-11	4 1/16	2 5/16	1.22	1.24	1.16	1.24	1.16	1.24	0.95	1.03
W34-6	4 5/16	2 3/16	1.26	1.29	1.20	1.29	1.20	1.31	0.97	1.06
W34-7	4 5/16	2 9/16	1.07	1.10	1.00	1.10	1.02	1.10	0.80	0.90
W34-8	4 1/4	2 3/16	1.26	1.29	1.17	1.29	1.20	1.29	0.94	1.06
W35-1	5 1/2	4 1/16	1.00	1.02	0.98	1.03	0.98	1.08	0.80	0.86
W35-2	5 1/2	4 1/8	0.98	1.00	0.97	1.02	0.97	1.06	0.79	0.85
W35-3	5 1/2	3 15/16	1.03	1.05	1.02	1.06	1.02	1.11	0.83	0.89
W35-7	4 3/16	2 1/2	1.10	1.13	1.03	1.13	1.05	1.13	0.83	0.93
W43-4	4 3/16	2 13/16	1.00	1.02	0.96	1.02	0.96	1.02	0.78	0.87
W43-5	4 3/16	3 1/8	0.90	0.92	0.86	0.92	0.86	0.92	0.70	0.78
W43-6	4 3/16	3 1/16	0.92	0.94	0.88	0.94	0.88	0.94	0.71	0.80
W43-8	4 3/16	2 15/16	0.96	0.98	0.91	0.98	0.91	0.98	0.74	0.83
W45-4	4 3/16	3 1/4	0.88	0.90	0.85	0.92	0.85	0.90	0.69	0.77
W45-5	4 3/16	2 3/4	1.05	1.07	1.00	1.09	1.00	1.07	0.82	0.91
W45-6	4 3/16	2 9/16	1.12	1.15	1.07	1.17	1.07	1.15	0.88	0.98
W45-7	4 3/16	2 3/8	1.21	1.24	1.18	1.26	1.18	1.26	0.97	1.05
W45-8	4 3/16	2 1/8	1.35	1.38	1.32	1.41	1.32	1.41	1.09	1.18

Values corresponding to each model are ratios of the predicted deflection to the measured deflection.

5.8 SUMMARY

The results of the study did not indicate that the use of any of the examined models yielded the most accurate predicted deflections across all beams and samples. Instead, there were models with more overall predictive accuracy than others, particularly when modulus of elasticity is predicted using the models (Figure 5.74). When modulus of elasticity is represented as the measured values, accuracy differences between models appear to reduce significantly (Figure 5.75). The Shams and Kahn model for creep, shrinkage, and modulus of elasticity resulted in the most accurate predicted beam deflections when used in conjunction with the incremental time step method as described in Chapter 4. The Gardner-Lockman (GL-2000) and AASHTO-LRFD Models were also observed to lead to similarly accurate overall predicted beam deflections.

The Shams and Kahn compressive strength equation best predicted the experimentally measured compressive strength obtained from cylinder testing. The measured modulus of elasticity was best represented by the predictive equation of ACI-363, although it is not time-dependent. A seasonal difference in compressive strength was observed, with summer compressive strength being lower than winter compressive strength for the same mix design.

The creep and shrinkage models considered in the present study are shown in Appendix A. The Shams and Kahn predicted compressive strength is also compared with the measured values for each beam. Finally, the remaining detailed charts for predicted beam deflection and residuals for Beam Sample 2 and 3 are presented. Conclusions and observations from the study are now presented in Chapter 6, as well as recommendations for future research.

CHAPTER 6. CONCLUSIONS AND RECOMMENDATIONS

6.1 CONCLUSIONS

The following conclusions and recommendations are presented based upon interpretation of the calculations, experimental measurements, and data collected during the study, as well as an analysis of the work of previous researchers.

6.1.1 Compressive Strength and Modulus of Elasticity

- Compressive strengths for the summer test cylinders exhibited lower long-term strength compared with winter test cylinders.
- Measured compressive strength was overpredicted by the considered models for nearly all beams cast in winter. For beams cast in summer, the Gardner-Lockman and CEB-MC90 models provided the best match to the measured compressive strengths.

6.1.2 Creep and Shrinkage

- The NCHRP model predicted the greatest shrinkage strains while the Bazant B3 model predicted the lowest shrinkage strains for the studied concrete mix.

- The AASHTO-LRFD model predicted the greatest time-dependent creep coefficient while the Shams and Kahn model predicted the lowest time-dependent creep coefficient for the concrete mix in the study.

6.1.3 Camber Prediction

- Thermal-induced same-day camber for 79 in. Bulb Tee beams with an approximate span length of 120 ft increased by ¼ in. for a partially shaded beam and by ½ in. for the beams fully exposed to the sun. This agreed well with the observations of previous researchers.

- For the 27 studied beams taken as a whole, time-step predicted camber using the theoretical creep strains, shrinkage strains, and modulus of elasticity equation of the Shams and Kahn model best matched the measured camber values.

- For all studied beams, using a Shams and Kahn approximated measured modulus of elasticity, no model was observed to be the definitive best model for predicting the measured camber values. Although predictive accuracy differences between models were extremely small, time-step predicted camber using the ACI-209 model (modified by Huo) best matched the measured camber values by a small margin.

- Camber predicted by the PCI Multiplier Method based on Martin (1977) was 48 percent greater than the measured beam camber at the assumed beam setting age of 60 days.

- Camber predicted by the Modified PCI Multiplier Method based on Tadros (1985) was 21 percent greater than the measured beam camber at the assumed beam setting age of 60 days.

- Camber predicted by the CONSPAN beam design software overpredicted measured camber by an average of 58 percent, which is a drastic overprediction.

6.2 RECOMMENDATIONS

- Based on the results of the study, the Shams and Kahn creep and shrinkage model, along with the Shams and Kahn modulus of elasticity equation and an incremental time step method, are recommended for calculating predicted beam camber for the beams constructed using the mix design described in the study. This recommendation should be revalidated before applying it to other situations.

- Further investigation of seasonal variation in camber growth is needed. Experimental measurements suggested a possible effect, but results were mixed, and small seasonal beam samples made it difficult to discern an overall trend.

- Future research should utilize strain gages to confirm the accuracy of the Shams and Kahn Model in predicting actual prestress losses in the beam.

- Camber prediction methodology used by computer programs such as CONSPAN should be examined, and their predicted camber should be verified using other methods, since the computer software used to design the studied beams overpredicted measured camber by an average of 58 percent.

- The Modified PCI Multiplier developed by Tadros (1985) is recommended for use over the original PCI Multiplier Method developed by Martin (1977), as it doubled the predictive accuracy when predicted results were compared with the measured beam deflections. Multiplier methods should only be used as a "rough estimate" of beam camber, since deflections were still overpredicted by an average of 21 percent at the assumed age of beam setting.

REFERENCES

Ahlborn, T.M.; Shield, C.K.; and French, C.W. (2000) "High-Performance Concrete Prestressed Bridge Girders: Long Term and Flexural Behavior." Report 2000-32, Minnesota Department of Transportation, St. Paul, MN 91 pp.

Aitcin, P.C. and Mehta, P.K. (1990). "Effect of Coarse-Aggregate Characteristics on Mechanical Properties of High-Strength Concrete." *ACI Materials Journal*, ACI, 87(2), 103-107.

Al-Omaishi, N. (2001). "Prestress Losses in Pretensioned High-Strength Concrete Bridge Girders." Ph.D. Dissertation, Department of Civil Engineering, University of Nebraska, Lincoln, NE.

Alexander, Mark G. (1996). "Aggregates and the Deformation Properties of Concrete." *ACI Materials Journal*, ACI, 94(6), 569-577.

American Association of State Highway and Transportation Officials. (1998). "AASHTO-LRFD Bridge Design Specifications." 2nd Edition. Washington, D.C.

American Association of State Highway and Transportation Officials. (2002). "AASHTO Standard Specifications for Highway Bridges." 17th Edition. Washington, D.C.

American Concrete Institute Committee 209. (1992). "Prediction of Creep, Shrinkage, and Temperature Effects in Concrete Structures." ACI Manual of Concrete Practice.

American Concrete Institute Committee 305. (1999). "Hot Weather Concreting." ACI Manual of Concrete Practice.

American Concrete Institute Committee 318. (1999). "Building Code Requirements for Structural Concrete." Detroit, MI.

American Concrete Institute Committee 363. (1992). "State of the Art Report on High-Strength Concrete." ACI Manual of Concrete Practice.

American Concrete Institute Committee 435. (1995). "Control of Deflection in Concrete Structures." Detroit, MI..

Baalbaki, W.; Benmokrane, B.; Chaallal, O.; and Aitcin, P. C. (1991). "Influence of Coarse Aggregate on Elastic Properties of High-Performance Concrete." *ACI Materials Journal*, ACI, 88(5), 499-503.

Baalbaki, W.; Aitcin, P. C. ; and Ballivy, G. (1992). "On Predicting Modulus of Elasticity in High-Strength Concrete." *ACI Materials Journal*, ACI, 89(5), 517-520.

Barr, P. ; Fekete, E. ; Eberhard, M. ; Stanton, J. ; Khaleghi, B. ; Hsieh, J. (2000). "High Performance Concrete in Washington State SR 18/SR 516 Overcrossing: Interim Report on Girder Monitoring." Report Number FHWA-RD-00-070. Federal Highway Administration (FHWA). Washington, D.C.

Bazant, Z.P. and Baweja, S. (1995). "Creep and Shrinkage Prediction Model for Analysis and Design of Concrete Structures – Model B3." *RILEM Recommendation, Materials and Structures*, 28, 357-365.

Branson, D.E., and Kripanarayanan, K. (1971). "Loss of Prestress, Camber, and Deflection of Non-Composite and Composite Prestressed Concrete Structures." *PCI Journal*., Precast/Prestressed Concrete Institute, 16(5), 22-52.

British Standards Institution (1985). "British Standard, Structural Use of Concrete." BS 8110.

Brown, K.M.; Nielsen, R.J.; and Schmeckpeper, E.R. (1999). "Camber Growth Prediction in Precast Prestressed Concrete Bridge Girders." Research Project FC#97-144, University of Idaho, National Center for Advanced Transportation Technology.

Burg, Ronald G. (1996). "The Influence of Casting and Curing Temperature on the Properties of Fresh and Hardened Concrete." Research and Development Bulletin RD113. Portland Cement Association. Skokie, Illinois.

Byle, K.A.; Burns, N.H.; and Carrasquillo, R.L. (1997). "Time-Dependent Deformation Behavior of Prestressed High Performance Concrete Bridge Beams." Research Report CTR 580-6, Center for Transportation Research – The University of Texas at Austin.

Canfield, Scott R. (2005). "Full Scale Testing of Prestressed, High Performance Concrete, Composite Bridge Girders." Master's Thesis, Georgia Institute of Technology, August, 2005, 308 pp.

Collins, Therese M. (1989). "Proportioning High Strength Concrete to Control Creep and Shrinkage." *ACI Materials Journal*, ACI, 86(6), 567-580.

Comite Euro-International du Beton-Federation Internationale de la Precontrainte. (1990). "CEB-FIP Model Code 1990." Lausanne, Switzerland.

Farrington, E.W.; Burns, N.H.; and Carrasquillo, R.L. (1996). "Creep and Shrinkage of High Performance Concrete." Research Report CTR 580-5, Center for Transportation Research – The University of Texas at Austin.

Fekete, E. ; Barr, P. ; Stanton, J.; Eberhard, M. ; Janssen, D. (2000). "High Performance Concrete in Washington State SR 18/SR 516 Overcrossing: Interim Report on Materials Tests." Report Number FHWA-RD-00-071. Federal Highway Administration (FHWA). Washington, D.C.

Gardner, N.J. and Lockman, M.J. (2001). "Design Provisions for Drying Shrinkage and Creep of Normal- Strength Concrete." *ACI Materials Journal,* ACI, 9(2), 159-167.

Gardner, N.J. and Zhao, J.W. (1993). "Creep and Shrinkage Revisited." *ACI Materials Journal,* ACI, 90(3), 236-246.

Gopalaratnam, V.S., and Eatherton, M. (2001). "Instrumentation and Monitoring of High Performance Concrete Prestressed Bridge Girders." Report No. RDT 01-007, Department of Civil and Environmental Engineering, University of Missouri – Columbia.

Haque, M.N. (1996). "Strength Development and Drying Shrinkage of High Strength Concretes." *Cement and Concrete Composites*, 18(5), 333-342.

Hover, Ken C. (2005). "Understanding Hot Weather Concrete – Getting the Most Out of the Summer Concrete Construction Season." *Structure Magazine*, July 2005, 26-31.

Huo, X.S. (1997). "Time-Dependent Analysis and Application of High Performance Concrete in Bridges." Ph.D. Dissertation, Department of Civil Engineering, University of Nebraska, Lincoln, NE. 211 pp.

Huo, X.S., Al-Omaishi, N., and Tadros, M.K. (2001). "Creep, Shrinkage, Modulus of Elasticity of High-Performance Concrete." *ACI Materials Journal*, 98(6), 440-449.

Kelly, D.J.; Bradberry, T.E.; and Breen, J.E. (1987). "Time Dependent Deflections of Pretensioned Beams." Research Report CTR 381-1, Center for Transportation Research – The University of Texas at Austin.

Klieger, Paul (1958). "Effect of Mixing and Curing Temperature on Concrete Strength." Research Department Bulletin RX103. Portland Cement Association. Skokie, Illinois.

Kosmatka, S. (2002). "Design and Control of Concrete Mixtures." 17th Edition. Portland Cement Association. Skokie, Illinois.

Lai, J.S.; Kahn, L.F.; Travis, D.; Champney, M.; Prada, J.; Shams, M.; and Saber, A. (1999). "Mix Design and Properties of High Performance Concrete– Task 4, Use of High Strength/High Performance Concrete for Precast Prestressed Concrete Bridges in Georgia." Georgia Tech Structural Engineering, Mechanics and Materials Research Report No. 99-1, Georgia Department of Transportation Research Project No. 9510, March, 1999, 199 pp.

Lai, J.S.; Kahn, L.F.; Travis, D.; Champney, M.; Prada, J.; Shams, M.; and Saber, A. (1999). "Evaluation of Field Production – Task 4, Use of High Strength/High Performance Concrete for Precast Prestressed Concrete Bridges in Georgia." Georgia Tech Structural Engineering, Mechanics and Materials Research Report No. 99-2, Georgia Department of Transportation Research Project No. 9510, June, 1999, 52 pp.

Lakshmikantan, S., "Evaluation of Concrete Shrinkage and Creep Models." Master of Science Thesis in Civil Engineering, San Jose State University, May 1999.

Luebkeman, C.L. ; Nilson, A.H.; and Slate, F.O. (1985). "Sustained Load Deflection of High-Strength Concrete Beams." Report No. 85-2, Department of Structural Engineering, Cornell University.

Magura, D. D.; Sozen, M.A.; and Siess, C.P. (1964). "A Study of Stress Relaxation in Prestressing Reinforcement." *PCI Journal*., Precast/Prestressed Concrete Institute, 41(5), 78-89.

Mangoba, N.; Mayberry, M.; and Saiidi, M. (1999). "Prestress Losses in Four Box Girder Bridges in Northern Nevada." Report No. CCEER-99-2, Civil Engineering Department, University of Nevada, Reno.

Martin, Leslie D. (1977). "A Rational Method for Estimating Camber and Deflection of Precast Prestressed Members." *PCI Journal*., Precast/Prestressed Concrete Institute, 22(1), 100-108.

McDonald, D.B. and Roper, H. (1993). "Accuracy of Prediction Models for Shrinkage of Concrete." *ACI Materials Journal*, 90, 265-271.

Meyerson, Richard. (2001). "Compressive Creep of Prestressed Concrete Mixtures With and Without Mineral Admixtures." Master of Science Thesis, Department of Civil and Environmental Engineering, Virginia Polytechnic Institute and State University. Blacksburg, VA.

Mokarem, David W. (2002). "Development of Concrete Shrinkage Performance Specifications." PhD. Thesis, Department of Civil and Environmental Engineering, Virginia Polytechnic Institute and State University. Blacksburg, VA.

Mokhtarzadeh, A. (1996). "Mechanical Properties of High Strength Concrete." Ph.D. Dissertation, Department of Civil Engineering, University of Minnesota, Minneapolis, MN.

Mokhtarzadeh, A. and French, C. (2000). "Time-dependent Properties of High-Strength Concrete with Consideration for Precast Applications." *ACI Materials Journal*, 97(3), 263-271.

Mortensen, C.; Saiidi, M.; and Ladkany, S. (2003). "Creep and Shrinkage Losses in Prestressed Concrete Bridges in Highly Variable Climates." *TRB 2003 Annual Meeting CD-ROM.*

Myers, J.J. and Carrasquillo, R.L. (1999). "Production and Quality Control of High Performance Concrete in Texas Bridge Structures." Research Report 580/589-1, Center for Transportation Research, University of Texas, Austin, TX, 176 pp.

National Association of Australian State Road Authorities (1976). "Bridge Design Specifications." NAASRA Section 6. Sydney, Australia.

Neville, Adam M. (1997). "Aggregate Bond and Modulus of Elasticity of Concrete." *PCI Journal*, PCI, 95(1), 71-74.

Nilson, Arthur H. *Design of Prestressed Concrete (2nd ed.).* John Wiley and Sons Inc. New York, New York. 1987.

Norwegian Council for Building Standardization (1992). "Norwegian Standard: Concrete Structures – Design Rules." NS 3473. Oslo, Norway.

Paulson, K.A.; Nilson, A.H.; and Hover, K.C. (1991). "Long Term Deflection of High Strength Concrete Beams." *ACI Materials Journal,* ACI, 88(2), 197-206.

PCI Committee on Prestress Losses. (1975). "Recommendations for Estimating Prestress Losses." *PCI Journal*., Precast/Prestressed Concrete Institute, 20(4), 42-75.

PCI Industry Handbook Committee. *PCI Design Handbook – Precast and Prestressed Concrete (5th ed.).* Precast/Prestressed Concrete Institute. Chicago, Illinois. 1999.

Roller, J.J.; Russell, H.G.; Bruce, R.N.; and Hassett, B. (2003). "Effect of Curing Temperatures on High Strength Concrete Bridge Girders." *PCI Journal*., Precast/Prestressed Concrete Institute, 48(2), 72-79.

Saiidi, M. S.; Shields, J.S.; O'Connor, D; and Hutchens, E. (1996). "Variation of Prestress Force in a Prestressed Concrete Bridge During the First 30 Months." *PCI Journal*., Precast/Prestressed Concrete Institute, 41(5), 66-72.

Sakata, K. (1993). "Prediction of Concrete Creep and Shrinkage." *Creep and Shrinkage of Concrete*, Proceedings of the Fifth International RILEM Symposium, Barcelona, Spain, pp. 649-654.

Sanek, Jonathan E. (2005). "Field Verification of Camber Estimates for Prestressed Concrete Bridge Girders." Master of Engineering Thesis, Department of Civil and Environmental Engineering, University of Florida. Gainesville, FL.

Shams, M. (2000). "Time Dependent Losses of High-Performance Concrete." Doctoral Thesis, Georgia Institute of Technology, May, 2000, 572 pp.

Shams, M. and Kahn, L.F. (2000). "Time-Dependent Behavior of High-Performance Concrete." Georgia Tech Structural Engineering, Mechanics and Materials Research Report No. 00-5, Georgia Department of Transportation Research Project No. 9510, April, 2000, 395 pp.

Slapkus, A., and Kahn, L.F. (2002). "Evaluation of Georgia's High Performance Concrete Bridge." Research Report No. 03-3, School of Civil and Environmental Engineering, Georgia Institute of Technology.

Stallings, J.M.and Eskildsen, S. (2001). "Camber and Prestress Losses in High Performance Concrete Bridge Girders." Highway Research Center, Harbert Engineering Center, Auburn University in cooperation with the Federal Highway Administration, 116 pp.

Stallings, J.M.and Glover, S. (2000). "High-Performance Bridge Concrete." Highway Research Center, Harbert Engineering Center, Auburn University in cooperation with the Federal Highway Administration, 360 pp.

Standards Association of Australia (1974). "SAA Australian Standard for Concrete Structures." AS1481.

Standards Association of Australia (1988). "SAA Australian Standard for Concrete Structures." AS3600.

Stanton, J.F.;Barr, P.; and Eberhard, M.O. (2000). "Behavior of High-Strength HPC Bridge Girders." Research Report SP-189, University of Washington, Seattle, WA.

Suttikan, C. (1978). "A Generalized Solution for Time-Dependent Response and Strength of Noncomposite and Composite Prestressed Concrete Beams." PhD. Thesis, Department of Civil, Architectural and Environmental Engineering, University of Texas. Austin, TX.

Tadros, M. K.; Ghali, A.; and Meyer, A.W. (1985). "Prestressed Loss and Deflection of Precast Concrete Members." *PCI Journal*., Precast/Prestressed Concrete Institute, 30(1), 114-141.

Tadros, M.K.; Seguirant, S.J.; and Gallt, J.G. (2003). "Prestress Losses in Pretensioned High-Strength Concrete Bridge Girders." NCHRP Report 496, National Cooperative Highway Research Program (NCHRP).

Torrenti, J.M. and Granger, L. (1999). "Modeling Concrete Shrinkage under Variable Ambient Conditions." *ACI Materials Journal*, ACI, 96(1), 35-39.

Townsend, Bradley D. (2003). "Creep and Shrinkage of a High Strength Concrete Mixture." Master of Science Thesis, Department of Civil and Environmental Engineering, Virginia Polytechnic Institute and State University. Blacksburg, VA.

Verbeck, George J. and Helmuth, R.A., (1968). "Structures and Physical Properties of Cement Pastes." Proceedings, Fifth International Symposium on the Chemistry of Cement. The Cement Association of Japan. Tokyo, Japan.

Waldron, Christopher J. (2004). "Investigation of Long-Term Prestress Losses in Pretensioned High Performance Concrete Girders." Doctor of Philosophy Dissertation, Department of Civil and Environmental Engineering, Virginia Polytechnic Institute and State University. Blacksburg, VA.

Will, J.J., and Sanders, D.H. (2000). "High-Performance Concrete Using Nevada Aggregates." Report No. RDT01-005, Nevada Department of Transportation.

Woolf, D., and French, C.E. (1998). "A Camber Study of Mn/DOT Prestressed Concrete I-Girders." Report Number 1998-08, University of Minnesota, Center for Transportation Studies.

Yazdani, N., and Mtenga, P. (1997). "Investigation of Camber in Precast Concrete Bridge Girders – Final Report." Report Number WPI-0510701, Florida Department of Transportation and Federal Highway Administration.

APPENDIX A

A.1 CREEP AND SHRINKAGE MODELS FOR LOSS CALCULATION

Prestress losses used in the Incremental Time Step Method are calculated using models that calculate creep and shrinkage strains as a function of time. These models include AASHTO-LRFD (1998), ACI-209 (1992), ACI-209 modified by Huo (1997), Bazant B3 (1995), CEB-MC90 (1990), Gardner-Lockman (GL-2000) (2001), Shams and Kahn (2000), and NCHRP 496 (2003). A few models predicted the prestress losses directly. The AASHTO-Standard model only calculates losses. The Shams and Kahn and NCHRP 496 Models calculate losses in addition to creep and shrinkage strains. The models that directly calculate losses divide the life of the member into fewer, longer time periods. These extremely long time periods do not allow the accuracy gained from an Incremental Time Step Method. It is for this reason that the models predicting time-dependent creep and shrinkage strains were used. The prediction equations and nomenclature for the various models considered in this study will now be presented in detail.

A.1.1 AASHTO-Standard Specifications Model

Nomenclature

Δf_s = total loss excluding friction (psi)
CR_c = loss due to creep of concrete (psi)
CR_s = loss due to relaxation of prestressing steel (psi)
E_s = modulus of elasticity of prestressing steel strand, which can be assumed to be 28 x 10^6 psi
E_{ci} = modulus of elasticity of concrete at stress transfer (psi)
ES = loss due to elastic shortening (psi)
f'_{ci} = compressive strength of concrete at initial prestress (psi)
f_{cir} = concrete stress at the center of gravity of prestressing steel due to prestressing force and dead load of beam immediately after transfer. The reduced strand stress can be taken as $0.63f'_s$ for stress-relieved strand or $0.60f'_s$ for low relaxation strand.
f_{cds} = concrete stress at the center of gravity of prestressing steel due to all dead loads except the dead load present at the time the prestressing force is applied.
RH = mean Annual Relative Humidity (%)
SH = loss due to concrete shrinkage (psi)
w = weight of concrete mix (lb/ft^3)

Prestress Losses

$$\Delta f_s = SH + ES + CR_c + CR_s \tag{A.1}$$

$$\text{SH} = 17{,}000 - 150(\text{RH}) \tag{A.2}$$

$$ES = \frac{E_s}{E_{ci}} f_{cir} \tag{A.3}$$

$$E_{ci} = 33w^{\frac{3}{2}}\sqrt{f'_{ci}} \tag{A.4}$$

where,

$$CR_c = 12 f_{cir} - f_{cds} \tag{A.5}$$

where,

Stress-Relieved Strand (250 to 270 ksi):

$$CR_s = 20{,}000 - 0.4ES - 0.2(SH + CR_c) \tag{A.6}$$

Low-Relaxation Strand (250 to 270 ksi):

$$CR_s = 5{,}000 - 0.10ES - 0.05(SH + CR_c) \tag{A.7}$$

A1.2 AASHTO-LRFD Model

Nomenclature

Δf_{pT} = total loss (ksi)

Δf_{pES} = loss due to elastic shortening (ksi)

Δf_{pSR} = loss due to shrinkage (ksi)

Δf_{pCR} = loss due to creep(ksi)

Δf_{pR2} = loss due to relaxation of steel after transfer (ksi)

Δf_{cdp} = change in concrete stress at center of gravity due to permanent loads, with the exception of the load acting at the time the prestressing force is applied. Values of Δf_{cdp} should be calculated at the same section or at sections for which f_{cgp} is calculated (ksi)

A_g = gross area of section (in.^{2})
A_{ps} = area of prestressing steel (in.^{2})
E_{ci} = modulus of elasticity of concrete at transfer (ksi)
E_p = modulus of elasticity of prestressing steel (ksi)
e_m = average eccentricity at midspan (in.)
f_{pbt} = stress in prestressing steel immediately prior to transfer (ksi)
f'_c = specified compressive strength of concrete (ksi)
f_{cgp} = sum of concrete stresses at the center of gravity of prestressing strands due to prestressing force at transfer and the self-weight of the member at the sections of maximum moment.
f_{pj} = initial stress in the strand at the end of stressing (ksi)
f_{py} = specified yield strength of prestressing steel (ksi)
H = relative humidity (%)
I_g = moment of inertia of the gross concrete section (in.^{4})
k_c = factor for the effect of the volume-to-surface ratio
k_f = factor for the effect of concrete strength
k_h = humidity Factor
k_s = size factor
M_g = midspan moment due to member self-weight (kip-in.)
t = maturity of concrete (days)
t_i = concrete age when load is initially applied (days)
V/S = volume to surface ratio (in.)
w_c = unit weight of concrete (kip/ft^3)

Modulus of Elasticity

$$E_c = 33{,}000 w_c^{1.5} \sqrt{f_c'} \tag{A.8}$$

Creep Coefficient

$$\psi(t, t_i) = 3.5 k_c k_f \left(1.58 - \frac{H}{120}\right) t_i^{-0.118} \frac{(t - t_i)^{0.6}}{10.0 + (t - t_i)^{0.6}} \tag{A.9}$$

$$k_f = \frac{1}{0.67 + \left(\frac{f_c'}{9}\right)} \tag{A.10}$$

$$k_c = \left[\frac{\frac{t}{26e^{0.36(V/S)} + t}}{\frac{t}{45 + t}}\right]\left[\frac{1.80 + 1.77e^{-0.54(V/S)}}{2.587}\right] \tag{A.11}$$

Shrinkage

Moist-Cured Concrete:

$$\varepsilon_{sh} = -k_s k_h \left(\frac{t}{55.0 + t}\right) 0.51 \times 10^{-3} \tag{A.12}$$

Steam-Cured Concrete:

$$\varepsilon_{sh} = -k_s k_h \left(\frac{t}{55.0 + t}\right) 0.56 \times 10^{-3} \tag{A.13}$$

$$k_s = \left[\frac{\frac{t}{26e^{0.36(V/S)} + t}}{\frac{t}{45 + t}}\right]\left[\frac{1064 - 94(V/S)}{923}\right] \tag{A.14}$$

$k_h = (140\text{-}H)/70$ for H<80% (A.15)

$k_h = 3(100\text{-}H)/70$ for H>80% (A.16)

$$k_c = \left[\frac{t}{\frac{26e^{0.36(V/S)}+t}{\frac{t}{45+t}}}\right]\left[\frac{1.80+1.77e}{}\right] \quad \text{(A.17)}$$

Prestress Losses

$$\Delta f_{pT} = \Delta f_{pES} + \Delta f_{pSR} + \Delta f_{pCR} + \Delta f_{pR1} \quad \text{(A.18)}$$

$$\Delta f_{pES} = \frac{E_p}{E_{ci}} f_{cgp} \quad \text{(A.19)}$$

$$\Delta f_{pES} = \frac{A_{ps} f_{pbt}\left(I_g + e_m^2 A_g\right) - e_m M_g A_g}{A_{ps}\left(I_g + e_m^2 A_g\right) + \frac{A_g I_g E_{ci}}{E_p}} \quad \text{(A.20)}$$

$$\Delta f_{pSR} = \left(17.0 - 0.150H\right) \quad \text{(A.21)}$$

$$\Delta f_{pCR} = 12.0 f_{cgp} - 7.0\Delta f_{cdp} \geq 0 \quad \text{(A.22)}$$

$$\Delta f_{pR1} = \frac{\log(24.0t)}{10.0}\left[\frac{f_{pj}}{f_{py}} - 0.55\right] f_{pj}\text{, for Stress-Relieved Strand} \quad \text{(A.23)}$$

$$\Delta f_{pR1} = \frac{\log(24.0t)}{40.0}\left[\frac{f_{pj}}{f_{py}} - 0.55\right] f_{pj}\text{, for Low-Relaxation Strand} \quad \text{(A.24)}$$

Table A.1 AASHTO-LRFD Model Input Values

Curing	H (%)	w_c (lb/ft^3)	A_g (in.^{2})	I_g (in.^{4})	V/S (in.)	Strand	A_{ps} (in.^{2})	e_m (in.)
Moist	80	147.72	1133	981196	3.8127	Low-Relaxation	0.217	9.583

f'_c (ksi)	f_{py} (ksi)	f_{pbt} (ksi)	f_{py} (ksi)	E_{ci} (ksi)	E_{ps} (ksi)	P_I (kips)	t_I (days)
9	270	206.6	270	4452	29000	43.9	1

A1.3 ACI-209 Model

Nomenclature

α=air content (percent)
β = constant (days)
$(\varepsilon_{sh})_u$ = ultimate shrinkage strain (recommended value = $780\gamma_{sh}$ x 10^{-6})
γ= relative humidity (percent)
γ_c = product of all applicable correction factors
γ_{sh} = product of all applicable correction factors
ψ= ratio of fine aggregate to total aggregate by weight
v_u = ultimate creep coefficient (recommended value=$2.35\gamma_c$)
a = constant (days)
c = cement content (lb/yd^3)
$f'_c(28)$ = compressive strength at 28 days (psi)
s = observed slump (in.)
t_{la}=loading age (days)
v/s = volume to surface ratio of member (in.)
w = unit weight of concrete (lb/ft^3)

Compressive Strength at time t (days)

$$f'_c(t) = \frac{t}{a + \beta t} f'_c(28) \tag{A.25}$$

Modulus of Elasticity at time t (days)

$$E_{ct} = g_{ct}\left[w^3 f'_c(t)\right]^{1/2} \tag{A.26}$$

where, $g_{ct} = 33$

Creep Strain at time t (days)

$$v_t = \frac{t^{0.6}}{10+t^{0.6}} v_u \tag{A.27}$$

Shrinkage Strain at time t (days)

$$(\varepsilon_{sh})_t = \frac{t}{35+t}(\varepsilon_{sh})_u \text{ for moist cured concrete after 7 days} \tag{A.28}$$

$$(\varepsilon_{sh})_t = \frac{t}{55+t}(\varepsilon_{sh})_u \text{ for steam cured concrete after 1 to 3 days} \tag{A.29}$$

Correction Factors

Loading Age:

$$\text{Creep: } \gamma_{la} = 1.25(t_{la})^{-0.118} \quad \text{for moist cured concrete} \tag{A.30}$$

$$\text{Creep: } \gamma_{la} = 1.13(t_{la})^{-0.094} \quad \text{for steam cured concrete} \tag{A.31}$$

Relative Humidity:

$$\text{Creep: } \gamma_{\lambda} = 1.27 - 0.0067\lambda, \text{ for } \lambda > 40 \tag{A.32}$$

$$\text{Shrinkage: } \gamma_{\lambda} = 1.40 - 0.010\lambda, \text{ for } 40 \leq \lambda \leq 80 \tag{A.33}$$

$$\gamma_{\lambda} = 3.00 - 0.030\lambda, \text{ for } 80 < \lambda \leq 100 \tag{A.34}$$

Volume Surface Ratio

$$\text{Creep: } \gamma_{vs} = 2/3[1 + 1.13 \exp(-0.54\ v/s)] \tag{A.35}$$

$$\text{Shrinkage: } \gamma_{vs} = 1.2 \exp(-0.12\ v/s) \tag{A.36}$$

Slump

$$\text{Creep: } \gamma_{s} = 0.82 + 0.067s \tag{A.37}$$

$$\text{Shrinkage: } \gamma_{s} = 0.89 + 0.041s \tag{A.38}$$

Fine Aggregate Percentage

$$\text{Creep: } \gamma_{\psi} = 0.88 + 0.0024\psi \tag{A.39}$$

$$\text{Shrinkage: } \gamma_{\psi} = 0.30 + 0.014\psi, \text{ for } \psi < 50\% \tag{A.40}$$

$$\gamma_{\psi} = 0.90 + 0.002\psi, \text{ for } \psi > 50\% \tag{A.41}$$

Cement Content

$$\text{Shrinkage: } \gamma_{c} = 0.75 + 0.00036c \tag{A.42}$$

Air Content

$$\text{Creep: } \gamma_\alpha = 0.46+0.09\alpha, \text{ but not less than 1.0} \quad \text{(A.43)}$$

$$\text{Shrinkage: } \gamma_\alpha = 0.95+0.08\alpha \quad \text{(A.44)}$$

Table A.2 ACI-209 Model Input Values

Curing	Cycle	Sustained Drying	H (%)	w_c (lb/ft^3)	ν_u	ε_{shu}	t_c (days)	t_{la} (days)
Moist	Wet/Dry	No	80	147.72	2.35	780x10^{-6}	1	1

s (in.)	ψ (%)	c (lb/yd^3)	a (%)	a (days)	b	$f_c'(28)$ (ksi)	V/S (in.)	g_{ct}
7.99	21.54	311.17	1.76	2.3	0.92	9	3.8127	33

A1.4 ACI-209, Modified by Huo

All elements of ACI 209 remain the same, with the addition of modification factors based on compressive strength.

Nomenclature

$(\varepsilon_{sh})_t$ = shrinkage strain at time t (in./in.)

$(\varepsilon_{sh})_u$ = ultimate shrinkage strain (in./in.)

$\gamma_{st,c}$ = creep correction factor for concrete strength

$\gamma_{st,s}$ = shrinkage correction factor for concrete strength

v_t = creep coefficient at time t

v_u = ultimate creep coefficient

f'_c = concrete compressive strength at 28 days (psi)

K_c = adjustment factor for early age creep coefficient

K_s = adjustment factor for early age shrinkage

t = age of concrete (days)

Creep

$$\gamma_{st,c} = 1.18\text{-}0.045(f'_c) \tag{A.45}$$

$$v_t = \frac{t^{0.6}}{K_C + t^{0.6}} v_u \tag{A.46}$$

where,

$$K_c = 12\text{-}0.50(f'_c) \tag{A.47}$$

Shrinkage

$$\gamma_{st,s} = 1.20\text{-}0.50(f'_c) \tag{A.48}$$

$$(\varepsilon_{sh})_t = \frac{t}{K_s + t}(\varepsilon_{sh})_u \tag{A.49}$$

$$K_s = 45 - 2.5(f'_c) \tag{A.50}$$

Table A.3 ACI-209 (modified by Huo) Model Input Values

Curing	Cycle	Sustained Drying	H (%)	w_c (lb/ft^3)	ν_u	ε_{shu}	t_c (days)	t_{la} (days)
Moist	Wet/Dry	No	80	147.72	2.35	780×10^{-6}	1	1

s (in.)	ψ (%)	c (lb/yd^3)	a (%)	a (days)	b	$f_c'(28)$ (ksi)	V/S (in.)	g_{ct}
7.99	21.54	311.17	1.76	2.3	0.92	9	3.8127	33

A1.5 Bazant B3 Model

Nomenclature

α = coefficient of thermal expansion
Δ = stress duration (days)
ε_{sh} = shrinkage strain, considered negative (except for swelling, when positive) (x 10^{-6})
$\varepsilon_{sh\infty}$ = ultimate shrinkage strain (x 10^{-6} in./in.)
$\varepsilon(t)$ = strain at time t (x 10^{6} in./in.)
$\phi(t,t')$ = creep coefficient
σ = stress applied at loading (psi)
τ_{sh} = shrinkage half-time (days)
a/c = ratio (by weight) of aggregate to cement
c = cement content of concrete (lb/ft^3)
$C_d(t,t',t_o)$ = compliance function for additional creep due to drying
$C_o(t,t')$ = compliance function for basic creep
D = 2v/s = effective cross-section thickness (in.)
E_o = Asymptotic Modulus of Elasticity (psi)
f'_c = 28-day standard cylinder compression strength (psi)
f_{ck} = design strength of concrete (psi)
h = relative humidity expressed as a decimal ($0 \leq h \leq 1$)
H = spatial average of pore relative humidity within the cross-section
J(t,t') = compliance function (strain at time t caused by a unit uniaxial constant stress applied at age t')
k_h = coefficient representing humidity dependence
k_s = cross-section shape factor
q_1 = instantaneous strain due to unit stress (x 10^{-6} psi^{-1})
q_2 = ageing viscoelastic compliance
q_3 = non-ageing viscoelastic compliance
q_4 = flow compliance
q_5 = creep at drying
S(t) = time function for shrinkage
t = time, representing the age of concrete (days)
t' = age at loading (days)
t_o = age when drying begins (Only $t_o \leq t'$ is considered) (days)
v/s = volume-to-surface ratio (in.)
w/c = ratio (by weight) of water to cementitious material
w = water content of concrete (lb/ft^3)

$$\varepsilon(t) = J(t,t')\sigma + \varepsilon_{sh}(t) \tag{A.51}$$

$$J(t,t') = q_1 + C_o(t,t') + C_d(t,t',t_o) \tag{A.52}$$

$$q_1 = \frac{0.6\times10^6}{E_{28}} \tag{A.53}$$

$$E_{28} = 57{,}000\sqrt{f_c'} \tag{A.54}$$

$$C_o(t,t') = q_2 Q(t,t') + q_3 \ln\left[1+(t-t')^n\right] + q_4 \ln\left(\frac{t}{t'}\right) \tag{A.55}$$

$$Q(t,t') = Q_f(t')\left[1+\left(\frac{Q_f(t')}{Z(t,t')}\right)^{r(t')}\right]^{\frac{-1}{r(t')}} \tag{A.56}$$

$$Q_f(t,t') = \left[0.086(t')^{\frac{2}{9}} + 1.21(t')^{\frac{4}{9}}\right]^{-1} \tag{A.57}$$

$$Z(t,t') = (t')^{-m}\ln\left[1+(t-t')^n\right] \tag{A.58}$$

$$r(t') = 1.7(t')^{0.12} + 8 \tag{A.59}$$

$$q_2 = 451.1c^{0.5}(f_c')^{-0.9} \tag{A.60}$$

$$q_3 = 0.29\left(\frac{w}{c}\right)^4 q_2 \tag{A.61}$$

$$q_4 = 0.14\left(\frac{a}{c}\right)^{-0.7} \tag{A.62}$$

$$C_d(t,t',t_o) = q_5\left[e^{-8H(t)} - e^{-8H(t')}\right]^{\frac{1}{2}} \tag{A.63}$$

$$q_5 = 7.57\times10^5 f_c'^{-1}\varepsilon_{sh\infty}{}^{-0.6} \tag{A.64}$$

$$H(t) = 1-(1-h)S(t) \tag{A.65}$$

$$\varepsilon_{sh}(t,t_o) = -\varepsilon_{sh\infty} k_h S(t) \tag{A.66}$$

$$k_h = \begin{cases} 1\text{-}h^3 & \text{for } h \le 0.98 \\ -0.2 & \text{for } h = 1 \text{ (swelling in water)} \\ \text{linear interpolation} & \text{for } 0.98 \le h \le 1 \end{cases} \tag{A.67}$$

$$S(t) = \tanh\left(\frac{t - t_o}{\tau_{sh}}\right)^{\frac{1}{2}} \tag{A.68}$$

$$\tau_{sh} = k_t (k_s D)^2 \tag{A.69}$$

$$k_t = 190.8 t_o^{-0.08} \left(f_c^{'}\right)^{-0.25} \tag{A.70}$$

$$D = 2\frac{v}{s} \tag{A.71}$$

$$\varepsilon_{sh\infty} = \alpha_1 \alpha_2 \left[26 w^{2.1} (f_c^{'})^{-0.28} + 270\right] \tag{A.72}$$

$\alpha 1 =$ 1.0 for Type I Cement
0.85 for Type II Cement
1.1 for Type III Cement

$\alpha 2 =$ 0.75 for Specimens that are Steam-Cured
1.0 for Specimens Cured in Water or at 100% RH
1.2 for Specimens Sealed During Curing

Table A.4 Bazant B3 Model Input Values

Curing	t' (days)	t_o (days)	Cement Type	h	V/S (in.)	m	n
Moist	1	0.75	3	0.80	3.8127	0.5	0.1

f_{ck} (psi)	f'_{ci} (psi)	E_{to} (10^6 psi)	c (lb/ft^3)	w (lb/ft^3)	w/c	a/c
9000	6100	4.11	34.57	10.59	0.31	2.96

A1.6 CEB-MC90 Model

Nomenclature

β_c = coefficient describing development of creep with time (after loading)
$\beta_{cc}(t)$ = coefficient depending on age of concrete
$\beta_E(t)$ = coefficient depending on the age of concrete, t
$\varepsilon_{c\sigma}(t)$ = stress dependent strain (Mpa)
$\varepsilon_{cn}(t)$ = stress independent strain (Mpa)
$\varepsilon_{cc}(t)$ = creep strain at time $t > t_o$ (Mpa)
$\varepsilon_{ci}(t_o)$ = initial strain at loading (Mpa)
$\varepsilon_{cs}(t)$ = shrinkage strain (Mpa)
$\varepsilon_{cT}(t)$ = thermal strain (Mpa)
$\phi(t,t_o)$ = creep coefficient
ϕ_o = notional creep coefficient
E_{ci} = modulus of elasticity of concrete at 28 days (Mpa)
$E_c(t_o)$ = modulus of elasticity at time of loading, t_o
f_{ck} = specific characteristic compressive strength (Mpa)
f_{cm} = mean compressive strength at 28 days (Mpa)
$f_{cm}(t)$ = mean concrete compressive strength at an age of t days (Mpa)
$J(t,t_o)$ = creep function, or creep compliance, strain per unit stress
s = coefficient depending on cement type
t = age of concrete (days)
t_1 = 1 day

Compressive Strength

$$f_{cm} = f_{ck} + \Delta f \tag{A.73}$$

where,

$\Delta f = 8$ Mpa

$$f_{cm}(t) = \beta_{cc}(t) f_{cm} \tag{A.74}$$

$$\beta_{cc}(t) = \exp\left\{ s\left[1 - \left(\frac{28}{t/t_1} \right)^{\frac{1}{2}} \right] \right\} \tag{A.75}$$

Table A.5 CEB-MC90 Model "s" Values based on Cement Type

Cement Type	s
Rapid Hardening High Strength (RS)	0.20
Normal and Rapid Hardening (N and R)	0.25
Slowly Hardening (SL)	0.38

Modulus of Elasticity

$$E_{ci} = E_{co}\left[\left(f_{ck} + \Delta f\right)/f_{cmo}\right]^{\frac{1}{3}} \tag{A.76}$$

where,

f_{cmo} = 10 MPa

$$E_{ci}(t) = \beta_E(t) E_{ci} \tag{A.77}$$

$$\beta_E(t) = \left[\beta_{cc}(t)\right]^{0.5} \tag{A.78}$$

Total Concrete Strain

$$\varepsilon_c(t) = \varepsilon_{ci}(t_o) + \varepsilon_{cc}(t) + \varepsilon_{cs}(t) + \varepsilon_{cT}(t) \tag{A.79}$$

$$\varepsilon_c(t) = \varepsilon_{c\sigma}(t) + \varepsilon_{cn}(t) \tag{A.80}$$

$$\varepsilon_{cc}(t,t_o) = \frac{\sigma_c(t_o)}{E_{ci}}\phi(t,t_o) \tag{A.81}$$

$$\varepsilon_{c\sigma}(t,t_o) = \sigma_c(t_o)\left[\frac{1}{E_c(t_o)} + \frac{\phi(t,t_o)}{E_{ci}}\right] = \sigma_c(t_o) J(t,t_o) \tag{A.82}$$

Creep Coefficient

$$\phi(t,t_o) = \phi_o \beta_c(t - t_o) \tag{A.83}$$

$$\phi_o = \phi_{RH}\beta\left(f_{cm}\right)\beta\left(t_o\right) \tag{A.84}$$

$$\phi_{RH} = 1 + \frac{(1 - RH)/RH}{0.46\left(h/h_o\right)^{\frac{1}{3}}} \tag{A.85}$$

$$\beta\left(f_{cm}\right) = \frac{5.3}{\left(f_{cm}/f_{cmo}\right)^{0.5}} \tag{A.86}$$

$$\beta(t_o) = \frac{1}{0.1 + (t_o / t_1)^{0.2}} \tag{A.87}$$

$$\beta_c(t - t_o) = \left[\frac{(t - t_o)/t_1}{\beta_H + (t - t_o)/t_1} \right]^{0.3} \tag{A.88}$$

$$\beta_H = 150\left\{1 + \left(1.2\frac{RH}{RH_o}\right)^{18}\right\}\frac{h}{h_o} + 250 \le 1500 \tag{A.89}$$

$$t_o = t_{0,T}\left[\frac{9}{2 + (t_{0,T}/t_{1,T})^{1.2}} + 1\right]^{\alpha} \ge 0.5 \text{ days} \tag{A.90}$$

Shrinkage Strain

$$\varepsilon_{cs}(t, t_s) = \varepsilon_{cso}\beta_s(t - t_s) \tag{A.91}$$

$$\varepsilon_{cso} = \varepsilon_s(f_{cm})\beta_{RH} \tag{A.92}$$

$$\varepsilon_s(f_{cm}) = [160 + 10\beta_{sc}(9 - f_{cm}/f_{cmo})] \times 10^{-6} \tag{A.93}$$

$$\beta_{RH} = -1.55\beta_{sRH} \quad \text{for } 40\% \le \text{RH} < 99\% \tag{A.94}$$

$$\beta_{RH} = +0.25 \quad \text{for RH} \ge 99\% \tag{A.95}$$

$$\beta_{RH} = 1 - \left(\frac{RH}{RH_o}\right)^3 \tag{A.96}$$

$$\beta_s(t - t_s) = \left[\frac{(t - t_s)/t_1}{350(h/h_o)^2 + (t - t_s)/t_1}\right]^{0.5} \tag{A.97}$$

$$t_T = \sum_{i=1}^{n} \Delta t_i \exp\left[13.65 - \frac{4000}{273 + T(\Delta t_i)/T_o}\right] \tag{A.98}$$

Table A.6 CEB-MC90 Model Input Values

Cement Type	σ (N/mm^2)	f'ck (N/mm^2)	t_s (days)	t_o (days)	α	H (%)	V/S (mm)
3	19.33	62.05	0.75	1	1	80	96.84

A1.7 Gardner-Lockman (GL-2000) Model

Nomenclature

$\beta(h)$ = correction term for effect of humidity on shrinkage
$\beta(t)$ = correction term for effect of time on shrinkage
ε_{sh} = shrinkage strain (x 10^{-6} in./in.)
ε_{shu} = notional ultimate shrinkage strain (x 10^{-6})
E_{cmt} = mean modulus of elasticity at age t days (psi)
E_{cmto} = mean modulus of elasticity at Loading (psi)
E_{cm28} = mean modulus of elasticity at 28 days (psi)
f_{ck28} = 28-day characteristic, or specified, concrete strength (psi)
f_{cm28} = 28-day mean concrete strength (psi)
f_{cmt} = mean concrete strength at age t days (psi)
f_{cmto} = mean concrete strength at loading (psi)
f_{cm28} = mean concrete strength at 28 days (psi)
h = humidity in decimal form
K = correction term for effect of cement type on shrinkage
t_c = age drying commenced (days)
t = age of concrete (days)
t_o = age load applied (days)
V/S = volume to surface ratio (in.)

Mean Compressive Strength

(Used only when experimental mean compressive strength is not available.)

$$f_{cm28} = 1.1(f_{ck28}) + 700 \quad \text{(psi)} \tag{A.99}$$

Mean Compressive Strength as a Function of Time

(Used only when experimental mean compressive strength at loading is not available.)

$$f_{cmt} = f_{cm28}\frac{t^{3/4}}{a + b(t)^{3/4}} \tag{A.100}$$

where,

a = 2.8 and b = 0.77 (Type I Cement Concrete)

a = 3.4 and b = 0.72 (Type II Cement Concrete)

a = 1.0 and b = 0.92 (Type III Cement Concrete)

Mean Modulus of Elasticity as a Function of Time

$$E_{cmt} = 500{,}000 + 52{,}000\sqrt{f_{cmt}} \quad \text{(psi)} \tag{A.101}$$

Shrinkage

$$\varepsilon_{sh} = \varepsilon_{shu}\beta(h)\beta(t) \tag{A.102}$$

$$\beta(h) = (1 - 1.18h^4) \tag{A.103}$$

$$\varepsilon_{shu} = 1000K\left(\frac{4350}{f_{cm28}}\right)^{1/2} \times 10^{-6} \tag{A.104}$$

$$\beta(t) = \sqrt{\frac{t - t_c}{t - t_c + 97\left(\frac{V}{S}\right)^2}} \tag{A.105}$$

where,

K = 1.0 (Type I Cement)

K = 0.70 (Type II Cement)

K = 1.15 (Type III Cement)

Creep

$$\phi_{28} = \Phi(t_c)\left[2\left(\frac{(t - t_c)^{0.3}}{(t - t_c)^{0.3} + 14}\right) + \left(\frac{7}{t_0}\right)^{0.5}\left(\frac{t - t_c}{t - t_c + 7}\right)^{0.5} + 2.5(1 - 1.086h^2)\left(\frac{t - t_0}{t - t_0 + 97(V/S)^2}\right)^{0.5}\right] \tag{A.106}$$

Table A.7 Gardner-Lockman (GL2000) Model Input Values

Cement Type	f'_{ck} (psi)	t_c (days)	t_o (days)	f_{ck28} (psi)	h	V/S (in.)
3	9000	0.75	1	9000	0.80	3.8127

A1.8 Shams and Kahn Model

Nomenclature

d = constant for member shape and size (days)
f = constant (23 days)
$E_c(t)$ = concrete modulus of elasticity at time t (ksi)
$f_c'(t)$ = concrete compressive strength at time t (ksi)
f_{c28}' = 28-day compressive strength (ksi)
H = relative humidity (%)
k_{f_c} = concrete strength factor
k_H = relative humidity factor (AASHTO-LRFD)
$k_{H'}$ = relative humidity factor (AASHTO-LRFD)
k_m = factor for moist curing period
$k_{t'}$ = factor for maturity at loading
k_{t_o} = factor for maturity at the beginning of drying
k_{vs} = volume to surface ratio factor (AASHTO-LRFD)
k_{vs}' = volume to surface ratio factor (AASHTO-LRFD)
k_σ = stress/strength ratio factor (CEB-MC90)
m = moist curing period (days)
t and t' = maturity of concrete (days) at the time considered and at initial loading per CEB-MC90 equation
$T(\Delta t_i)$ = temperature (^oC) during the period Δt_i (days)
T_o = 1 ^oC
v/s = volume to surface ratio (in.)
$\varepsilon_{sh}(t,t_o)$ = shrinkage strain (in./in.)
$\varepsilon_{sh\infty}$ = ultimate shrinkage strain (in./in.)
Γ = stress/strength ratio at loading
ϕ_∞ = creep coefficient at infinity
$\phi(t,t')$ = creep coefficient at time t

Compressive Strength

$$f_c'(t) = \frac{t^{0.28}}{1.11 + 0.56t^{0.28}} f_{c28}' \quad \text{(for Moist-Cured, Type III Cement)} \qquad \text{(A.107)}$$

Modulus of Elasticity

$$E_c(t) = 41000\sqrt{f_c^{'}(t)} + 410000 \quad \text{(psi)} \tag{A.108}$$

Creep Model

$$\phi(t,t^{'}) = \phi_{\infty} k_{vs} k_{f_c} k_H k_{t^{'}} k_{\sigma} k_m \frac{(t-t^{'})^{0.6}}{d + (t-t^{'})^{0.6}} \tag{A.109}$$

$$\phi_{\infty} = 2.73 \tag{A.110}$$

$$k_{vs} = \left[\frac{\frac{t}{26e^{0.36(V/S)} + t}}{\frac{t}{45+t}}\right]\left[\frac{1.80 + 1.77e^{-0.54(v/s)}}{2.587}\right] \tag{A.111}$$

$$k_{f_c} = \frac{4.8}{1.645 + f_c^{'}} \tag{A.112}$$

$$k_H = 1.58 - \frac{H}{120} \tag{A.113}$$

$$k_{t^{'}} = 0.65 \cdot e^{\frac{0.7}{t^{'}+0.57}} \tag{A.114}$$

$$k_{\sigma} = e^{1.5(\Gamma - 0.4)} \quad \text{for } 0.4 < \Gamma \le 0.6$$
$$k_{\sigma} = 1.0 \quad \text{for } 0.4 \ge \Gamma \tag{A.115}$$

$$k_m = 1 + 0.65\left(1 - e^{-0.59m}\right)^{5.73} \tag{A.116}$$

$$d = \frac{t^{'}}{0.356 + 0.09t^{'}} \tag{A.117}$$

$$\text{t or t`} = \sum_{i=1}^{n} \Delta t_i \exp\left[13.65 - \frac{4000}{273 + T(\Delta t_i)/T_o}\right] \tag{A.118}$$

Shrinkage Model

$$\varepsilon_{sh}(t,t_o) = \varepsilon_{sh\infty} k_{vs}^{'} k_H^{'} k_{t_o} \left[\frac{t - t_o}{f + (t - t_o)} \right]^{0.5} \tag{A.119}$$

$$\varepsilon_{sh\infty} = 405 \times 10^{-6} \text{ in/in} \quad \text{for member-cured concrete}$$
$$\varepsilon_{sh\infty} = 380 \times 10^{-6} \text{ in/in} \quad \text{for moist-cured concrete} \tag{A.120}$$

$$k_{vs}^{'} = \left[\frac{t}{\frac{26e^{0.36(V/S)} + t}{\frac{t}{45 + t}}} \right] \left[\frac{1064 - 94(v/s)}{923} \right] \tag{A.121}$$

$$k_{H'} = \frac{140 - H}{70} \quad \text{for H} < 80\%$$
$$k_{H'} = \frac{3(100 - H)}{70} \quad \text{for H} \geq 80\% \tag{A.122}$$

$$k_{t_o} = 0.67 e^{\frac{4.2}{9.45 + t_o}} \tag{A.123}$$

$$f = 23 \text{ days} \tag{A.124}$$

Table A.8 Shams and Kahn Model Input Values

Curing	m (days)	f'ck (ksi)	t' (days)	to (days)	H (%)	ϕ_∞	G	V/S (in.)
Moist	0.75	9.0	1	0.75	80	2.73	0.4	3.8127

A1.9 NCHRP 496 Model

Nomenclature

A_n = net cross-sectional area of precast member (in.^{2})
A_{ps} = area of prestressing steel (in.^{2})
A_{ti}=transformed area of cross-section at transfer (in.^{2})
E'_{c1} = age-adjusted effective modulus of elasticity of concrete at time 1 due to sustained stress (ksi)
E''_{c1} = age-adjusted effective concrete modulus of elasticity at time 1
E_c = concrete modulus of elasticity (ksi)
E_{ci} = concrete modulus of elasticity at transfer (ksi)
E_p = modulus of elasticity of prestressing steel (ksi)
e_{pn} = eccentricity of steel with respect to net precast section, always positive (in.)
e_{pti}=eccentricity of strands with respect to the transformed section centroid, always positive (in.)
f'_c = specified 28-day concrete compressive strength (ksi)
f'_{ci} = compressive strength of concrete at transfer (ksi)
f_{cgp} = concrete stress at center of prestressing steel due to initial prestressing force and beam weight at section of maximum moment (ksi)
f_{po} = initial stress in prestressing steel (ksi)
f_{py} = yield strength of prestressing steel (ksi)
H = average annual ambient relative humidity (%)
I_n = moment of inertia of net precast cross-section at transfer (in.^{4})
I_{ti}=transformed moment of inertia at transfer (in.^{4})
K_1 = correction factor for aggregate type in predicting average value
K_2 = correction factor for aggregate type in predicting upper and lower bounds
K_{id}=transformed section age-adjusted effectve modulus of elasticity factor, for adjustment between time of transfer and deck placement
k_f = concrete strength creep correction factor
k_{hc} = humidity correction factor for creep
k_{hs} = humidity correction factor for shrinkage
k_{la} = loading age correction factor
k_s = volume to surface ratio shrinkage correction factor
k_{td} = time-development correction factor
L_i = intrinsic relaxation loss between transfer and deck placement (ksi)
M_g = maximum moment due to self-weight (kip-in.)
n = modular ratio
P_i = initial prestressing force (kips)
t = age of concrete (days)
t_d = age of concrete at deck placement (days)

t_i = age of concrete at transfer (days)
V/S = volume to surface ratio of the member (in.)

α_n= net precast section properties factor
$\triangle f_{pCR}$ = loss of steel stress due to creep of beam concrete (ksi)
$\triangle f_{pES}$ = loss of steel stress due to elastic shortening (ksi)
$\triangle f_{pR}$ = loss of steel stress due to relaxation (ksi)
$\triangle f_{pR2}$ = loss of steel stress due to relaxation between transfer and deck placement (ksi)
$\triangle f_{pSR}$ = loss of steel stress due to shrinkage of beam concrete (ksi)
$\triangle f_{pT}$ = total loss of steel stress (ksi)
ΔP_P = change in prestressing force (kips)
ε_{bid}=shrinkage of beam concrete between transfer and deck placement (in./in.)
ε_{sh} = shrinkage strain at a given time, t (in./in.)
γ_{cr} = combined creep correction factor
γ_{sh} = combined shrinkage correction factor
ϕ_i = reduction factor that reflects the steady decrease in strand prestressing due to creep and shrinkage of concrete
ρ_n=tensile reinforcement ratio for initial net section
χ=aging coefficient accounting for concrete stress variability with time and may be considered constant for all concrete members at age 1 to 3 days = 0.7
$\psi(t,t_i)$ = creep coefficient minus the ratio of the strain that exists t days after casting to the elastic strain caused when load is applied t_i days after casting
ψ_{bid} = beam creep coefficient minus the ratio of the strain that exists at the time of deck placement to the elastic strain caused when the load is applied at the time of transfer
ψ_{bif} = beam creep coefficient minus the ratio of the strain that exists at final time to the elastic strain caused when load is applied at the time of deck loading

Concrete Modulus of Elasticity Model

$$E_c = 33{,}0000K_1K_2\left(0.140+\frac{f_c^{'}}{1000}\right)^{1.5}\sqrt{f_c^{'}} \tag{A.125}$$

Prestress Loss Model

$$\triangle f_{pT} = \triangle f_{pES}+(\triangle f_{pSR}+\triangle f_{pCR}+\triangle f_{pR})_{id} \tag{A.126}$$

$$\triangle f_{pES}=n_i f_{cgp}=(E_p/E_{ci})f_{cgp} \tag{A.127}$$

$$f_{cgp}=P_i(1/A_{ti} + e^2_{pti}/I_{ti}) - M_g e_{pti}/I_{ti} \tag{A.128}$$

Prestress Loss Due to Shrinkage

$$\triangle\varepsilon_p = \triangle\varepsilon_c \tag{A.129}$$

$$\frac{\Delta P_P}{A_{ps}E_p} = \varepsilon_{bid} - \left(\frac{\Delta P_p}{E''_{c1}A_n} + \frac{\Delta P_p}{E''_{c1}} \frac{e_{pn}^2}{I_n} \right) \tag{A.130}$$

$$\frac{\Delta P_p}{A_{ps}} \left[1 + \frac{E_p}{E''_{cl}} \frac{A_{ps}}{A_n} \left(1 + \frac{A_n e_{pn}^2}{I_n} \right) \right] = \varepsilon_{bid} E_p \tag{A.131}$$

$$E''_{c1} = \frac{E_{ci}}{1 + \chi\psi_{bif}} \tag{A.132}$$

$$\alpha_n = \left(1 + \frac{A_n e_{pn}^2}{I_n} \right) \tag{A.133}$$

$$\rho_n = \frac{A_{ps}}{A_n} \tag{A.134}$$

$$K_{id} = \frac{1}{1 + n_i \rho_n \alpha_n \left(1 + \chi\psi_{bif} \right)} \tag{A.135}$$

$$\Delta f_{pSR} = \frac{\Delta P_p}{A_{ps}} \tag{A.136}$$

$$\Delta f_{pSR} = \varepsilon_{bid} E_p K_{id} \tag{A.137}$$

Prestress Loss Due to Creep

$$\Delta\varepsilon_p = \Delta\varepsilon_{pc} \tag{A.138}$$

$$\frac{\Delta P_p}{A_{ps}E_p} = \frac{f_{cgp}}{E'_{cl}} - \left(\frac{\Delta P_p}{E'_{cl}A_n} + \frac{\Delta P_p}{E''_{cl}} \frac{e_{pn}^2}{I_n} \right) \tag{A.139}$$

$$\frac{\Delta P_p}{A_{ps}E_p} = \frac{f_{cgp}}{E''_{cl}} \psi_{bid} - \left(\frac{\Delta P_p}{E'_{cl}A_n} + \frac{\Delta P_p}{E''_{cl}} \frac{e_{pn}^2}{I_n} \right) \left(1 + \chi\psi_{bif} \right) \tag{A.140}$$

$$E_{cl}^{'} = \frac{E_{ci}}{\psi_{bid}} \tag{A.141}$$

$$E_{c1}^{"} = \frac{E_{ci}}{1+\chi\psi_{bif}} \tag{A.142}$$

$$\frac{\Delta P_p}{A_{ps}}\left[1+\frac{E_p}{E_{ci}}\frac{A_{ps}}{A_n}\left(1+\frac{A_n e_{pn}^2}{I_n}\right)\left(1+\chi\psi_{bif}\right)\right] = \frac{E_p}{E_{ci}} f_{cgp}\psi_{bid} \tag{A.143}$$

$$K_{id} = \frac{1}{1+n_i\rho_n\alpha_n\left(1+\chi\psi_{bif}\right)} \tag{A.144}$$

$$\Delta f_{pCR} = \frac{\Delta P_p}{A_{ps}} \quad \Delta f_{pCR} = \frac{\Delta P_p}{A_{ps}} \tag{A.145}$$

$$\Delta f_{pCR} = n_i f_{cgp}\psi_{bid} K_{id} \tag{A.146}$$

Prestress Loss Due to Relaxation

$$\Delta f_{pR2} = \phi_i L_i K_{id} \tag{A.147}$$

$$\text{for,} \frac{f_{po}}{f_{py}} \geq 0.50\ ,\ L_i = \frac{f_{po}}{45}\left(\frac{f_{po}}{f_{py}} - 0.55\right)\log\left(\frac{24t_d+1}{24t_i+1}\right) \tag{A.148}$$

for, $\frac{f_{po}}{f_{py}} \leq 0.50$, No relaxation loss is assumed to take place.

$$\phi_i = 1 - \frac{3\left(\Delta f_{pSR} + \Delta f_{pCR}\right)}{f_{po}} \tag{A.149}$$

Shrinkage and Creep Strain Models

$$\varepsilon_{sh} = 480\cdot 10^{-6}\gamma_{sh} \tag{A.150}$$

$$\psi(t,t_i) = 1.90\gamma_{cr} \tag{A.151}$$

where,

$$\gamma_{sh} = k_{td} k_s k_{hs} k_f \tag{A.152}$$

$$\gamma_{cr} = k_{td} k_{la} k_s k_{hc} k_f \tag{A.153}$$

$$k_{td} = \frac{t}{61 - 4 f'_{ci} + t} \tag{A.154}$$

$$k_s = \frac{1064 - 94 V/S}{735} \tag{A.155}$$

$$k_{hs} = 2.00 - 0.0143 H \tag{A.156}$$

$$k_{hc} = 1.56 - 0.008 H \tag{A.157}$$

$$k_f = \frac{5}{1 + f'_{ci}} \tag{A.158}$$

$$k_{la} = t_i^{-0.118} \tag{A.159}$$

Table A.9 NCHRP 496 Model Input Values

f'_c (ksi)	f'_{ci} (ksi)	H (%)	K_1	K_2	V/S (in.)
9.0	6.1	80	1.0	1.115	3.8127

A.2 Modified Shams and Kahn / ACI-209 Compressive Strength Prediction Equation Results

A.2.1 Winter Beams

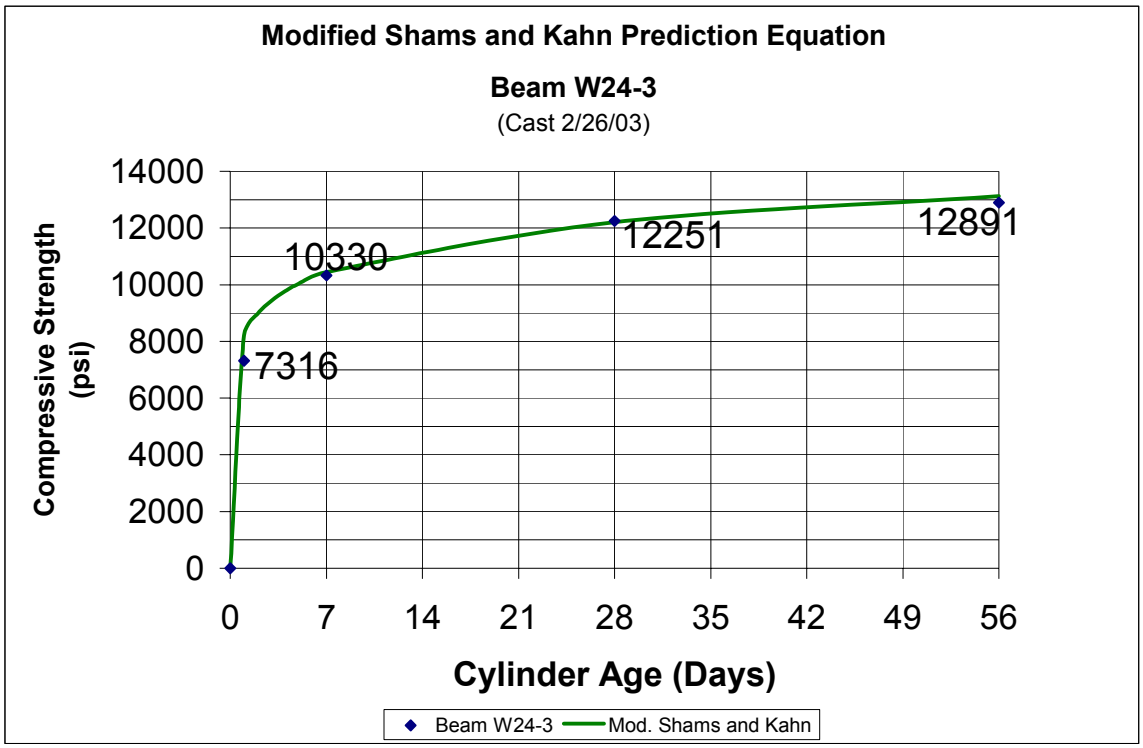

Figure A.1 Beam W24-3: Modified Shams and Kahn Prediction Equation

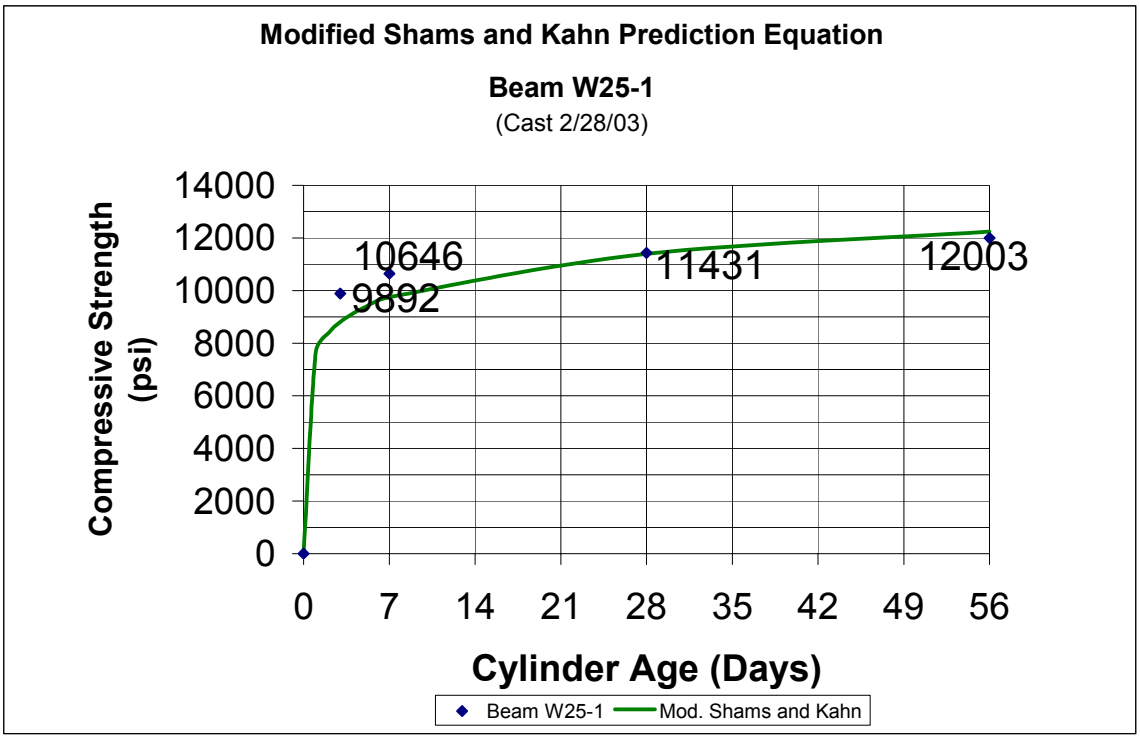

Figure A.2 Beam W25-1: Modified Shams and Kahn Prediction Equation

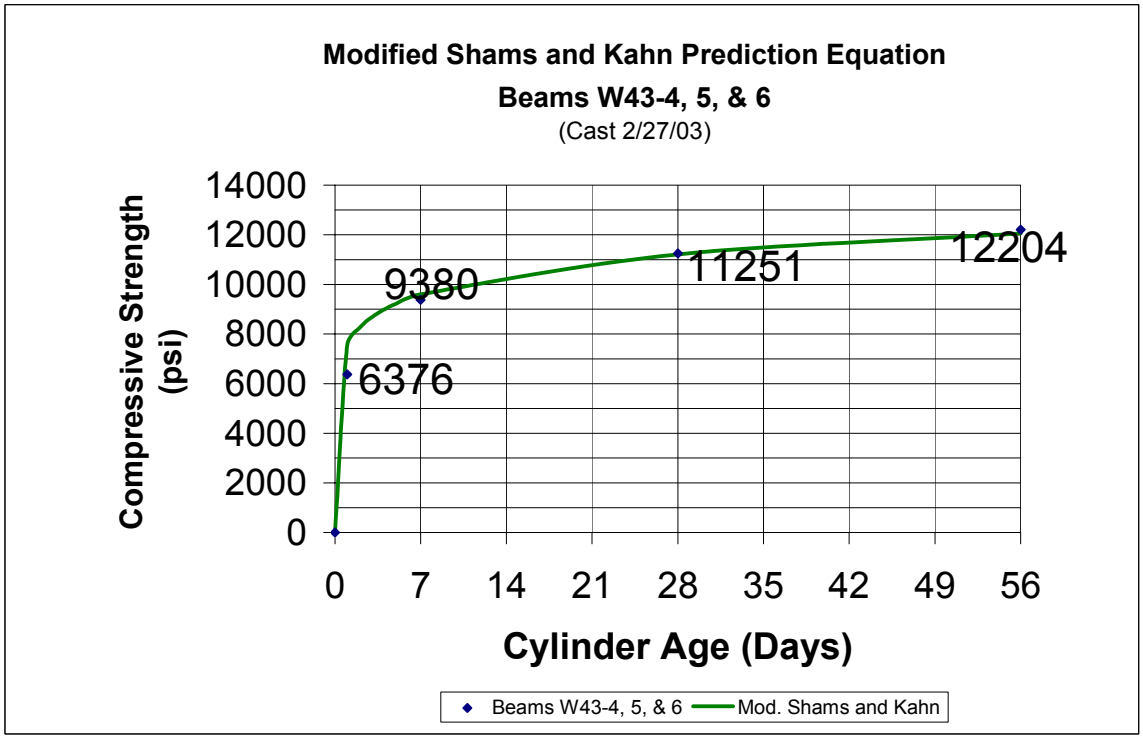

Figure A.3 Beams W43-4, 5, & 6: Modified Shams and Kahn Prediction Equation

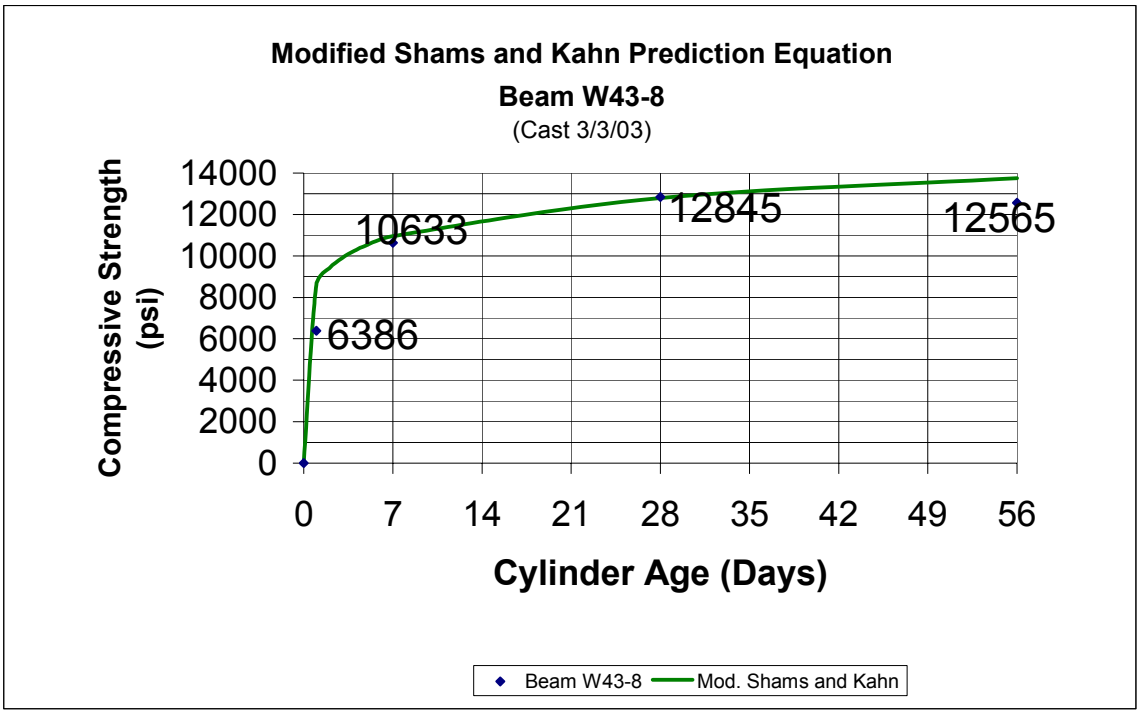

Figure A.4 Beam W43-8: Modified Shams and Kahn Prediction Equation

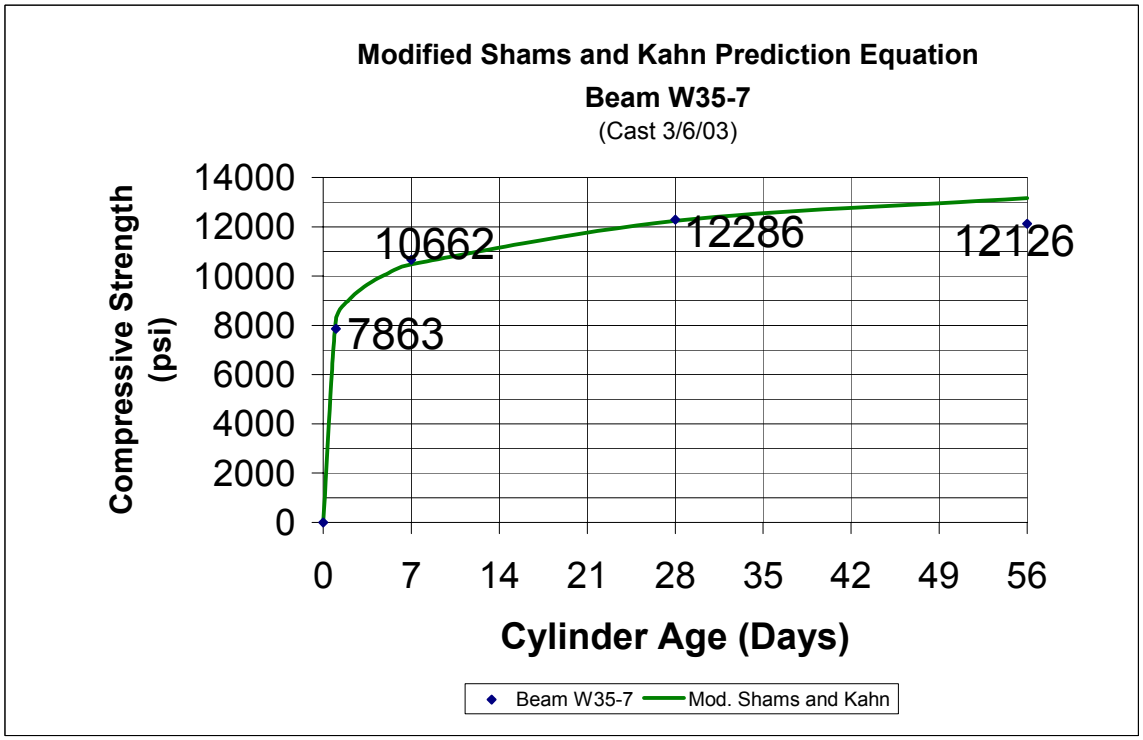

Figure A.5 Beam W35-7: Modified Shams and Kahn Prediction Equation

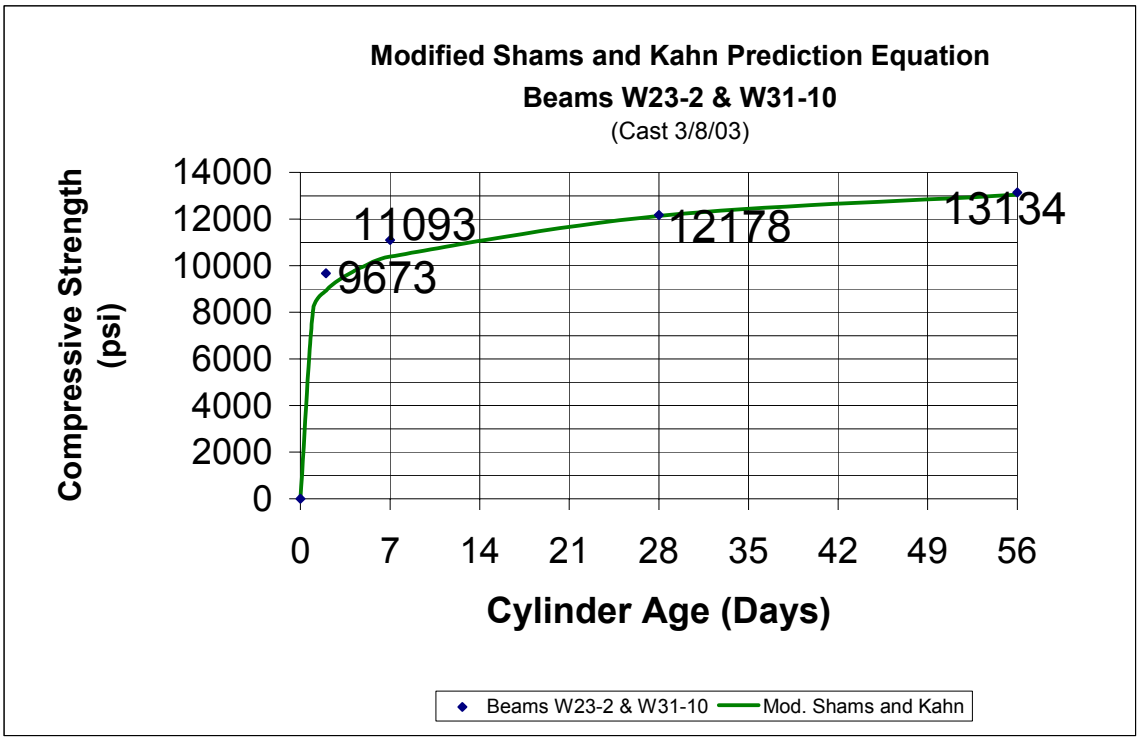

Figure A.6 Beams W23-2, & W31-10: Modified Shams and Kahn Prediction Equation

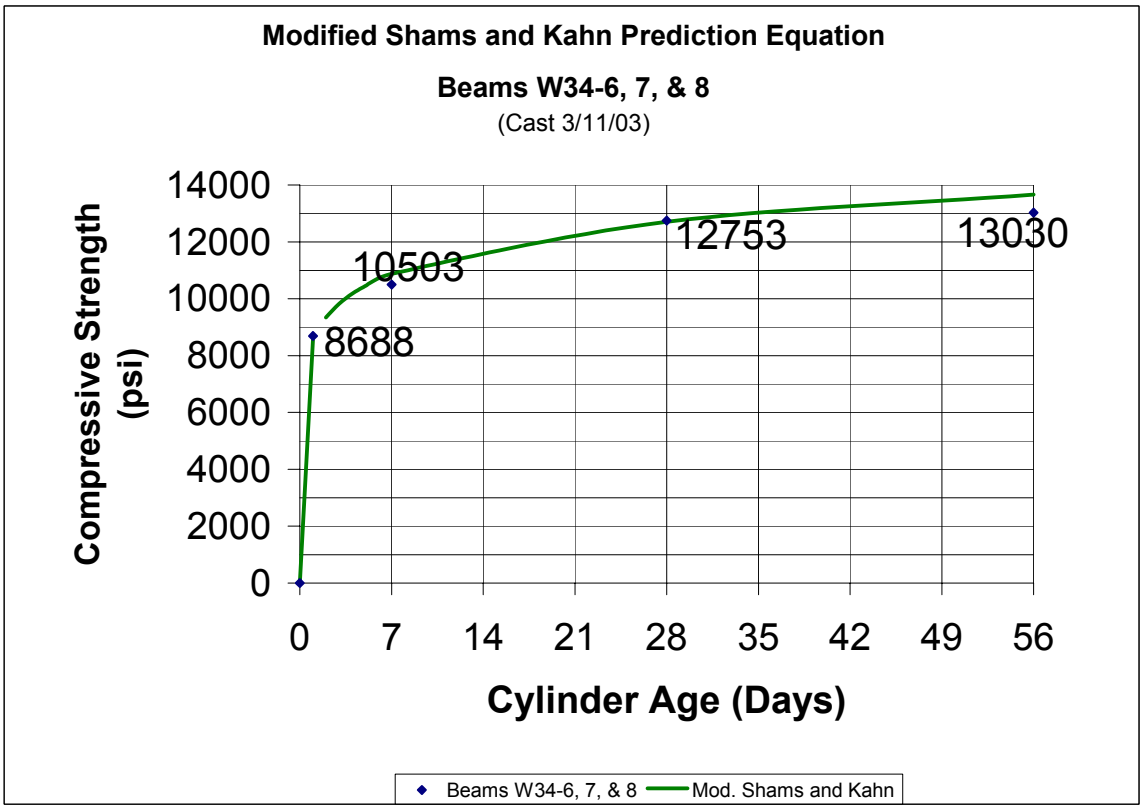

Figure A.7 Beams W34-6, 7, & 8: Modified Shams and Kahn Prediction Equation

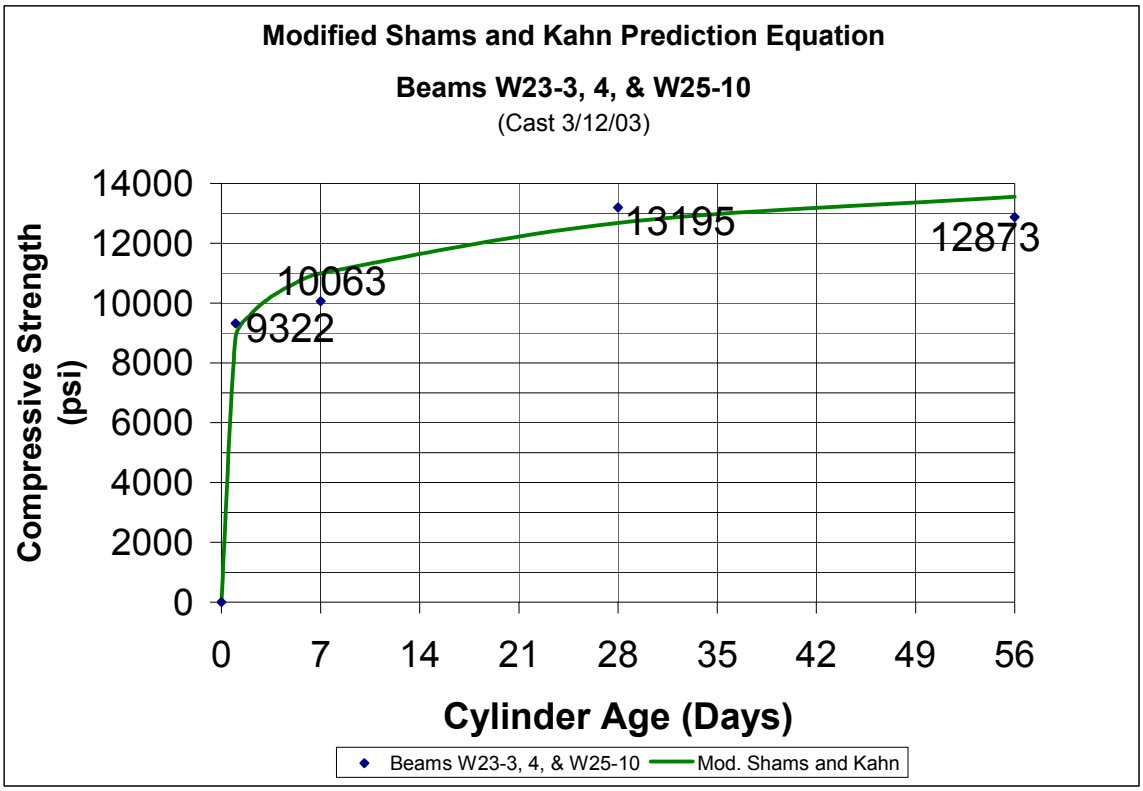

Figure A.8 Beams W23-3, 4, & W25-10: Modified Shams and Kahn Prediction Equation

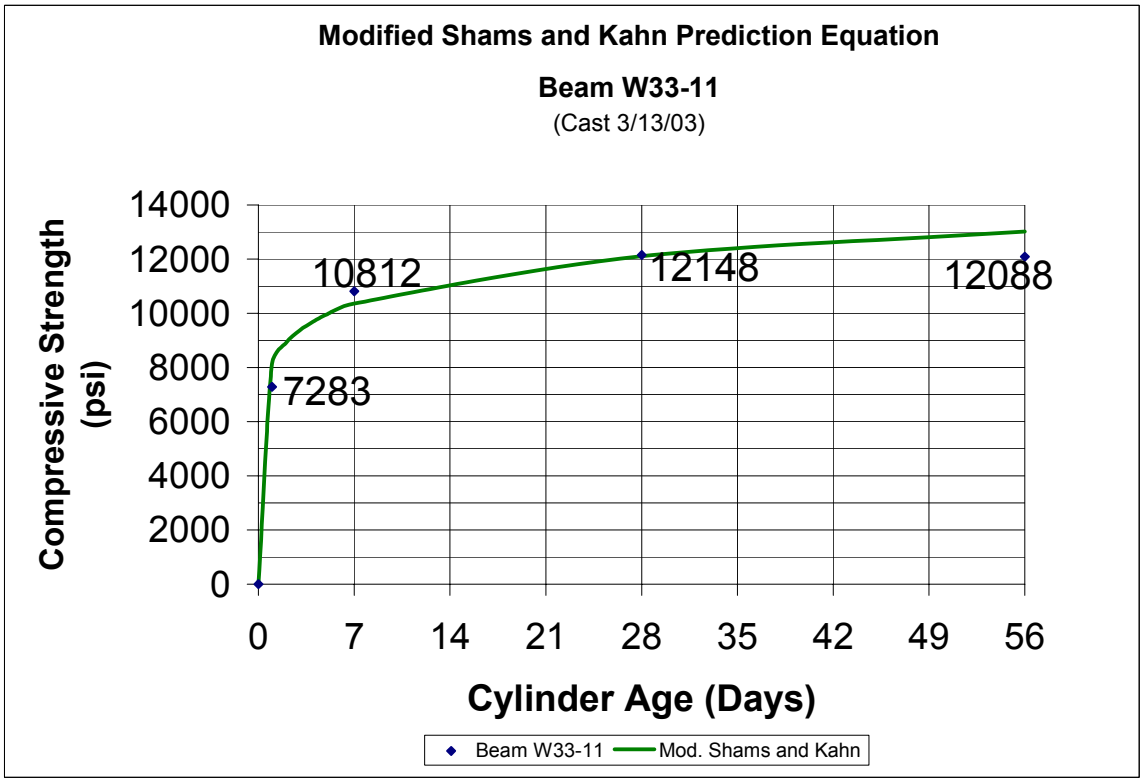

Figure A.9 Beam W33-11: Modified Shams and Kahn Prediction Equation

A.2.2 Summer Beams

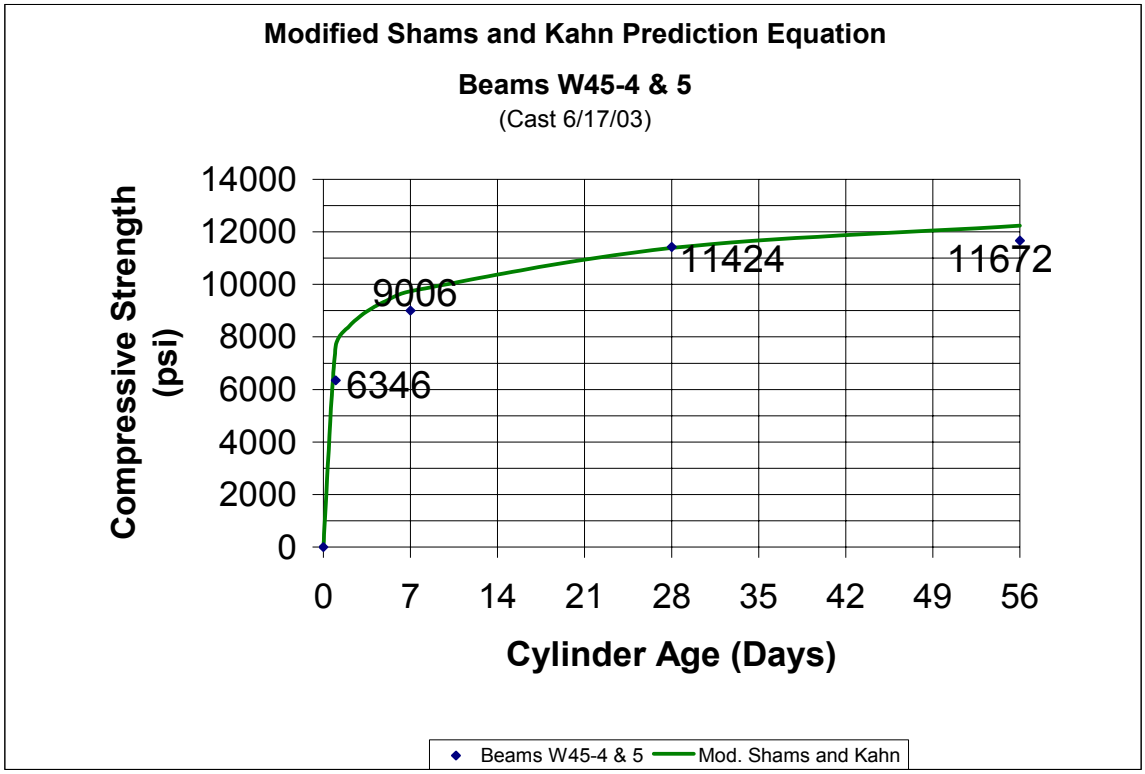

Figure A.10 Beams W45-4 & 5: Modified Shams and Kahn Prediction Equation

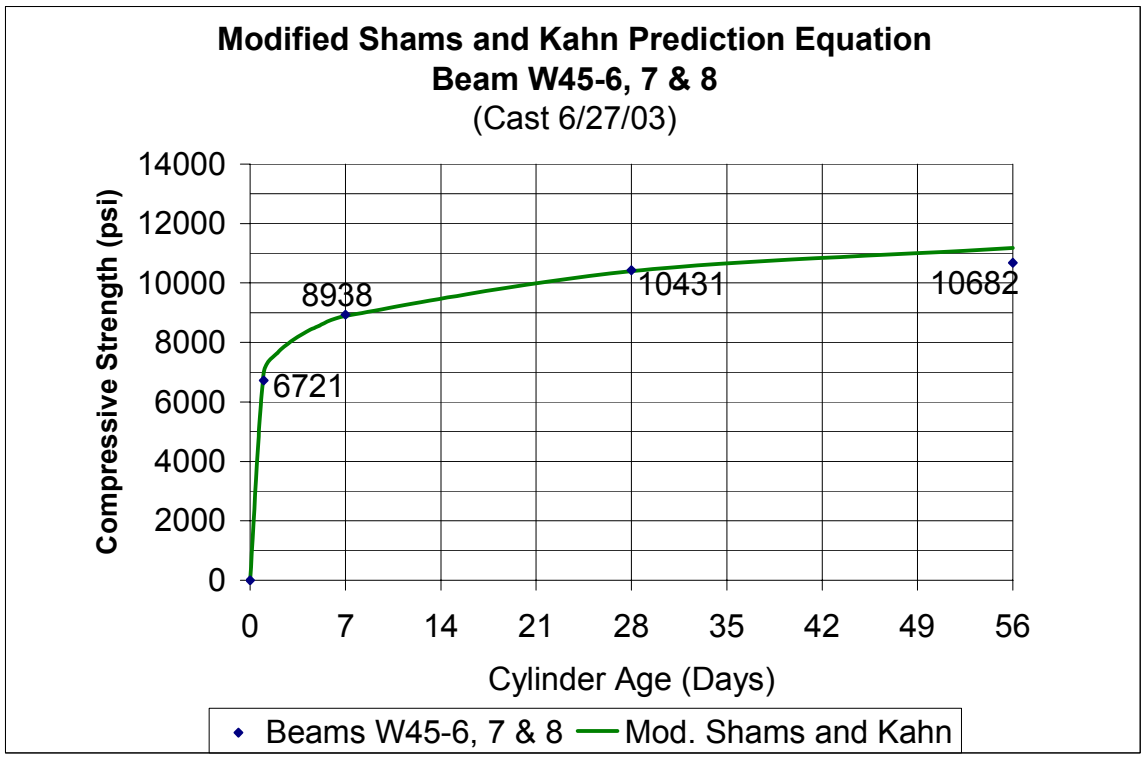

Figure A.11 Beams W45-6, 7, & 8: Modified Shams and Kahn Prediction Equation

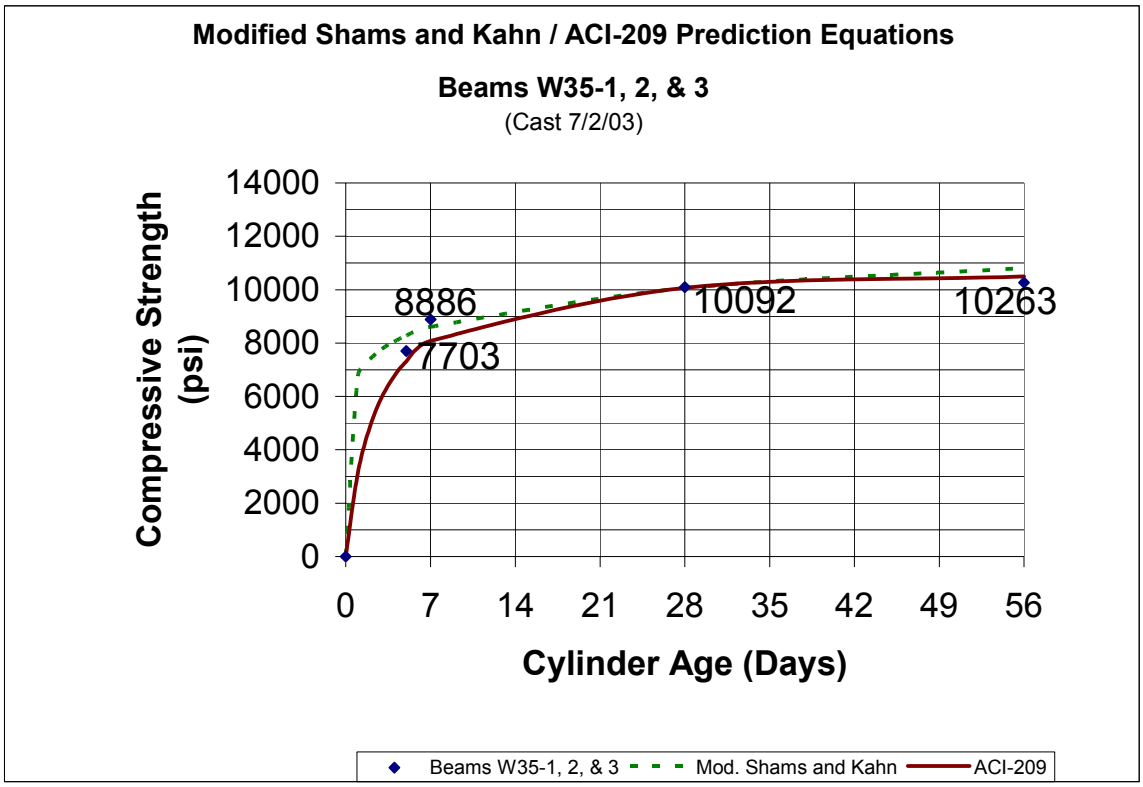

Figure A.12 Beams W35-1, 2, & 3: Modified Shams and Kahn Prediction Equation

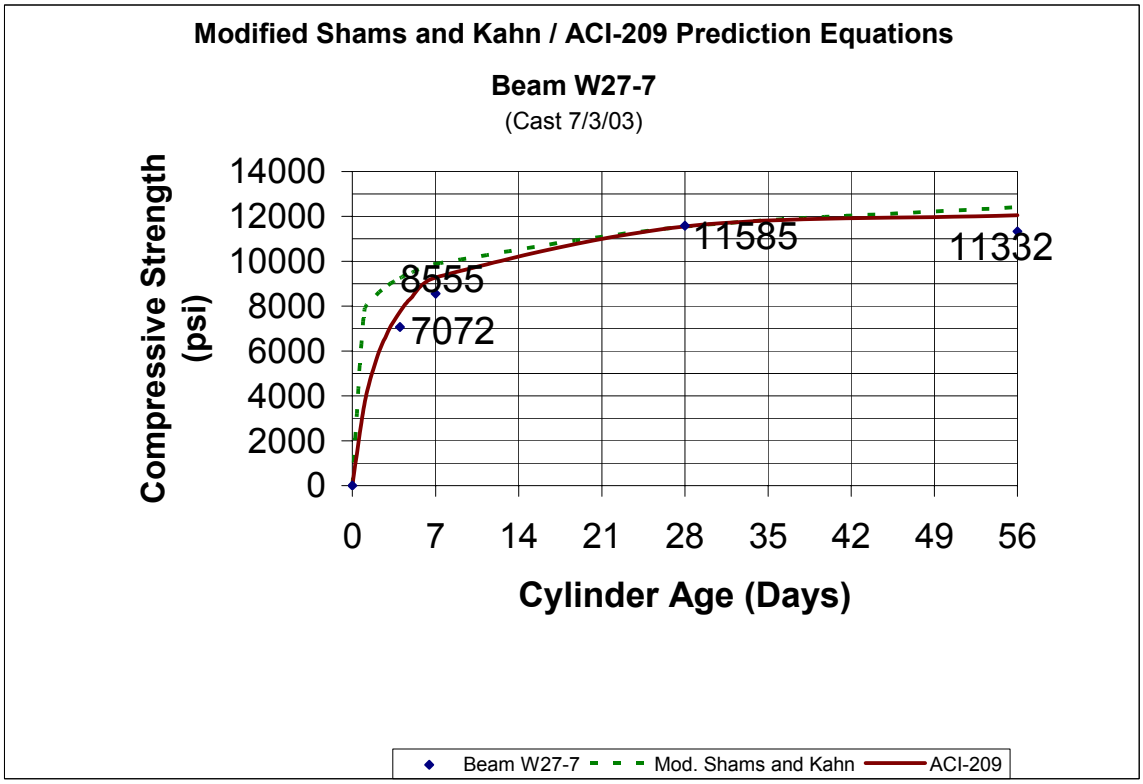

Figure A.13 Beam W27-7: Modified Shams and Kahn Prediction Equation

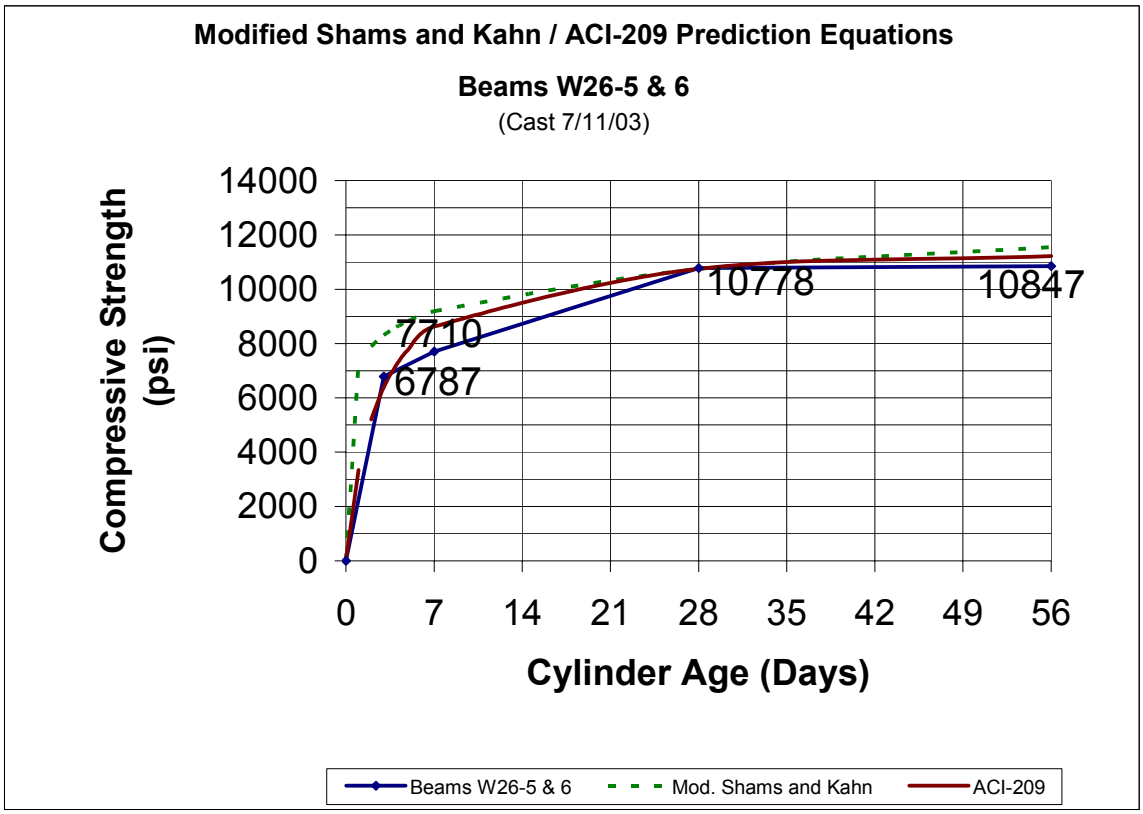

Figure A.14 Beams W26-5 & 6: Modified Shams and Kahn Prediction Equation

A.3 Predicted Deflections, Beam Sample 2

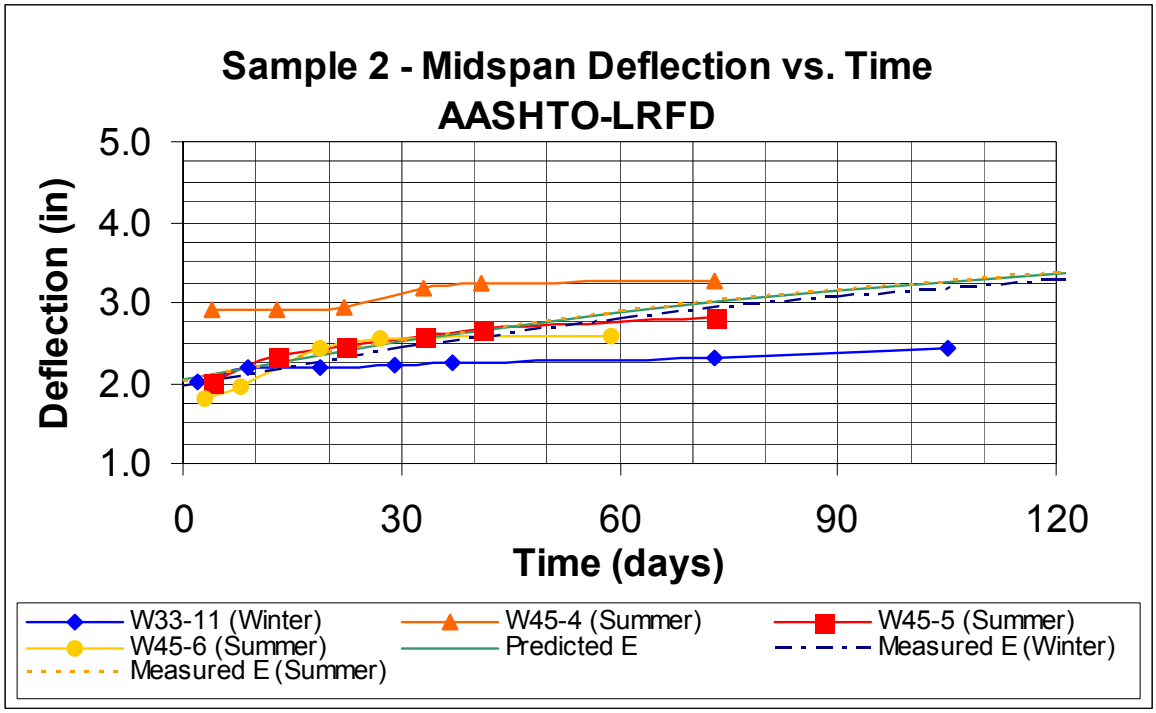

Figure A.15 Beam Sample 2 - AASHTO-LRFD Predicted Deflection vs. Time

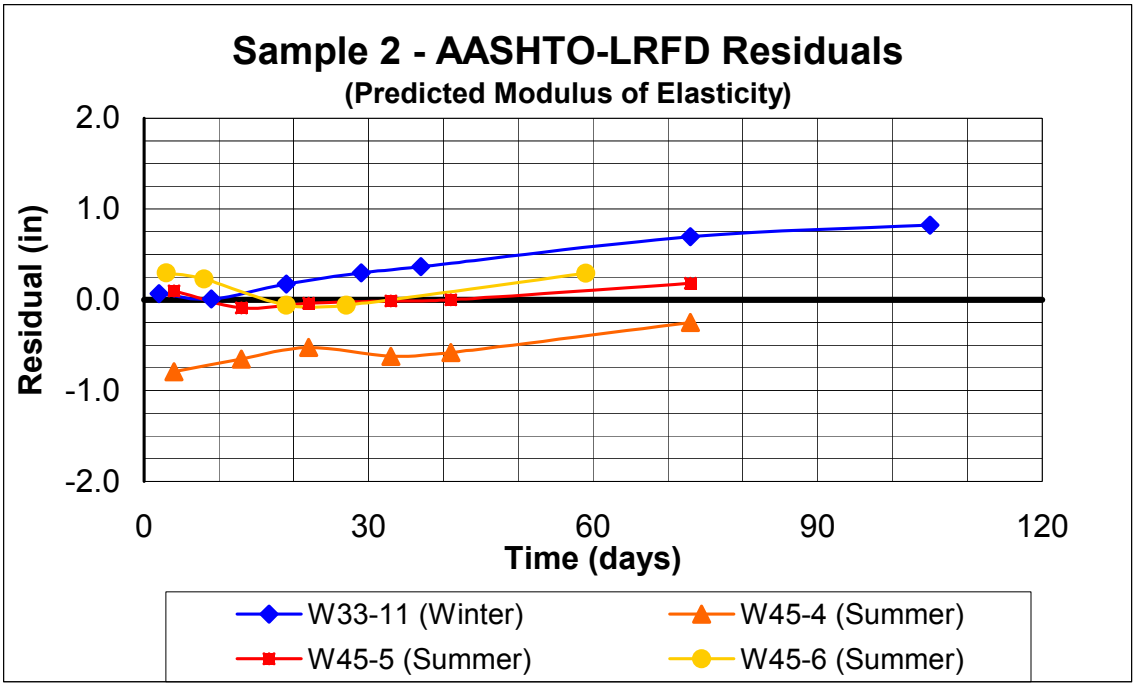

Figure A.16 Beam Sample 2 - AASHTO-LRFD Residuals vs. Time (Predicted Modulus of Elasticity)

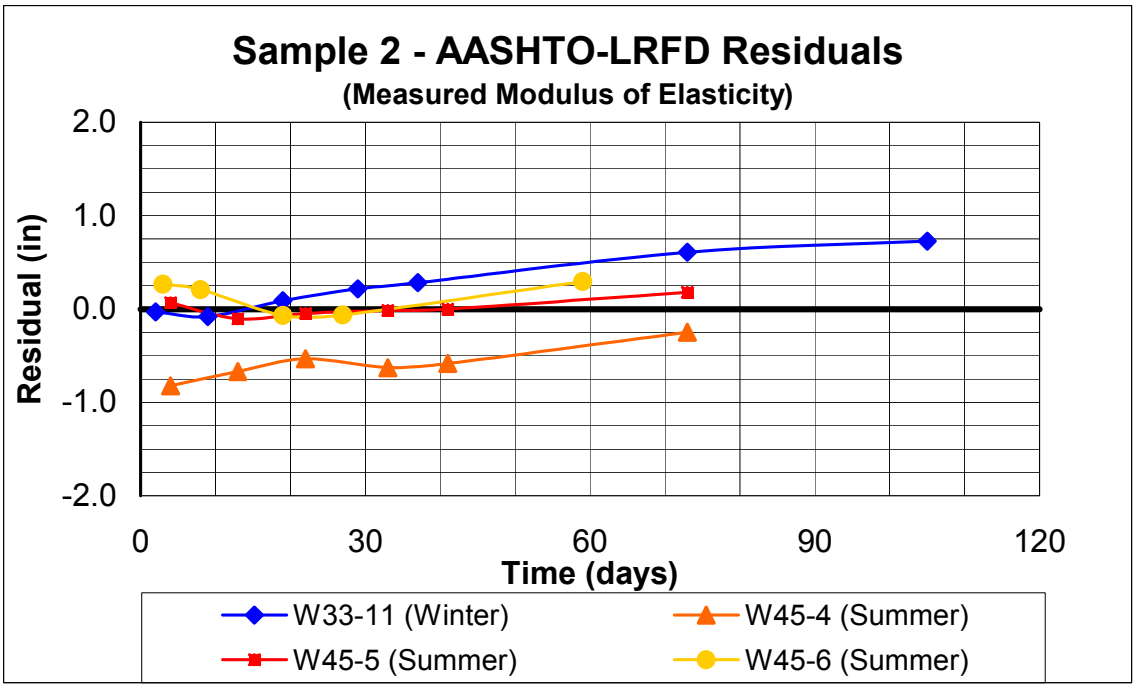

Figure A.17 Beam Sample 2 - AASHTO-LRFD Residuals vs. Time (Measured Modulus of Elasticity)

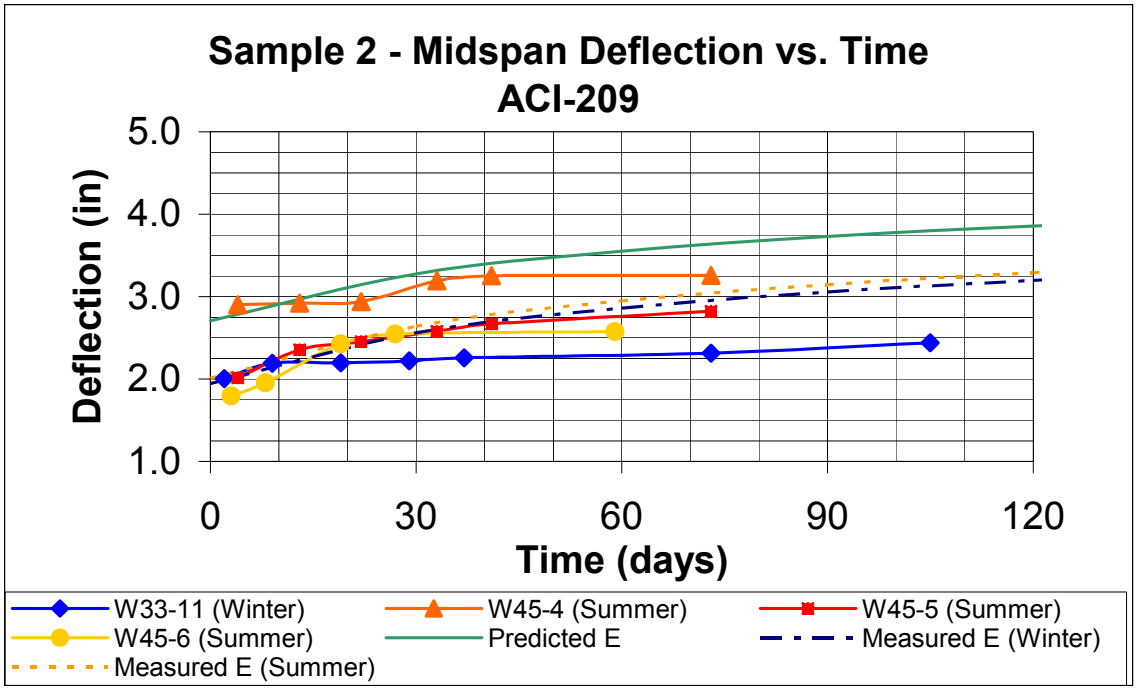

Figure A.18 Beam Sample 2 - ACI-209 Predicted Deflection vs. Time

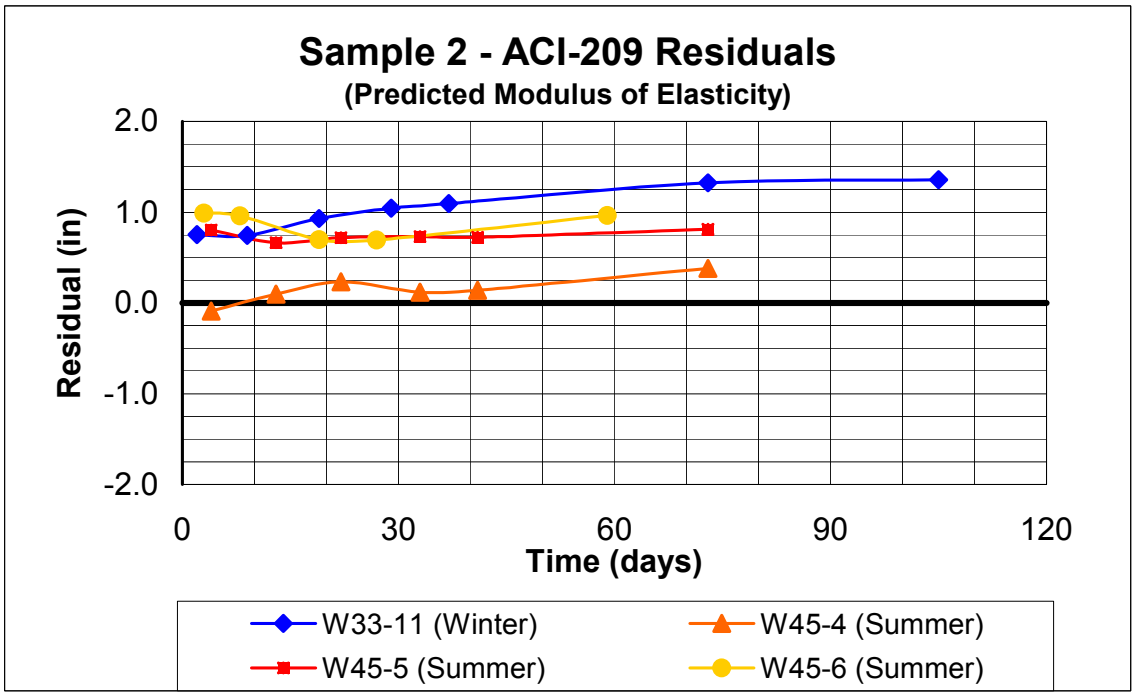

Figure A.19 Beam Sample 2 - ACI-209 Residuals vs. Time (Predicted Modulus of Elasticity)

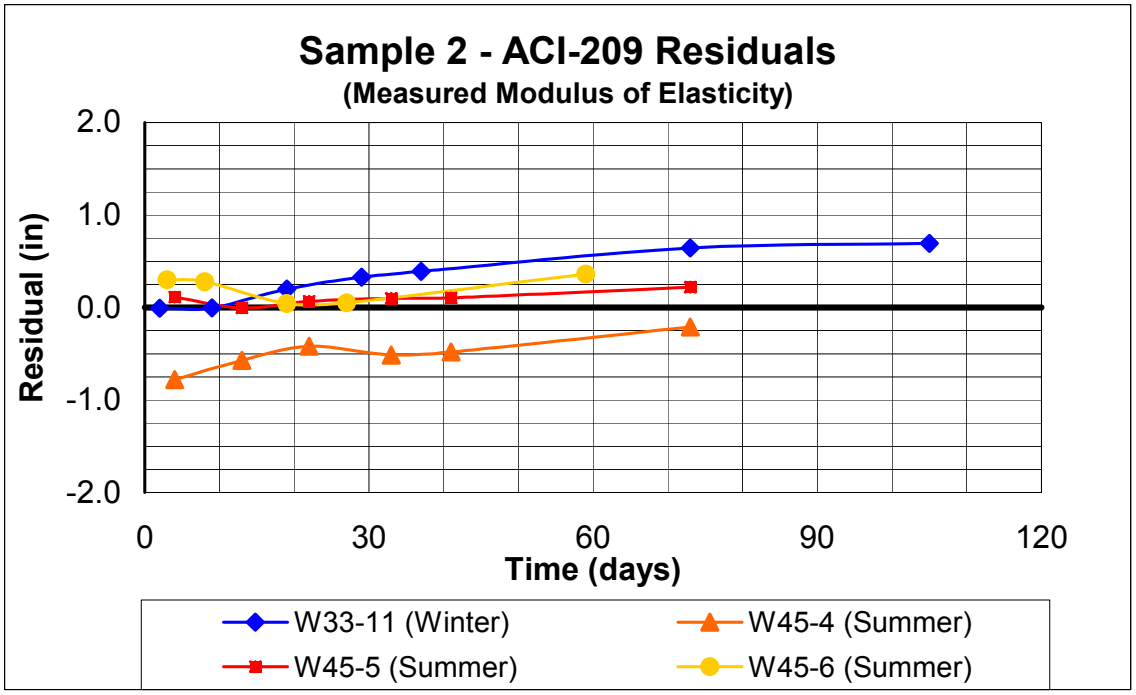

Figure A.20 Beam Sample 2 - ACI-209 Residuals vs. Time (Measured Modulus of Elasticity)

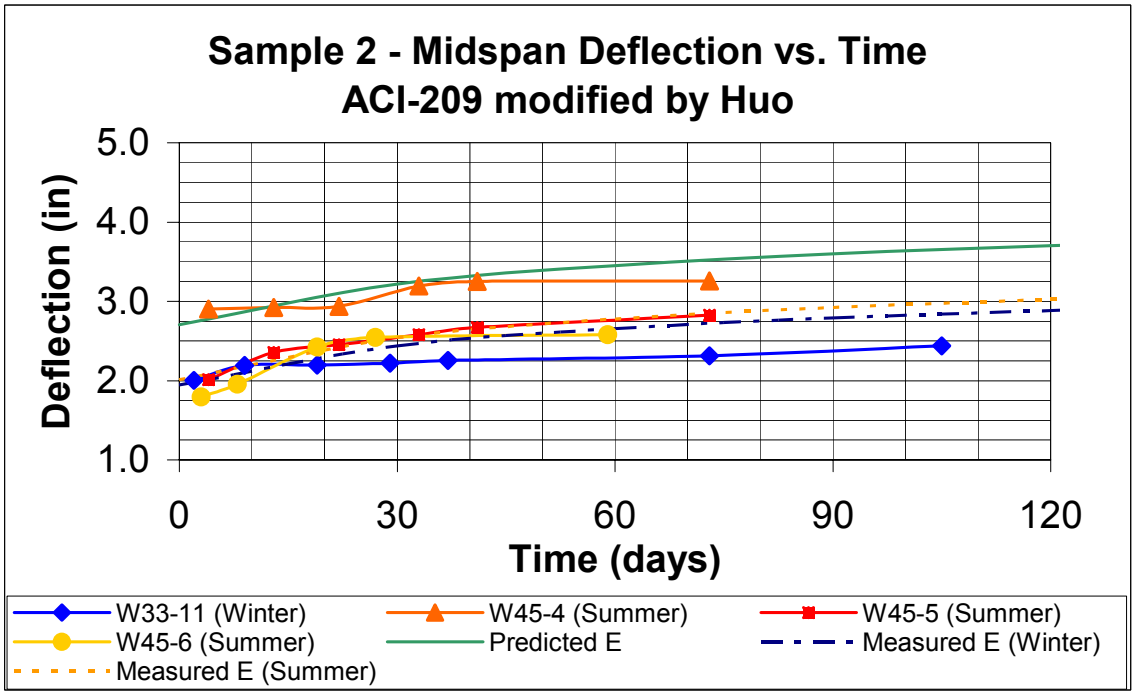

Figure A.21 Beam Sample 2 - ACI-209 (Modified by Huo) Predicted Deflection vs. Time

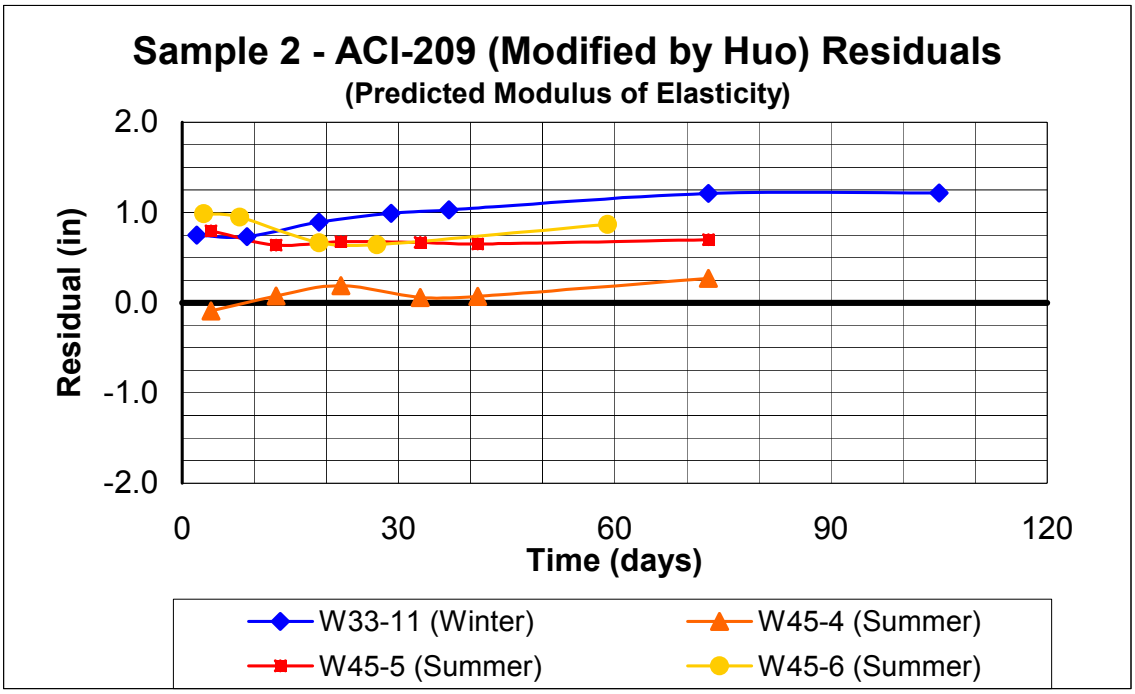

Figure A.22 Beam Sample 2 - ACI-209 (Modified by Huo) Residuals vs. Time (Predicted Modulus of Elasticity)

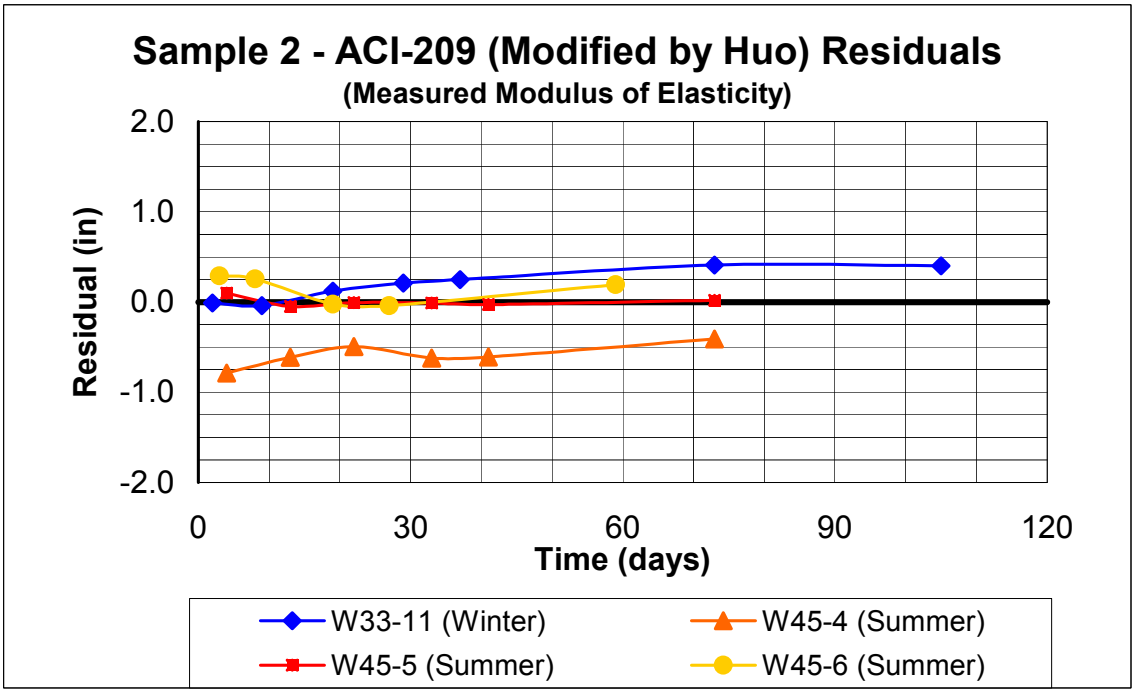

Figure A.23 Beam Sample 2 - ACI-209 (Modified by Huo) Residuals vs. Time (Measured Modulus of Elasticity)

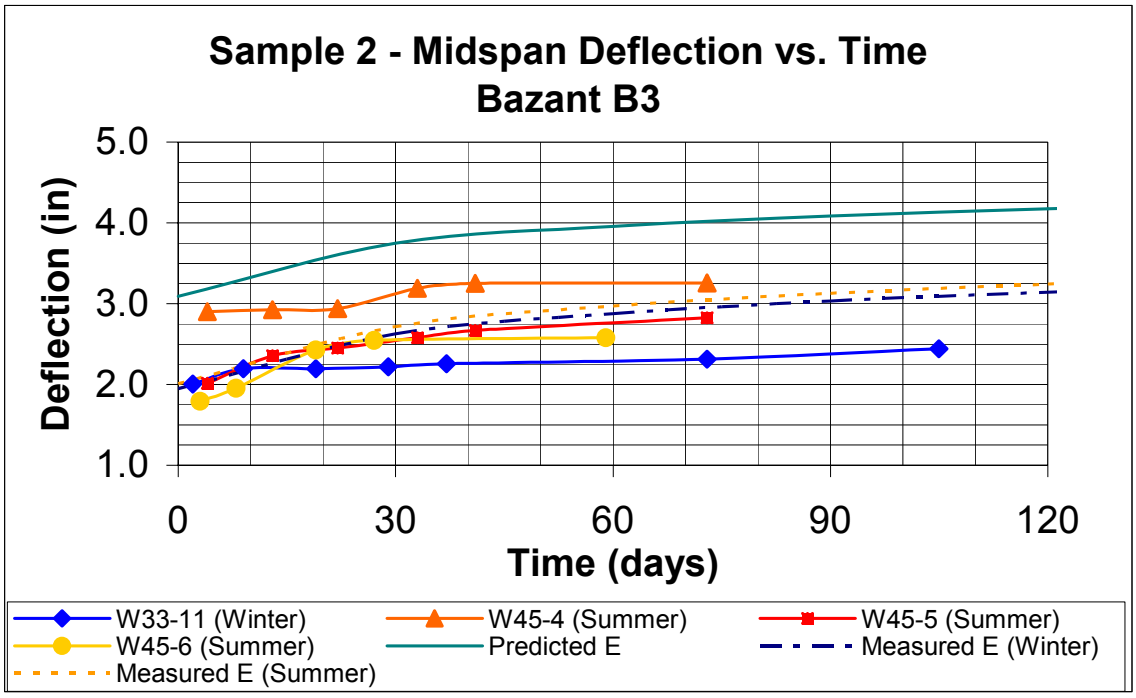

Figure A.24 Beam Sample 2 - Bazant B3 Predicted Deflection vs. Time

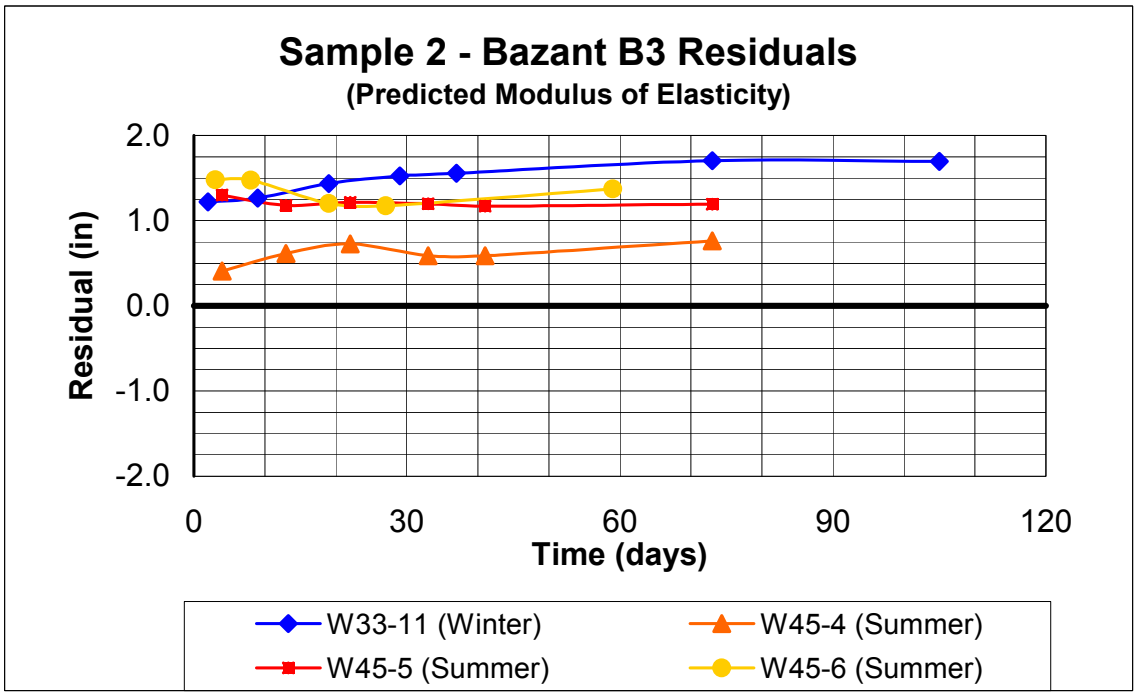

Figure A.25 Beam Sample 2 - Bazant B3 Residuals vs. Time (Predicted Modulus of Elasticity)

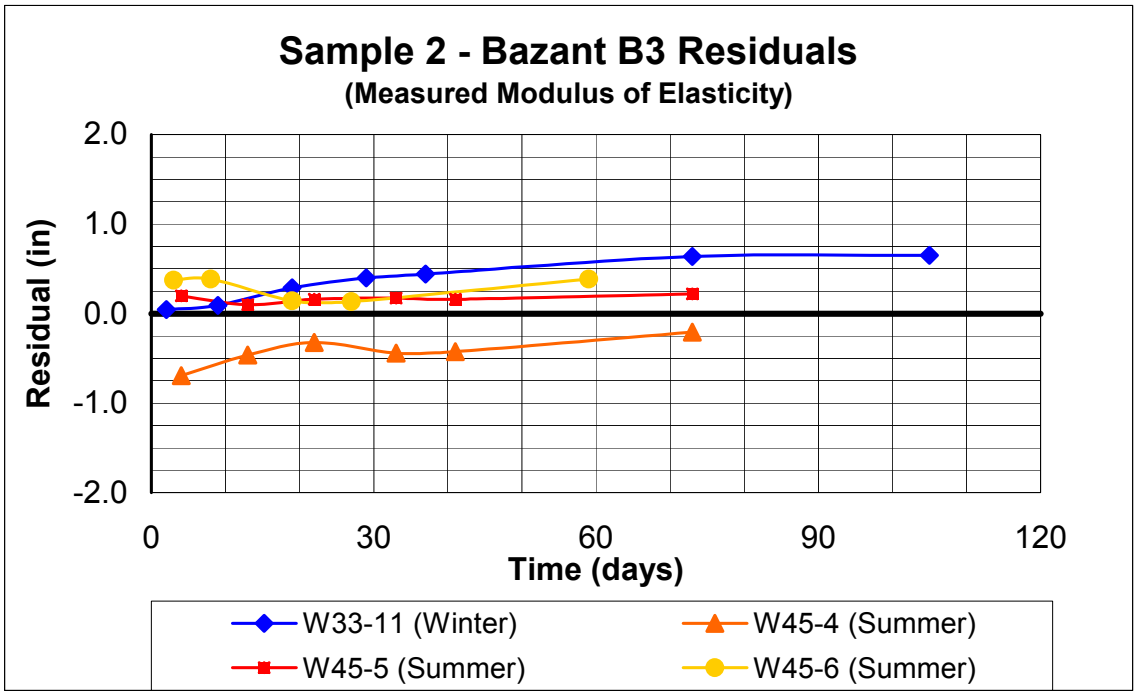

Figure A.26 Beam Sample 2 - Bazant B3 Residuals vs. Time (Measured Modulus of Elasticity)

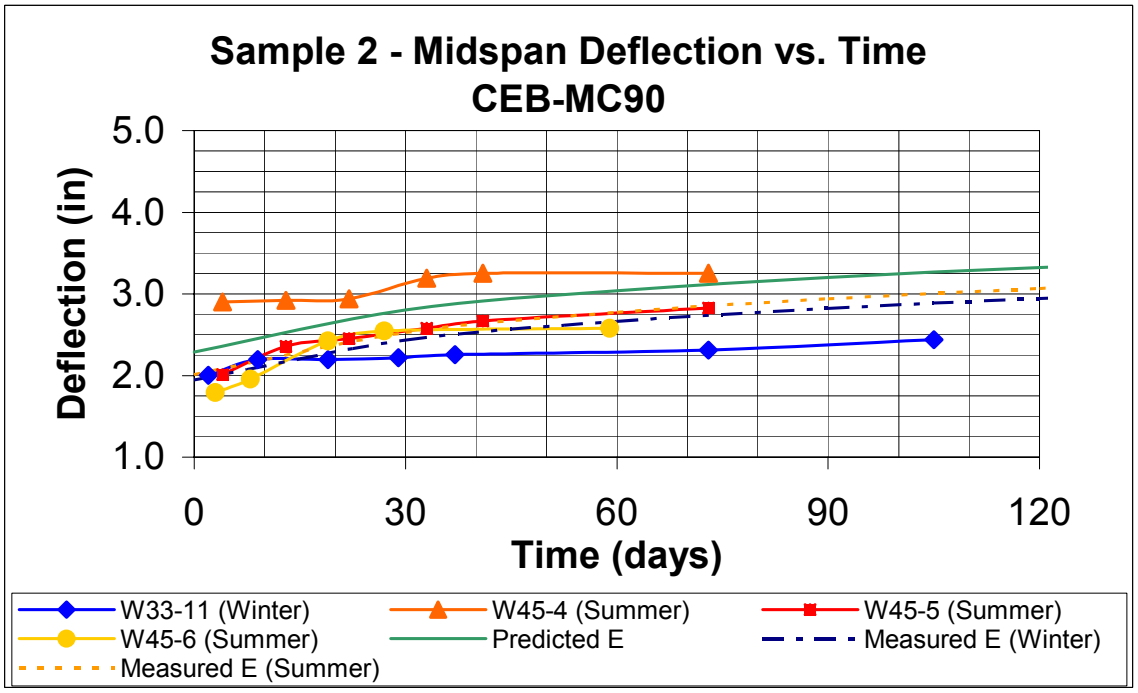

Figure A.27 Beam Sample 2 - CEB-MC90 Predicted Deflection vs. Time

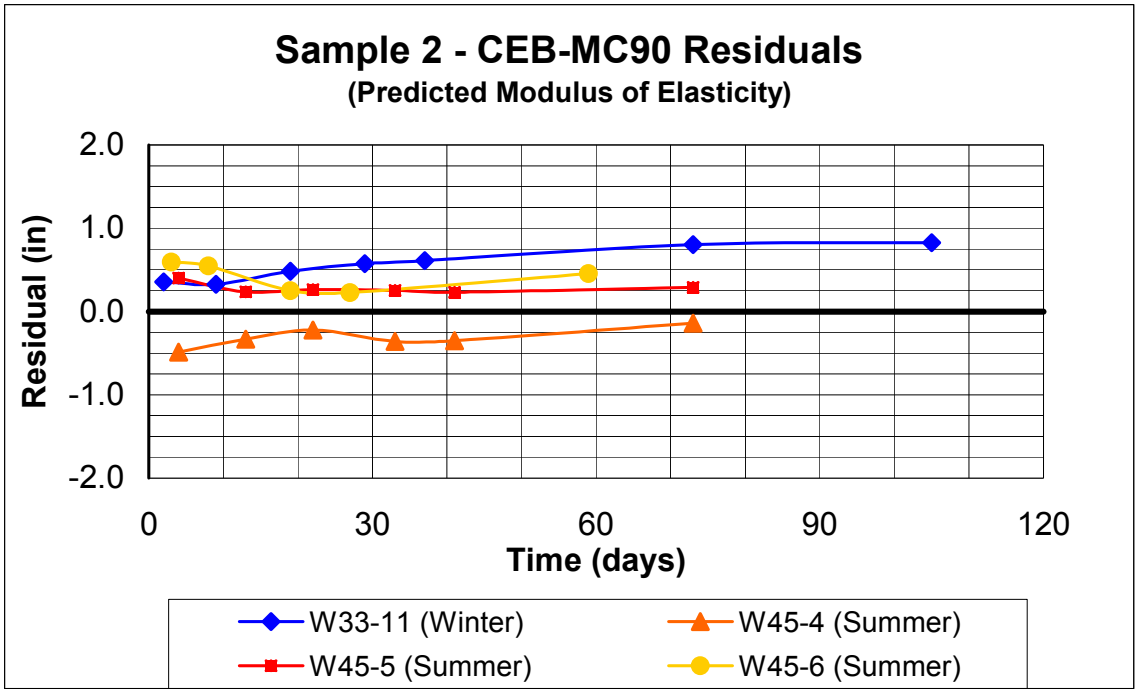

Figure A.28 Beam Sample 2 - CEB-MC90 Residuals vs. Time (Predicted Modulus of Elasticity)

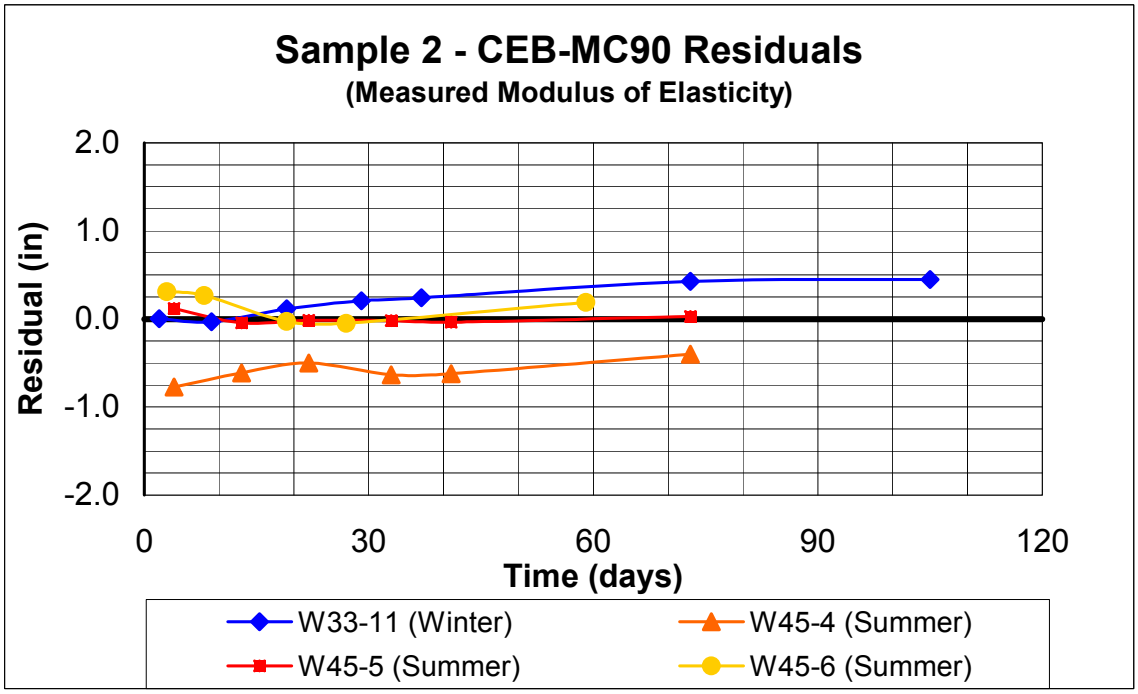

Figure A.29 Beam Sample 2 - CEB-MC90 Residuals vs. Time (Measured Modulus of Elasticity)

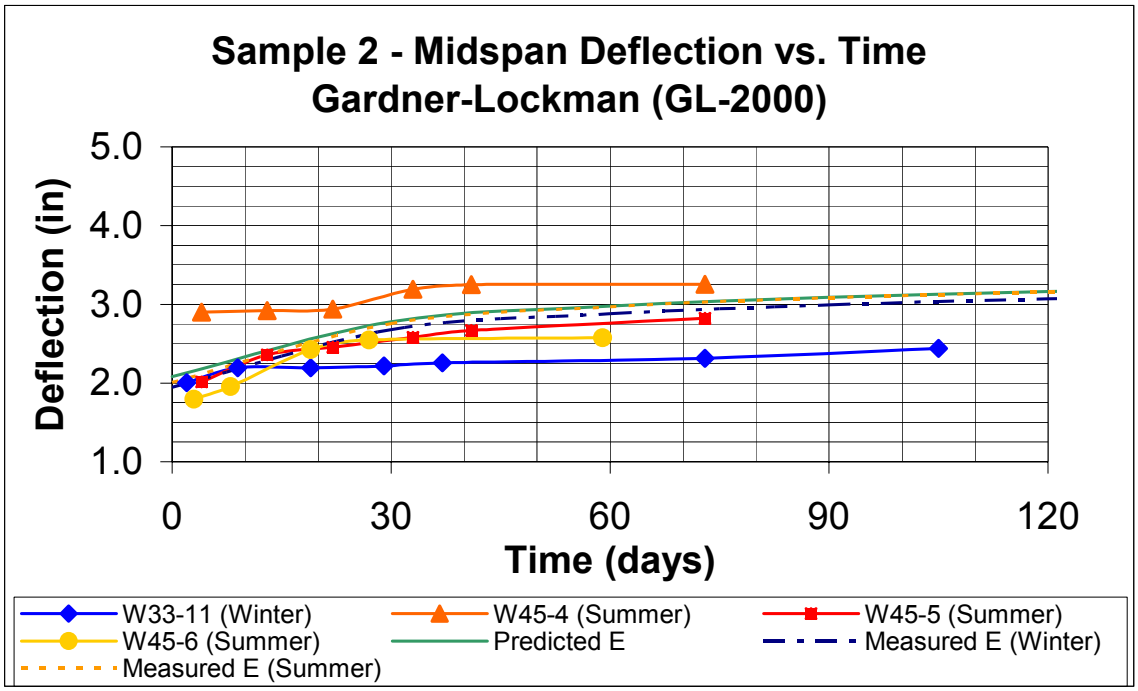

Figure A.30 Beam Sample 2 - Gardner-Lockman (GL-2000) Predicted Deflection vs. Time

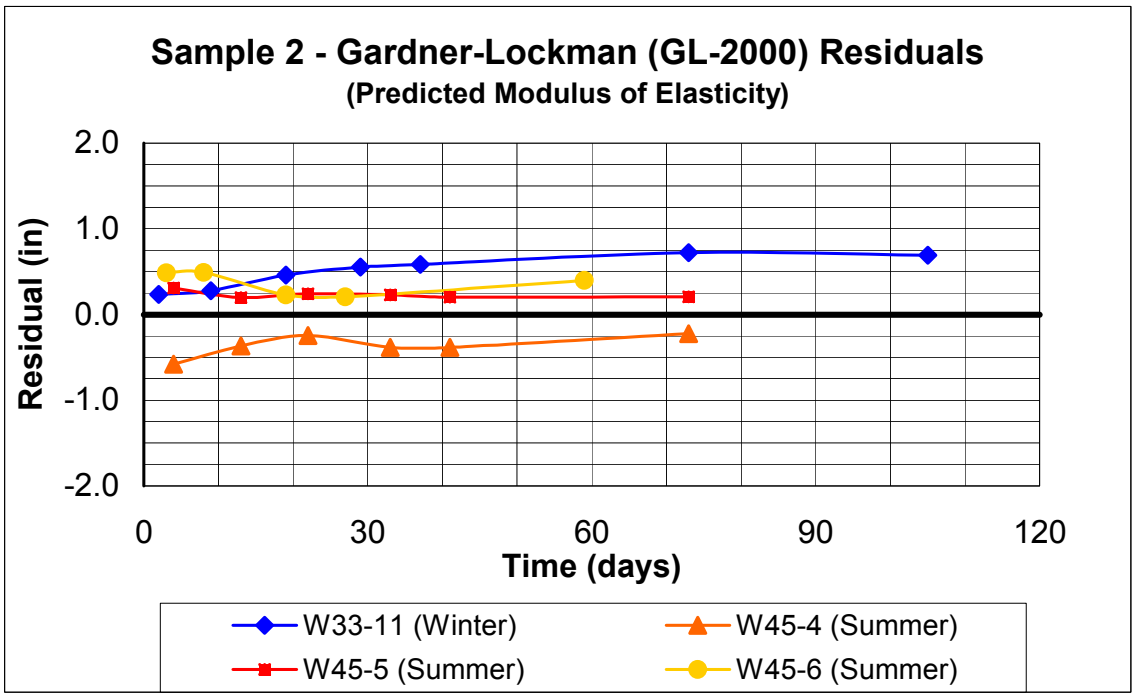

Figure A.31 Beam Sample 2 - Gardner-Lockman Residuals vs. Time (Predicted Modulus of Elasticity)

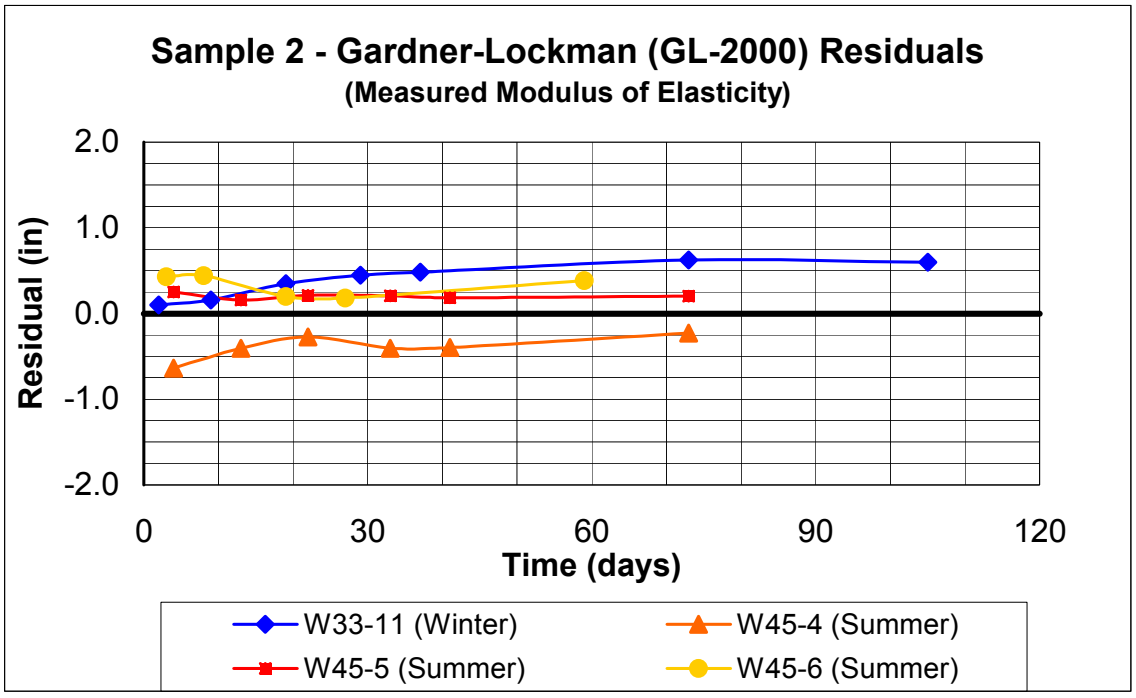

Figure A.32 Beam Sample 2 - Gardner-Lockman Residuals vs. Time (Measured Modulus of Elasticity)

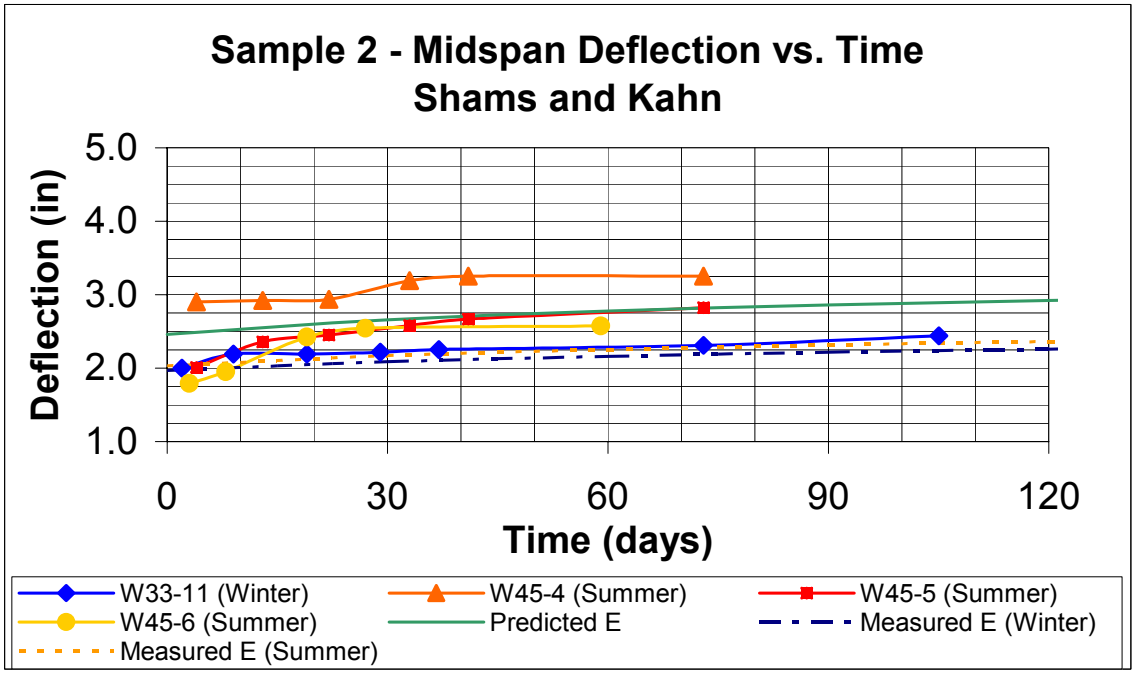

Figure A.33 Beam Sample 2 - Shams and Kahn Predicted Deflection vs. Time

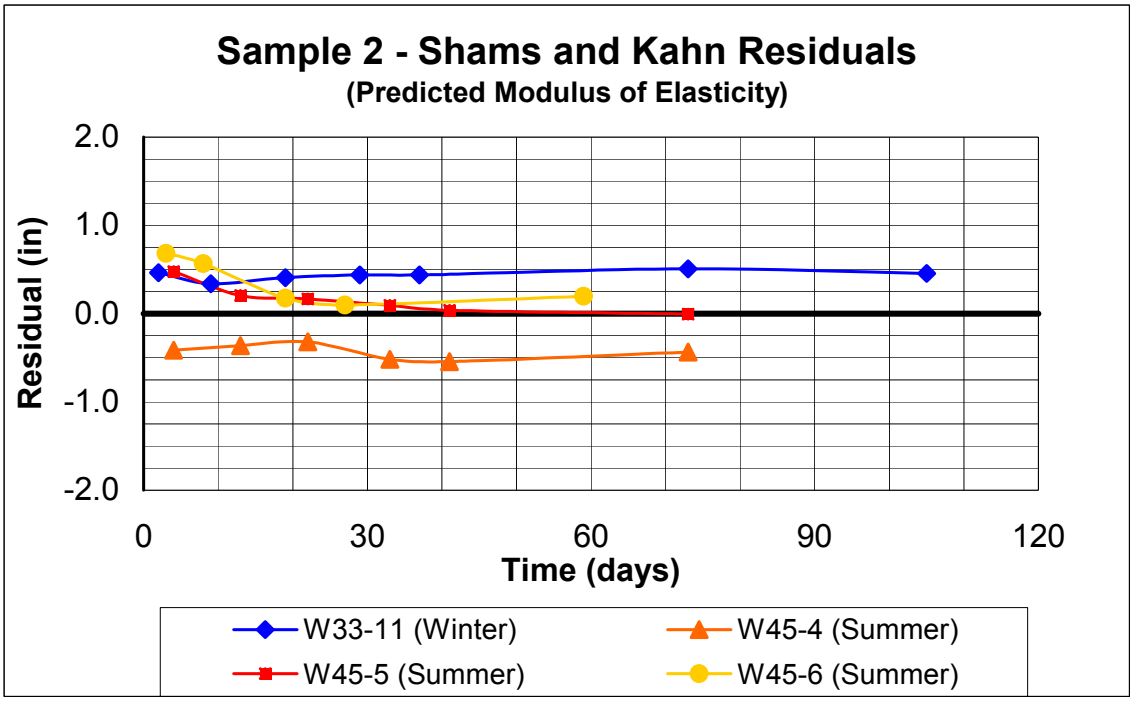

Figure A.34 Beam Sample 2 - Shams and Kahn Residuals vs. Time (Predicted Modulus of Elasticity)

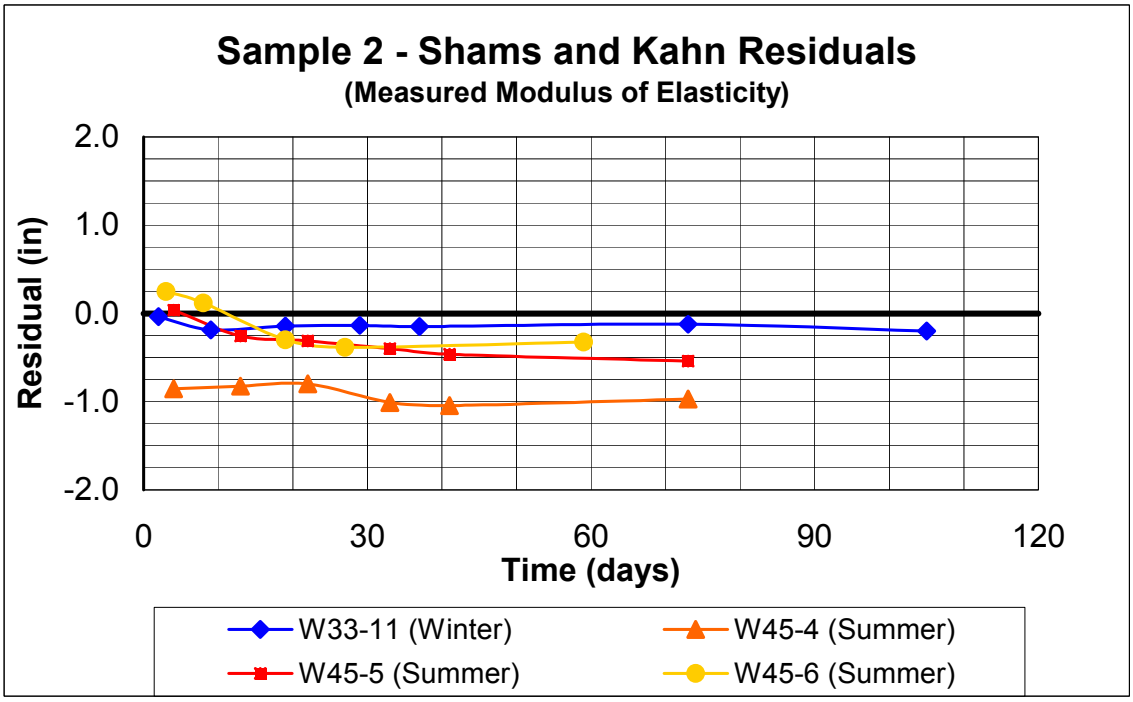

Figure A.35 Beam Sample 2 - Shams and Kahn Residuals vs. Time (Measured Modulus of Elasticity)

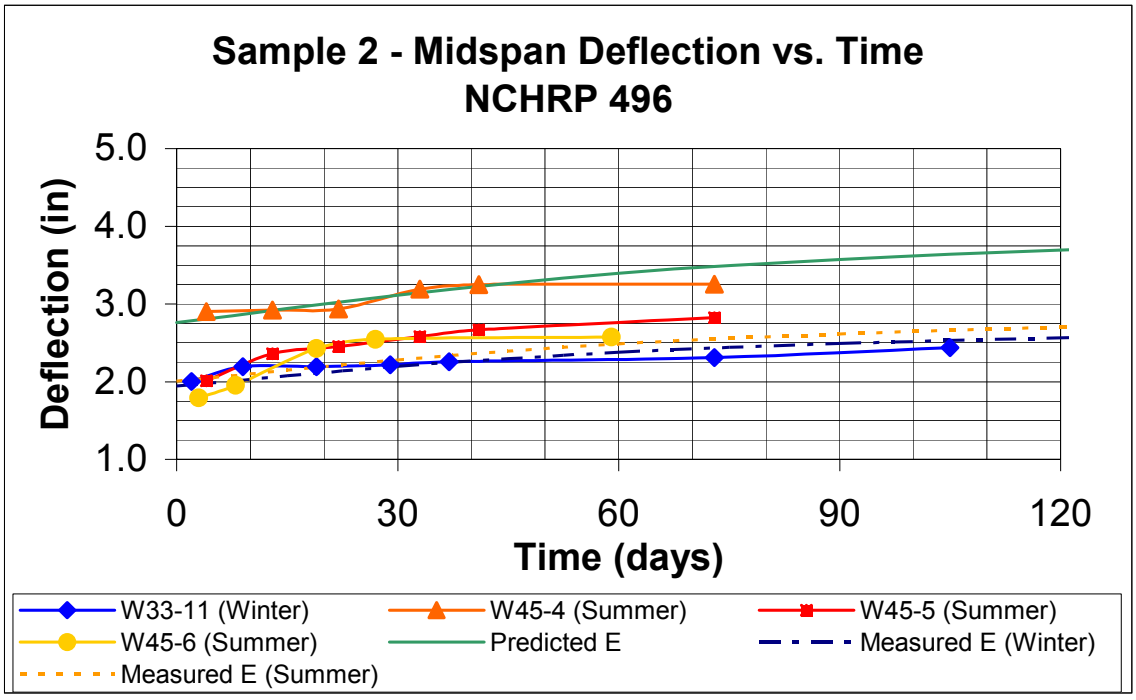

Figure A.36 Beam Sample 2 - NCHRP 496 Predicted Deflection vs. Time

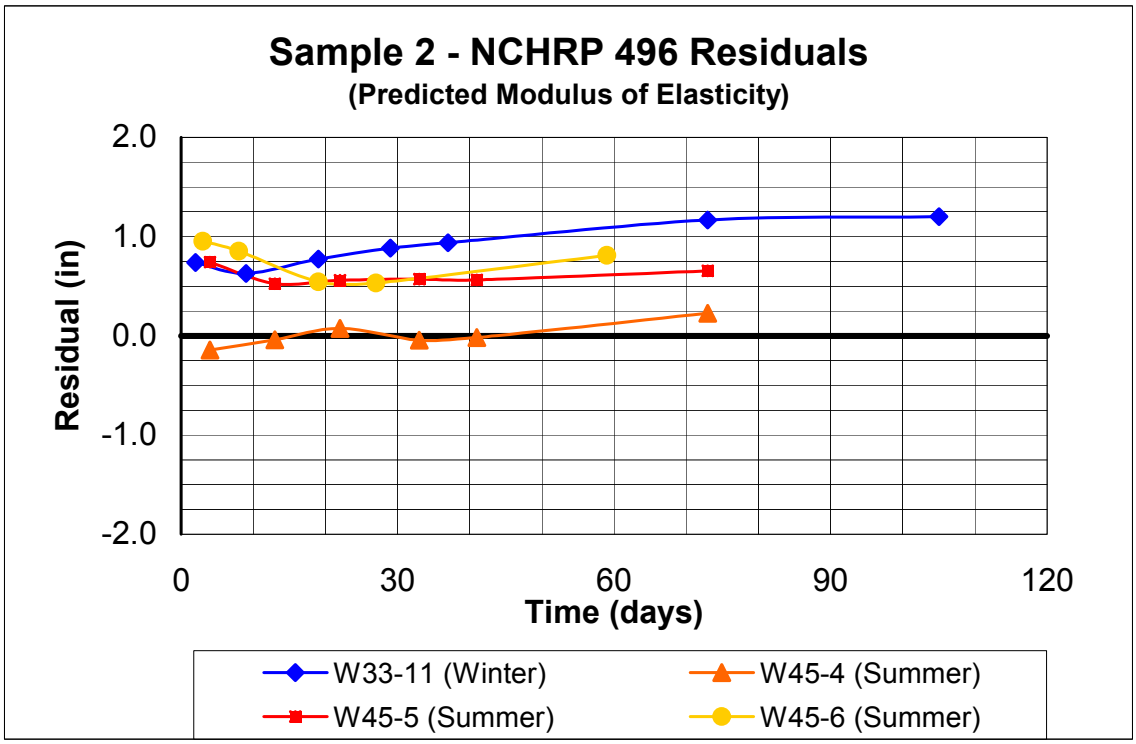

Figure A.37 Beam Sample 2 - NCHRP 496 Residuals vs. Time (Predicted Modulus of Elasticity)

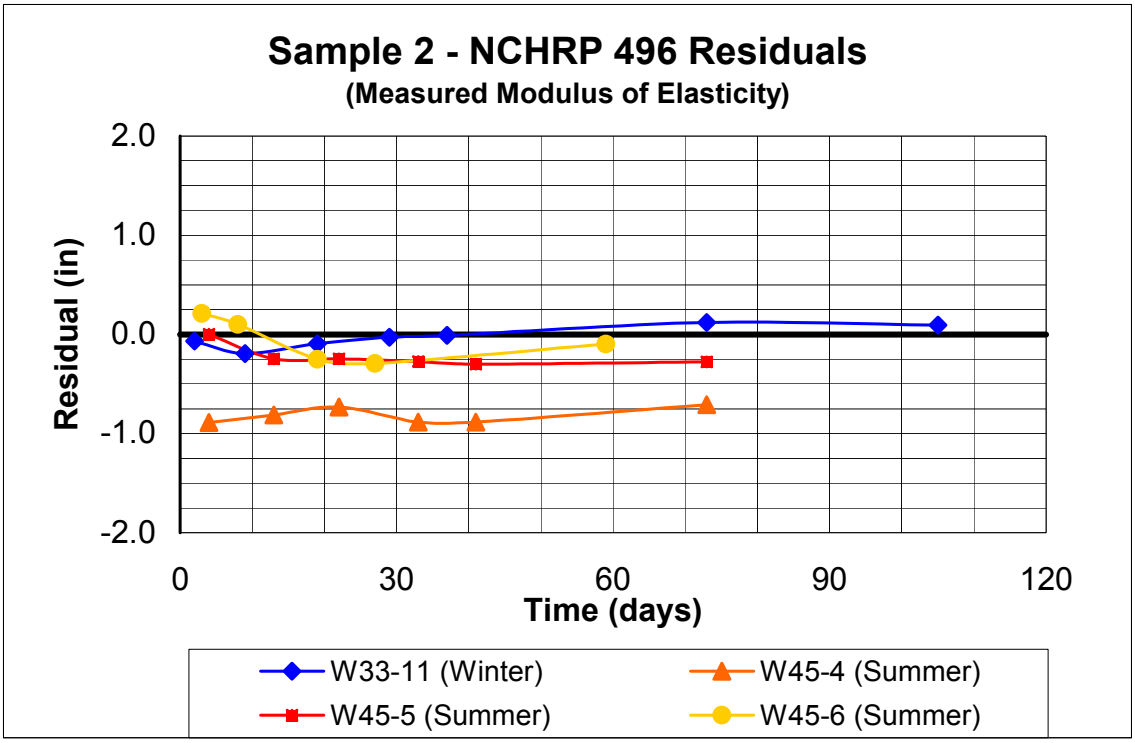

Figure A.38 Beam Sample 2 - NCHRP 496 Residuals vs. Time (Measured Modulus of Elasticity)

A.4 Predicted Deflections, Beam Sample 3

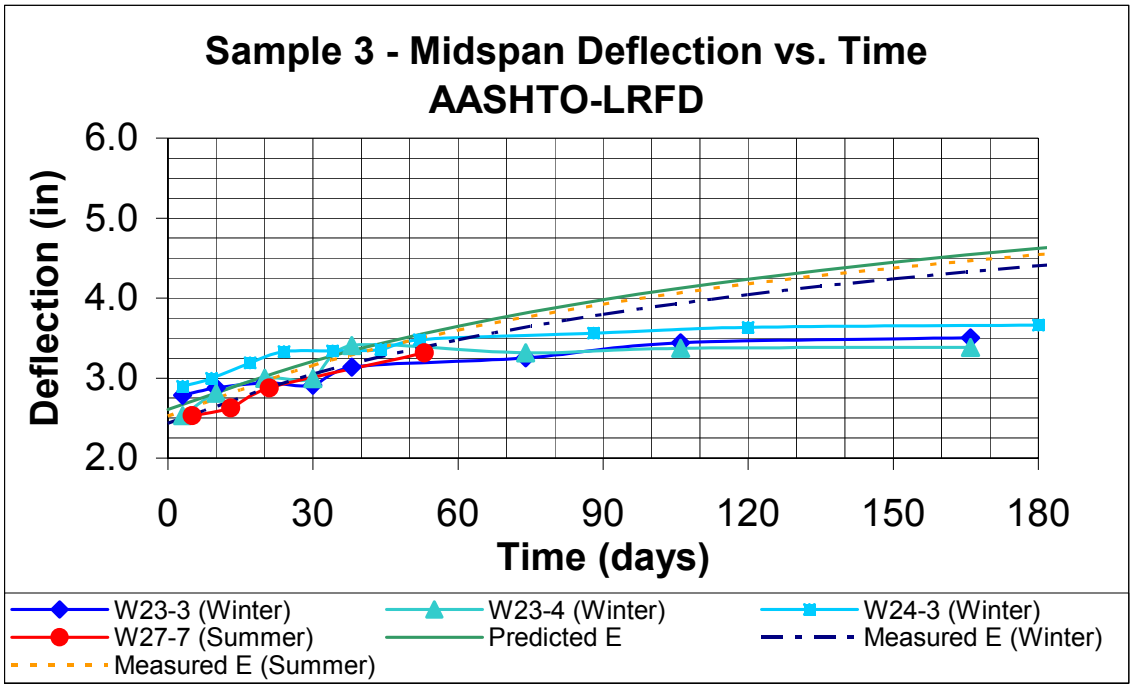

Figure A.39 Beam Sample 3 - AASHTO-LRFD Predicted Deflection vs. Time

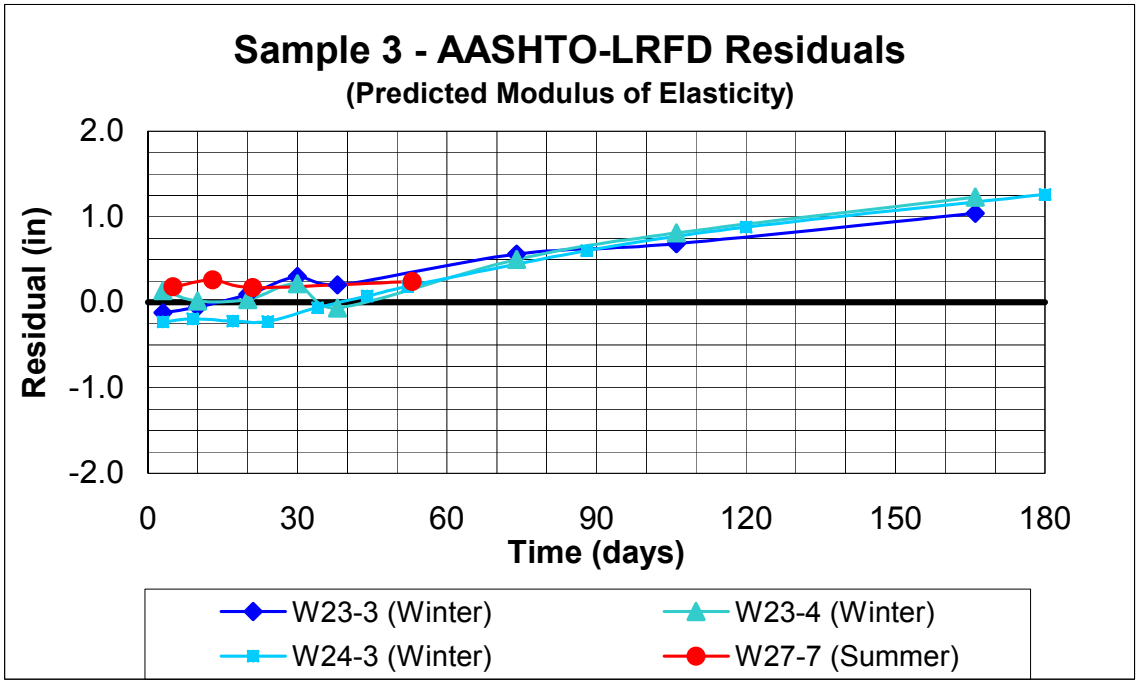

Figure A.40 Beam Sample 3 - AASHTO-LRFD Residuals vs. Time (Predicted Modulus of Elasticity)

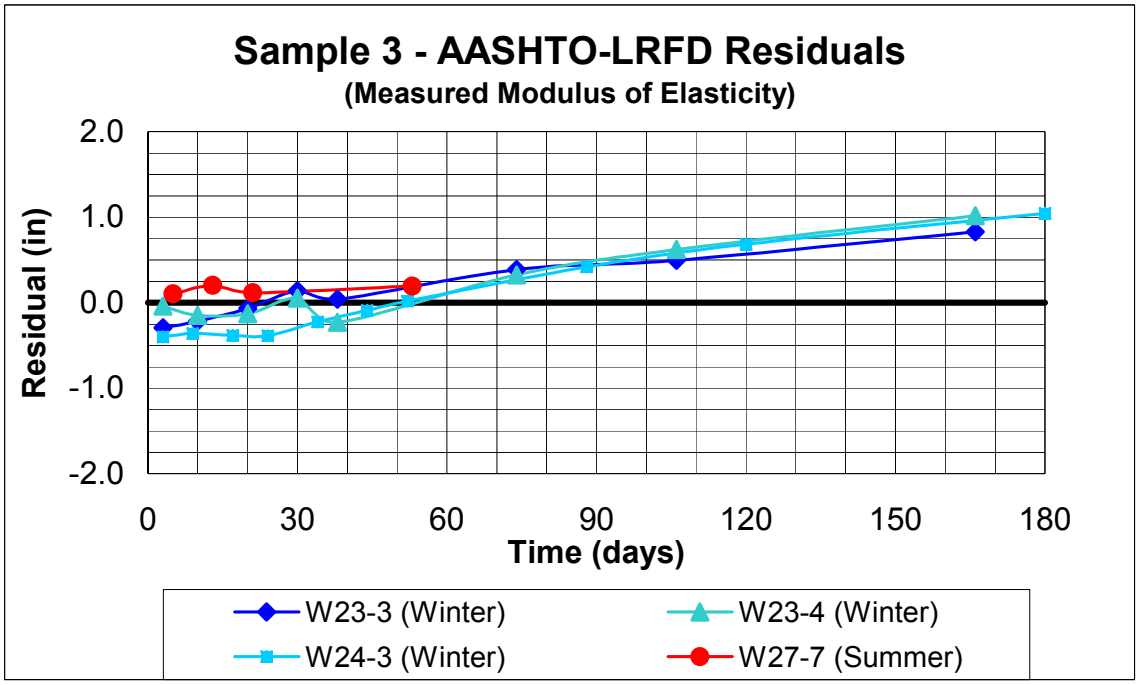

Figure A.41 Beam Sample 3 - AASHTO-LRFD Residuals vs. Time (Measured Modulus of Elasticity)

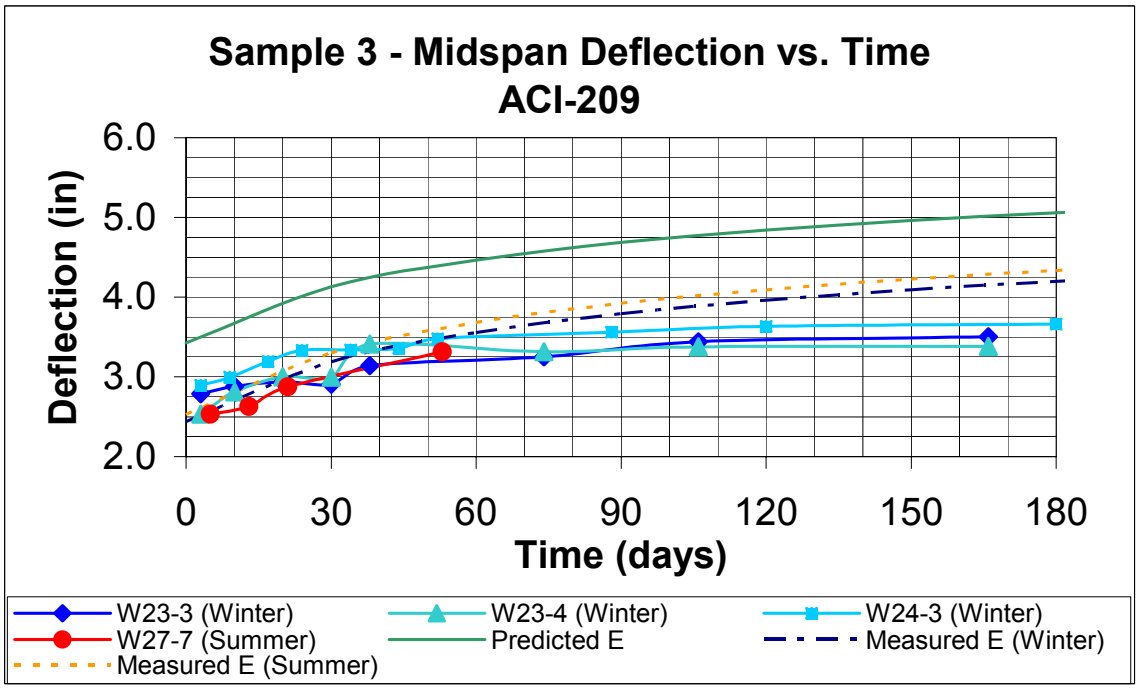

Figure A.42 Beam Sample 3 - ACI-209 Predicted Deflection vs. Time

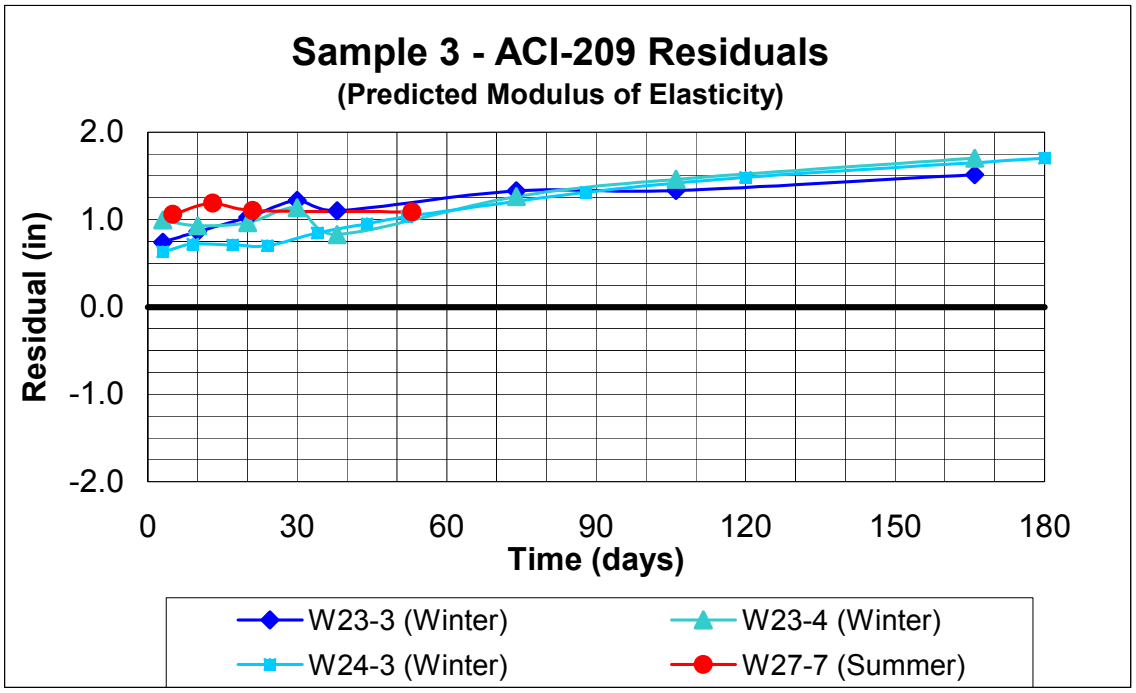

Figure A.43 Beam Sample 3 - ACI-209 Residuals vs. Time (Predicted Modulus of Elasticity)

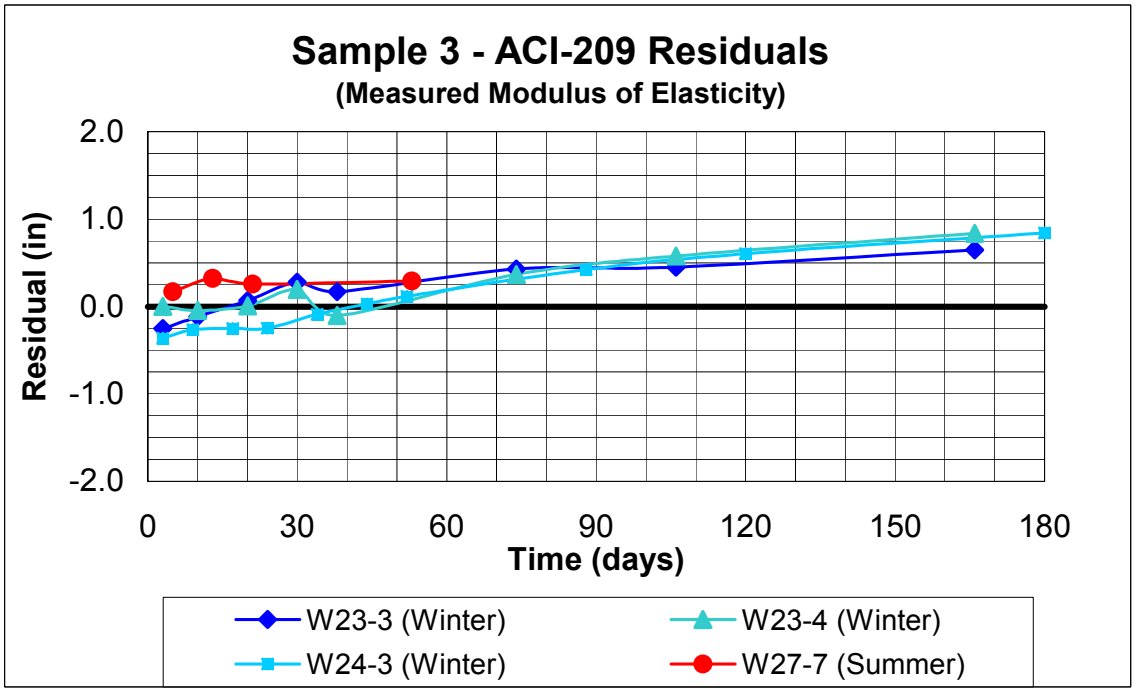

Figure A.44 Beam Sample 3 - ACI-209 Residuals vs. Time (Measured Modulus of Elasticity)

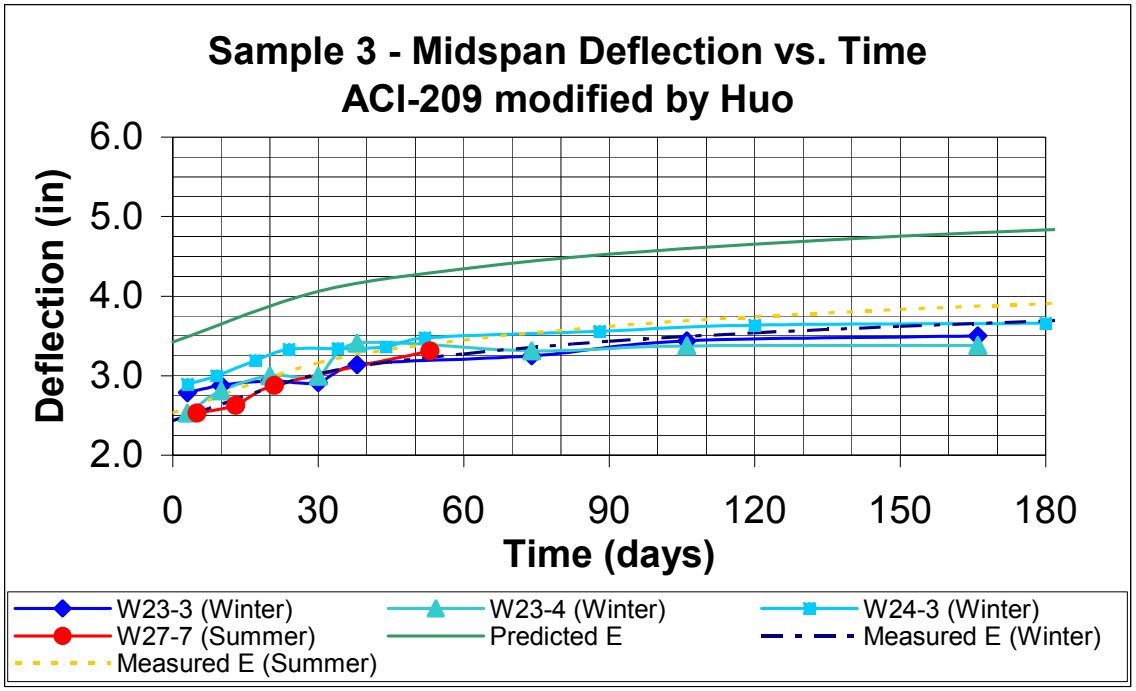

Figure A.45 Beam Sample 3 - ACI-209 (Modified by Huo) Predicted Deflection vs. Time

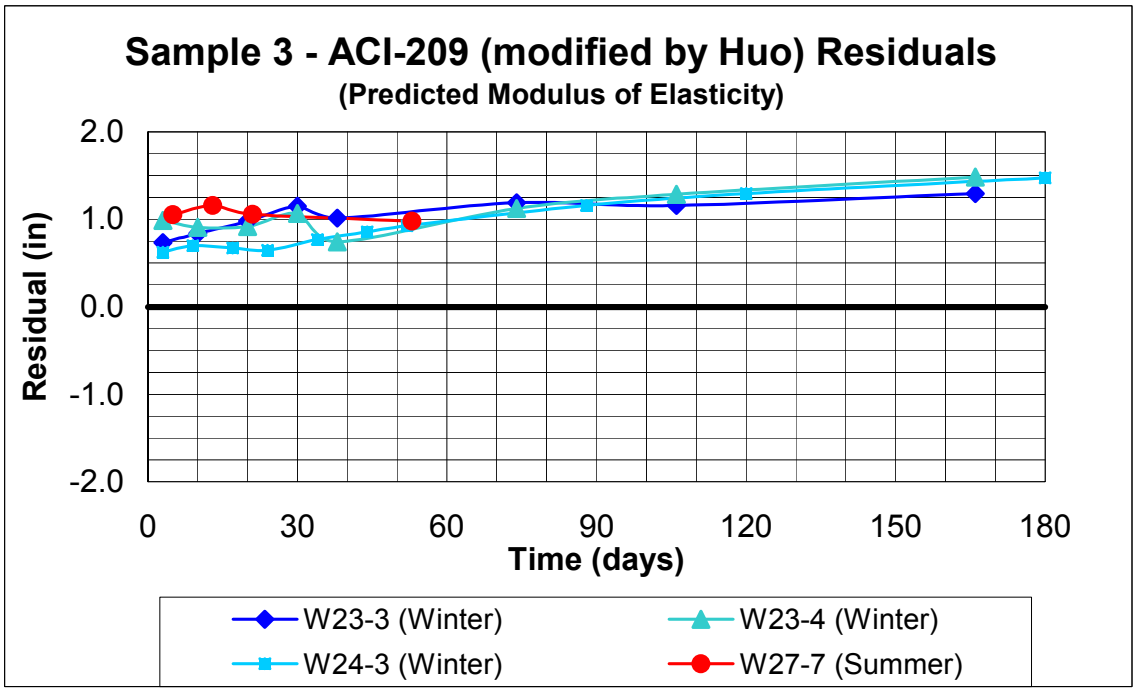

Figure A.46 Beam Sample 3 - ACI-209 Residuals vs. Time (Predicted Modulus of Elasticity)

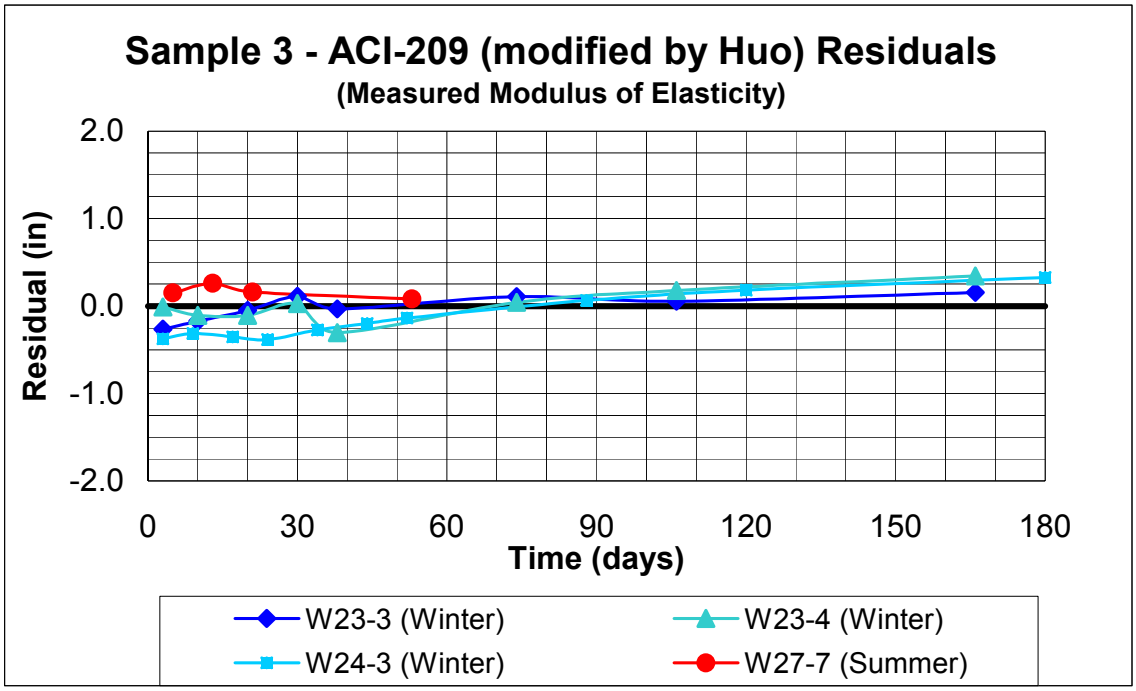

Figure A.47 Beam Sample 3 - ACI-209 Residuals vs. Time (Measured Modulus of Elasticity)

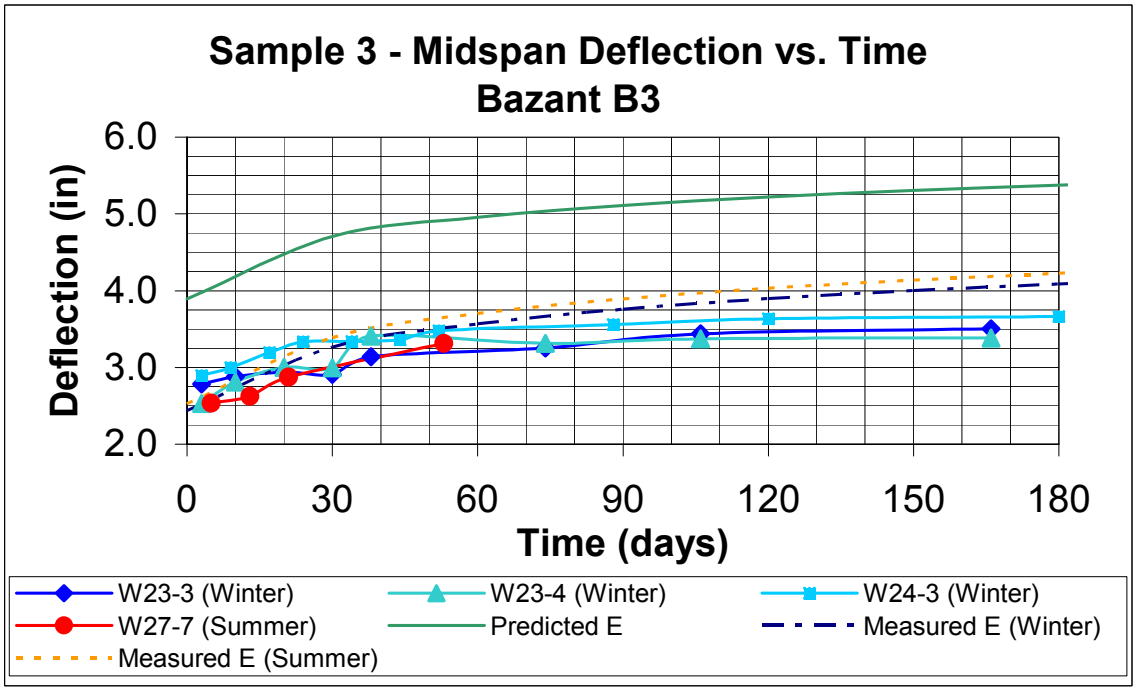

Figure A.48 Beam Sample 3 - Bazant B3 Predicted Deflection vs. Time

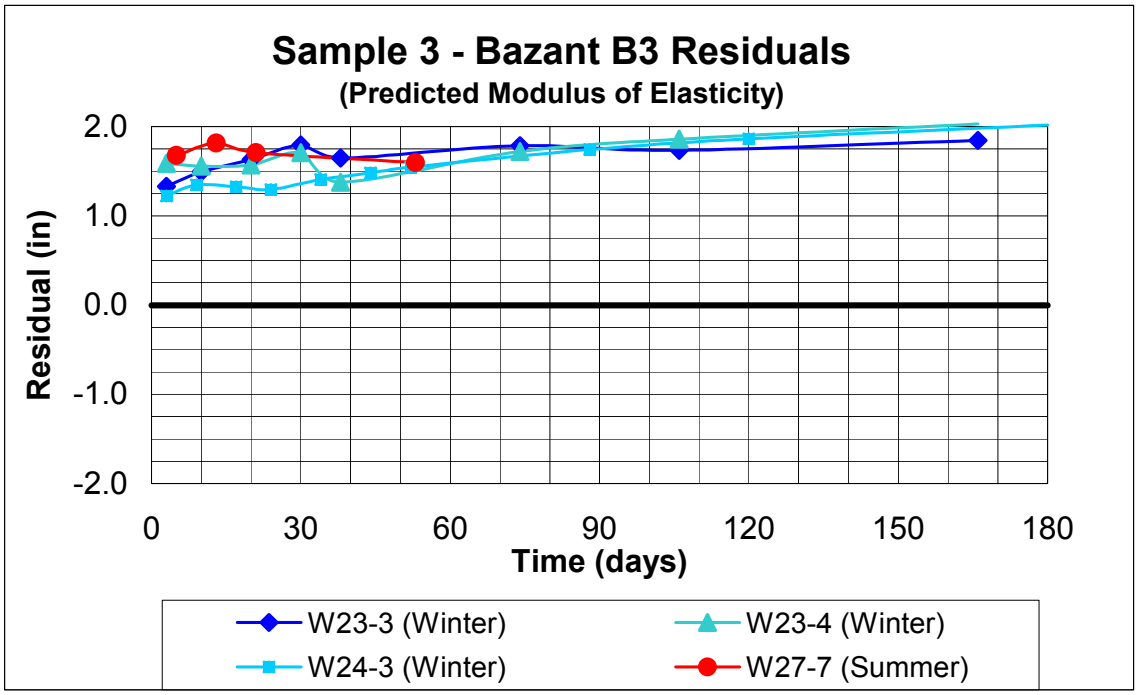

Figure A.49 Beam Sample 3 - Bazant B3 Residuals vs. Time (Predicted Modulus of Elasticity)

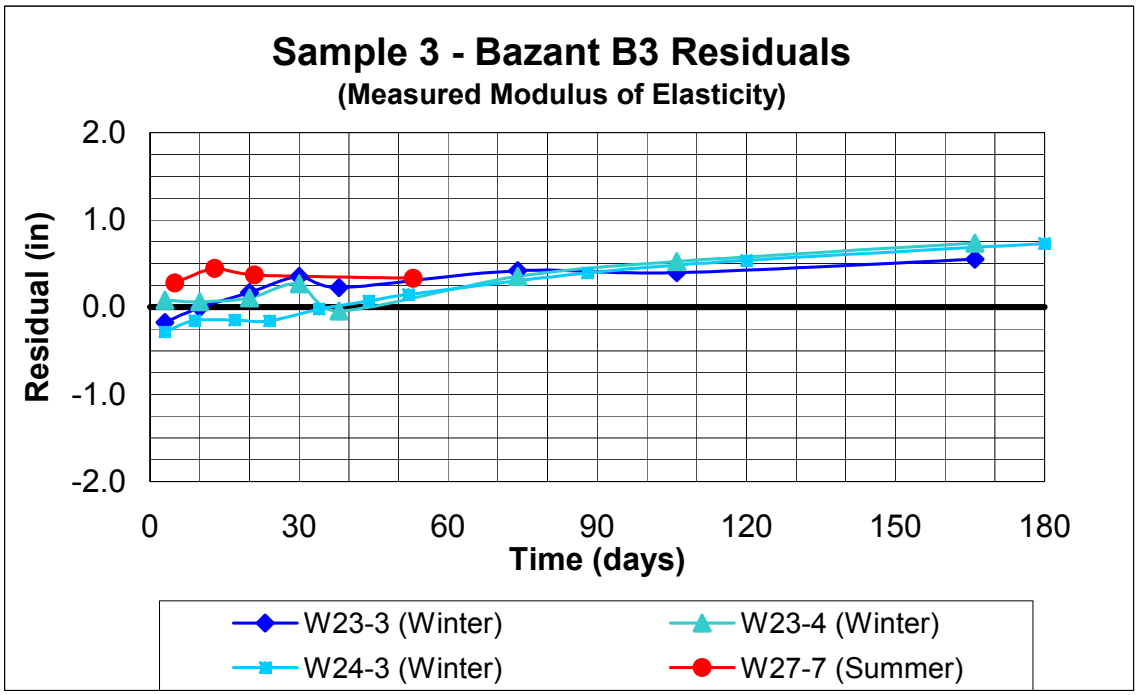

Figure A.50 Beam Sample 3 - Bazant B3 Residuals vs. Time (Measured Modulus of Elasticity)

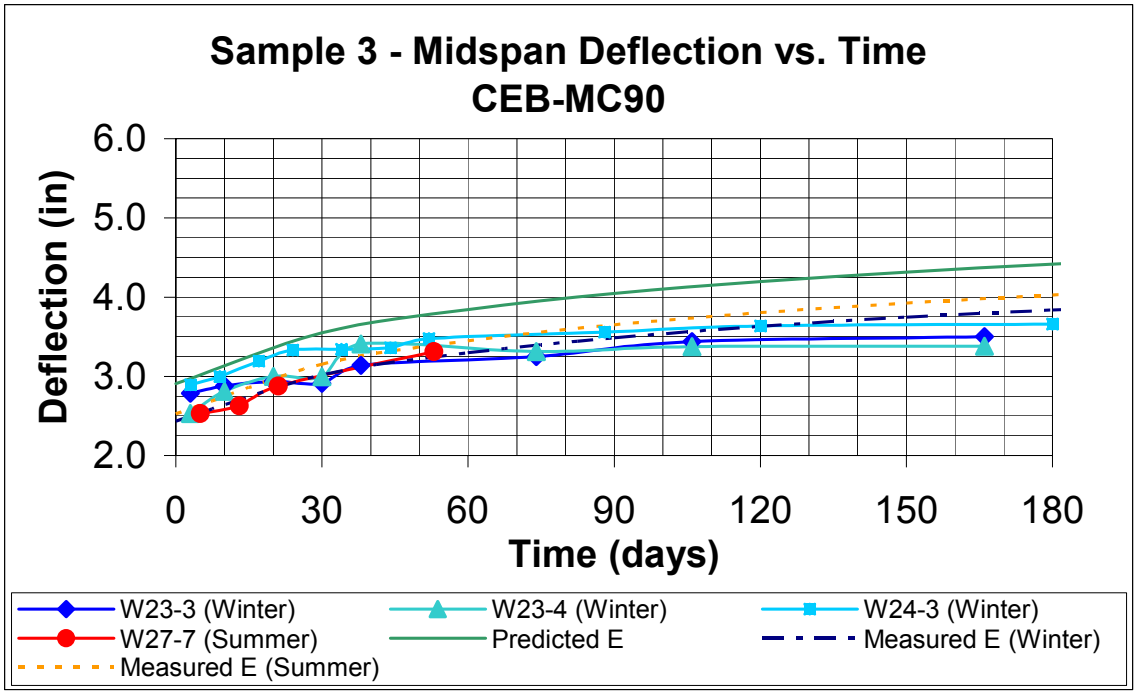

Figure A.51 Beam Sample 3 - CEB-MC90 Predicted Deflection vs. Time

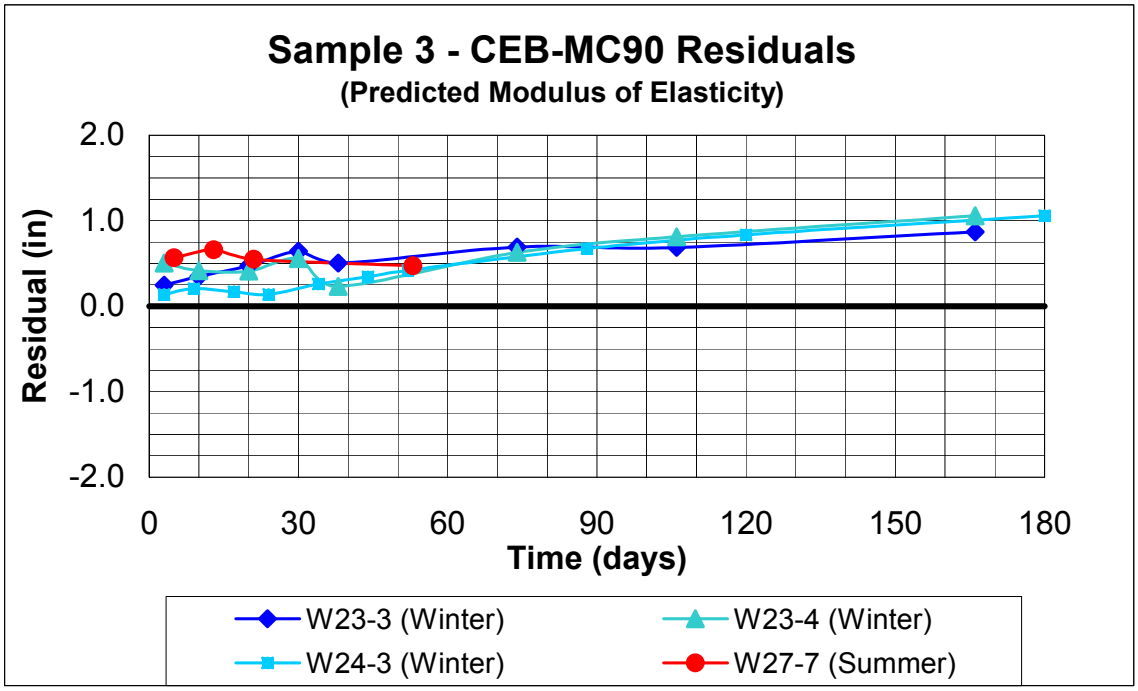

Figure A.52 Beam Sample 3 - CEB-MC90 Residuals vs. Time (Predicted Modulus of Elasticity)

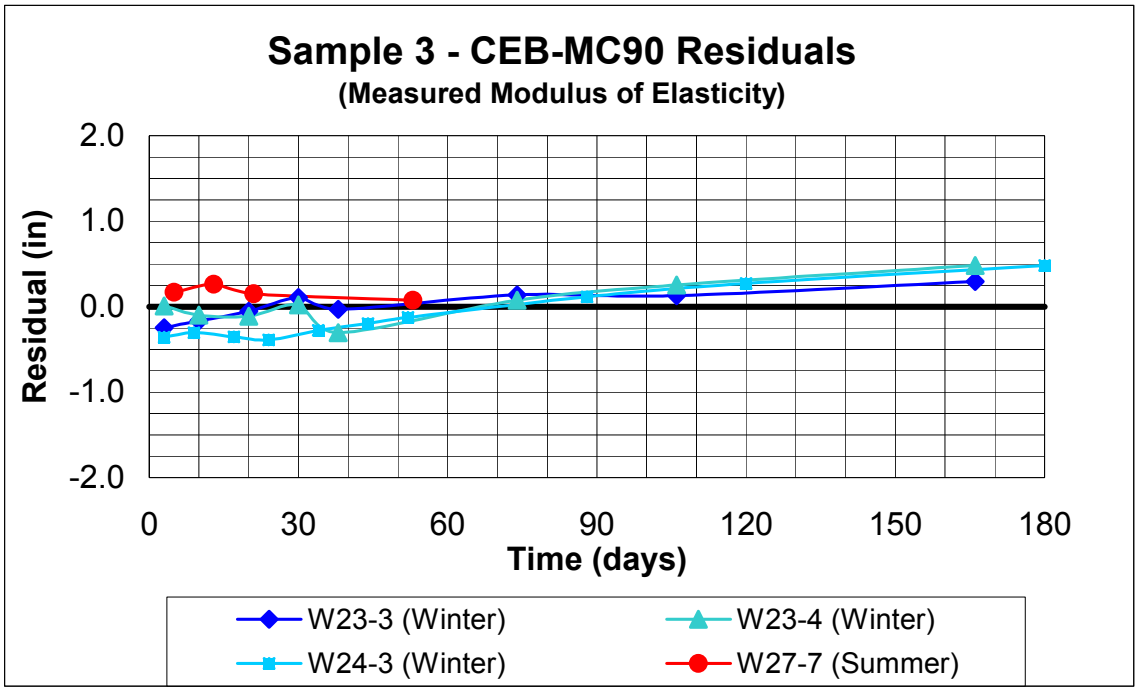

Figure A.53 Beam Sample 3 - CEB-MC90 Residuals vs. Time (Measured Modulus of Elasticity)

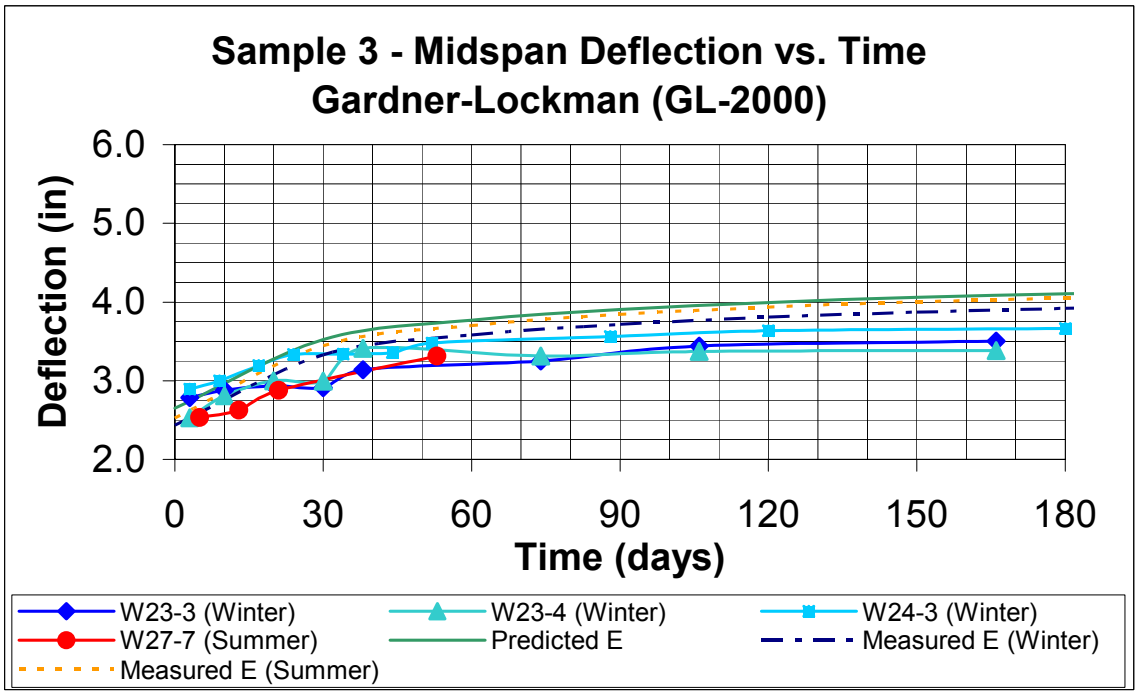

Figure A.54 Beam Sample 3 - Gardner-Lockman (GL-2000) Predicted Deflection vs. Time

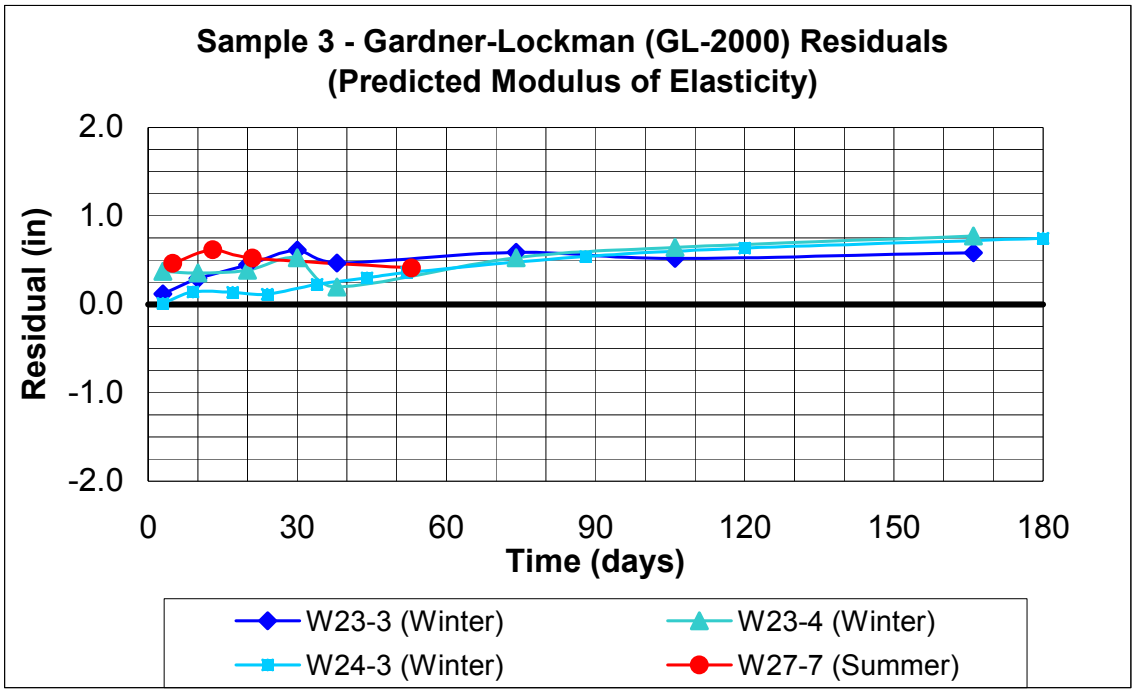

Figure A.55 Beam Sample 3 - Gardner-Lockman Residuals vs. Time (Predicted Modulus of Elasticity)

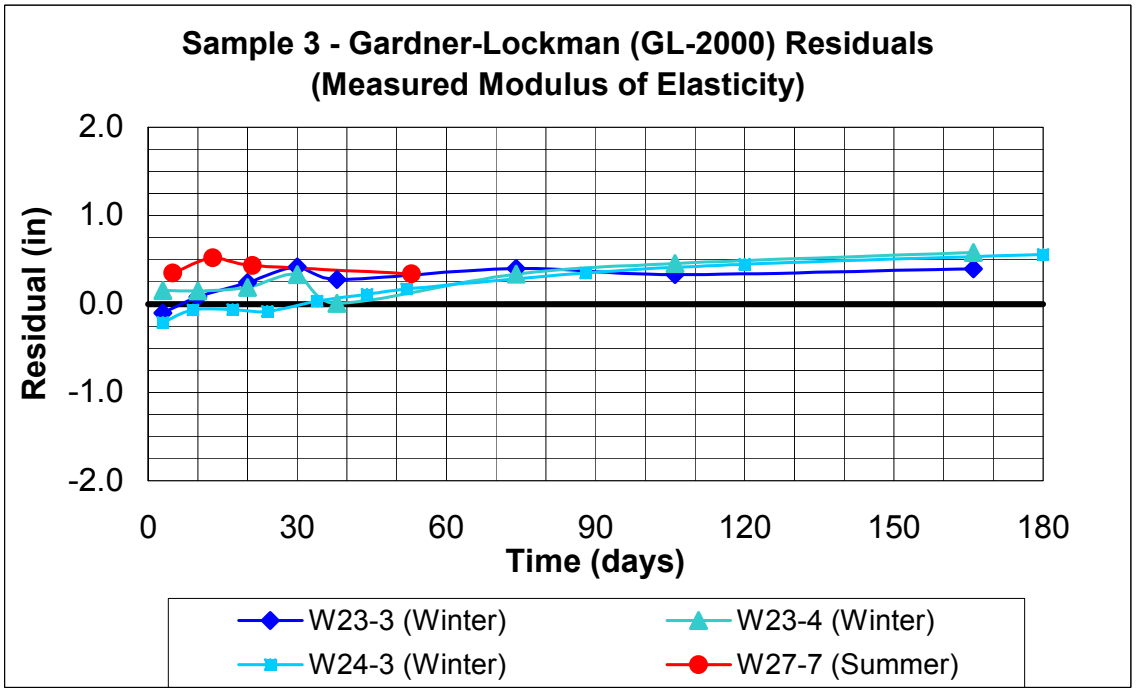

Figure A.56 Beam Sample 3 - Gardner-Lockman Residuals vs. Time (Measured Modulus of Elasticity)

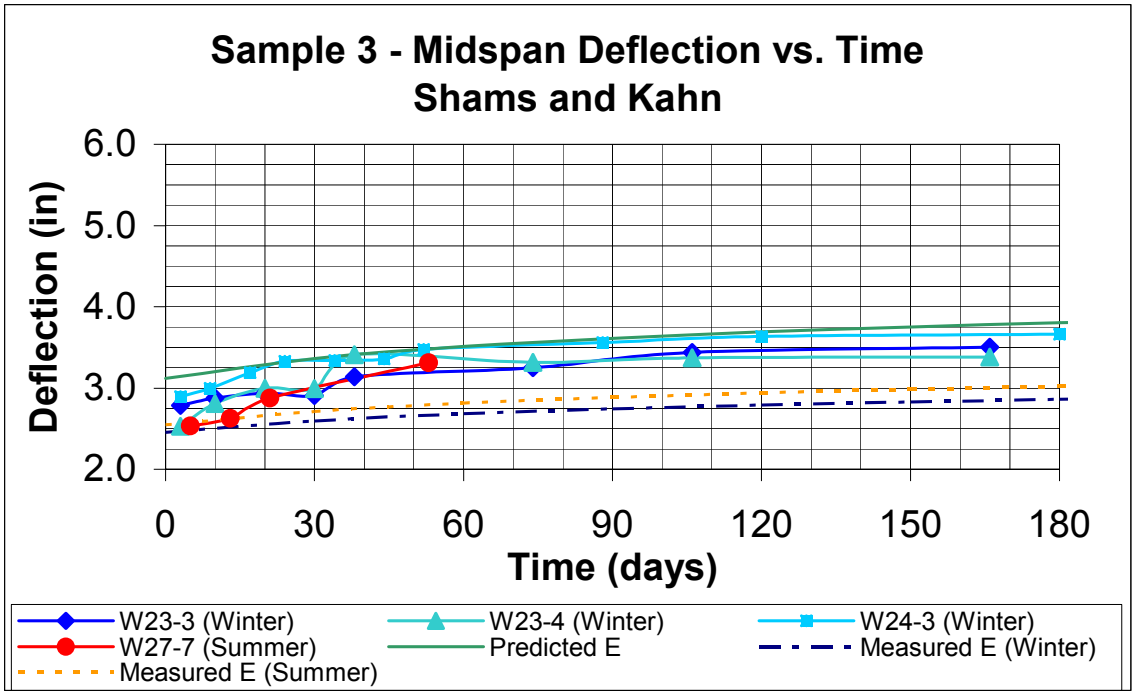

Figure A.57 Beam Sample 3 - Shams and Kahn Predicted Deflection vs. Time

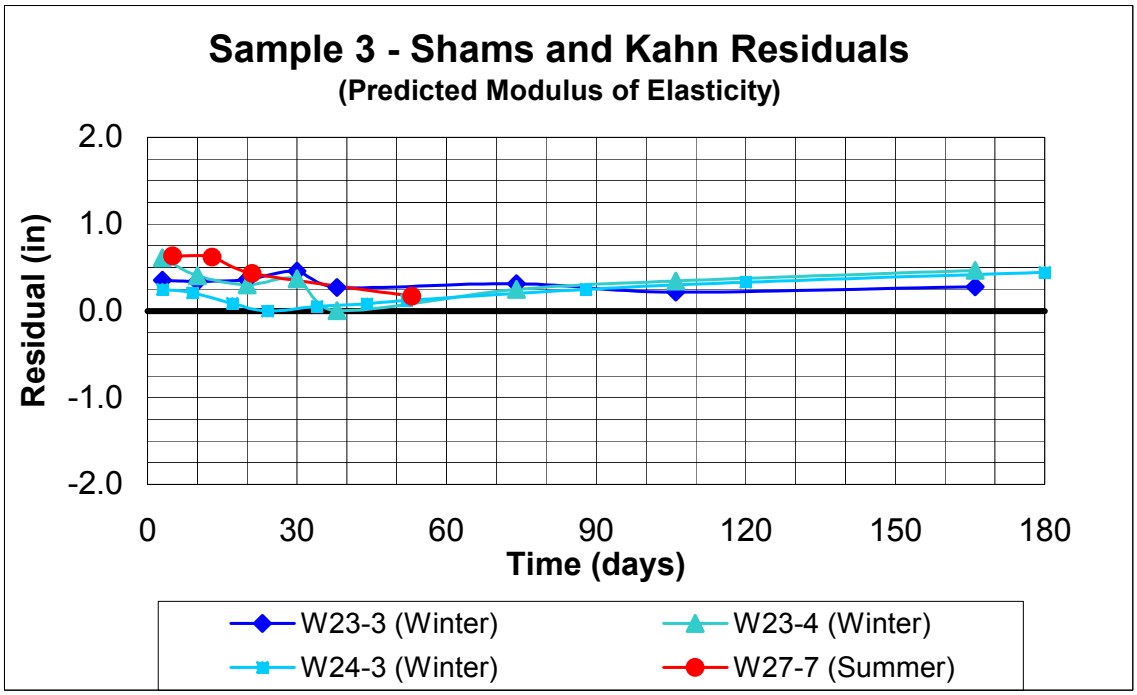

Figure A.58 Beam Sample 3 - Shams and Kahn Residuals vs. Time (Predicted Modulus of Elasticity)

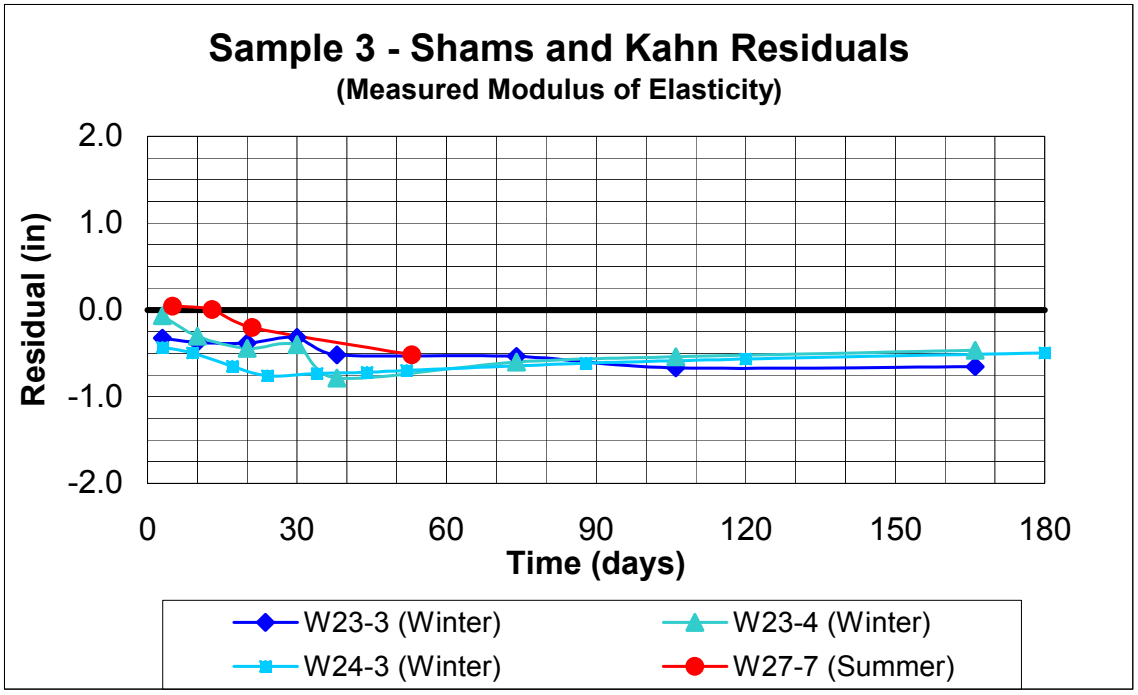

Figure A.59 Beam Sample 3 - Shams and Kahn Residuals vs. Time (Measured Modulus of Elasticity)

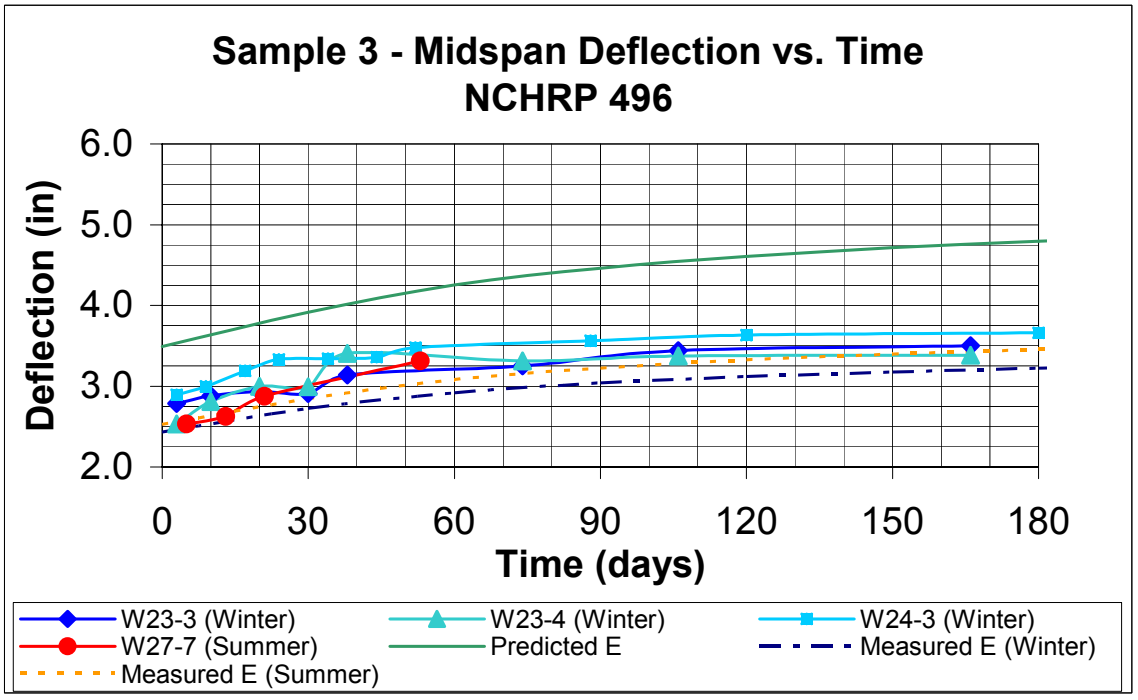

Figure A.60 Beam Sample 3 - NCHRP 496 Predicted Deflection vs. Time

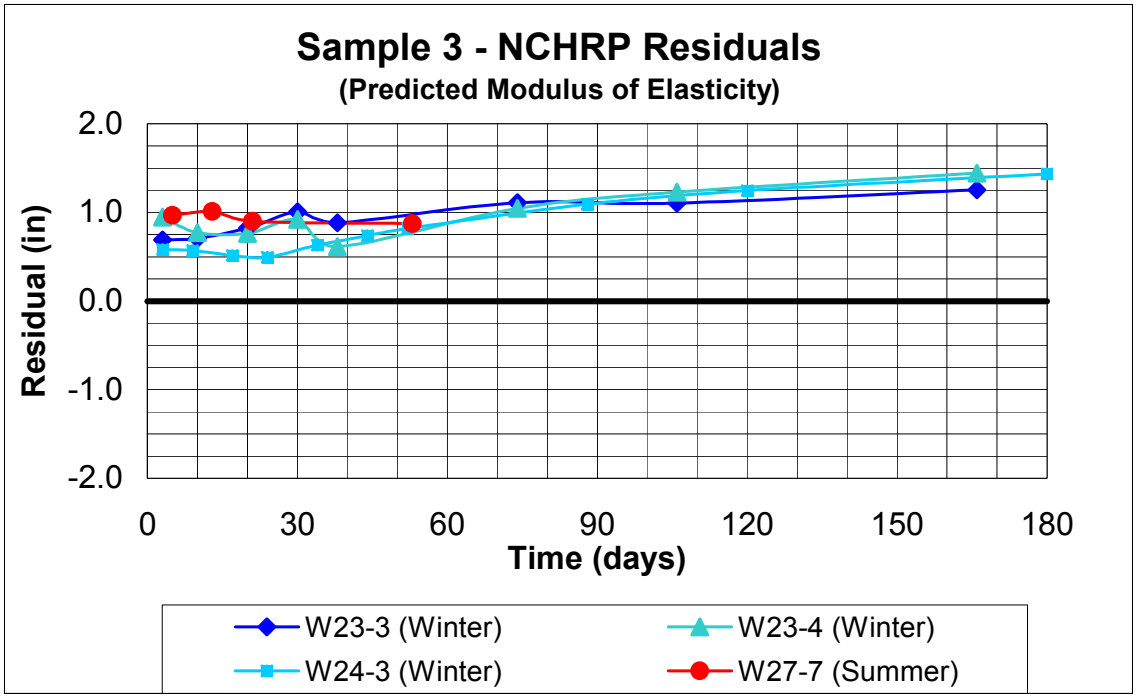

Figure A.61 Beam Sample 3 - NCHRP 496 Residuals vs. Time (Predicted Modulus of Elasticity)

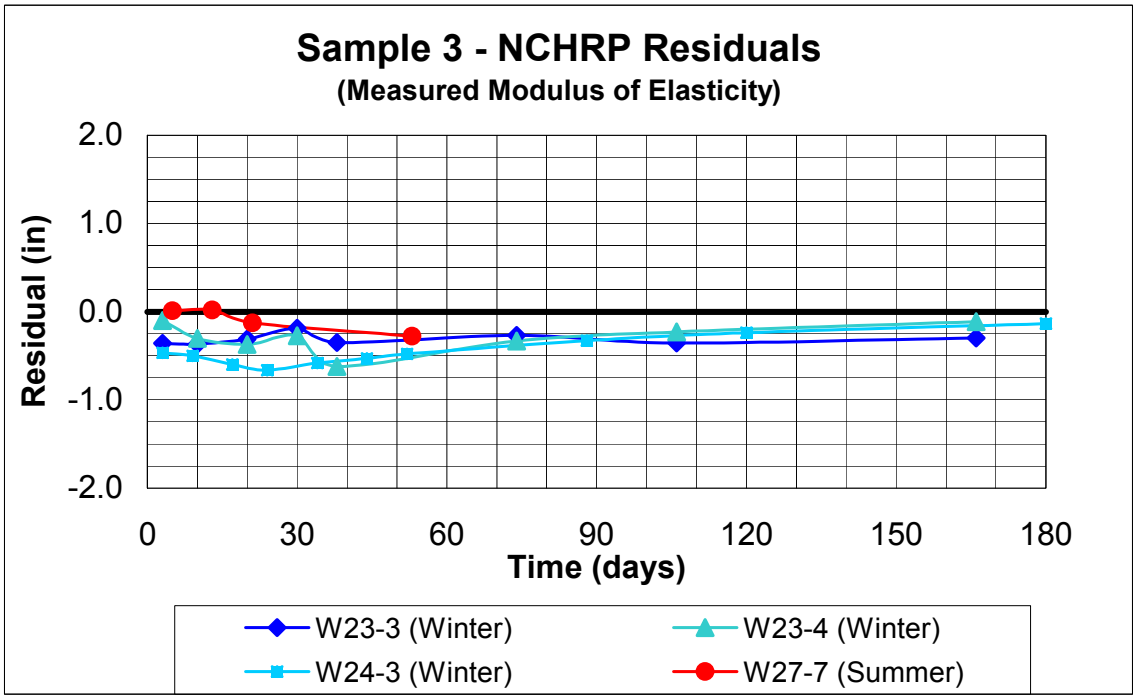

Figure A.62 Beam Sample 3 - NCHRP 496 Residuals vs. Time (Measured Modulus of Elasticity)

APPENDIX B

B.1 Additional Beams W26-5 & 6

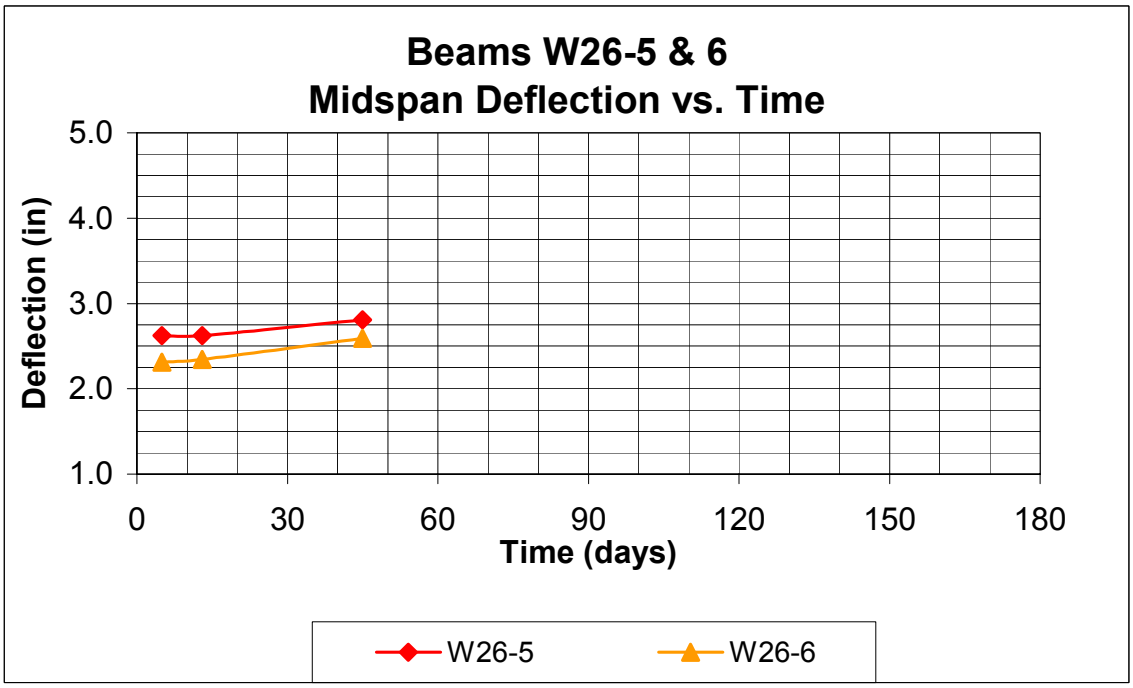

Figure B.1 Beams W26-5 & 6, Deflection vs. Time

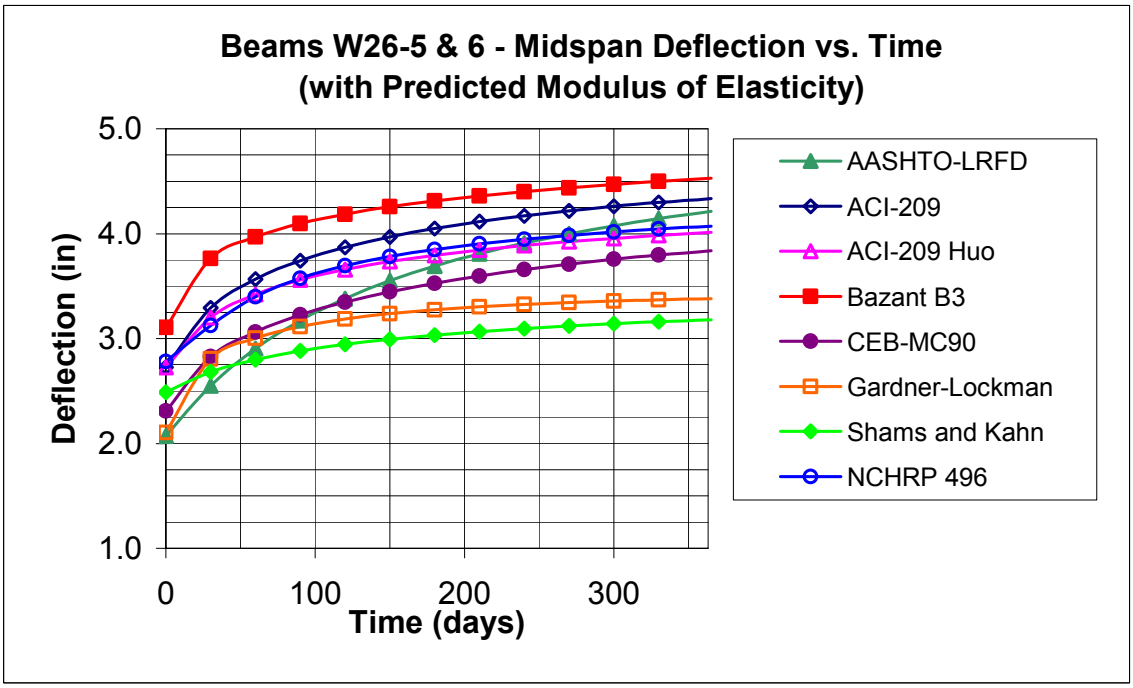

Figure B.2 Beams W26-5 & 6, Predicted Deflection vs. Time (Predicted E)

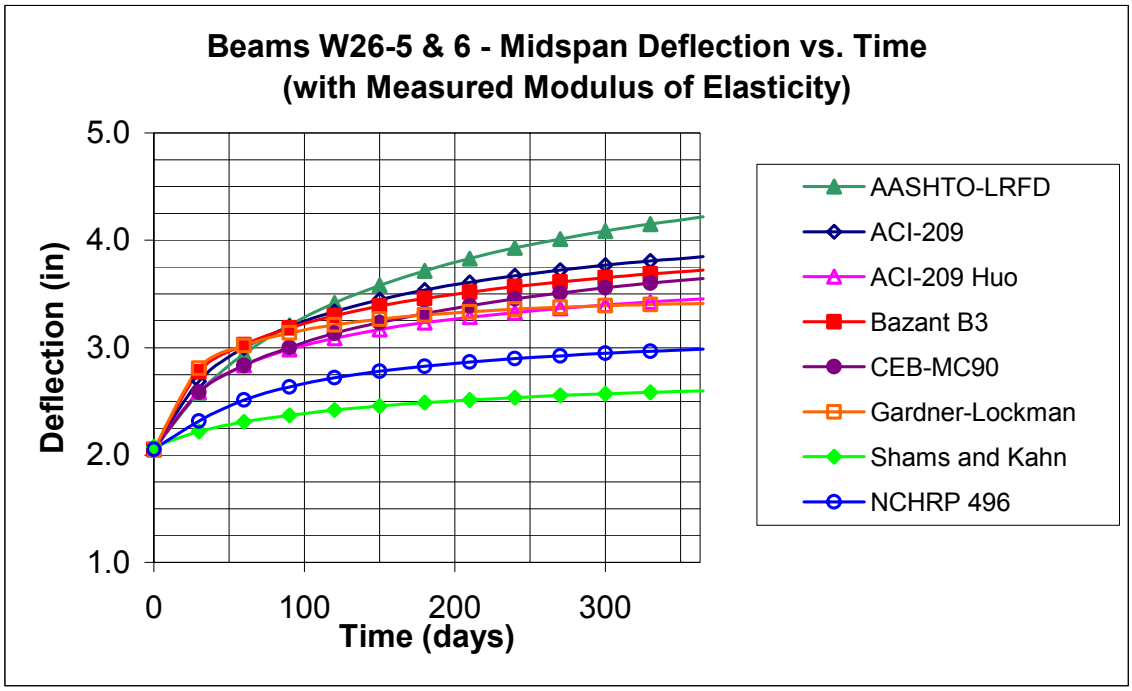

Figure B.3 Beams W26-5 & 6, Predicted Deflection vs. Time (Measured E)

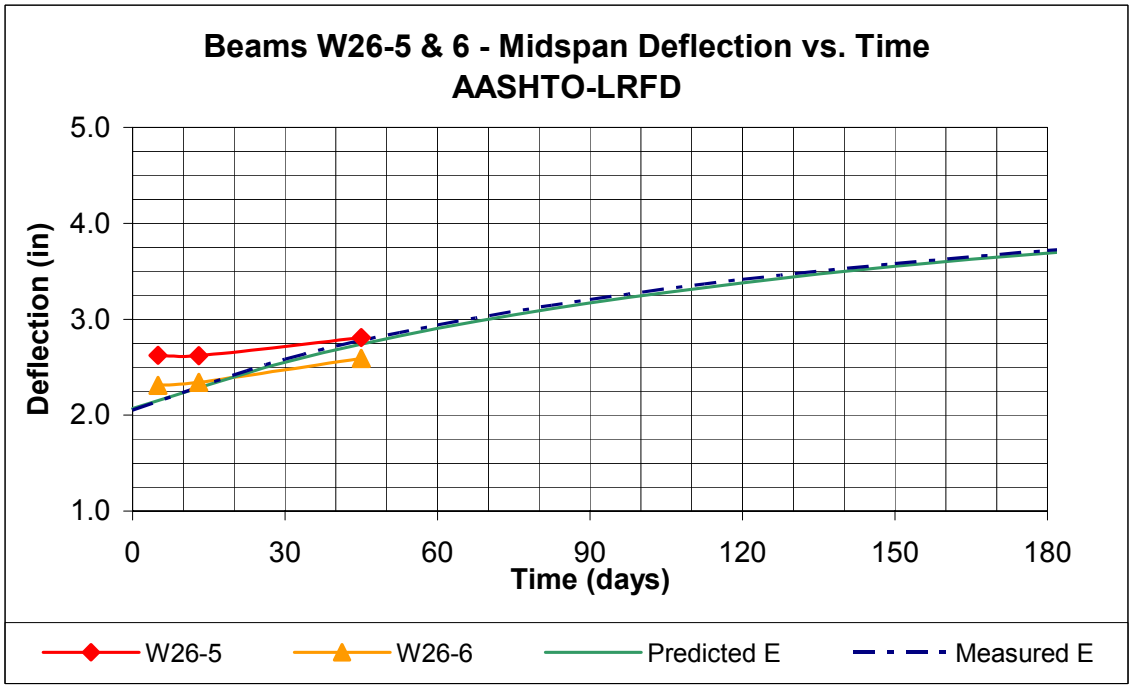

Figure B.4 Beams W26-5 & 6 AASHTO-LRFD Predicted Deflection vs. Time

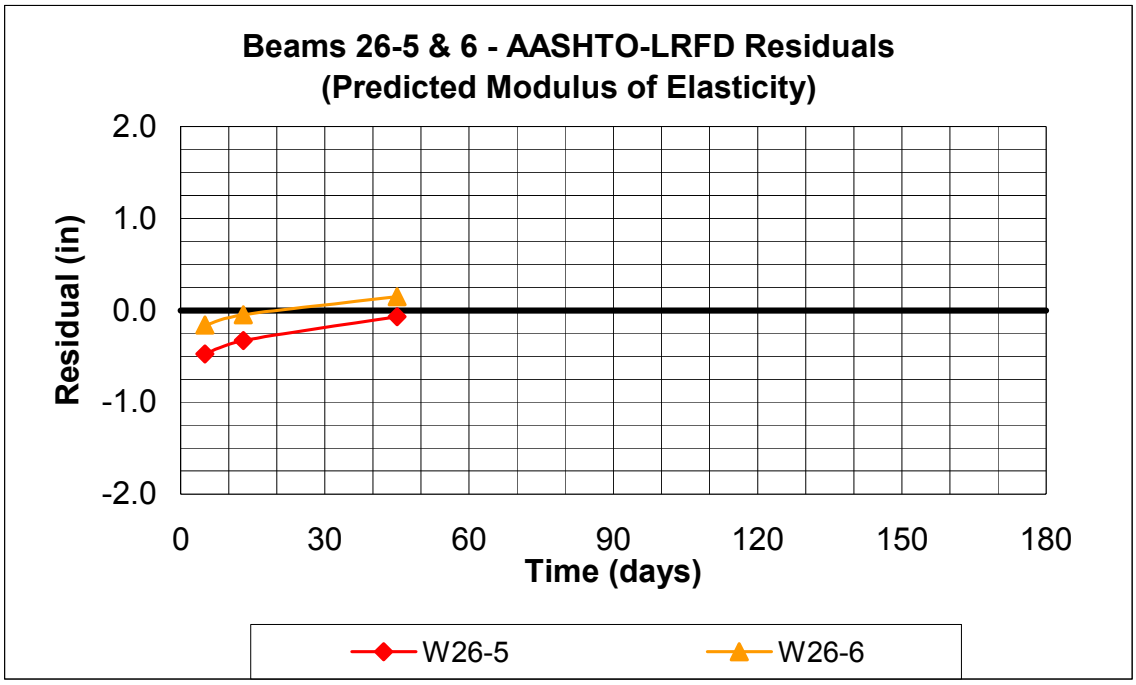

Figure B.5 Beams W26-5 & 6 AASHTO-LRFD Residuals (Predicted Modulus of Elasticity)

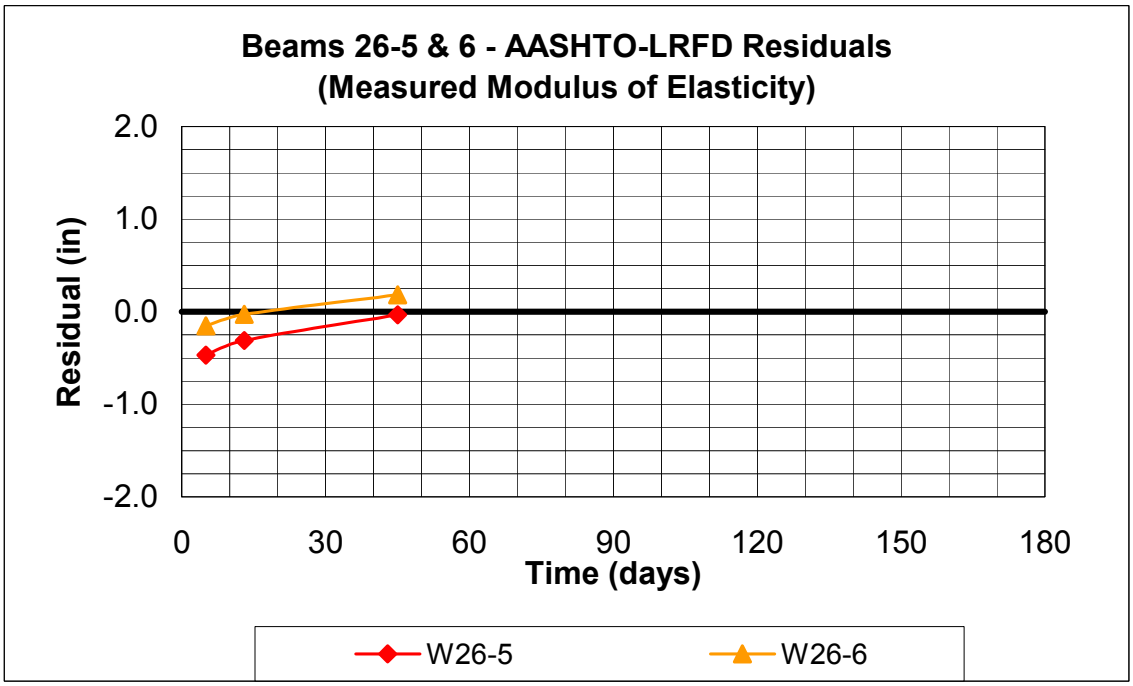

Figure B.6 Beams W26-5 & 6 AASHTO-LRFD Residuals (Measured Modulus of Elasticity)

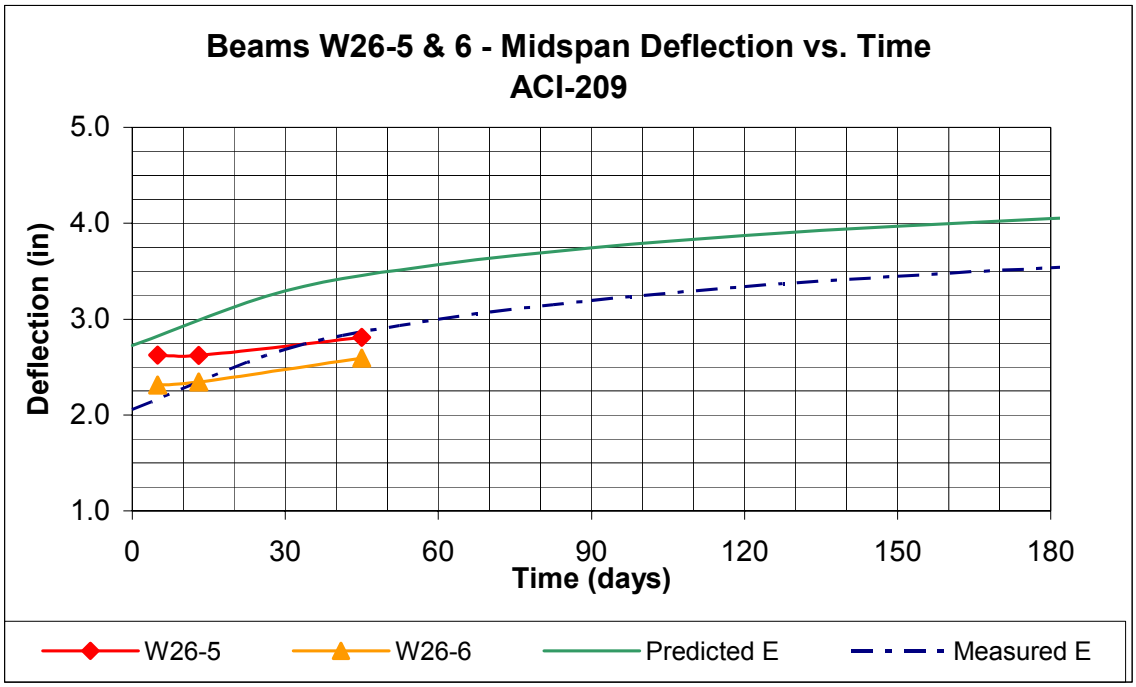

Figure B.7 Beams W26-5 & 6 ACI-209 Predicted Deflection vs. Time

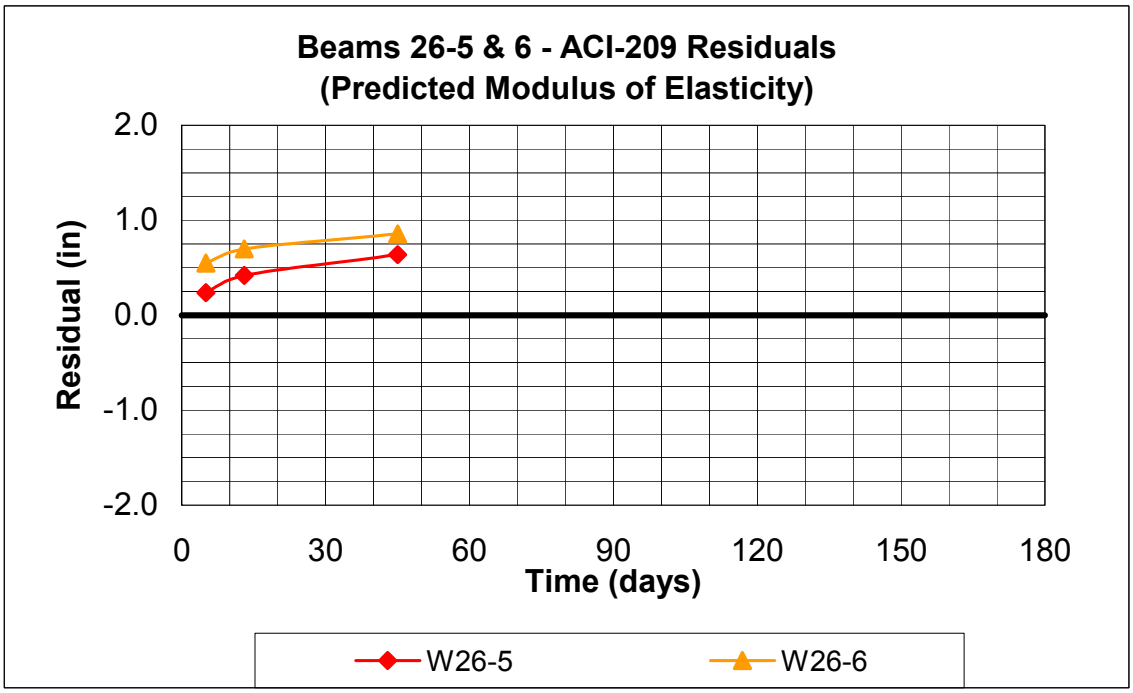

Figure B.8 Beams W26-5 & 6 ACI-209 Residuals (Predicted Modulus of Elasticity)

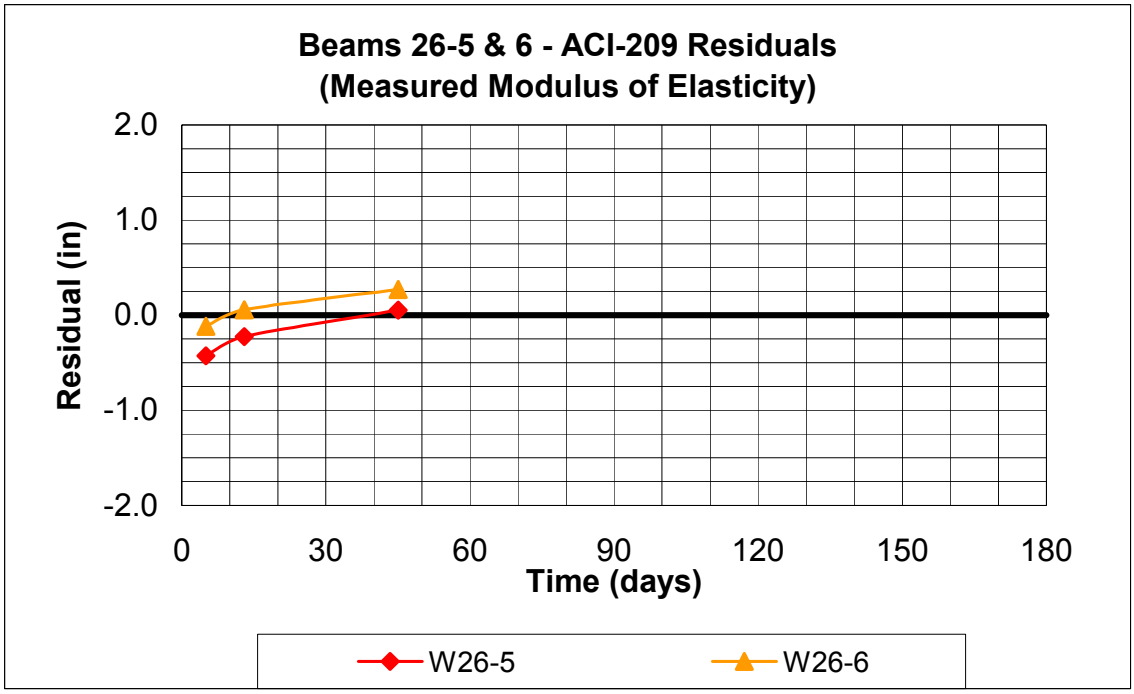

Figure B.9 Beams W26-5 & 6 ACI-209 Residuals (Measured Modulus of Elasticity)

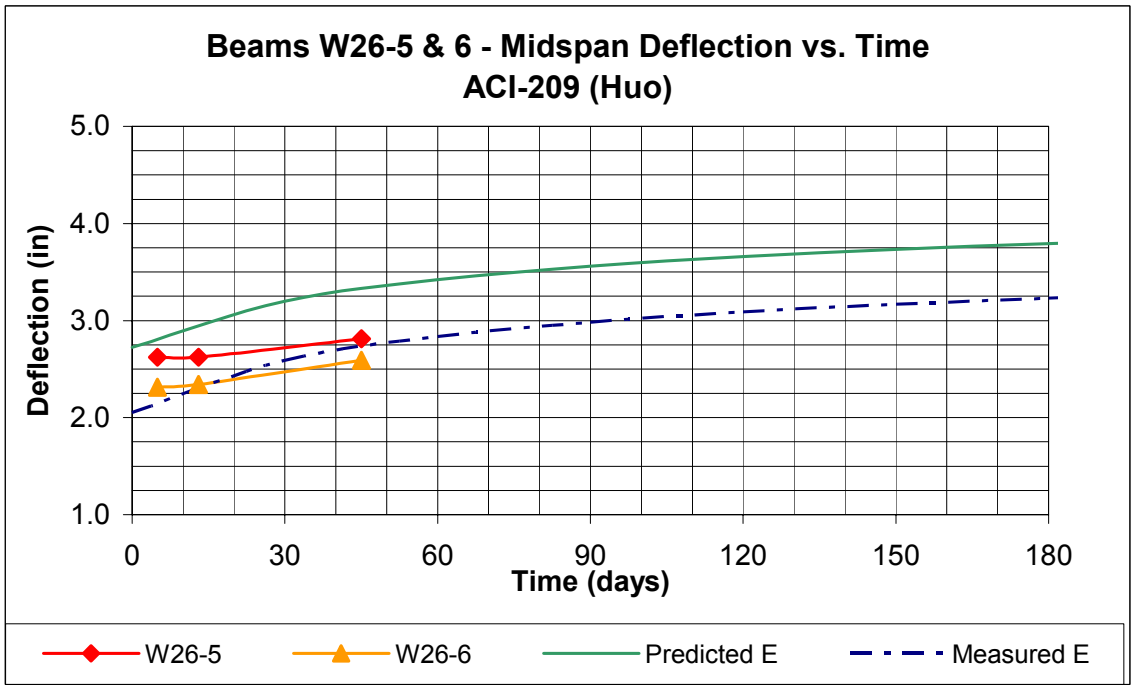

Figure B.10 Beams W26-5 & 6 ACI-209 (Huo) Predicted Deflection vs. Time

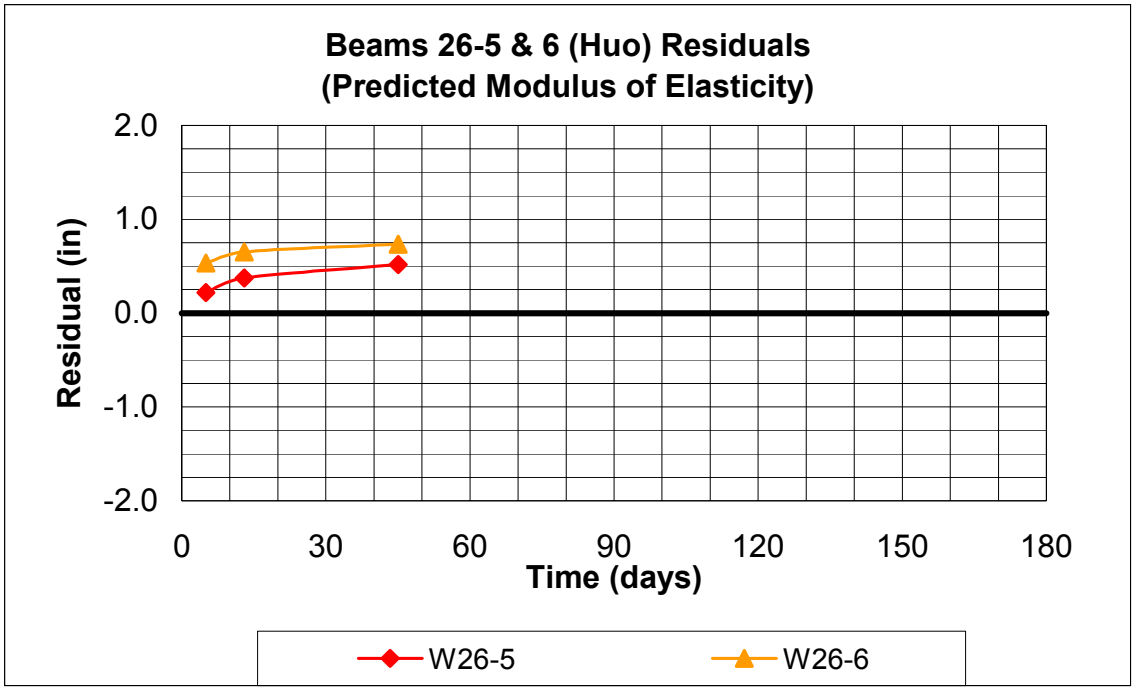

Figure B.11 Beams W26-5 & 6 ACI-209 (Huo) Residuals (Predicted Modulus of Elasticity)

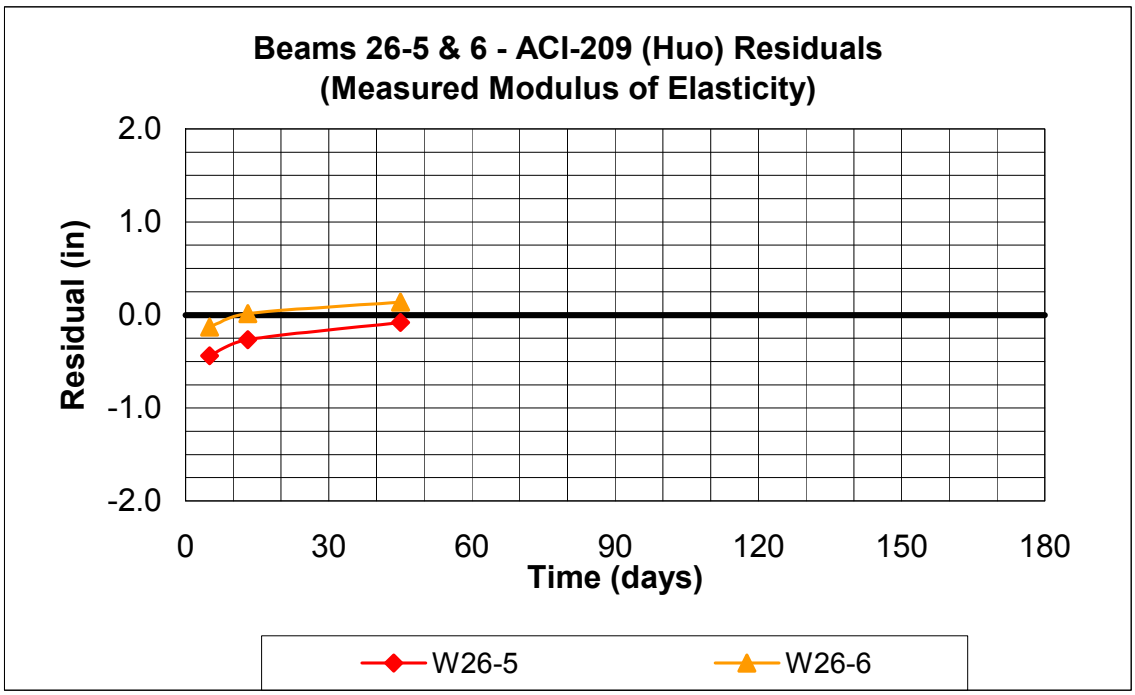

Figure B.12 Beams W26-5 & 6 ACI-209 Residuals (Measured Modulus of Elasticity)

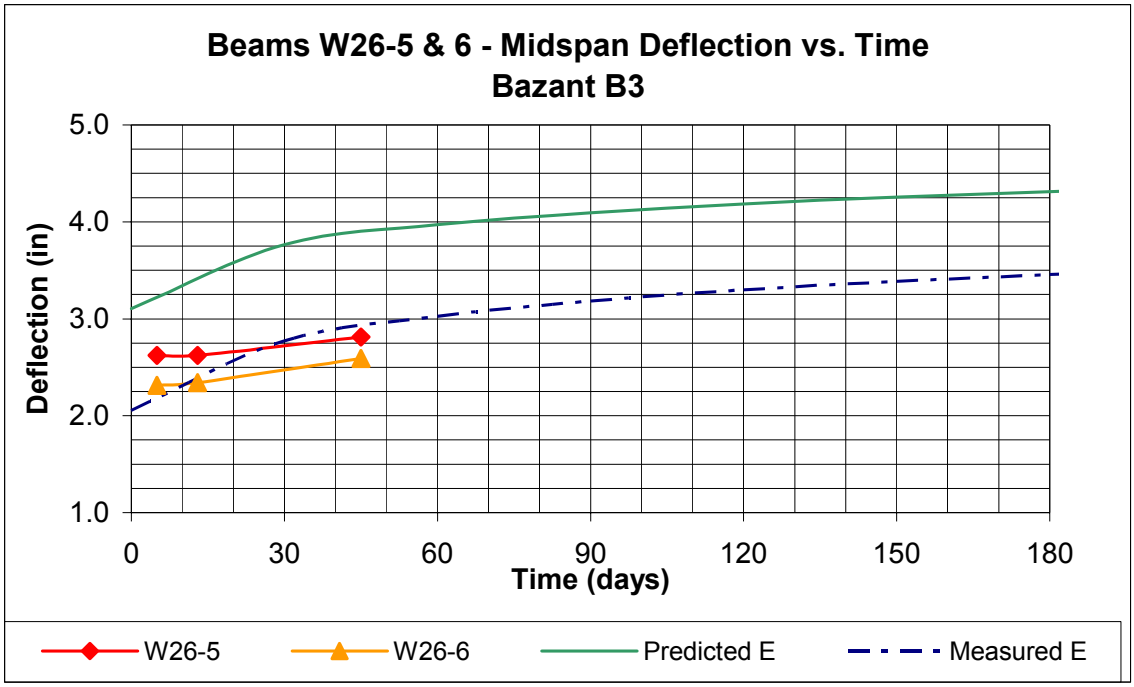

Figure B.13 Beams W26-5 & 6 Bazant B3 Predicted Deflection vs. Time

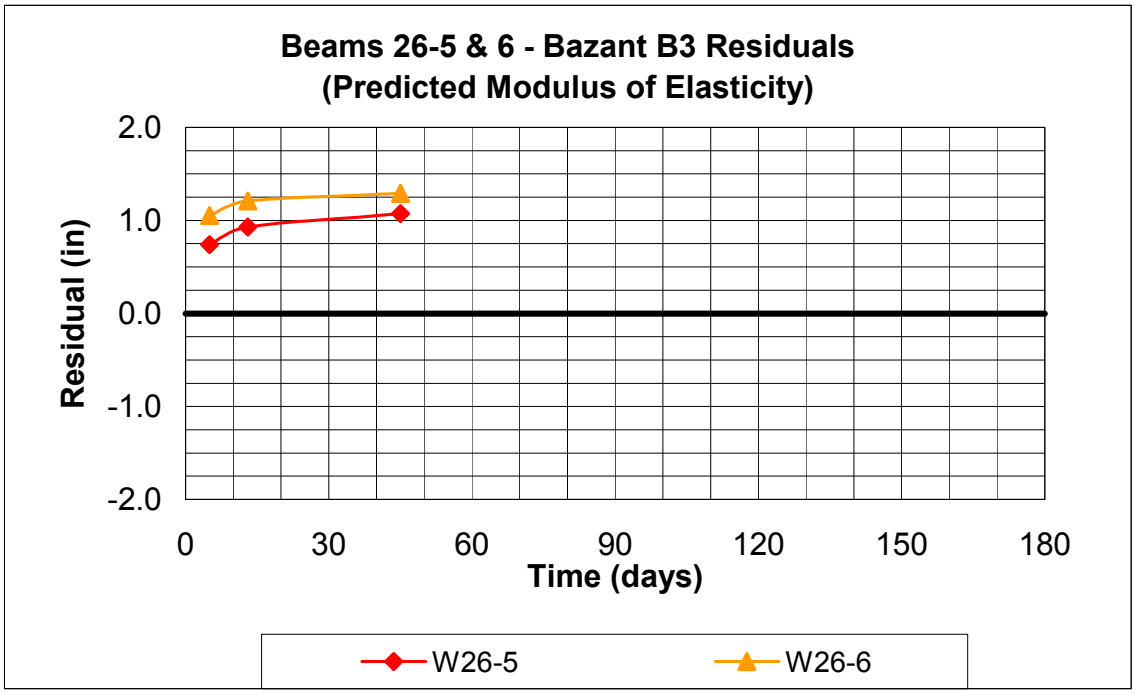

Figure B.14 Beams W26-5 & 6 Bazant B3 Residuals (Predicted Modulus of Elasticity)

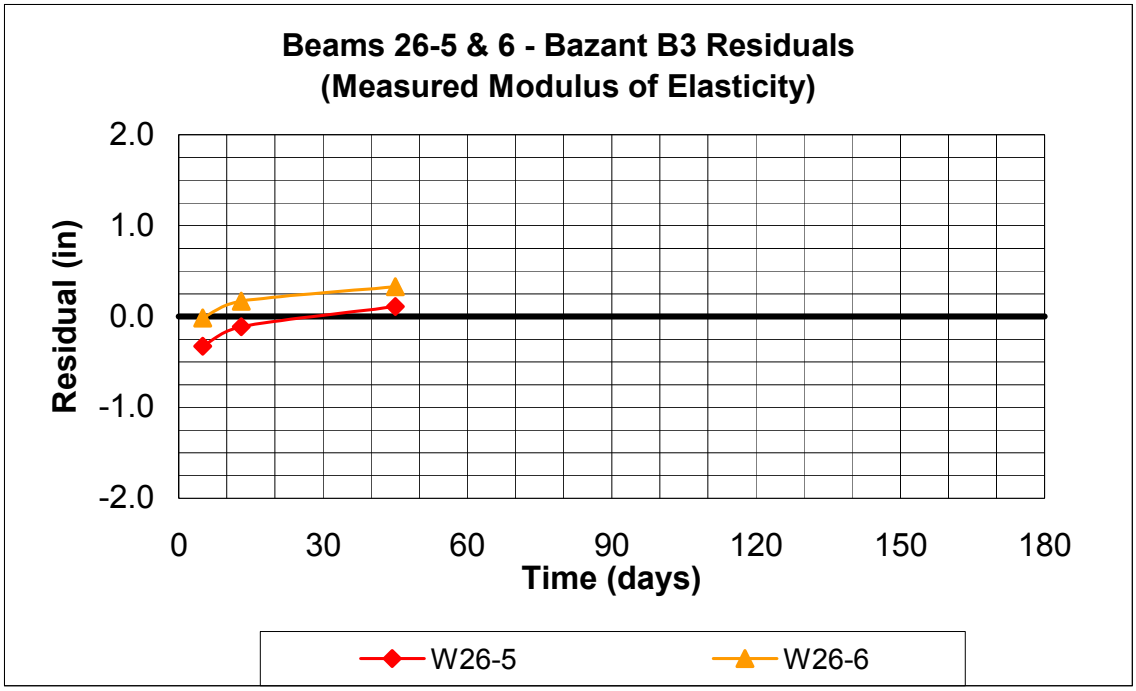

Figure B.15 Beams W26-5 & 6 Bazant B3 Residuals (Measured Modulus of Elasticity)

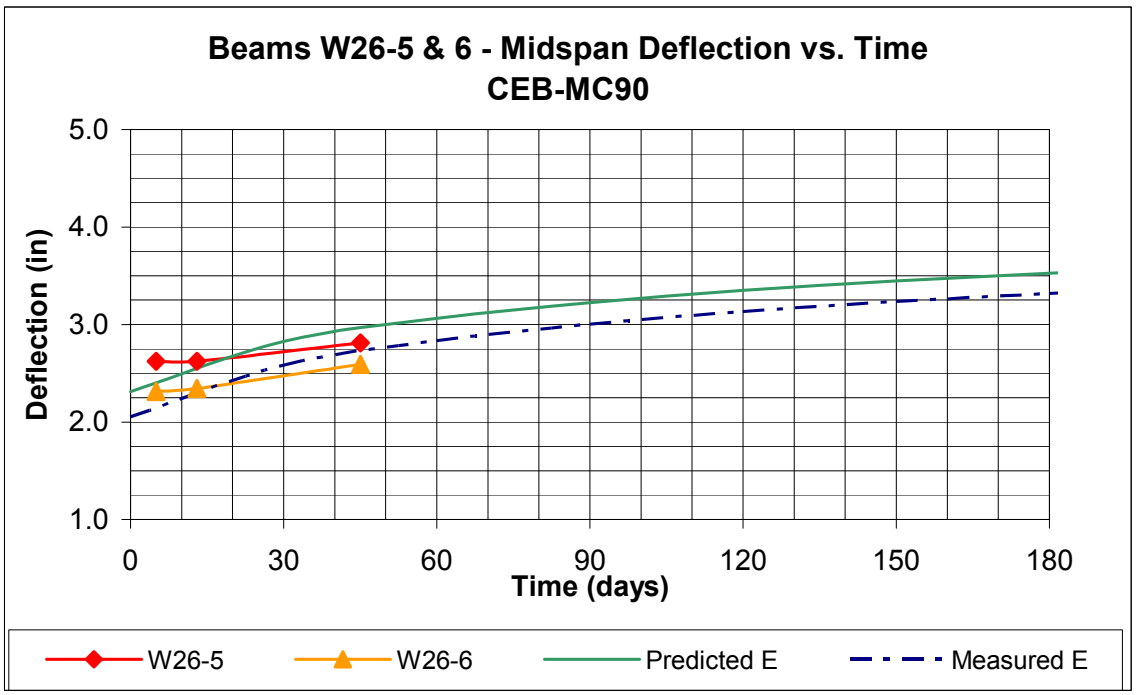

Figure B.16 Beams W26-5 & 6 CEB-MC90 Predicted Deflection vs. Time

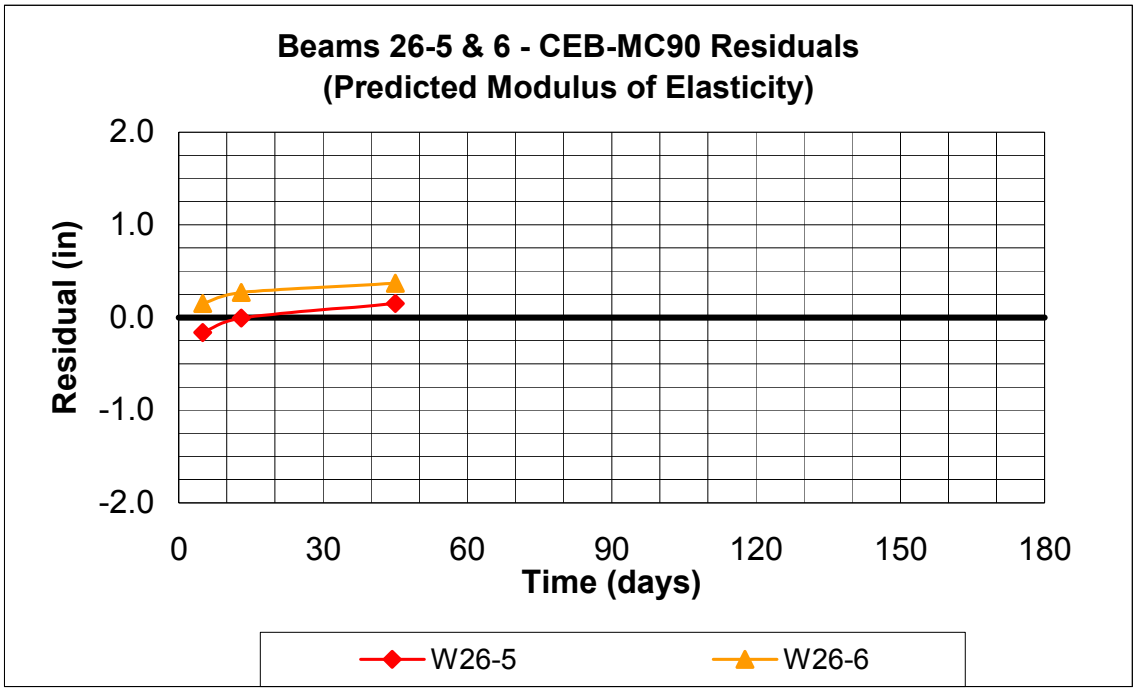

Figure B.17 Beams W26-5 & 6 CEB-MC90 Residuals (Predicted Modulus of Elasticity)

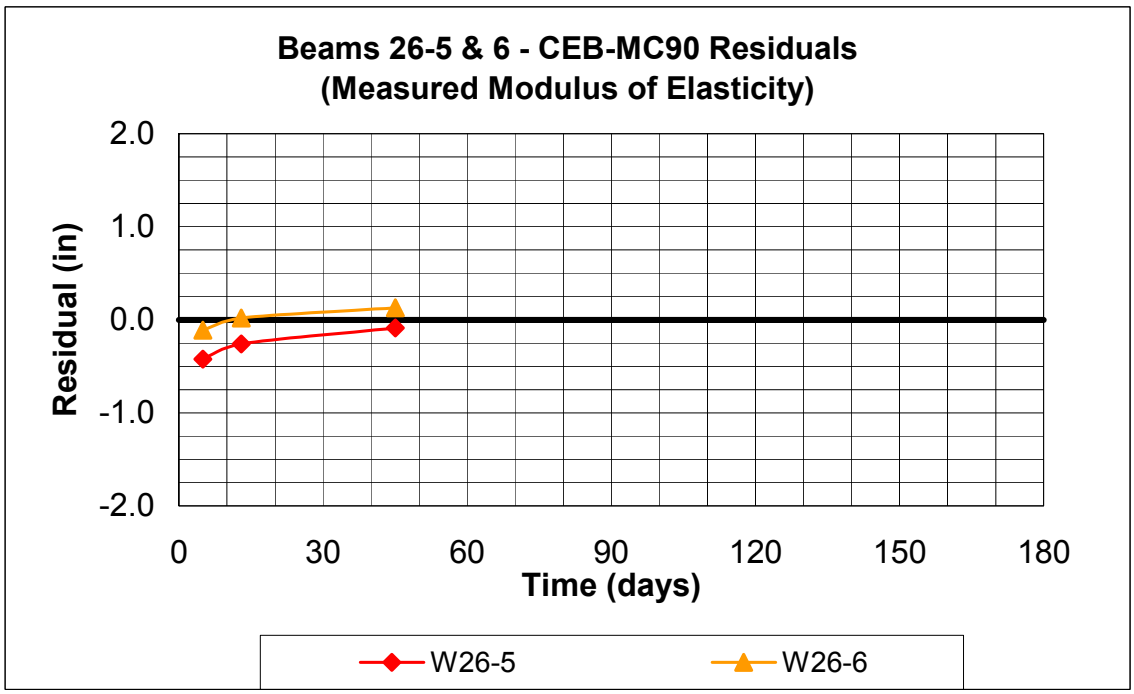

Figure B.18 Beams W26-5 & 6 CEB-MC90 Residuals (Measured Modulus of Elasticity)

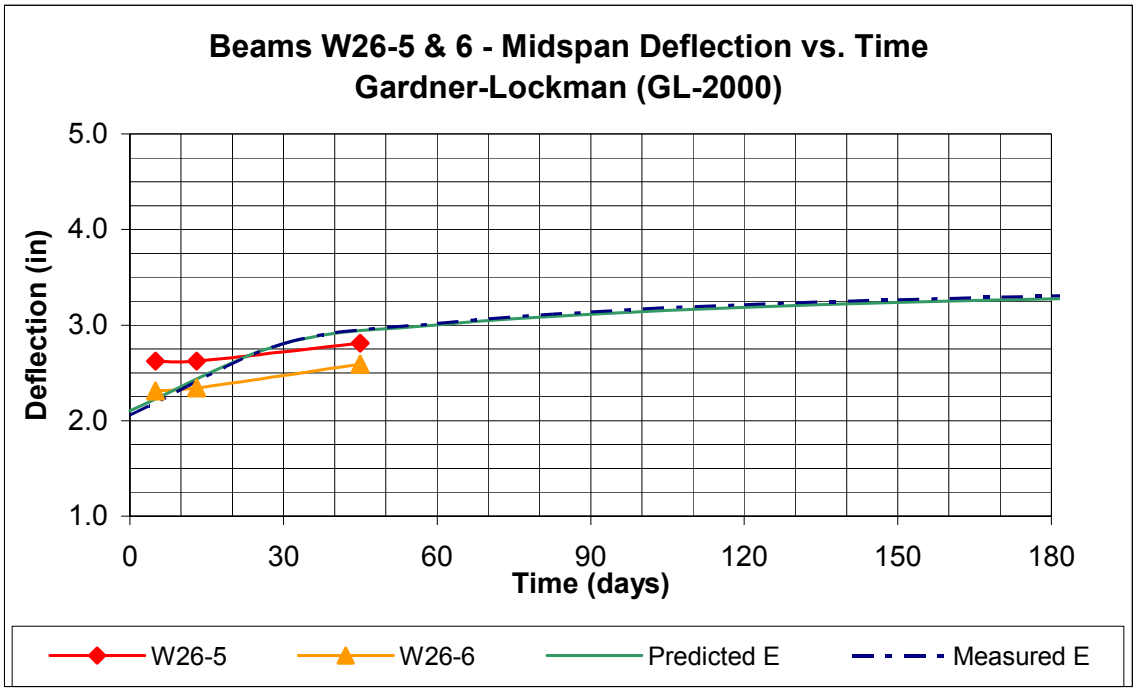

Figure B.19 Beams W26-5 & 6 GL-2000 Predicted Deflection vs. Time

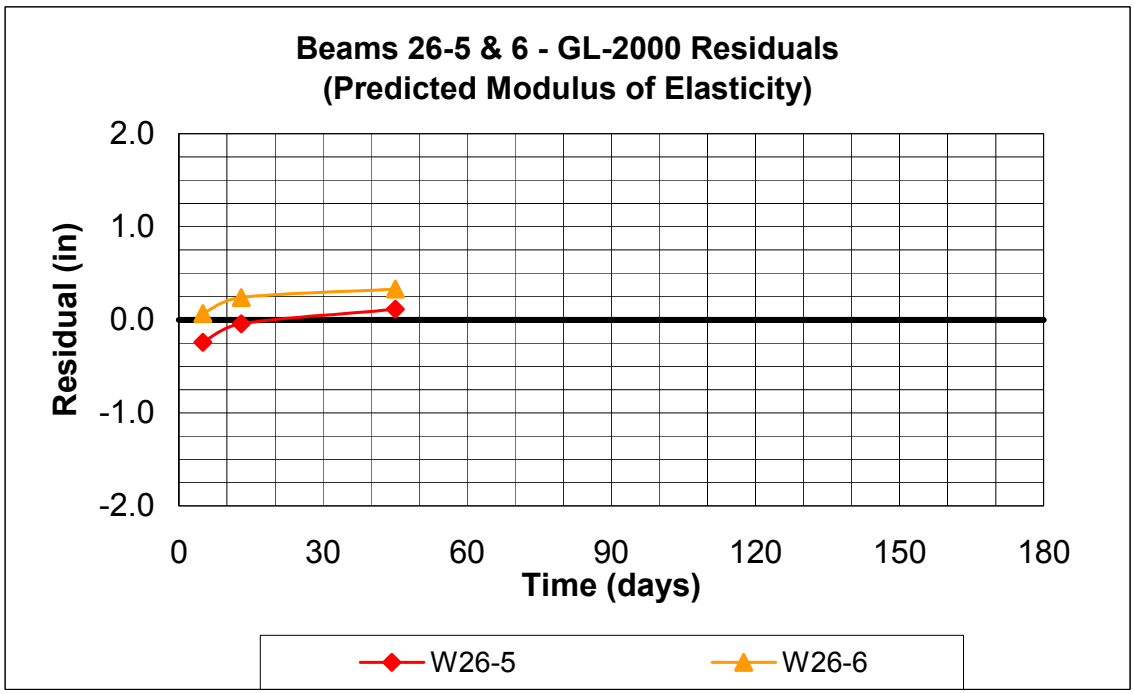

Figure B.20 Beams W26-5 & 6 GL-2000 Residuals (Predicted Modulus of Elasticity)

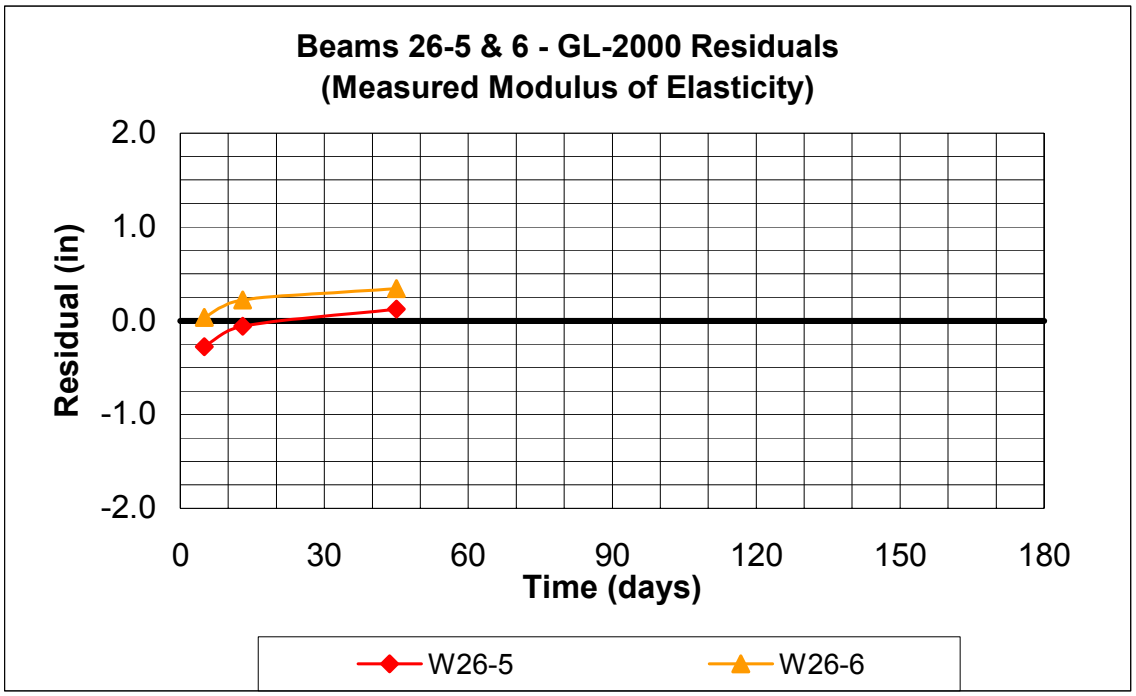

Figure B.21 Beams W26-5 & 6 GL-2000 Residuals (Measured Modulus of Elasticity)

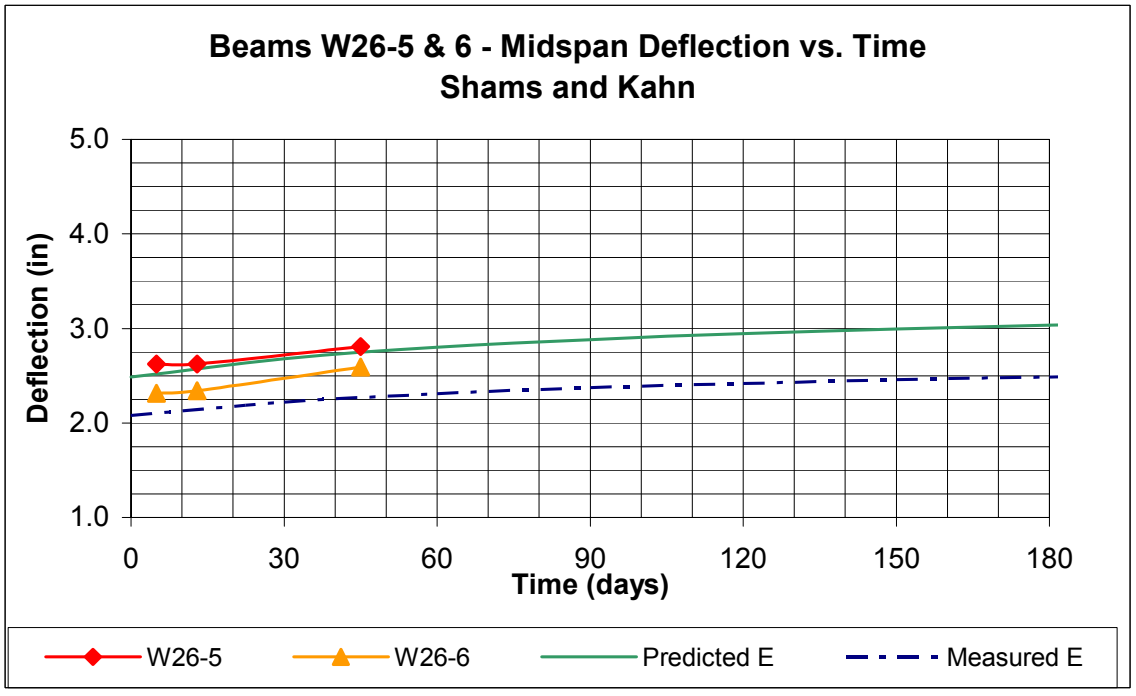

Figure B.22 Beams W26-5 & 6 Kahn & Shams Predicted Deflection vs. Time

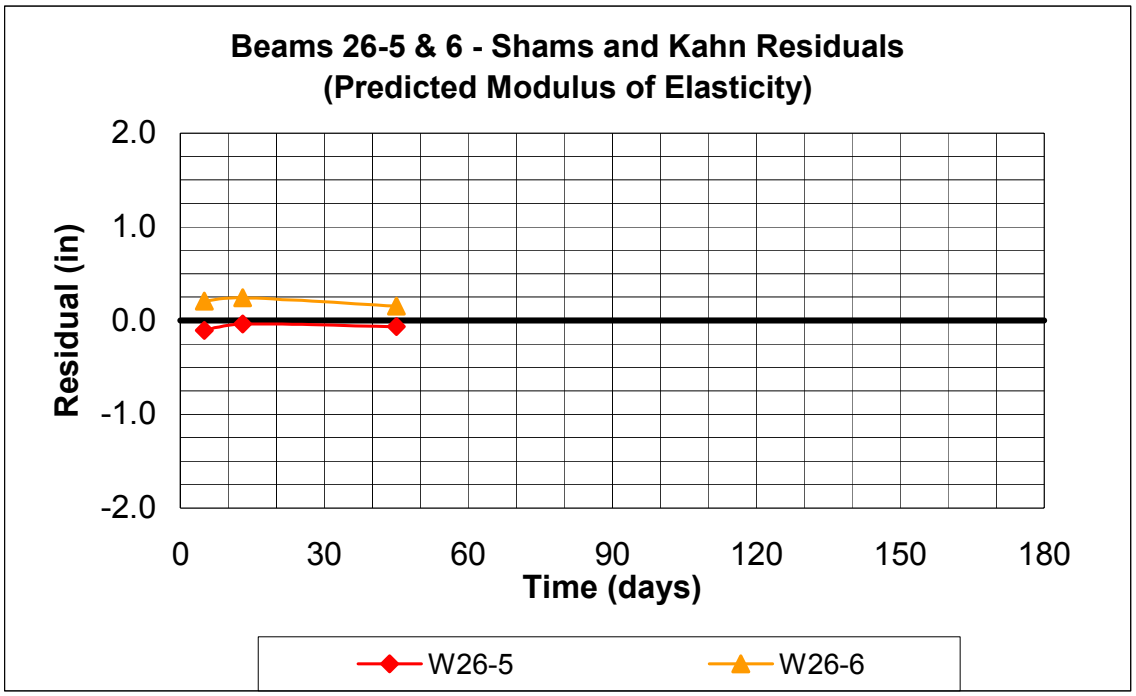

Figure B.23 Beams W26-5 & 6 Kahn & Shams Residuals (Predicted Modulus of Elasticity)

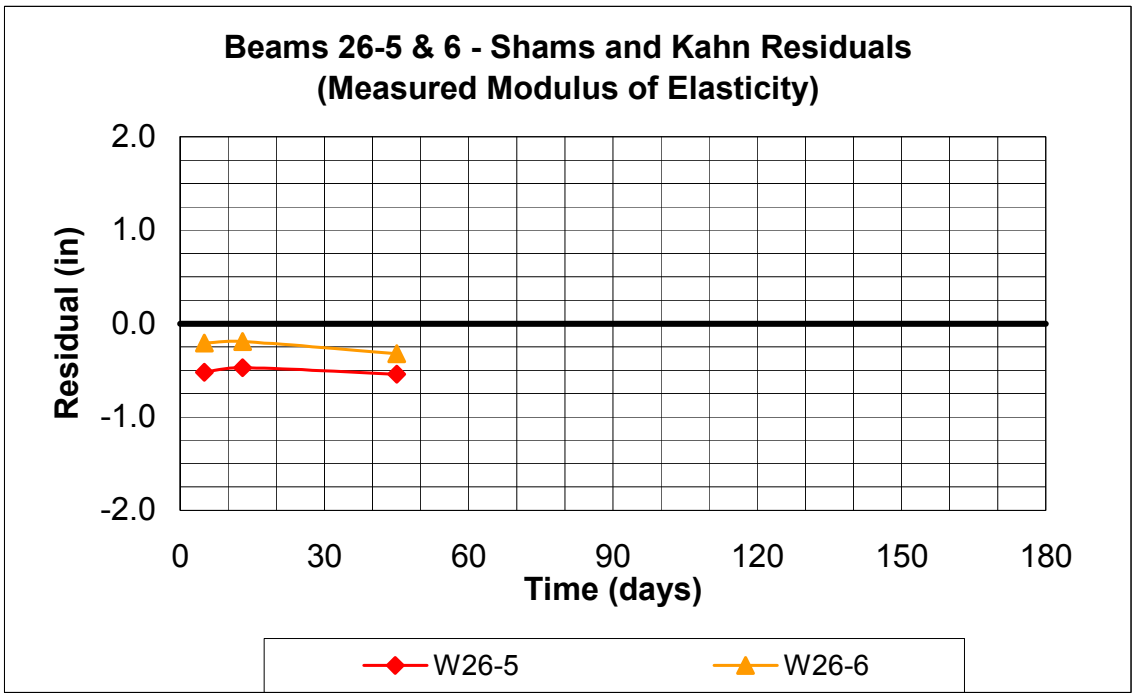

Figure B.24 Beams W26-5 & 6 Kahn & Shams Residuals (Measured Modulus of Elasticity)

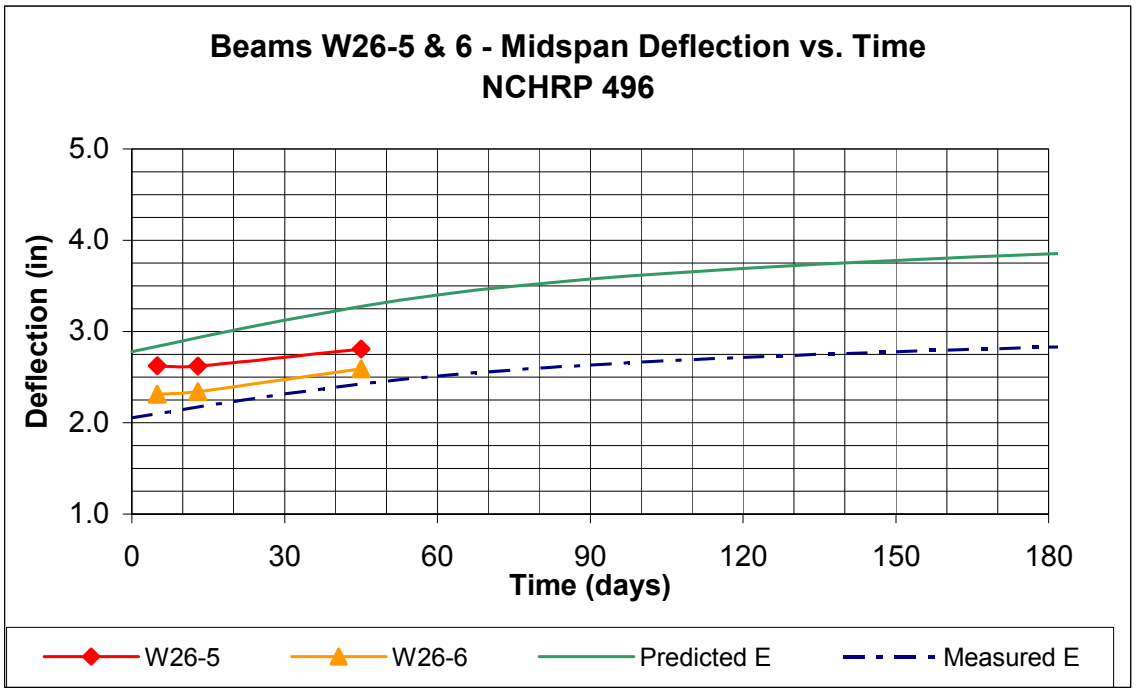

Figure B.25 Beams W26-5 & 6 NCHRP 496 Predicted Deflection vs. Time

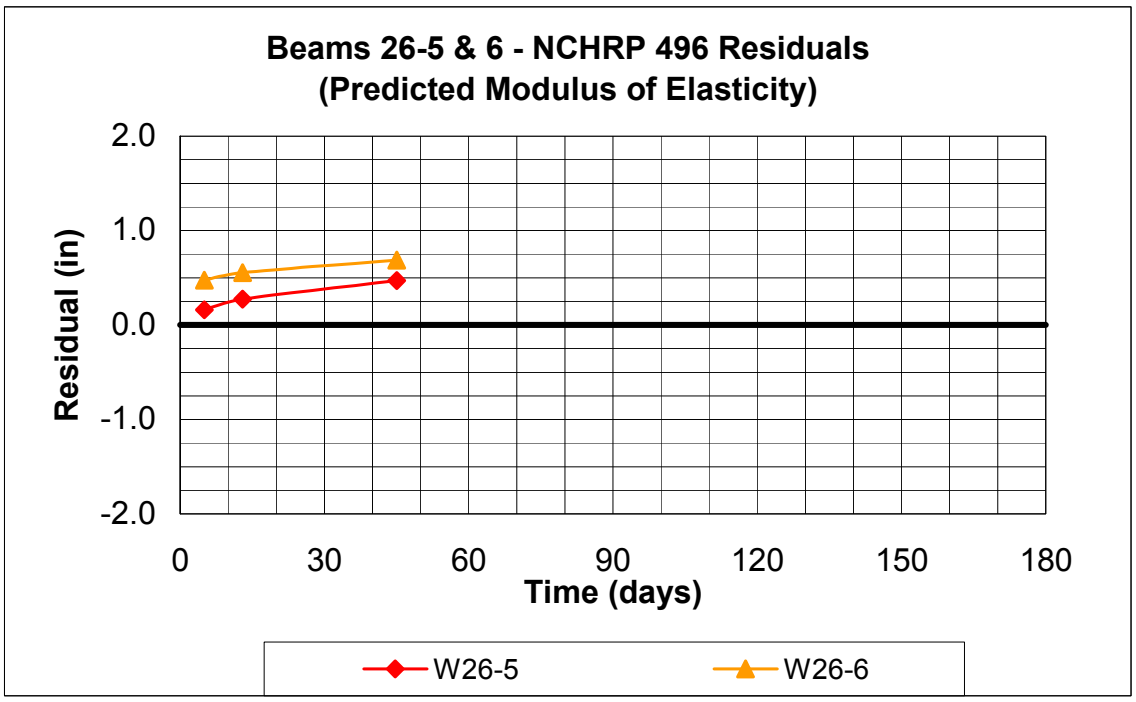

Figure B.26 Beams W26-5 & 6 NCHRP 496 Residuals (Predicted Modulus of Elasticity)

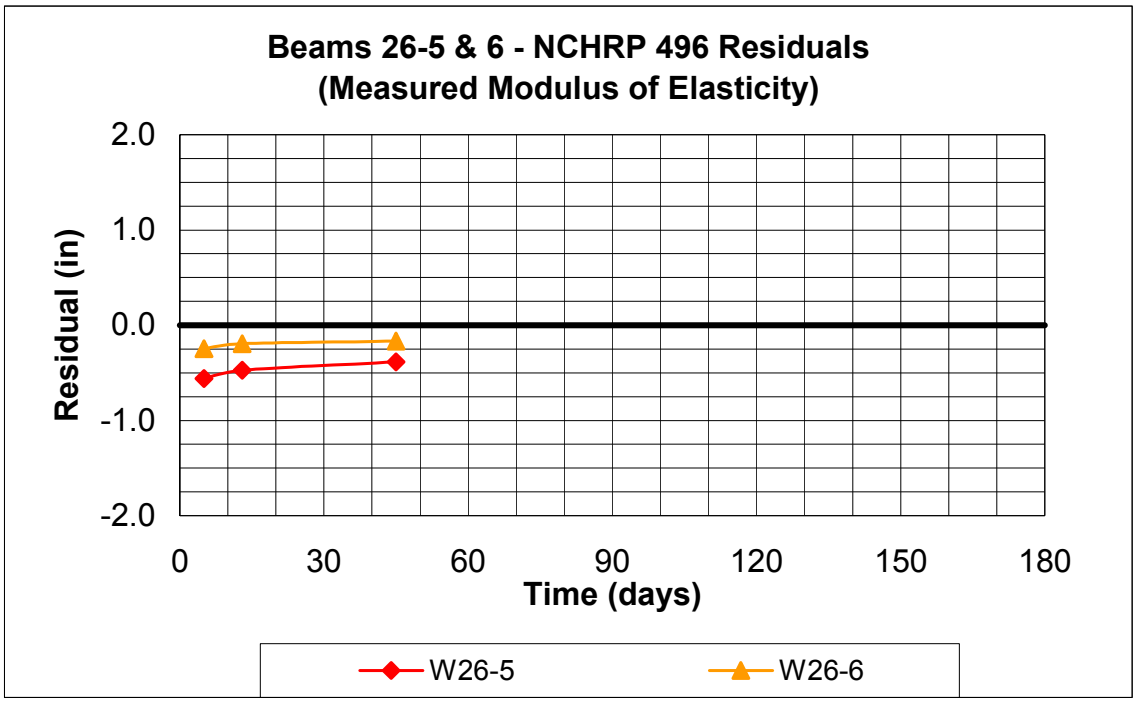

Figure B.27 Beams W26-5 & 6 NCHRP 496 Residuals (Measured Modulus of Elasticity)

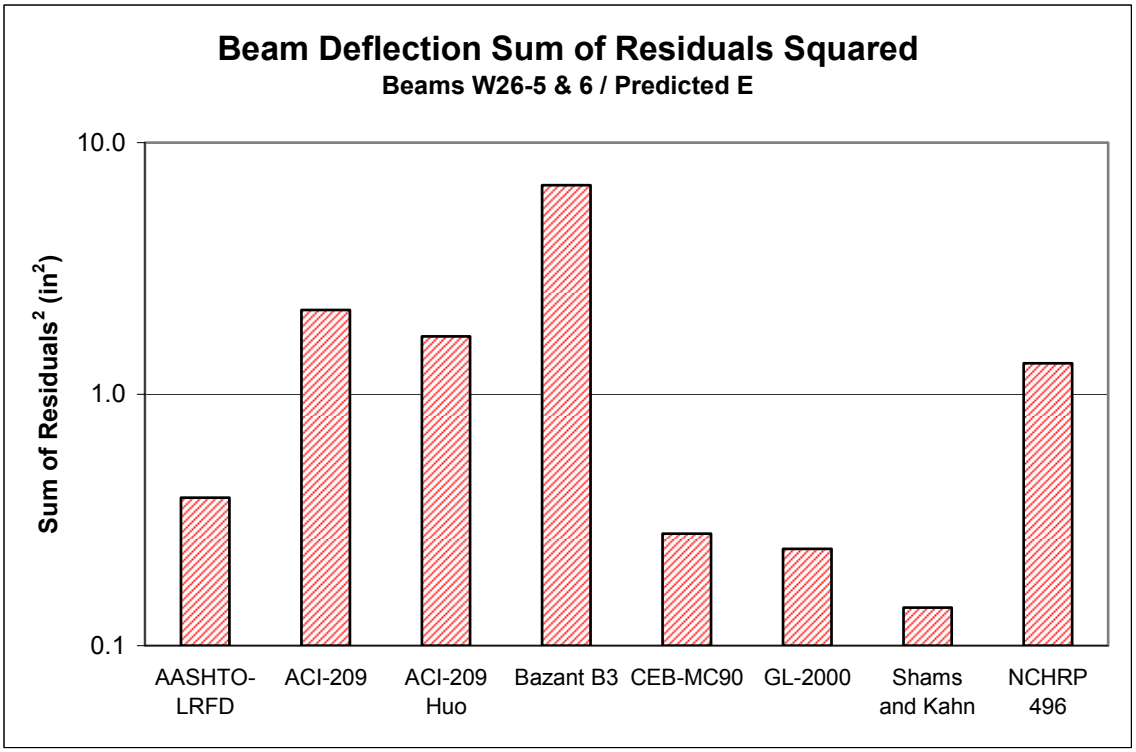

Figure B.28 Beams W26-5 & 6 Deflection Sum of Residuals Squared, Predicted E

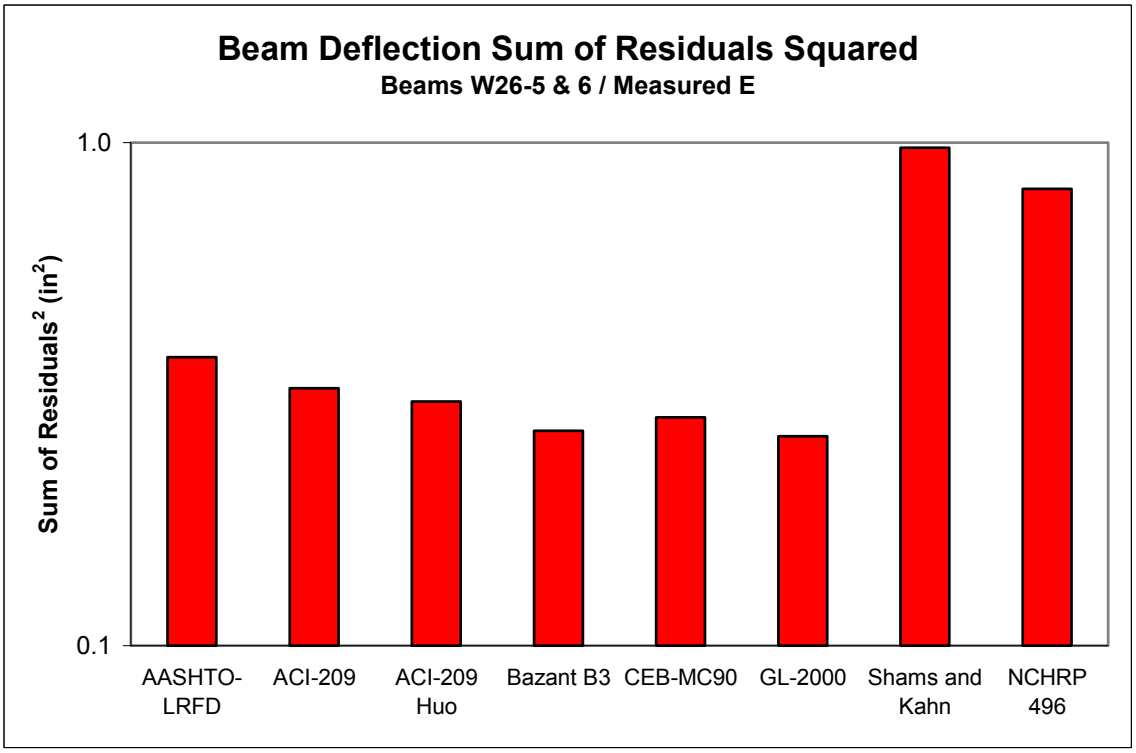

Figure B.29 Beams W26-5 & 6 Deflection Sum of Residuals Squared, Measured E

Table B.1 Beams W26-5 & 6 Model Ranking with Predicted E

Rank	Model
1	**Shams and Kahn**
2	CEB-MC90
3	NCHRP 496
4	AASHTO-LRFD
5	ACI-209
6	ACI-209, modified by Huo
7	GL-2000
8	Bazant B3

Table B.2 Beams W26-5 & 6 Model Ranking with Measured E

Rank	Model
1	**Bazant B3**
2	CEB-MC90
3	ACI-209
4	ACI-209, modified by Huo
5	AASHTO-LRFD
6	NCHRP 496
7	Shams and Kahn
8	GL-2000

B.2 Additional Beam W34-6

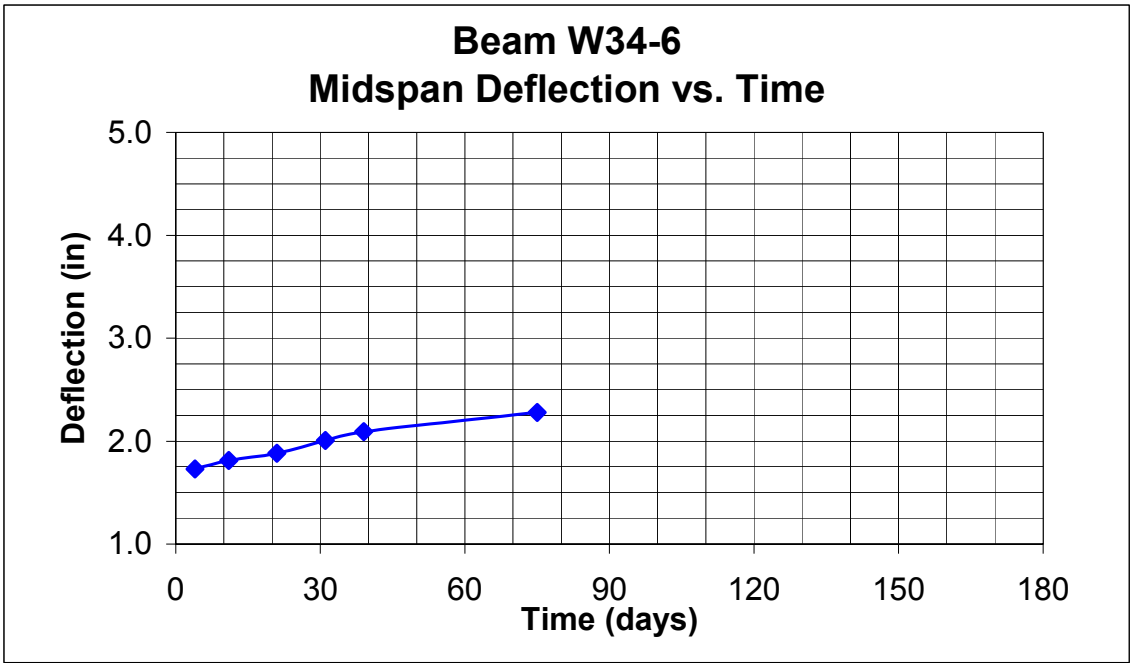

Figure B.30 Beam W34-6, Deflection vs. Time

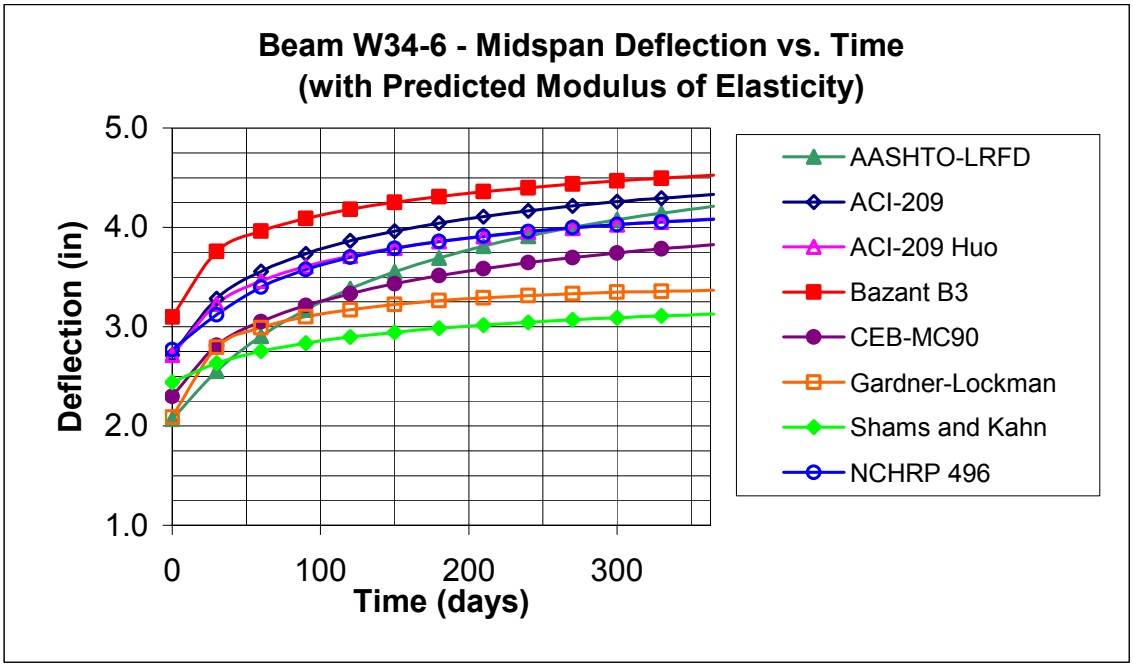

Figure B.31 Beam W34-6, Predicted Deflection vs. Time (Predicted E)

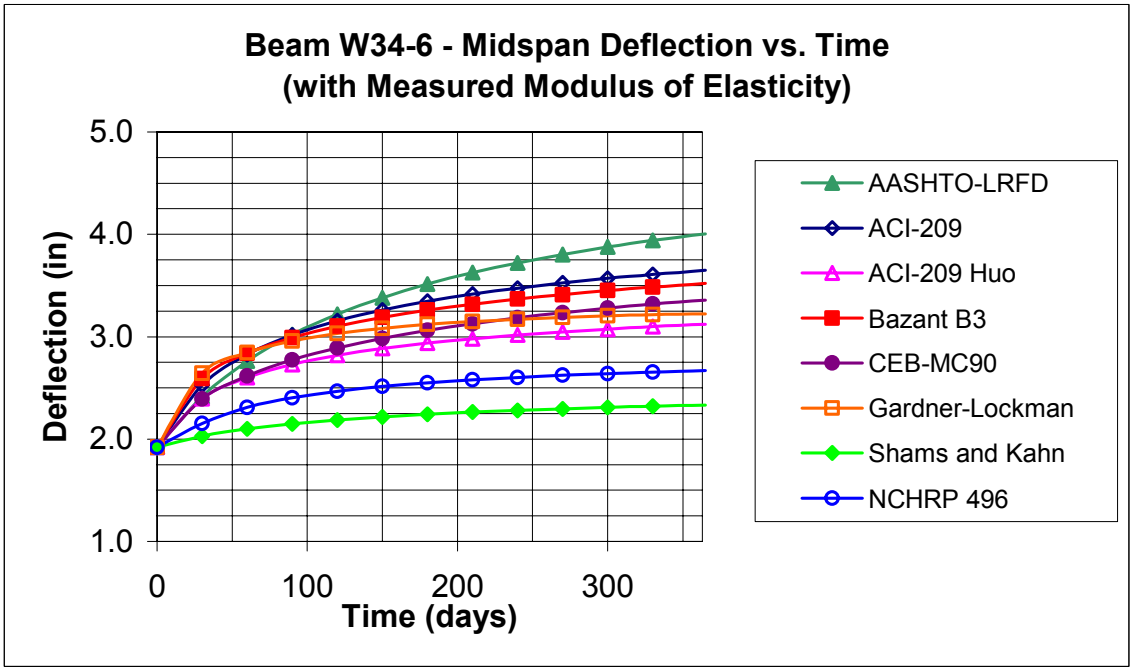

Figure B.32 Beam W34-6, Predicted Deflection vs. Time (Measured E)

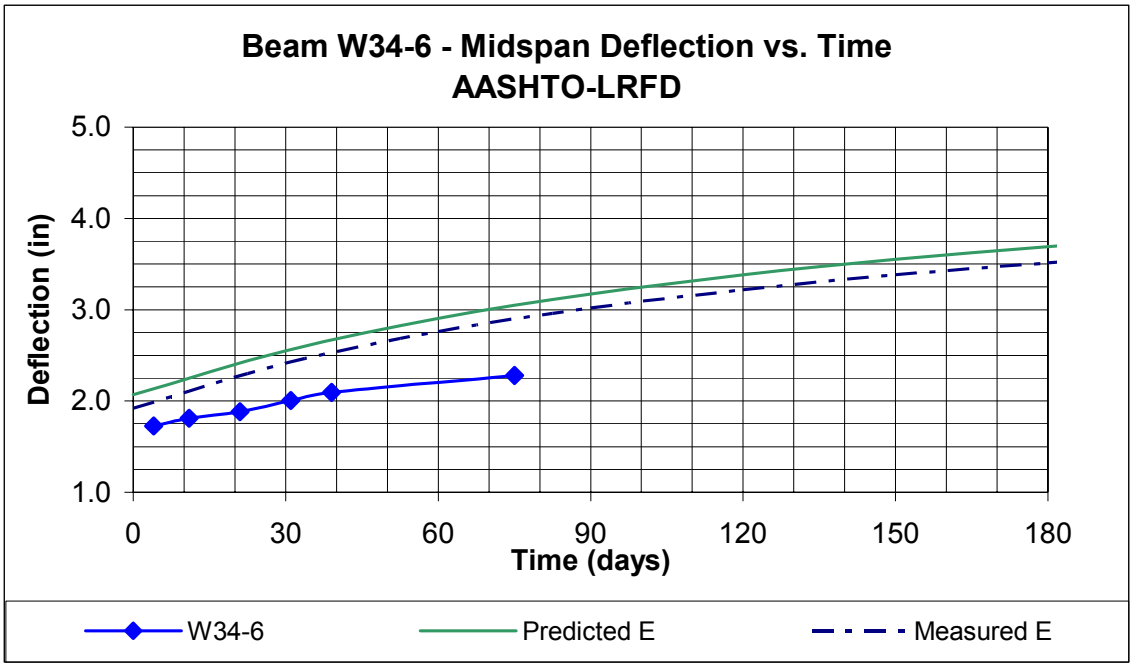

Figure B.33 Beam W34-6 AASHTO-LRFD Predicted Deflection vs. Time

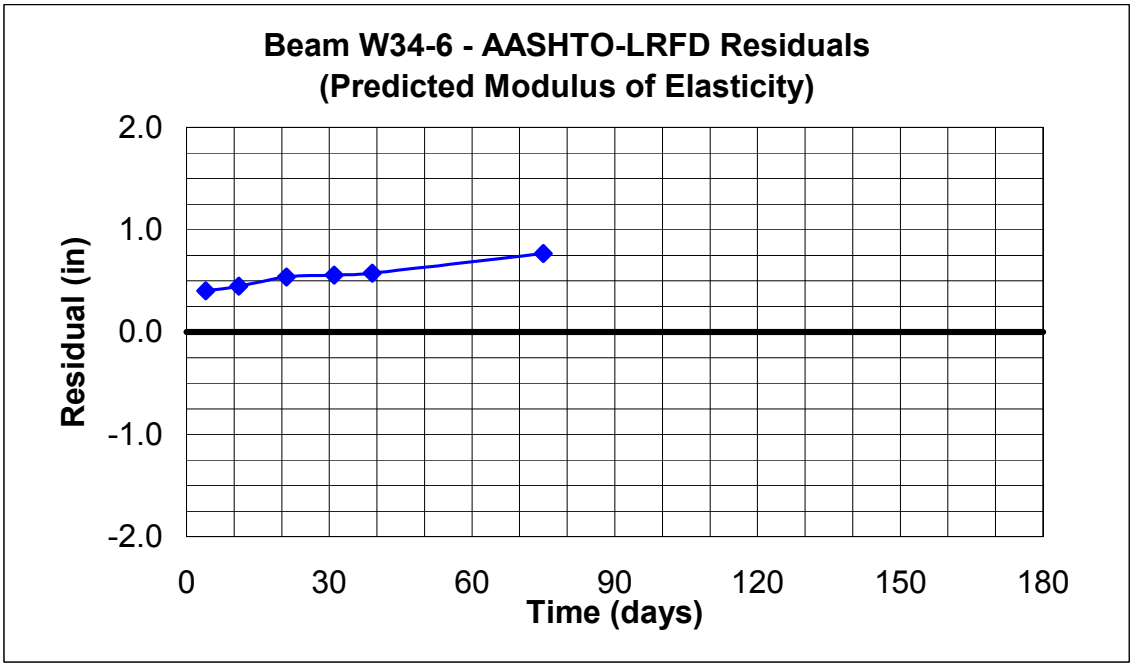

Figure B.34 Beam W34-6 AASHTO-LRFD Residuals (Predicted Modulus of Elasticity)

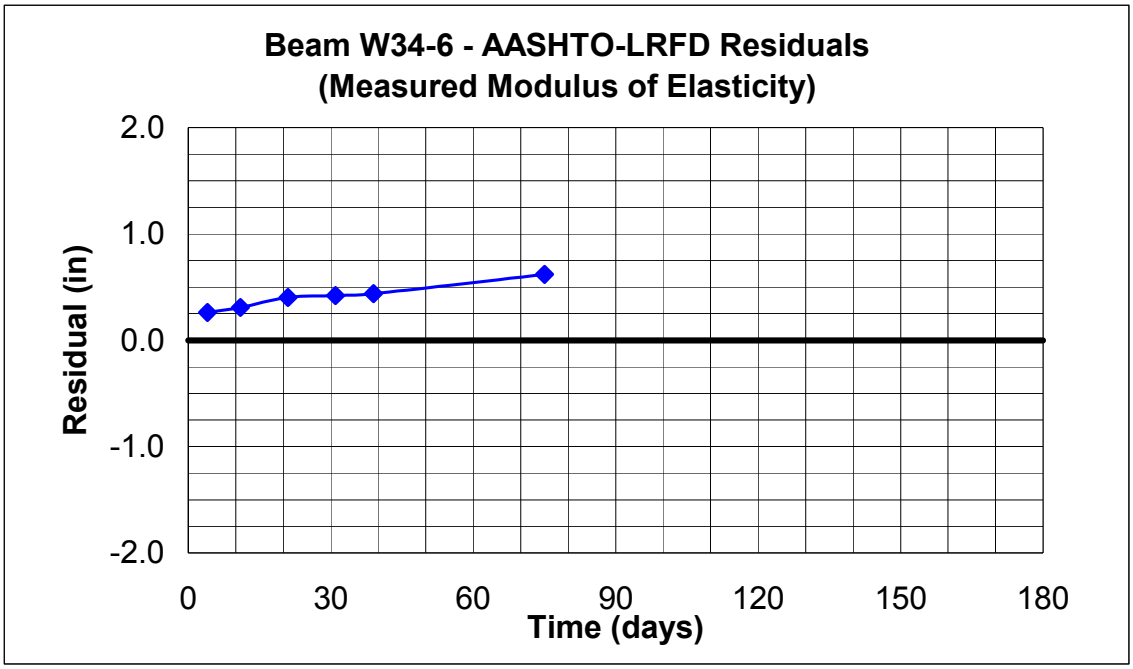

Figure B.35 Beam W34-6 AASHTO-LRFD Residuals (Measured Modulus of Elasticity)

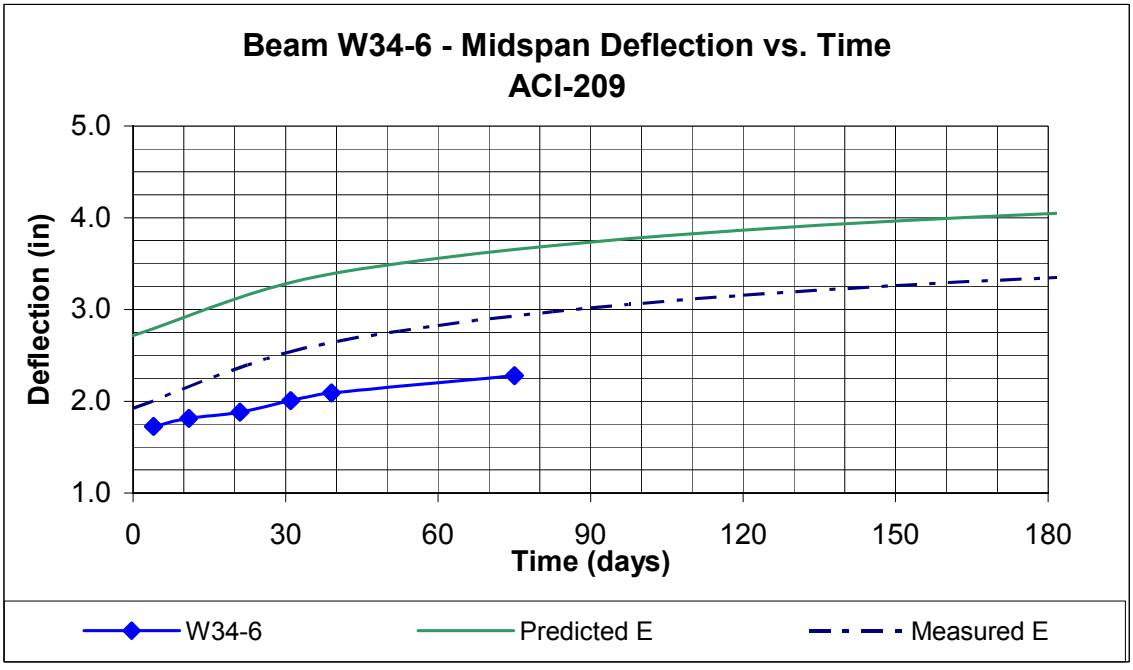

Figure B.36 Beam W34-6 ACI-209 Predicted Deflection vs. Time

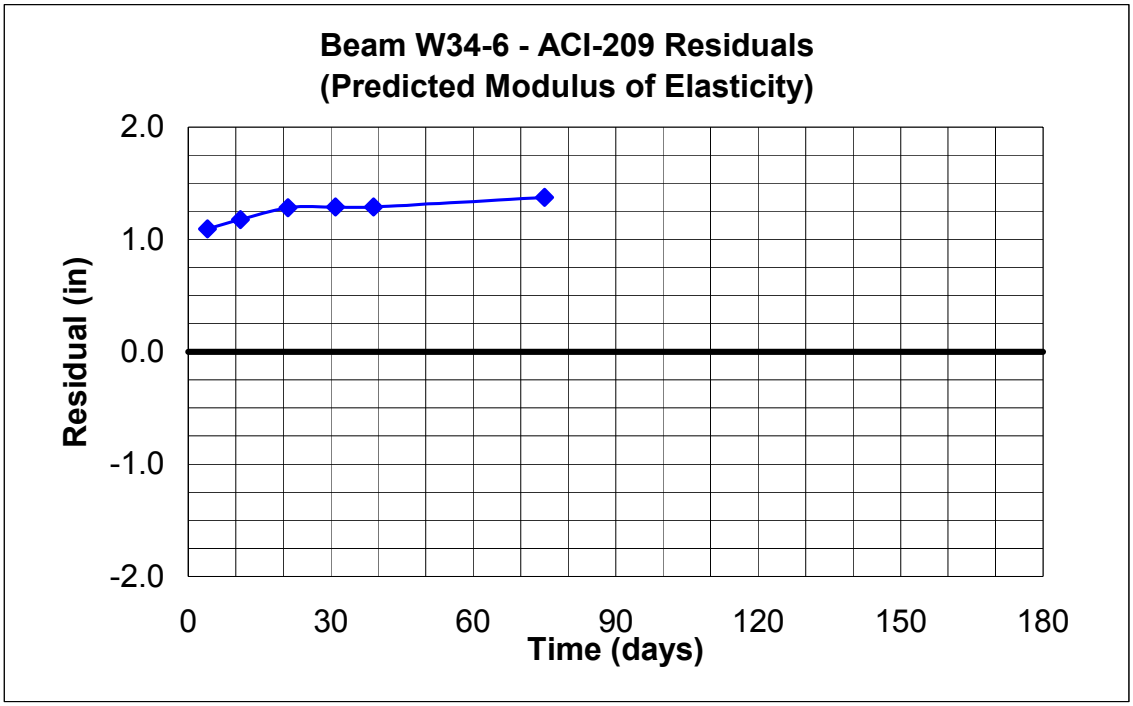

Figure B.37 Beam W34-6 ACI-209 Residuals (Predicted Modulus of Elasticity)

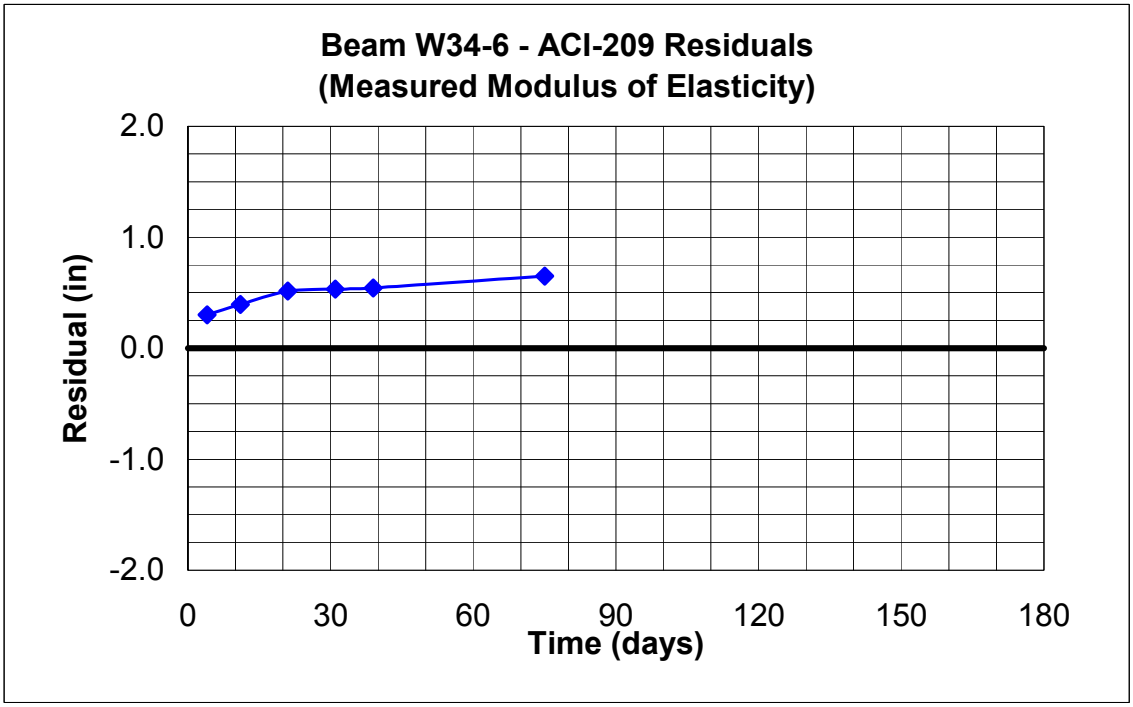

Figure B.38 Beam W34-6 ACI-209 Residuals (Measured Modulus of Elasticity)

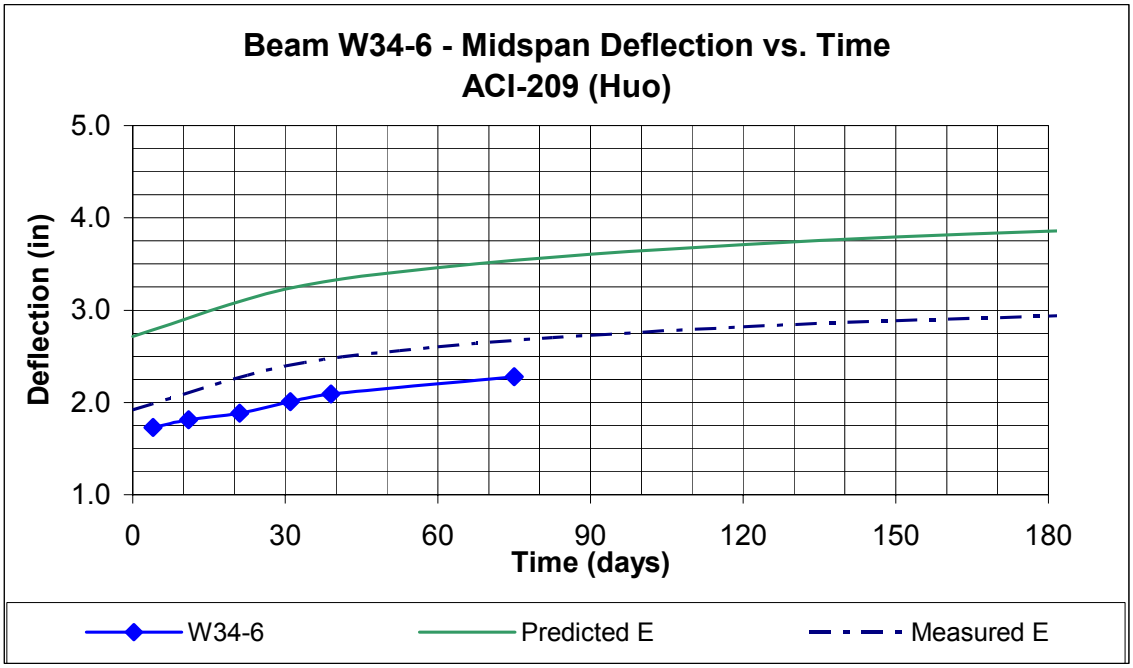

Figure B.39 Beam W34-6 ACI-209 (Huo) Predicted Deflection vs. Time

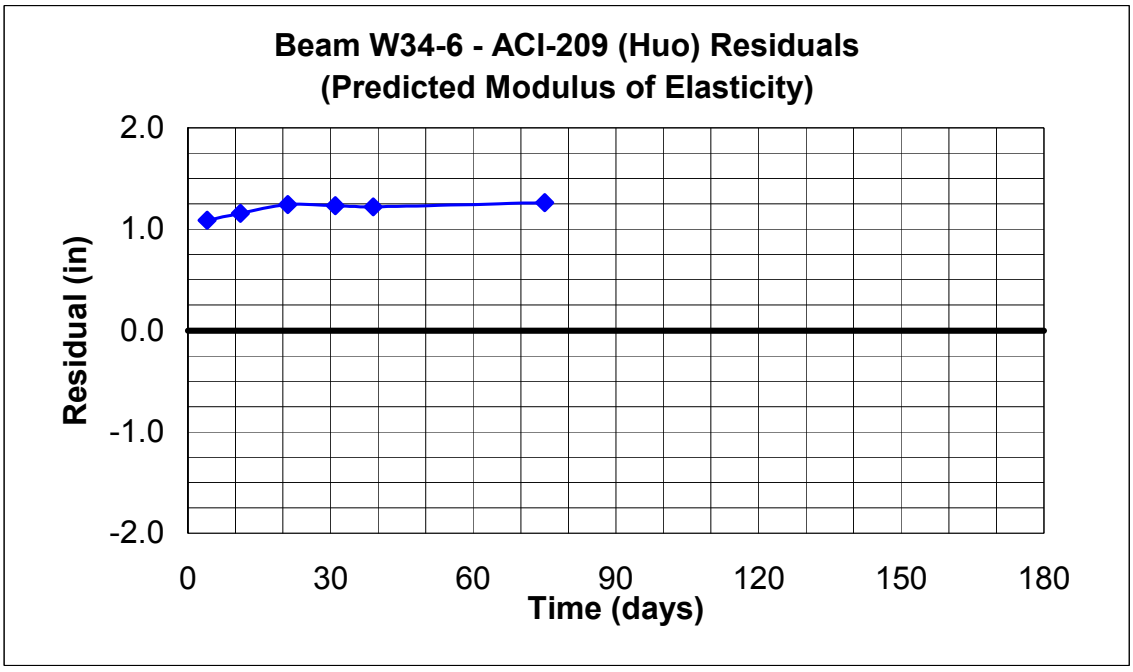

Figure B.40 Beam W34-6 ACI-209 (Huo) Residuals (Predicted Modulus of Elasticity)

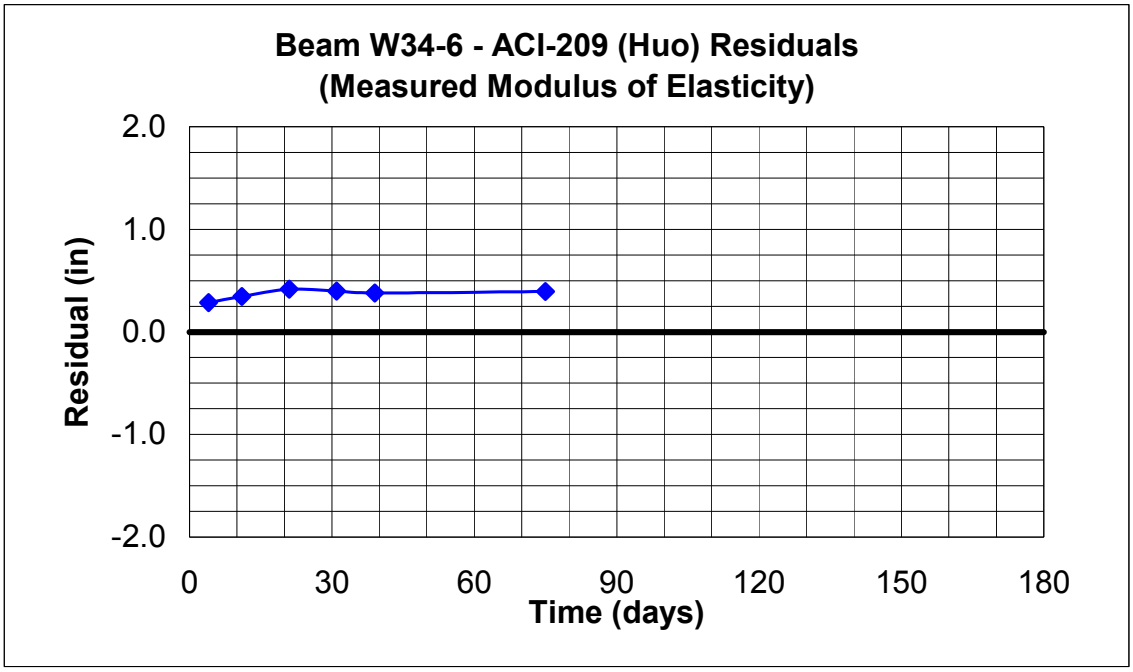

Figure B.41 Beam W34-6 ACI-209 (Huo) Residuals (Measured Modulus of Elasticity)

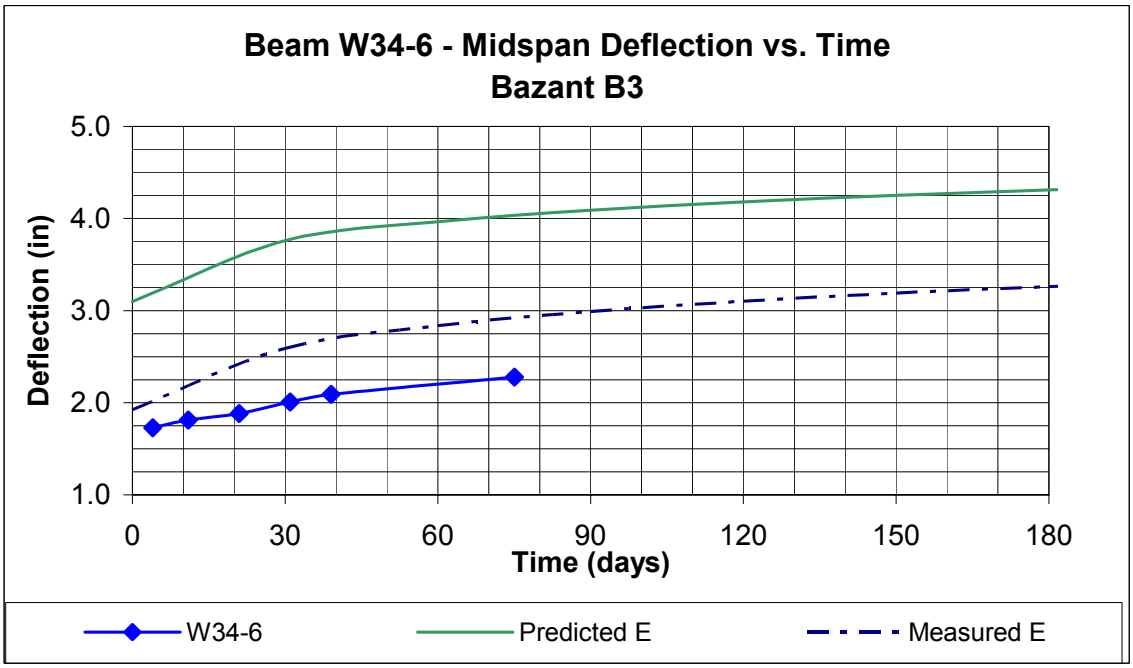

Figure B.42 Beam W34-6 Bazant B3 Predicted Deflection vs. Time

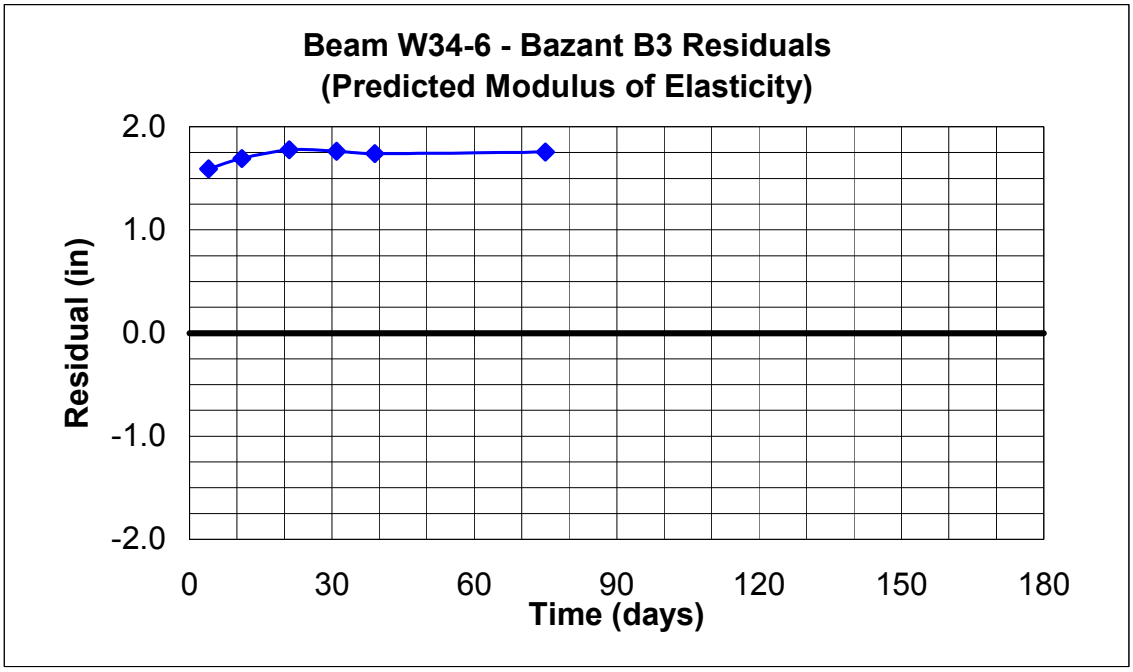

Figure B.43 Beam W34-6 Bazant B3 Residuals (Predicted Modulus of Elasticity)

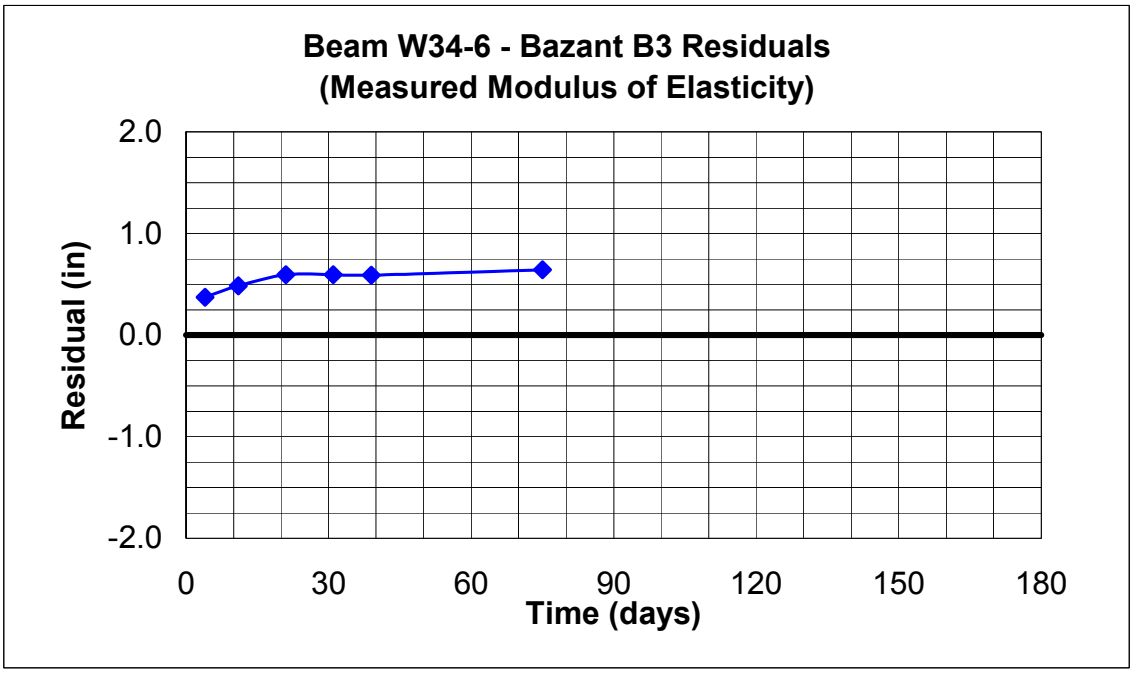

Figure B.44 Beam W34-6 Bazant B3 Residuals (Measured Modulus of Elasticity)

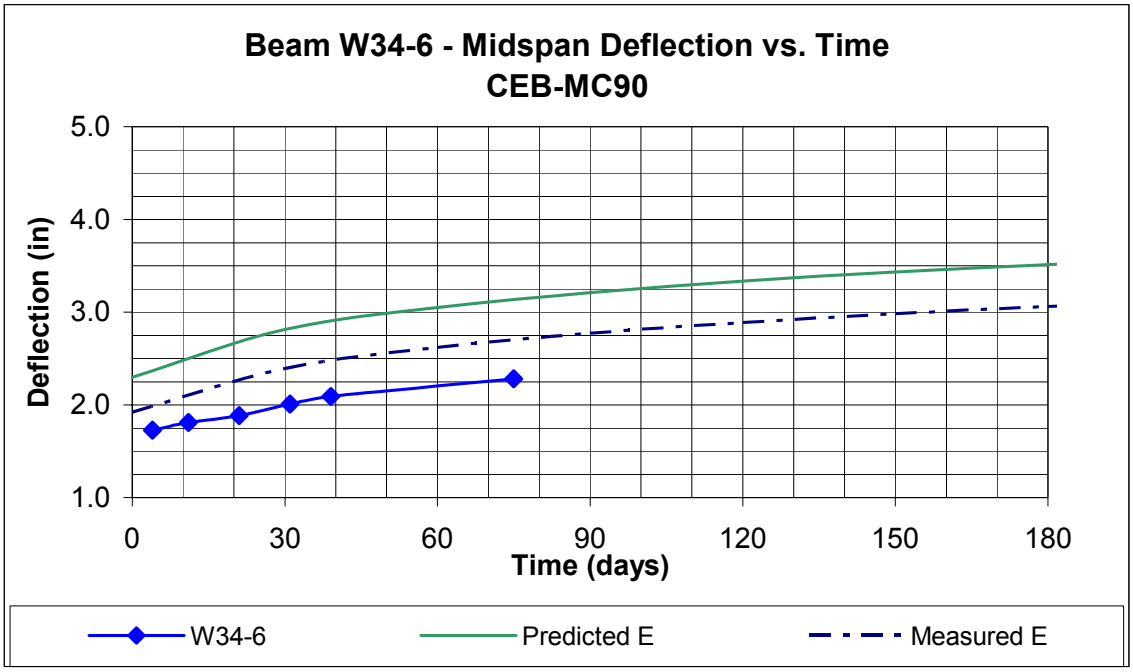

Figure B.45 Beam W34-6 CEB-MC90 Predicted Deflection vs. Time

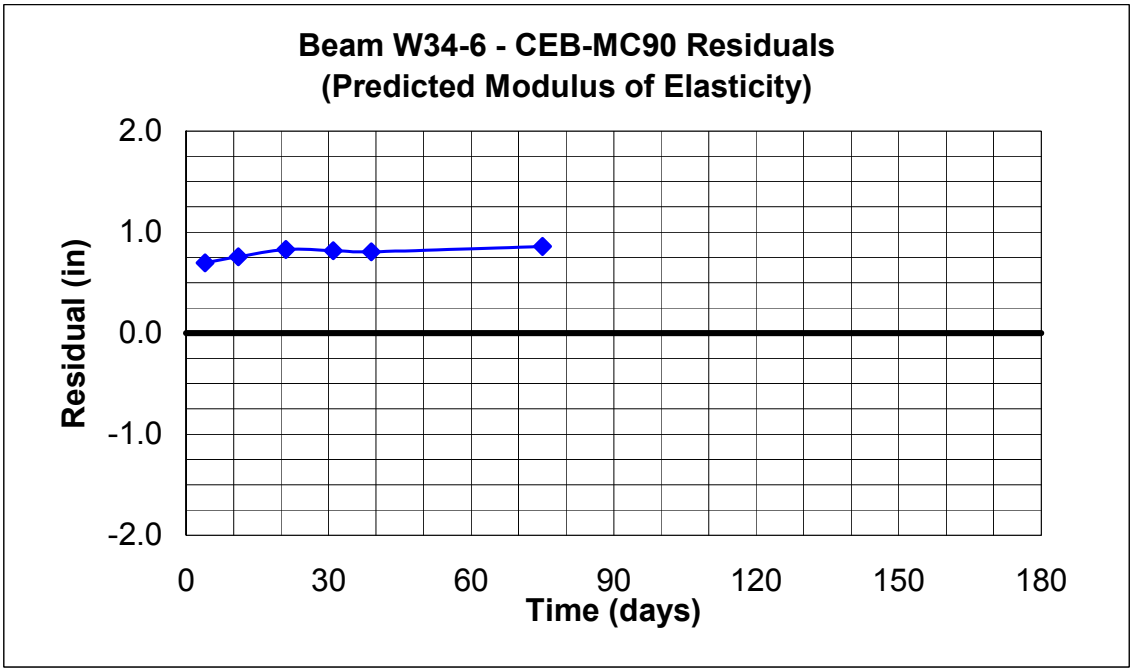

Figure B.46 Beam W34-6 CEB-MC90 Residuals (Predicted Modulus of Elasticity)

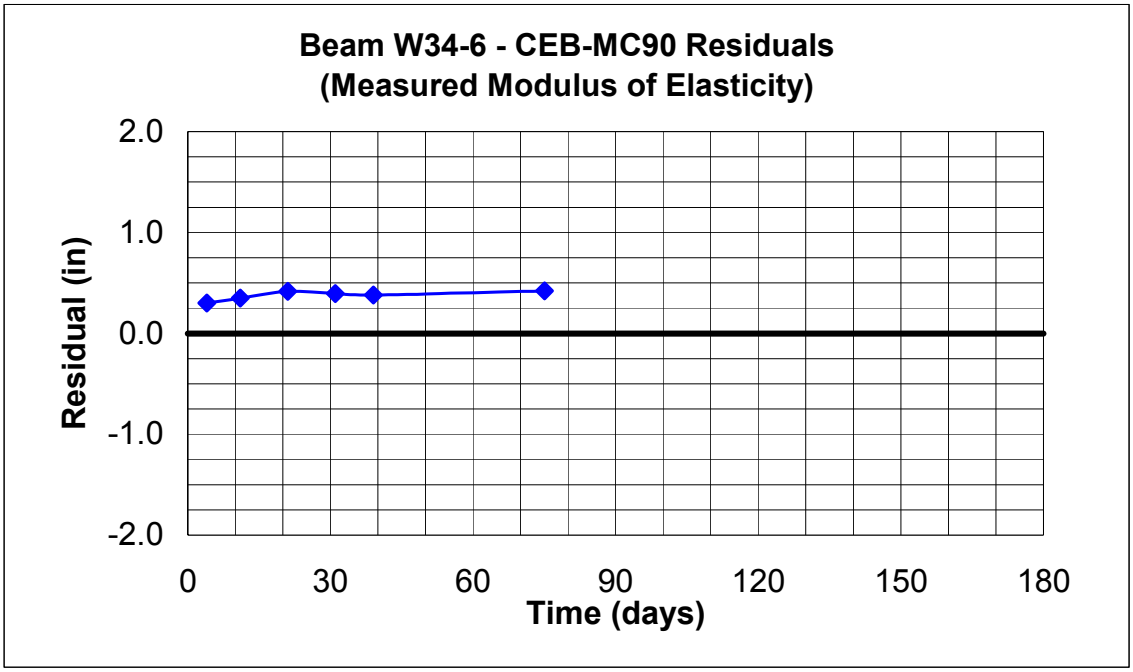

Figure B.47 Beam W34-6 CEB-MC90 Residuals (Measured Modulus of Elasticity)

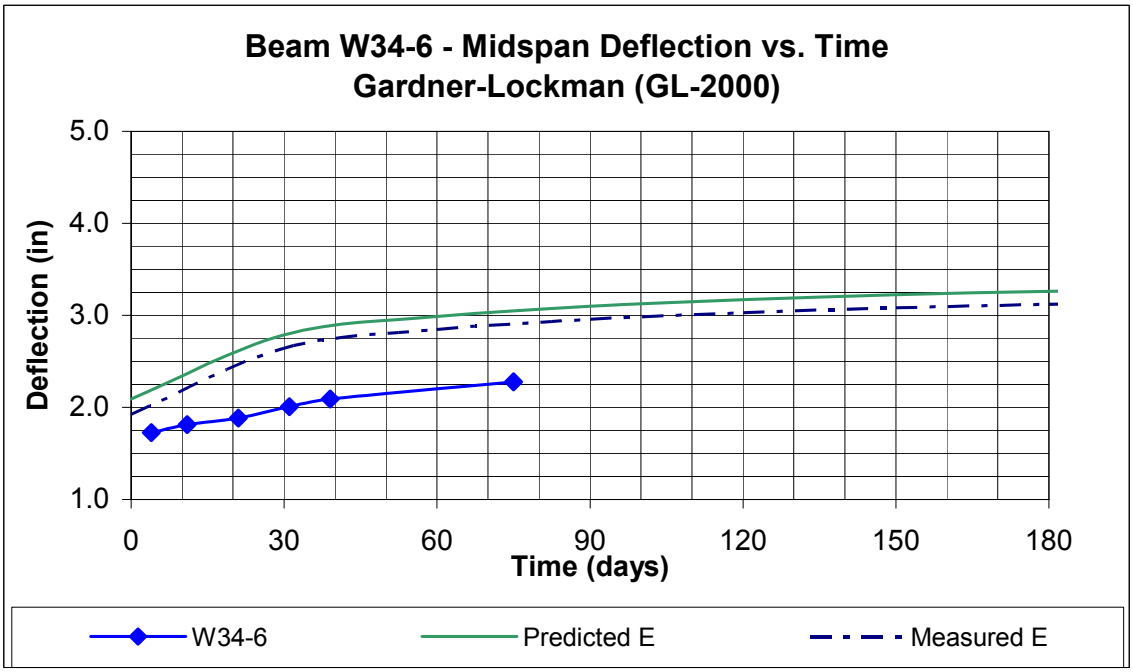

Figure B.48 Beam W34-6 GL-2000 Predicted Deflection vs. Time

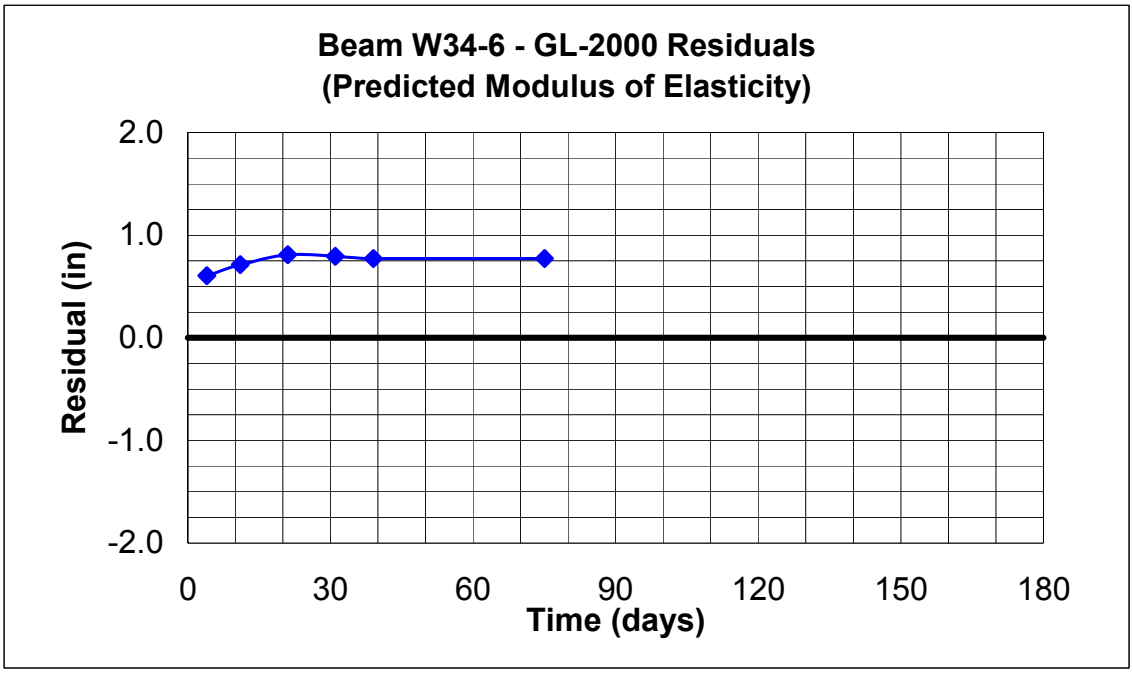

Figure B.49 Beam W34-6 GL-2000 Residuals (Predicted Modulus of Elasticity)

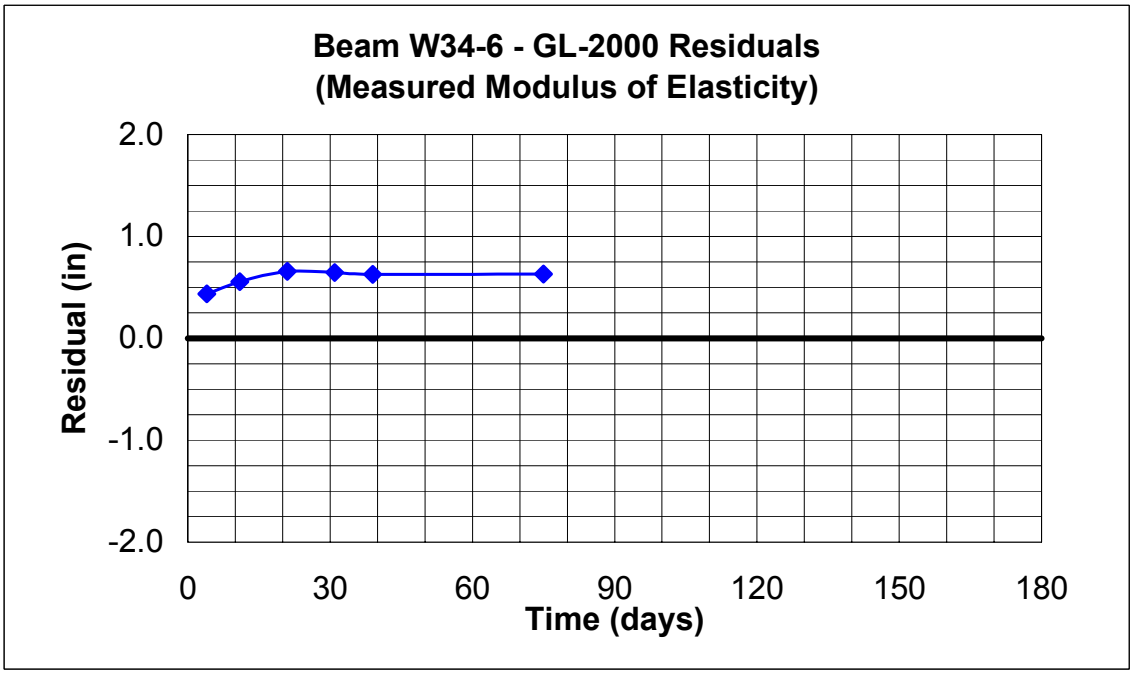

Figure B.50 Beam W34-6 GL-2000 Residuals (Measured Modulus of Elasticity)

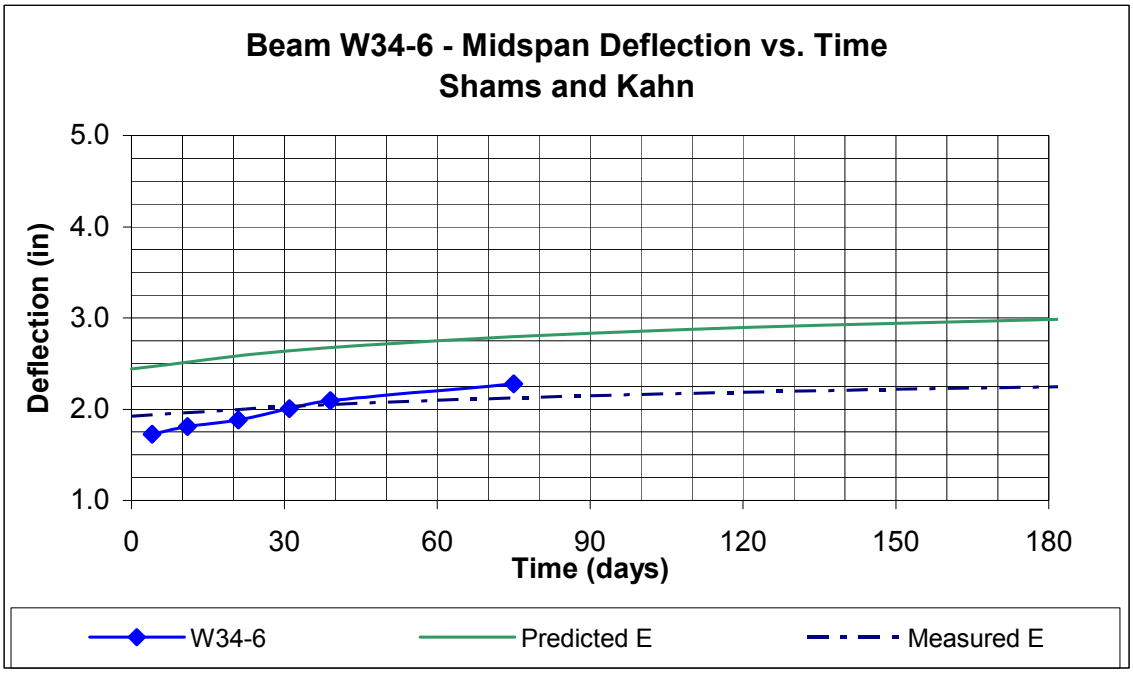

Figure B.51 Beam W34-6 Kahn & Shams Predicted Deflection vs. Time

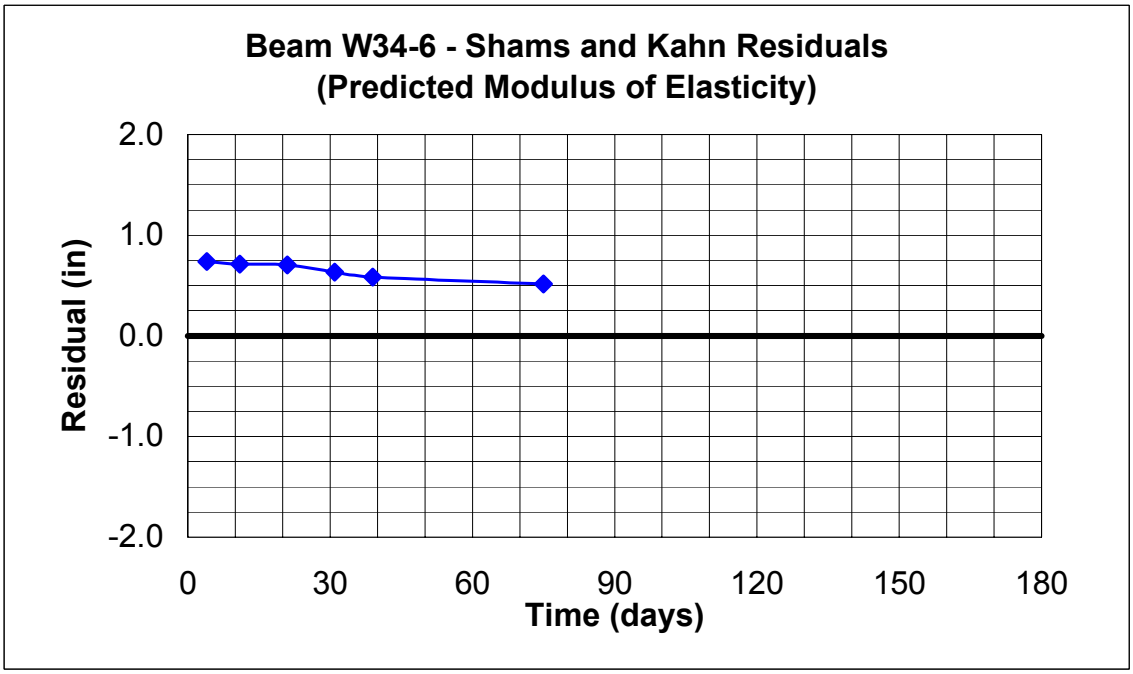

Figure B.52 Beam W34-6 Kahn & Shams Residuals (Predicted Modulus of Elasticity)

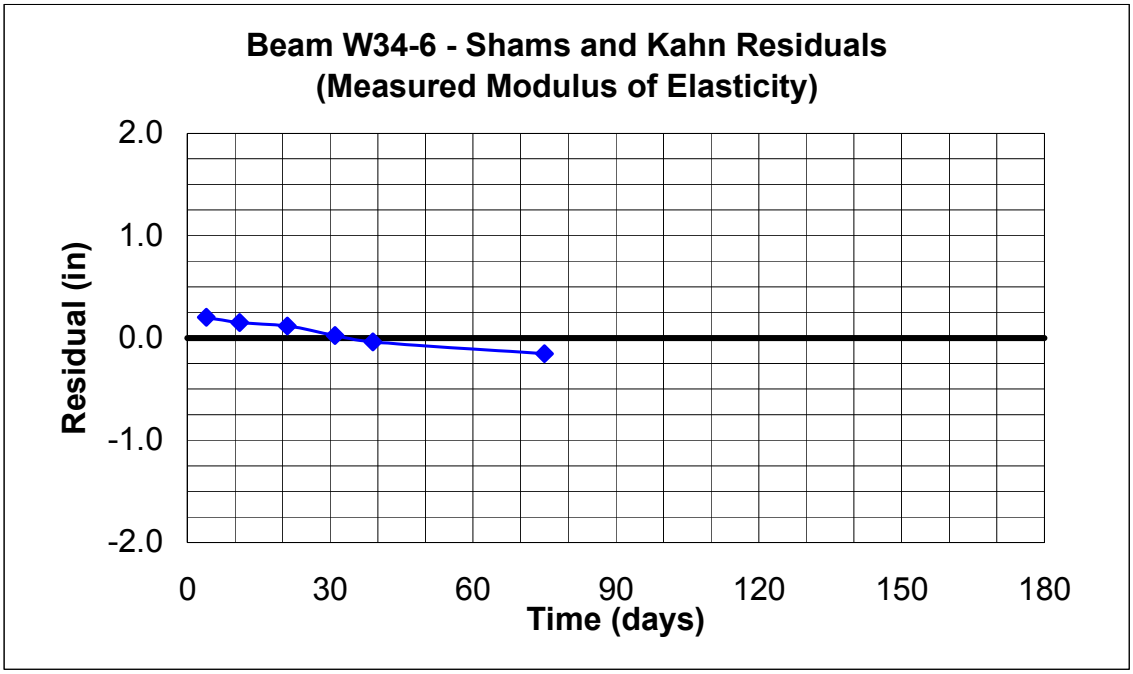

Figure B.53 Beam W34-6 Kahn & Shams Residuals (Measured Modulus of Elasticity)

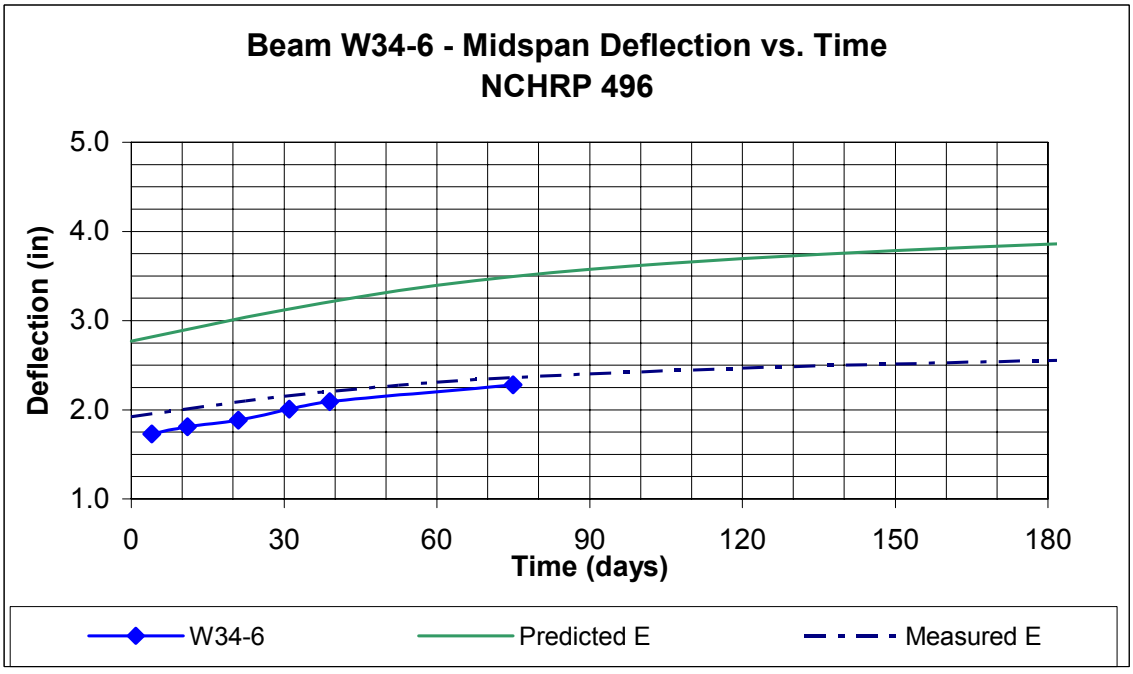

Figure B.54 Beam W34-6 NCHRP 496 Predicted Deflection vs. Time

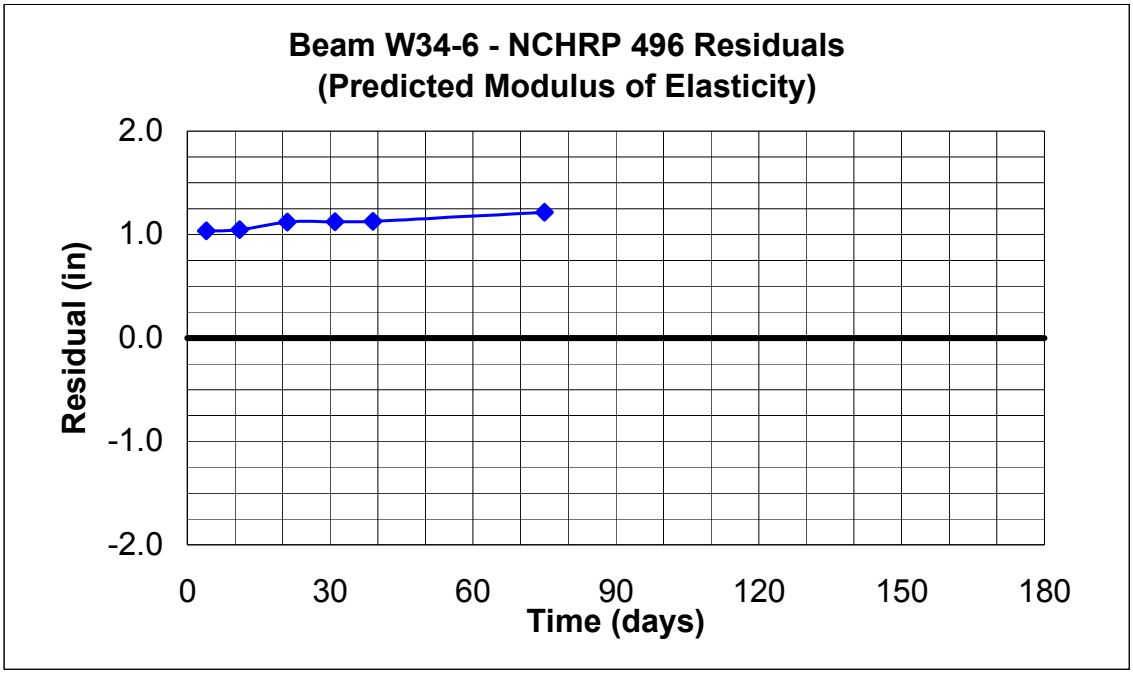

Figure B.55 Beam W34-6 NCHRP 496 Residuals (Predicted Modulus of Elasticity)

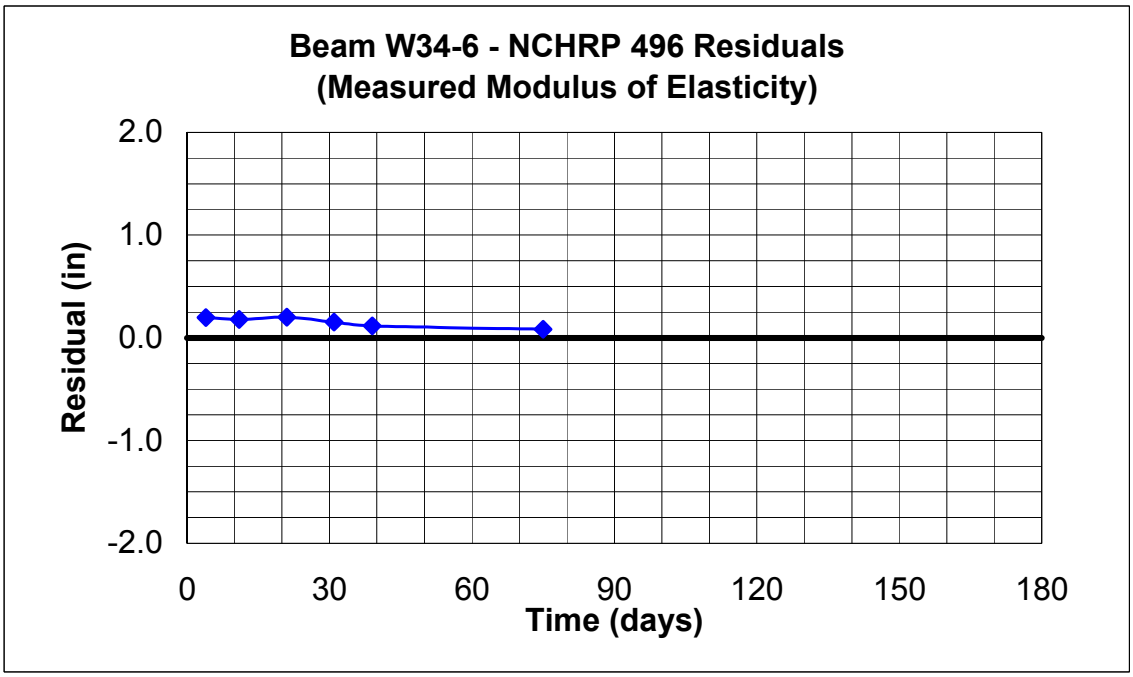

Figure B.56 Beam W34-6 NCHRP 496 Residuals (Measured Modulus of Elasticity)

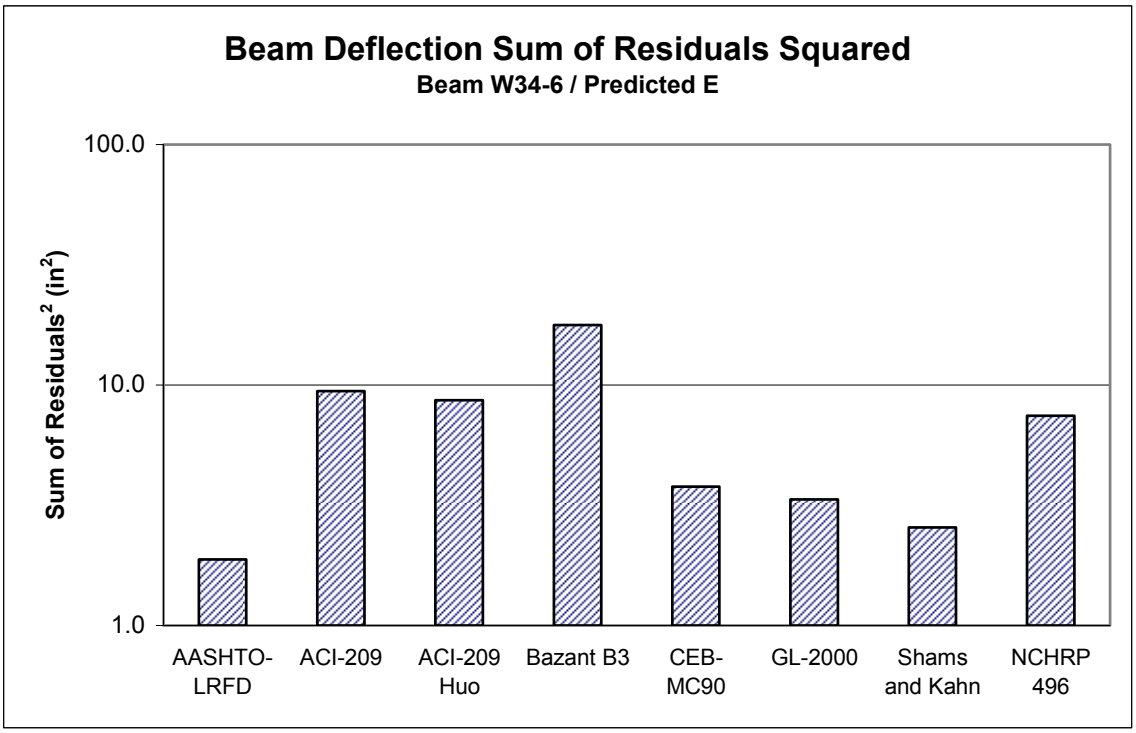

Figure B.57 Beam W34-6 Deflection Sum of Residuals Squared, Predicted E

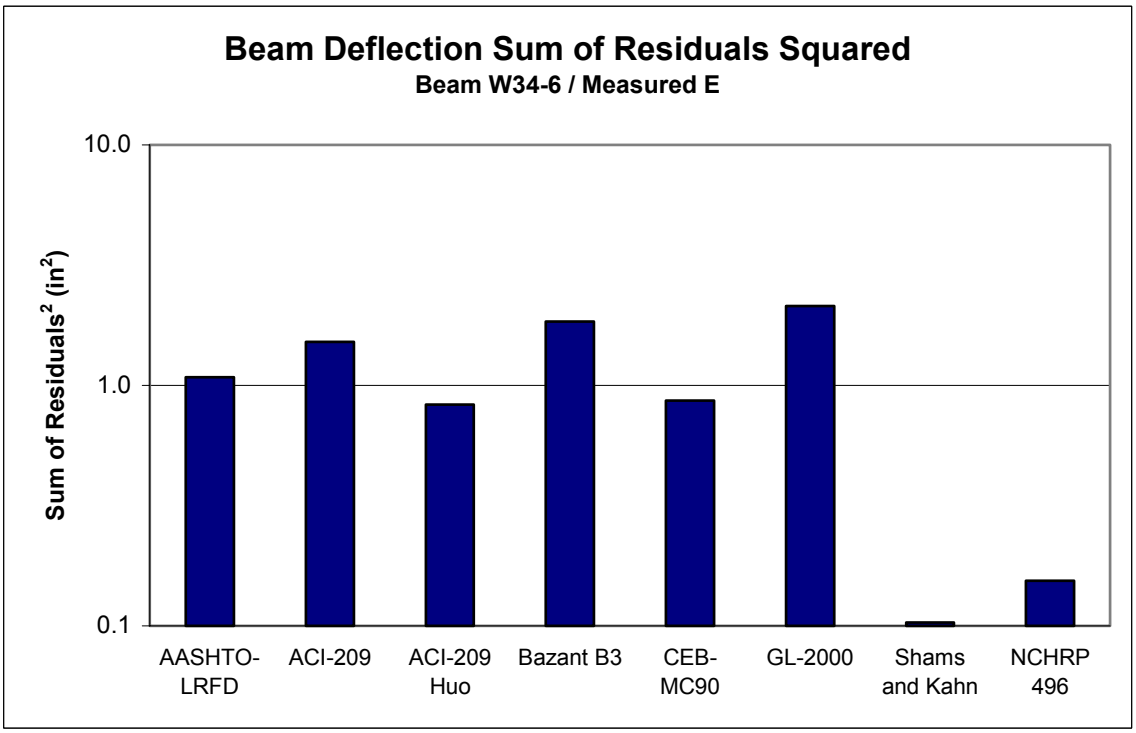

Figure B.58 Beam W34-6 Deflection Sum of Residuals Squared, Predicted E

Table B.3 Beam W34-6 Model Ranking with Predicted E

Rank	Model
1	**AASHTO-LRFD**
2	Shams and Kahn
3	CEB-MC90
4	NCHRP 496
5	ACI-209
6	ACI-209, modified by Huo
7	GL-2000
8	Bazant B3

Table B.4 Beam W34-6 Model Ranking with Measured E

Rank	Model
1	**Shams and Kahn**
2	NCHRP 496
3	CEB-MC90
4	AASHTO-LRFD
5	ACI-209
6	ACI-209, modified by Huo
7	Bazant B3
8	GL-2000

B.3 Additional Beams W34-7, 8, & W35-7

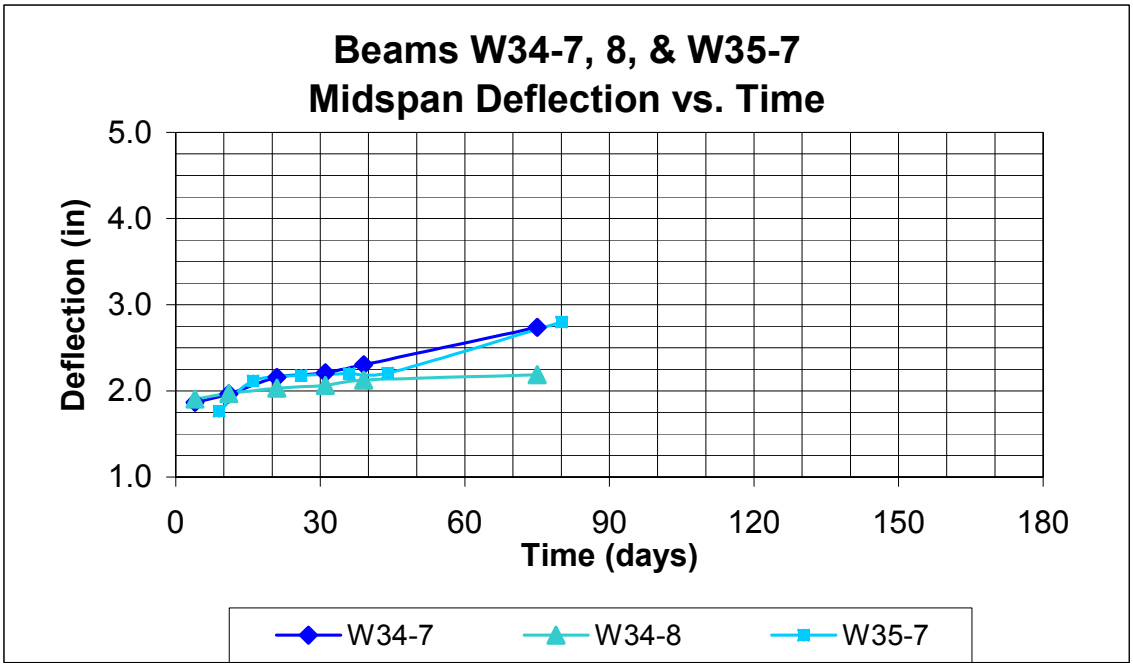

Figure B.59 Beams W34-7, 8, & W35-7, Deflection vs. Time

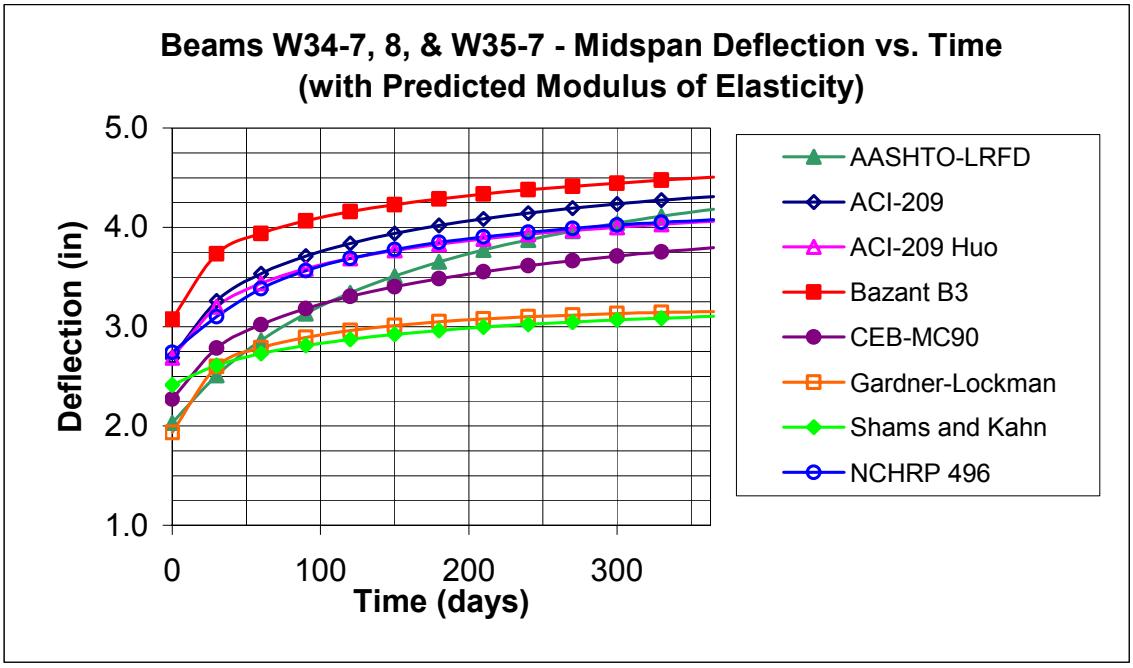

Figure B.60 Beams W34-7, 8, & W35-7, Predicted Deflection vs. Time (Predicted E)

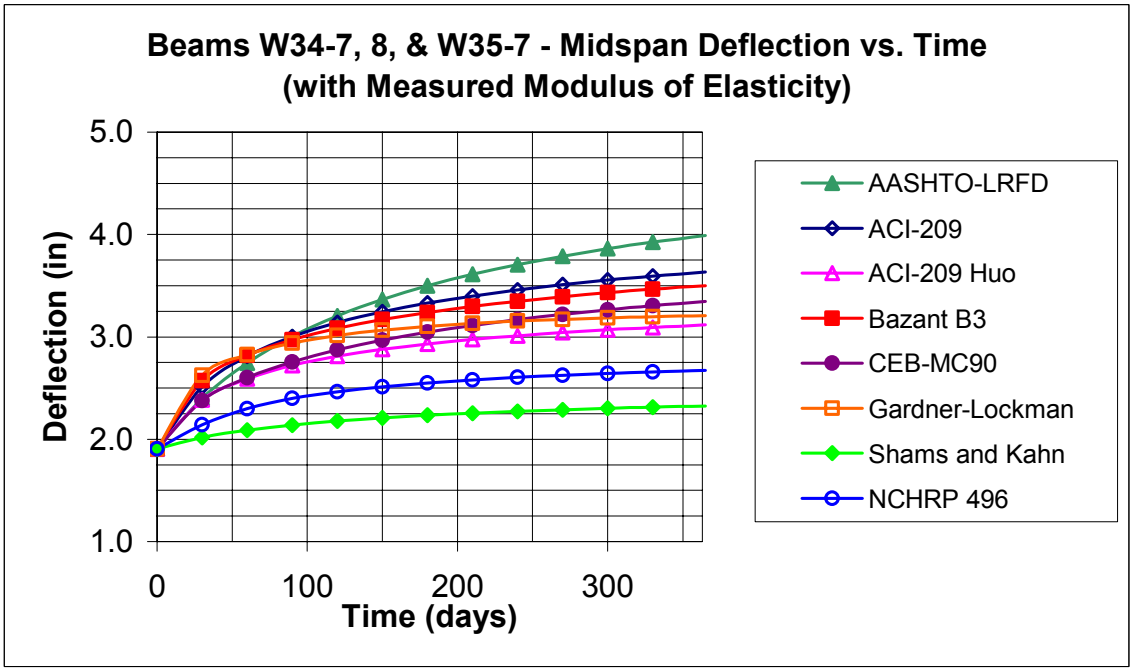

Figure B.61 Beams W34-7, 8, & W35-7, Predicted Deflection vs. Time (Measured E)

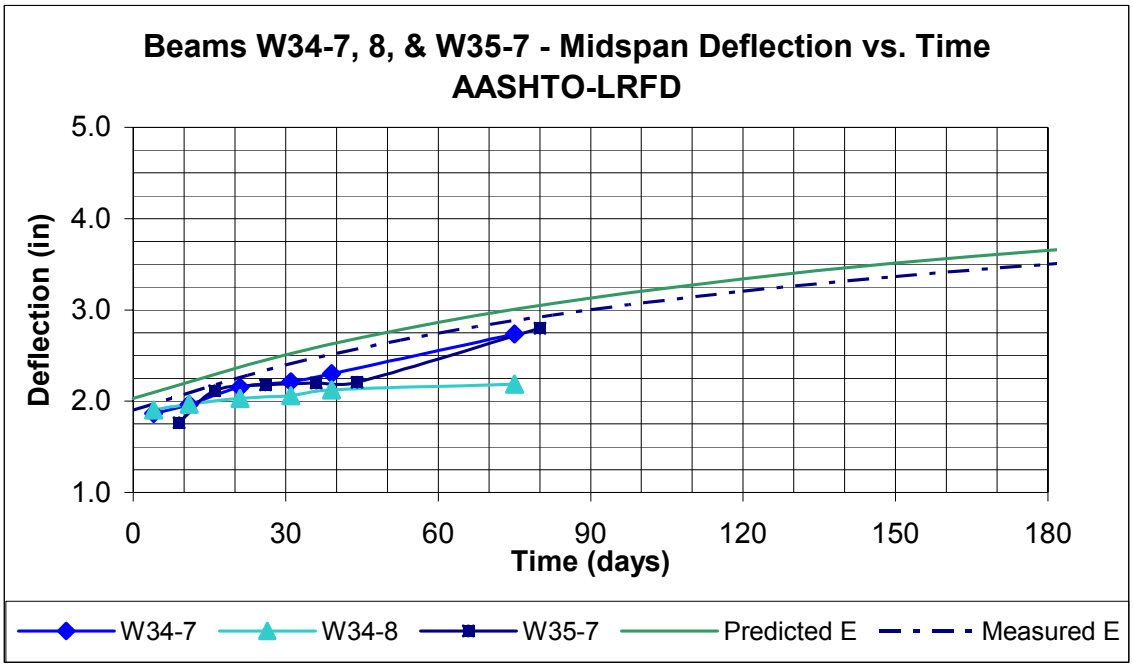

Figure B.62 Beams W34-7, 8, & W35-7 AASHTO-LRFD Predicted Deflection vs. Time

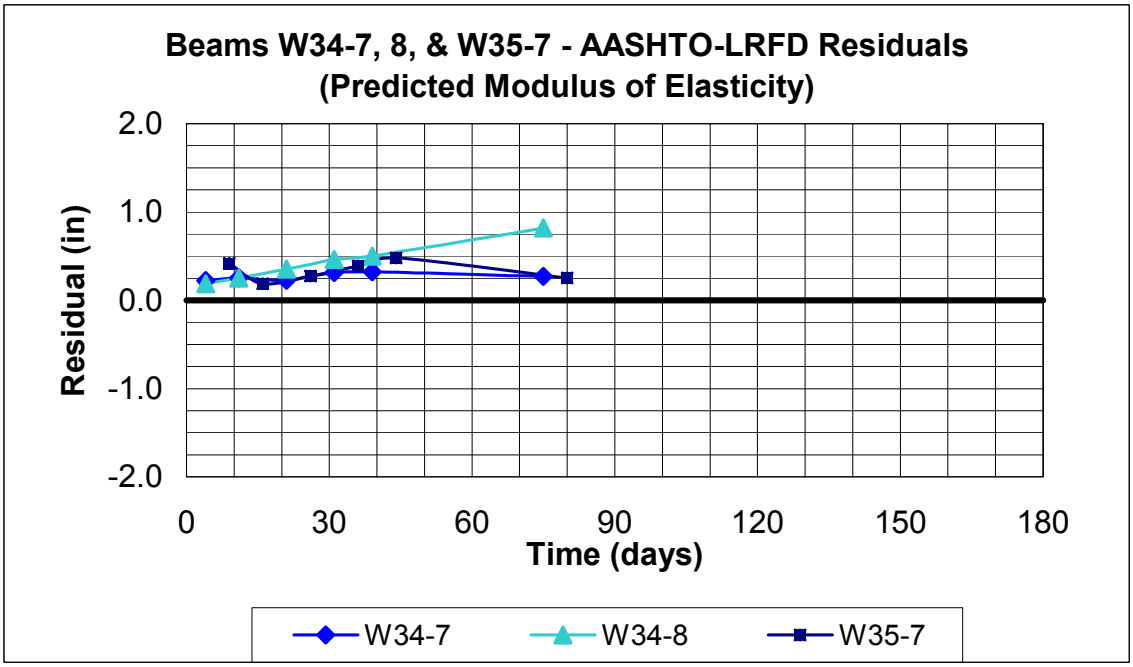

Figure B.63 Beams W34-7, 8, & W35-7 AASHTO-LRFD Residuals (Predicted Modulus of Elasticity)

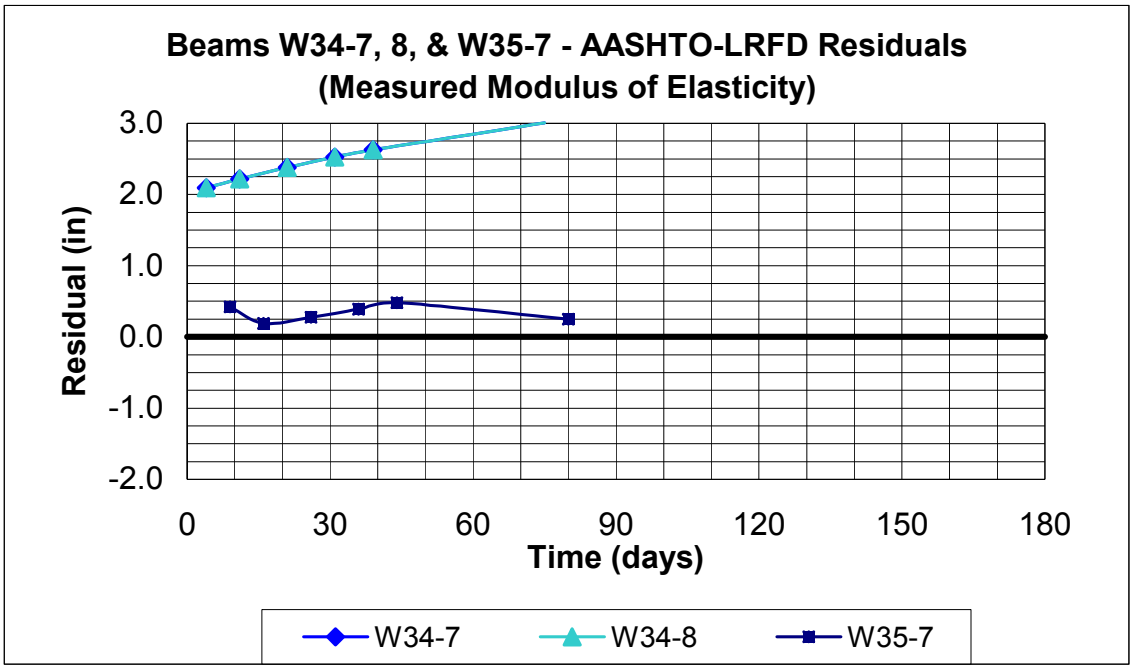

Figure B.64 Beams W34-7, 8, & W35-7 AASHTO-LRFD Residuals (Measured Modulus of Elasticity)

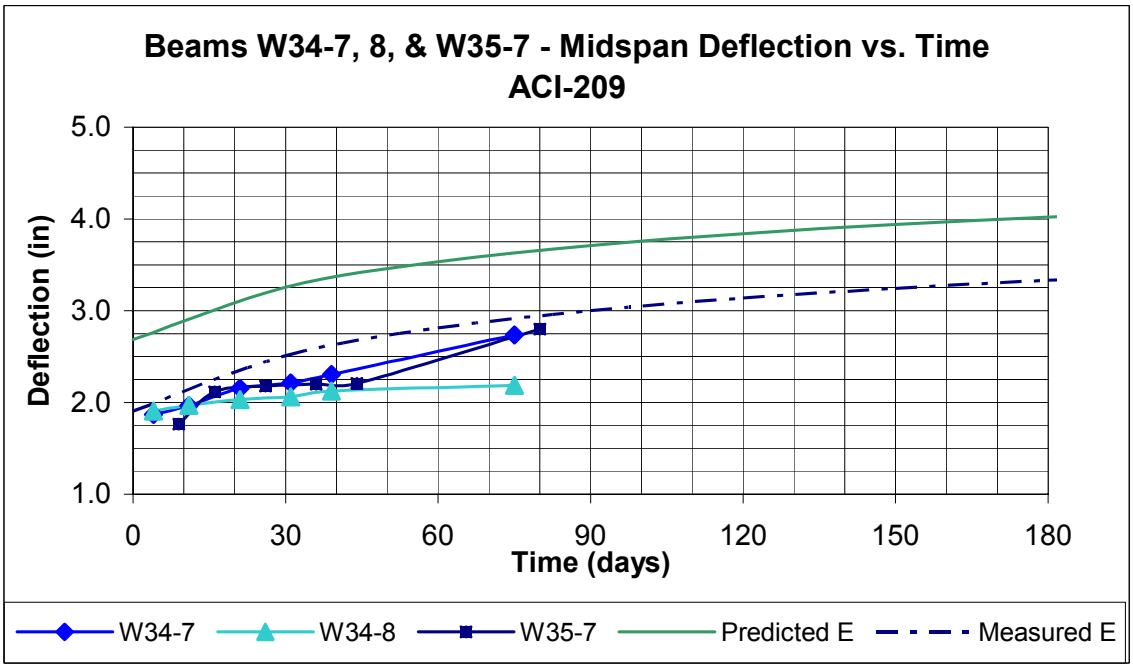

Figure B.65 Beams W34-7, 8, & W35-7 ACI-209 Predicted Deflection vs. Time

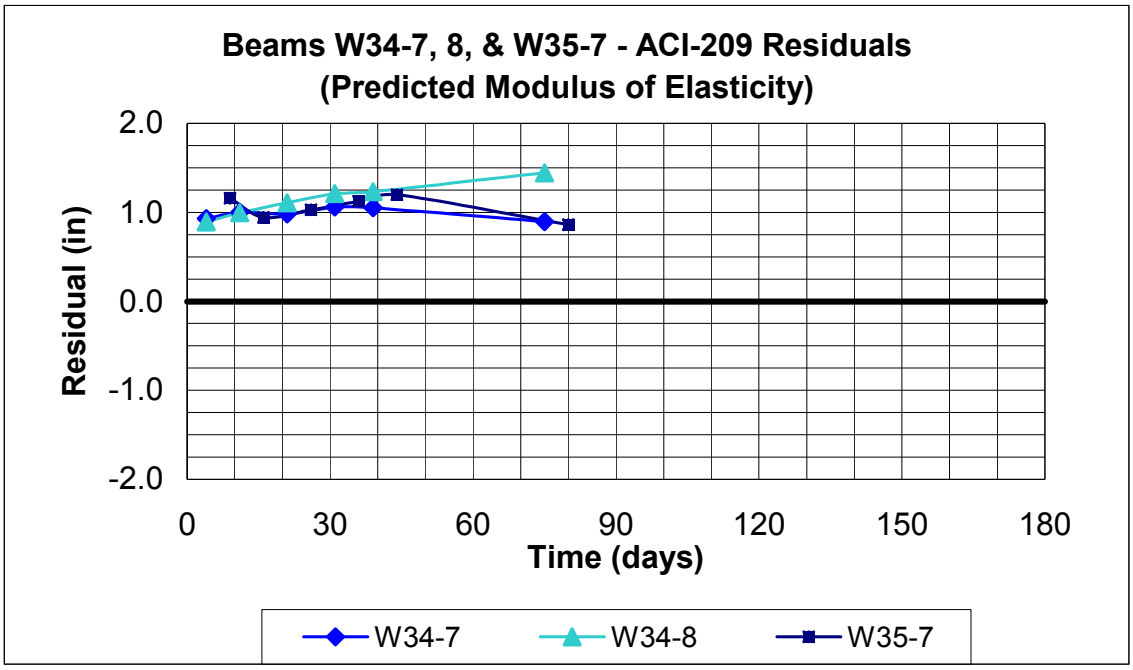

Figure B.66 Beams W34-7, 8, & W35-7 ACI-209 Residuals (Predicted Modulus of Elasticity)

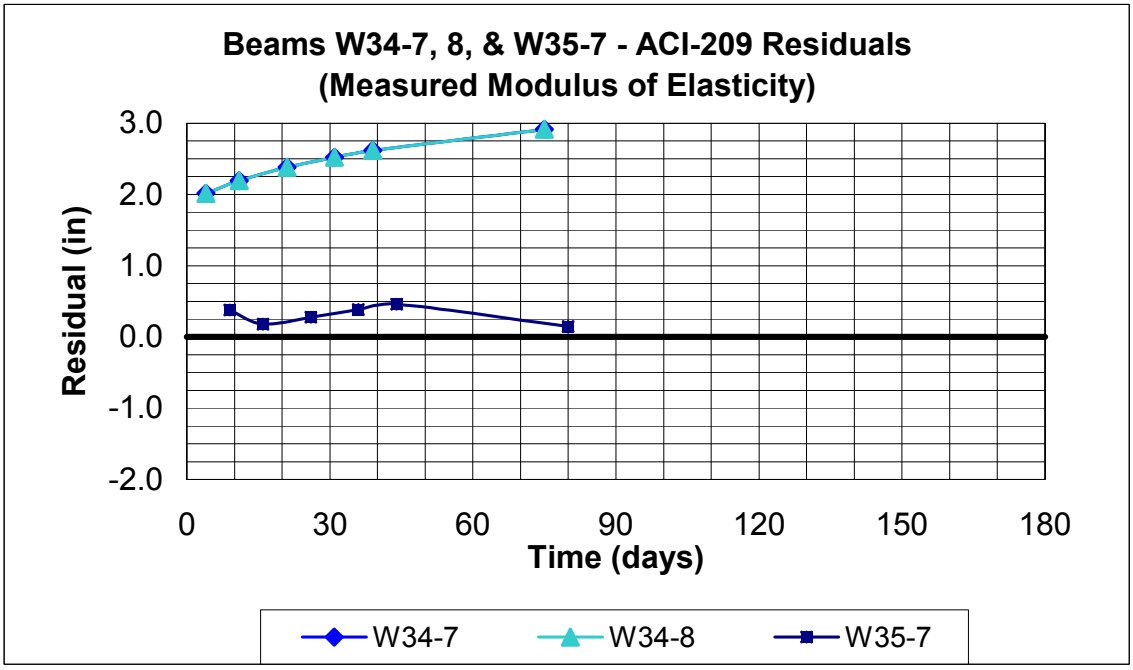

Figure B.67 Beams W34-7, 8, & W35-7 ACI-209 Residuals (Measured Modulus of Elasticity)

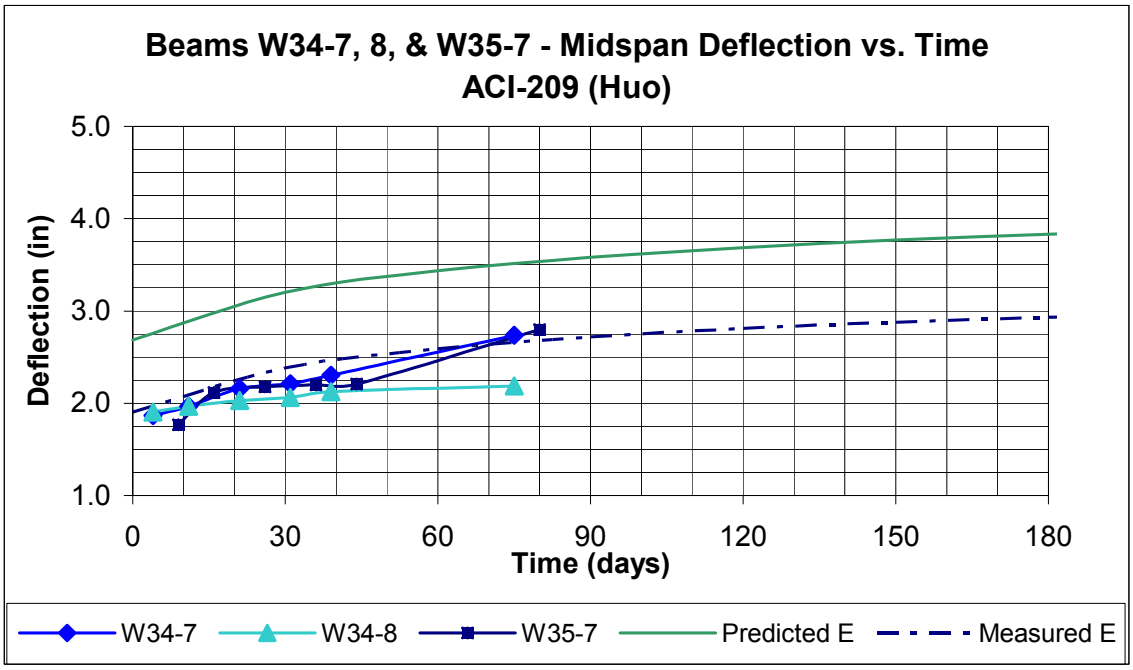

Figure B.68 Beams W34-7, 8, & W35-7 ACI-209 (Huo) Predicted Deflection vs. Time

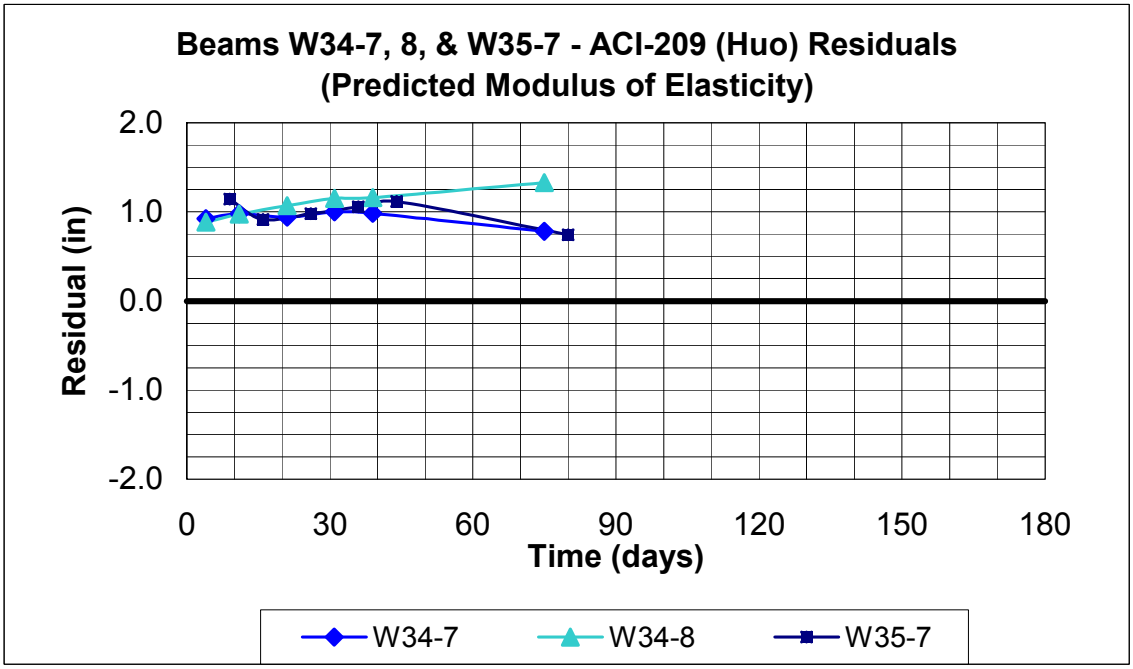

Figure B.69 Beams W34-7, 8, & W35-7 ACI-209 (Huo) Residuals (Predicted Modulus of Elasticity)

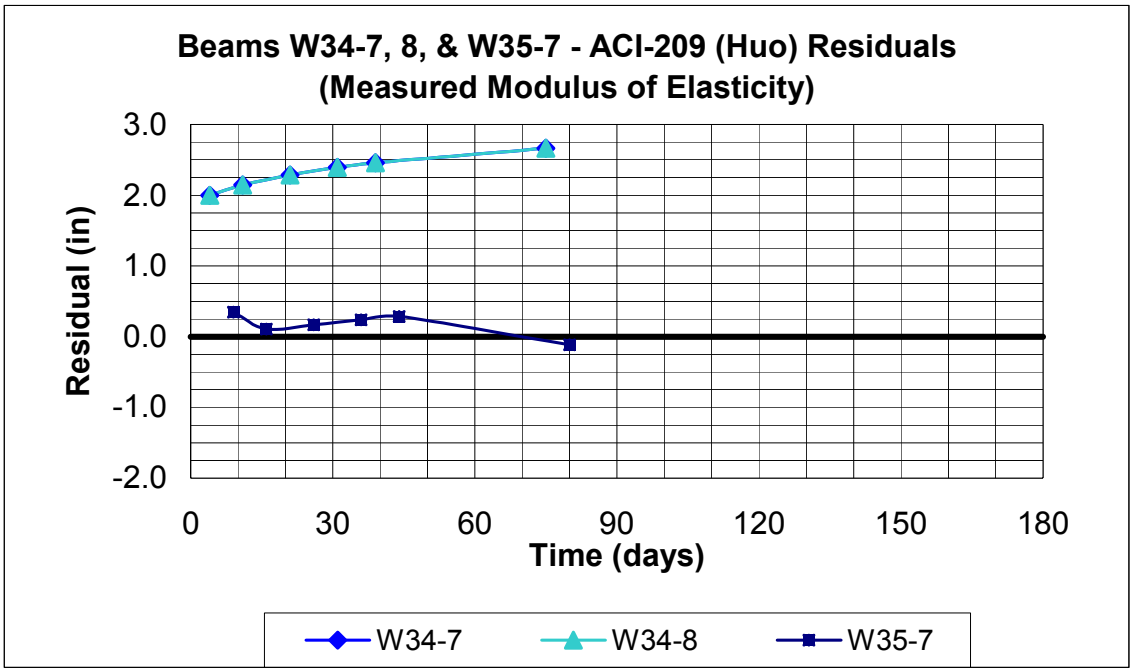

Figure B.70 Beams W34-7, 8, & W35-7 ACI-209 (Huo) Residuals (Measured Modulus of Elasticity)

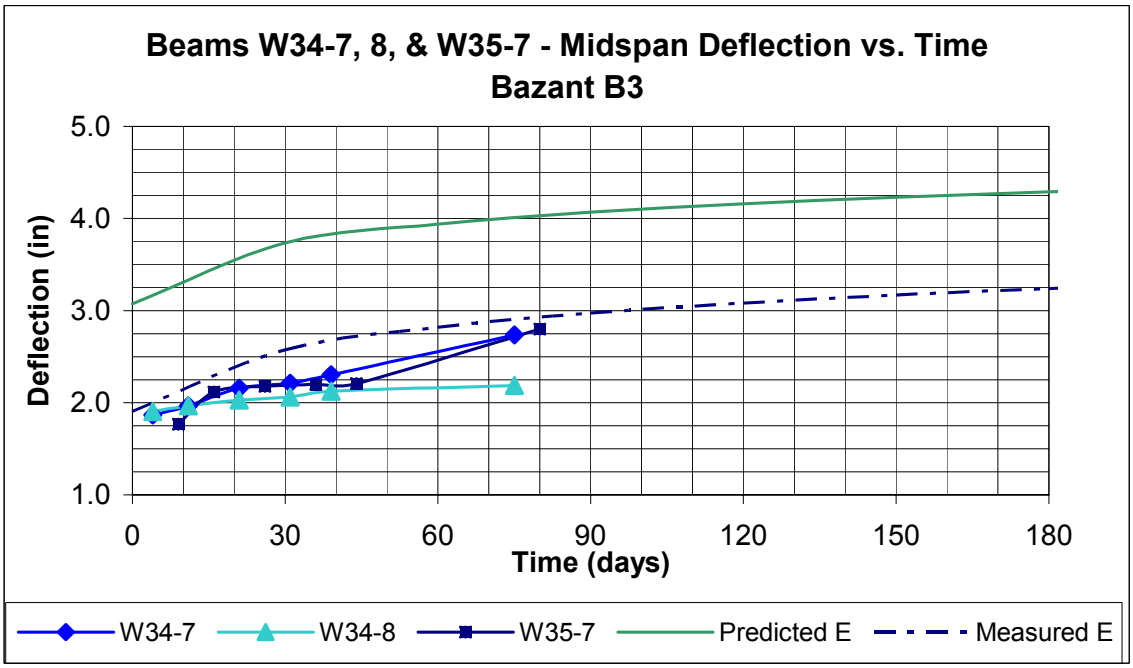

Figure B.71 Beams W34-7, 8, & W35-7 Bazant B3 Predicted Deflection vs. Time

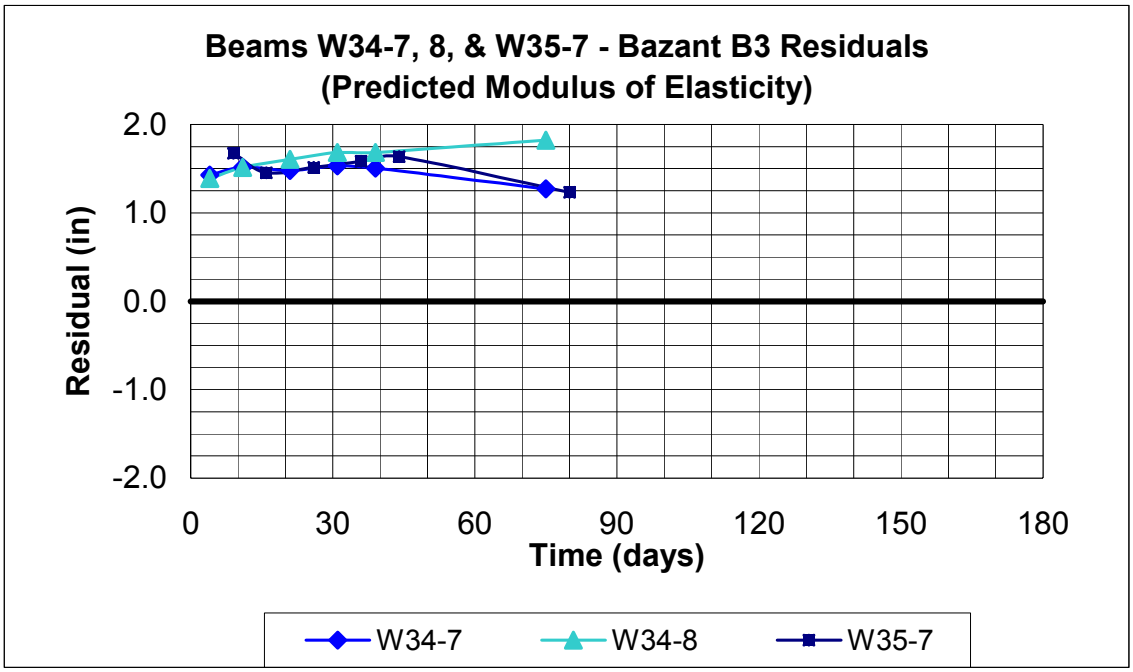

Figure B.72 Beams W34-7, 8, & W35-7 Bazant B3 Residuals (Predicted Modulus of Elasticity)

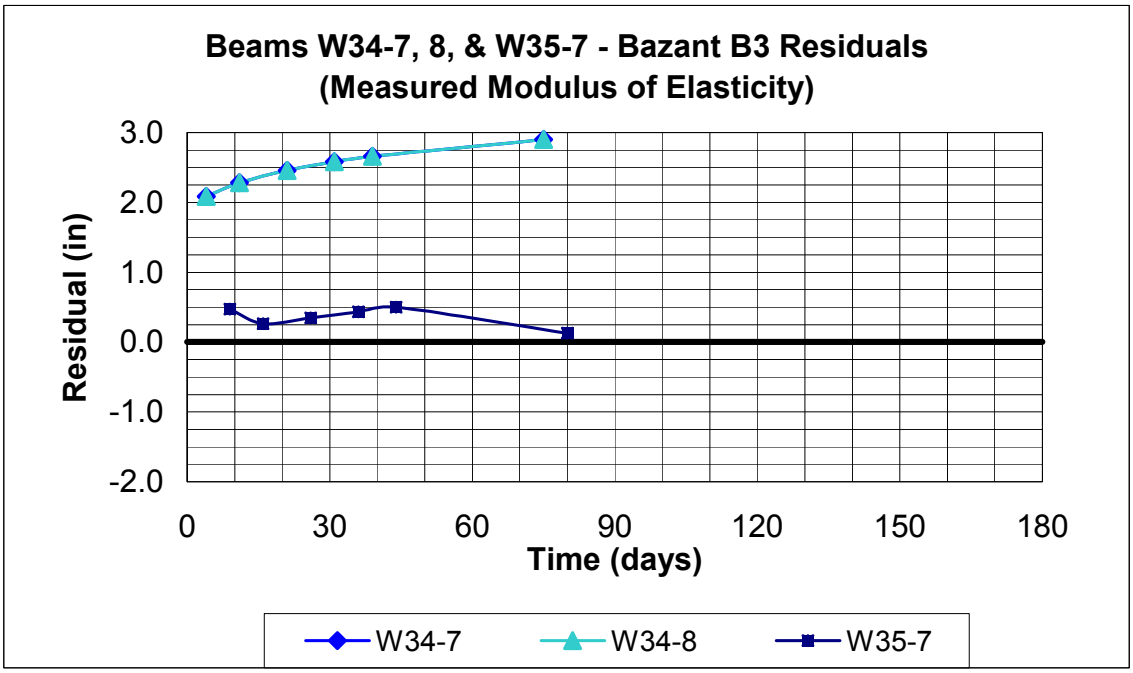

Figure B.73 Beams W34-7, 8, & W35-7 Bazant B3 Residuals (Measured Modulus of Elasticity)

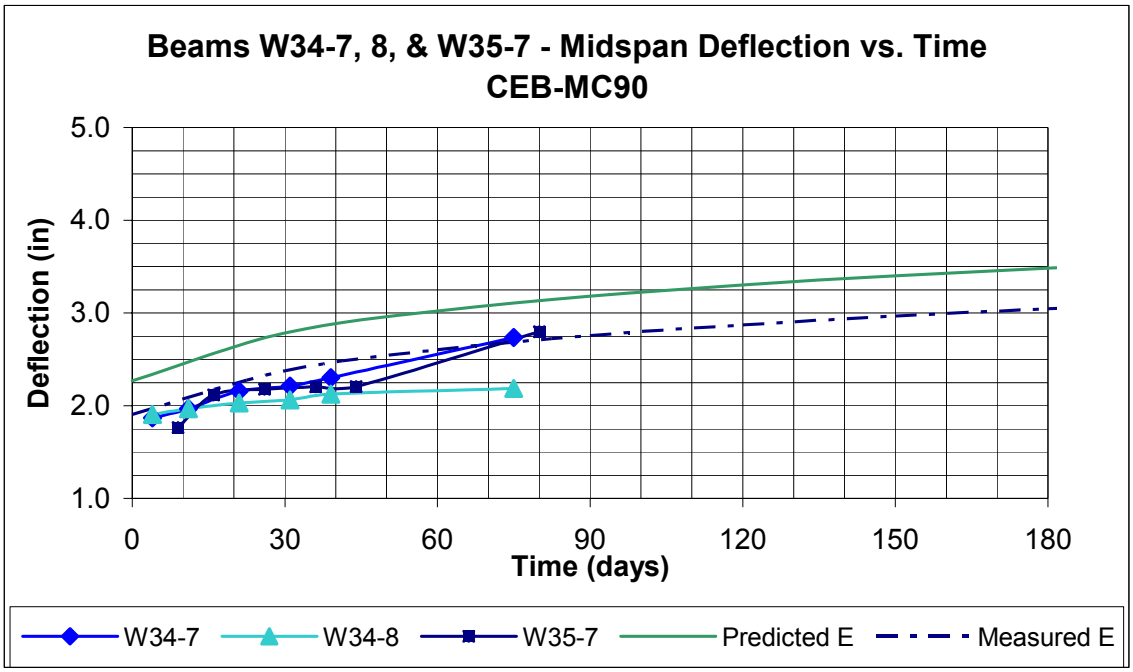

Figure B.74 Beams W34-7, 8, & W35-7 CEB-MC90 Predicted Deflection vs. Time

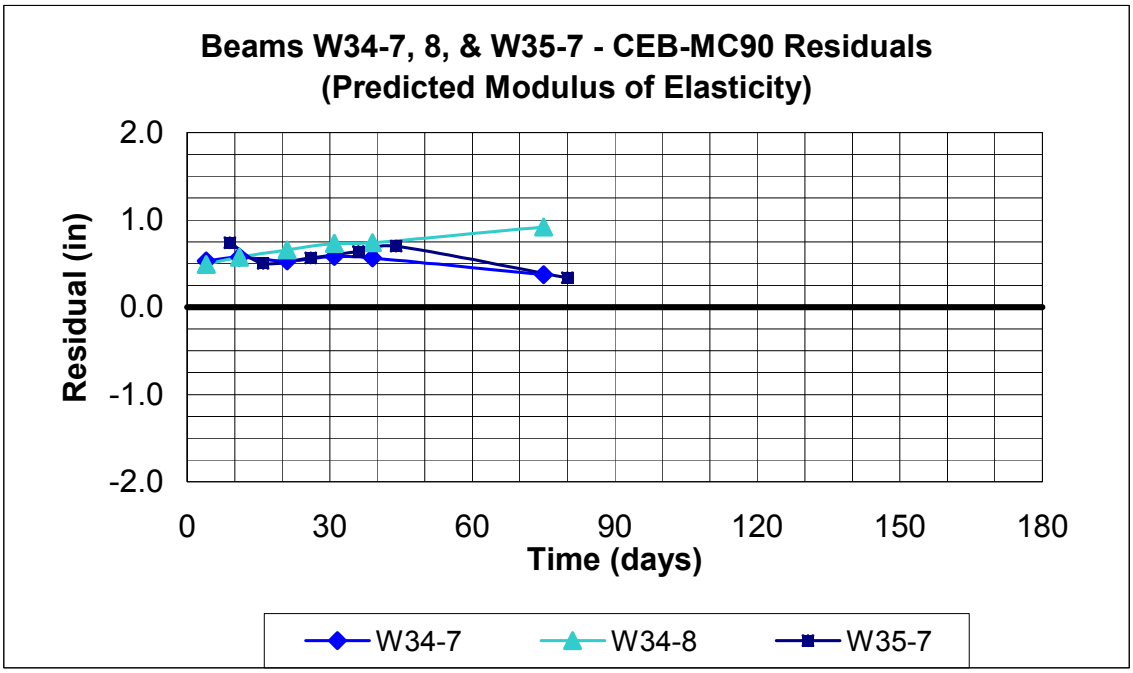

Figure B.75 Beams W34-7, 8, & W35-7 CEB-MC90 Residuals (Predicted Modulus of Elasticity)

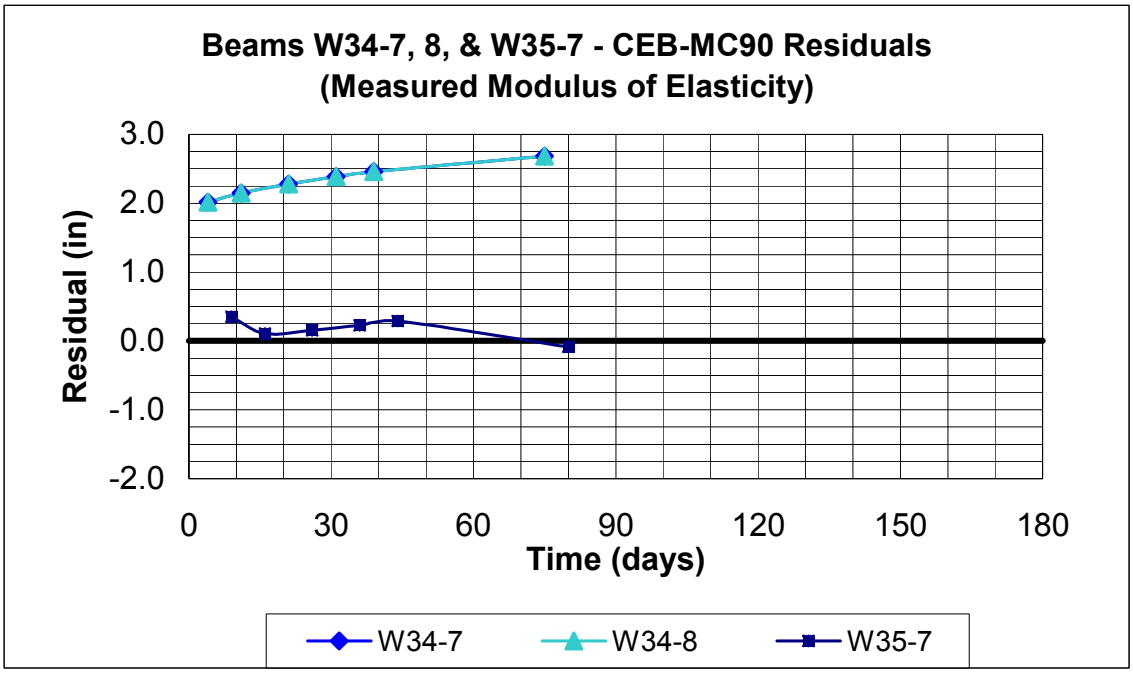

Figure B.76 Beams W34-7, 8, & W35-7 CEB-MC90 Residuals (Measured Modulus of Elasticity)

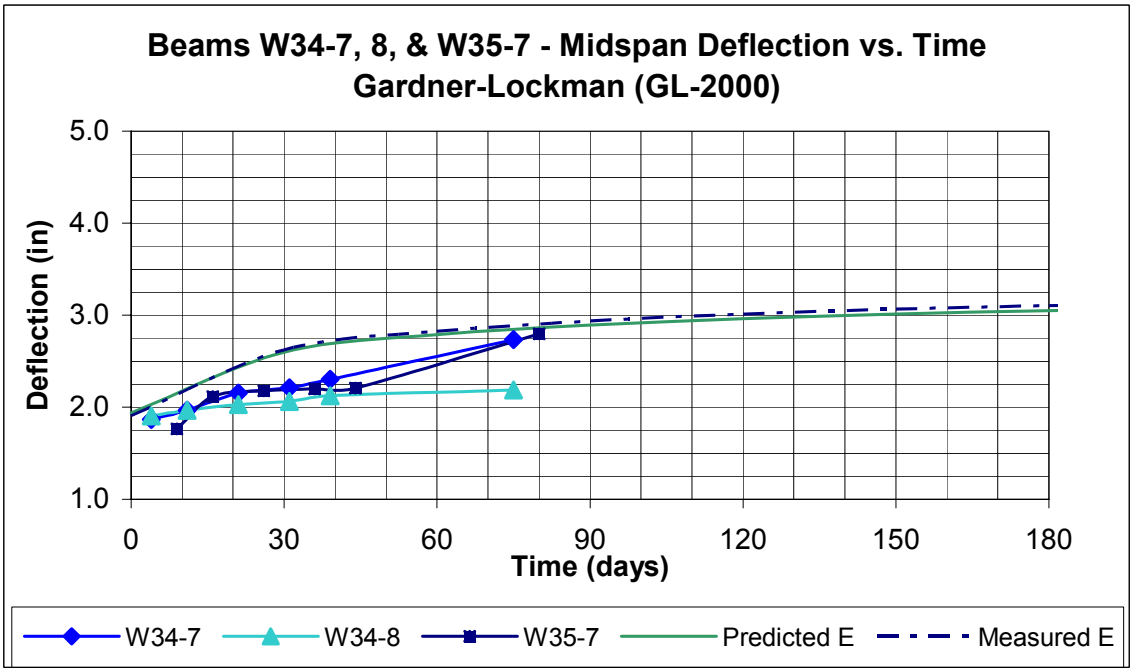

Figure B.77 Beams W34-7, 8, & W35-7 GL-2000 Predicted Deflection vs. Time

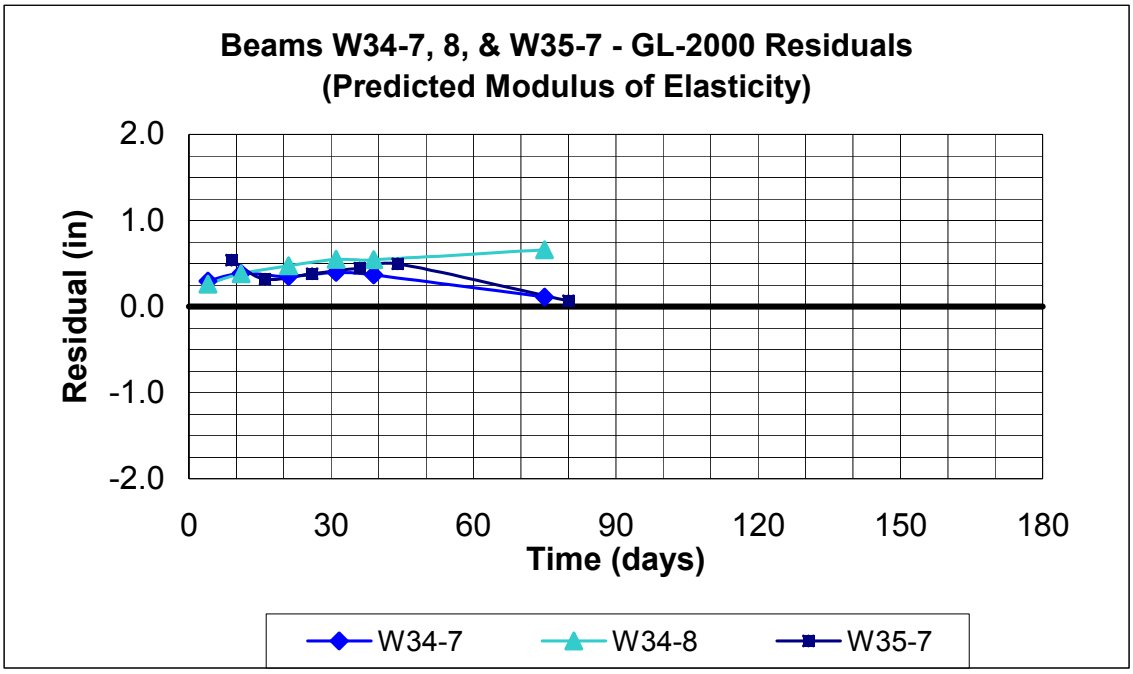

Figure B.78 Beams W34-7, 8, & W35-7 GL-2000 Residuals (Predicted Modulus of Elasticity)

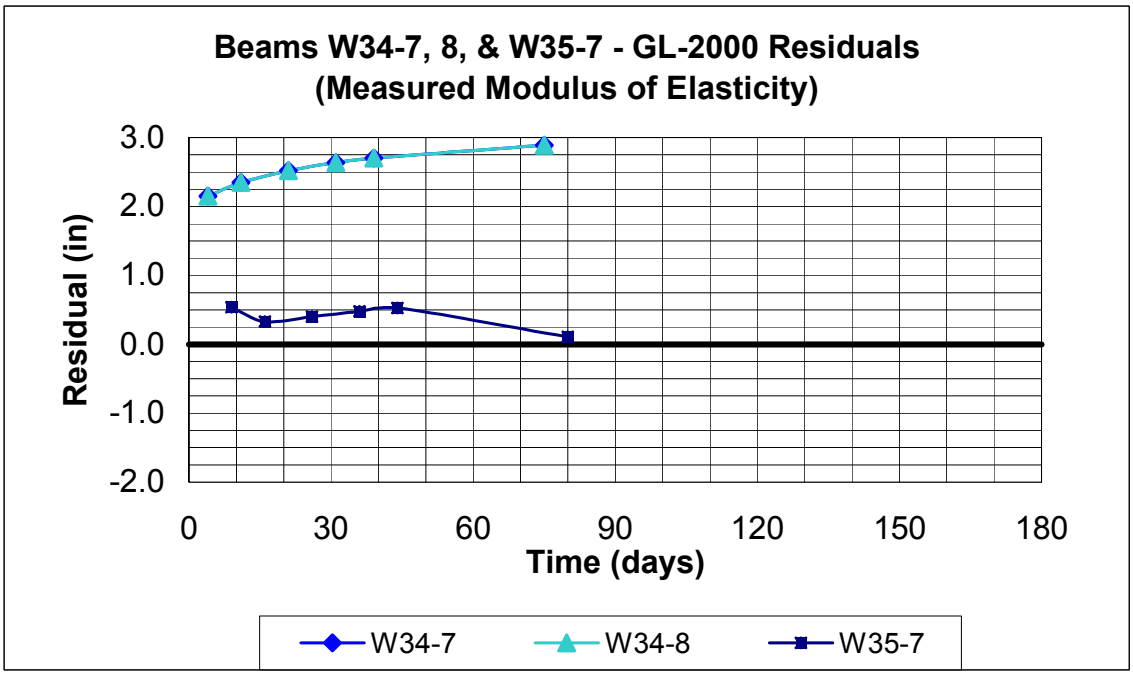

Figure B.79 Beams W34-7, 8, & W35-7 GL-2000 Residuals (Measured Modulus of Elasticity)

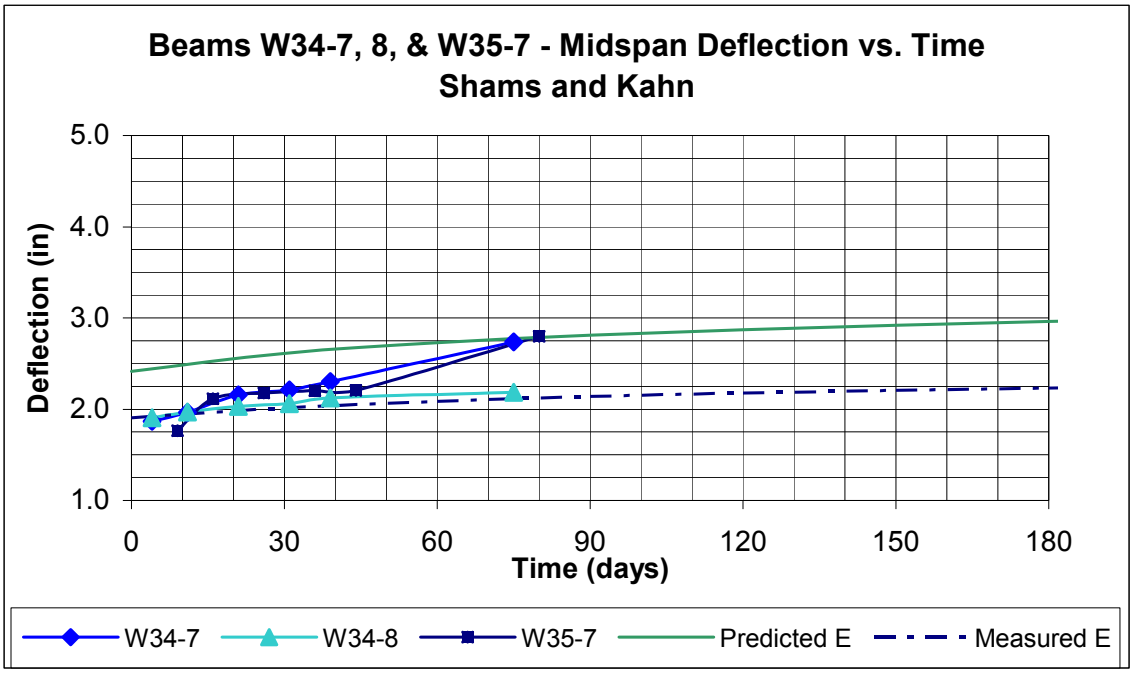

Figure B.80 Beams W34-7, 8, & W35-7 Kahn & Shams Predicted Deflection vs. Time

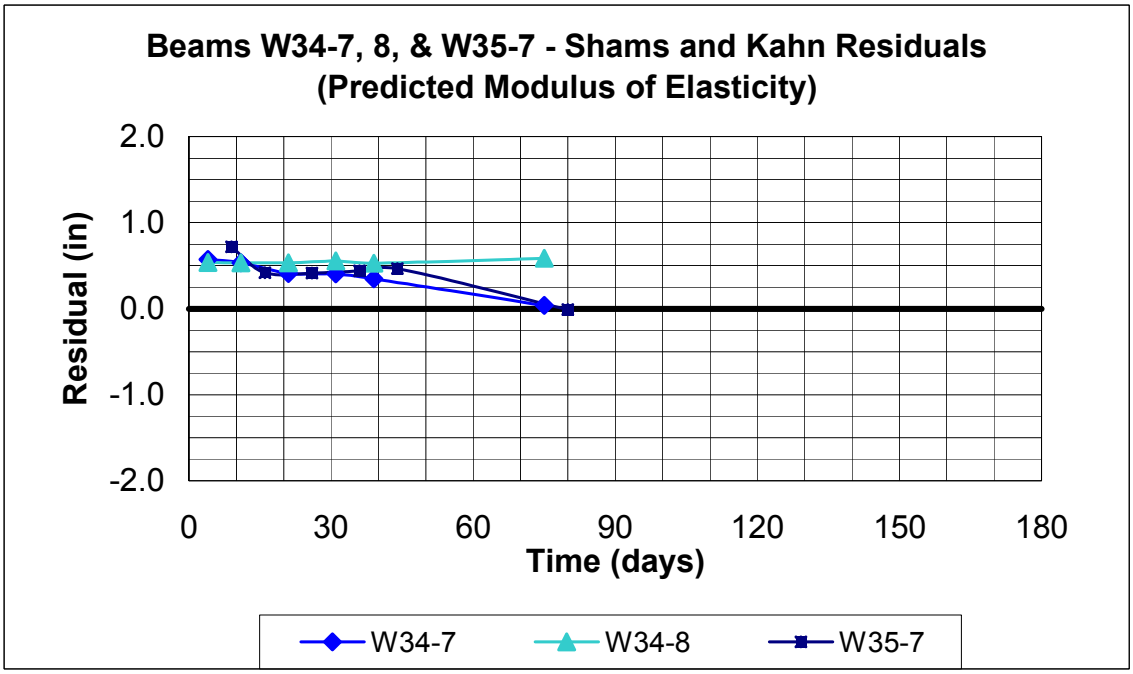

Figure B.81 Beams W34-7, 8, & W35-7 Kahn & Shams Residuals (Predicted Modulus of Elasticity)

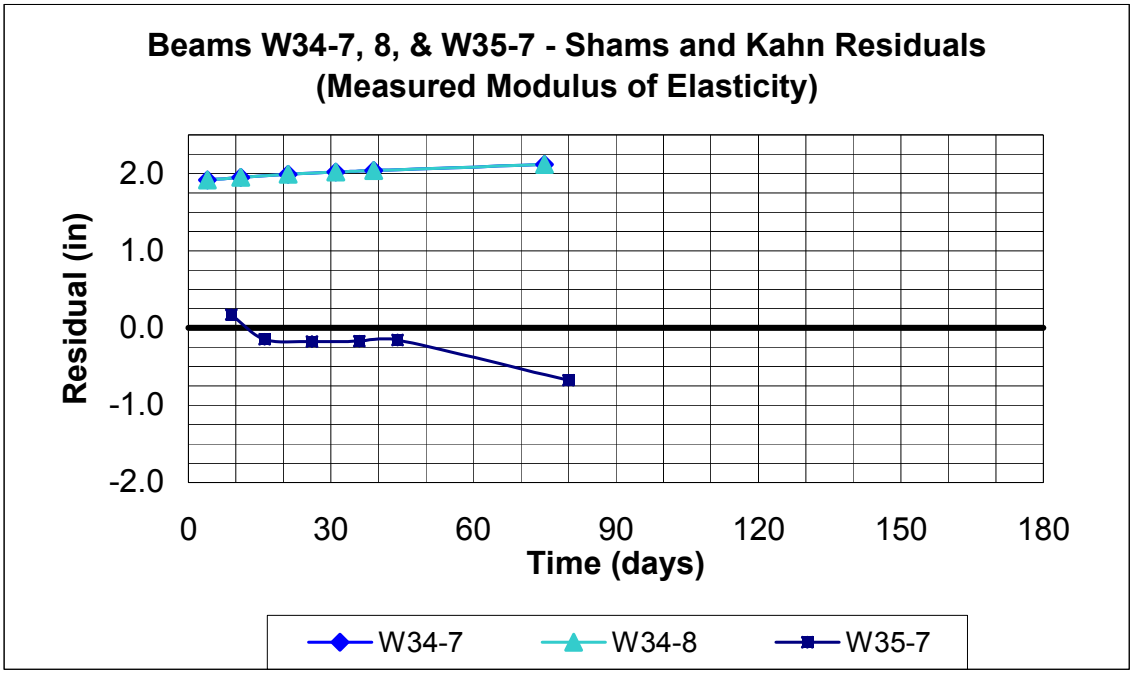

Figure B.82 Beams W34-7, 8, & W35-7 Kahn & Shams Residuals (Measured Modulus of Elasticity)

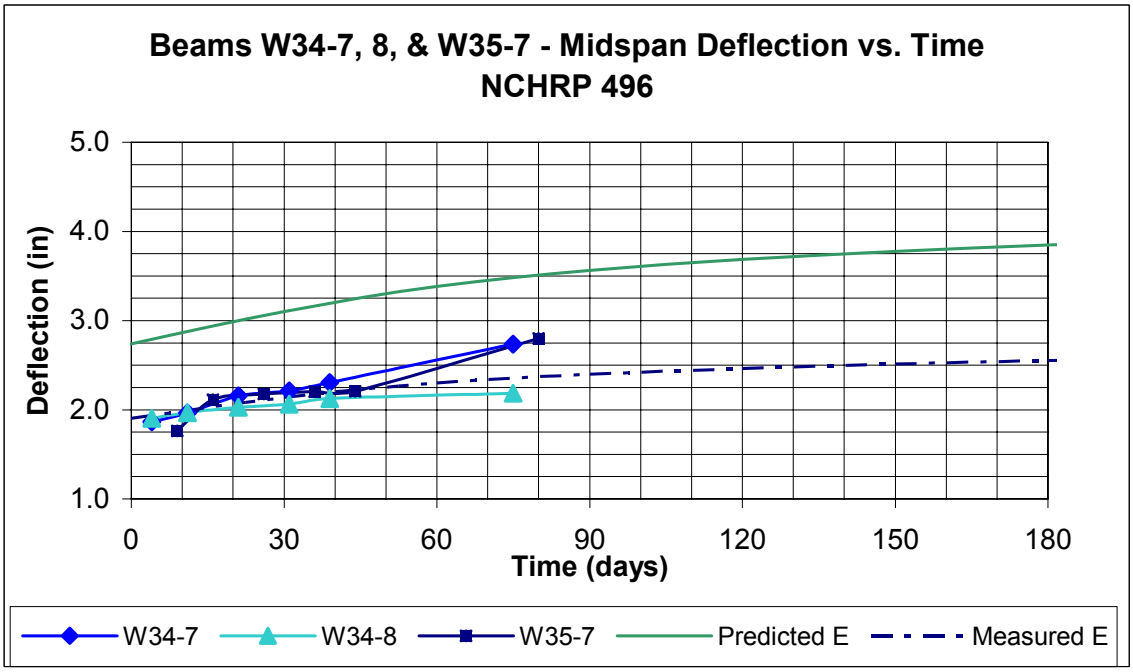

Figure B.83 Beams W34-7, 8, & W35-7 NCHRP 496 Predicted Deflection vs. Time

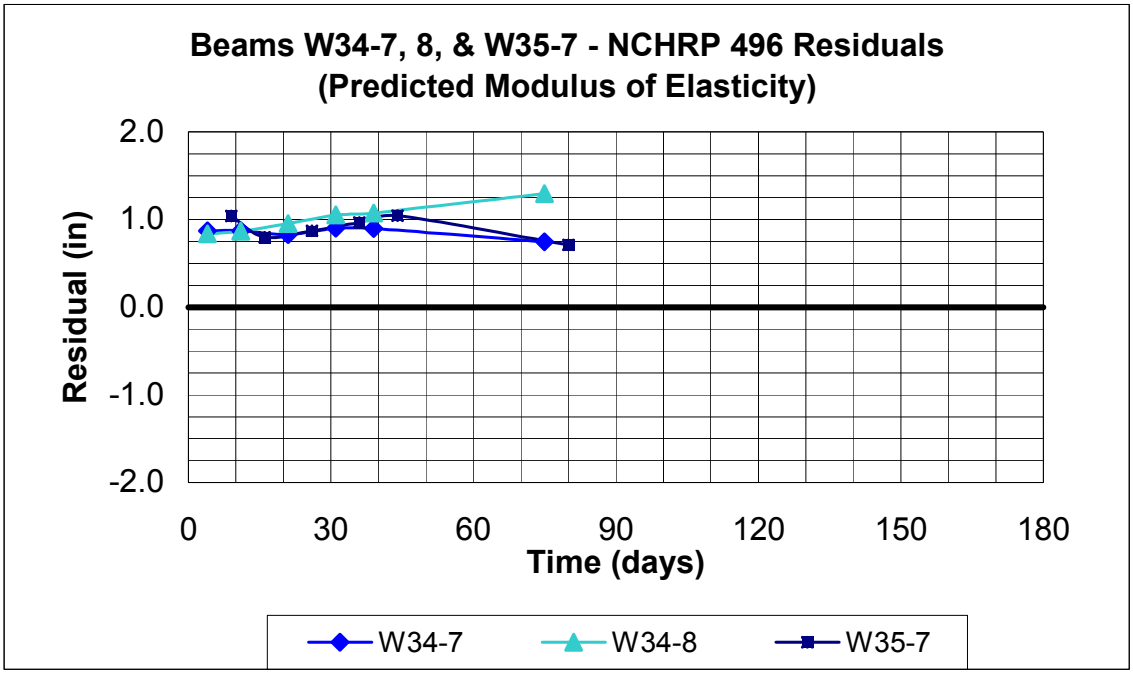

Figure B.84 Beams W34-7, 8, & W35-7 NCHRP 496 Residuals (Predicted Modulus of Elasticity)

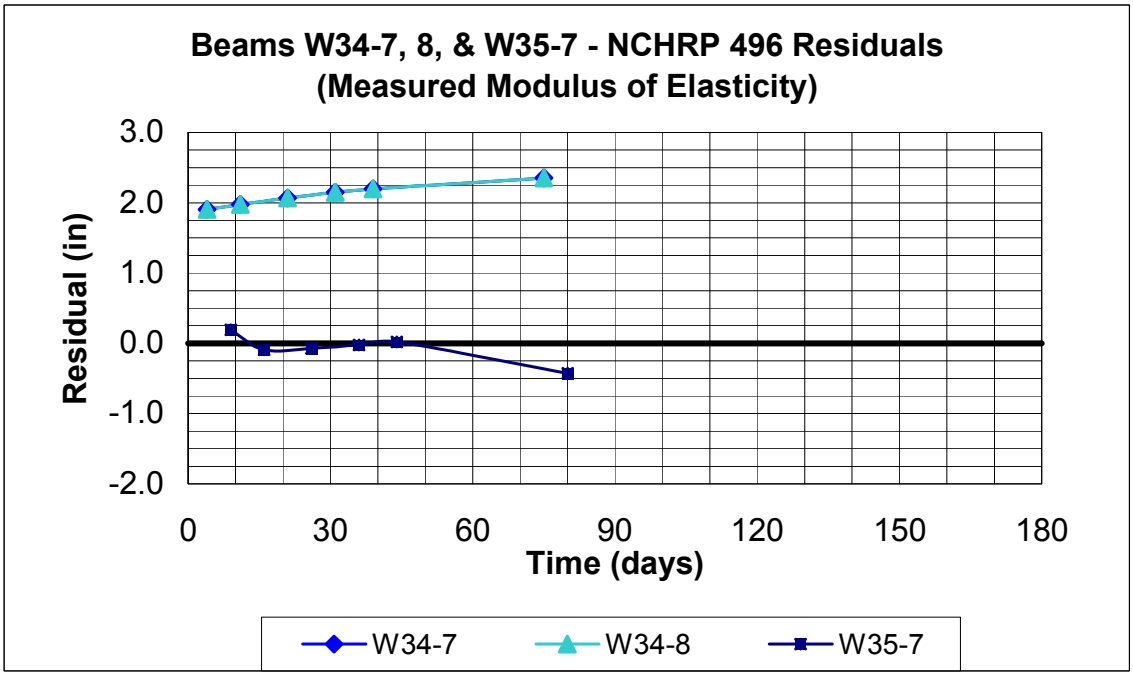

Figure B.85 Beams W34-7, 8, & W35-7 NCHRP 496 Residuals (Measured Modulus of Elasticity)

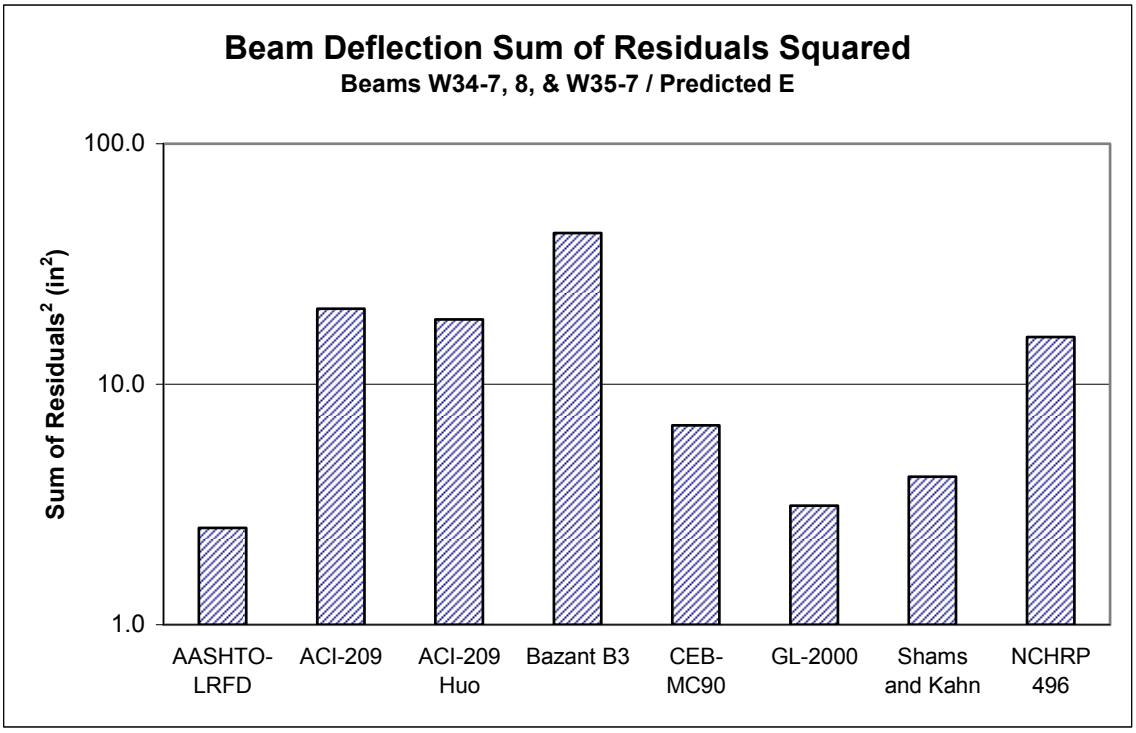

Figure B.86 Beams W34-7, 8, & W35-7 Deflection Sum of Residuals Squared, Predicted E

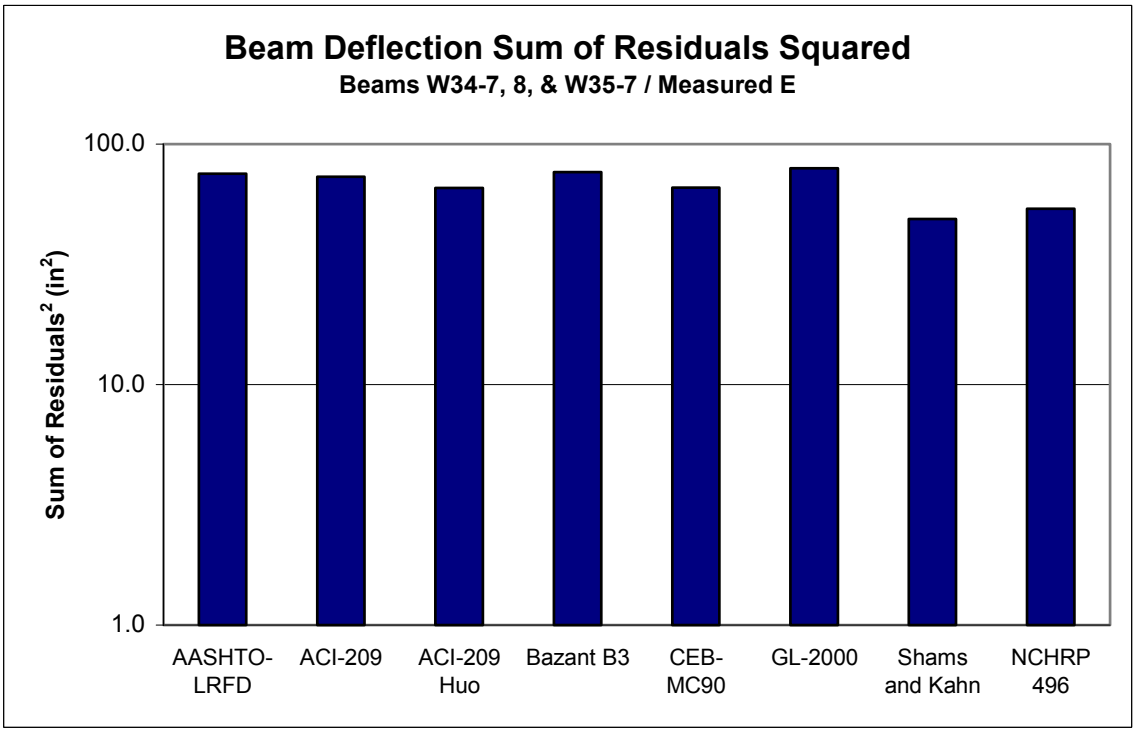

Figure B.87 Beams W34-7, 8, & W35-7 Deflection Sum of Residuals Squared, Predicted E

Table B.5 Beams W34-7, 8, & W35-7 Model Ranking with Predicted E

Rank	Model
1	**AASHTO-LRFD**
2	Shams and Kahn
3	CEB-MC90
4	NCHRP 496
5	ACI-209
6	ACI-209, modified by Huo
7	GL-2000
8	Bazant B3

Table B.6 Beams W34-7, 8, & W35-7 Model Ranking with Measured E

Rank	Model
1	**Shams and Kahn**
2	NCHRP 496
3	AASHTO-LRFD
4	CEB-MC90
5	ACI-209
6	ACI-209, modified by Huo
7	Bazant B3
8	GL-2000

B.4 Additional Beams W23-2 & W25-1

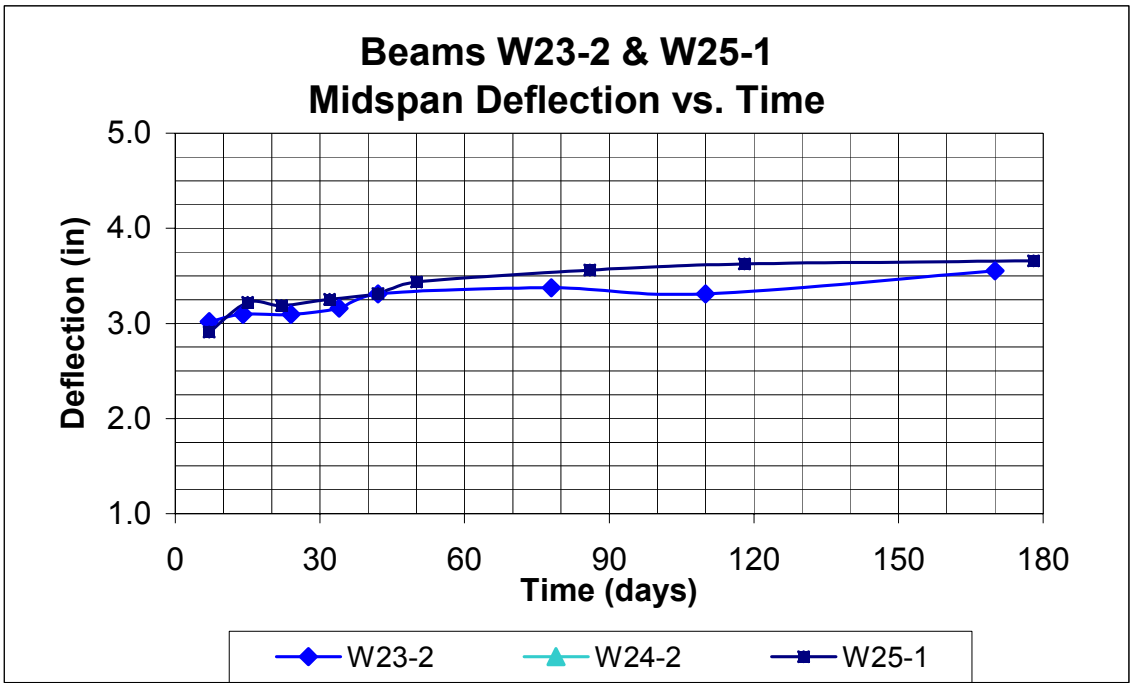

Figure B.88 Beams W23-2 & W25-1, Deflection vs. Time

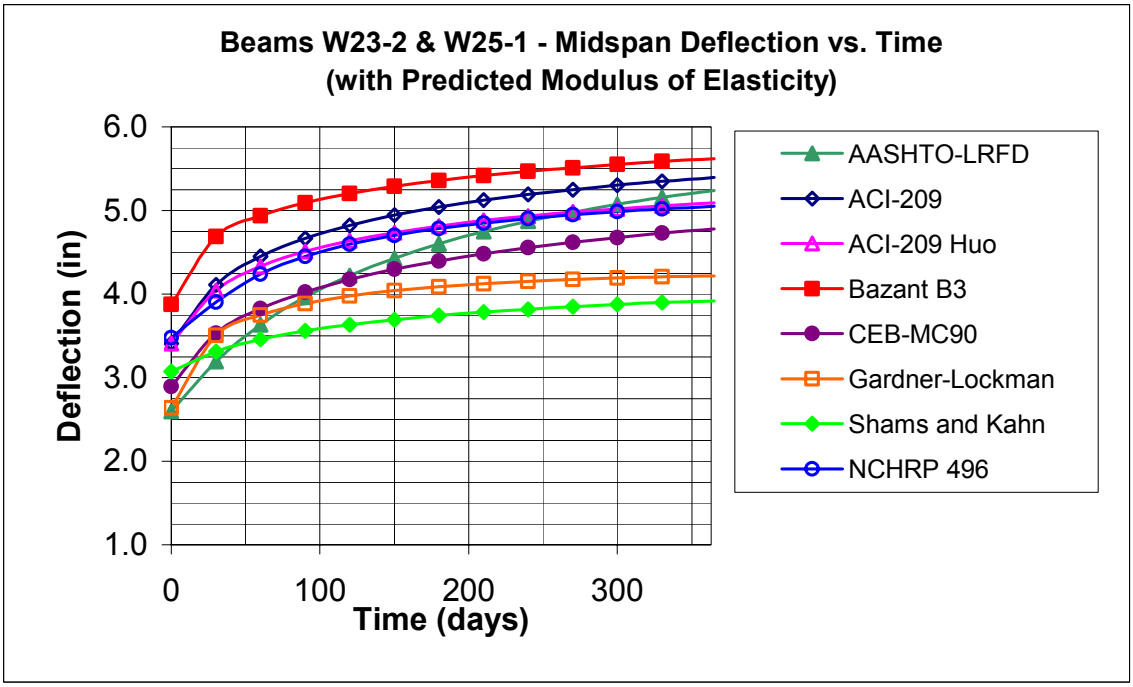

Figure B.89 Beams W23-2 & W25-1, Predicted Deflection vs. Time (Predicted E)

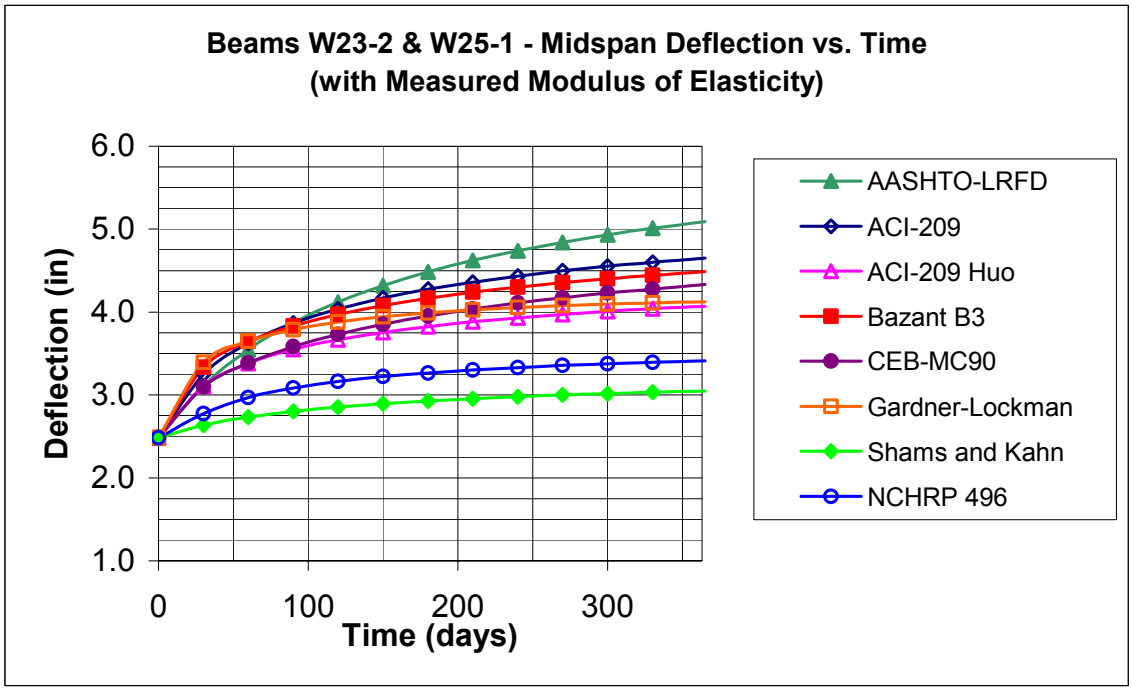

Figure B.90 Beams W23-2 & W25-1, Predicted Deflection vs. Time (Measured E)

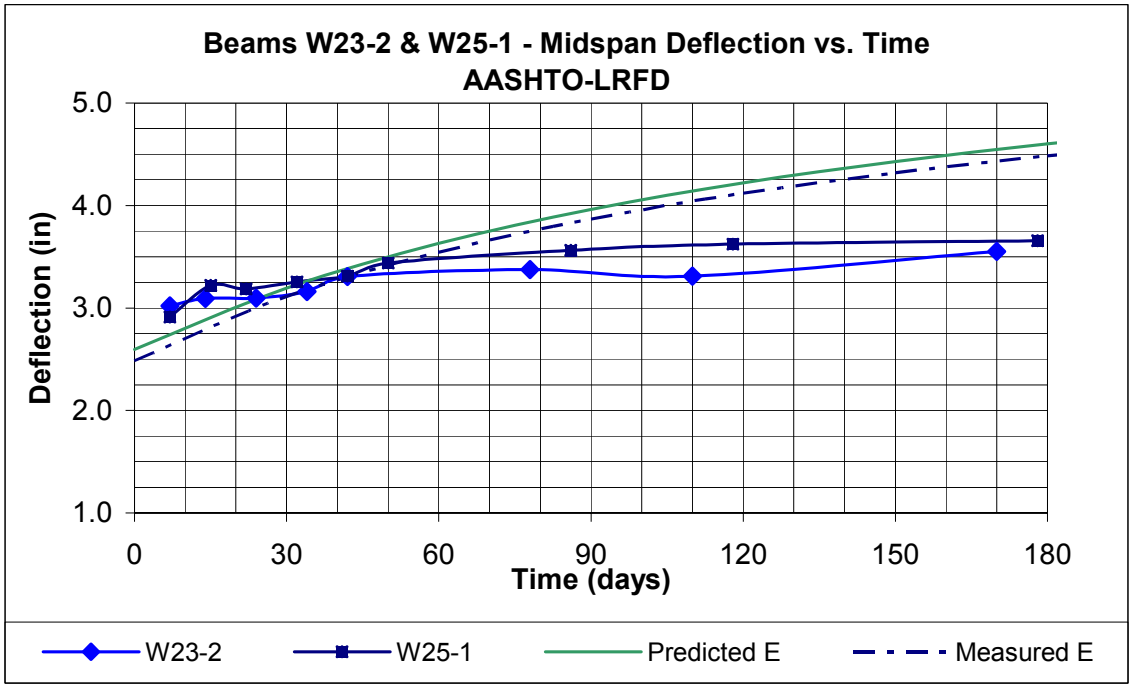

Figure B.91 Beams W23-2 & W25-1 AASHTO-LRFD Predicted Deflection vs. Time

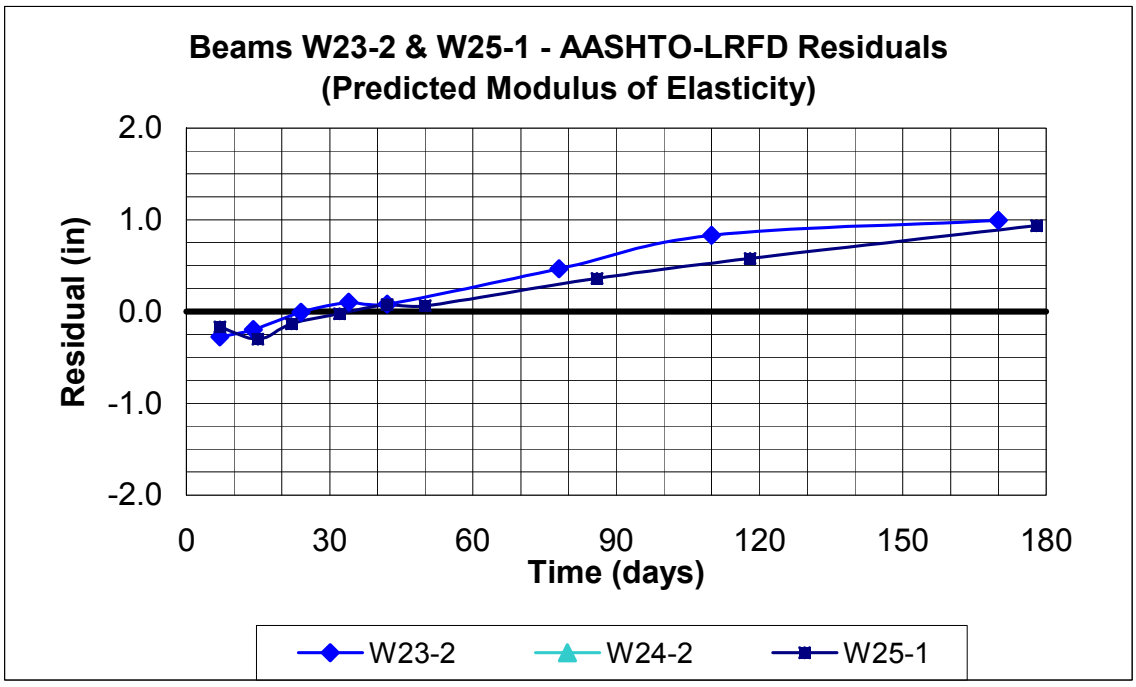

Figure B.92 Beams W23-2 & W25-1 AASHTO-LRFD Residuals (Predicted Modulus of Elasticity)

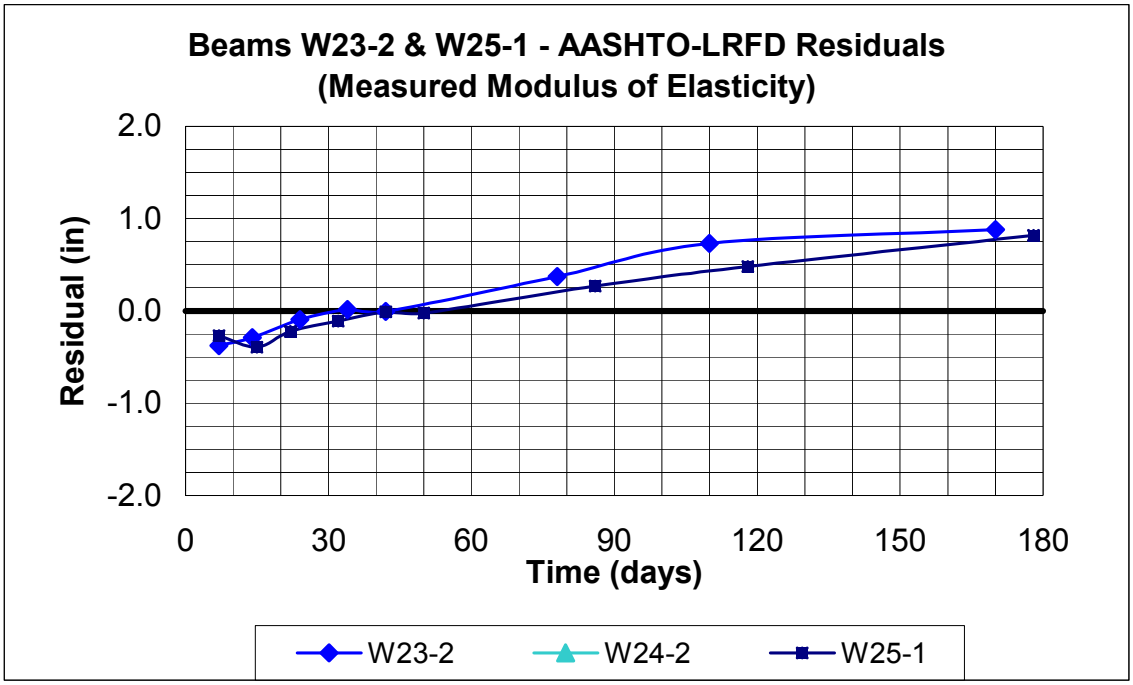

Figure B.93 Beams W23-2 & W25-1 AASHTO-LRFD Residuals (Measured Modulus of Elasticity)

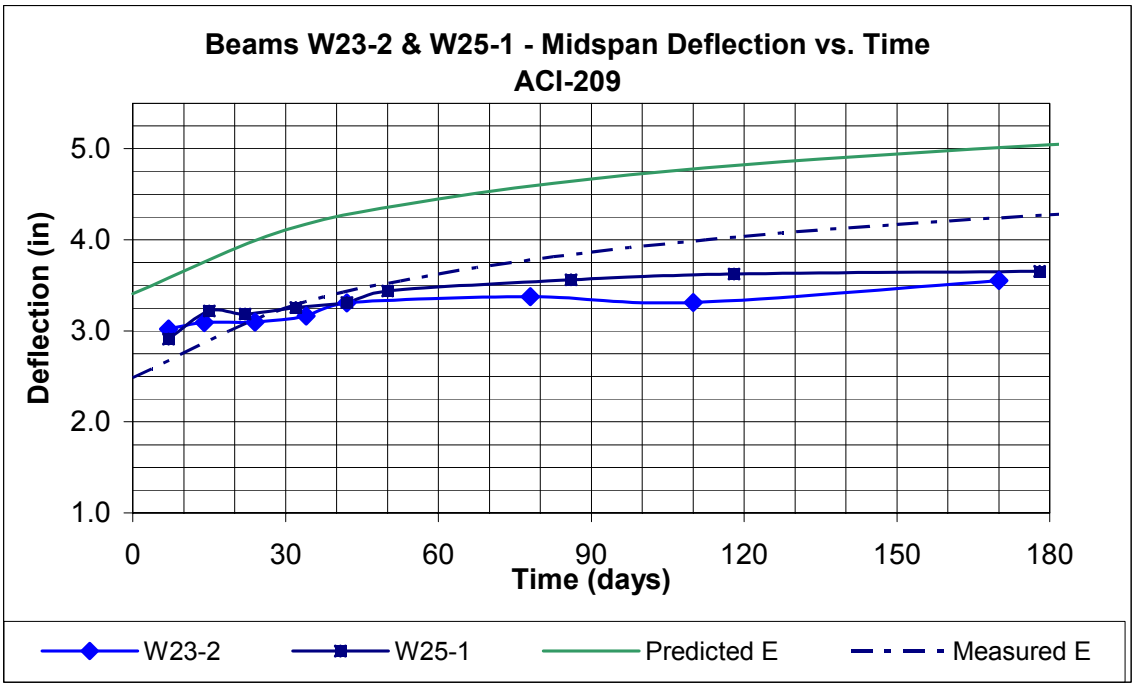

Figure B.94 Beams W23-2 & W25-1 ACI-209 Predicted Deflection vs. Time

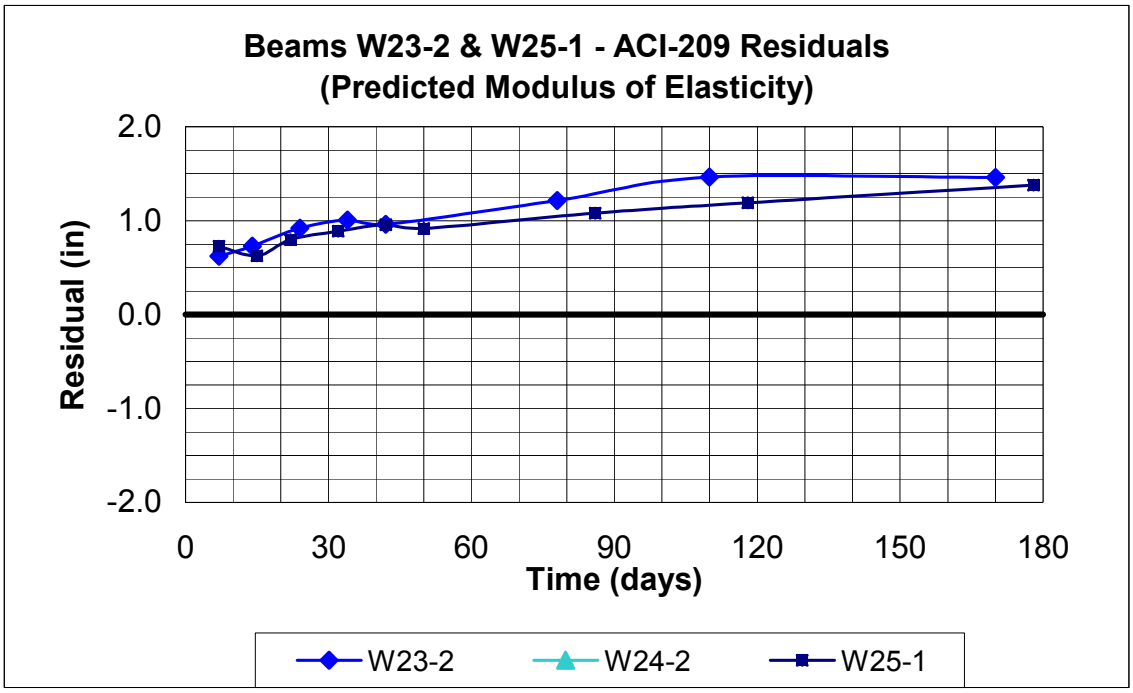

Figure B.95 Beams W23-2 & W25-1 ACI-209 Residuals (Predicted Modulus of Elasticity)

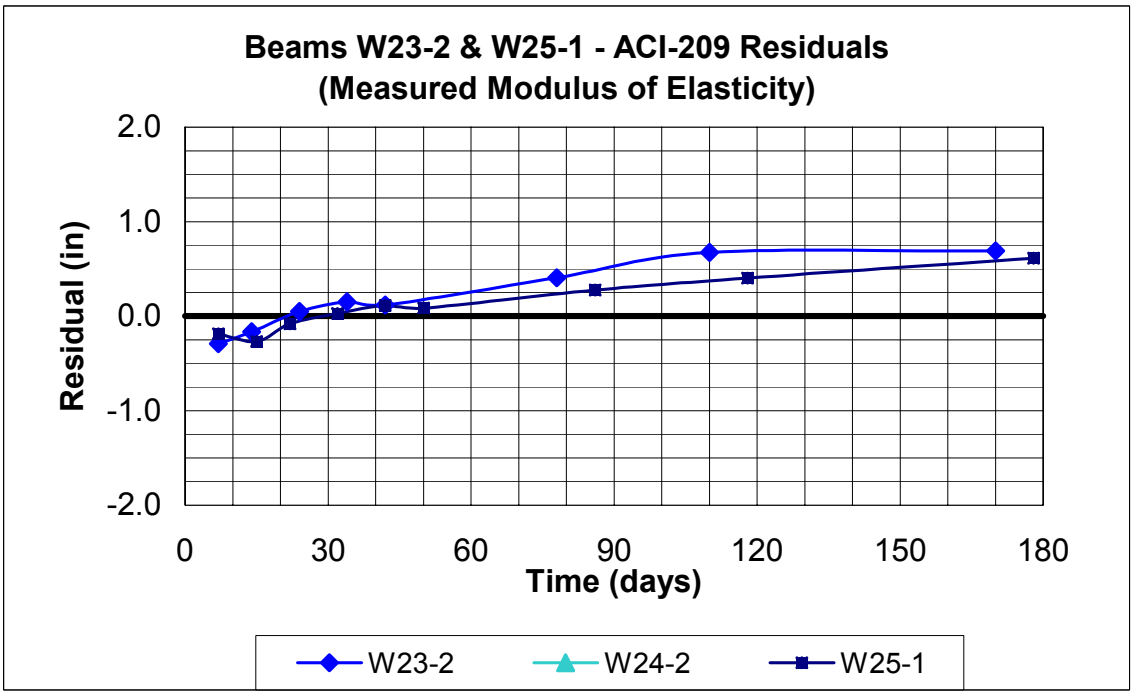

Figure B.96 Beams W23-2 & W25-1 ACI-209 Residuals (Measured Modulus of Elasticity)

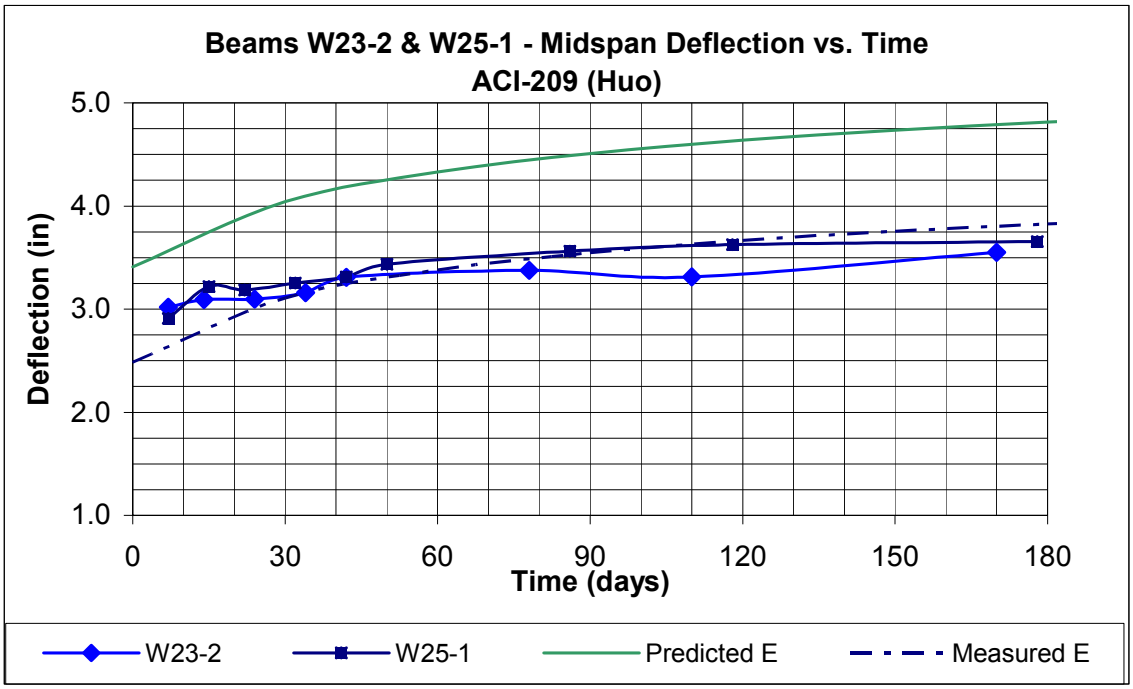

Figure B.97 Beams W23-2 & W25-1 ACI-209 (Huo) Predicted Deflection vs. Time

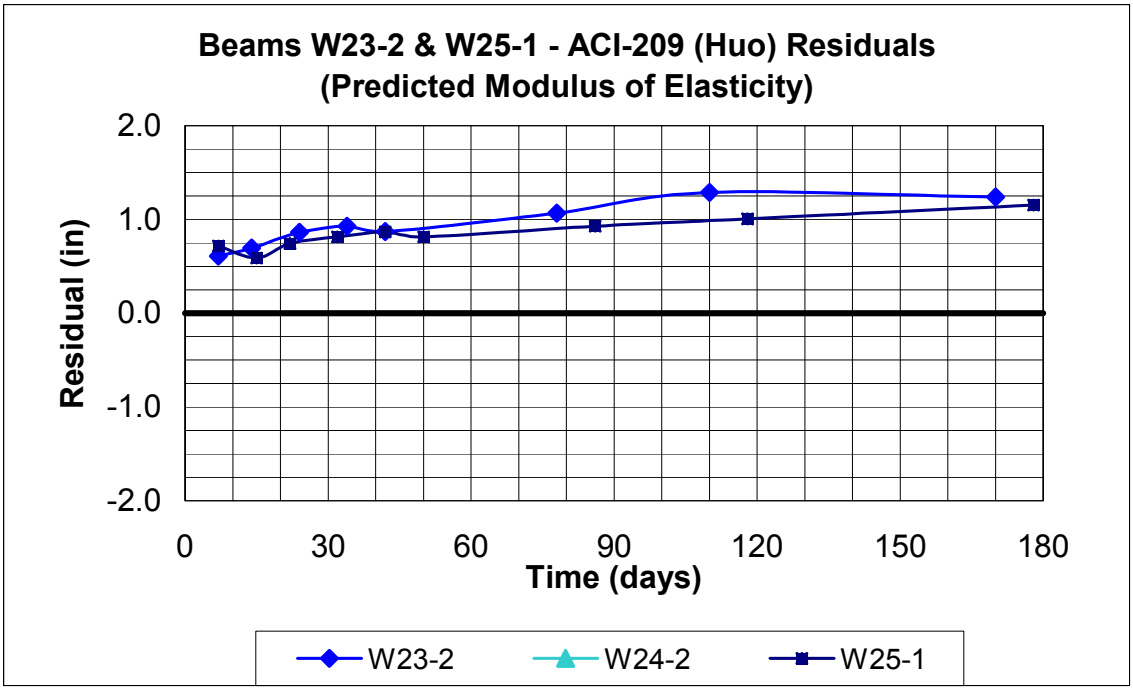

Figure B.98 Beams W23-2 & W25-1 ACI-209 (Huo) Residuals (Predicted Modulus of Elasticity)

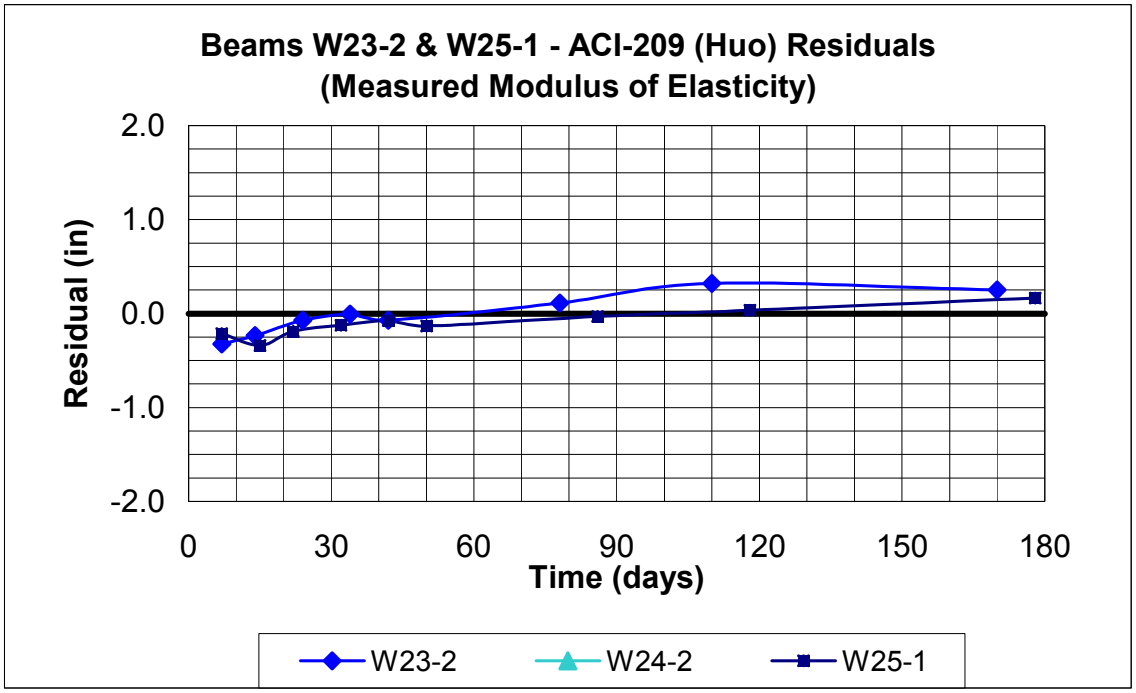

Figure B.99 Beams W23-2 & W25-1 ACI-209 (Huo) Residuals (Measured Modulus of Elasticity)

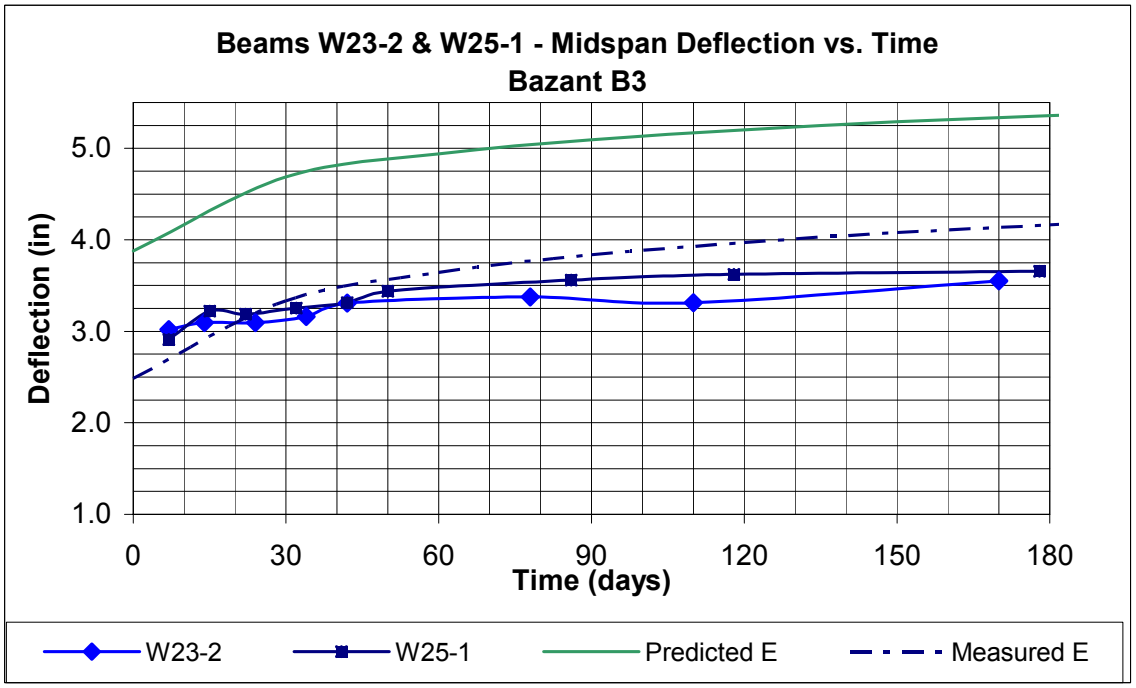

Figure B.100 Beams W23-2 & W25-1 Bazant B3 Predicted Deflection vs. Time

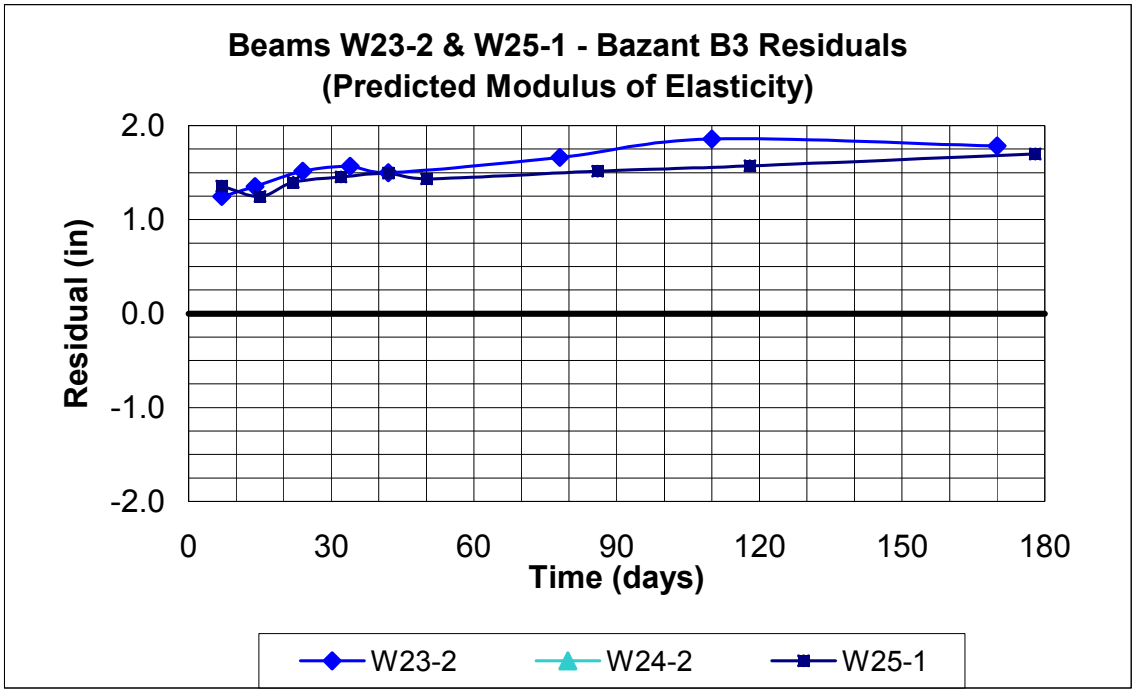

Figure B.101 Beams W23-2 & W25-1 Bazant B3 Residuals (Predicted Modulus of Elasticity)

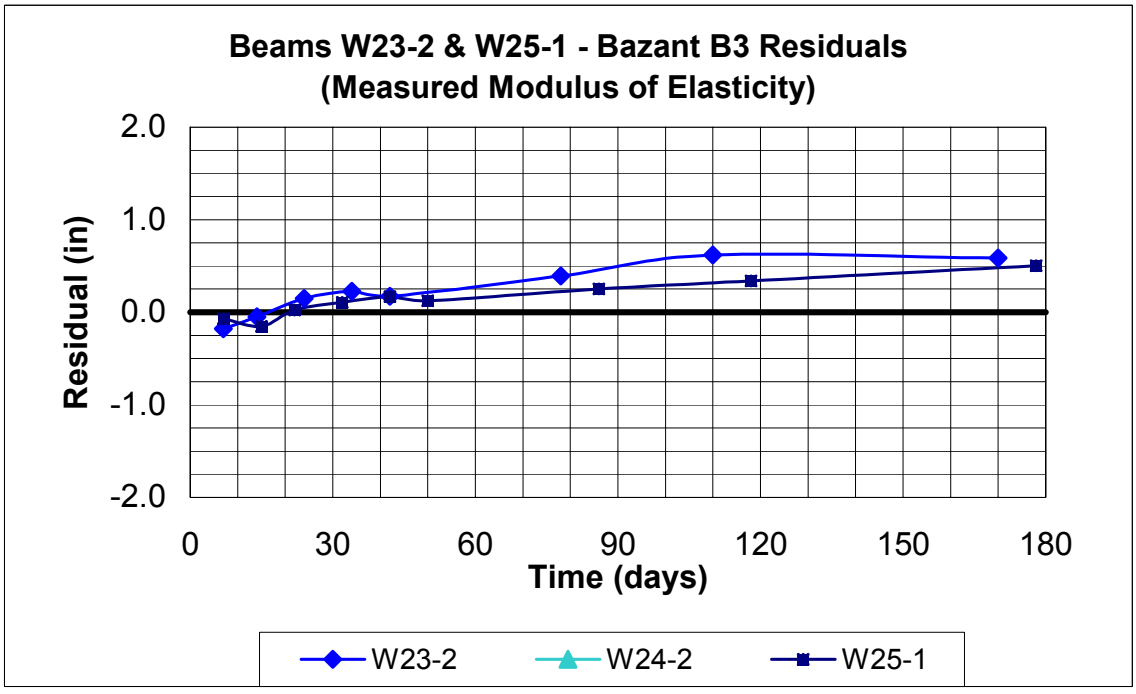

Figure B.102 Beams W23-2 & W25-1 Bazant B3 Residuals (Measured Modulus of Elasticity)

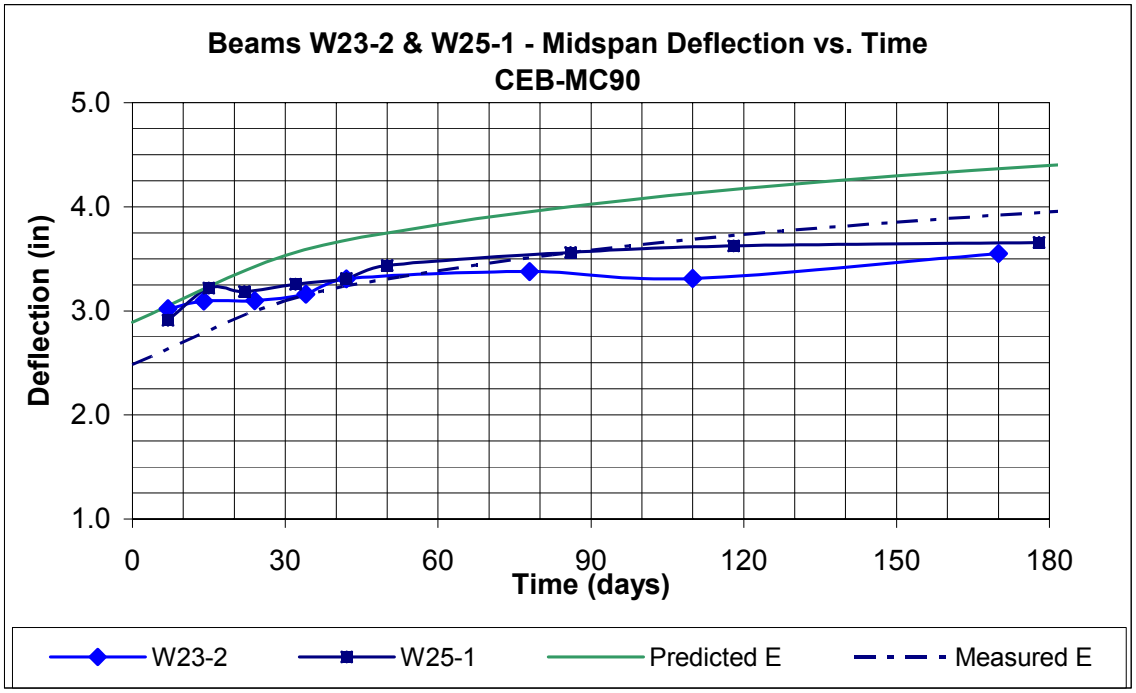

Figure B.103 Beams W23-2 & W25-1 CEB-MC90 Predicted Deflection vs. Time

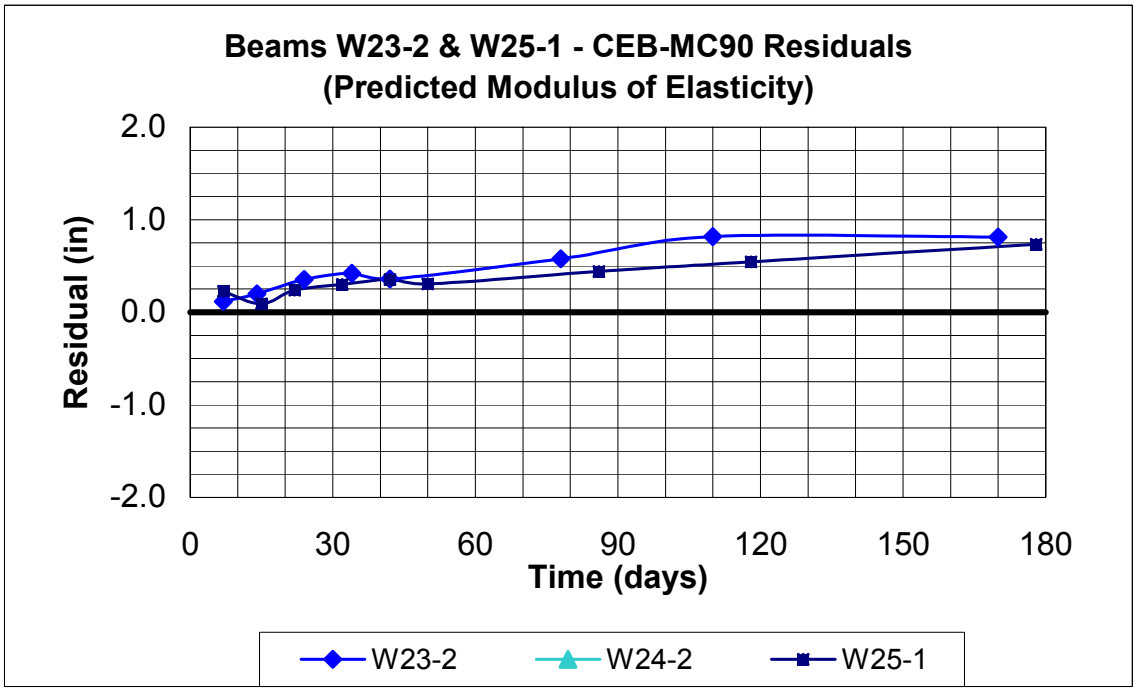

Figure B.104 Beams W23-2 & W25-1 CEB-MC90 Residuals (Predicted Modulus of Elasticity)

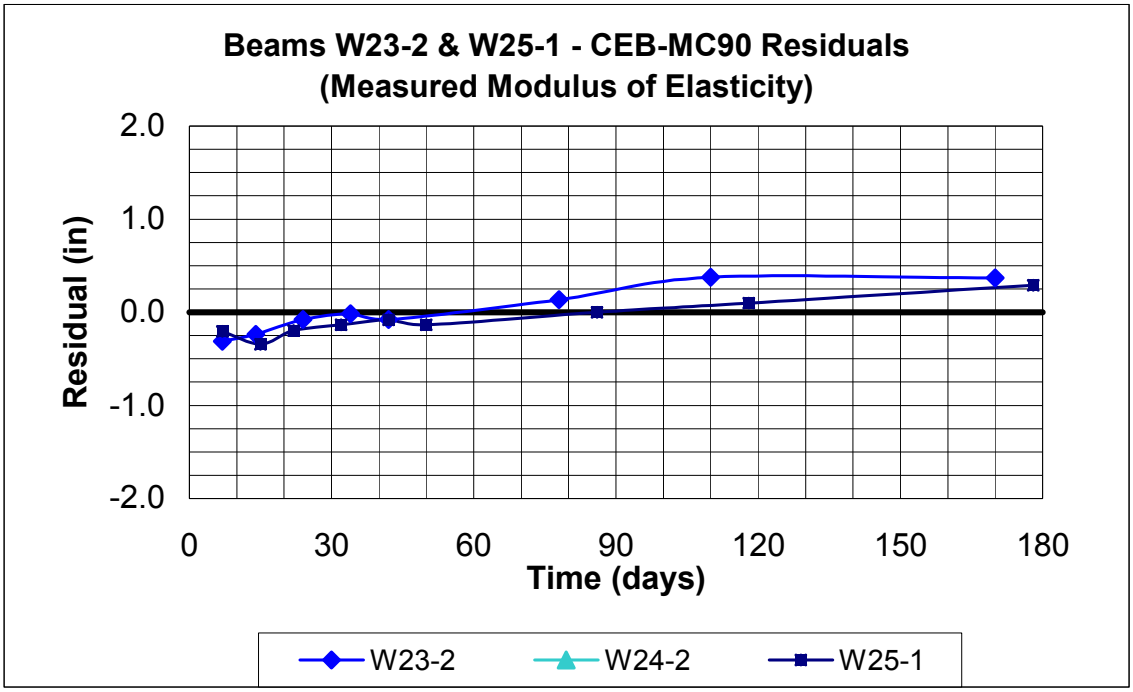

Figure B.105 Beams W23-2 & W25-1 CEB-MC90 Residuals (Measured Modulus of Elasticity)

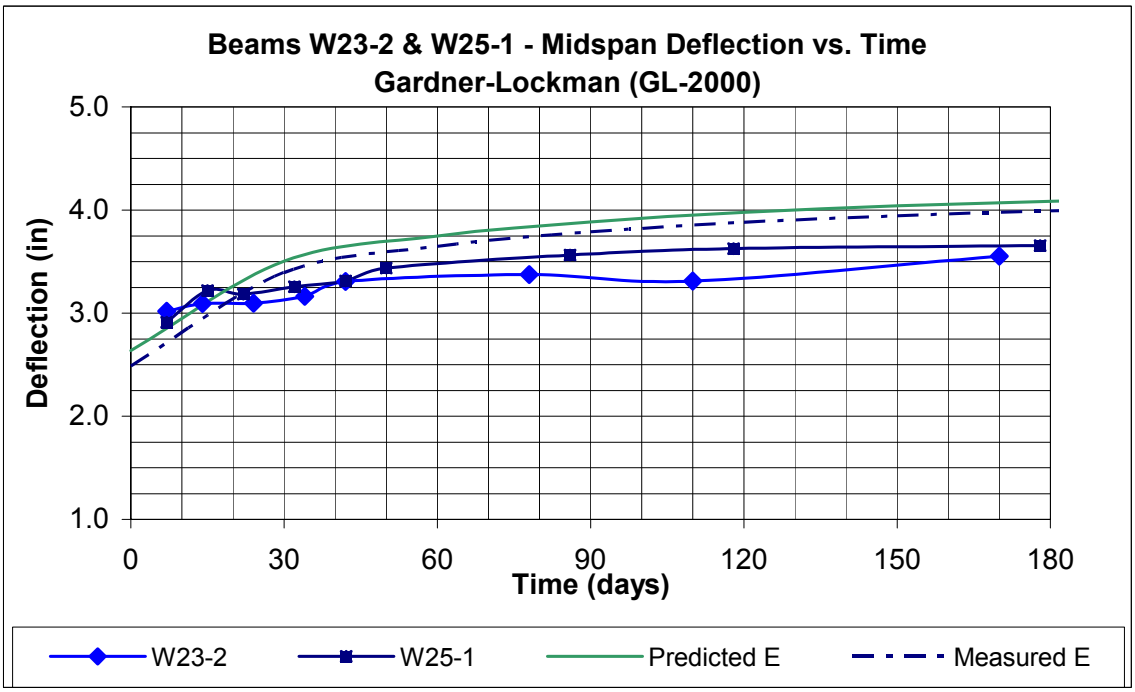

Figure B.106 Beams W23-2 & W25-1 GL-2000 Predicted Deflection vs. Time

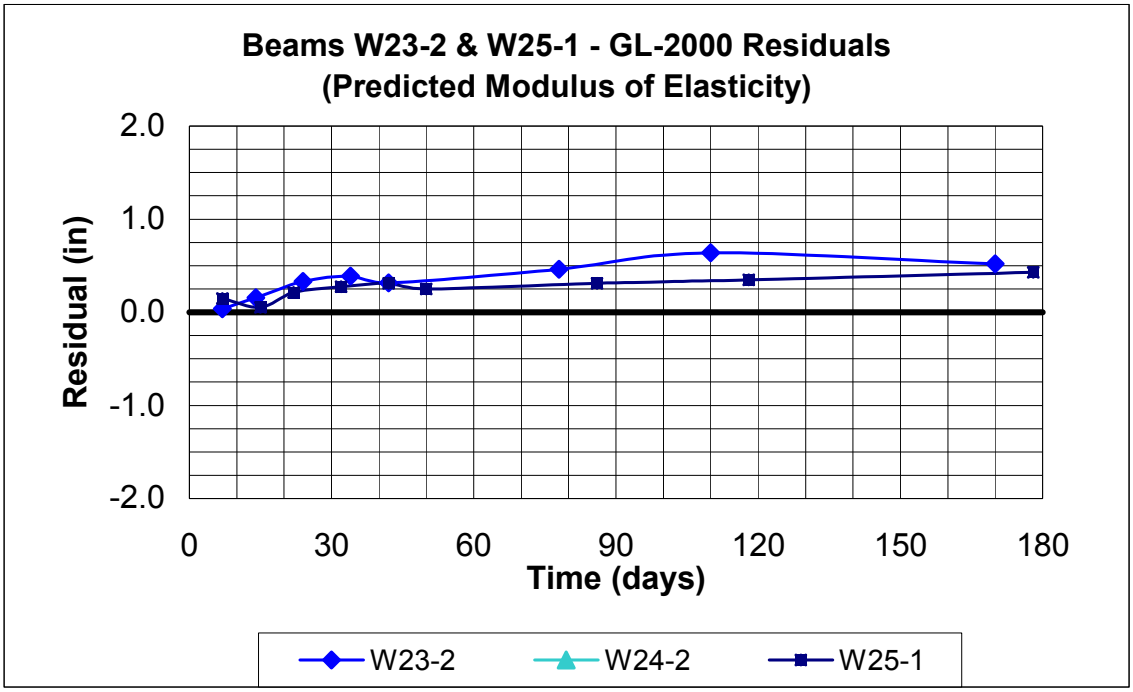

Figure B.107 Beams W23-2 & W25-1 GL-2000 Residuals (Predicted Modulus of Elasticity)

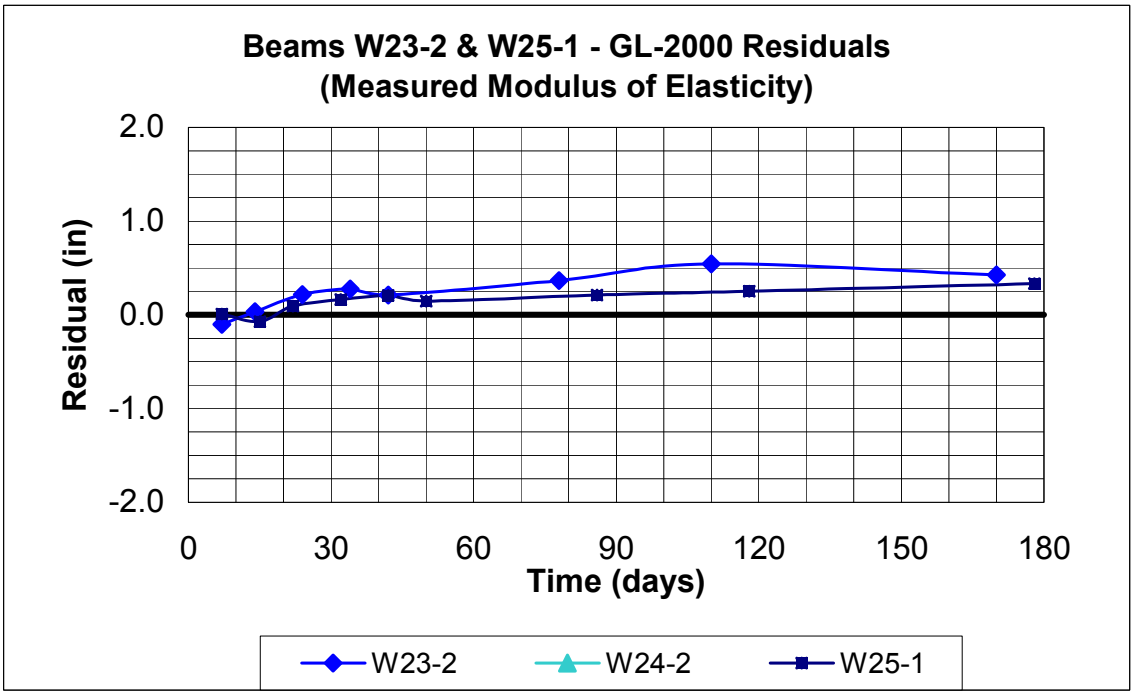

Figure B.108 Beams W23-2 & W25-1 GL-2000 Residuals (Measured Modulus of Elasticity)

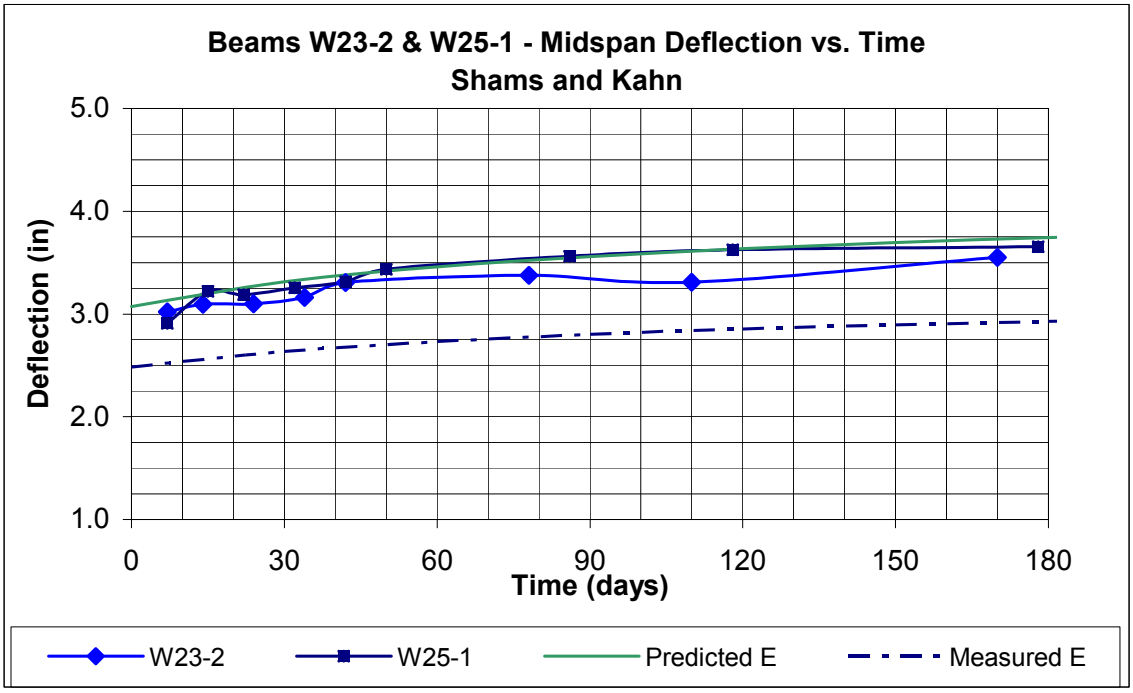

Figure B.109 Beams W23-2 & W25-1 Kahn & Shams Predicted Deflection vs. Time

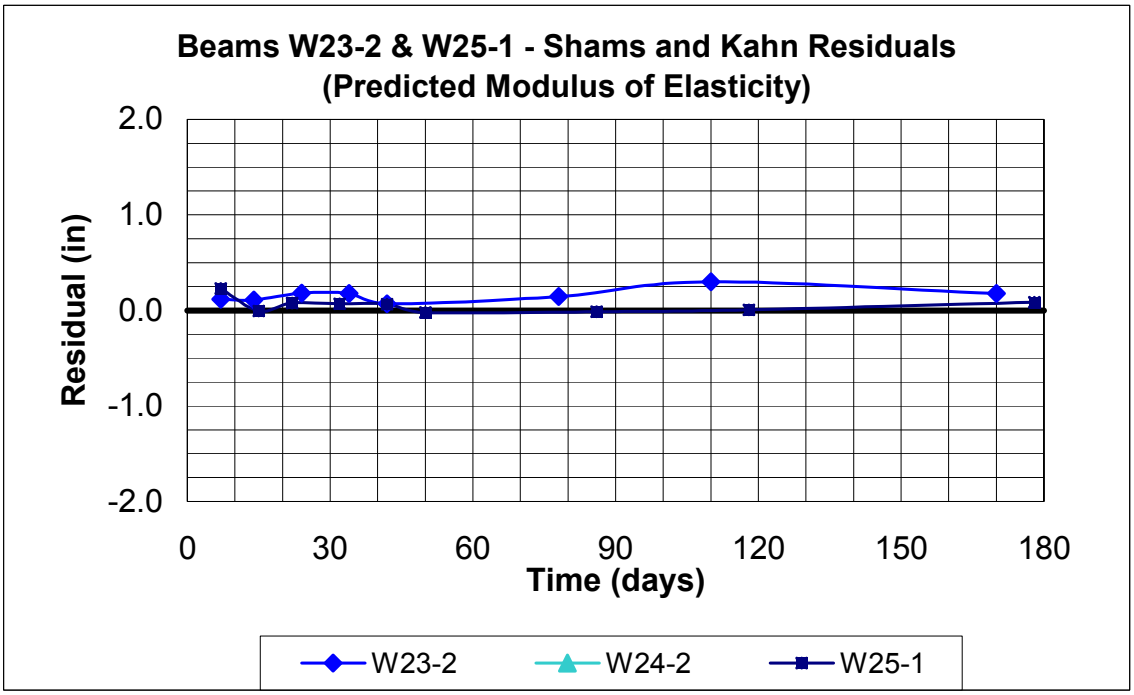

Figure B.110 Beams W23-2 & W25-1 Kahn & Shams Residuals (Predicted Modulus of Elasticity)

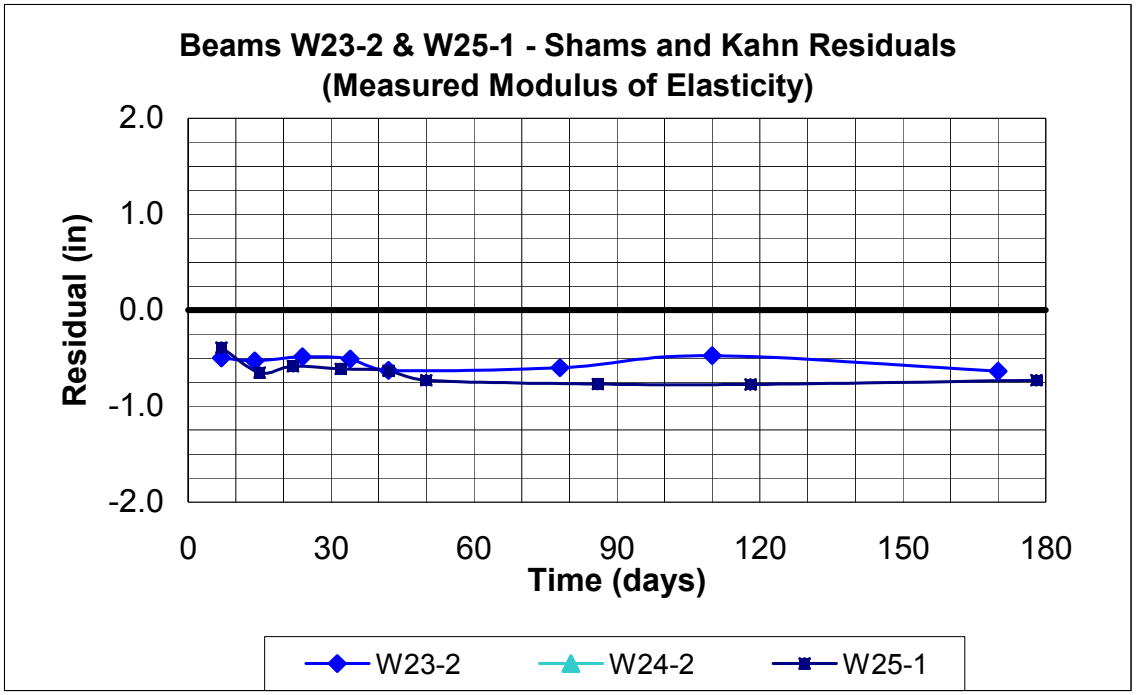

Figure B.111 Beams W23-2 & W25-1 Kahn & Shams Residuals (Measured Modulus of Elasticity)

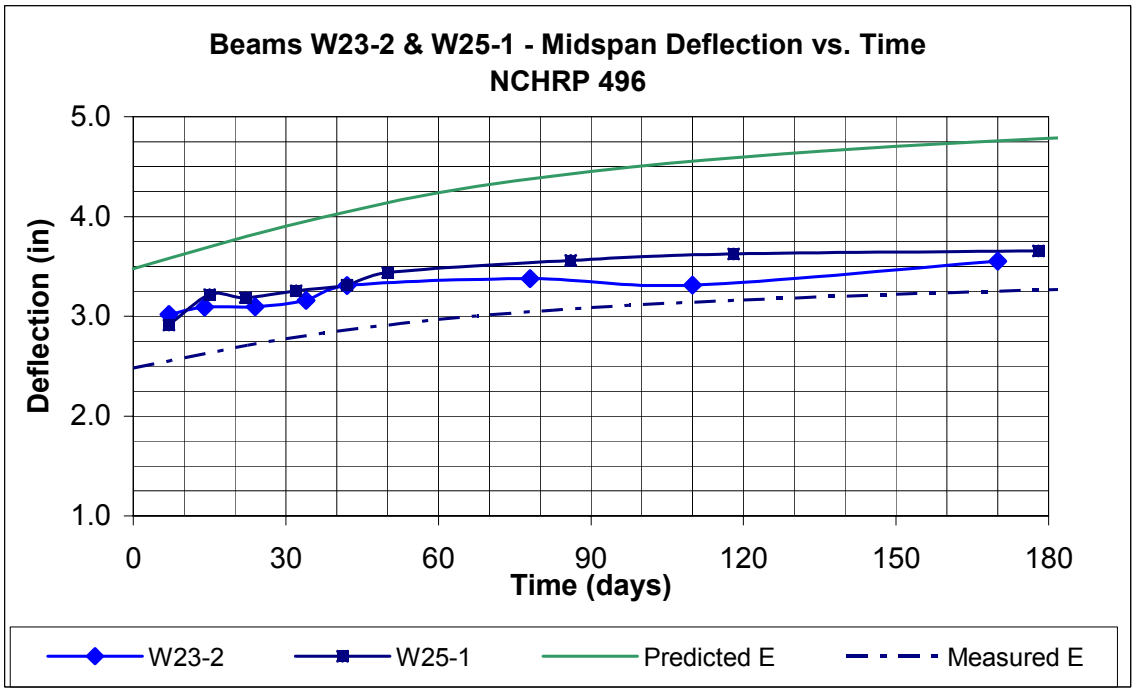

Figure B.112 Beams W23-2 & W25-1 NCHRP 496 Predicted Deflection vs. Time

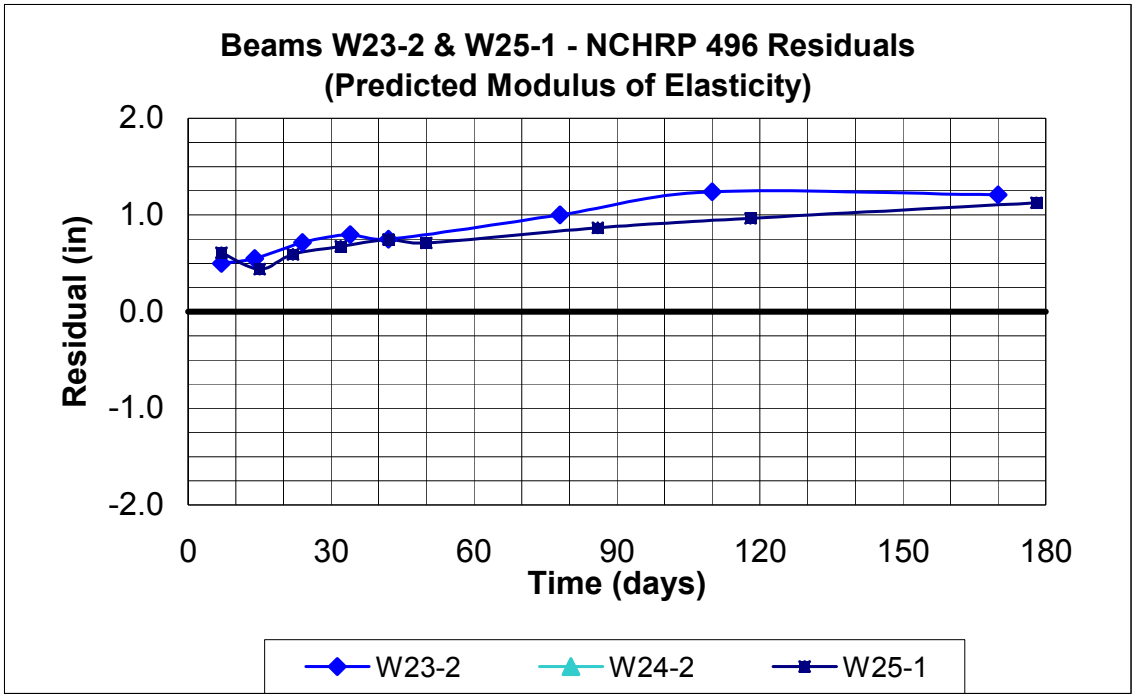

Figure B.113 Beams W23-2 & W25-1 NCHRP 496 Residuals (Predicted Modulus of Elasticity)

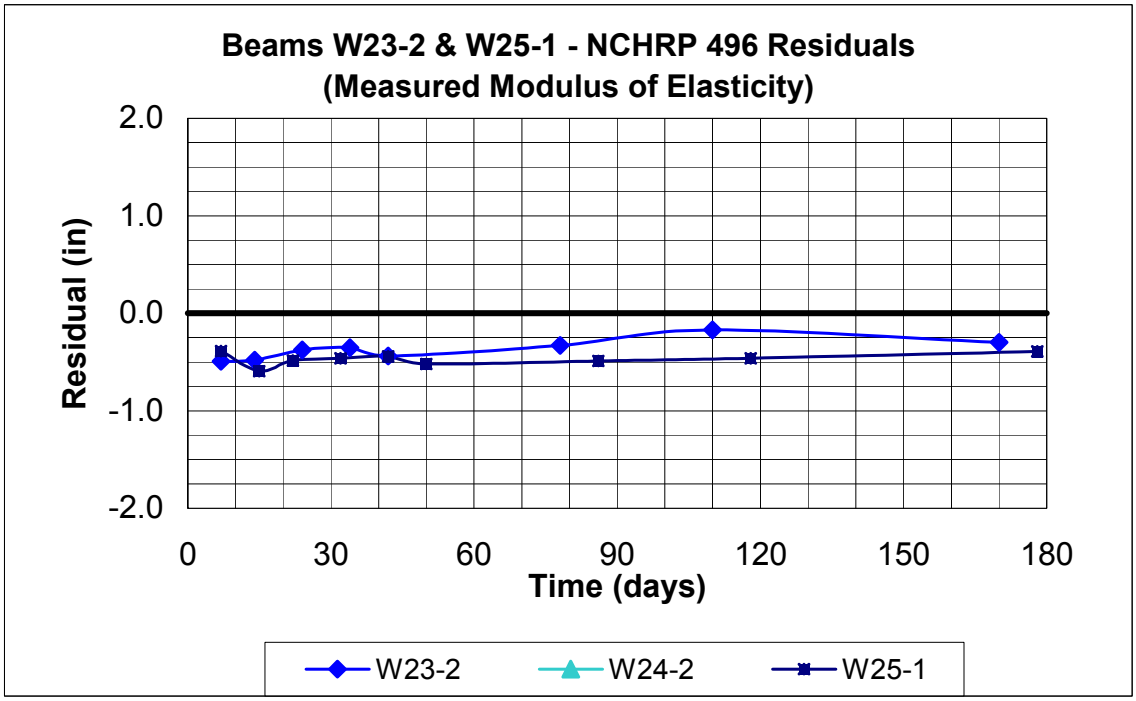

Figure B.114 Beams W23-2 & W25-1 NCHRP 496 Residuals (Measured Modulus of Elasticity)

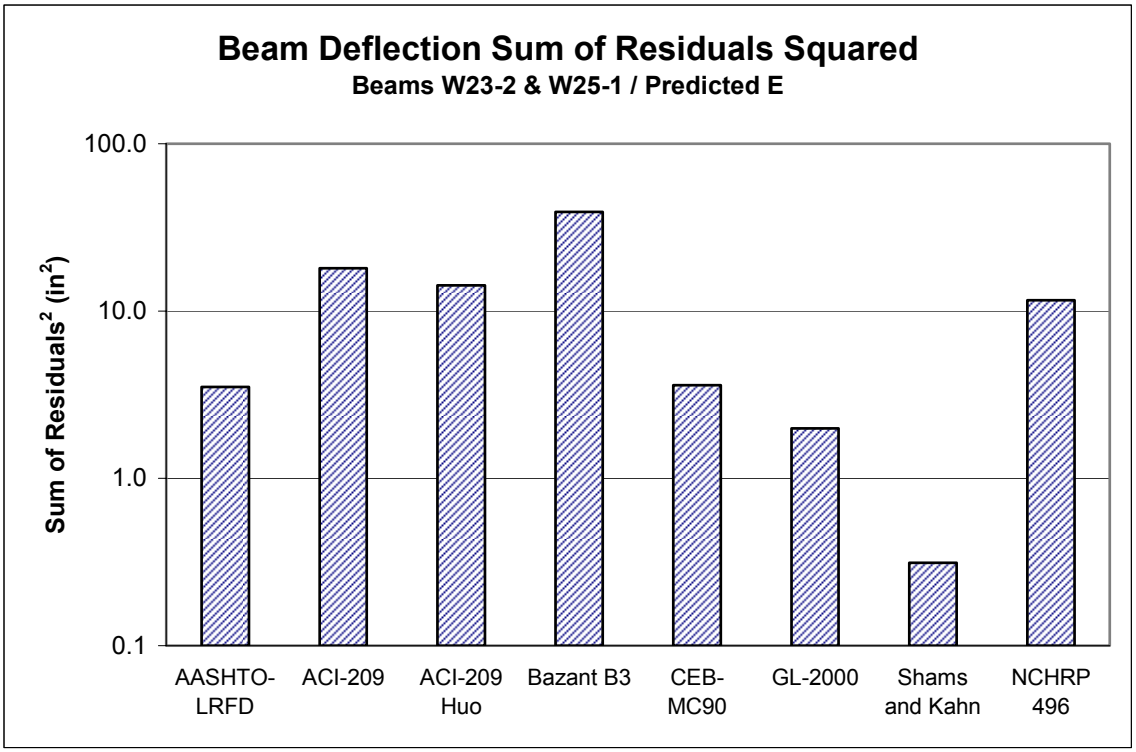

Figure B.115 Beams W23-2 & W25-1 Deflection Sum of Residuals Squared, Predicted E

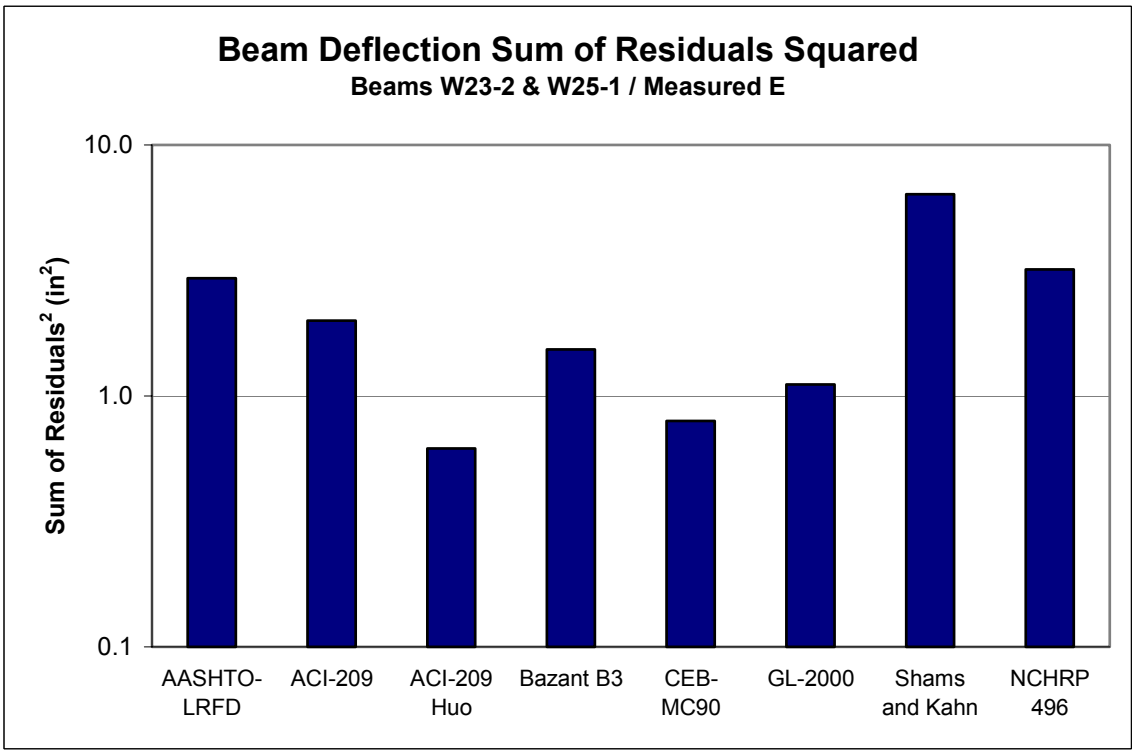

Figure B.116 Beams W23-2 & W25-1 Deflection Sum of Residuals Squared, Predicted E

Table B.7 Beams W23-2 & W25-1 Model Ranking with Predicted E

Rank	Model
1	**Shams and Kahn**
2	CEB-MC90
3	AASHTO-LRFD
4	NCHRP 496
5	ACI-209
6	ACI-209, modified by Huo
7	GL-2000
8	Bazant B3

Table B.8 Beams W23-2 & W25-1 Model Ranking with Measured E

Rank	Model
1	**CEB-MC90**
2	Bazant B3
3	ACI-209
4	ACI-209, modified by Huo
5	AASHTO-LRFD
6	NCHRP 496
7	Shams and Kahn
8	GL-2000

B.5 Additional Beam W25-10

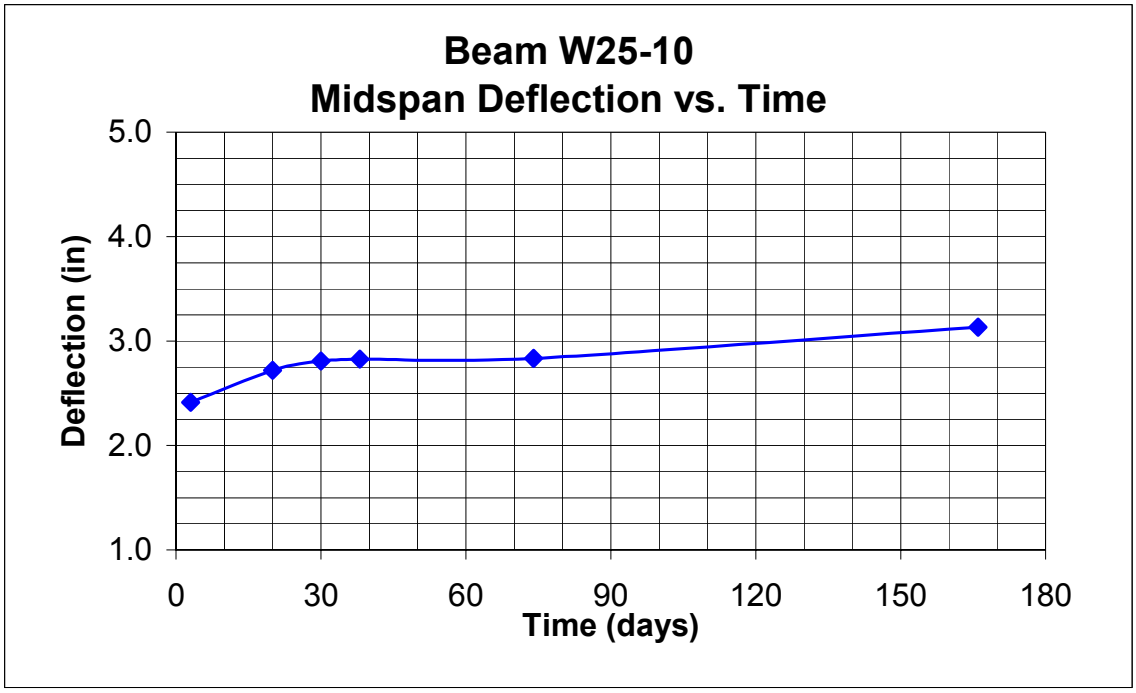

Figure B.117 Beam W25-10, Deflection vs. Time

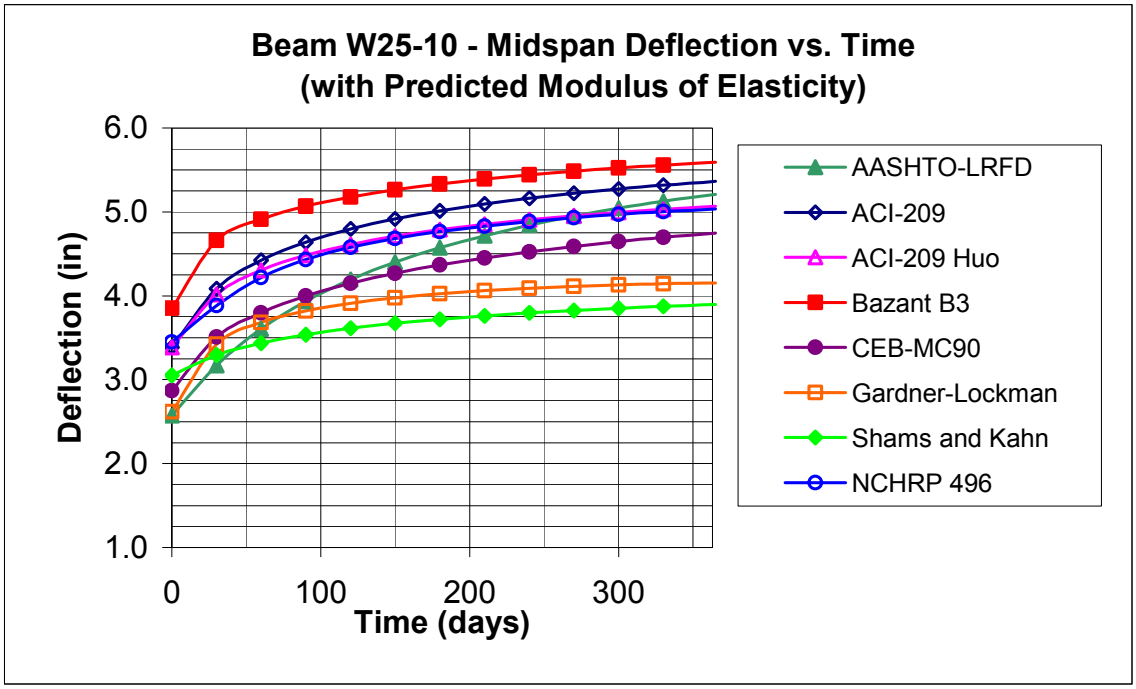

Figure B.118 Beam W25-10, Predicted Deflection vs. Time (Predicted E)

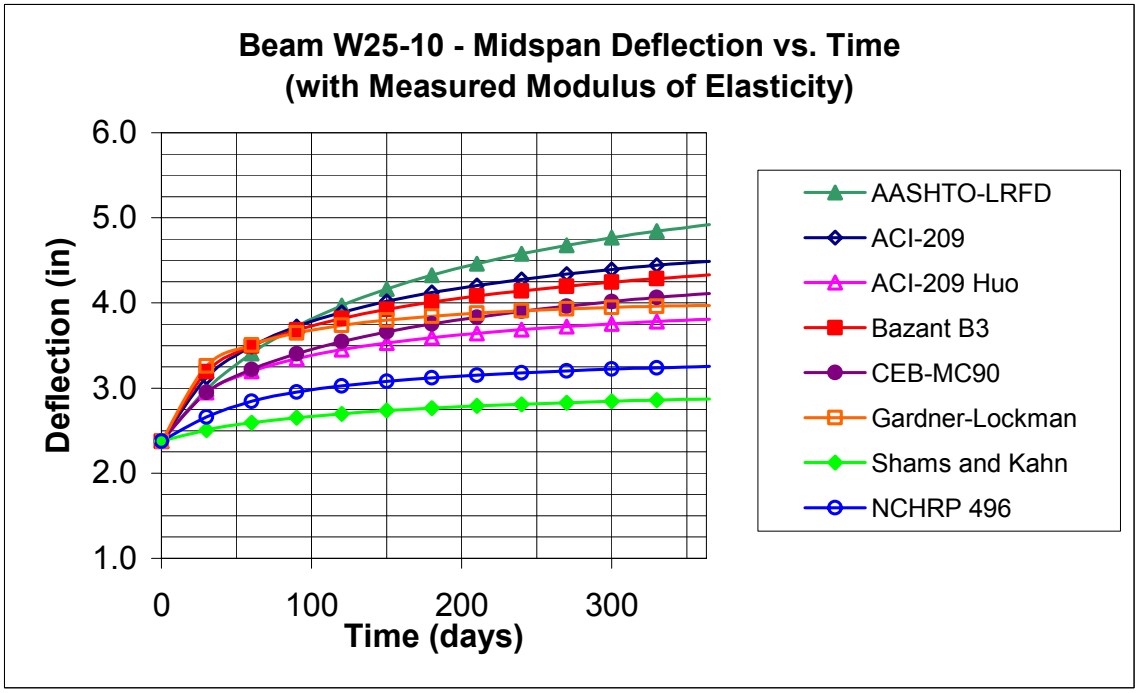

Figure B.119 Beam W25-10, Predicted Deflection vs. Time (Measured E)

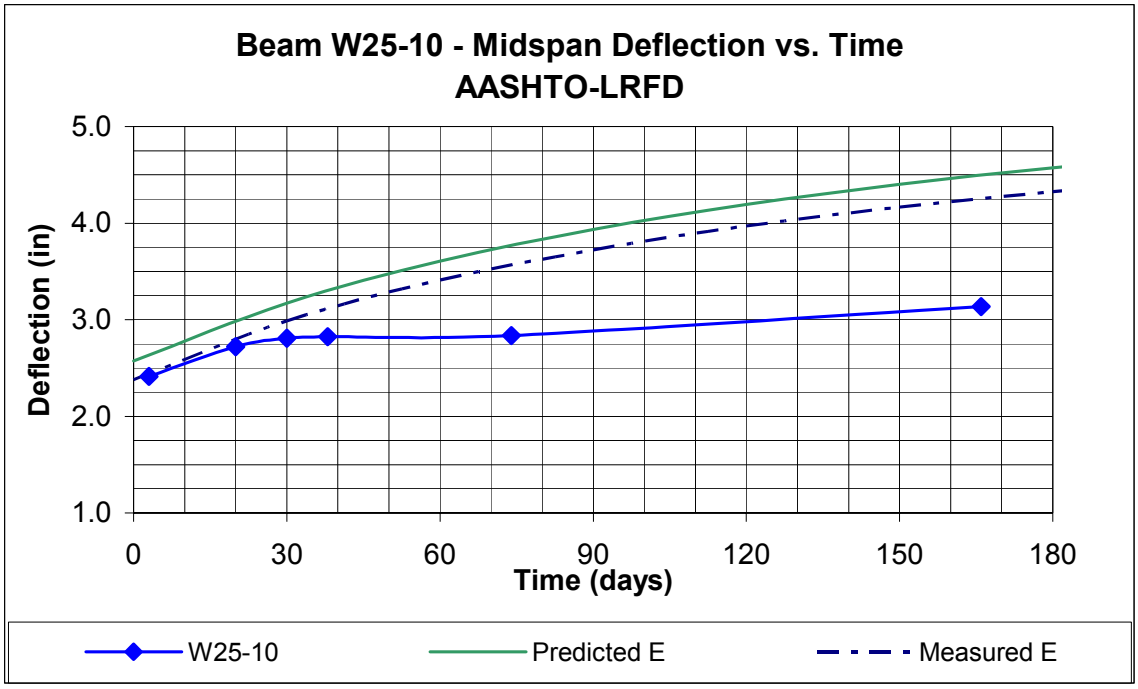

Figure B.120 Beam W25-10 AASHTO-LRFD Predicted Deflection vs. Time

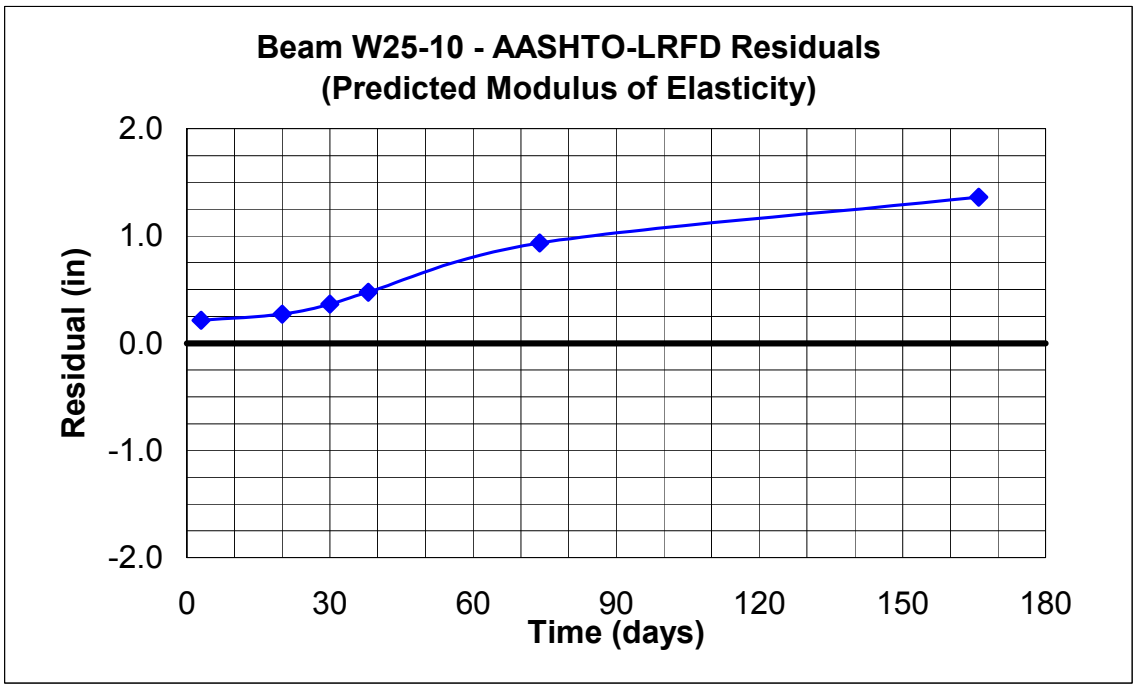

Figure B.121 Beam W25-10 AASHTO-LRFD Residuals (Predicted Modulus of Elasticity)

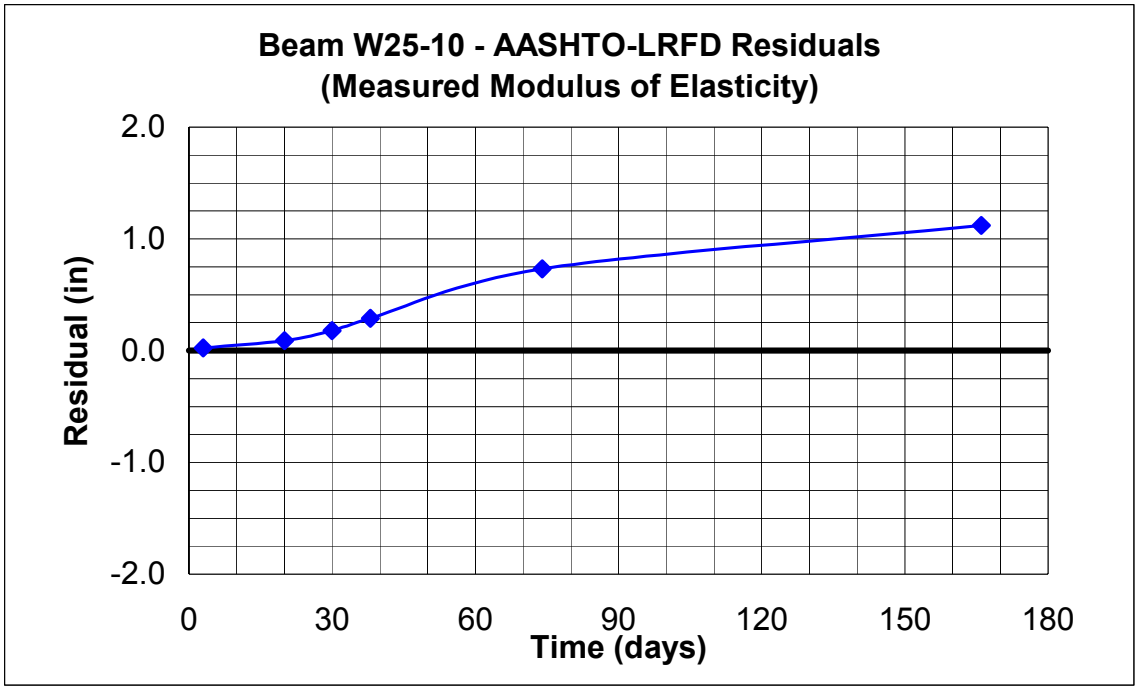

Figure B.122 Beam W25-10 AASHTO-LRFD Residuals (Measured Modulus of Elasticity)

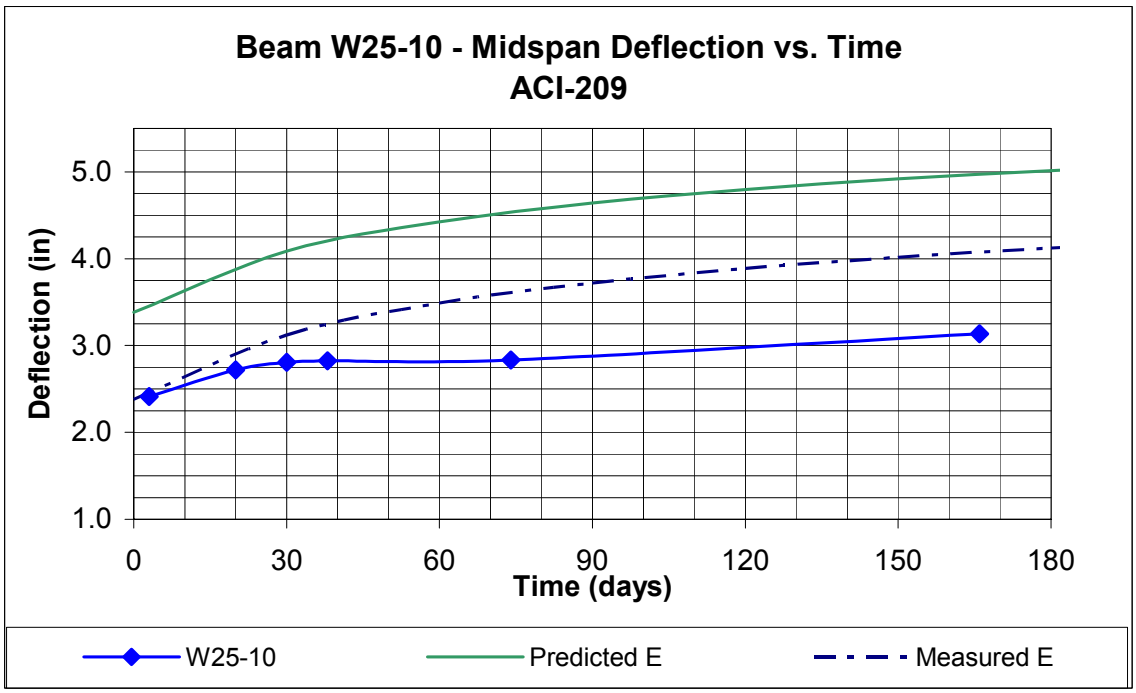

Figure B.123 Beam W25-10 ACI-209 Predicted Deflection vs. Time

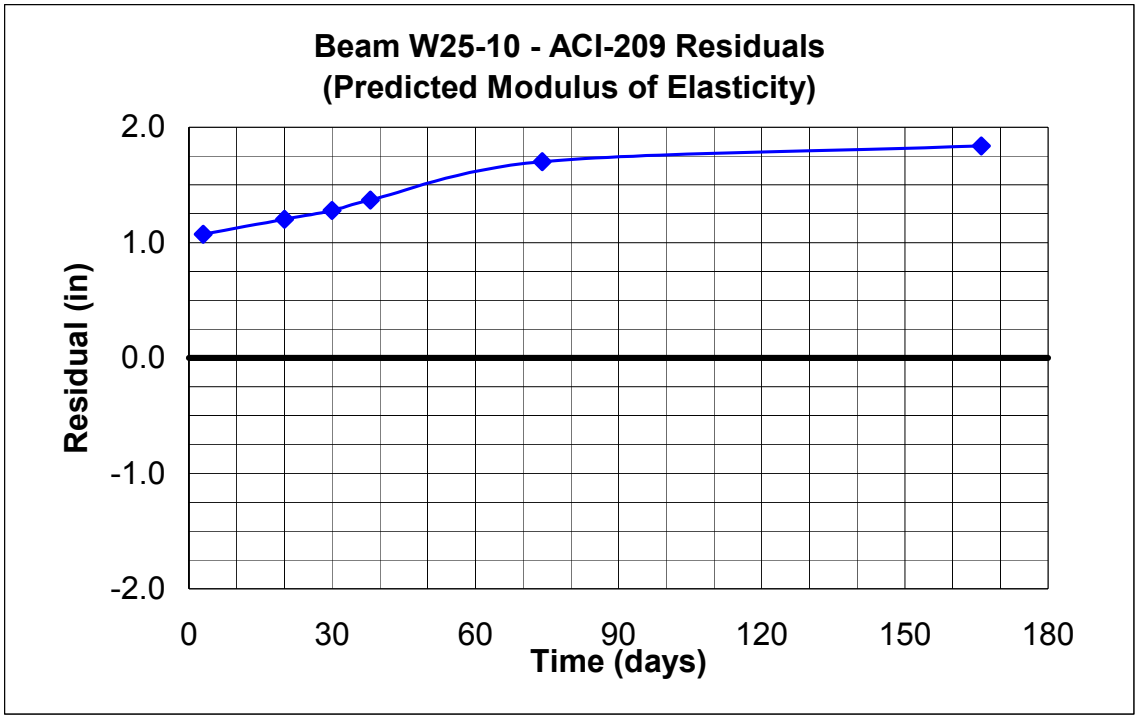

Figure B.124 Beam W25-10 ACI-209 Residuals (Predicted Modulus of Elasticity)

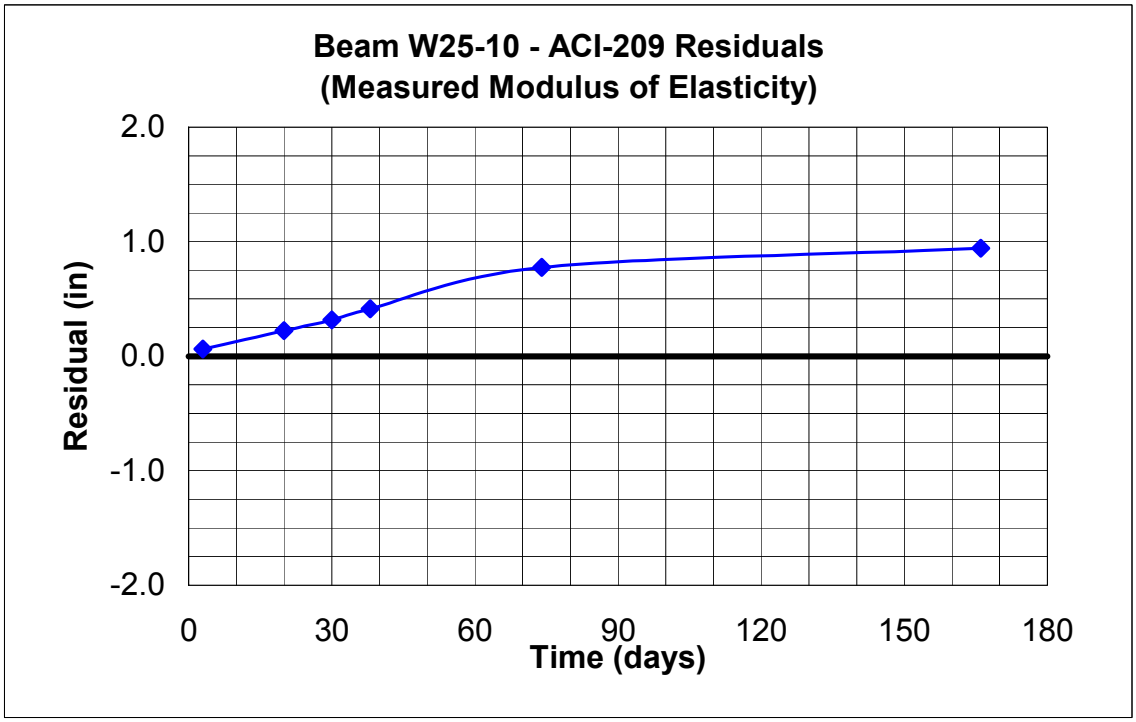

Figure B.125 Beam W25-10 ACI-209 Residuals (Measured Modulus of Elasticity)

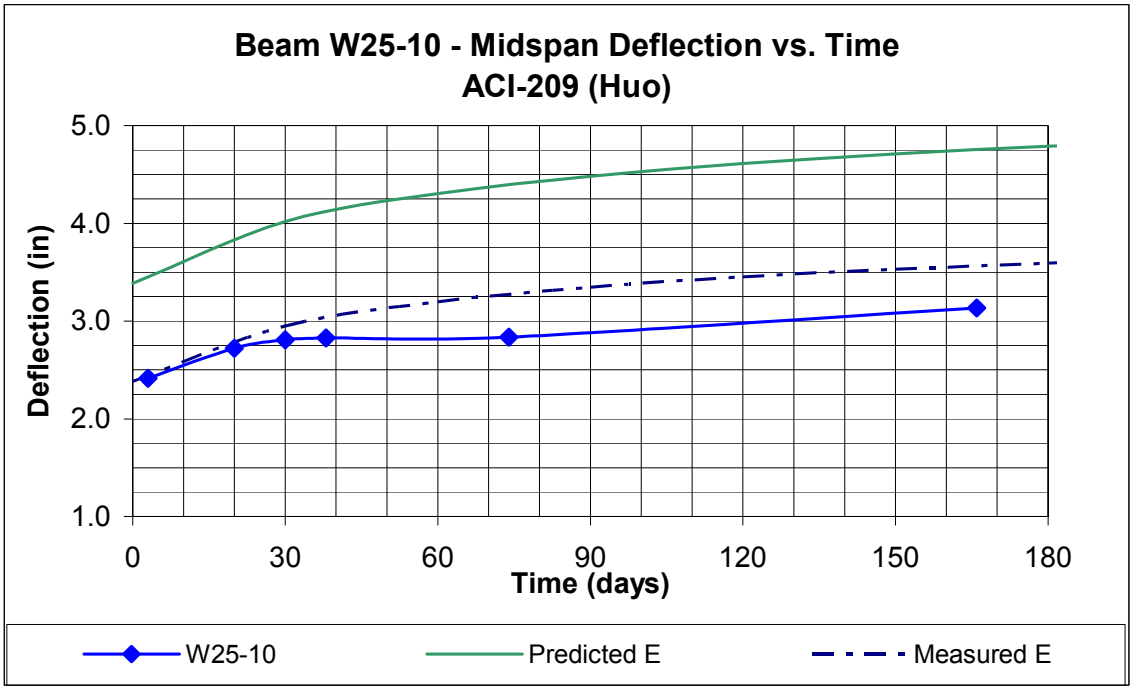

Figure B.126 Beam W25-10 ACI-209 (Huo) Predicted Deflection vs. Time

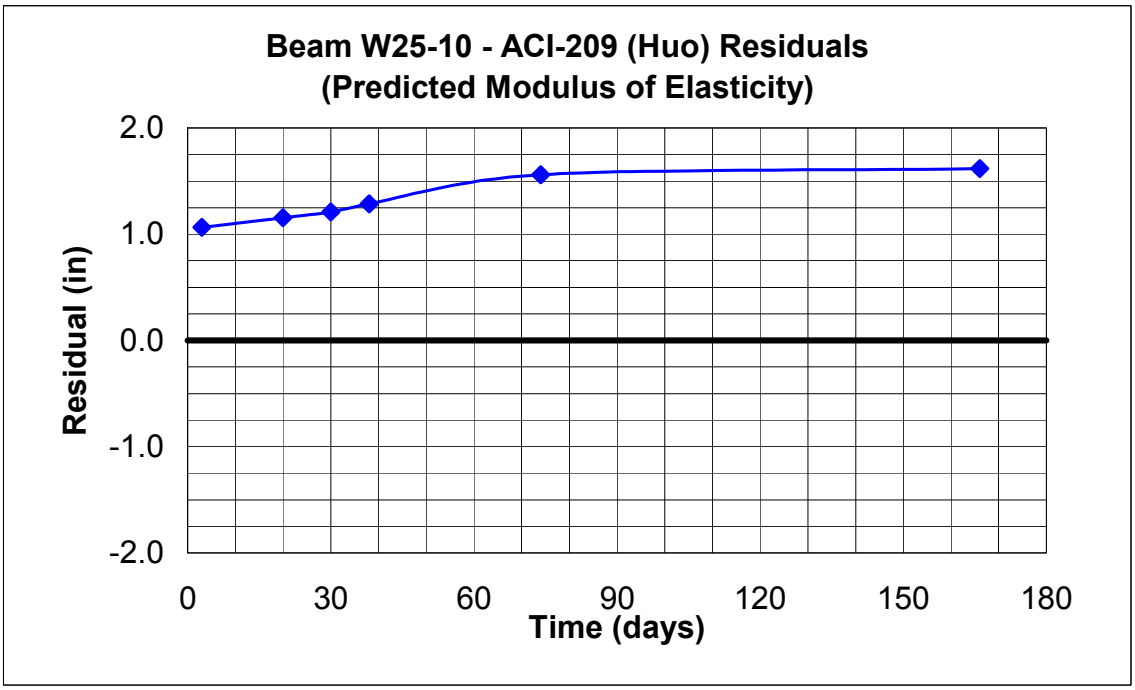

Figure B.127 Beam W25-10 ACI-209 (Huo) Residuals (Predicted Modulus of Elasticity)

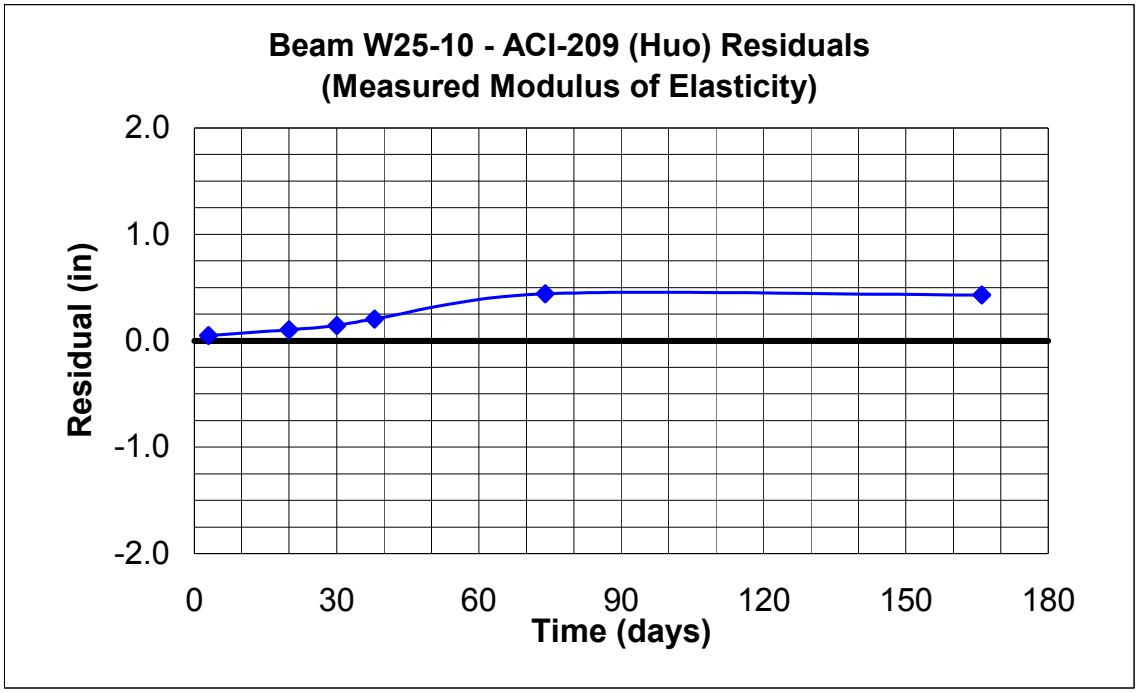

Figure B.128 Beam W25-10 ACI-209 (Huo) Residuals (Measured Modulus of Elasticity)

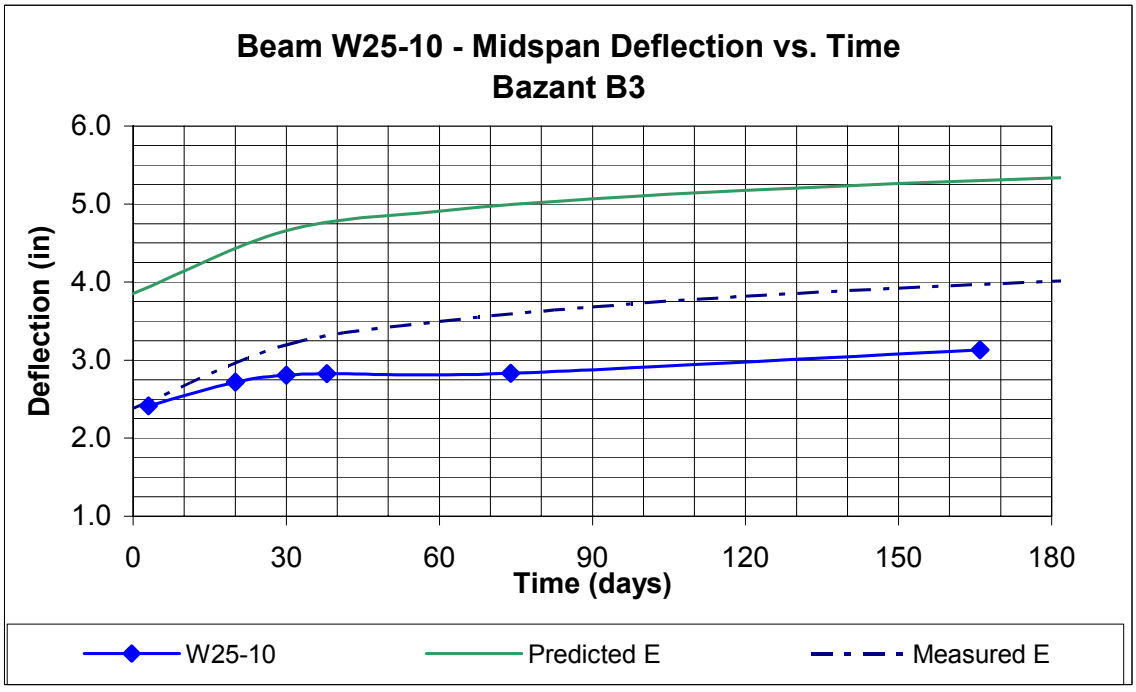

Figure B.129 Beam W25-10 Bazant B3 Predicted Deflection vs. Time

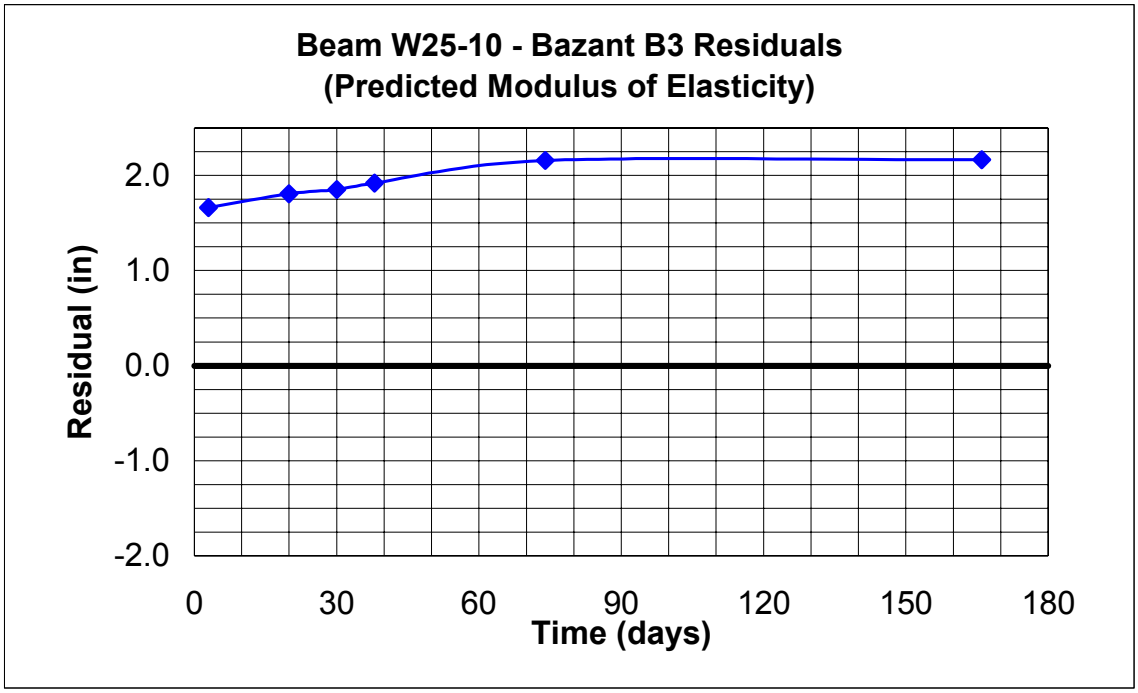

Figure B.130 Beam W25-10 Bazant B3 Residuals (Predicted Modulus of Elasticity)

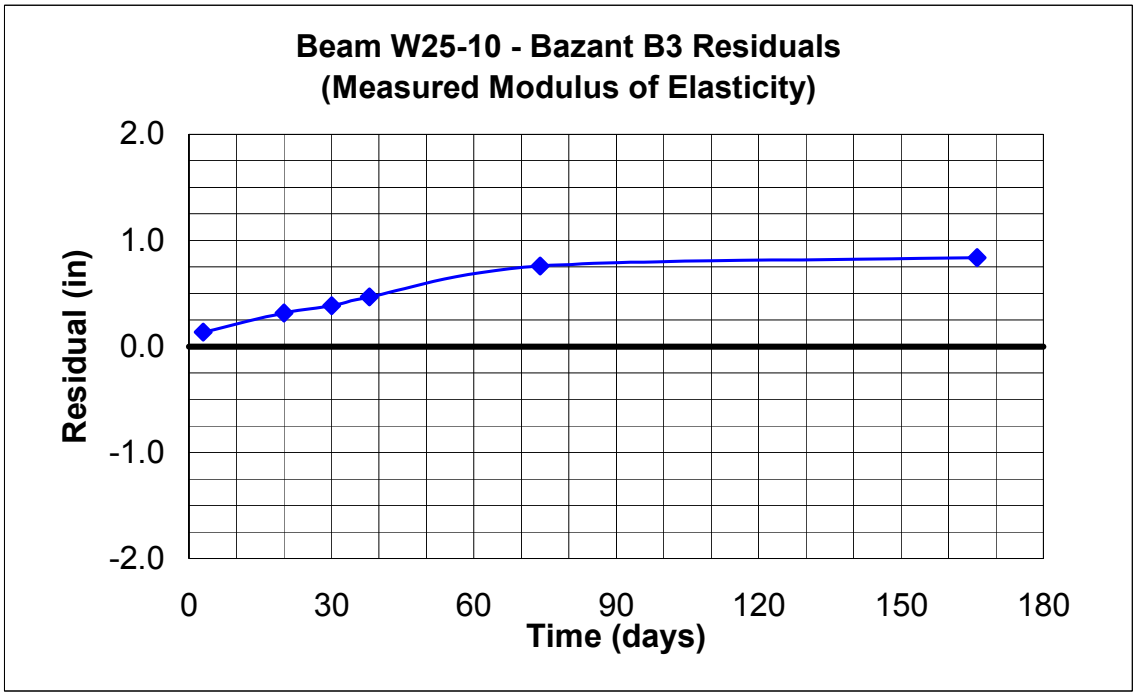

Figure B.131 Beam W25-10 Bazant B3 Residuals (Measured Modulus of Elasticity)

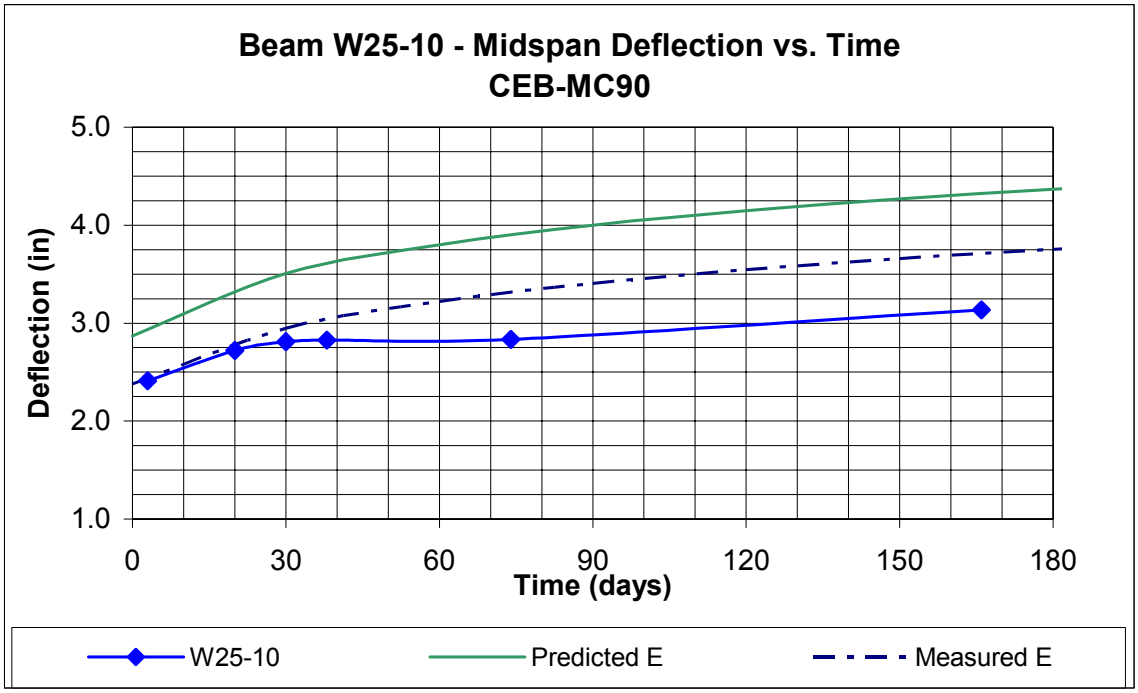

Figure B.132 Beam W25-10 CEB-MC90 Predicted Deflection vs. Time

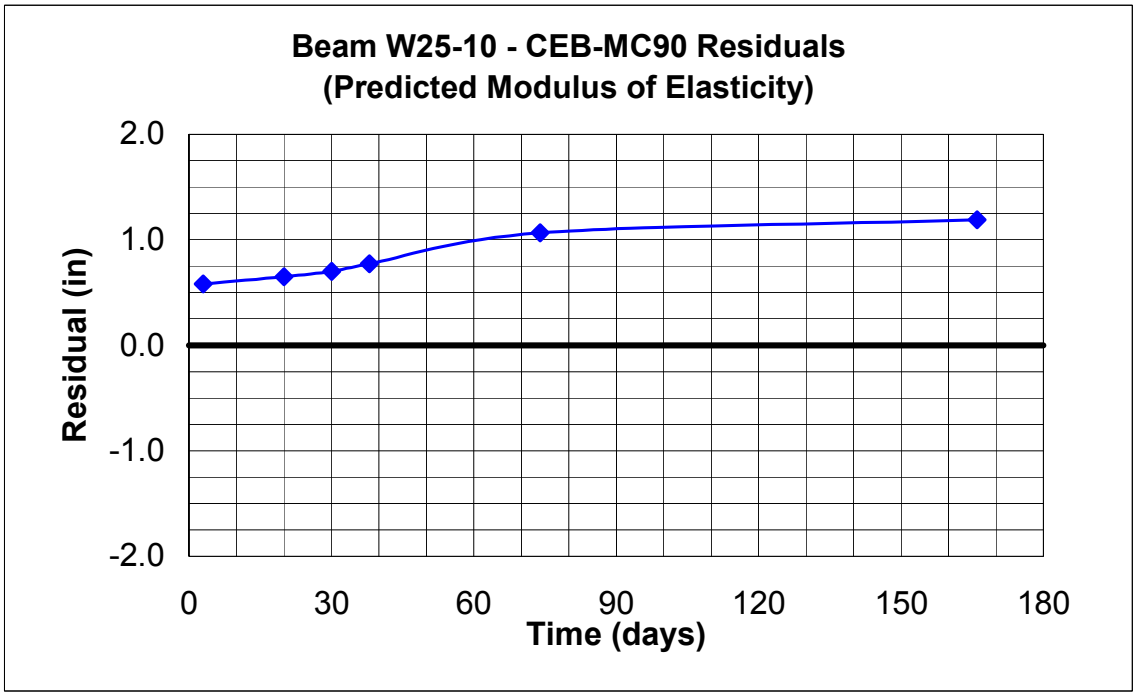

Figure B.133 Beam W25-10 CEB-MC90 Residuals (Predicted Modulus of Elasticity)

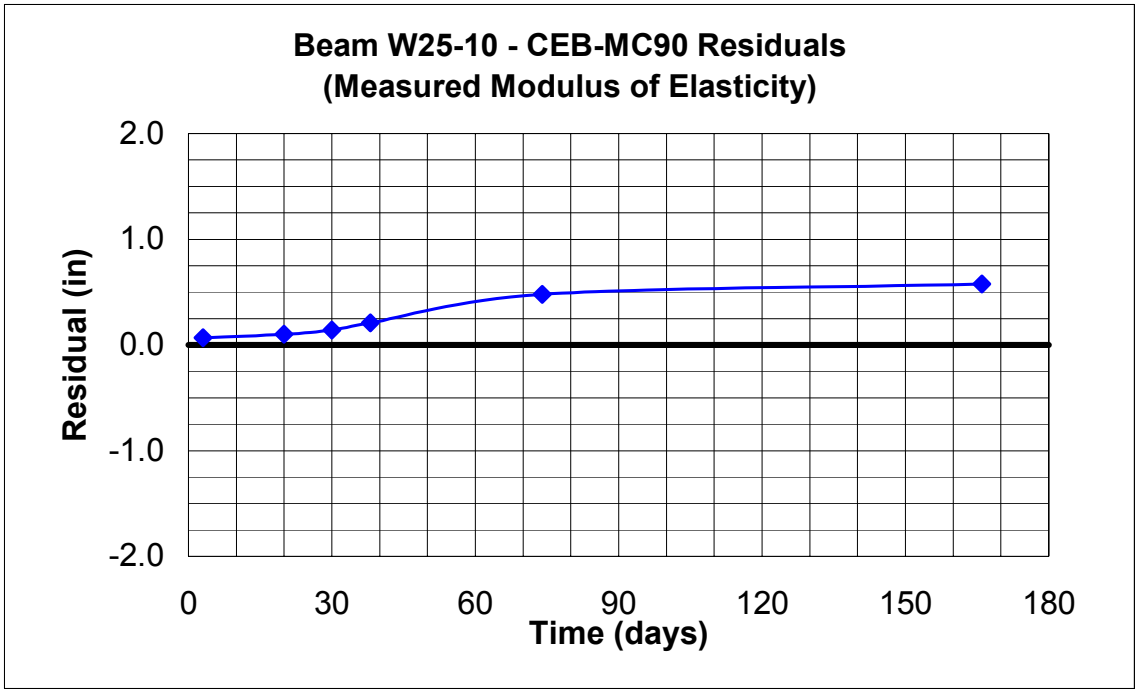

Figure B.134 Beam W25-10 CEB-MC90 Residuals (Measured Modulus of Elasticity)

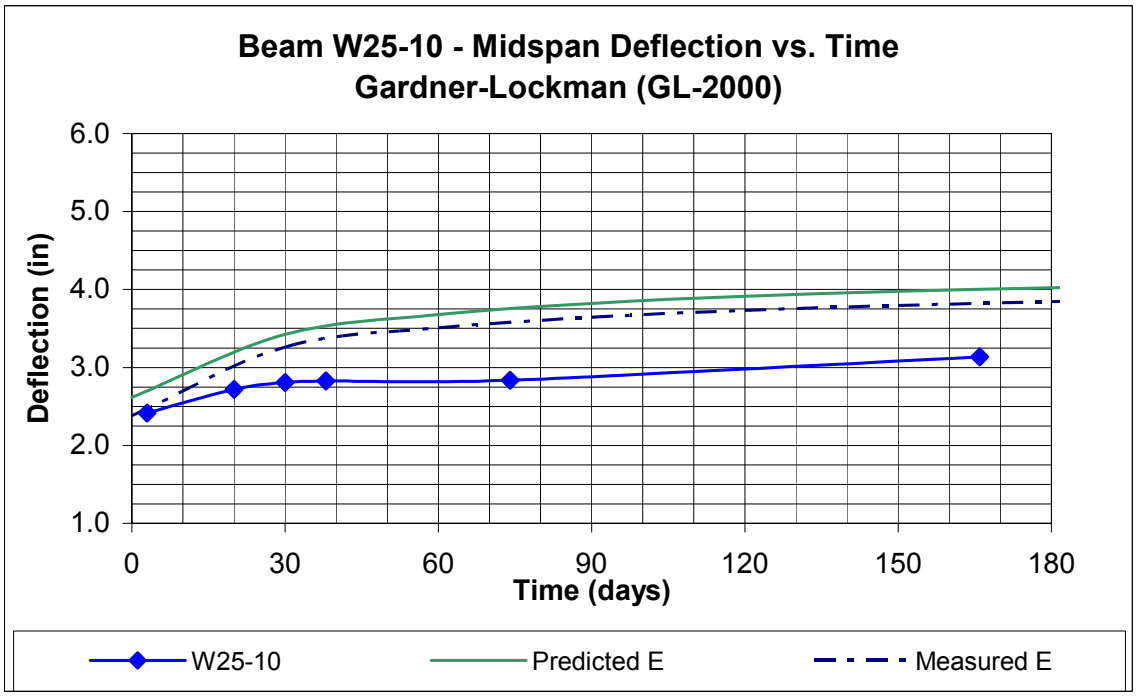

Figure B.135 Beam W25-10 GL-2000 Predicted Deflection vs. Time

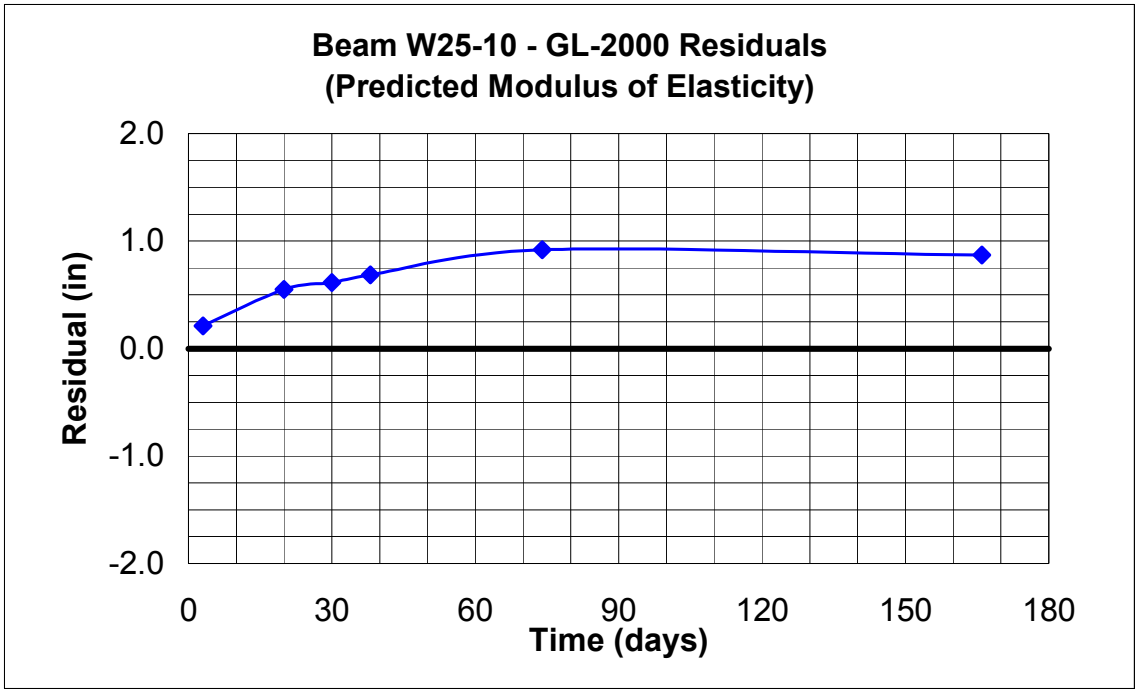

Figure B.136 Beam W25-10 GL-2000 Residuals (Predicted Modulus of Elasticity)

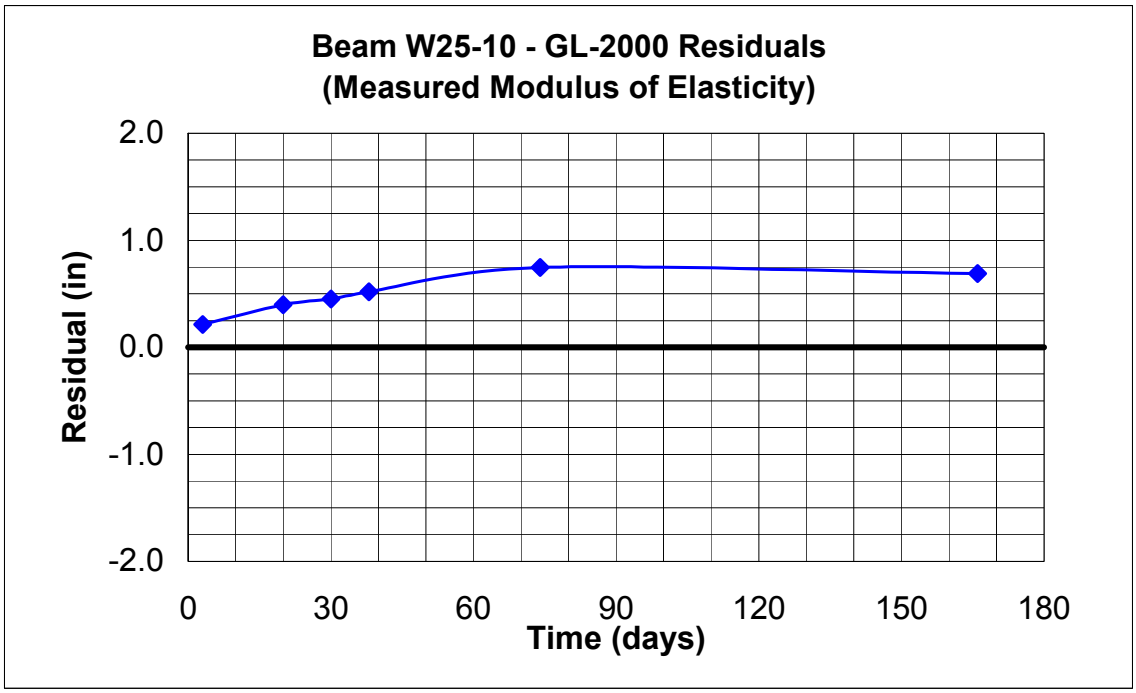

Figure B.137 Beam W25-10 GL-2000 Residuals (Measured Modulus of Elasticity)

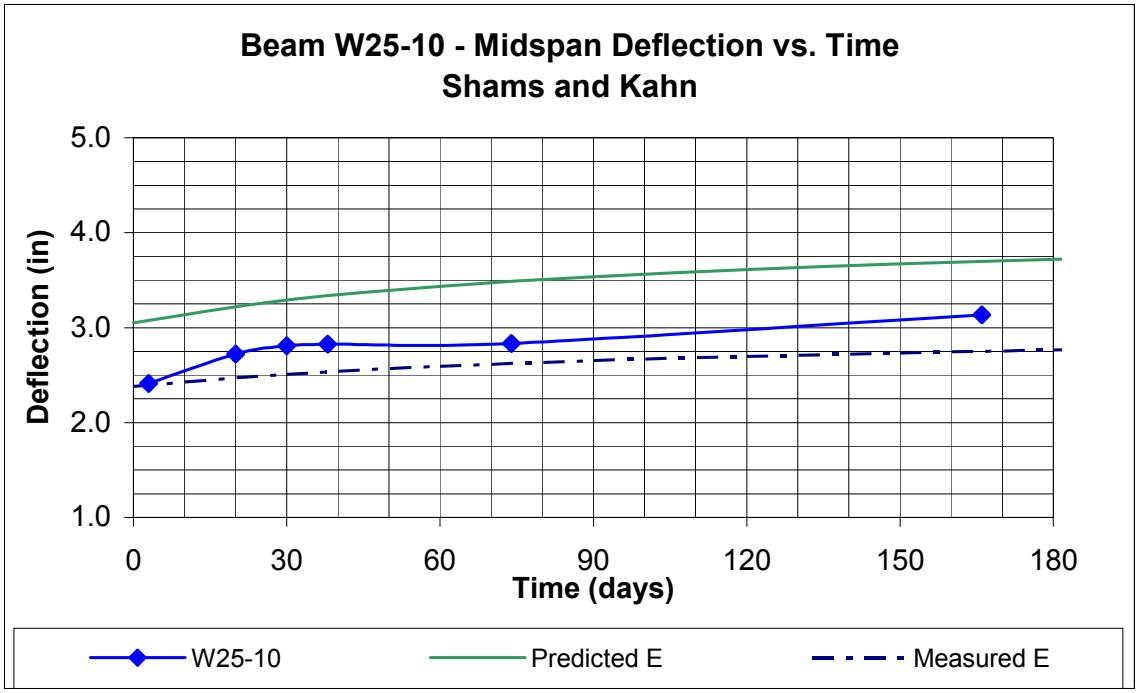

Figure B.138 Beam W25-10 Kahn & Shams Predicted Deflection vs. Time

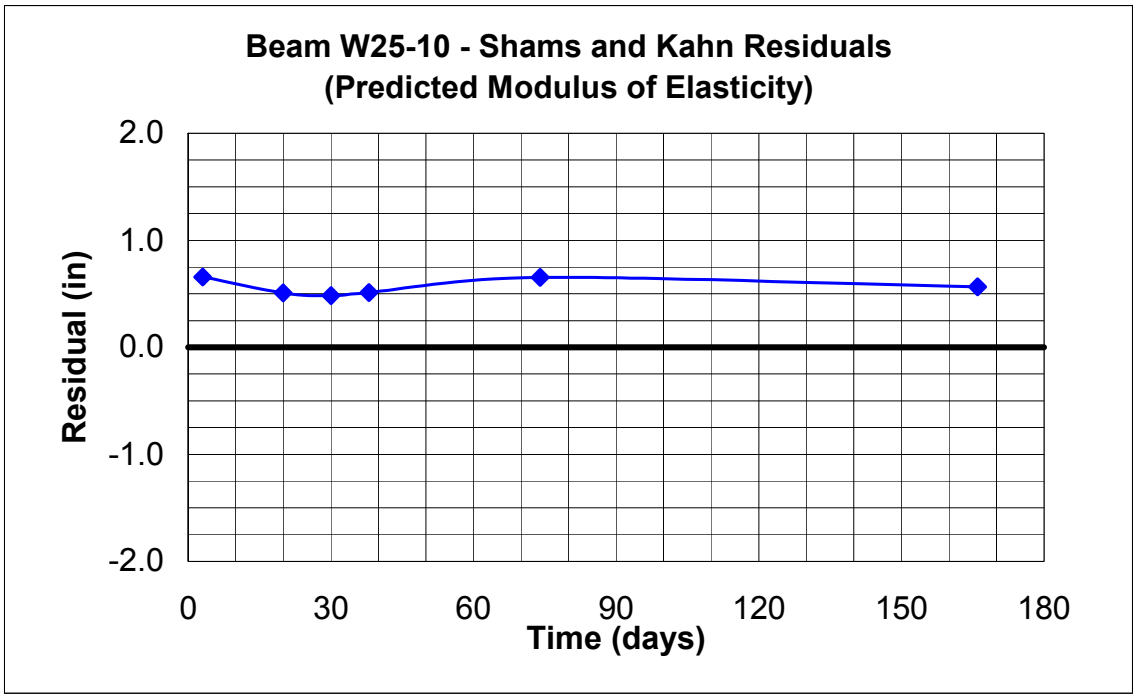

Figure B.139 Beam W25-10 Kahn & Shams Residuals (Predicted Modulus of Elasticity

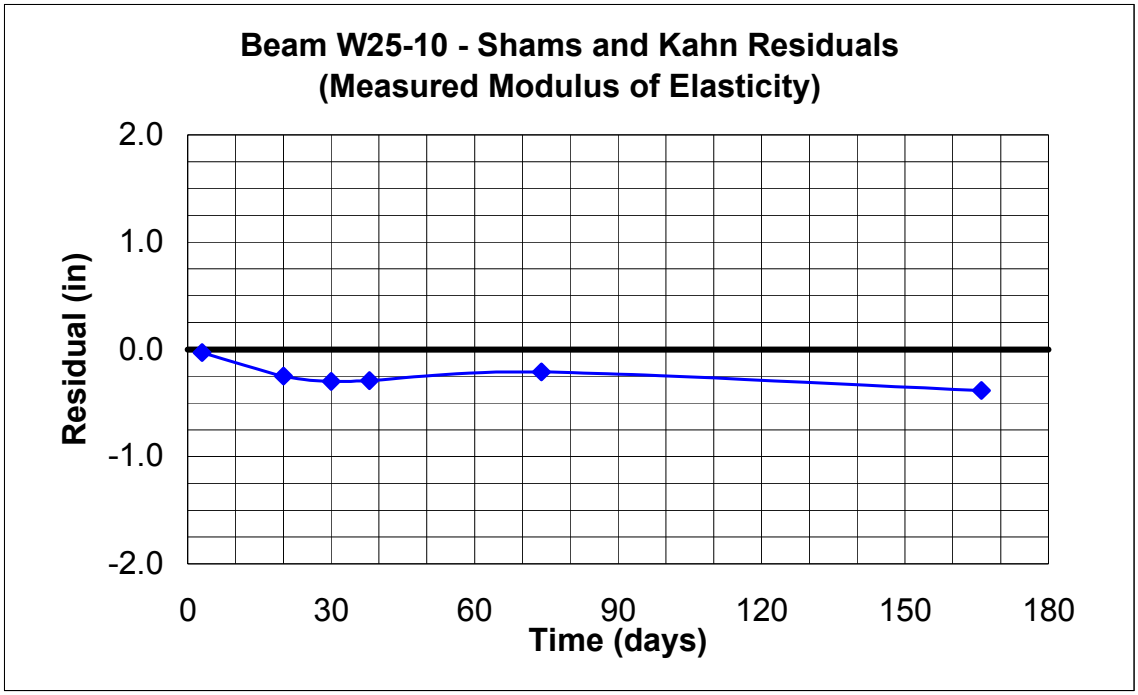

Figure B.140 Beam W25-10 Kahn & Shams Residuals (Measured Modulus of Elasticity)

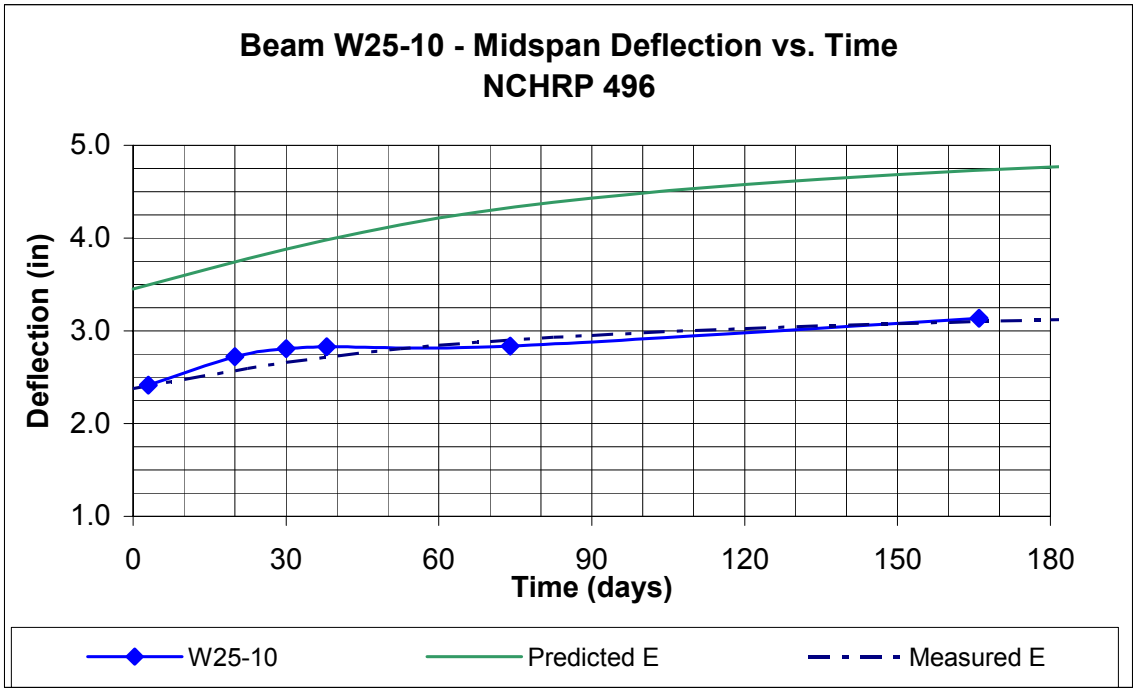

Figure B.141 Beam W25-10 NCHRP 496 Predicted Deflection vs. Time

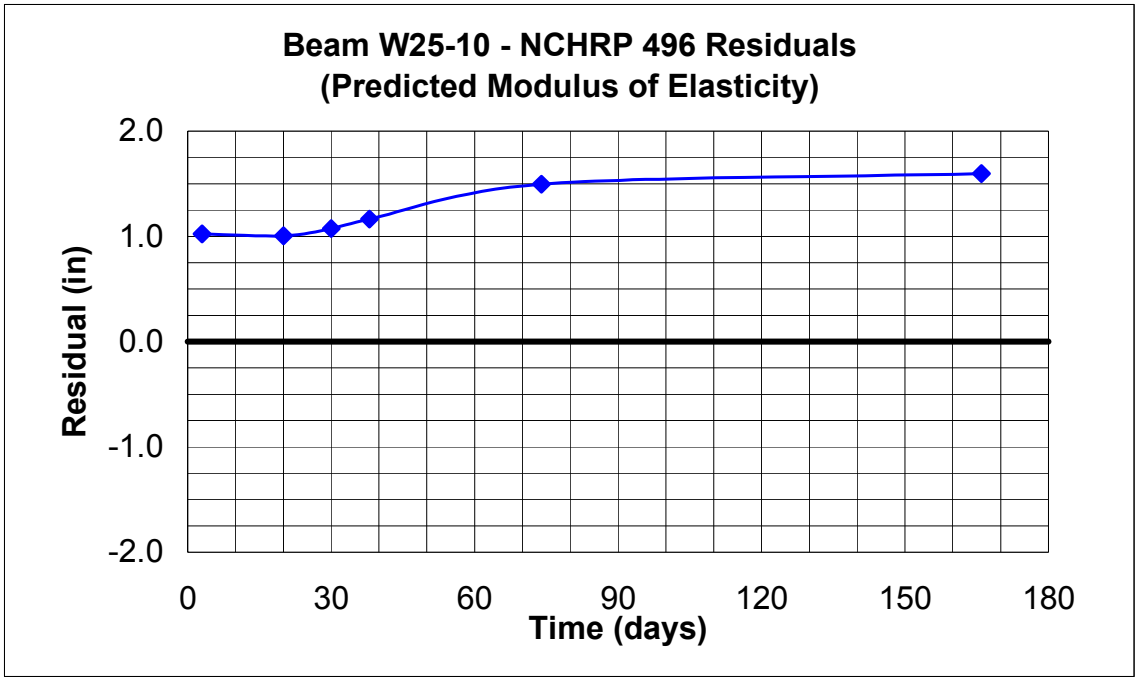

Figure B.142 Beam W25-10 NCHRP 496 Residuals (Predicted Modulus of Elasticity)

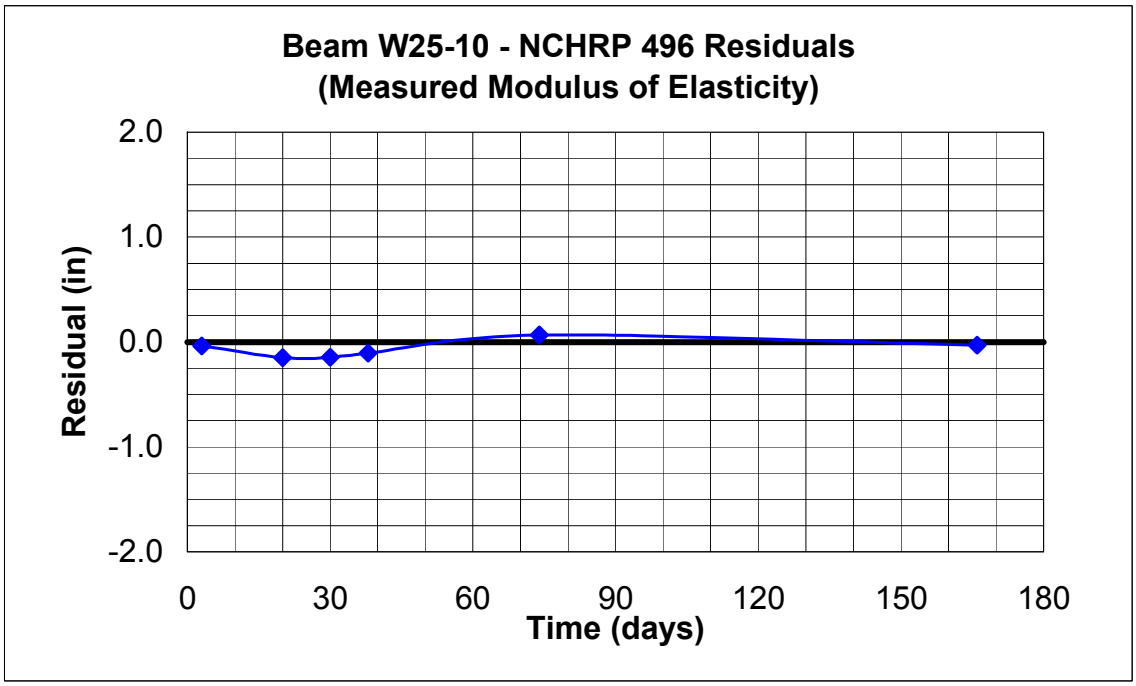

Figure B.143 Beam W25-10 NCHRP 496 Residuals (Measured Modulus of Elasticity)

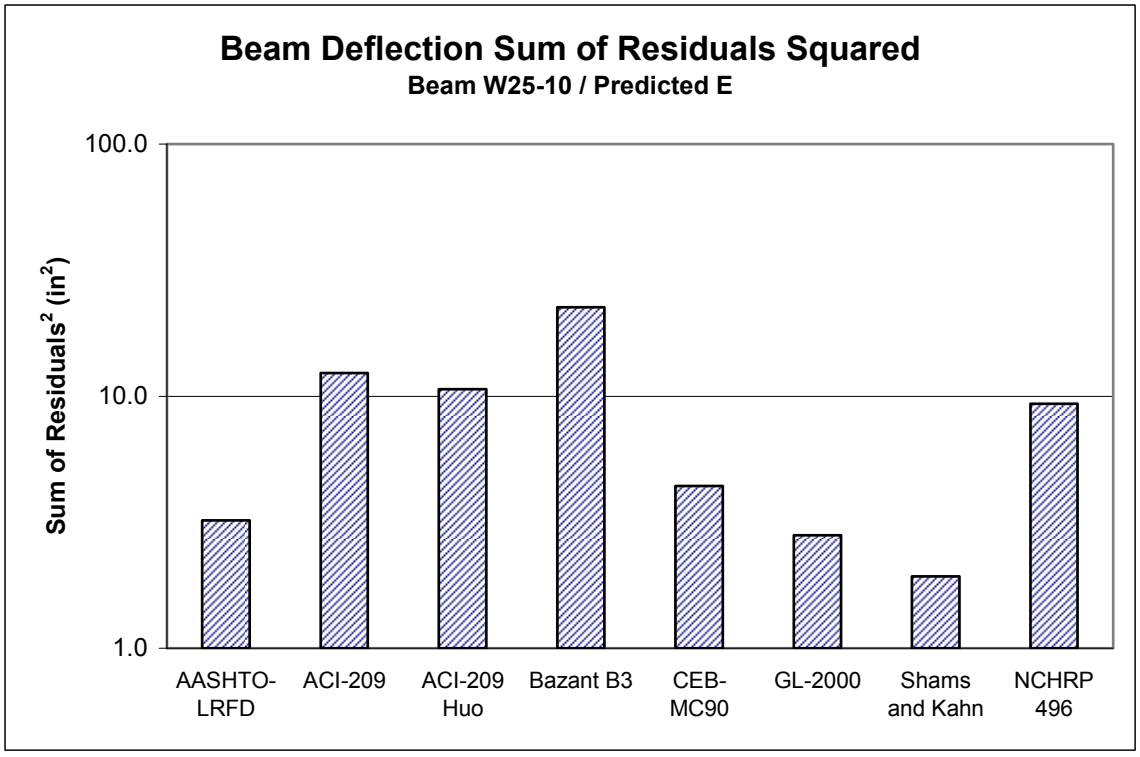

Figure B.144 Beam W25-10 Deflection Sum of Residuals Squared, Predicted E

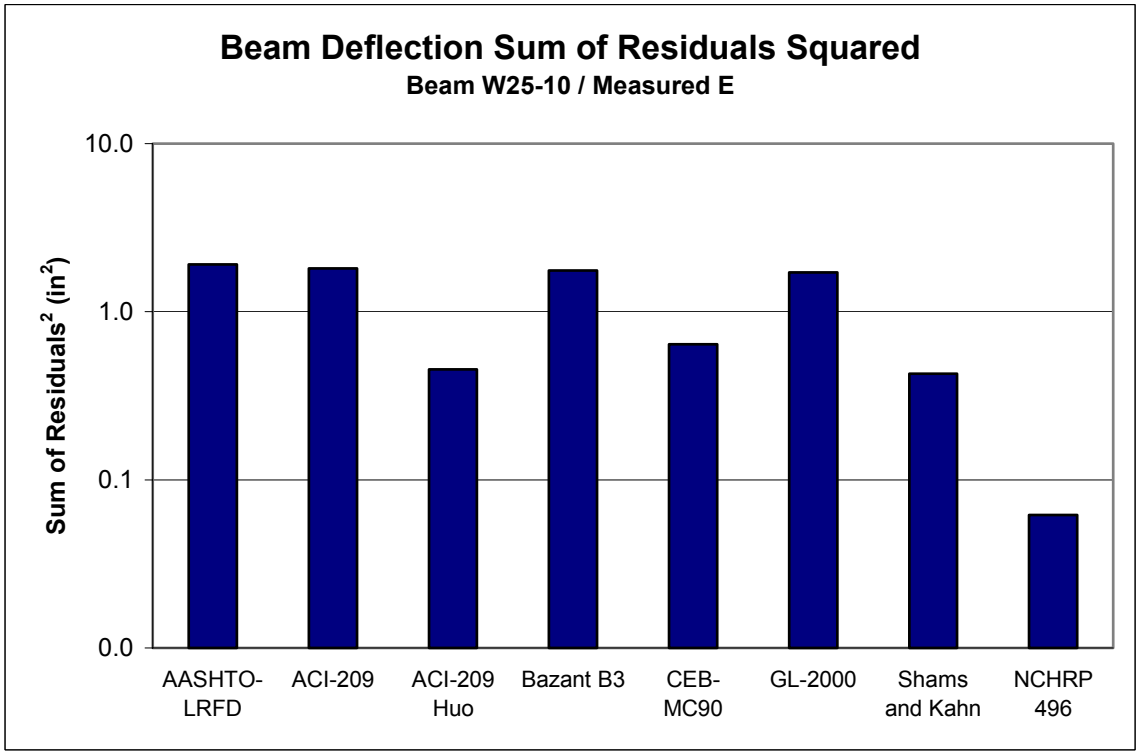

Figure B.145 Beam W25-10 Deflection Sum of Residuals Squared, Measured E

Table B.9 Beam W25-10 Model Ranking with Predicted E

Rank	Model
1	**AASHTO-LRFD**
2	Shams and Kahn
3	CEB-MC90
4	NCHRP 496
5	ACI-209
6	ACI-209, modified by Huo
7	GL-2000
8	Bazant B3

Table B.10 Beam W25-10 Model Ranking with Measured E

Rank	Model
1	**NCHRP 496**
2	Shams and Kahn
3	CEB-MC90
4	ACI-209
5	ACI-209, modified by Huo
6	Bazant B3
7	AASHTO-LRFD
8	GL-2000

B.6 Additional Beam W31-10

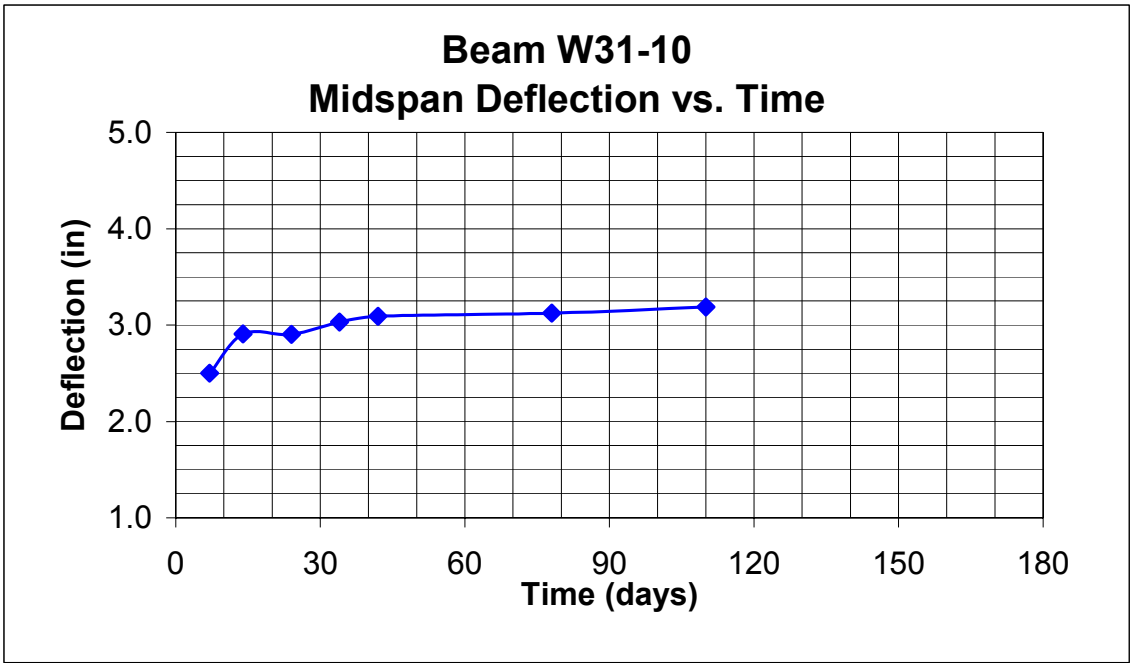

Figure B.146 Beam W31-10, Deflection vs. Time

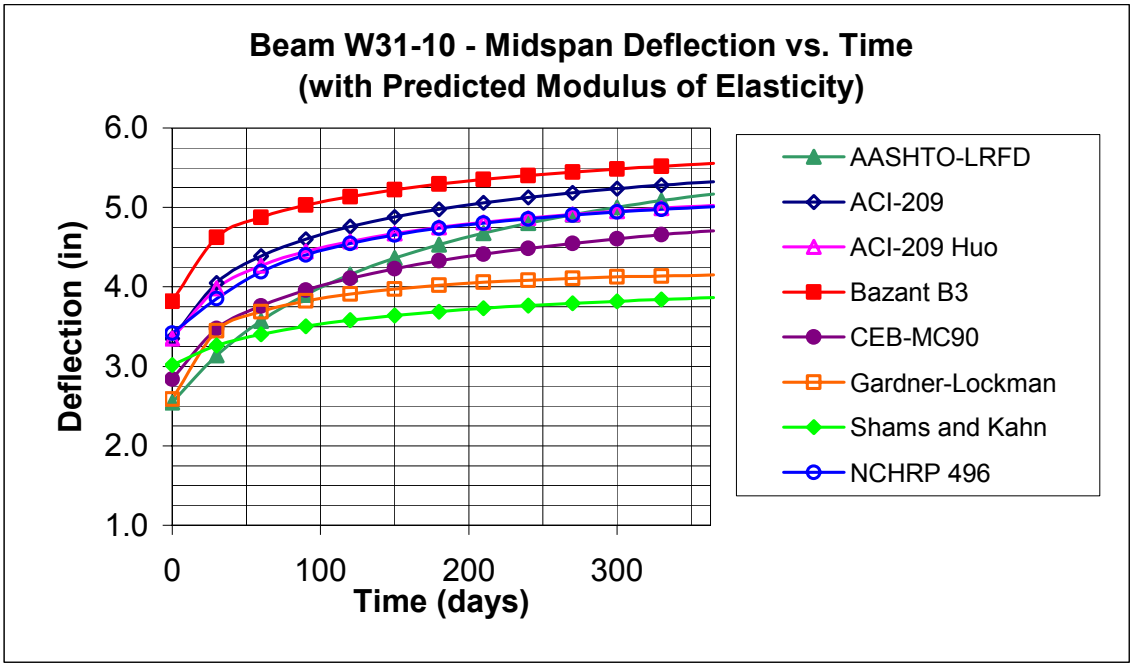

Figure B.147 Beam W31-10, Predicted Deflection vs. Time (Predicted E)

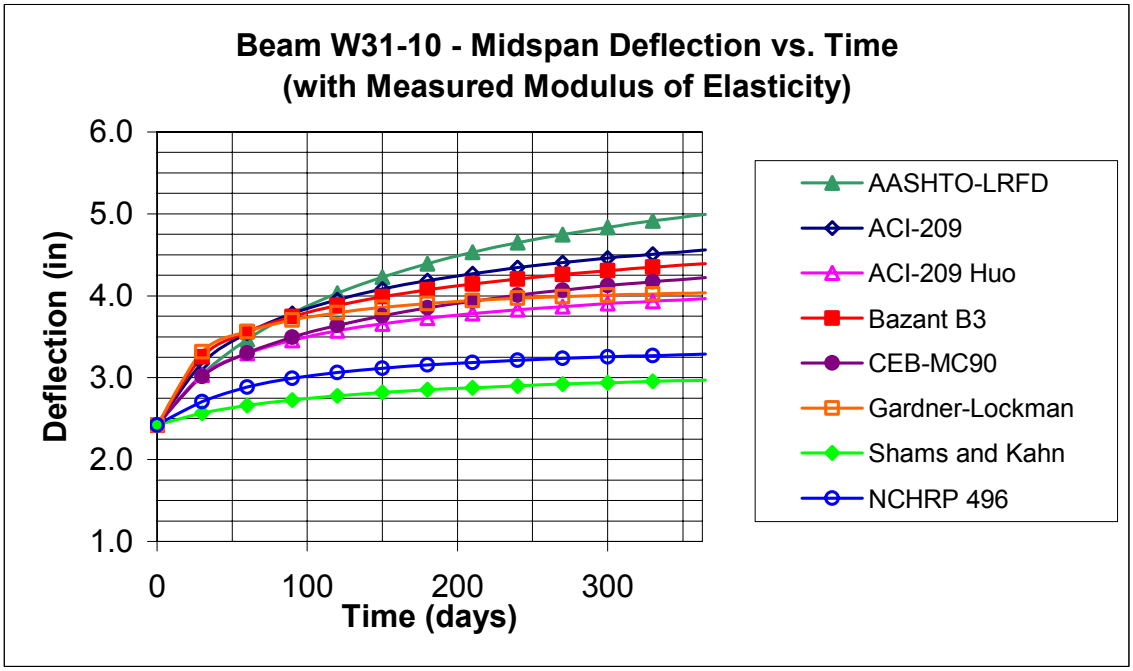

Figure B.148 Beam W31-10, Predicted Deflection vs. Time (Measured E)

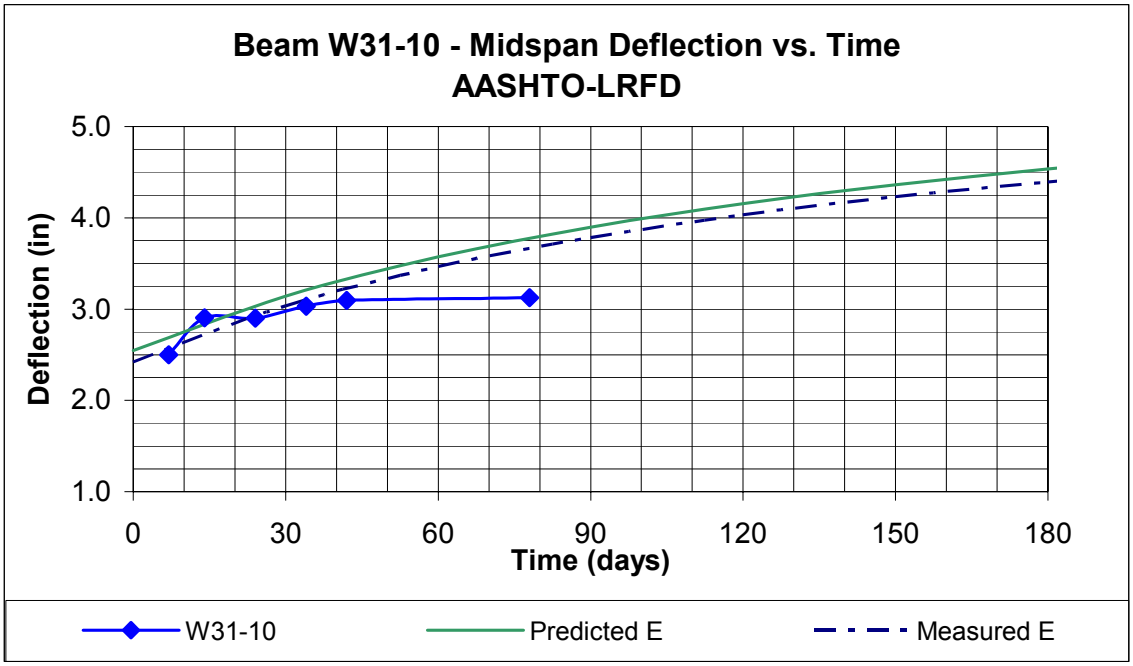

Figure B.149 Beam W31-10 AASHTO-LRFD Predicted Deflection vs. Time

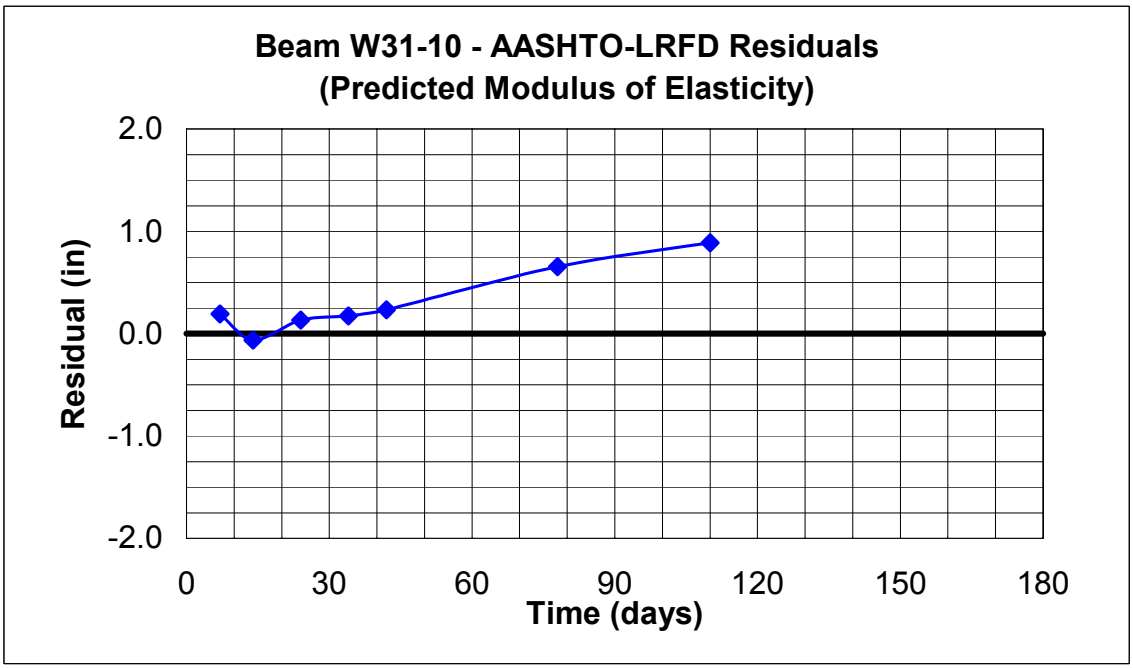

Figure B.150 Beam W31-10 AASHTO-LRFD Residuals (Predicted Modulus of Elasticity)

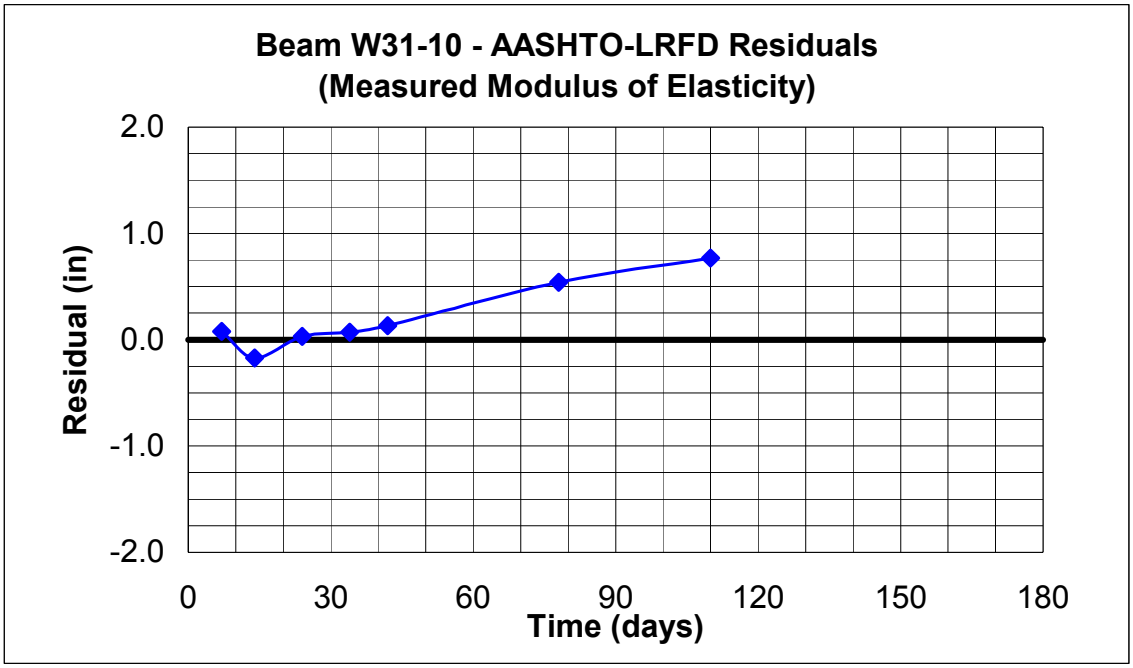

Figure B.151 Beam W31-10 AASHTO-LRFD Residuals (Measured Modulus of Elasticity)

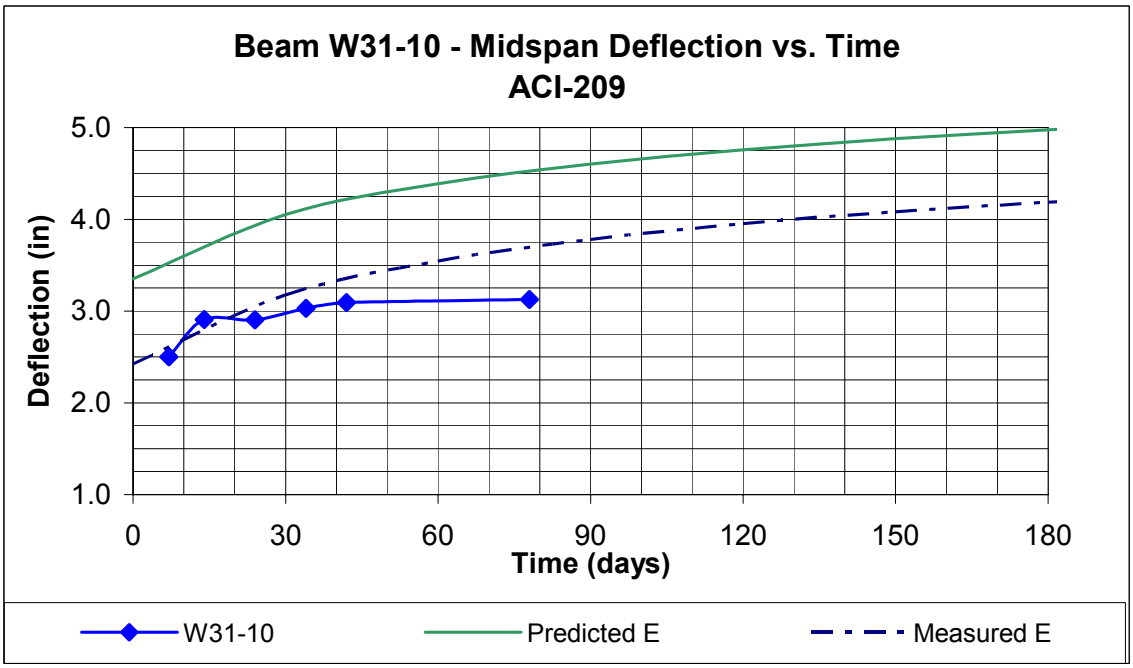

Figure B.152 Beam W31-10 ACI-209 Predicted Deflection vs. Time

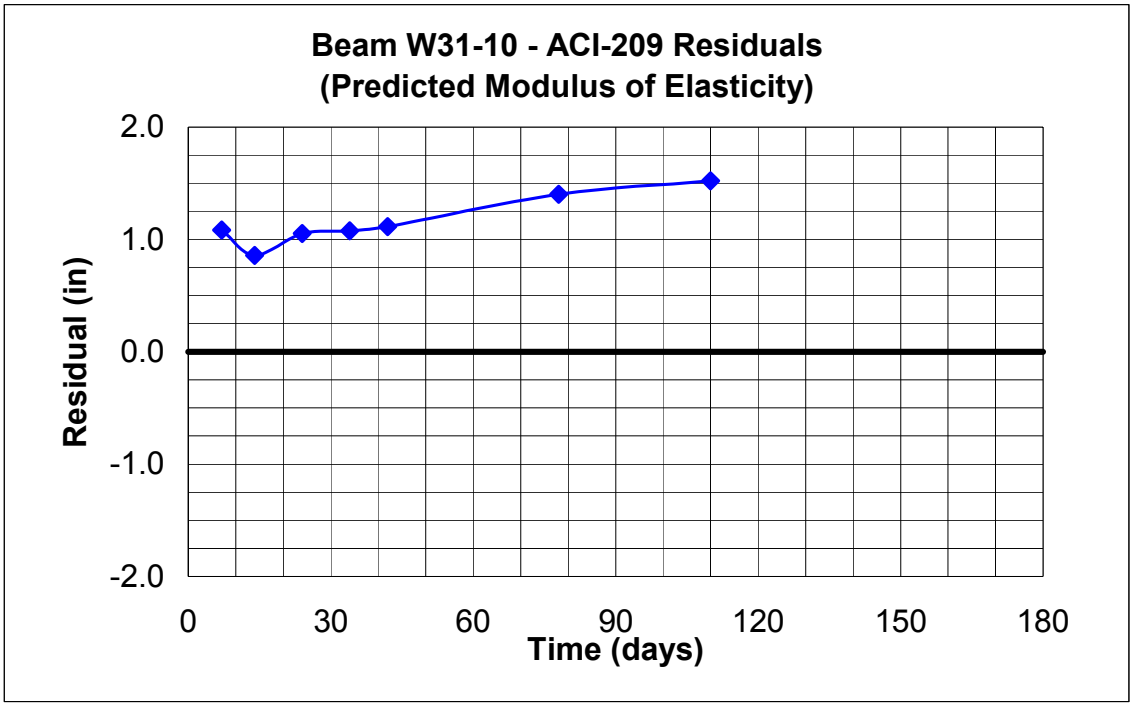

Figure B.153 Beam W31-10 ACI-209 Residuals (Predicted Modulus of Elasticity)

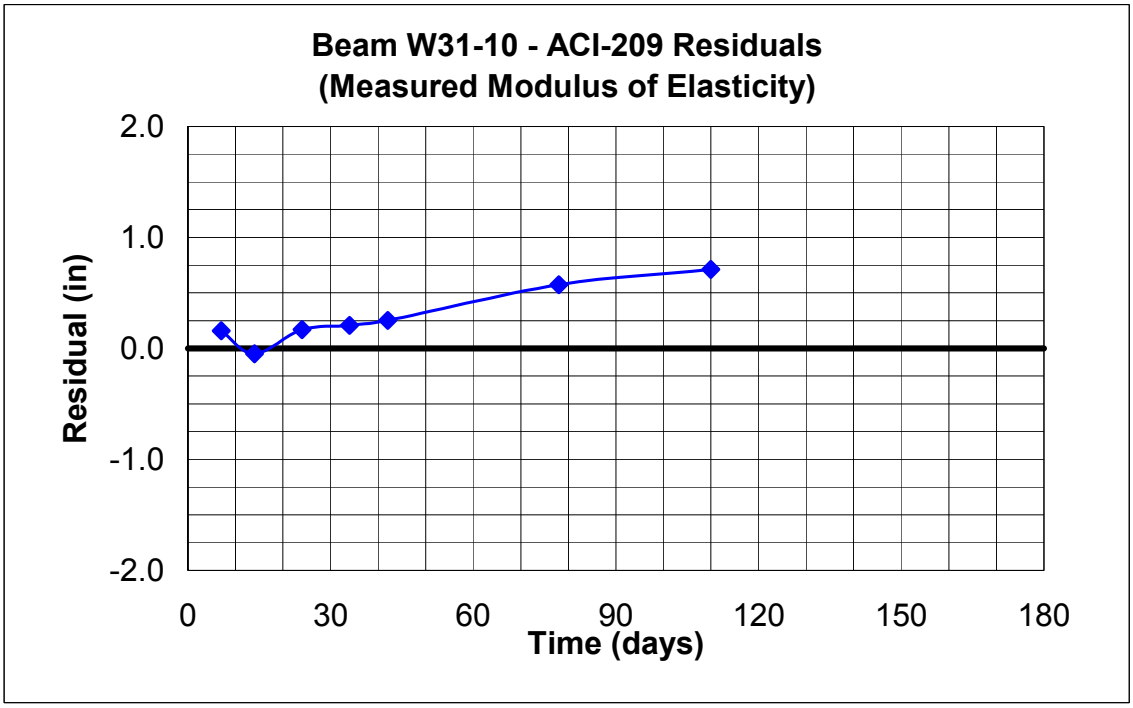

Figure B.154 Beam W31-10 ACI-209 Residuals (Measured Modulus of Elasticity)

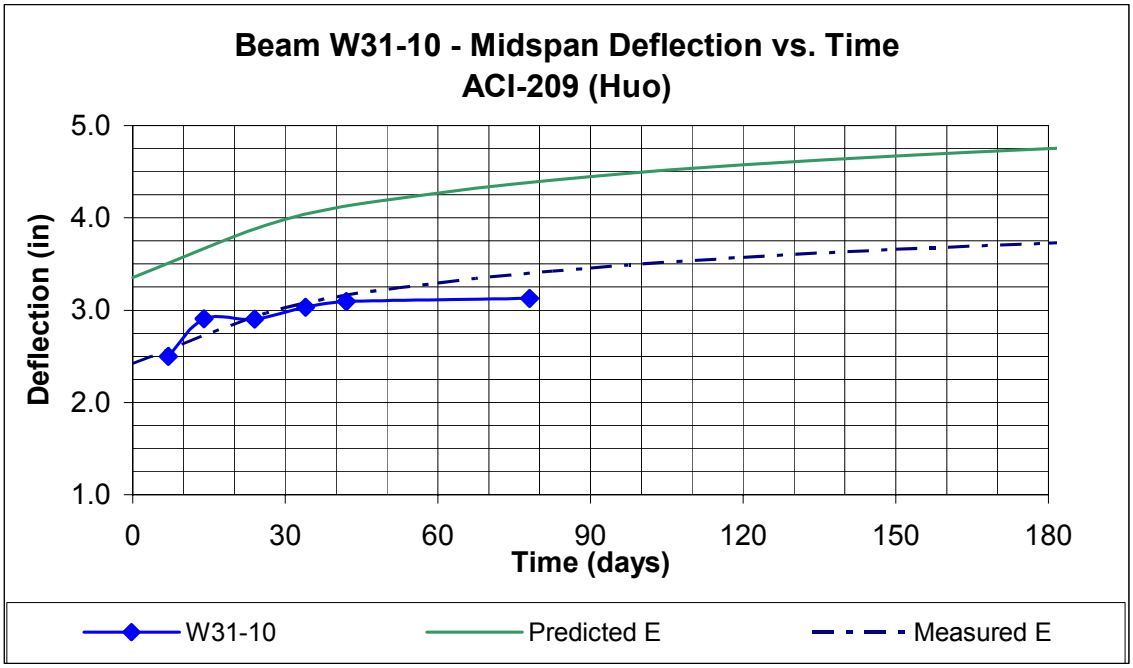

Figure B.155 Beam W31-10 ACI-209 (Huo) Predicted Deflection vs. Time

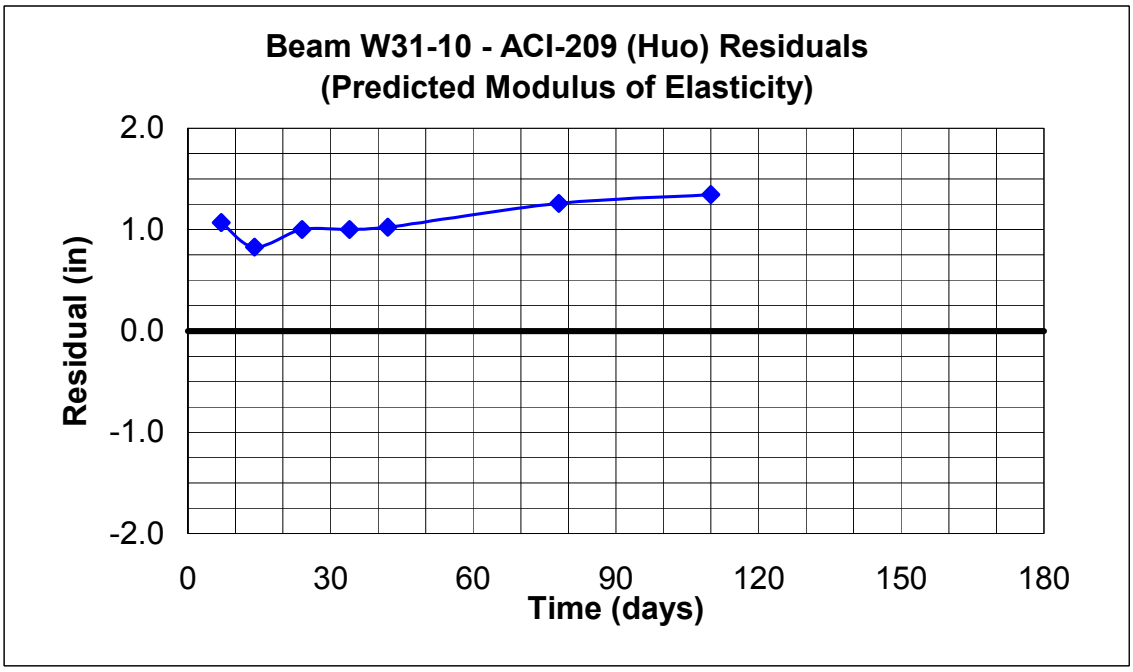

Figure B.156 Beam W31-10 ACI-209 (Huo) Residuals (Predicted Modulus of Elasticity)

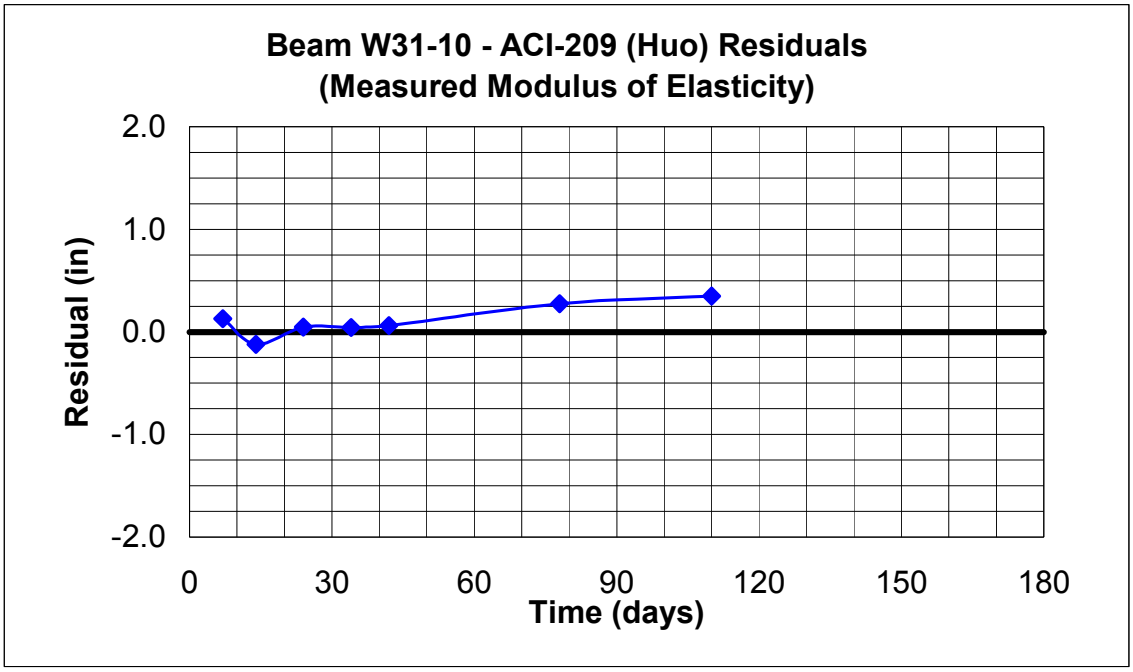

Figure B.157 Beam W31-10 ACI-209 (Huo) Residuals (Measured Modulus of Elasticity)

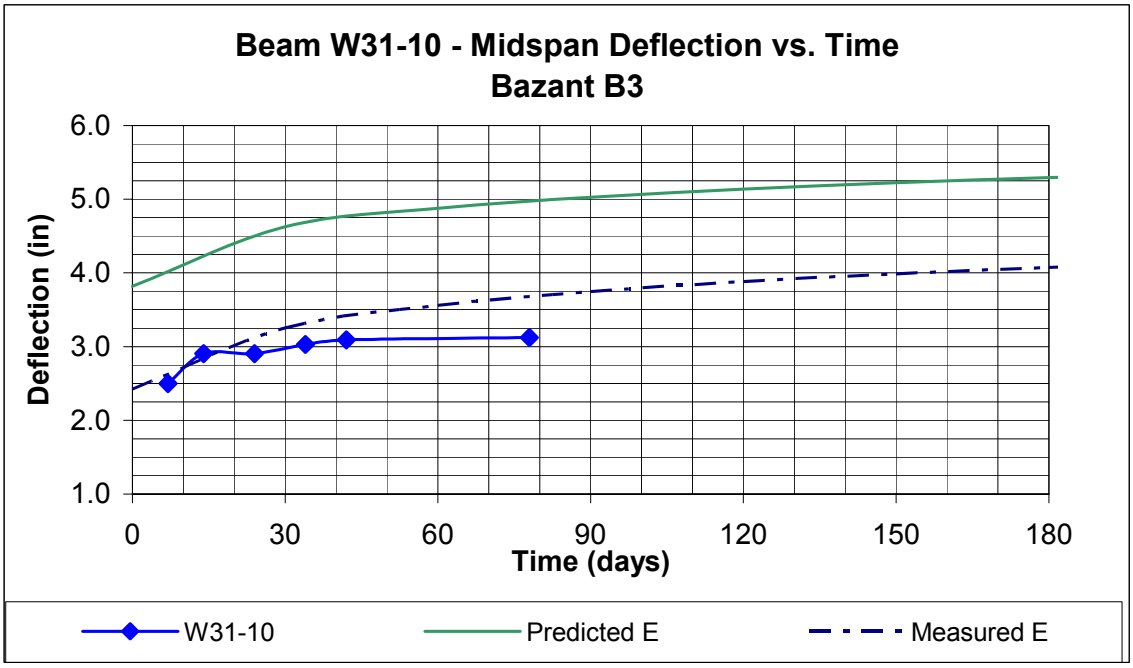

Figure B.158 Beam W31-10 Bazant B3 Predicted Deflection vs. Time

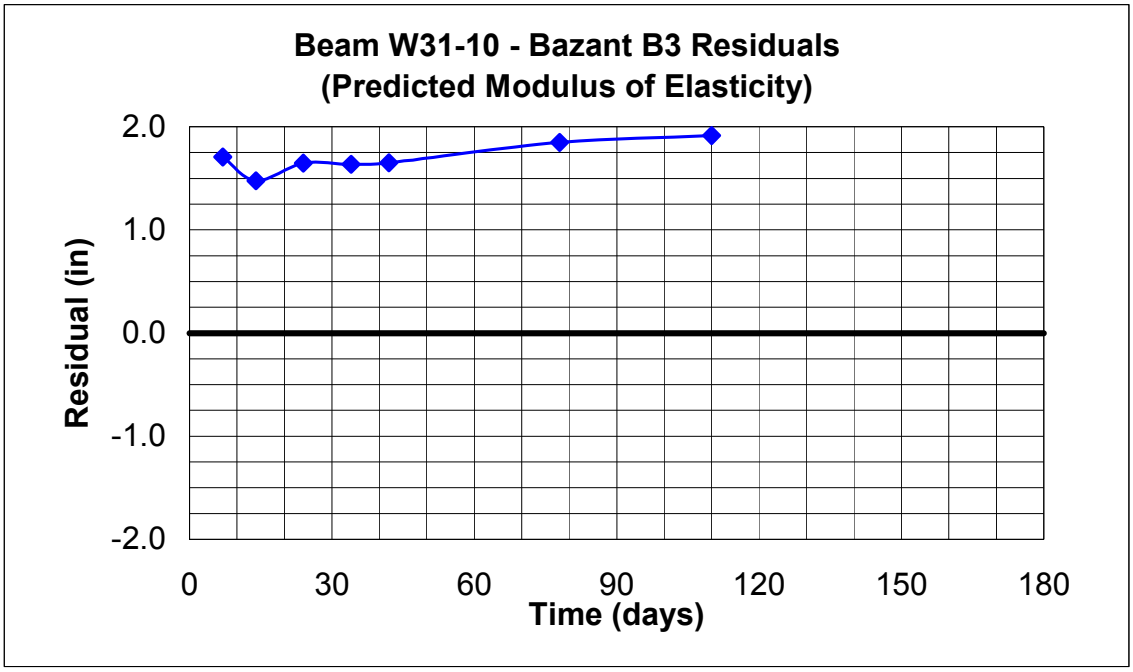

Figure B.159 Beam W31-10 Bazant B3 Residuals (Predicted Modulus of Elasticity)

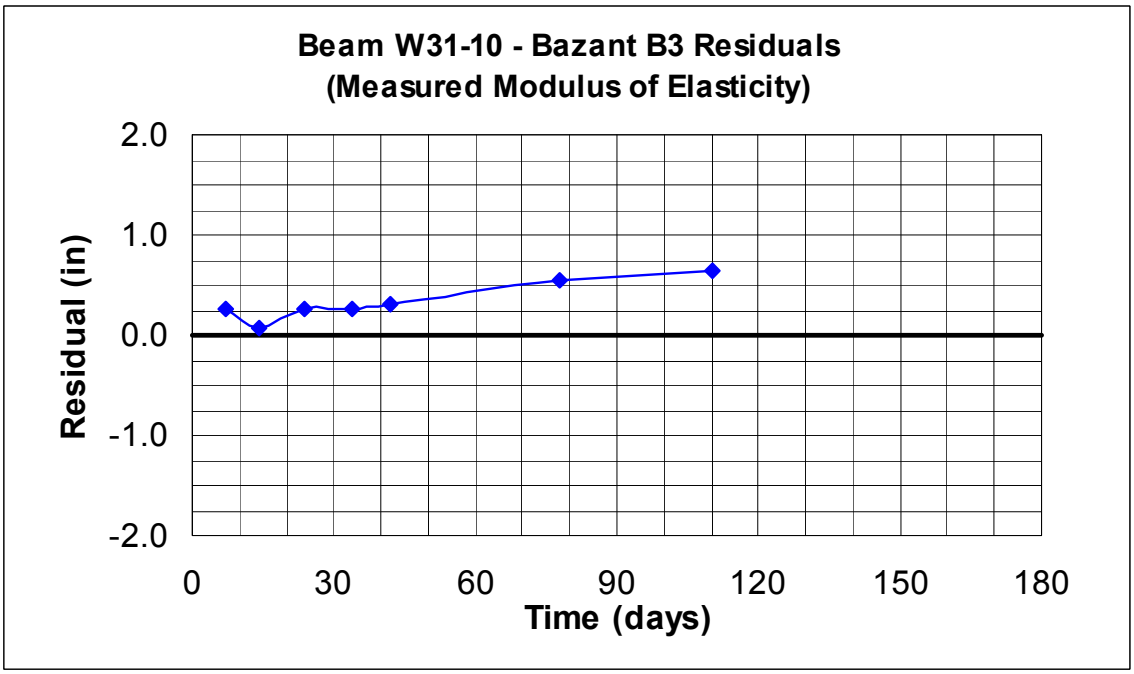

Figure B.160 Beam W31-10 Bazant B3 Residuals (Measured Modulus of Elasticity)

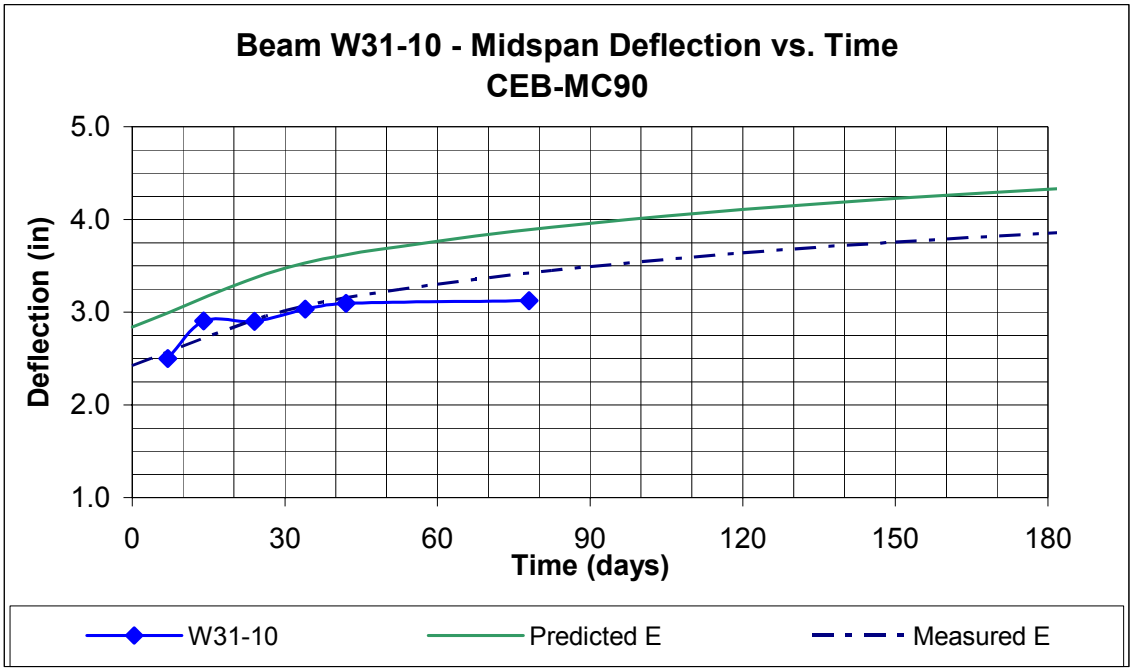

Figure B.161 Beam W31-10 CEB-MC90 Predicted Deflection vs. Time

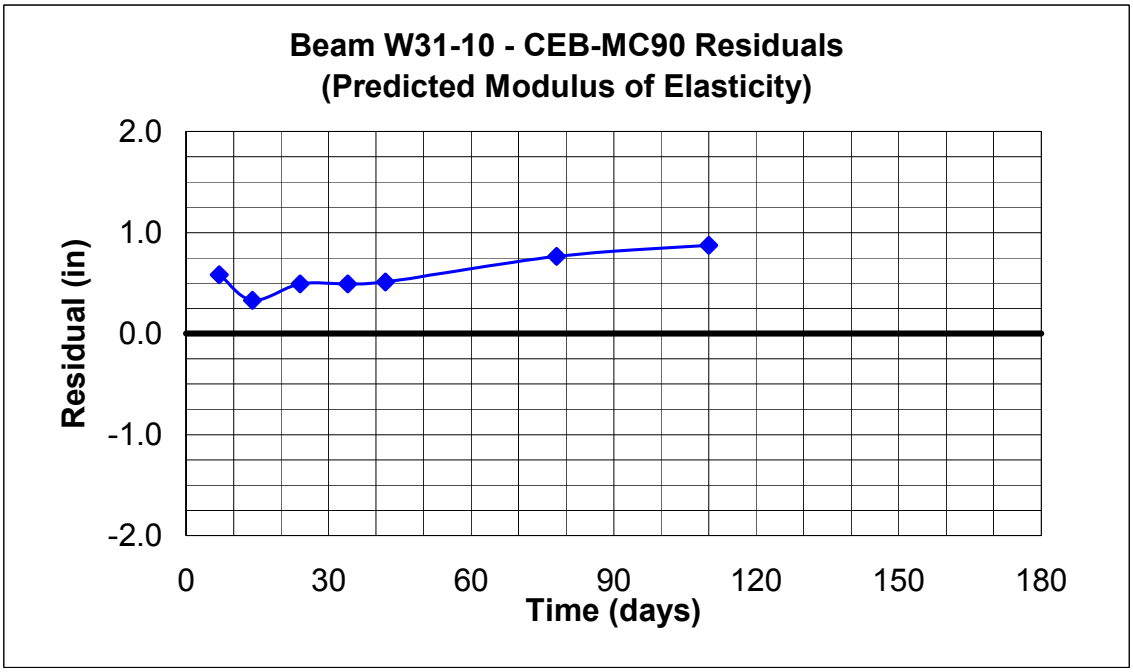

Figure B.162 Beam W31-10 CEB-MC90 Residuals (Predicted Modulus of Elasticity)

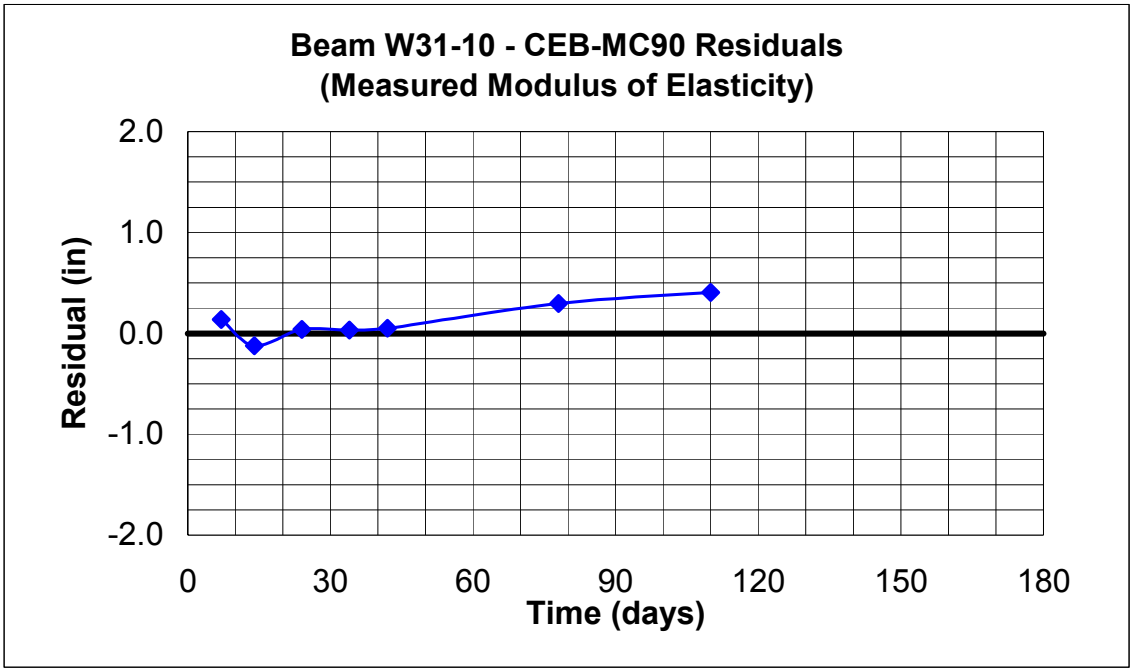

Figure B.163 Beam W31-10 CEB-MC90 Residuals (Measured Modulus of Elasticity)

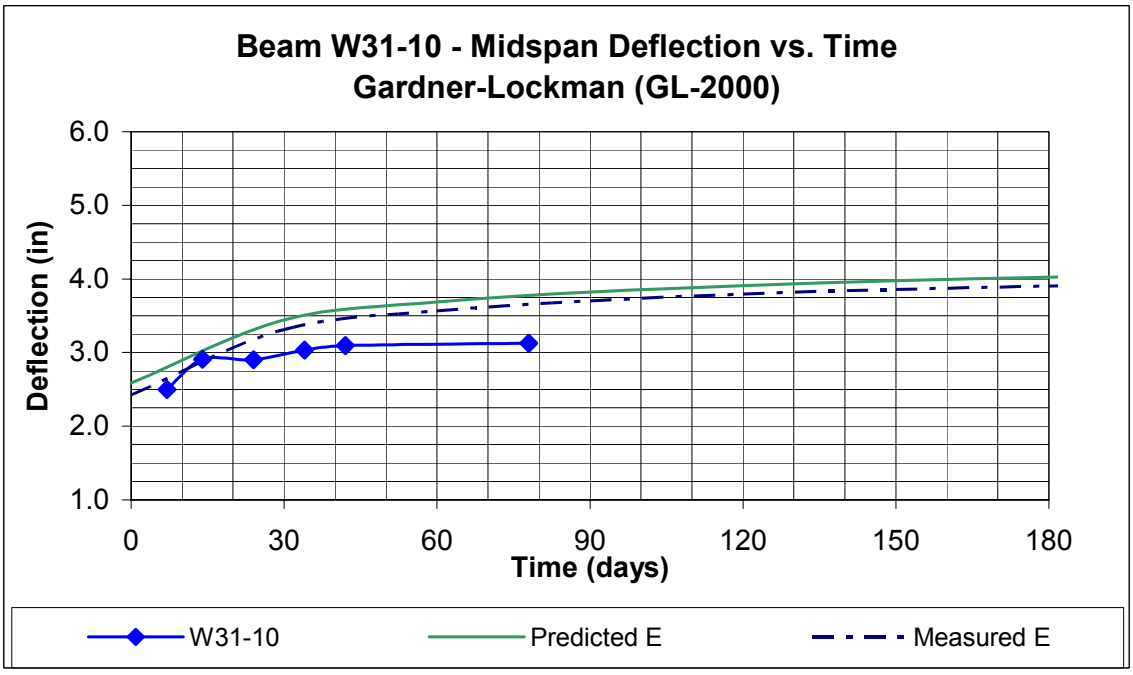

Figure B.164 Beam W31-10 GL-2000 Predicted Deflection vs. Time

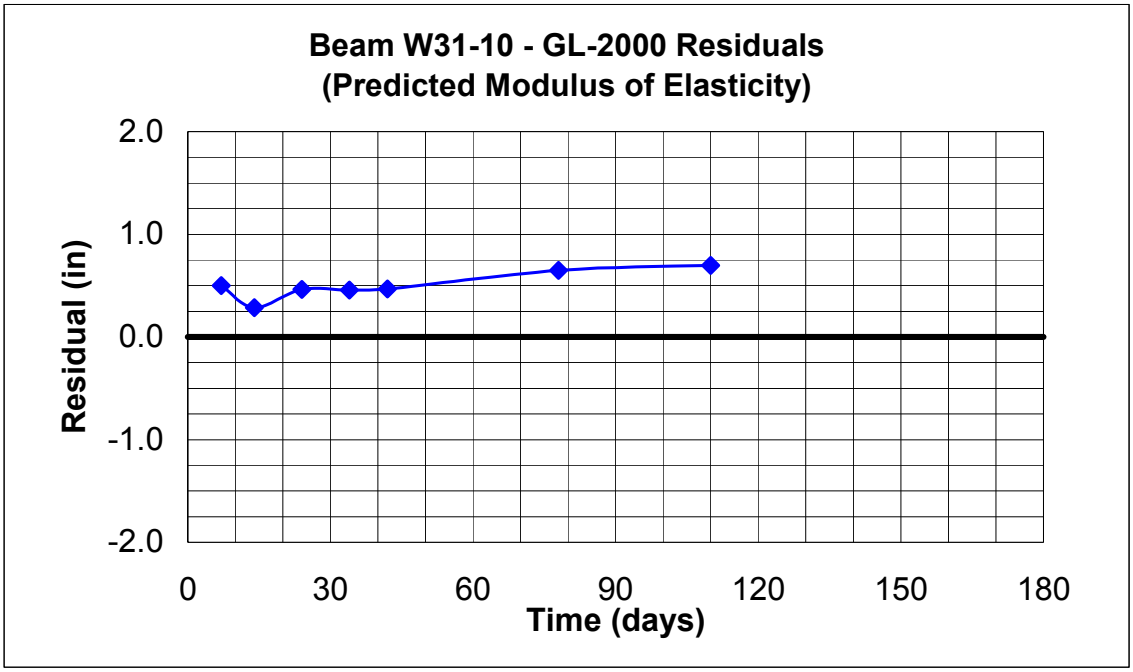

Figure B.165 Beam W31-10 GL-2000 Residuals (Predicted Modulus of Elasticity)

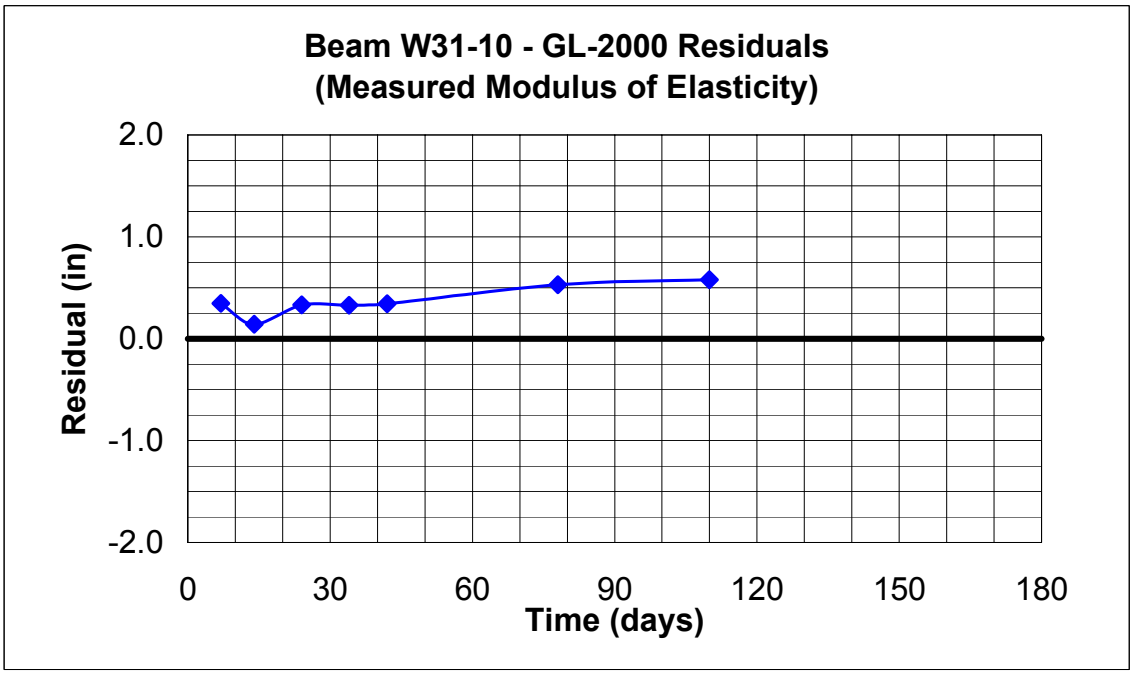

Figure B.166 Beam W31-10 GL-2000 Residuals (Measured Modulus of Elasticity)

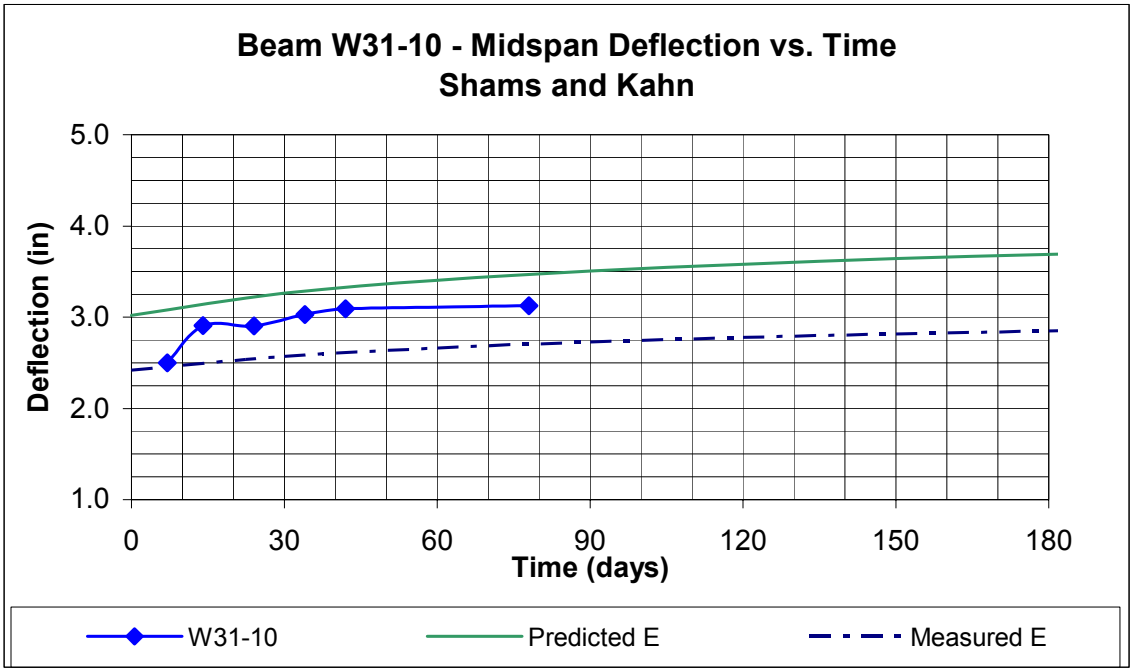

Figure B.167 Beam W31-10 Kahn & Shams Predicted Deflection vs. Time

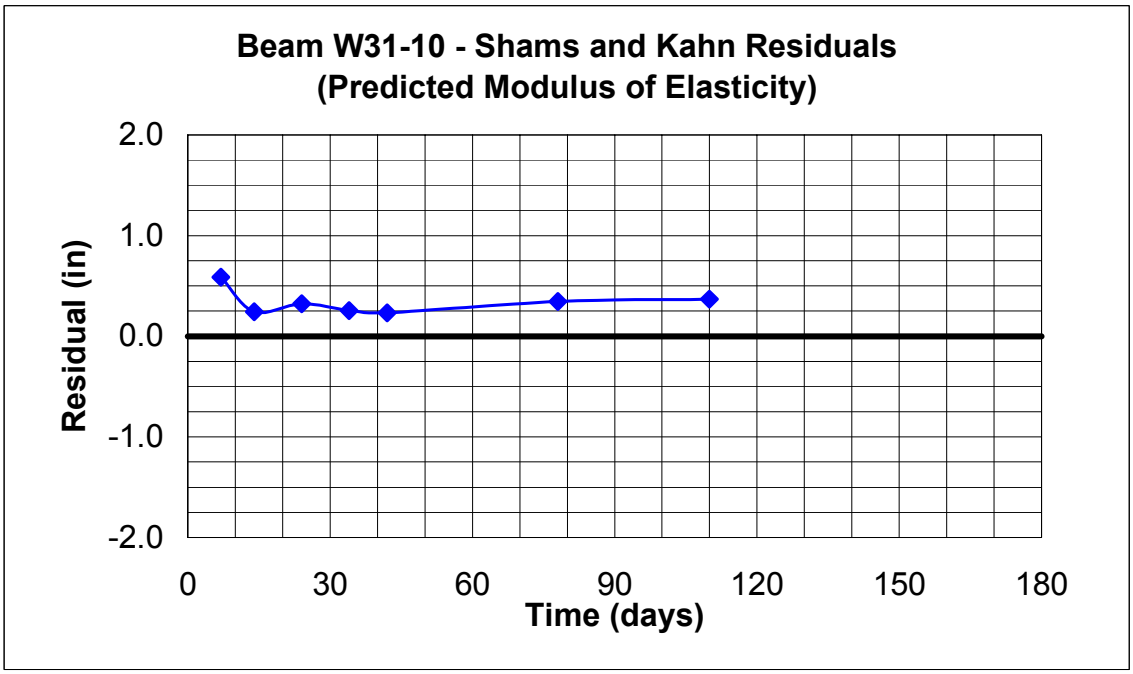

Figure B.168 Beam W31-10 Kahn & Shams Residuals (Predicted Modulus of Elasticity)

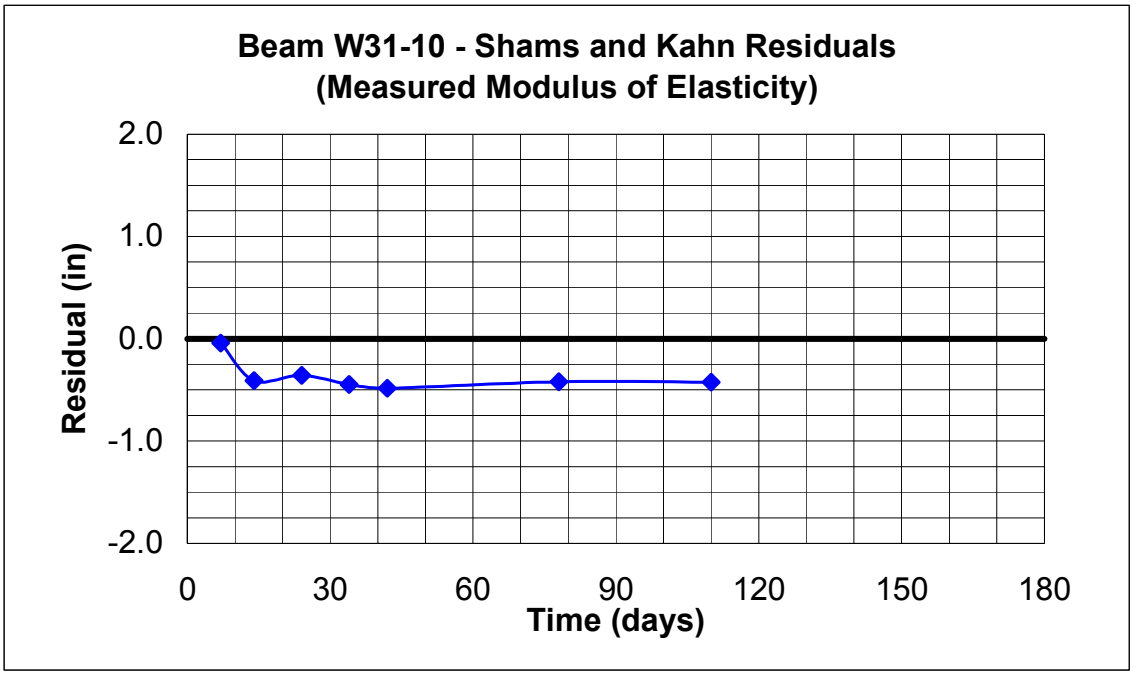

Figure B.169 Beam W31-10 Kahn & Shams Residuals (Measured Modulus of Elasticity)

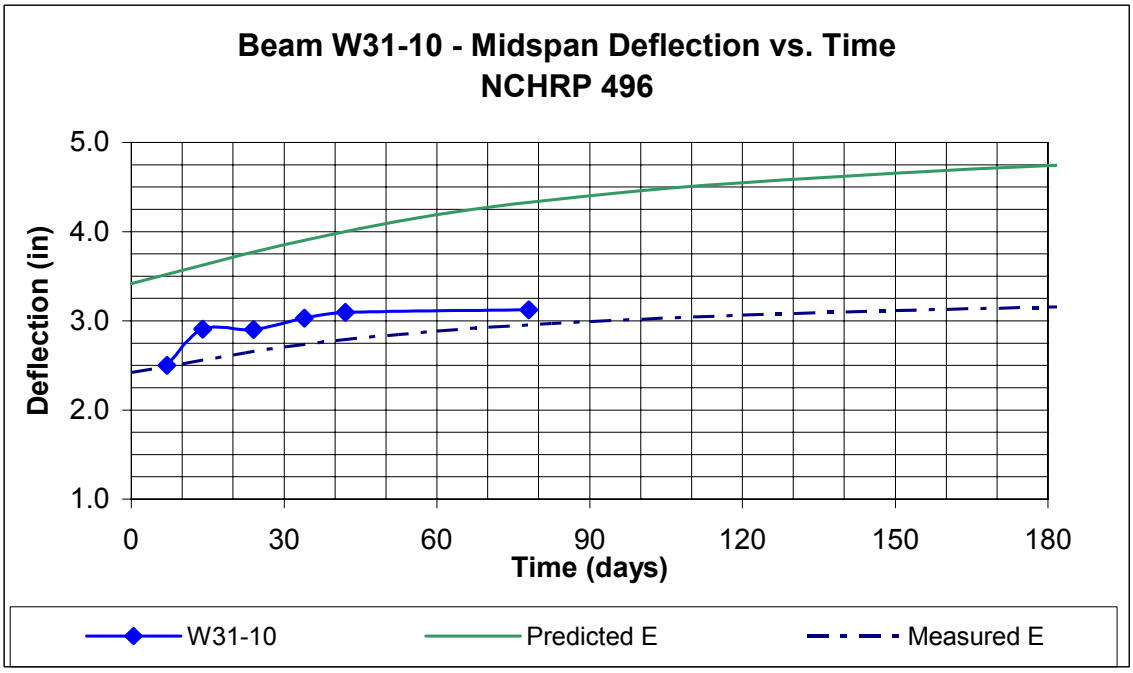

Figure B.170 Beam W31-10 NCHRP 496 Predicted Deflection vs. Time

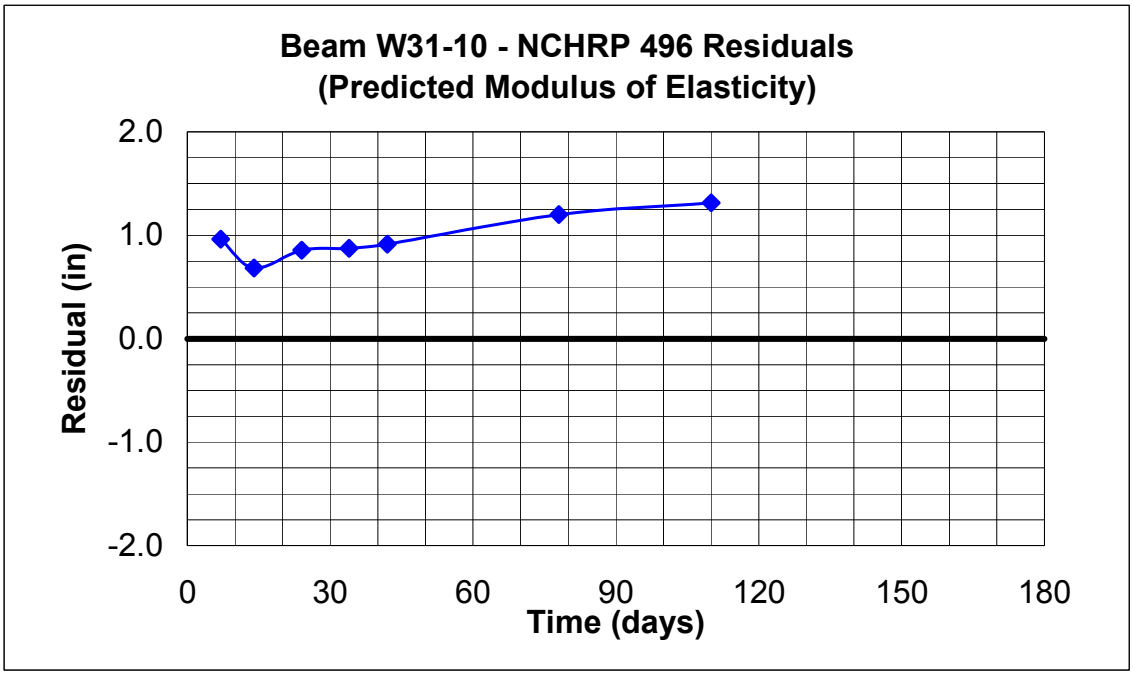

Figure B.171 Beam W31-10 NCHRP 496 Residuals (Predicted Modulus of Elasticity)

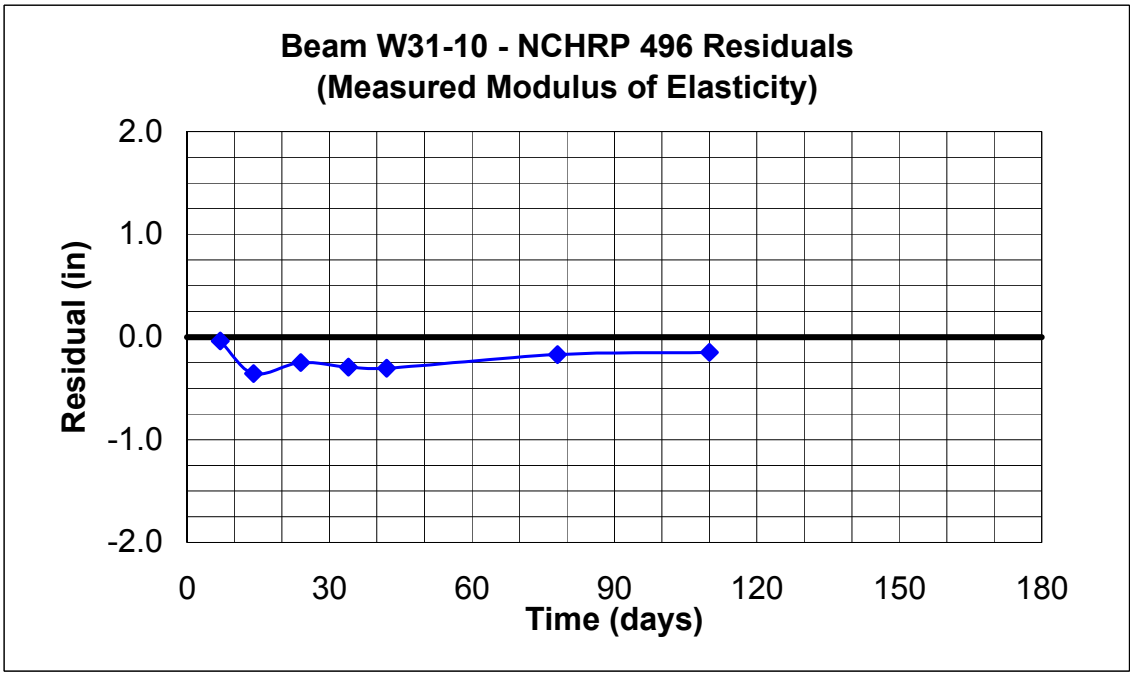

Figure B.172 Beam W31-10 NCHRP 496 Residuals (Measured Modulus of Elasticity)

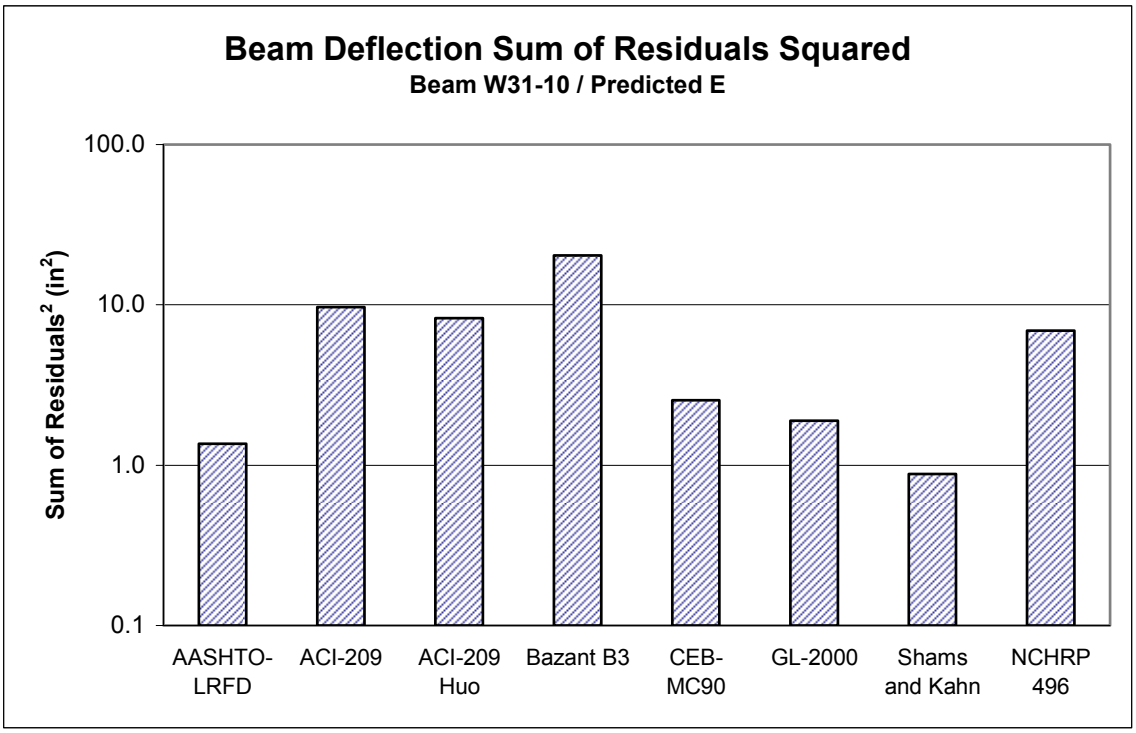

Figure B.173 Beam W31-10 Deflection Sum of Residuals Squared, Predicted E

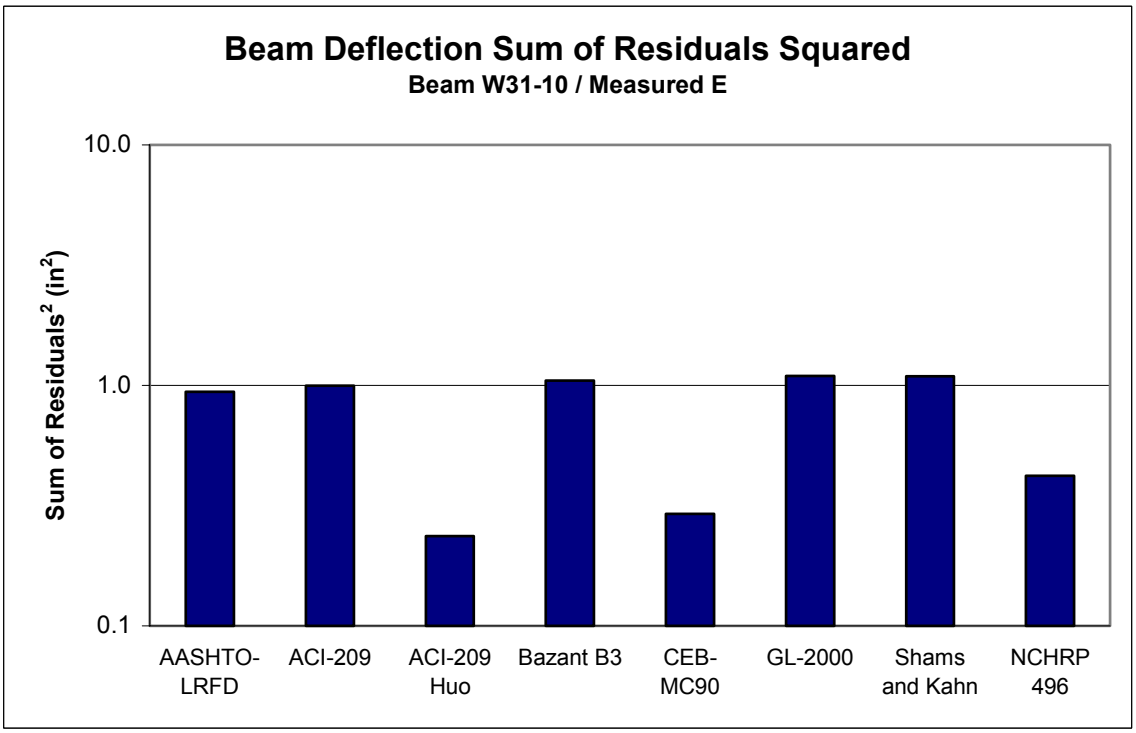

Figure B.174 Beam W31-10 Deflection Sum of Residuals Squared, Measured E

Table B.11 Beam W31-10 Model Ranking with Predicted E

Rank	Model
1	**AASHTO-LRFD**
2	Shams and Kahn
3	CEB-MC90
4	NCHRP 496
5	ACI-209
6	ACI-209, modified by Huo
7	GL-2000
8	Bazant B3

Table B.12 Beam W31-10 Model Ranking with Measured E

Rank	Model
1	**CEB-MC90**
2	NCHRP 496
3	ACI-209
4	ACI-209, modified by Huo
5	AASHTO-LRFD
6	Bazant B3
7	Shams and Kahn
8	GL-2000

B.7 Additional Beams W35-1, 2 & 3

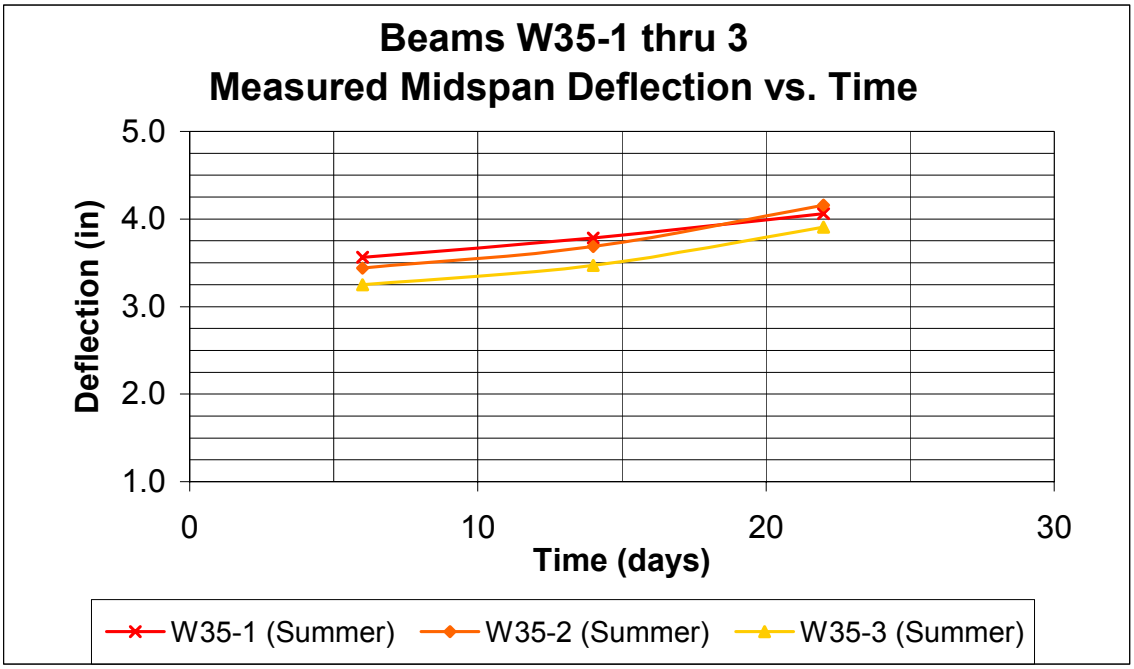

Figure B. 175 Beams W35-1 thru 3, Deflection vs. Time

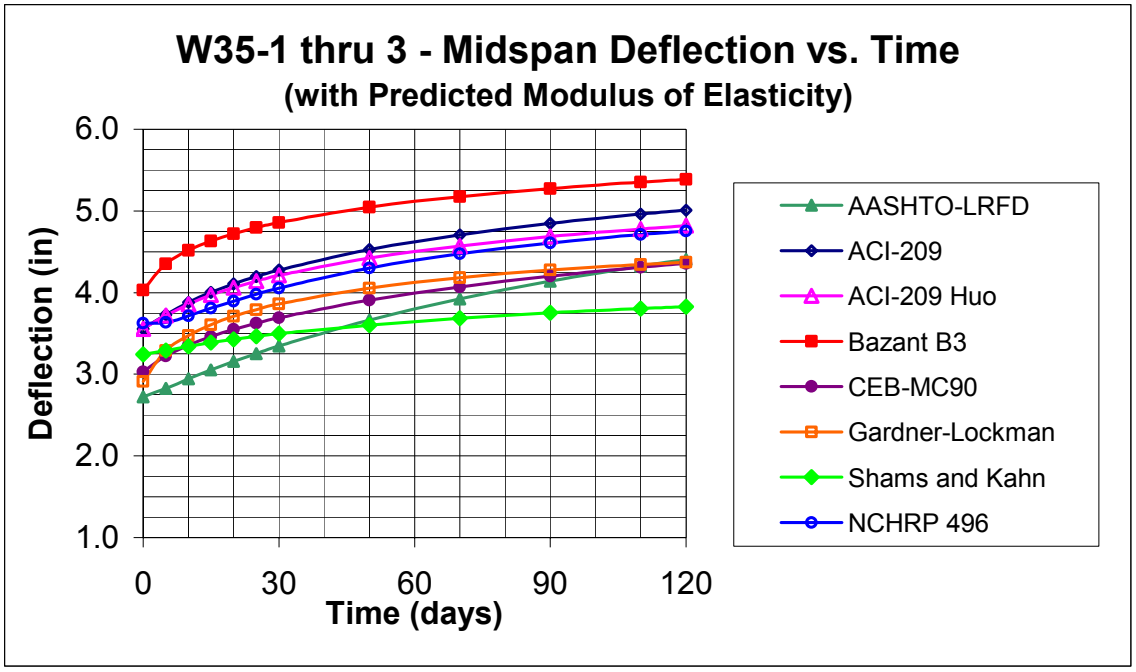

Figure B.176 Beams W35-1 thru 3, Predicted Deflection vs. Time (Predicted E)

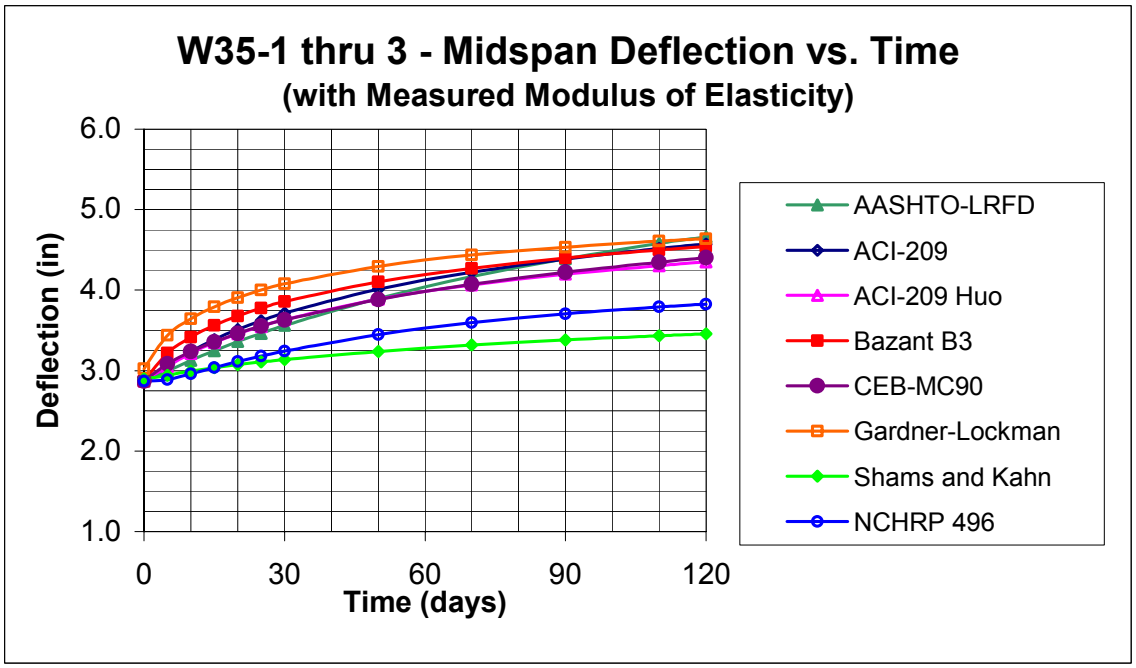

Figure B.177 Beams W35-1 thru 3, Predicted Deflection vs. Time (Measured E)

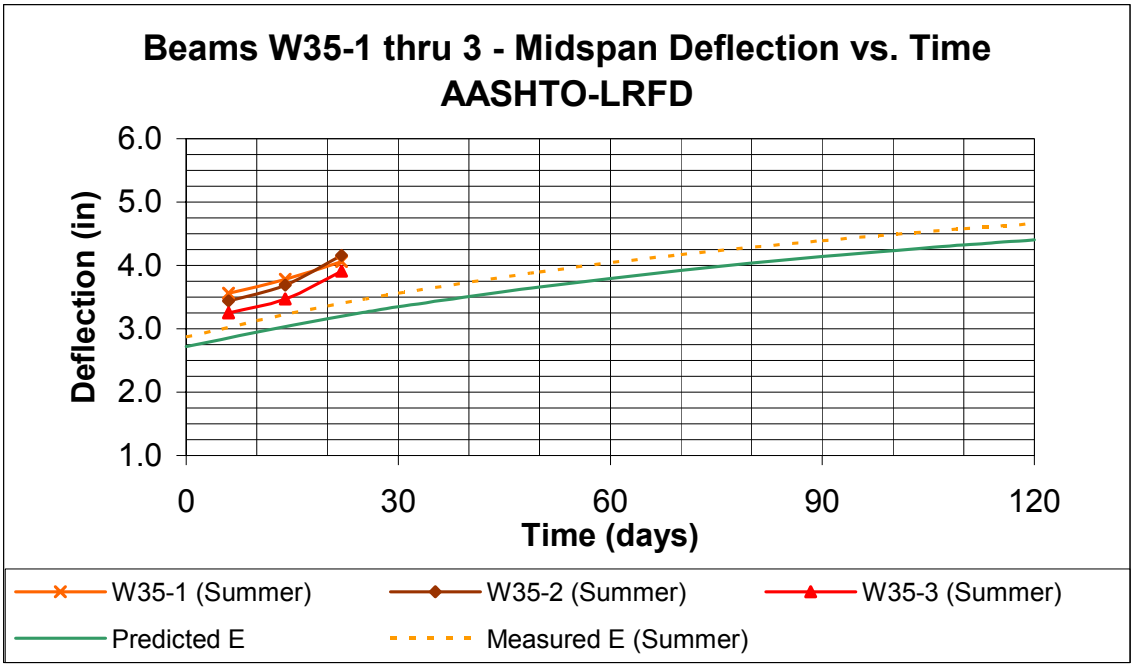

Figure B.178 Beams W35-1 thru 3 AASHTO-LRFD Predicted Deflection vs. Time

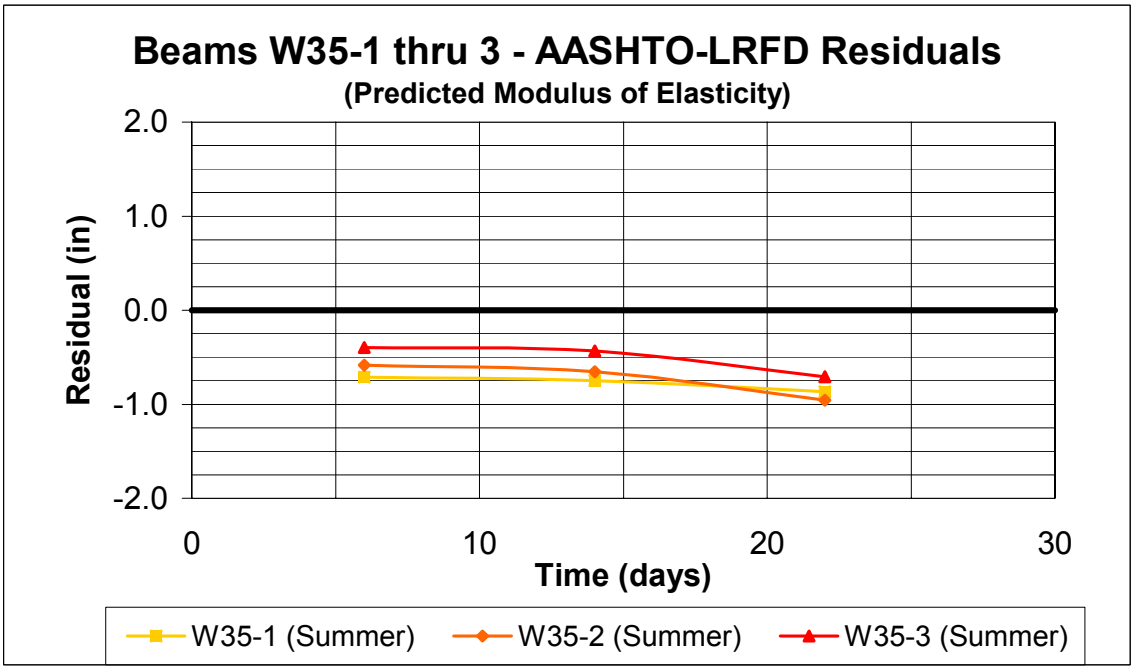

Figure B.179 Beams W35-1 thru 3 AASHTO-LRFD Residuals (Predicted Modulus of Elasticity)

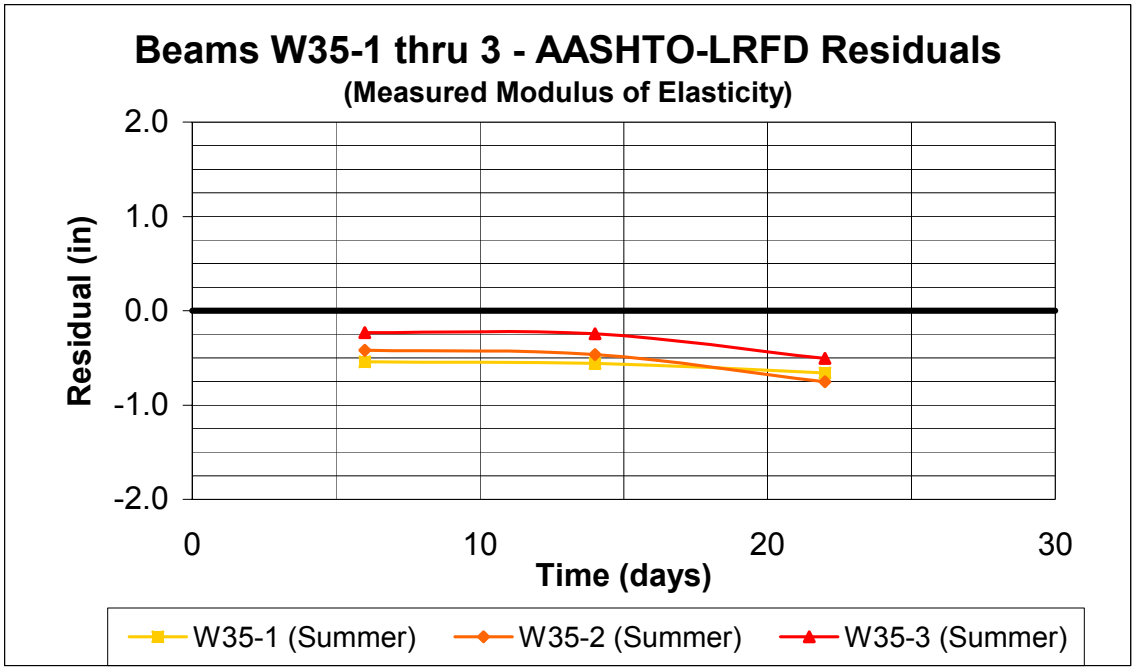

Figure B.180 Beams W35-1 thru 3 AASHTO-LRFD Residuals (Measured Modulus of Elasticity)

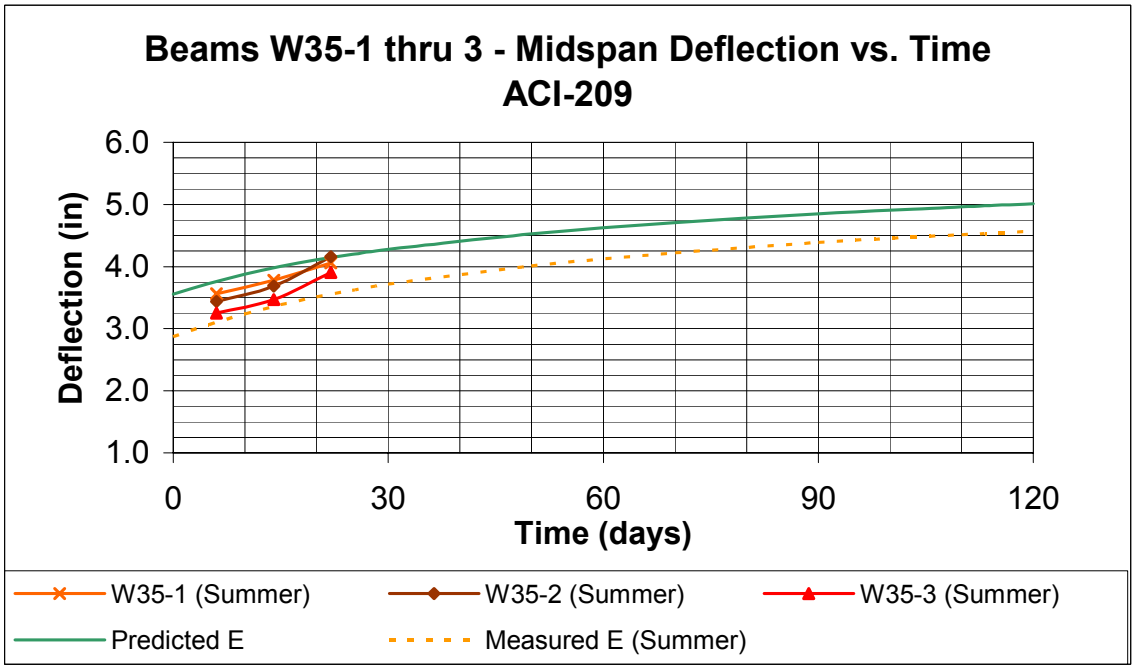

Figure B.181 Beams W35-1 thru 3 ACI-209 Predicted Deflection vs. Time

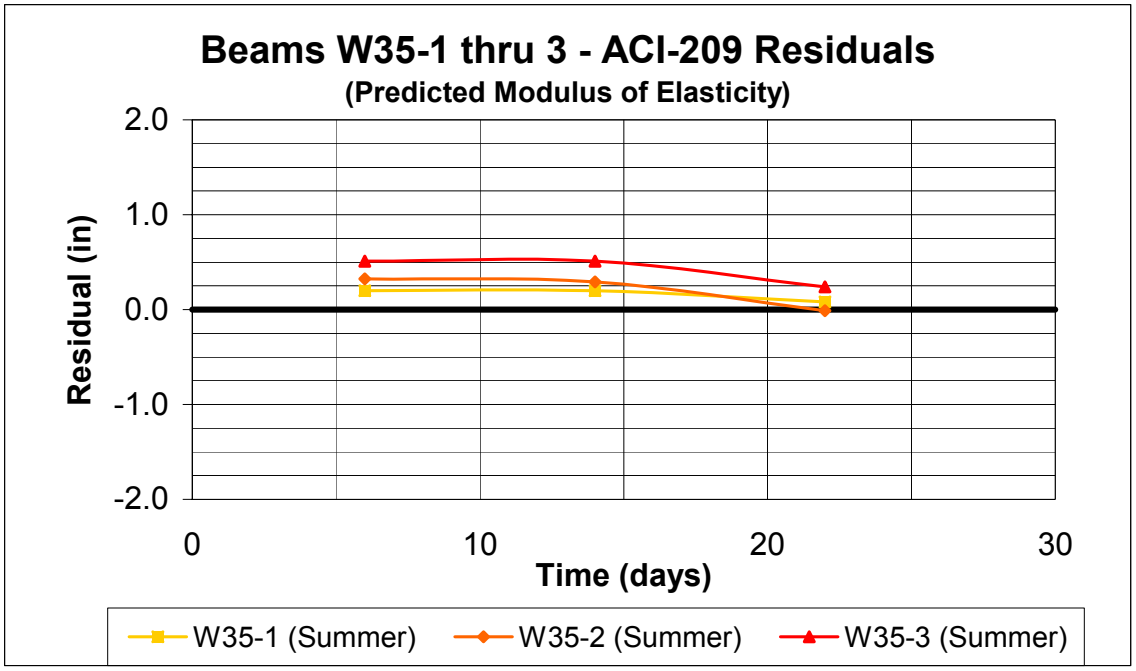

Figure B.182 Beams W35-1 thru 3 ACI-209 Residuals (Predicted Modulus of Elasticity)

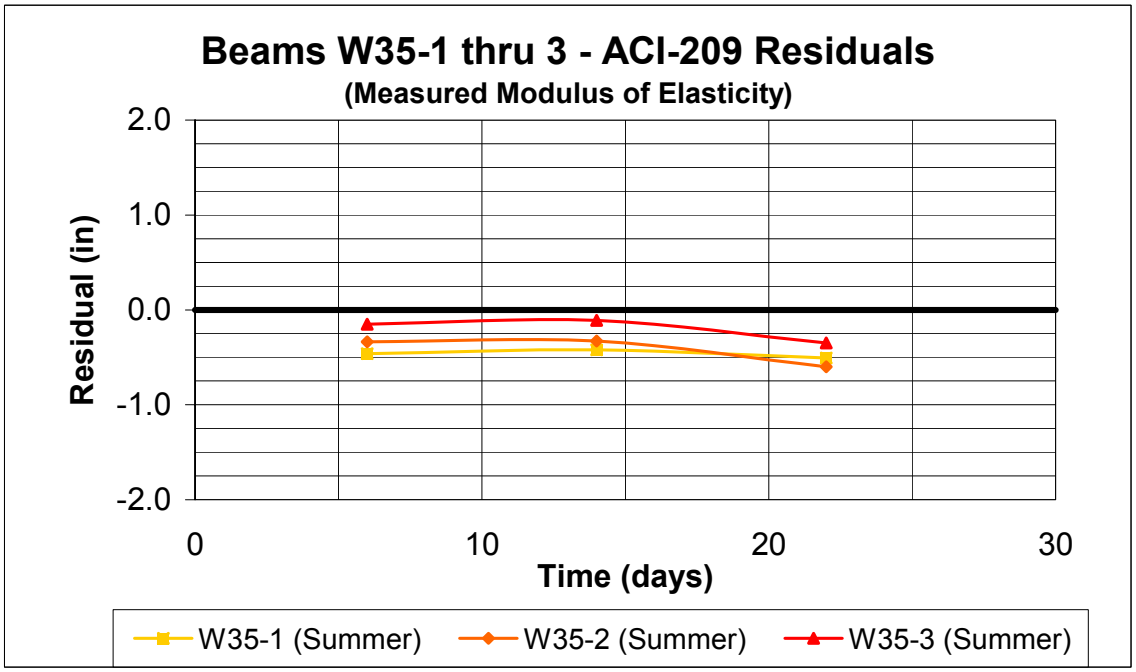

Figure B.183 Beams W35-1 thru 3 ACI-209 Residuals (Measured Modulus of Elasticity)

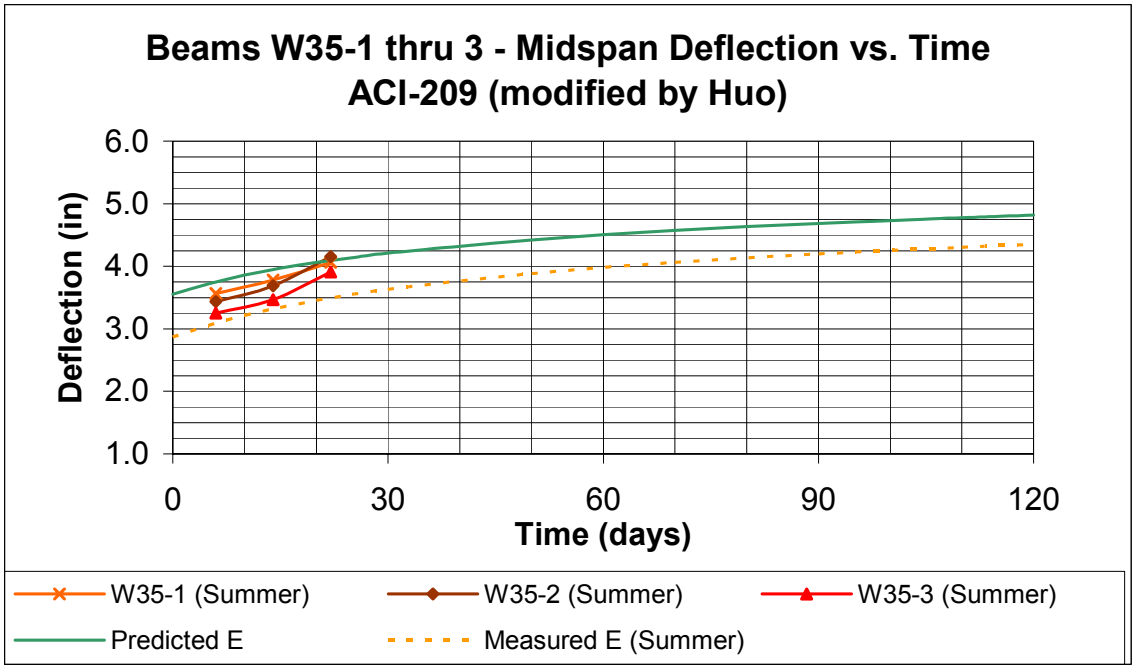

Figure B.184 Beams W35-1 thru 3 ACI-209 (Huo) Predicted Deflection vs. Time

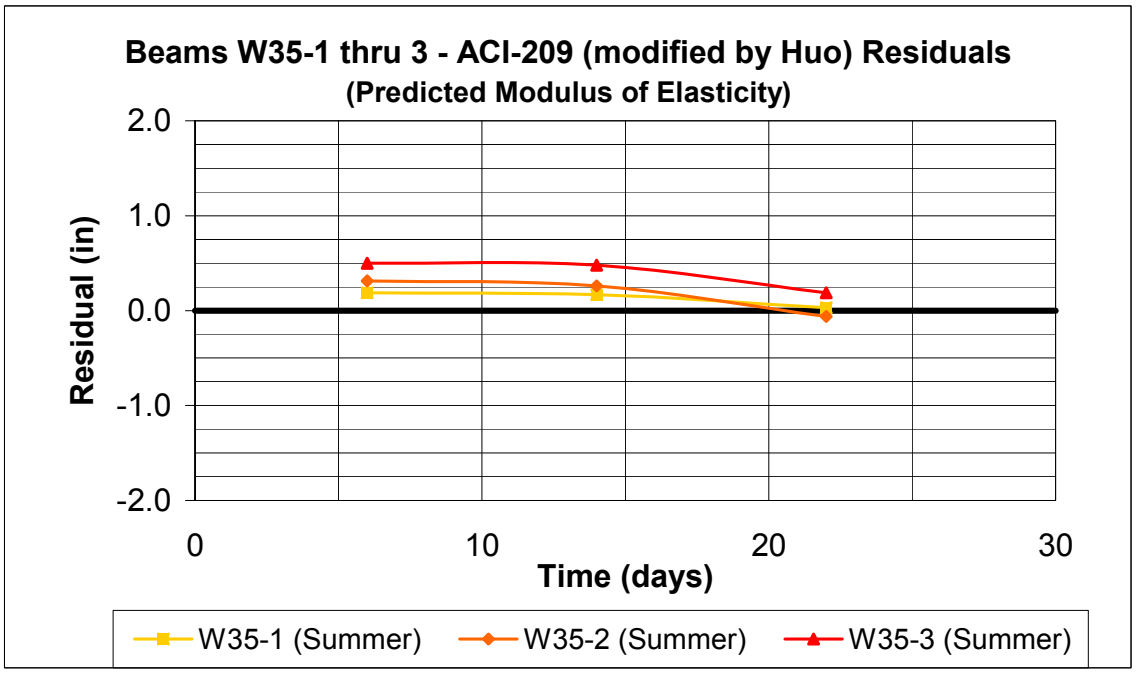

Figure B.185 Beams W35-1 thru 3 ACI-209 (Huo) Residuals (Predicted Modulus of Elasticity)

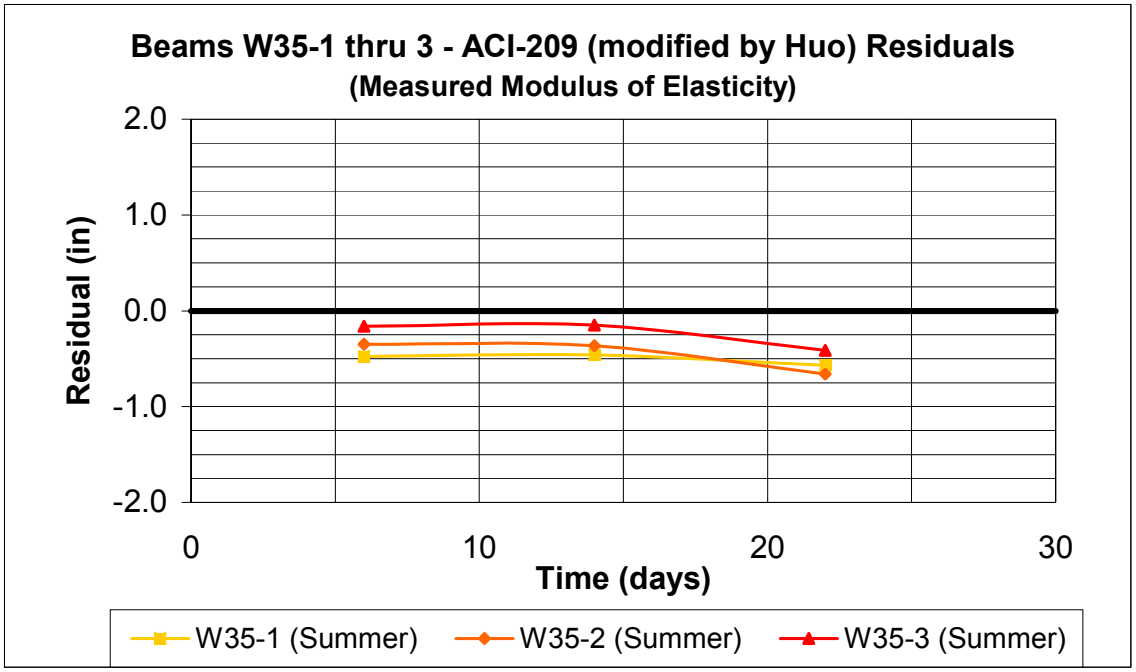

Figure B.186 Beams W35-1 thru 3 ACI-209 (Huo) Residuals (Measured Modulus of Elasticity)

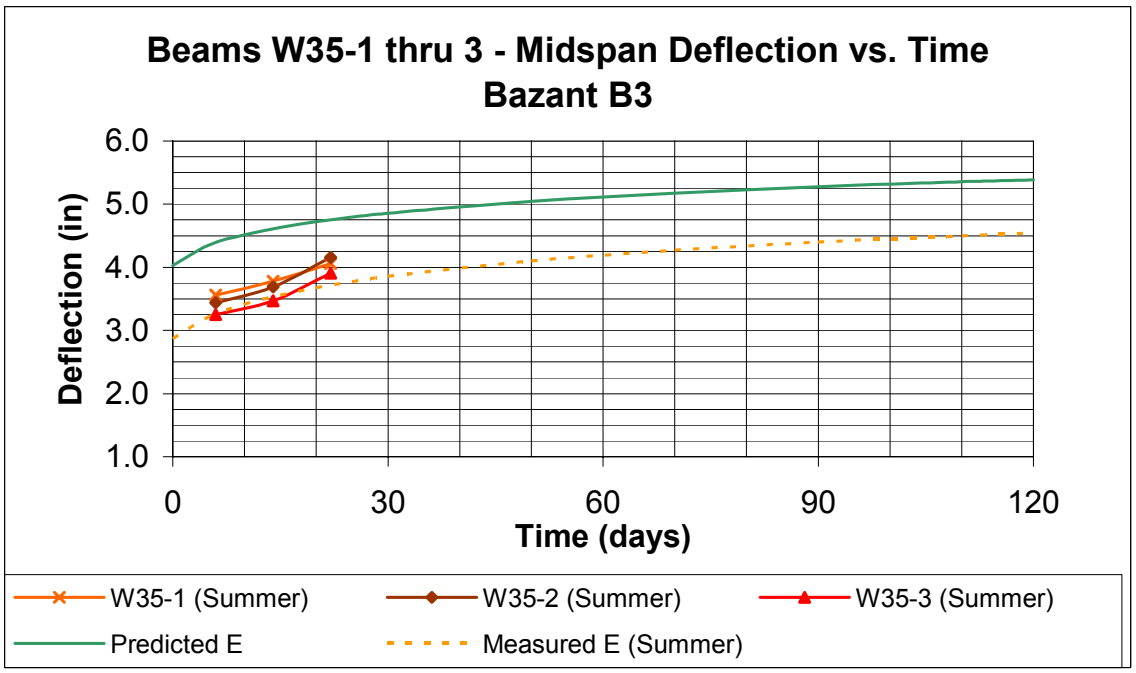

Figure B.187 Beams W35-1 thru 3 Bazant B3 Predicted Deflection vs. Time

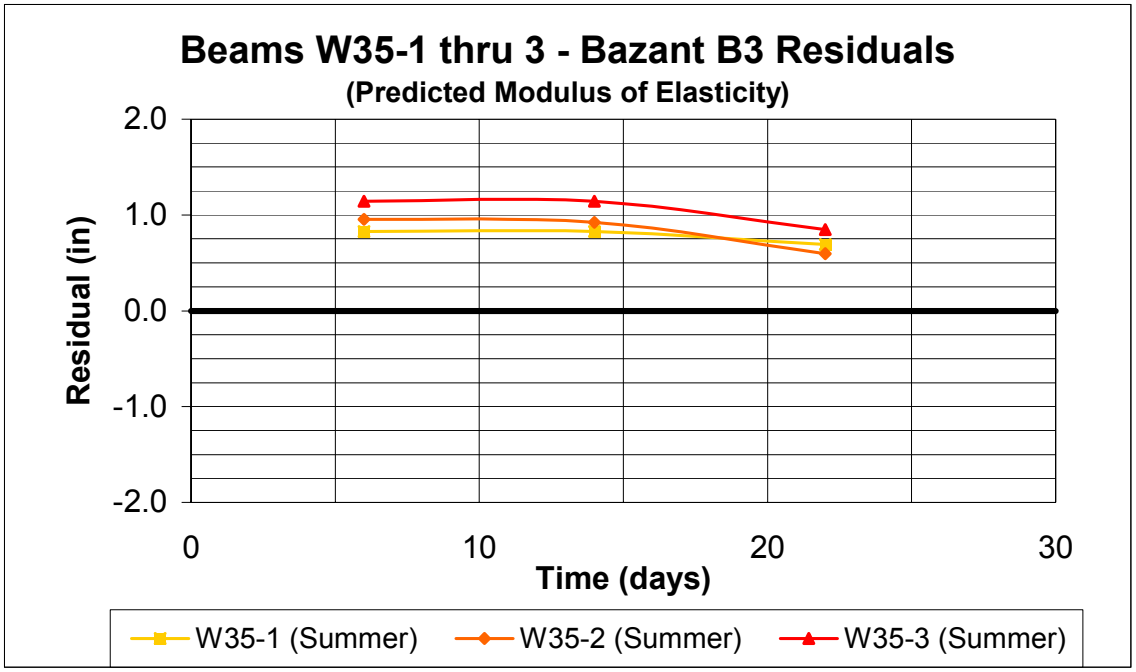

Figure B.188 Beams W35-1 thru 3 Bazant B3 Residuals (Predicted Modulus of Elasticity)

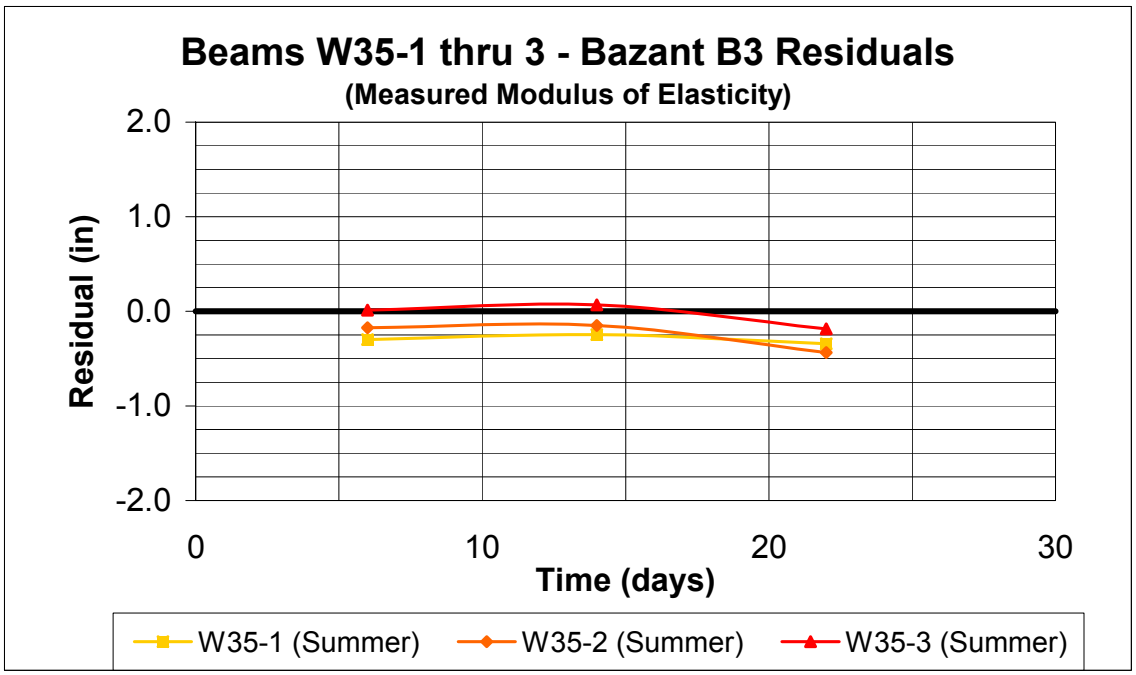

Figure B.189 Beams W35-1 thru 3 Bazant B3 Residuals (Measured Modulus of Elasticity)

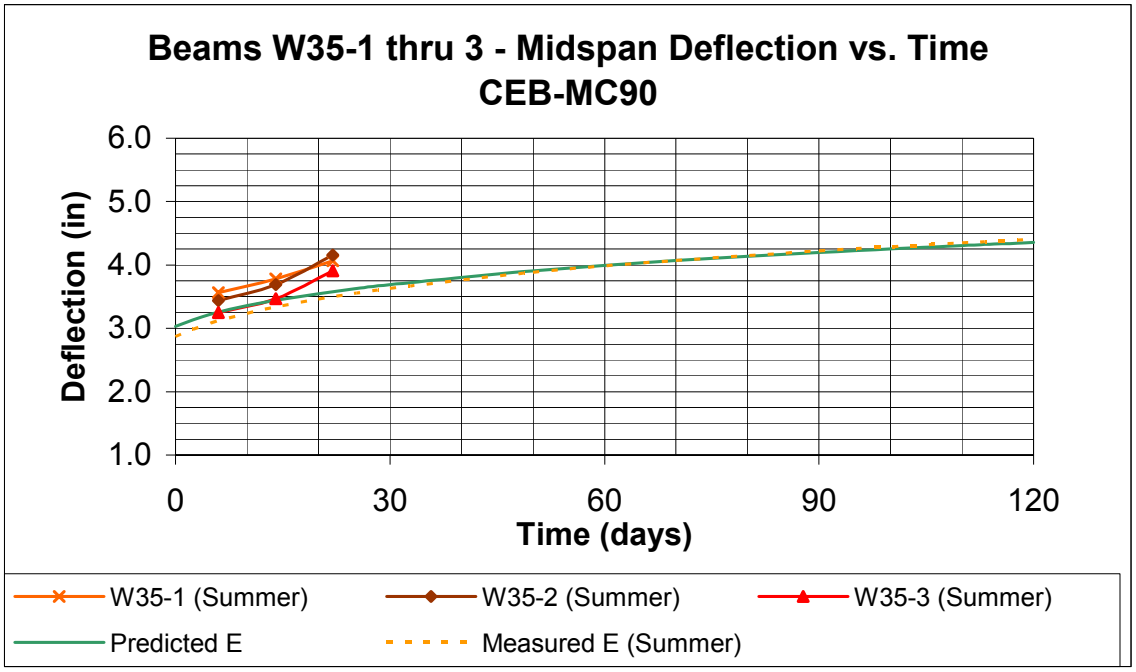

Figure B.190 Beams W35-1 thru 3 CEB-MC90 Predicted Deflection vs. Time

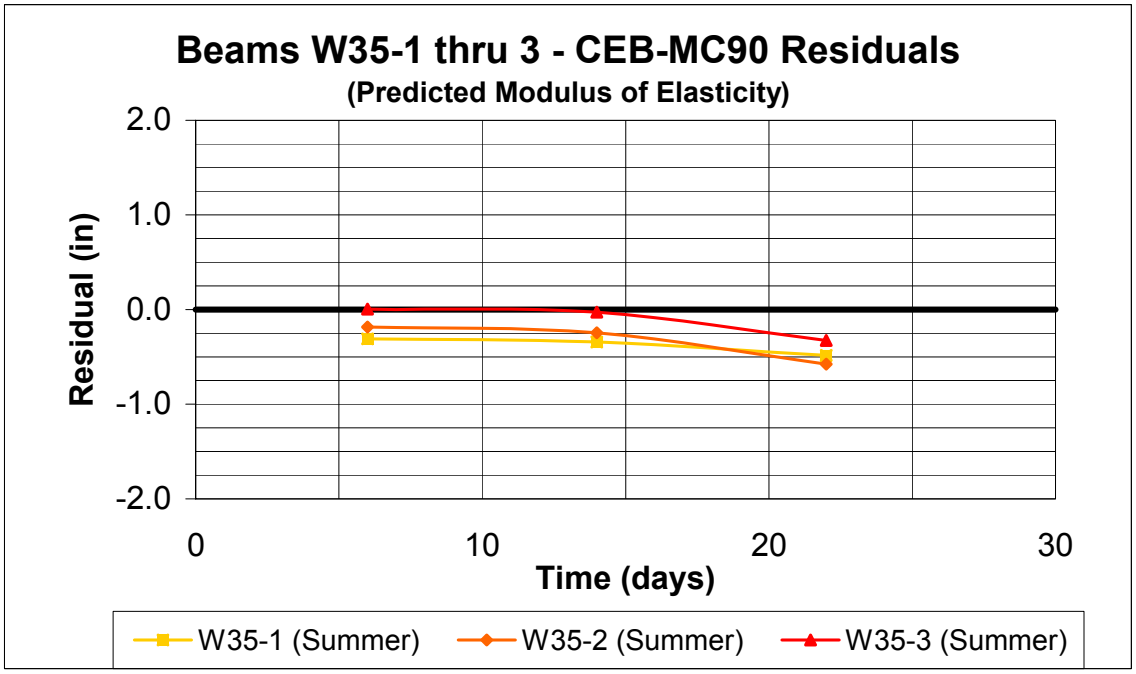

Figure B.191 Beams W35-1 thru 3 CEB-MC90 Residuals (Predicted Modulus of Elasticity)

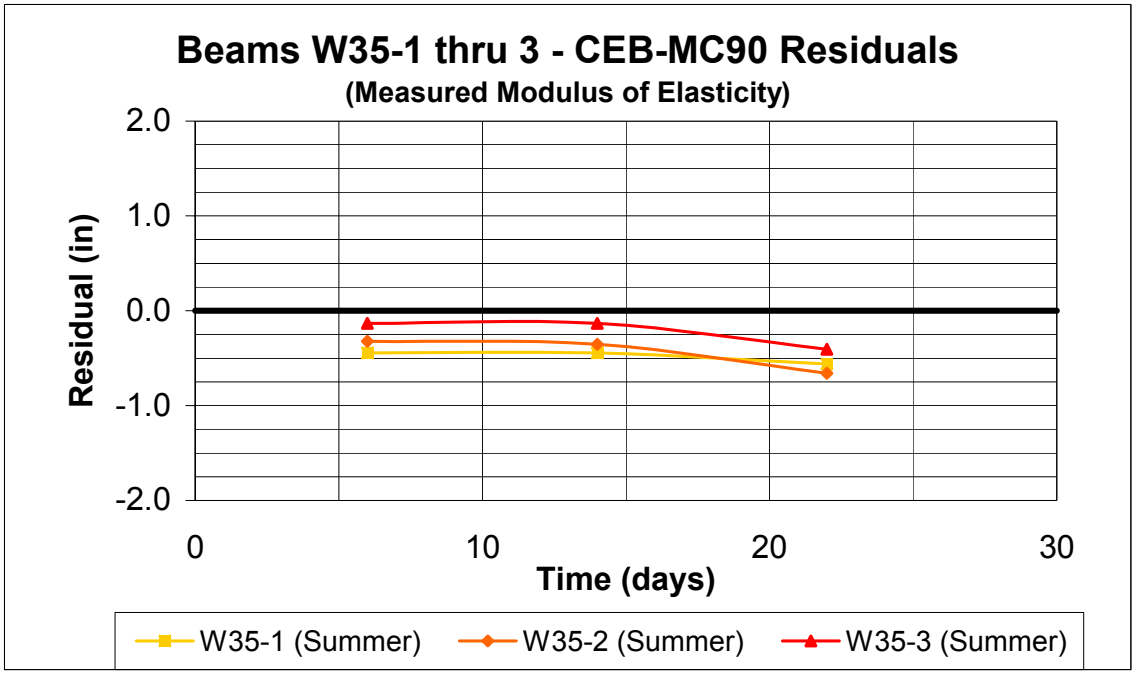

Figure B.192 Beams W35-1 thru 3 CEB-MC90 Residuals (Measured Modulus of Elasticity)

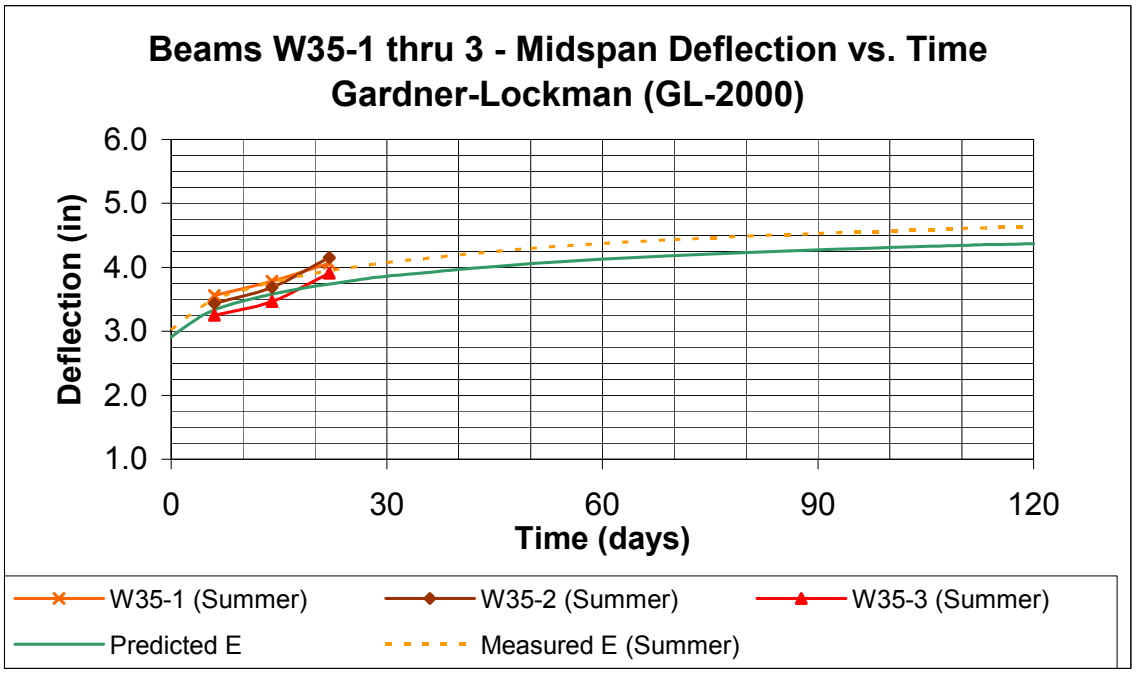

Figure B.193 Beams W35-1 thru 3 GL-2000 Predicted Deflection vs. Time

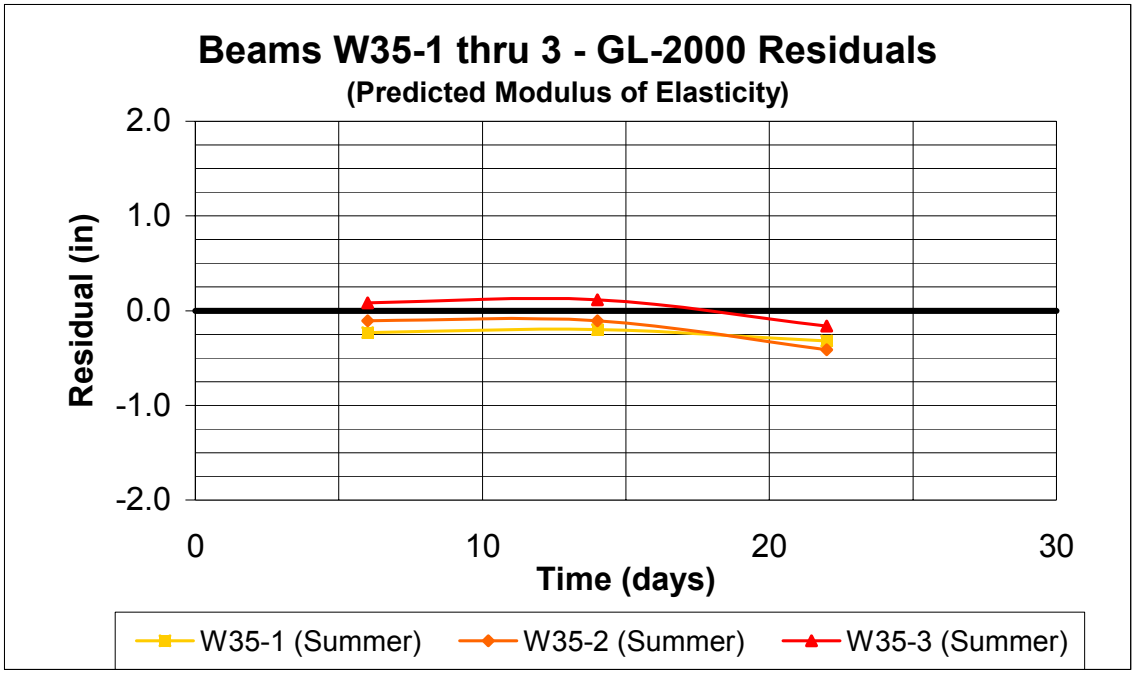

Figure B.194 Beams W35-1 thru 3 GL-2000 Residuals (Predicted Modulus of Elasticity)

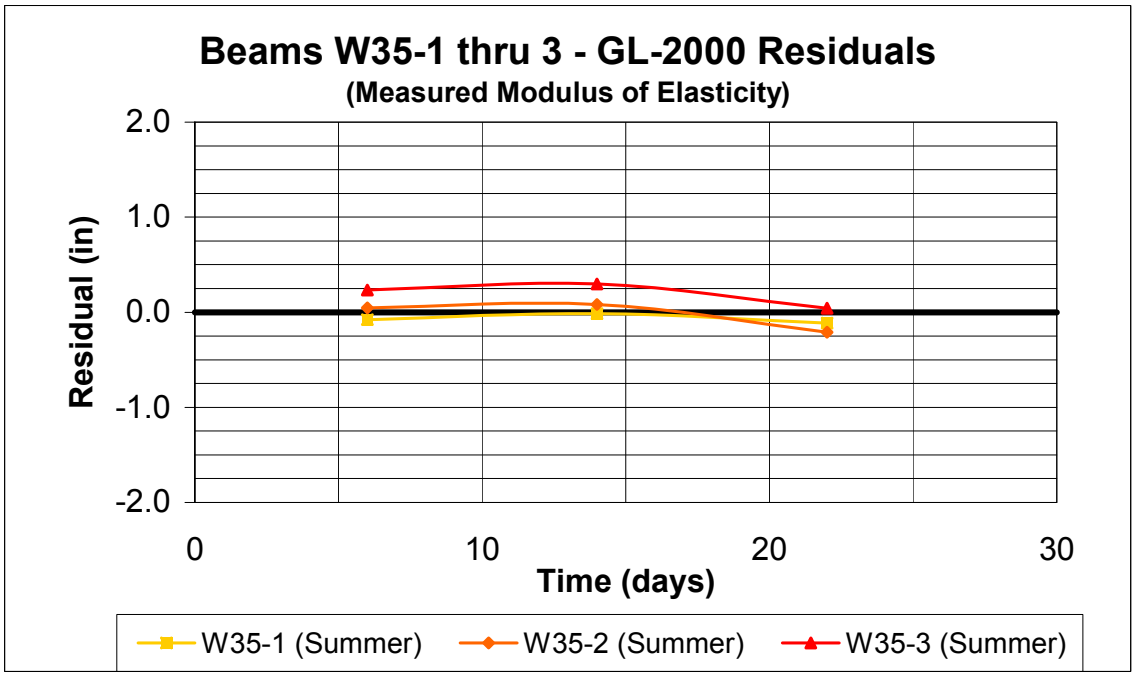

Figure B.195 Beams W35-1 thru 3 GL-2000 Residuals (Measured Modulus of Elasticity)

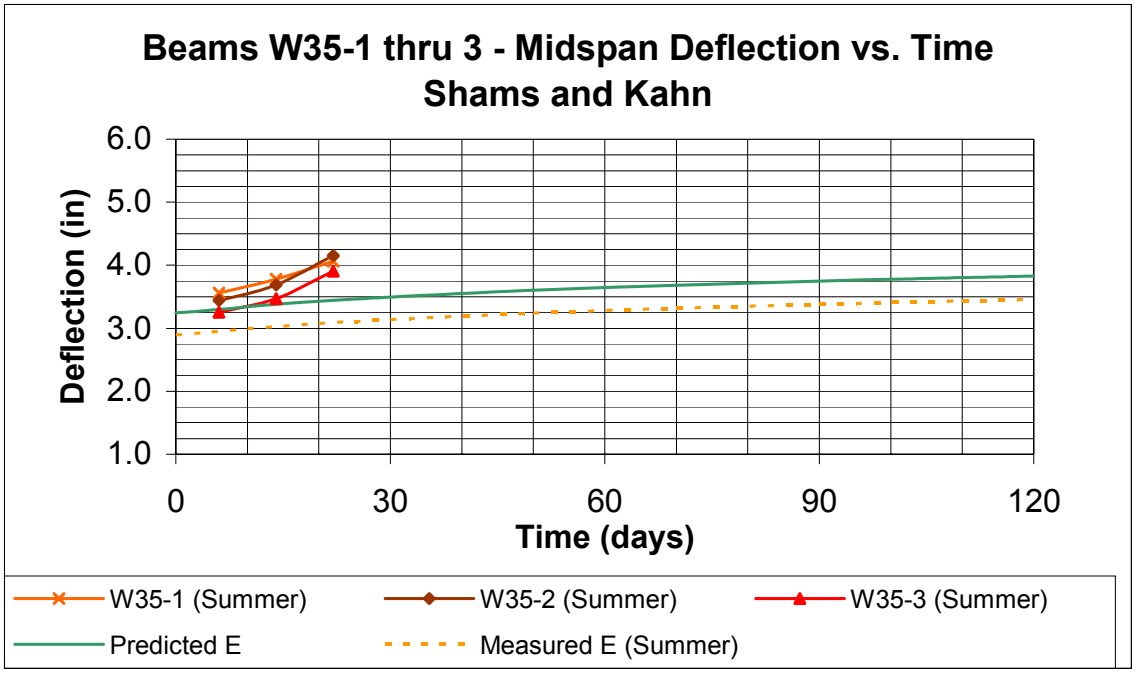

Figure B.196 Beams W35-1 thru 3 Shams and Kahn Predicted Deflection vs. Time

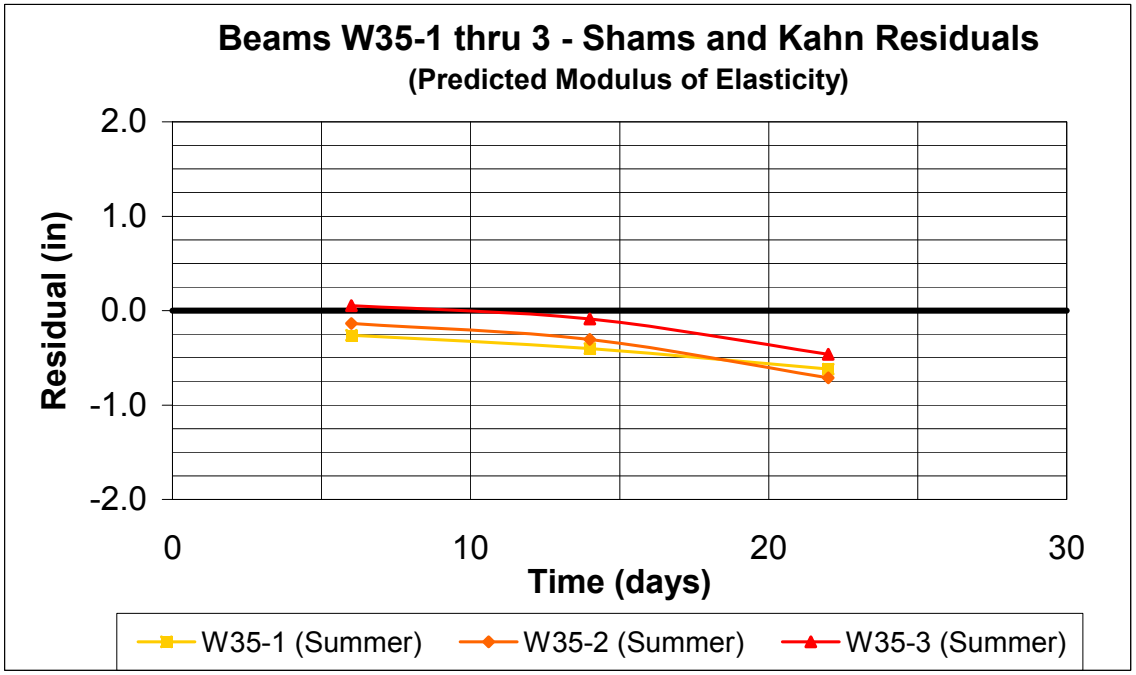

Figure B.197 Beams W35-1 thru 3 Shams and Kahn Residuals (Predicted Modulus of Elasticity)

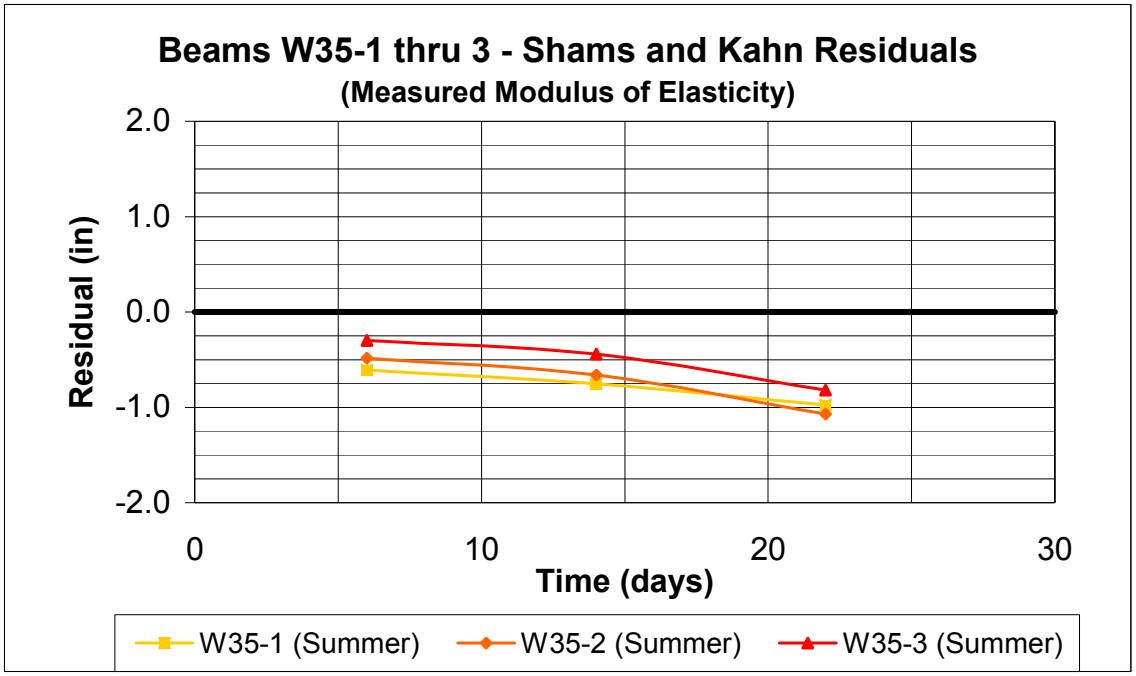

Figure B.198 Beams W35-1 thru 3 Shams and Kahn Residuals (Measured Modulus of Elasticity)

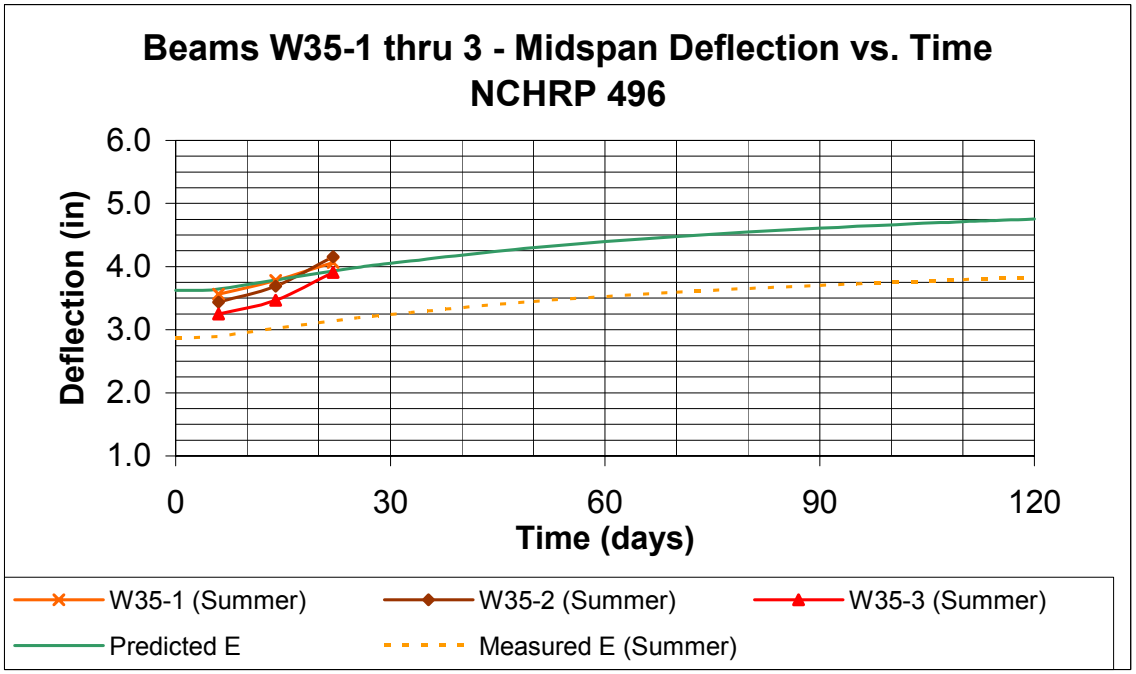

Figure B.199 Beams W35-1 thru 3 NCHRP 496 Predicted Deflection vs. Time

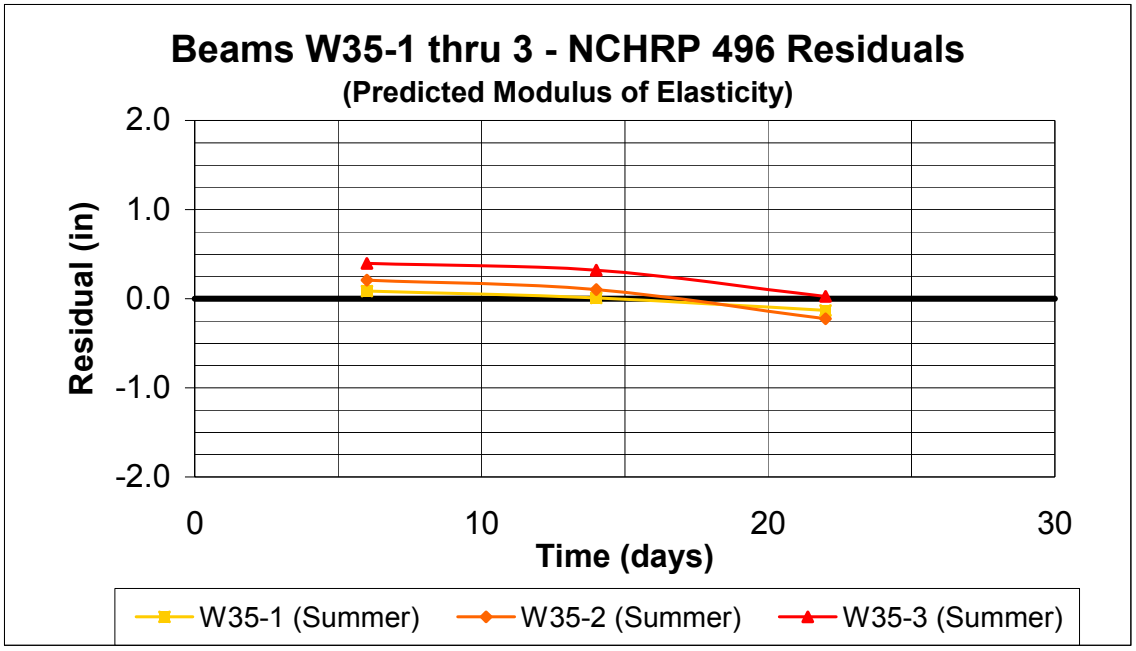

Figure B.200 Beams W35-1 thru 3 NCHRP 496 Residuals (Predicted Modulus of Elasticity)

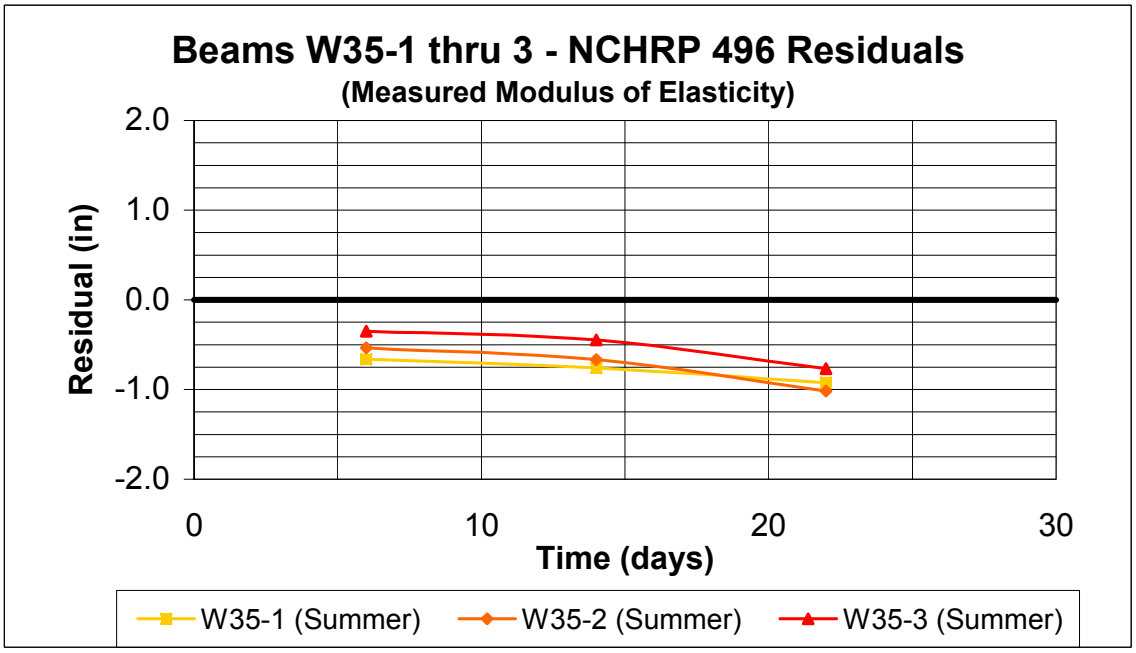

Figure B.201 Beams W35-1 thru 3 NCHRP 496 Residuals (Measured Modulus of Elasticity)

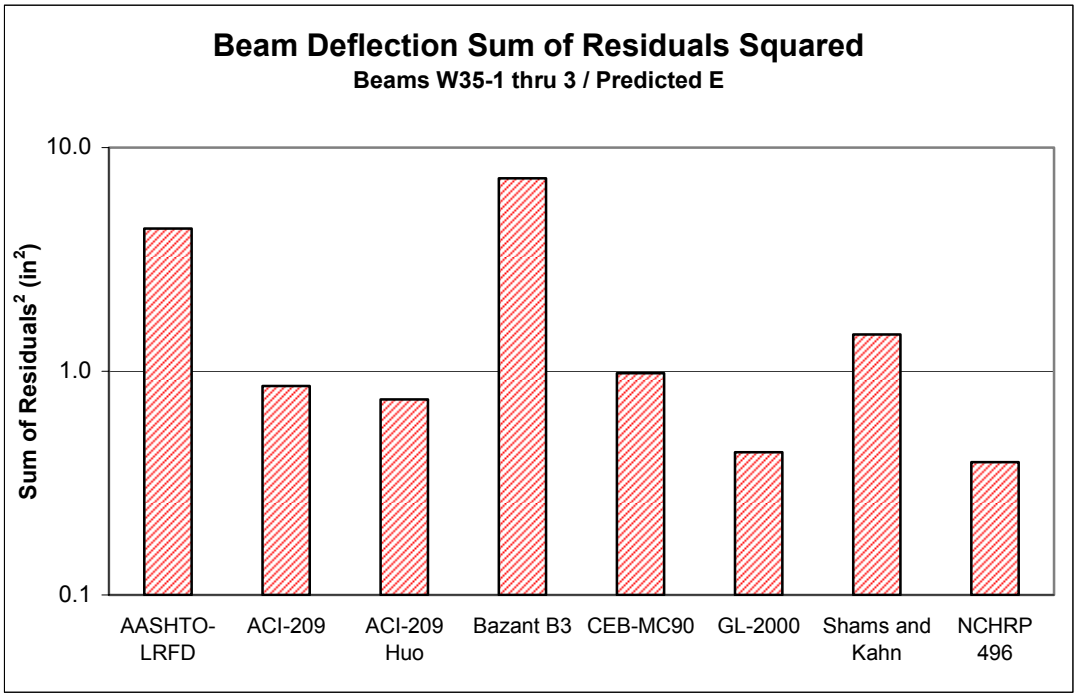

Figure B.202 Beams W35-1 thru 3 Deflection Sum of Residuals Squared, Predicted E

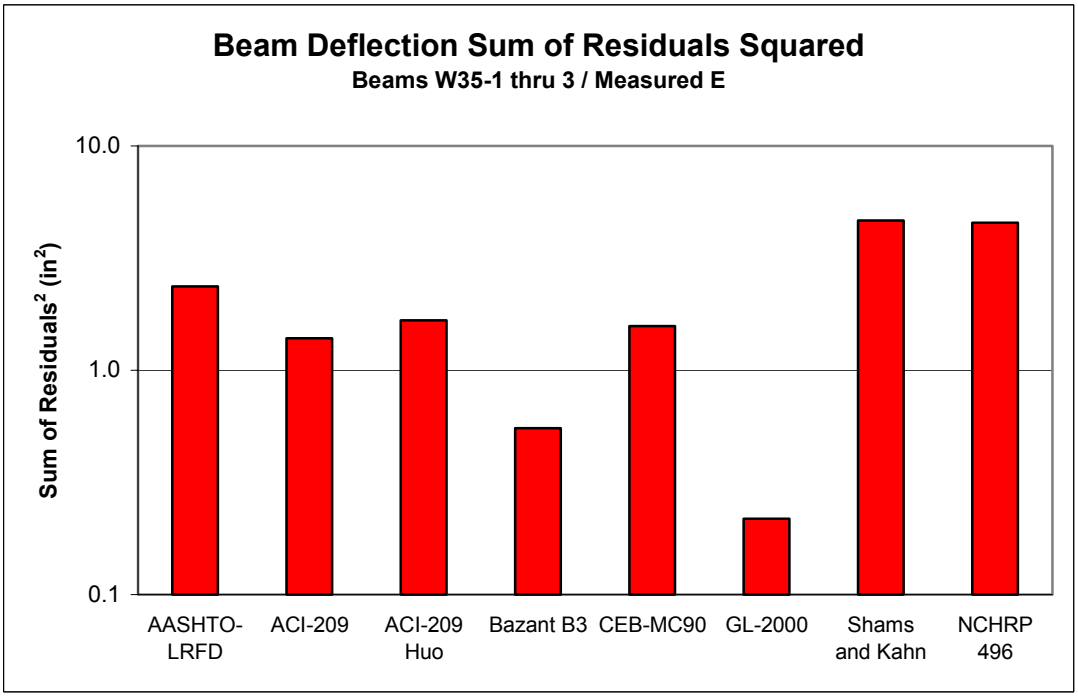

Figure B.203 Beams W35-1 thru 3 Deflection Sum of Residuals Squared, Measured E

Table B.13 Beams W35-1 thru 3 Model Ranking with Predicted E

Rank	Model
1	**NCHRP 496**
2	GL-2000
3	ACI-209, modified by Huo
4	ACI-209
5	CEB-MC90
6	Shams and Kahn
7	AASHTO-LRFD
8	Bazant B3

Table B.14 Beams W35-1 thru 3 Model Ranking with Measured E

Rank	Model
1	**GL-2000**
2	Bazant B3
3	ACI-209
4	CEB-MC90
5	ACI-209, modified by Huo
6	AASHTO-LRFD
7	NCHRP 496
8	Shams and Kahn

VITA

Stephen Dock Hinkle was born in Summersville, West Virginia in 1973. He spent the first eighteen years of his life there and graduated from Nicholas County High School in 1992. He began his Civil Engineering studies at West Virginia University (WVU) in the Fall of 1992. During his undergraduate years, he interned at the NASA Marshall Space Flight Center in Huntsville, Alabama and the West Virginia Division of Highways in Charleston, West Virginia. He graduated from West Virginia University in 1997 magna cum laude with a B.A. in Communication Studies, and a B.S in Civil Engineering. He was accepted to Virginia Polytechnic Institute and State University and was selected as a Via Scholar. Upon being unable to proceed with his initial thesis topic, he left Virginia Polytechnic Institute and State University and accepted a position as a bridge engineer with Parsons Brinckerhoff in Atlanta, GA. The continued goal of completing his Master's Degree led him to contact Dr. Carin Roberts-Wollmann, at Virginia Polytechnic Institute and State University, who allowed him the opportunity to begin a new thesis topic in the area of camber growth in prestressed concrete bridge beams. This work represents the fruition of that effort.